Edited by Reiner Salzer
and Heinz W. Siesler

WILEY-VCH

Infrared and Raman Spectroscopic Imaging

**Infrared and Raman
Spectroscopic Imaging**

Edited by
Reiner Salzer and Heinz W. Siesler

Further Reading

Diem, M., Griffiths, P. R., Chalmers, J. M. (eds.)
Vibrational Spectroscopy for Medical Diagnosis

2008
Hardcover
ISBN: 978-0-470-01214-7

Lasch, P., Kneipp, J. (eds.)
Biomedical Vibrational Spectroscopy

2008
Hardcover
ISBN: 978-0-470-22945-3

Sasic, S.
Pharmaceutical Applications of Raman Spectroscopy

2007
Hardcover
ISBN: 978-0-8138-1013-3

Siebert, F., Hildebrandt, P.
Vibrational Spectroscopy in Life Science

2007
Hardcover
ISBN: 978-3-527-40506-0

Ozaki, Y., McClure, W. F., Christy, A. A. (eds.)
Near-Infrared Spectroscopy in Food Science and Technology

2006
Hardcover
ISBN: 978-0-471-67201-2

Infrared and Raman Spectroscopic Imaging

Edited by
Reiner Salzer and Heinz W. Siesler

The Editors

Prof. Dr. Reiner Salzer
Technische Universität Dresden
Bioanalytische Chemie
01062 Dresden

Prof. H. W. Siesler
Inst. f. Physikalische Chemie
Universität Duisburg Essen
Schützenbahn 70
45127 Essen

Contents

4   Vibrational Spectroscopic Imaging of Hard Tissues   *149*

Michael D. Morris, Matthew V. Schulmerich, Kathryn A. Dooley, and Karen A. Esmonde-White

5   Infrared and Raman Spectroscopy and Spectral Imaging of Individual Cells   *173*

Max Diem, Christian Matthäus, Tatyana Chernenko, Melissa J. Romeo, Miloš Miljković, Benjamin Bird, Jennifer Schubert, Kostas Papamarkakis, and Nora Laver

Part Four   Polymers and Pharmaceuticals

Preface

The breakthrough of Raman, mid-infrared and near-infrared spectroscopy as practical imaging tools with rational measurement and evaluation times has only taken place in recent years, although Raman and infrared spectroscopy are well-established analytical techniques for research, quality assurance and process control since many decades. The driving force behind this technology jump was on the one hand the increasing demand for imaging techniques with high chemical selectivity and specificity and on the other hand the commercial availability of suitable high-performance multi-channel detectors and the development of efficient evaluation and representation software. Thus, today not only the frequently asked questions about the qualitative and quantitative composition of a sample ('what' and 'how much') can be answered, but imaging investigations now also provide information as to 'where' different chemical species are located and how they are distributed among a heterogeneous sample. This book is devoted to illustrate the new insights which can be achieved and the multiplicity of applications which can be tackled in a variety of fields with this new technology.

Basically, the book can be subdivided into three parts. In the first part the fundamentals of the instrumentation for infrared and Raman imaging and mapping and an overview on the chemometric tools for image analysis are covered in two introductory chapters. The second part comprises the chapters 3–9 and describes a wide variety of applications ranging from biomedical via food and agriculture to polymers and pharmaceuticals. Some historical insights are given as well. In the third part the chapters 10–15 cover special methodical developments and their utility in specific fields.

We would like to thank all authors for their efforts and commitments to the timely publication of this volume being completely aware that writing a chapter for a book is an activity that is taken on in addition to one's daily work. We would also like to acknowledge the superb job and support by WILEY-VCH in the final composition and edition of the book. Our greatest debt of gratitude goes to our wives for their patience and encouragement.

Dresden and Essen, January 2009 _Reiner Salzer and Heinz W. Siesler_

List of Contributors

Keith R. Bambery
Monash University
Centre for Biospectroscopy and
School of Chemistry
3800 Victoria
Australia

Véronique Bellon-Maurel
UMR Cemagref–Montpellier
Supagro
'Information and Technologies
for AgroProcesses'
BP 50 95
34033 Montpellier Cedex 1
France

Benjamin Bird
Northeastern University
Department of Chemistry and
Chemical Biology
Boston
MA 02115
USA

K. L. Andrew Chan
Department of Chemical
Engineering
Imperial College London
London SW7 2AZ
United Kingdom

Tatyana Chernenko
Northeastern University
Department of Chemistry and
Chemical Biology
Boston
MA 02115
USA

Timothy C. Cox
University of Washington
Division of Craniofacial Medicine
Department of Pediatrics and
Oral Biology
98195-6320 Seattle
Washington
USA

Anna de Juan
Grup de Quimiometria
Facultat de Química
Universitat de Barcelona
Diagonal 647
08028 Barcelona
Spain

Jörg Detlef Drenckhahn
Max-Delbrück-Centre for Molecular
Medicine (MDC)
Berlin-Buch
Robert-Rössle-Straße 10
13092 Berlin
Germany

Max Diem
Northeastern University
Department of Chemistry and
Chemical Biology
Boston
MA 02115
USA

Kathryn A. Dooley
University of Michigan
Department of Chemistry
Ann Arbor
Michigan 48109-1055
USA

Janie Dubois
Malvern Instruments
Analytical Imaging
7221 Lee Deforest Drive
Suite 300
Columbia
MD 21046
USA

Ludovic Duponchel
Université des Sciences et
Technologies de Lille (USTL)
Laboratoire de Spectrochimie
Infrarouge et Raman (LASIR
CNRS UMR 8516)
Bâtiment C5
59655 Villeneuve d'Ascq
France

Karen A. Esmonde-White
University of Michigan
Department of Chemistry
Ann Arbor
Michigan 48109-1055
USA

Peter R. Griffiths
University of Idaho
Department of Chemistry
Moscow
ID 83844-2343
USA

Thomas Hancewicz
Unilever Research & Development
Trumbull
40 Merrit Blvd
Trumbull
CT 06611
USA

Uwe Hoffmann
NIR-Tools
Katernberger Straße 107
45327 Essen
Germany

Sergei G. Kazarian
Department of Chemical Engineering
Imperial College London
London SW7 2AZ
United Kingdom

Olga Kolomiets
Department of Physical Chemistry
University of Duisburg-Essen
45117 Essen
Germany

Christoph Krafft
Institute for Photonic Technology
07745 Jena
Germany

Nora Laver
New England Medical Center – Tufts
University
Department of Pathology
Washington Street
Boston
MA 02111
USA

Eunah Lee
HORIBA Jobin Yvon
3008 Park Avenue
Edison
NJ 08820
USA

Marcel Maeder
The University of Newcastle
Department of Chemistry
Callaghan
NSW 2308
Australia

Pavel Matousek
Central Laser Facility
Science and Technology Facilities
Council
Rutherford Appleton Laboratory
Harwell Science and Innovation
Campus
Didcot
Oxfordshire OX11 0QX
United Kingdom

Christian Matthäus
Northeastern University
Department of Chemistry and
Chemical Biology
Boston
MA 02115
USA

Don McNaughton
Monash University
Centre for Biospectroscopy and
School of Chemistry
3800 Victoria
Australia

Miloš Miljković
Northeastern University
Department of Chemistry and
Chemical Biology
Boston
MA 02115
USA

Lisa M. Miller
National Synchrotron Light Source
Brookhaven National Laboratory
75 Brookhaven Avenue
Upton
NY
USA

Michael D. Morris
University of Michigan
Department of Chemistry
Ann Arbor
Michigan 48109-1055
USA

Kostas Papamarkakis
Northeastern University
Department of Chemistry and
Chemical Biology
Boston
MA 02115
USA

Christian Pellerin
Université de Montréal
Département de chimie
Montréal QC
H3C 3J7
Canada

Melissa J. Romeo
Northeastern University
Department of Chemistry and
Chemical Biology
Boston
MA 02115
USA

Thomas Schmid
Department of Chemistry
and Applied Biosciences
ETH Zürich
8093 Zürich
Switzerland

Jennifer Schubert
Northeastern University
Department of Chemistry and
Chemical Biology
Boston
MA 02115
USA

Matthew V. Schulmerich
SABIC Innovative Plastics
1 Lexan Lane
Mt Vernon
IN 47620
USA

Heinz W. Siesler
Department of Physical
Chemistry
University of Duisburg-Essen
45117 Essen
Germany

Romà Tauler
IIQAB-CSIC
Jordi Girona 18
Barcelona 08034
Spain

Feng H. Tay
Department of Chemical
Engineering
Imperial College London
London SW7 2AZ
United Kingdom

Christian Vogel
Department of Physical
Chemistry
University of Duisburg-Essen
45117 Essen
Germany

Elke Wessel
Beiersdorf AG
Research & Development
Unnastraße 48
20253 Hamburg
Germany

David L. Wetzel
Kansas State University
Microbeam Molecular Spectroscopy
Laboratory
Shellenberger Hall
Manhattan
Kansas 66506
USA

Bayden R. Wood
Monash University
Centre for Biospectroscopy and School
of Chemistry
3800 Victoria
Australia

Boon-Siang Yeo
Department of Chemistry
and Applied Biosciences
ETH Zürich
8093 Zürich
Switzerland

Weihua Zhang
Department of Chemistry
and Applied Biosciences
ETH Zürich
8093 Zürich
Switzerland

Renato Zenobi
Department of Chemistry
and Applied Biosciences
ETH Zürich
8093 Zürich
Switzerland

Part One   Basic Methodology

1
Infrared and Raman Instrumentation for Mapping and Imaging

Peter R. Griffiths

1.1
Introduction to Mapping and Imaging

The analysis of localized regions of samples by vibrational microspectroscopy can be accomplished in two ways, by mapping or imaging.

Mapping involves the sequential measurement of the spectra of adjacent regions of a sample. This is achieved by moving each region of that sample into the beam focus of a microscope after the spectrum of the previous region has been measured; the measurement is then repeated until the entire region of interest has been covered.

Imaging, on the other hand, requires an image of the sample to be focused onto an array detector, where the intensity of the radiation passing through each region of the sample is measured at each pixel. In a mapping experiment in which the sample is only moved in one direction – say the x direction – the measurement is called line mapping. If the sample is moved in both the x and y dimensions, the measurement cannot be properly called imaging, as the spectra have not been acquired by an array detector. However, the spectra that are obtained can be treated in exactly the same way as if they had been acquired with an array detector.

In hyperspectral imaging, the images at more than ten wavelength regions are recorded simultaneously with a two-dimensional (2-D) array detector. Vibrational hyperspectral imaging can be accomplished through the measurement of either the mid-infrared, near-infrared (NIR) or Raman spectrum. The measurement of each type of spectrum is accomplished in different ways, although the instruments that have been developed for the measurement of NIR and Raman spectra are more closely related than are mid-infrared hyperspectral imaging spectrometers. In NIR and Raman instruments, the signal at a given wavelength is recorded at each pixel. In NIR imaging instruments, the light is usually passed through a monochromator or narrow band-pass filter (e.g., a liquid crystal tunable filter) before being focused on the sample, and from there onto the array detector. The image from one wavelength region is measured at all pixels simultaneously. The wavelength region is then changed (usually, but not necessarily, to an adjacent

spectral region) and the intensity at each pixel is measured again. This process is repeated until all wavelengths of interest in the spectrum have been measured.

An analogous approach is used for Raman imaging, except that the monochromator must be located after the sample. The signal from all pixels for a given wavelength setting is acquired rapidly in NIR imaging instruments, where the signal-to-noise ratio (SNR) is usually high. The SNR for Raman imaging is much lower, so that a much longer integration time is needed. Thus, Raman imaging can be painfully slow unless only a few wavelength regions are measured. In both NIR and Raman imaging spectrometers, the bandpass of the monochromator or filter determines the spectral resolution. Occasionally, only a short spectral range or a few wavelength regions may be sufficient to classify samples that are composed of just a few components. On the other hand, for complex or previously uncharacterized samples, it is usually necessary to measure data over the entire spectral range. In mid-IR imaging instruments, it is more common to couple the array to an interferometer, so that interferograms from different spatial regions of the sample are recorded at each detector element. Subsequent Fourier transformation yields the desired hyperspectral data set. All types of systems will be described in this chapter.

In addition to the mapping and imaging approaches outlined above, a hybrid technique is also available where a linear array of detectors is used to measure the spectra over a line of points on a sample simultaneously, so that a line image is measured. By using the same approach as for mapping measurements, and with a single-element detector, the sample is moved after each measurement so that the spectra of the next linear region of interest are measured. The spectra are then 'stitched' together to form the complete image. This 'push-broom' approach has proved to be useful for mid-IR imaging (as will be discussed later in the chapter). Of course, it may well be that even the region that can be monitored with a 2-D array detector (especially the smaller arrays, such as 16×16 pixels) does not cover the entire sample of interest. In that case, the sample is also moved after each measurement so that a hyperspectral image of the adjacent region is acquired. These data can then also be stitched together (a procedure sometimes known as *quilting* or *mosaicing*) to allow an image to be observed over a wider area.

The end result of either spectroscopic mapping or hyperspectral imaging is an array of spectra (sometimes called a hyperspectral cube) from which the identifying characteristics of inhomogeneous samples can be obtained. For Raman imaging, the sample need not be of constant thickness, although ideally it should be as flat as possible. Conversely, when mid-IR or NIR absorption spectra are to be measured, the thickness of the sample should be as uniform as possible. In this case, it is sometimes possible to synthesize an image that shows the concentration of a certain component by simply plotting the absorbance at a certain wavelength of a band that is isolated from all others in the spectrum (e.g., the C≡N stretching mode of polyacrylonitrile, *vide infra*; Figure 1.24). If this approach proves to be feasible, the image may either be plotted as a gray scale, with white representing the absence of the component and dark gray representing its greatest concentration, or – more commonly nowadays – through the use of color.

(a)   (b)
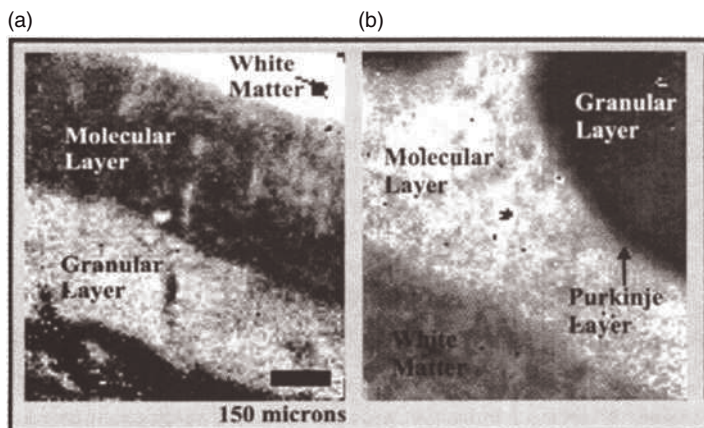
Figure 1.1 Infrared spectroscopic gray-scale images of thin cerebellar sections from (a) a control rat and (b) a rat treated with the drug cytarabine, showing the spatial distribution of lipid and protein by ratioing the absorbance of the CH_2 antisymmetric stretching band at $2927\,cm^{-1}$ and the N–H stretching band at $3350\,cm^{-1}$. Reproduced with permission from Ref. [1].

It is usually not possible to obtain samples of absolutely constant thickness, and in this case the ratio of the peak absorbance or integrated absorbance of bands that can be assigned to particular components must be calculated [1, 2]. An example of this approach can be seen in Figure 1.1, which shows the infrared images of thin cerebellar sections from an untreated rat and a rat treated with the drug cytarabine. The images demonstrate the spatial distribution of lipid and protein by ratioing the absorbance of the CH_2 antisymmetric stretching band at $2927\,cm^{-1}$ and the N–H stretching band at $3350\,cm^{-1}$. For more complex samples, principal component analysis or more sophisticated chemometric algorithms may be applied (as described in Chapter 2 in this book and also by Diem *et al.* [3] and Šašić and Clark [4]). Although many applications of imaging spectroscopy will be described throughout this volume, only the design of the instruments used to acquire these data will be described in this chapter.

1.2
Mid-Infrared Microspectroscopy and Mapping

1.2.1
Microscopes and Sampling Techniques

Although many noble efforts at fabricating a microscope for infrared spectrometry using a prism monochromator were made during the 1940s and 1950s [5–10], and Perkin-Elmer actually advertised a microscope that could be installed in one of

their prism spectrometers [11], the performance of these instruments was marginal and the use of infrared microscopes never caught on commercially until the early 1990s. Until that time, the mid-IR spectra of minute samples were measured by mounting the sample behind a pinhole of the appropriate dimensions, so that only the region of the sample of interest was irradiated. The sample was then held at the focus of a simple beam condenser that fitted in the sample compartment of the spectrometer. As the size of the region of interest decreased, locating the sample so that the region of interest corresponded to the position of the pinhole became increasingly difficult. However, the situation was dramatically improved when a standard reflecting microscope was interfaced to a Fourier transform infrared (FT-IR) spectrometer. In this case, the previous function of the pinhole was replaced by a remote aperture at a conjugate focus of the sample. A simplified schematic of a typical infrared microscope is shown in Figure 1.2.

The microscope shown in Figure 1.2 is designed to operate in either the transmission or reflection mode. In the transmission mode, the beam from the interferometer is passed onto a toroidal coupling optic and thence to the Cassegrainian condenser. The condenser focuses the beam into a small spot where the sample is mounted. The radiation that is transmitted through the sample is collected by the objective and refocused at a remote adjustable aperture. The part of beam that passes through the aperture is imaged onto an optical viewer (or, more frequently nowadays, a video camera) so that the image of the sample that is passed by the aperture can be viewed. The sample is usually mounted on an x,y,z stage The height of the sample is adjusted with the z control to ensure that the position of
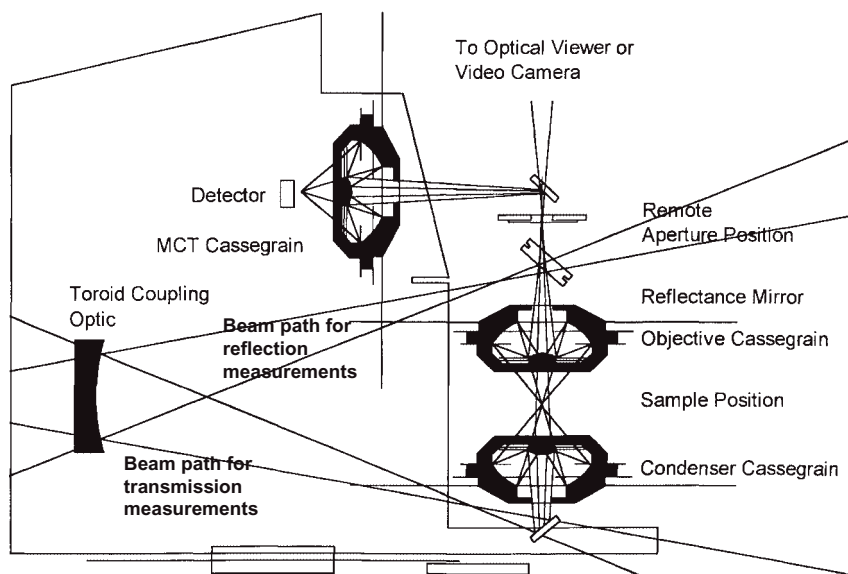
Figure 1.2 Simplified schematic of a typical microscope interfaced to an FT-IR spectrometer. Courtesy of PerkinElmer Inc.

the sample is coincident with the beam focus. The x and y controls are then used to adjust the location of the sample so that the region of interest is at the center of the beam. The jaws of the aperture are then adjusted so that only the region of interest is seen at the viewer. The aperture is often rectangular and can be rotated through 180° to allow the greatest amount of light transmitted through the region of interest in the sample to pass through the aperture. When the conditions have been optimized, a 45° mirror is slid into position so the light that is transmitted through the remote aperture is collected by the third Cassegrain and focused onto the detector, which measures the spectrum of the desired region of the sample.

The condenser goes by two names: some call it a *Cassegrain*, while others call it a *Schwarzschild* objective. The present author has always been rather confused about the difference between a Cassegrain and a Schwarzschild objective but, aiming to resolve such confusion, contacted one of the designers of the first FT-IR microscopes, Bob Messerschmidt (now with Rare Light, Inc.), as to their difference. His reply to this question was as follows:

> The Schwarzschild objective has been used in almost all FT-IR microscopes, and is still used to this day. The design is attributable to the German physicist and astronomer Karl Schwarzschild (1873–1916). The Schwarzschild objective is an all-reflective two-mirror system in which the mirrors are very nearly concentric. The system employs one concave and one convex mirror, and is on-axis, with a hole in one mirror for the light to pass through. The beauty of the system is in its simplicity. It has excellent imaging characteristics over a surprisingly wide field of view, a fact that arises from the mirror concentricity. The first commercial FT-IR microscope, the Digilab IRMA, used this design because the designers were aware that the 1953 Perkin-Elmer microscope for dispersive spectrometers used such a Schwarzschild objective.

> The Schwarzschild objective can be considered a special case of a Cassegrainian system. In fact, the Schwarzschild objective is sometimes simply referred to as a Cassegrainian or Cassegrain microscope objective. This name comes from an optical design attributed to Laurent Cassegrain, a Catholic priest who was born in the region of Chartres around 1629 and died in 1693. The invention seems to have occurred in 1672, the same year Isaac Newton reported his first invention, the Newtonian telescope, using a similar yet not the same two-mirror configuration. Most modern telescopes are Cassegrain designs, or very similar. A Cassegrain system is any two-mirror objective with a convex and concave mirror, with a hole in the latter for the light to travel through. There is no requirement of concentricity. So, all Schwarzschild objectives are Cassegrain objectives. The key performance feature of the Schwarzschild design is the concentricity, or near-concentricity, of the two mirrors. It took over 200 years to be invented from the time of Laurent Cassegrain's original design.

When the microscope shown in Figure 1.2 is used in the external reflection mode, the same Cassegrain is used both as the condenser and the objective. In the external reflection mode, the angle at which the toroidal coupling optic is held is switched so that the beam is passed to the top of the objective via a small deflection mirror. The size and location of this mirror are such that half the beam enters the Cassegrain. The beam is demagnified by the primary and secondary mirrors and focused on the sample, which is at the same location as for transmission measurements. The reflected beam is then reconfigured by the secondary and primary mirrors, the optical properties of which are such that the beam misses the small deflection mirror and passes to the remote aperture. Even if a perfect mirror is held at the sample focus, it can be seen that, in comparison to a transmission measurement, only half the signal can be measured when the microscope is used in its reflection mode.

Three types of external reflection spectra can be measured with the microscope optics in the reflection mode shown in Figure 1.2, for which the angle of incidence on the sample is about 30°. In the first type, *transflection spectroscopy* (which is of increasing popularity for mid-IR spectroscopy), a sample of thickness between 5 and 10 µm is deposited on a reflective substrate and the transflection spectrum measured. In measurements of this type, the beam passes through the sample, is reflected from the substrate, and then passes back through the sample before it re-emerges from the surface of the sample and passes to the detector. This type of measurement has occasionally been used for tissue samples, and has proved quite beneficial when the sample is deposited on a 'low-e glass' (low emissivity) slide (Kevley Technologies, Chesterland, OH, USA). These slides, which are fabricated by coating glass with a very thin layer of silver-doped tin oxide, were originally developed for the windows of tall buildings. The coating is thin enough to be transparent to visible light, yet is highly reflective in the mid-IR region. Thus, while any tissue sample on these slides can be inspected by visual microscopy, it still allows the transflection spectrum to be measured [12].

Transflection spectra have the disadvantage that radiation reflected from the front surface of the sample will also reach the detector and give rise to a distortion of the pure transflection spectrum. Merklin and Griffiths [13] showed that the contribution by front-surface reflection can be eliminated by measuring the spectrum at Brewster's angle using p-polarized radiation; that is, radiation polarized such that its electric vector is parallel to the plane of incidence. Brewster's angle for tissue samples is about 50°, which is somewhat higher than the angle of incidence of most infrared microscopes, although the distortion introduced by front-surface reflection will be reduced significantly. It should be noted, however, that the use of a polarizer will reduce the SNR of the spectrum by between a factor of 2 and 3, so this approach may not be beneficial if very small samples, such as single cells, are being investigated.

The other two types of external reflection microspectroscopy are less well suited to the characterization of tissue samples. In the first type, which is variously called *specular reflection*, *front-surface reflection* or *Kramers–Kronig reflection*, the reflectance

spectrum of thick, nonscattering, bulk samples is measured and converted to the wavenumber-dependent optical constants – that is, the refractive index, $n(\tilde{v})$ and the absorption index, $k(\tilde{v})$ – by the Kramers–Kronig transform, as discussed by Griffiths and de Haseth [14]. As the requirement for the lack of scattering by the sample is essentially never met for tissue samples of the type obtained in medical diagnosis, this will not be discussed further.

The final type of measurement that can be made with the microscope in its reflection mode is diffuse reflection (DR) spectroscopy. Today, very few applications of mid-IR microspectroscopy of neat samples are available, because for mid-IR DR spectrometry the samples should be diluted to a concentration of between 0.5 and 5% with a nonabsorbing diluent (e.g., KBr powder) to preclude band saturation and severe distortion by reflection from the front surface of the particles. However, this mode has substantial application for NIR measurements, where sample dilution is not needed. Because the absorption of NIR radiation by most samples is rather weak, they must either be at least 1 mm thick or be mounted on a reflective or diffusing substrate, such as a ceramic or Teflon disk. In the latter case, the spectrum is caused by a combination of diffuse reflection, transflection and front-surface reflection (hopefully with diffuse reflection being the dominant process).

1.2.2
Detectors for Mid-Infrared Microspectroscopy

Essentially all mid-IR spectra are measured today using FT-IR spectrometers for which the optical path difference (opd) of the interferometers is varied continuously; these are often referred to as 'continuous' or 'rapid-scan' interferometers. Most standard laboratory FT-IR spectrometers are equipped with a 1 mm × 1 mm or 2 mm × 2 mm deuterated triglycine sulfate (DTGS) detector operating at ambient temperature. However, the sensitivity of DTGS detectors is too low to allow them to be used to measure the relatively weak signals encountered after the beam has been passed through the small aperture of a microscope. Instead, the more sensitive liquid-nitrogen-cooled mercury cadmium telluride (MCT) detector is almost invariably used. These detectors operate in the photoconductive mode; that is, when infrared radiation is incident on them the photons promote electrons from the valence band to the conduction band, and the increase in conductivity is a measure of photon flux.

The properties of MCT detectors depend on their composition, that is their Hg : Cd ratio. 'Narrow-band' MCT detectors are typically about 50-fold more sensitive than DTGS, but do not respond to radiation below ~750 cm^{-1}. The cut-off can be extended to a lower wavenumber, but at the expense of sensitivity. Thus, 'mid-band' MCT detectors have a cut-off of about 600 cm^{-1}, while their sensitivity is about half that of the narrow-band detector. 'Wide-band' detectors cut off at ~ 450 cm^{-1} but are even less sensitive. Fortunately, few spectra of organic samples contain useful bands below 700 cm^{-1}, as a result, FT-IR microscopes are almost invariably equipped with narrow-band MCT detectors.

The noise equivalent power (NEP) of an infrared detector is a measure of the noise generated by the detector and is given by:

$$\text{NEP} = \frac{\sqrt{A_D}}{D*} \qquad (1.1)$$

where A_D is the area of the detector element and $D*$ is the specific detectivity of the detector (which is typically a constant for a given wavelength, detector composition and temperature.) The greater the NEP, the lower is the sensitivity of the detector. Most detectors are specified in terms of their $D*$ rather than their NEP. The $D*$ of a narrow-band MCT detector is close to the value given by the background limit for infrared photons, and their performance can only be improved significantly by switching to a liquid-helium-cooled bolometer. To the present author's knowledge, the use of such a bolometer for mid-IR microspectroscopy has not been reported.

From Equation 1.1 it can be seen that the area of any detector used for infrared microspectroscopy should be as small as possible. Provided that all the radiation that passes through the sample is focused on the detector, the use of a 0.25 mm detector gives a SNR that is fourfold greater than if a 1 mm detector were used for the characterization of microsamples. For mid-IR microspectroscopy, the detector is usually a $250 \times 250\,\mu m$ narrow-band MCT photoconductive detector, although some vendors do provide options for $100 \times 100\,\mu m$ or even $50 \times 50\,\mu m$-sized elements. As identical objectives are usually used to focus the beam onto the sample and the detector (e.g., see Figure 1.2), there is 1× magnification and the *largest* sample that can be measured with a 250 μm detector is $250 \times 250\,\mu m$; however, this is rarely a significant limitation in mid-IR microspectroscopy when samples *smaller* than 250 μm are usually of interest.

The SNR of a FT-IR spectrum (i.e., the reciprocal of the noise of a 100% line measured in transmittance) is given by the following equation [15]:

$$\text{SNR} = \frac{U_v(T)\Theta\Delta\tilde{v}\,D*\,t^{-1/2}\,\xi}{A_D^{1/2}} \qquad (1.2)$$

where $U_v(T)$ is the spectral energy density of the source radiation (W (sr cm^2 cm^{-1})), Θ is the optical throughput or *étendue* (cm^2 sr), $\Delta\tilde{v}$ is the resolution at which the spectrum is measured (cm^{-1}), t is the measurement time (s), $D*$ is the specific detectivity of the detector (cm Hz$^{1/2}$ W^{-1}), ξ is the efficiency of the optics and A_D is the detector area (cm^2). Microscopes are designed to have a high optical efficiency, ξ, and a numerical aperture that gives the highest étendue, Θ, for small samples. The spectral resolution, $\Delta\tilde{v}$, is governed by the nature of the sample and the information required by the operator.

The data acquisition rate (sampling frequency) for mid-IR interferograms is usually equal to the frequency, f_L Hz, of the interferogram that is generated by a laser (usually a helium-neon laser at 632.8 nm) simultaneously with the infrared interferogram. f_L is equal to the product of the wavenumber of the laser and the

optical velocity (i.e., the rate of change of opd) of the interferometer. For a standard Michelson interferometer, the optical velocity is twice the mechanical velocity of the moving mirror. The scan speed is usually determined by the effect of the frequency on the signal being detected on the D* of the detector [15]. For example, the D* of the DTGS detector that is supplied as standard with most FT-IR spectrometers is greatest when the modulation frequencies of the signals in the interferogram are low. For the most efficient operation with a DTGS detector, therefore, the optical velocity of the interferometer must also be low. The typical optical velocity used in this case is $0.316\,cm\,(opd)\,s^{-1}$, corresponding to a 5 kHz signal from the interferogram generated by the 632.8 nm line of a He–Ne laser and hence a 5 kHz data acquisition rate. Conversely, the D* of the MCT detector is approximately constant for modulation frequencies between 1 kHz and 1 MHz, but decreases at lower modulation frequencies. Many continuous-scanning interferometers are operated at an optical velocity of $1.264\,cm\,(opd)\,s^{-1}$, corresponding to a 20 kHz signal from the 632.8 nm line of a He–Ne laser. In this case, the modulation frequency for $750\,cm^{-1}$ radiation is ~950 Hz and radiation at all higher wavenumbers is modulated at a frequency greater than 1 kHz. Obviously, the D* remains relatively constant over the range at which the fastest instruments can scan (>100 kHz).

Most FT-IR spectra measured through a microscope are acquired at a resolution of $4\,cm^{-1}$, which requires 8K data points for each symmetric (double-sided) interferogram. If the data acquisition frequency with a He–Ne laser is 20 kHz, then the time to measure each interferogram is 0.4 s. Assuming that the mirror can be turned around fairly efficiently, this implies that about 2.5 scans can be measured per second. For mapping purposes, it is fairly common to average 16 scans before advancing the position of the microscope stage; however, the number of scans required to achieve the desired SNR will depend heavily on the size of the sample aperture employed, with smaller apertures (for higher spatial resolution) requiring many more scans, typically hundreds.

Although contemporary FT-IR spectrometers and microscopes are well matched, for spectra measured when using sample apertures that approach the diffraction limit (<20 μm) even a 30 s collection may result in a spectrum with a rather poor SNR. It may be noted that if the measurement of each spectrum takes 30 s and a 64×64 map is required at 20 μm spatial resolution, it would take over 34 h to acquire all the spectra required for the image!

At this point, it may be asked if certain parameters can be changed to decrease the measurement time to allow maps to be acquired in reasonable times. As the size of the remote aperture for most applications is smaller than 250 μm, it is valid to suggest that even smaller detectors should be installed in FT-IR microscopes, so that the SNR is optimized for samples that are 50 μm or smaller in dimension. The answer is a very practical one: it is simply very difficult to keep the beam aligned with the tighter tolerance required for the beam to be focused accurately on a detector that is smaller than 250 μm. As we will see later, the situation is different when array detectors with very small pixels are used for hyperspectral imaging.

The measurement time, t, is largely determined by the goal of the experiment. If only a few regions of the sample are of interest, then several minutes can be used for each measurement. However, if the sample is to be mapped, hundreds of spectra are often needed and the time for each should be less than 1 min if the measurement is to be completed in a reasonable time.

1.2.3
Sources for Mid-Infrared Microspectroscopy

One parameter in Equation 1.2 has not yet been discussed, namely the spectral energy density, $U_\nu(T)$. The only parameter that can lead to a significantly improved SNR is the spectral energy density of the source radiation, $U_\nu(T)$. In general, the operators of laboratory FT-IR spectrometers have little control over the source installed in their instruments. Most instruments are equipped with an incandescent silicon carbide source, such as a Globar, operating at about 1400 K. The emission characteristics of mid-IR sources are usually similar to those of a blackbody, so that it is possible to increase the spectral energy density by increasing the temperature of the source. However, increasing the temperature of a Globar often leads to cracking and the rapid degradation of electrical contacts at the end of the rod. One material that has been reported to be operable to over 1950 K is molybdenum silicide; another source that can be taken up to a temperature close to 2000 K is a homogeneous material with the chemical formula $Mo_xW_{1-x}Si_2$, which is available commercially as Kanthal Super 1900. The molybdenum and tungsten atoms are isomorphous in this chemical formula, and can thus replace each other in the same structure. However, a detailed comparison of any of these materials with a Globar with respect to infrared microspectroscopy has, to the present author's knowledge, never been reported.

Provided that samples can be removed from the laboratory, there are two alternative sources of infrared radiation that are far better than incandescent sources for mid-IR microspectroscopy, namely the synchrotron and the free electron laser (FEL) [16].

A synchrotron is a particular type of cyclic particle accelerator, or cyclotron, in which the particles are electrons. A magnetic field is used to bend the path of the electrons and an electric field is used to accelerate them. Both fields are carefully synchronized with the traveling beam of electrons. By increasing the two fields appropriately as the particles gain energy, their path can be controlled as they are accelerated. This allows the particles to be contained within a large narrow ring, with some straight sections between the bending magnets and some bent sections within the magnets giving the ring the shape of a round-cornered polygon. This shape also allows (and, in fact, requires) the use of multiple magnets to bend the particle beam. The strength of the transverse magnetic field is varied periodically by arranging magnets with alternating poles along the beam path. This array of magnets is sometimes called an undulator, or 'wiggler', because it forces the electrons in the beam to assume a sinusoidal path. The acceleration of the electrons along this path results in the release of a photon.

In a typical cyclotron, the maximum radius is quite limited as the particles start at the center and spiral outward; thus, the entire path must be a self-supporting, disc-shaped evacuated chamber. As the radius is limited, the power of the device becomes limited by the strength of the magnetic field, but synchrotrons overcome this limitation through the use of a narrow beam pipe that can be surrounded by much smaller and more tightly focused magnets. The ability of this device to accelerate particles is limited by the fact that the particles must be charged to be accelerated at all, and all charged particles under acceleration emit photons, thereby losing energy. The limiting beam energy is reached when the energy lost to the lateral acceleration required to maintain the beam path in a circle equals the energy added each cycle. More powerful accelerators are built using larger radius paths and by using more numerous and more powerful microwave cavities to accelerate the particle beam between corners.

A FEL shares the same optical property as a conventional laser; that is, the emission of a beam of coherent electromagnetic radiation that can reach high power. However, FELs use some very different operating principles than a conventional laser to form the beam. Unlike conventional lasers, which rely on bound atomic or molecular states, FELs use a relativistic electron beam as the lasing medium, which gives them the widest frequency range of any laser type, and makes many of them widely tunable, currently ranging in wavelength from microwaves to soft X-rays. In certain respects, the FEL is similar to a synchrotron. To create a FEL, a beam of electrons is accelerated to relativistic speeds. As in the operation of a synchrotron, the beam passes through a periodic, transverse magnetic field. However, in an FEL, the undulator is placed in an optical cavity, or resonator, that reflects the emitted light back and forth. The electrons become tightly bunched because of interactions with a light beam that is also passing through the undulator. The light may either be introduced from an external 'seed' laser or, more frequently, is radiation that has been generated from a previous bunch of electrons that is reflected from mirrors that form an optical cavity outside the undulator.

Viewed relativistically in the rest frame of the electron, the magnetic field can be treated as if it were a virtual photon. The collision of the electron with this virtual photon creates an actual photon by Compton scattering. Mirrors capture the released photons to generate a resonant gain, while the wavelength can be tuned over a wide range by adjusting either the energy of the electrons or the field strength. As the energy of the emitted photons is governed by the speed of the electron beam and magnetic field strength, an FEL can be tuned. Furthermore, because the resonance is specific for light of a given wavelength, the power of the beam is significantly greater than that of a synchrotron, for which broadband radiation is emitted.

What makes this device a laser is that the electron motion is in-phase with the field of the light already emitted, so that the fields add coherently. As the intensity of the emitted light depends on the square of the field, the light output is increased. In the rest frame moving along the undulator, any radiation will still move with the speed of light and pass over the electrons, allowing their motion to become synchronized. The phase of the emitted light is introduced from the outside.

Depending on the position along the undulator, the oscillation of the electrons is either in-phase or out-of-phase with the radiation introduced from the outside. The light either tries to accelerate or decelerate these electrons, thereby gaining or losing kinetic energy, and so moves faster or slower along the undulator. This causes the electrons to form bunches; when they are synchronized they will in turn emit synchronized (i.e., coherent) radiation.

Steiner *et al.* have reported the measurement of maps of octadecanephosphonic acid (OPA) molecules deposited on a microstructured aluminum oxide/gold surface using an FEL source [17]. The beam from the FEL was first passed through an interferometer to modulate the beam at a frequency of a few kilohertz. (Note that as the FEL emits monochromatic radiation, the interferometer was only used as a modulator and served no spectroscopic function.) The beam was then passed through a wire-grid polarizer and a photoelastic modulator so that the polarization was switched at a rate of 75 kHz, and then through a pinhole to be focused onto the sample with a Cassegrainian objective at an incidence angle of approximately 60°; in this way the diameter of the Airy disk (*vide infra*) was about 15 μm. Radiation that was polarized such that the electric vector was parallel to the surface was absorbed by the surface species, whereas radiation polarized such that the electric vector was perpendicular to the surface was not absorbed. The beam was collected by a second Cassegrain and then refocused at the detector. As the detector signal is passed into a lock-in amplifier referenced to the polarization modulation frequency, the interferogram was caused only by the surface species [18]. The sample was then moved in a raster fashion in order to generate a spectroscopic map that showed OPA to be attached on the aluminum oxide surface, and not to the gold. Although the attached molecules formed a highly ordered film, a lower degree of ordering was found for phosphonic acid adsorbed onto gold.

For these investigations, Steiner *et al.* measured either 40×40 or 20×20 pixels per image, with three scans being averaged for each data point. The measurement time per pixel for a single wavelength was ~5 s, with an additional 2 s for data processing; hence, the total measurement time per image for a single wavelength was 190 min for the 40×40 pixel image and 45 min for the 20×20 pixel image. Under normal conditions, the operators of the FEL require 10–20 min to change the wavelength of the FEL; thus, to measure the image at three wavelengths required at least a day.

From a spectroscopic standpoint, the main difference between a synchrotron and an FEL is that a synchrotron emits broadband radiation, while the FEL emits monochromatic radiation with several orders of magnitude higher brilliance than a synchrotron. Thus, radiation from a synchrotron can be expanded and passed into a FT-IR spectrometer, for which the interferometer and all the subsequent optics are no different from those in a conventional FT-IR spectrometer (or microspectrometer.) When a FEL is used for spectroscopy, the monochromatic radiation generated can be modulated in any appropriate manner (e.g., by a tuning fork chopper) before being passed onto the sample and detector. In principle, FELs can

be used for imaging by passing monochromatic radiation onto a focal plane array detector and measuring the signal from each pixel (*vide infra*), although such experiments have not yet been reported. The laser would then be tuned to the next wavelength of interest, and this process would be repeated for as many wavelengths as were needed to characterize the sample. This is rarely a fast process, as it usually takes several minutes to change from one wavelength to the next.

The synchrotron has an equivalent black-body temperature of 10 000 K [19]. The effective diameter of the beam from a synchrotron is typically about 100 μm; moreover, the light is emitted into a narrow range of angles, making this an almost perfect radiation source for mid-IR microspectroscopy. Not all synchtrotrons are equipped with infrared beam lines, although as the importance of the results obtained continues to increase this situation is changing. Beam time on most synchrotrons is highly prized, and potential users may often have to write a short proposal to be granted beam time. However, since FT-IR microscopes with a synchrotron source allow spectra with diffraction-limited spatial resolution and high SNR to be measured in a few seconds, many spectroscopists are starting to use the combination of synchrotron source, FT IR spectrometer and either a single-element detector or an array detector [20–23].

1.2.4
Spatial Resolution

Today, FT-IR microscopes are designed to allow the spectra of physically small samples, or regions of small samples, to be measured as quickly and easily as possible. An example of such a system is shown in Figure 1.3. On this microscope, a video image of the sample is displayed on the monitor screen immediately adjacent to the sample; this allows the position of the sample and the jaws of the aperture to be optimized prior to measurement of the spectrum. A motorized sample stage allows mapping to be readily accomplished.

The spatial resolution of a microscope is ultimately determined by diffraction of the radiation. If monochromatic radiation from a point source is passed into the microscope, then a series of concentric rings of decreasing intensity is seen at the beam focus. The Airy disk is the central bright circular region of the pattern produced by light diffracted when passing through a small circular aperture. The size of the Airy disk depends on the wavelength of the radiation and the optics of the microscope. The radius of the Airy disk is the distance between the central maximum and the first minimum of the diffraction pattern and is given by:

$$r = 0.61 \frac{\lambda}{NA} \tag{1.3}$$

Here, NA is the numerical aperture, defined as:

$$NA = n \sin \theta \tag{1.4}$$

Figure 1.3 The Bruker Optics Hyperion microscope. Courtesy of Bruker Optics.

where n is the refractive index of the medium in which the optics are immersed (i.e., 1.0 for air and up to 1.56 for oils) and θ is the half-angle of the maximum cone of light that can enter or exit the condenser or objective. (Immersion optics are almost never used for infrared microspectroscopy because of absorption by the oil, but have occasionally been used to improve the spatial resolution in Raman microspectroscopy. Immersion oils have been shown to be essential in order to obtain good depth resolution with confocal Raman microscopy [24].)

Two objects are completely resolved if they are separated by $2r$, and barely resolved if they are separated by r. The latter condition is sometimes known as the *Rayleigh criterion of resolution*. The largest numerical aperture that can generally be achieved for a Cassegrainian optic is approximately 0.6, so the diffraction-limited spatial resolution is approximately equal to the wavelength of the light when $n = 1.0$.

Although it was stated that the spatial resolution of a microscope is ultimately limited by diffraction, all modes of chemical imaging employ detector elements of finite size. When the image of the pixel at the sample plane becomes the limit-

ing aperture, it can often become the limiting factor determining the ultimate spatial resolution before wavelength-limited diffraction effects become apparent. As the wavelengths of radiation across the mid-IR spectrum typically range from 2 to 14 μm, and if the pixel size at the sample plane (which is a function of native detector pixel size and overall system magnification) is larger than the wavelength being used to measure it, then the system is said to be 'pixel size-limited'. Conversely, if the wavelength of light being used to measure the sample is smaller than the pixel size at the sample plane, the system is said to be 'diffraction-limited'. This is an important – yet often misunderstood – concept. For example, the use of higher magnification objectives (e.g., 36×) results in very small images at the sample plane. However, this does not necessarily result in an improved spatial resolution, as these systems are often already diffraction-limited. Some focal plane array (FPA) imaging systems, report a pixel size of 1.1 μm when a 36× objective is used, but this is a 'waste of pixels' as the pixel size is significantly smaller than the wavelengths of light in the mid-IR; that is, the resolution is already diffraction-limited. In the example of the 36× objective providing a 1.1 μm pixel size, this spatial resolution could only really be achieved at 9000 cm^{-1}, well beyond the high wavenumber cut-off of the FPA.

In practice, even though the size of the images of the pixels at the sample plane is smaller than the wavelengths of light being used to measured the sample, the finite thickness of the sample (typically 5–20 μm) can degrade the achievable spatial resolution significantly. This effect is discussed further in Section 1.4.

While several types of microscope are commercially available for mid-IR microspectroscopy, these differ in how the sample is apertured and how the light is transferred within the microscope. The first has the simple design concept shown in Figure 1.2, namely that the beam from the interferometer is focused at the sample; thus, the sample is at an image of either the source or the Jacquinot stop (for higher-resolution FT-IR spectrometers). The beam is then refocused at the remote aperture and then again onto the detector. In the alternative design, the beam from the interferometer is passed through two apertures, one before and one after the sample, as shown schematically in Figure 1.4. This approach, which originally was called *redundant aperturing* and is now more frequently known as *dual aperturing*, provides a slightly higher spatial resolution near the diffraction limit than the single-aperture design, as shown on a theoretical basis in Figure 1.5. The second aperture serves much the same purpose as the pinhole in a confocal microscope (*vide infra.*)

Sommer and Katon [25] reported an elegant experiment that verified the improvement of spatial resolution through the use of dual aperturing. These authors mounted a free-standing polymer film at the beam focus of a microscope with dual rectangular apertures of 8×240 μm, and then measured a series of spectra as the edge of the film was moved into the beam. The spectra were measured with both apertures installed, and also with a single aperture mounted before or after the sample. By measuring the intensity of the polymer bands, it could be shown that the worst resolution was obtained when a single aperture was located after the sample. The performance for dual remote apertures and a single aperture

Preaperture
(aperture before sample)

Objective
(15X, N.A.=0.58)

Sample plane →

Condenser
(10X, N.A.= 0.71)

Postaperture
(aperture after sample)
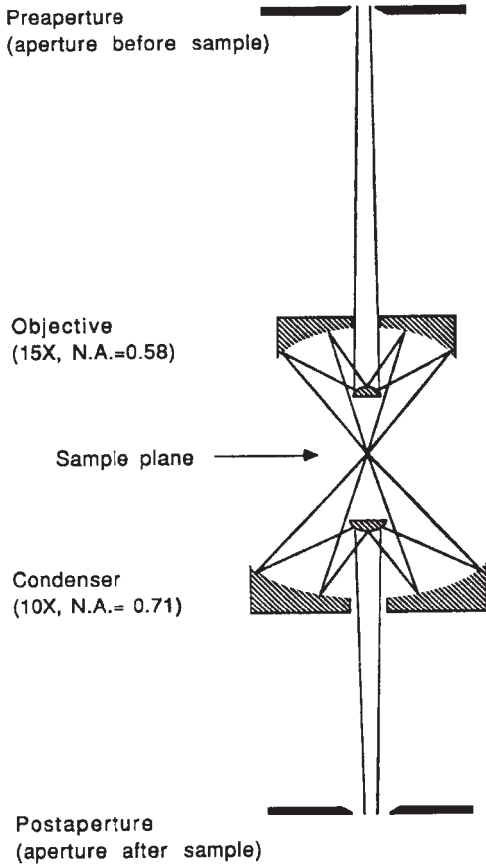
Figure 1.4 Dual-aperture microscope similar to the optics of an IRPlan microscope. Reproduced with permission from Ref. [25].

(a) (b)
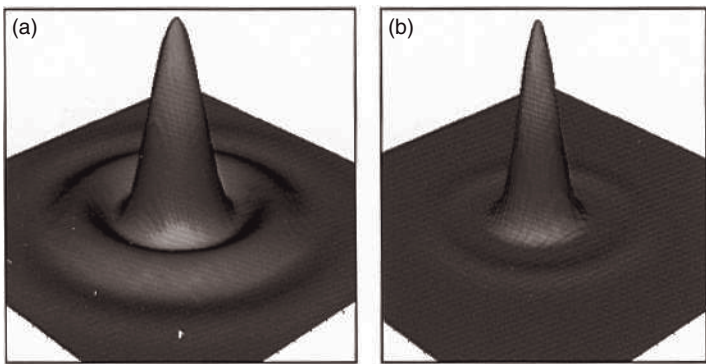
Figure 1.5 (a) Energy profile showing the diffracted radiation outside the area defined by a single aperture; (b) Corresponding profile obtained with masks located before and after the sample. Reproduced from *Infrared Fourier Transform Spectrometry* by P. R. Griffiths and J. A. de Haseth; © 2007, p. 307.
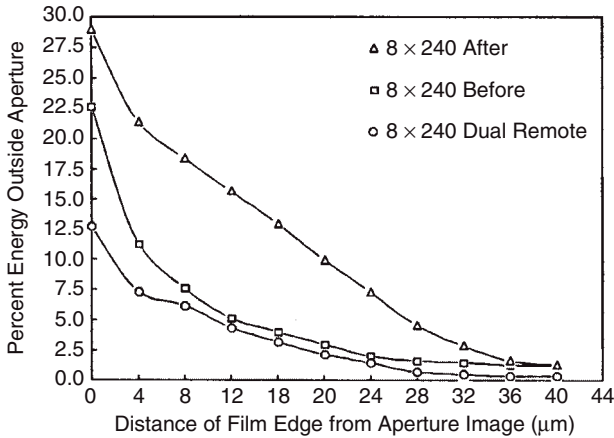
Figure 1.6 Percentage of stray energy outside the area defined by an $8 \times 240\,\mu m$ rectangular aperture for various imaging modes. Reproduced with permission from Ref. [25].

located before the sample was comparable, as shown in Figure 1.6. However, it should be noted that the dual-aperture design has the limitation that less energy reaches the detector than with the single-aperture design, so that the SNR for a given spatial resolution is decreased.

It was found that keeping the apertures of a dual-aperture microscope in alignment over a long period of use was not an easy task, especially when a high spatial resolution is desired and the apertures must be very small. Consequently, Thermo-Electron devised a clever scheme to overcome this problem by using the same aperture twice, as shown in Figure 1.7.[1] The dual-aperture concept is similar to that of a confocal microscope (*vide infra*; Section 1.5). Both, the dual-aperture design and confocal microscopes preclude imaging measurements, however, because in order to image a sample all regions of that sample which are of interest must be completely illuminated by the source radiation, while the detector pixels serve the purpose of the remote aperture that would normally be located after the sample. The dual-aperture system is ideally suited to mapping measurements with diffraction-limited spatial resolution, in which case a source of very high brightness such as a synchrotron is needed.

The manufacturers of infrared microscopes are split almost evenly between those that produce 'infinity-corrected' and those producing 'non-infinity-corrected' microscopes. Infinity correction effectively refers to a collimation of the beam throughout the microscope (other than at the condenser and objective outputs), and is frequently used in research-grade optical microscopes. Despite the added

1) Nicolet Corporation made its first FT-IR spectrometer in 1971 and became the market leader shortly afterwards. In 1995, Thermo-Electron Corporation purchased Nicolet and dropped the Nicolet name. In 2006, Thermo Electron purchased Fisher Scientific and the corporation is now known as Thermo-Fisher.
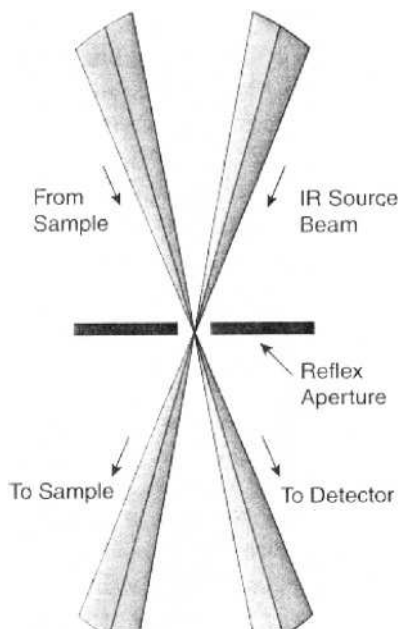
Figure 1.7 Dual confocal aperturing achieved with a single physical aperture. Reproduced from Infrared Fourier Transform Spectrometry by P. R. Griffiths and J. A. de Haseth; © 2007, p. 307.

complexity in microscope design, 'infinity correction' provides for added flexibility in the choice of 'off-the-shelf' visible objectives (as most are for infinity-corrected systems), and also in that filters and other optical components can be placed anywhere where the beam is collimated. Infinity correction can also provide for improved image clarity and focus. Non-infinity-corrected microscopes (otherwise known as 'finite tube length' microscopes), although less complex in design, are limited in terms of available options, such as other objectives, the placement of filters and other optical components, and sometimes also in the quality of the images in terms of clarity and focus. For those microscopes that are most commonly used in conjunction with FT-IR spectrometers, Varian and Thermo-Fisher employ the infinity-corrected type, while Bruker and PerkinElmer use non-infinity-corrected optics.

1.2.5
Transmission Microspectroscopy

Occasionally, transmission spectra of small inhomogeneous samples show the presence of artifacts. For example, the effect of scattering may cause symmetrical bands to lose their symmetry. Instead of having the symmetric shape of the absorption index spectrum, the stronger bands begin to take on the appearance of the

refractive index spectrum (this phenomenon is sometimes called the Christiansen effect [26]). Romeo *et al.* [27, 28] observed a second effect caused by light scattering while measuring the infrared spectrum of whole cells using FT-IR microspectroscopy. These authors showed that light scattering by the nucleus introduces a broad undulating spectral feature into the baseline of the spectrum, which they attributed to Mie-type scattering by the cell nucleus. Dielectric spheres are known to scatter electromagnetic radiation if the wavelength of the light is comparable to the sphere's size. The theory of this scattering process was first described (on a theoretical basis) by Mie [29], and has been nicely summarized by Romeo *et al.* [27, 28]. The same effect is visible in Raman spectroscopy, causing baseline ripples and perturbation of band intensities. In Raman spectroscopy the effect is sometimes termed 'morphology-dependent resonance'.

Mie theory assumes a spherical scattering particle in the field of a plane electromagnetic wave. The scattering cross-section Q_{sca} of a dielectric sphere interacting with a plane electromagnetic wave is given by a series expansion of the size parameter, ρ, and complicated expressions in the half-integer order Bessel (Ricatti–Bessel) functions of the first type and their complex equivalents (Hankel functions). The size parameter ρ is defined by

$$\rho = 2\pi r\, m_{\mathrm{o}}/\lambda \qquad\qquad (1.5)$$

where r is the radius of the sphere, λ the wavelength of the light, and m_{o} the ratio of the refractive indices between the sphere and the surroundings. The Bessel functions account for the undulating wavelength dependence of Mie scattering.

The angular dependence of Mie scattering is given by series expansions in the Legendre polynomials and their derivatives with respect to the scattering angle. While the exact solution of this problem is rather complex, Diem's group also used an approximate formula, which was first reported by Walstra [30]:

$$Q_{sca} = 2 - (4/\rho)\sin\rho + (4/\rho^2)(1-\cos\rho) \qquad\qquad (1.6)$$

where ρ is the size factor as defined above. This approximation reproduces the rigorous calculation to within 1%, and matches the spectra remarkably well. By using the approximate calculations, Romeo *et al.* were able to model the Mie scattering background satisfactorily, and corrected the distorted spectra by subtracting the modeled Mie background.

1.2.6
Attenuated Total Reflection Microspectroscopy

It can be seen from Equations 1.2 and 1.3 that the spatial resolution of infrared microspectroscopy can be improved by immersing the sample in a medium of high refractive index. This exactly what is done in attenuated total reflection (ATR) spectroscopy using a single-reflection hemispherical internal reflection element (IRE). For example, if a germanium ($n = 4.0$) hemispherical IRE is used, not only

(a)

(b)

Contracted beam size = $\dfrac{\text{Original beam size}}{\text{Refractive index of hemisphere}}$

Beam size does not change

Original beam size

Defocusing occurs

No defocusing occurs
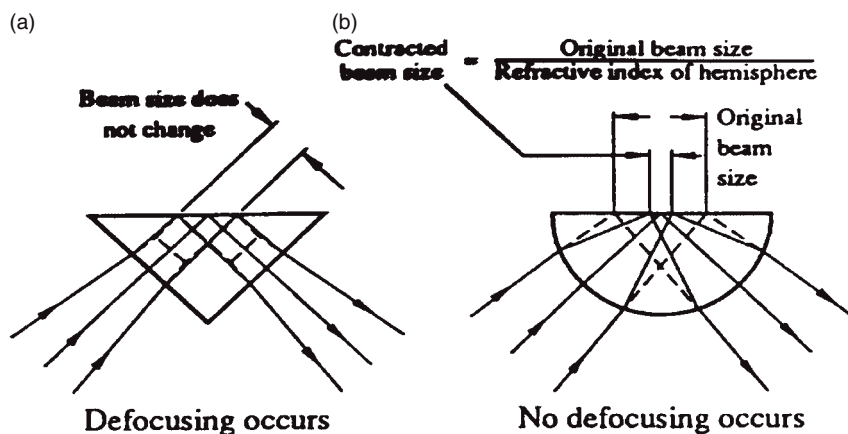
Figure 1.8 Beam focusing through (a) prismatic and (b) hemispherical internal reflection elements.

is an increase in the numerical aperture obtained (because of the increased refractive index of Ge), but the outer ray angle of incidence (which defines *NA*) is also increased, as the light is refracted inwards. The difference between the focusing that occurs with a triangular prism and a hemispherical IRE is seen in Figure 1.8a and b.

The first ATR accessory to make use of a single-reflection IRE with approximately hemispherical geometry was the Split Pea (Harrick Scientific), the usual image size of which is about 250 μm when used with a germanium IRE. Although germanium has the highest refractive index of infrared transparent materials (and therefore gives the greatest demagnification), it has the great disadvantage in that it is not transparent to visible light. As a result, sample alignment in some of the earlier devices was quite tricky. Since the introduction of the Split Pea, a number of analogous accessories have been introduced for ATR microspectroscopy, including several that have been explicitly designed to replace the objective in a standard infrared microscope. The Bruker Optics Hyperion, as shown in Figures 1.9 and 1.10, is just one example of a microscope designed for FT-IR microspectroscopy; analogous systems are available from a number of different vendors. Several manufacturers have designed accessories where the sample can be aligned without being in contact with the IRE. When the appropriate region has been selected, the IRE is moved into place. With the Bruker Hyperion, the tip of the internal reflection element is 100 μm in linear dimension to achieve high spatial resolution; this instrument is equipped with an electronic pressure sensor to ensure good contact with the sample, which is particularly important for mapping by ATR microscopy. The IRE is spring-loaded to avoid damage, and there are five different pressure steps to allow optimal contact for hard and soft samples.

Like germanium, silicon also has a fairly high refractive index ($n = 3.4$). Silicon is rarely used for the fabrication of large IREs (for which the optical path may be

(a)

(b)

IRE
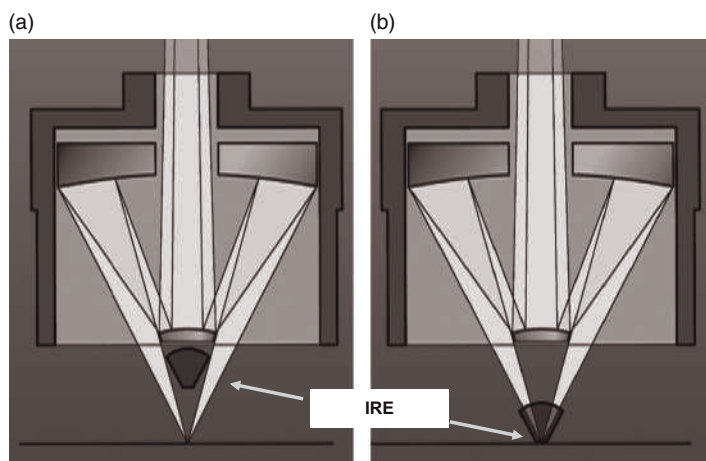
Figure 1.9 Optical schematic of the Bruker Optics ATR objective used in (a) alignment mode and (b) spectral acquisition mode. Illustration courtesy of Bruker Optics.

Figure 1.10 Photograph of the Bruker Optics ATR objective. Illustration courtesy of Bruker Optics.

several centimeters) because the presence of trace impurities leads to excessive absorption of the radiation below about $1200\,cm^{-1}$. With the very short path through the IRE installed in a microscope objective, however, this is no longer a problem. Thus, either silicon or germanium can be used productively as the IRE in an ATR objective.
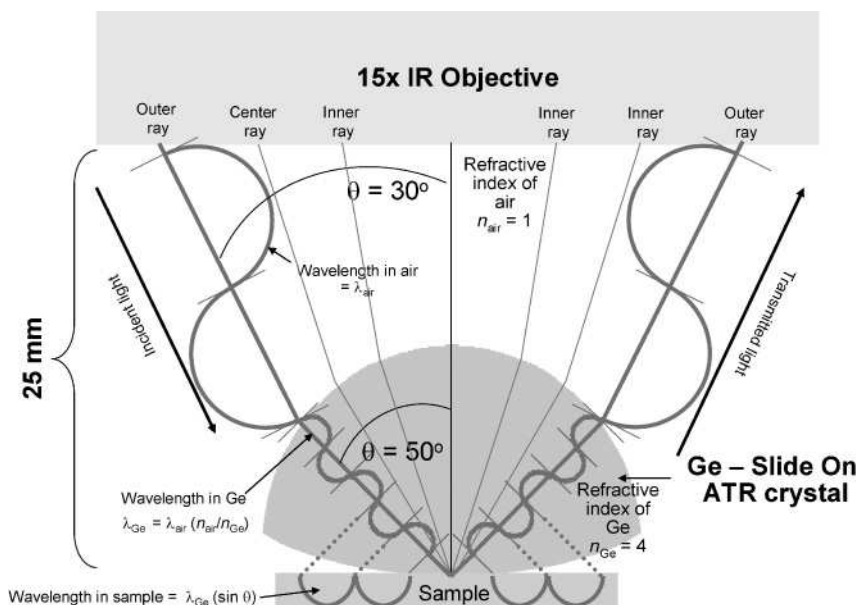
Figure 1.11 Schematic of Varian's Ge slide-on ATR objective, showing how the spatial resolution is enhanced by increasing the refraction index of the medium to 4 with Ge and increasing the outer ray angle of incidence to 50°, resulting in a numerical aperture of 3.1. Illustration courtesy of Varian Corporation.

The increase in numerical aperture achieved through the use of hemispherical IREs can be seen more quantitatively by considering the design of Varian's slide-on Ge ATR accessory, shown in Figure 1.11. On refraction, the outer ray angle which is normally 30° (for a *NA* of 0.5) is increased to 50° after refraction through the Ge IRE. In the Varian design, the underside of the hemisphere (which is in contact with the sample) has a relatively large radius of curvature, such that over the field-of-view of the IRE (~$100 \times 100\,\mu m$), it is effectively flat.

1.3
Raman Microspectroscopy and Mapping

1.3.1
Introduction to Raman Microspectroscopy

In principle, Raman microspectroscopy is attractive because the practical diffraction limit is on the order of the excitation wavelength, which is about 10-fold smaller for Raman spectroscopy with a visible laser than for mid-IR spectroscopy. It is therefore possible to focus visible or NIR laser light to much smaller spot

sizes (~1 μm or less) than may be examined by mid-IR radiation. Until the mid 1980s, however, Raman spectrometry was a time-consuming and relatively unpopular technique for the characterization of both macro- and micro-samples for the following reasons:

- The intensities of strong bands in Raman spectra are usually at least 10^8-fold weaker than the intensity of the incident monochromatic beam.

- When photomultiplier tubes (PMTs) were used for the detection of Raman spectra, high-power gas lasers (e.g., Ar^+) were required to yield enough photons for the measurement of Raman spectra in less than 1 h; the power supplies for the early versions of these lasers generated so much heat that they often required water cooling.

- Inefficient double and triple monochromators were required to eliminate stray light from the Rayleigh line.

- No multiplex or multichannel technique was available for the measurement of Raman spectra; hence, the instruments were based on scanning monochromators with a single PMT detector.

- Many 'real-world' samples fluoresce when illuminated with visible light, especially green light from a frequency-doubled neodymium-doped yttrium aluminum garnet (Nd-YAG) laser at 532 nm or from an argon ion laser at 488 or 514.5 nm.

Although nothing can be done to make the Raman cross-section of vibrational bands any greater without the application of techniques such as resonance Raman spectroscopy or surface-enhanced Raman scattering, several important technological developments have led to the design of today's truly powerful Raman spectrometers. These included (in no particular historical order) the development of:

- Highly efficient notch filters that eliminate the Rayleigh line and transmit both the Stokes- and anti-Stokes Raman bands, or edge filters that transmit only the Stokes Raman bands and block all shorter-wavelength radiation.

- Small, efficient single monochromators based on concave holographic gratings, transmission holographic gratings or standard Czerny–Turner monochromators in combination with a notch filter.

- 'Scientific' CCD array detectors with quantum efficiencies close to 100%.

- Visible lasers operating at much lower input power than the earlier gas lasers; the most important of these is the He–Ne laser (632.8 nm), while argon ion (488.0 and 514.5 nm) and krypton lasers (647.1, 568.2 and 530.9 nm) are also useful for Raman spectroscopy.

- Diode lasers emitting at 785 and 840 nm, which minimize fluorescence and are still compatible with silicon-based CCD detectors over much of the Raman spectrum.

- Diode-pumped Nd : YAG lasers emitting at 1064 nm: with a laser operating at this long wavelength, fluorescence from the sample is often minimized and sometimes eliminated.

- The frequency-doubled Nd : YAG laser emitting at 532 nm.

- The recent development of blue/green diode lasers operating at, for example, 472 nm.

- FT Raman spectrometry, which was needed because the Raman spectrum-generated 1064 nm radiation was at too long a wavelength for silicon-based CCD detectors.

- Efficient fiber-optic probes.

The first report of the design and testing of an FT-Raman spectrometer was by Hirschfeld and Chase in 1986 [31], and this became available commercially during the following year. With these instruments, the sample is illuminated with 1064-nm radiation from a Nd : YAG laser, while the Rayleigh- and Raman-scattered light is modulated by a two-beam interferometer. After removal of the Rayleigh-scattered radiation by a notch or edge filter, the Raman interferogram is detected using either an indium gallium arsenide (InGaAs) or germanium detector. Within another year, however, Raman spectrometers based on a polychromator and a CCD array detector were also brought onto the market. These instruments were compatible with essentially any laser that led to the generation of a Raman spectrum at shorter wavelength than the 1100 nm cut-off of silicon-based CCD detectors. Thus, instruments became available with, *inter alia*, a doubled Nd : YAG laser (532 nm), a low-power He–Ne laser (632.8 nm) or NIR diode lasers, of which 785 nm and 840 nm were the most common wavelengths. Neither of these diode lasers is capable of measuring the complete Raman spectrum. For example, if an 840 nm (11 900 cm^{-1}) diode laser is used, the Raman spectrum beyond about 2500 cm^{-1} is beyond the cut-off of a silicon CCD.

These FT-Raman and CCD-Raman spectrometers revolutionized Raman spectroscopy such that, within the space of about five years, about ten different Raman spectrometers based on multiplex and multichannel technologies had been introduced commercially [32, 33]. Several of the CCD-Raman spectrometers were either designed for, or could be readily modified for, microspectroscopy. Although FT-Raman microspectrometers have been reported (e.g., Ref. [34]), they have not proved very popular for three reasons:

- Safety: the 1064 nm beam of a FT-Raman spectrometer is high powered, completely invisible and quite dangerous.

- When the beam from a Nd : YAG laser is focused on a sample that absorbs 1064 nm radiation, even the weakest absorption band will cause significant heating. In fact, it is quite common for samples to ignite, or at least to generate background blackbody radiation.

- FT-Raman spectroscopy is relatively insensitive compared to dispersive Raman spectroscopy, due to the longer wavelength of excitation and the poor noise performance of detectors in the NIR. This means that FT-Raman microscopes lack the sensitivity to analyze small samples unless high laser powers are employed, which leads to the problems noted above.

In practice, therefore, CCD-Raman spectrometers have proved to be far more successful for Raman microspectroscopy than FT-Raman spectrometers, and most instruments are based on this concept.

Raman microspectroscopy was not a completely new concept. In 1966, Delhaye and Migeon [35] showed that a laser beam could be tightly focused at a sample, and that Raman-scattered light could be collected and transferred to a spectrometer, with minimal loss. Their calculations showed that the increased irradiance more than compensated for the decrease in the size of the irradiated volume. The first Raman microscope was reported by Delhaye and Dhamelincourt in 1975 [36], and an instrument based on these principles (the MOLE) was introduced by Jobin Yvon at about the same time. However, the optical scheme used for imaging, which employed global illumination, was inefficient and it was not until the advent of CCD-Raman spectrometers that the advantages of Raman microscopy became apparent.

Arguably the most important advantage of many microscopes used for Raman microspectroscopy is the fact that they have a confocal design. In such a design (see Figure 1.12) the laser beam is first focused on a small aperture (to clean up the beam profile and present a diffraction-limited source), and then refocused by an objective lens with a large numerical aperture onto a small (ideally diffraction-limited) focal volume within the sample. A mixture of the Raman- and Rayleigh-scattered light from the illuminated spot is then collected by the objective lens. The high *NA* of these optics allows the light to be collected over a solid angle of almost a full hemisphere. An objective with a *NA*-value of 0.95 collects about 70% of the radiation emitted over 2π steradians. A dichroic beamsplitter (typically a
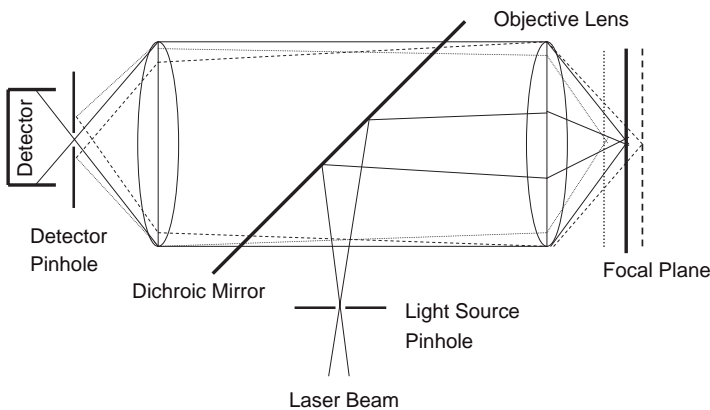
Figure 1.12 Schematic representation of the optics of a confocal microscope.

notch filter or an edge filter) reflects the radiation from the Rayleigh line and transmits the Stokes-shifted Raman-scattered radiation at longer wavelength. After passing through a pinhole, the Raman-scattered light is passed into the monochromator and the intensity at each wavelength is measured. The small spot enables the image to be transferred to the spectrometer though the narrow (typically ca. 100 µm) entrance slit with a minimal loss in energy. Today, several Raman microspectrometers employ confocal optics, which provide the capability to produce blur-free images of thick samples at various depths. It may be noted, however, that spherical aberration limits sampling with diffraction-limited resolution at depths much greater than 10 µm.

As seen in Figure 1.12, the detector pinhole obstructs the so-called out-of-focus (or out-of-plane) light, especially light from adjacent spatial regions and fluorescent emission not originating from the focal plane of the objective lens. Light rays from below the focal plane come to a focus before reaching the detector pinhole, and then expand out so that most of the rays are physically blocked from reaching the detector by the pinhole. In the same way, light from above the focal plane is focused behind the detector pinhole, so that most of this light is also vignetted by the pinhole and is not detected. However, all the light from the illuminated focus (solid lines) is imaged at the pinhole and passed to the detector. The detected light originating from an illuminated volume element within the specimen is then focused on the entrance slit of a polychromator and the spectrum measured using a CCD detector. As the out-of-focus rays from above and below the focal plane are largely removed, sharper images are measured than can be acquired from conventional (non-confocal) microscopy techniques. Mapping is accomplished by moving the sample by small amounts after each spectrum has been recorded.

Several modes of operation are available in state-of-the-art confocal Raman microspectroscopy, including the measurement of samples with a spatial resolution of less than 1 µm, depth profiling and line mapping. LaPlant and Ben-Amotz have provided a detailed description of the design and construction of a confocal Raman microspectrometer [37], and several instruments are now available commercially. In the case of the HORIBA Jobin Yvon LabRAM ARAMIS Raman spectrometer (see Figure 1.13), up to four lasers (three internal, one external), four gratings and four notch filters may be automatically switched in order to optimize the performance for a given sample, as illustrated in Figure 1.14. While not every sample is an efficient Raman scatterer, this instrument ensures that many types of sample can be routinely mapped using fast point acquisitions.

Several companies, including Horiba, Renishaw and Witec, market Raman spectrometers with confocal optical configurations. The WITec alpha300 R confocal Raman microscope differs from other confocal Raman microspectrometers in that it has been designed especially for fast microspectroscopy. The data acquisition time for an entire spectrum can be less than 1 ms, which allows Raman mapping of over 10 000 spectra in less than one minute when the Raman signal is adequate. These data sets can already be evaluated during data acquisition by using filters. For example, the integrated intensities of certain bands of interest may be calculated or the position or full width at half maximum of the bands may

Figure 1.13 The HORIBA Jobin Yvon LabRAM ARAMIS Raman spectrometer. Illustration courtesy of Horiba Jobin-Yvon Corporation.
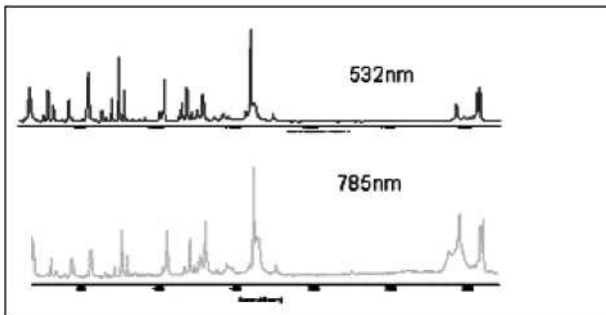
Figure 1.14 Spectra of aspirin measured with seconds of each other using a frequency-doubled Nd : YAG laser (532 nm) and a semiconductor diode laser (785 nm). Illustration courtesy of Horiba Jobin-Yvon Corporation.

be evaluated. Band fitting to Gaussian or Lorenzian shapes, as well as various other fitting algorithms, can also be applied to the data set. By using these filters, several three-dimensional (3-D) data sets that can be displayed as images are created from the four-dimensional hyperspectral data.

The WITec alpha300 R confocal Raman microscope can be upgraded to perform atomic force microscopy (AFM), tip-enhanced Raman spectrometry and near-field scanning optical microscopy, and is arguably the most versatile instrument for Raman microspectroscopy available today.

1.3.2
CCD Detectors

The quantum efficiency of contemporary array detectors can be remarkably high – in excess of 90% in the case of back-illuminated CCDs. The two main sources of noise for CCD cameras are:

- A dark current, which is largely caused by thermal emission and is usually reduced to a negligibly low level by thermoelectrically cooling the detector below −60 °C.

- Readout noise, which is the number of electrons introduced per pixel into the final signal upon the readout of the device and is caused by: (i) a lack of repeatability of the conversion from an analogue signal to a digital number; and (ii) the introduction of spurious electrons into the camera electronics, leading to unwanted random fluctuations in the output. Readout noise, which is usually given in terms of electrons, is dependent on the readout rate; typical values are 5–10 electrons for a 50 kHz readout rate to ~30 electrons for a 2.5 MHz readout rate.

The combination of these two random effects produces an uncertainty in the final output value for each pixel. In the output of the CCD image, readout noise is added into every pixel each time the array is read out. This means that a CCD with a readout noise of 30 electrons will, on average, contain 30 extra electrons of charge in each pixel upon readout. As a consequence, CCDs with a high readout noise (more than 80–100 electrons) are not very good to use if a sequence of short exposure frames is co-added instead of using one long exposure. However, for modern scientific CCDs, readout noise values are very low, in the range of 10 electrons per pixel per read or less. Ideally, the limiting noise source in any Raman spectrometer should be photon shot noise. Because photons follow Poisson statistics, for a given signal the uncertainty is the square root of the signals in electrons. In this case, the SNR of many Raman spectra can be remarkably high, even though the signal is so low. For example, even if only 100 photons are detected (converted to electrons), the SNR is still 10 – provided that the only noise source is photon shot noise.

For Raman mapping measurements, the readout time per pixel must be very short. For example, if an image consisting of 128 pixels per line and 128 lines is acquired with an integration time of 1 s per pixel, then the total acquisition time will be a little over 4.5 h. Reducing the readout time to 100 ms per pixel decreases the measurement time to 27 min. A further 10-fold reduction in the readout rate decreases the acquisition time to less than 3 min. The latter situation would allow hundreds of images to be acquired per day, instead of just one or two. Unfortunately, this condition is not readily achievable in practice because the faster the readout time of the detector electronics, the noisier is the readout amplifier.

Hollricher and Ibach [38] have described how the SNR of Raman spectra can be increased through the use of an electron multiplying CCD (EMCCD). This device is a normal CCD with an additional readout register that is driven with a significantly higher clock voltage than a normal CCD readout register. The effect of the high clock voltage is to effect an electron multiplication through impact ionization. In practice, the gain may be increased by a factor of up to 1000 in this way, so that the photon shot noise is always much greater than the readout noise. The SNR of the signal from the CH_2 stretching band of poly(methyl methacrylate) (PMMA) is shown as a function of the gain in Figure 1.15. The improved SNR allows superb
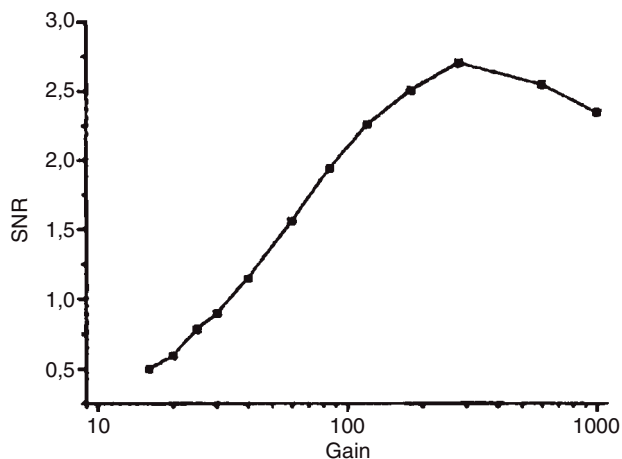
Figure 1.15 Signal-to-noise ratio of the CH_2 symmetric stretching band of PMMA plotted against the gain of the EMCCD. Reproduced with permission from Ref. [38].

images to be acquired from Raman mapping experiments in a remarkably short time. For example, a 200×200 pixel color-coded image of a 7.1 nm-thick layer of PMMA contaminated with 4.2 nm-diameter fibers acquired with a WITec alpha300R confocal Raman microscope is shown in Figure 1.16. The integration time was 7 ms per spectrum, and the total acquisition time 5.4 min. This fast response makes it feasible to map relatively large areas in minutes or hours, and is critical for practical mapping applications.

Another source of 'noise' in spectra measured using a CCD is caused by the pixel-to-pixel variation in the quantum efficiency of neighboring pixels. This variation can be corrected by illuminating the detector array with a uniform light source and measuring the signal from each pixel. Once the relative response of each pixel has been determined, a correction known as a *flat field correction* can be applied.

Despite all efforts to minimize the noise in Raman spectra measured in the short times needed for mapping measurements, it is rare that the spectroscopist would not be more satisfied if the SNR were higher. Cai *et al.* [39] reported a more powerful way of reducing the noise in Raman spectra a below that achievable by Savitzky–Golay smoothing with minimal band broadening [40]. In their approach, multiresolution wavelet transformation and block thresholding was used to both suppress the background caused by fluorescence and to reduce the noise without a significant loss in spectral resolution.

1.3.3
Spatial Resolution

For diffraction-limited microscopy, it may be thought that the image should be focused on the CCD such that the Airy disk fills one pixel. However, Adar *et al.* [41]
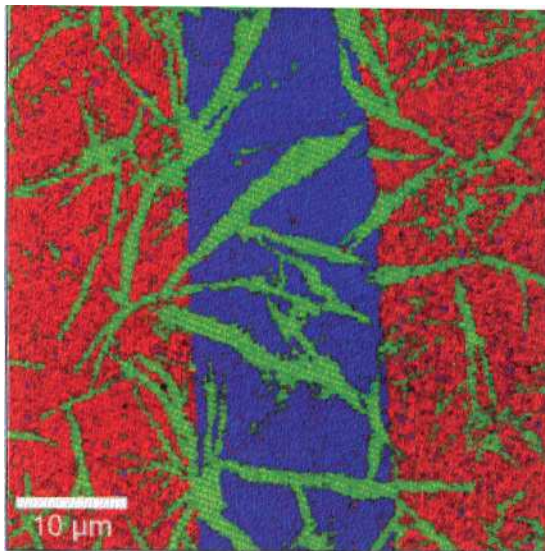
Figure 1.16 Color-coded confocal Raman map of a 7.1 nm-thick PMMA layer (red) and a 4.2 nm contaminant layer (green) on glass (blue). The map was computed from 200×200 spectra, with an integration time of 7 ms per spectrum, for a total acquisition time of 5.4 min. Reproduced with permission from Ref. [38].

demonstrated that image quality could be improved significantly if the sample step is much smaller than the spatial resolution of the measurement. As an example, Figure 1.17a shows the Raman map of an 8 μm polystyrene bead on a silicon substrate recorded with a 100× objective with steps of 1.0, 0.5 and 0.1 μm. The visual image recorded through a standard optical microscope is shown for comparison. Clearly, reconstructing the image from data taken with steps smaller than the resolution given by the Rayleigh criterion gives a higher quality Raman image.

The strength of the objective is, of course, also important, as it controls the numerical aperture. Figure 1.18a shows Raman maps of five 5.18 μm polystyrene spheres recorded with 100×, 50× and 20× objectives, with the increment between data points being 0.2 μm; Figure 1.18b shows the line profiles across the two beads at the top right of these images.

Information can also be collected from different focal planes by raising or lowering the microscope stage. The computer can generate a 3-D picture of a specimen by assembling a stack of these 2-D images from successive focal planes. Some care is needed in the interpretation of the results obtained by depth profiling with a confocal Raman microscope, however. For example, Everall *et al.* [24] have shown that when using metallurgical objectives, which are typically supplied as standard with confocal Raman microscopes, the focus is both much deeper than might be first thought, and is also blurred due to spherical aberration (see Figure 1.19). Even

(a)

(b)
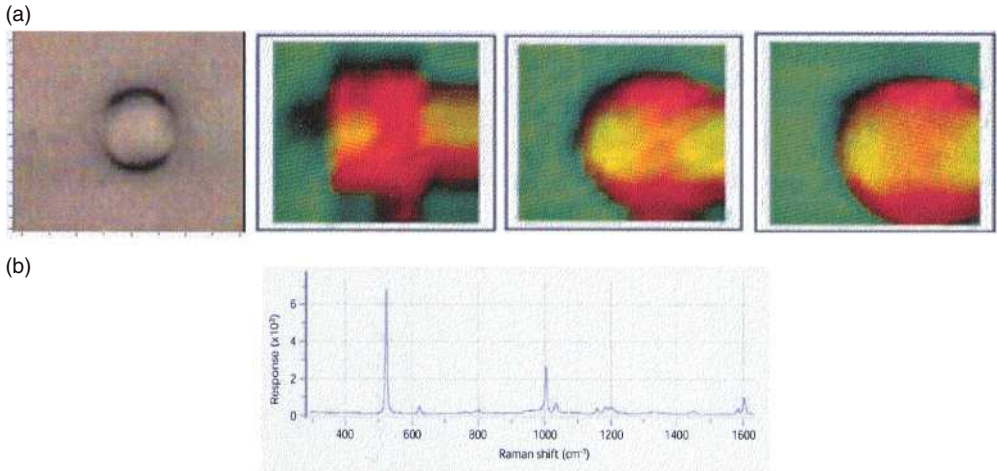
Figure 1.17 (a) Visual image of a 1 μm-diameter polystyrene bead. The lower images show Raman images of the bead, recorded with a 100× (*NA* = 0.95) infinity-corrected microscope objective at increments of (left to right) 1.0, 0.5 and 0.1 μm per step, respectively; (b) Raman spectrum measured from the center of one of these beads. Reproduced with permission from Ref. [41].

in the absence of spherical aberration, Everall has shown that bands originating from sample regions far above and below the optimum focal plane can still contribute significantly to the spectrum [42]. He demonstrated this by investigating the Raman spectra of a 20 μm-thick layer of polyethylene (PE) over a 100 μm-thick sheet of poly(ethylene terephthalate) (PET). The spectra measured at different depths, including locating the focus 10 μm above the sample, are shown in Figure 1.20. It is clear that signals from the PET contribute significantly to the spectrum, even when focused in or well above the PE. Everall demonstrated a similar effect when scanning laterally across the same sample. These results were found because, for every point within the entire illuminated volume of a transparent sample (not just the beam waist), there are some rays that can reach the detector. When all of these paths are added together, there can be a significant signal originating from those parts of the sample that are out of focus. Macdonald and Vaughn have developed a simple mathematical model to quantify the contribution of 'out of focus' regions of the sample [43].

1.3.4
Tip-Enhanced Raman Spectroscopy

By using the techniques discussed in the previous sections of this chapter, it can be seen that the spatial resolution achievable by infrared or Raman microspectroscopy is governed by the diffraction limit shown in Equation 1.3. It is possible to
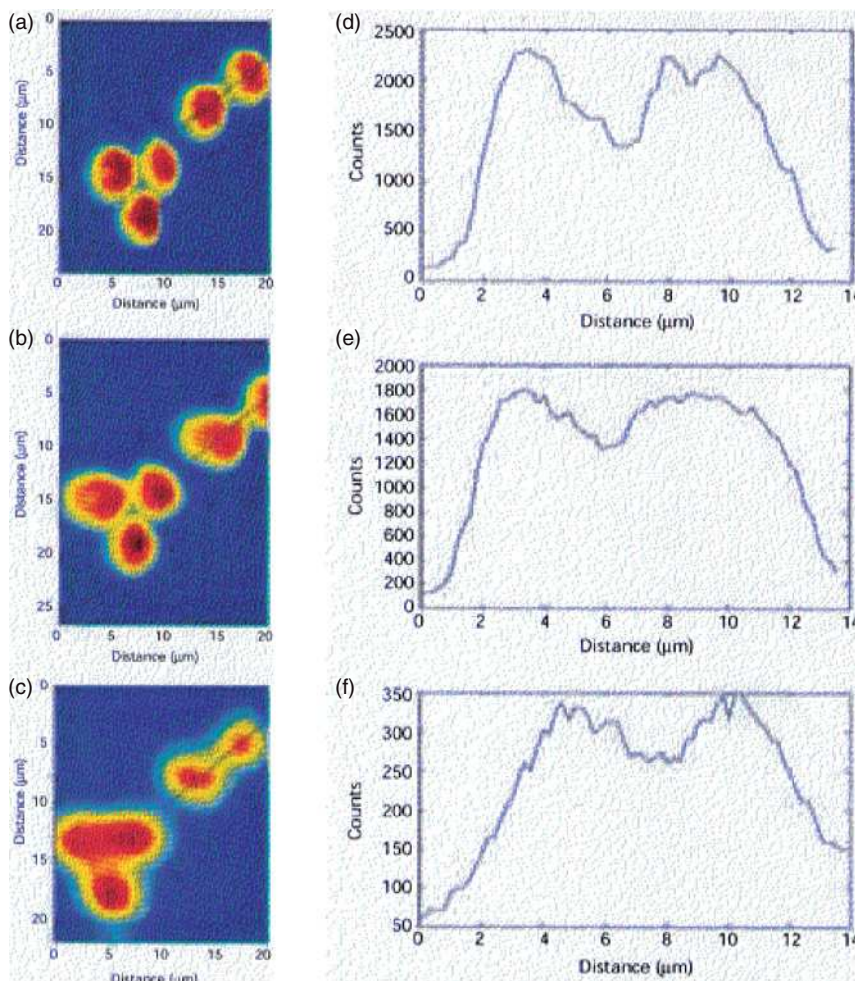
Figure 1.18 (a–c) Raman maps of 5.18 µm-diameter polystyrene beads recorded with 100×, 50× and 20× objectives, respectively. Increments between data points were 0.2 µm for all three images; (d–f) Line profiles of the two beads at the upper right in panels (a–c).Reproduced with permission from Ref. [41].

improve on the diffraction limit by near-field scanning optical microscopy (NSOM), although most of the vibrational NSOM techniques are currently in the developmental stage (see Chapter 2). However, there is one technique – known as tip-enhanced Raman spectroscopy (TERS) – whereby the spatial resolution of Raman spectroscopy can be reduced significantly below the diffraction limit [44]. TERS is a hybrid system that combines the nanometer resolution afforded by scanning probe microscopy (e.g., AFM) with the molecular specificity of surface-enhanced
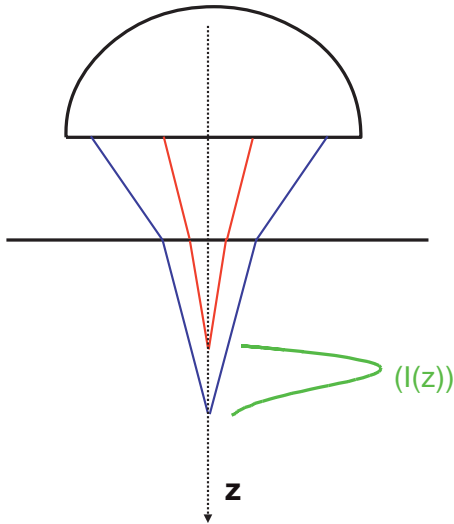
Figure 1.19 Schematic diagram showing how the effect of refraction leads to an increase in the depth of field for Raman microscopy. Illustration courtesy of Dr Neil Everall, Measurement Science Group, Intertek Corporation.
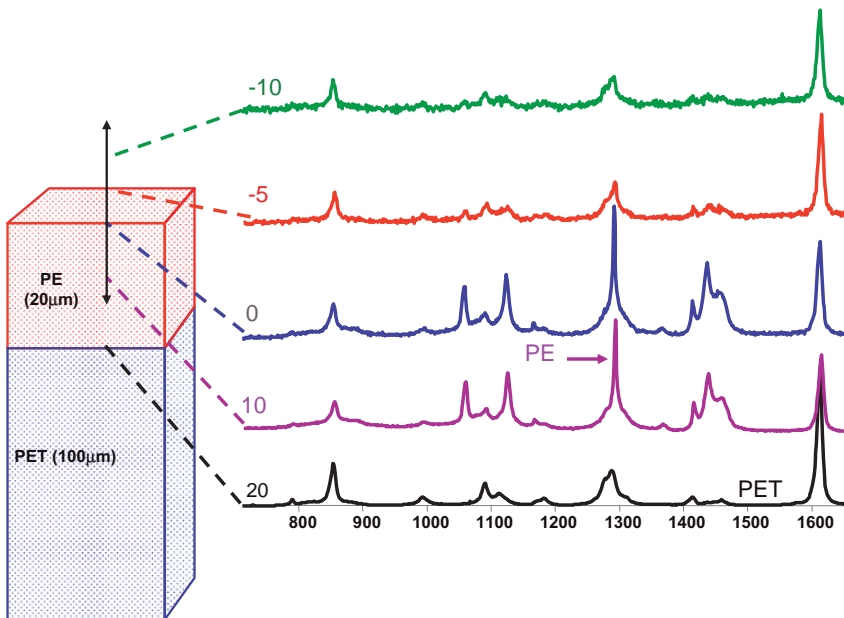
Figure 1.20 Spectra measured by raising the level of a polymer laminate sample consisting of a 100 μm-thick layer of poly(ethylene terephthalate) (PET) under a 20 μm-thick layer of poly(ethylene) (PE). The strongest bands in the Raman spectra of PE and PET are marked with arrows. Illustration courtesy of Dr Neil Everall, Measurement Science Group, Intertek Corporation.

Raman scattering (SERS). It is well known that the Raman spectrum of species with a few nanometers of roughened silver or gold surfaces is enhanced by at least four orders of magnitude. The primary enhancement in SERS arises from the electric field of the radiation being greatly increased because of resonance between the wavelength of the illumination laser and the nearby Raman signals and the wavelengths of the surface plasmon resonance of the metal nanostructures, λ_{SPR}.

It has been shown that localized plasmon polaritons in the region of sharp metal tips act in an analogous fashion, giving rise to TERS. In one mode of operation, TERS employs a sharp metal tip, which is illuminated from the outside to create a localized light source [45]. Alternatively, silver nanoparticles have been deposited on silica or titania surfaces and a silicon tip is used [46, 47]. That these tips are not easy to prepare most likely accounts for the fact that TERS is not yet widely used. Nonetheless, preliminary results have indicated the feasibility of detecting and characterizing single molecules [45] with atomic site sensitivity [48]. The investigation of bacterial surfaces [49] and single-walled carbon nanotubes [50] has also recently been reported. Although these early results are very promising, TERS is not yet widely used and will not be described in any great depth in this chapter (although a more detailed account can be found in Chapter 2).

1.4
Near-Infrared Hyperspectral Imaging

Following the above introduction to the types of microscopes used for single-point sampling and sample mapping, the instrumentation used for hyperspectral imaging by vibrational spectrometry will now be described. NIR imaging instruments will be introduced first, as these are the simplest in design. Raman imaging spectrometers will then be discussed, as these bear considerable similarity to their NIR counterparts. The instrumentation for mid-IR imaging will be described subsequently, as their operating principles are somewhat different to those of NIR and Raman imaging systems. Finally, terahertz imaging, which is based on a completely different principle to any of the other types of imaging instruments will be introduced.

Perhaps the simplest type of instrument for NIR hyperspectral imaging spectrometer is that originally developed by Spectral Dimensions, Inc. (Olney, MD, USA, now Malvern Instruments.) In this instrument, the radiation from a broadband source of NIR radiation (a simple tungsten or quartz–tungsten–halogen lamp) is passed through a liquid crystal tunable filter (LCTF) so that a narrow region of the NIR spectrum is isolated. A typical LCTF is constructed from an interwoven stack of Lyot stages (linear polarizers and liquid-crystal variable retarders mounted on birefringent quartz crystals), usually mounted in a temperature-controlled housing. A single Lyot stage of an LCTF system is shown in Figure 1.21. Varying the voltage applied to the liquid crystals shifts the pass band in less than 1 ms, without any mechanical motion or vibration of the optics. Thus, the filter can be tuned an almost infinite number of times as there is no wear and tear.
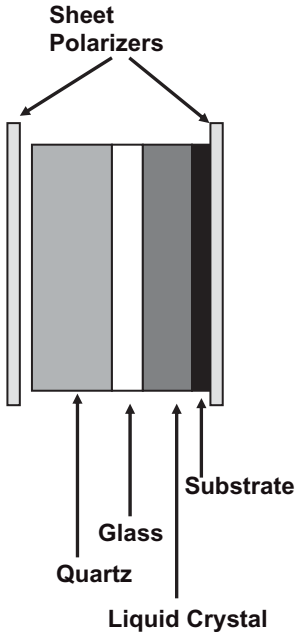
Figure 1.21 A typical Lyot stage of a liquid crystal tunable filter (LCTF) system.

The operation of an LCTF may be understood by considering a simplified Lyot filter stack, in which $(N+1)$ polarizers are separated by N layers of liquid crystals sandwiched between birefringent crystals. The optical retardation, R nm, introduced by birefringent crystals is dependent on the thickness of the crystal, d nm, and the difference between the refractive index of the ordinary ray, n_o, and the extraordinary ray, n_e, at the wavelength of interest:

$$R = d(n_e - n_o) \qquad (1.7)$$

The velocities of the extraordinary and ordinary ray differ, and these emerge from the stack with a phase delay, Γ radians, that is dependent upon the wavelength, λ, of the radiation:

$$\Gamma = \frac{2\pi R}{\lambda} \qquad (1.8)$$

The transmittance of the crystal, T, is given by:

$$T = 0.5\cos^2(\Gamma/2) \qquad (1.9)$$

In a typical Lyot filter, crystals are often selected so that transmission has its maximum value at the wavelength determined by the thickest crystal retarder, with

other stages in the filter serving to block the transmission of unwanted wavelengths. The spectral region passed by the LCTF is dependent upon the choice of polarizer, the optical coating and the liquid crystal characteristics (nematic, cholesteric, smectic, etc.) In practice, a Lyot LCTF may have as many as 11 polarizers and 10 liquid crystalline layers, and is sometimes equipped with an internal microprocessor to tune all of the stages.

Wavelength scanning in NIR hyperspectral imaging spectrometers has also been accomplished with both a scanning monochromator and an acousto-optic tunable filter (AOTF.) AOTFs are also frequently used in confocal fluorescence microscopes. AOTFs are electro-optical devices that function as electronically tunable filters and rely on a birefringent crystal, the optical properties of which vary upon interaction of the crystal with an acoustic wave. The resulting compression and rarefaction of the crystal give it the properties of a diffraction grating. Changes in the acoustic frequency alter the grating constant, which enables the wavelength to be tuned very rapidly. The switching time is limited only by the acoustic transit time across the crystal, and is rarely greater than 50 μs. AOTFs designed for operation in the NIR region typically consist of an optically anisotropic tellurium dioxide crystal to which a piezoelectric transducer is bonded. In response to the application of an oscillating radiofrequency electrical signal, the transducer generates a high-frequency acoustic wave that propagates into the crystal. The alternating ultrasonic acoustic wave induces a periodic redistribution of the refractive index through the crystal, which then acts as a transmission diffraction grating. Changing the frequency of the transducer signal applied to the crystal alters the period of the refractive index variation and, therefore, the angle through which the radiation is diffracted, and hence the wavelength band that reaches the detector. The design parameters that affect resolution include the dispersion constant of the crystalline material (related to degree of birefringence), the incidence angle and the acousto-optic interaction length. The relative intensity of the diffracted beam is determined by the amplitude (power) of the signal applied to the crystal and by the widths of the entrance and exit slits of the monochromator.

One of the more important parameters governing which of these wavelength selection devices to use is their bandpass – that is, the full-width at half height (FWHH) of their transmittance window. The typical bandpass of a LCTF is 5 nm. As the FWHH of most bands in the NIR spectrum is greater than 10 nm, a bandpass of 5 nm is more than adequate for NIR hyperspectral imaging. The LCTF has a far higher optical throughput than a monochromator operated at 5 nm resolution (although when the size of the sample being examined is very small, as it is in any microscopic measurement, the potential throughput advantage is rarely met in practice).

The bandpass of a typical AOTF ranges from several nanometers to tens of nanometers for the visible and NIR spectral regions. This resolution is suitable for fluorescence spectroscopy where bands are very broad, and is just adequate for Raman hyperspectral imaging, albeit with lower resolution than may be achieved with a monochromator (see Section 1.5). A NIR spectrometer based on an AOTF has also been sold commercially. However, the transmission of these devices for

NIR hyperspectral imaging is somewhat poorer than that of LCTFs, and they degrade the image quality slightly more than LCTFs. The optical efficiency of monochromators for NIR hyperspectral imaging is poorer than that of both LCTFs and AOTFs. Thus, despite the fact that the FWHH of the pass-band of a mono-chromator can be made much narrower than that of LCTFs and AOTFs, the highest performance for NIR microspectroscopy is usually found when wave-length selection is accomplished through the use of one of these devices rather than a monochromator.

The NIR hyperspectral imaging spectrometers designed by Malvern Instru-ments are equipped with a Stirling-engine-cooled indium antimonide (InSb) FPA detector with 320 pixels in one dimension and 256 in the other (total 81 920 pixels) that operates in the range 1200 to 2450 nm. Wavelength tuning is achieved by an LCTF, such that the entire spectral range can be covered in 2 min. Alternatively, as described above, if the signal from just a few wavelengths is all that needs to be measured, the LCTF allows rapid switching between a few selected wavelengths and the measurement is over in a few seconds. A short-wavelength alternative instrument is also available that is equipped with an InGaAs FPA detector that operates in the range from 950 to 1720 nm.

Because this instrument is designed for NIR operation, it is possible to use a microscope with refractive optics. In the case of the Malvern Instruments system, a refractive objective that has 1× magnification is used. With this lens, the sample is imaged directly onto the FPA detector. This objective can be easily removed and objectives with higher (micro mode) or lower (macro mode) magnification installed. The initial alignment of the sample is performed manually, although if a series of samples is to be measured then a programmable sample stage enables the sequen-tial analysis of multiple samples.

It is probably true to say that instruments for NIR hyperspectral imaging are more versatile and rugged than corresponding instruments used to measure mid-IR and Raman spectra. However, they have two disadvantages. The first problem is that the absorptivities of the overtone and combination bands in the NIR spec-trum are far weaker than those of corresponding fundamentals from which they are derived. For measurements in the transmission mode, the ideal sample thick-ness is one that yields a low-noise spectrum with bands that are strong enough to allow rapid identification or quantification. For mid-IR spectrometry, this thick-ness is about 10 μm. As the center wavelength of mid-IR spectra is about 5 μm, the sample thickness is approximately equal to the smallest dimension in the xy plane that can be observed – that is, the diffraction limit when NA is approximately equal to 0.6. For conventional NIR spectrometry (1200–2450 nm), on the other hand, the absorptivities of the stronger bands are an order of magnitude less than the stronger fundamentals from which they are derived, and so the sample thick-ness should be at least 100 μm. However, the diffraction limited spatial resolution for NIR measurements is less than 3 μm if optics with a NA-value of 0.6 are used. Thus, even though the ultimate spatial resolution is, in principle, determined by the optics of the spectrometer, in practice this resolution is never achievable because the thickness of the sample means that the diameter of the beam waist

at the top or bottom surface of the sample is larger than the diffraction-limited spatial resolution.

For short-wavelength NIR spectra (950–1720 nm), where the absorption bands are caused by transitions to the third or fourth vibrational states of C–H, N–H and O–H stretching modes, along with weak combination bands, the situation is even worse because bands are so weak that the sample thickness must be increased to about 500 μm, even though the diffraction limit is less than 2 μm. It is at least in part for this reason that NIR hyperspectral imaging is rarely used for measurements with very high spatial resolution. Thus, the standard objective of the Malvern Instruments imaging spectrometer, for example, is a refractive lens with 1× magnification and a low numerical aperture.

The second disadvantage of NIR hyperspectral imaging is more subtle, as it is only evident for measurements of powders. Perhaps the most common application of NIR hyperspectral imaging is in the characterization of intact pharmaceutical tablets by DR spectrometry. These measurements have a significant limitation in terms of their spatial resolution caused by the effect of light scattering. Photon time-of-flight measurements [51–57] have shown that photons in diffuse transmission and reflection measurements emerge from compacted powdered samples (e.g., pharmaceutical tablets) in a time that is much greater than would be expected if no scattering had taken place. In analogous measurements made by mid-IR DR spectrometry, Averett and Griffiths [58] estimated that the average path traveled by mid-infrared photons through very weakly absorbing samples is at least 100 particles, strongly implying that photons do not emerge from the same point at which they enter the sample. The greater the particle size, the more strongly a given particle will absorb at a given wavelength. Similarly, the greater is the scattering coefficient, the fewer particles are encountered by photons in a DR measurement and the better the spatial resolution. For scattering samples, this effect clearly has a highly deleterious effect on spatial resolution. In DR measurements, photons are extensively scattered on entering the sample, passing through several particles (often much more than ten) before re-emerging from the top surface.

The effect of scattering on spatial resolution in DR/NIR imaging has recently been discussed by Hudak *et al.* [59]. These authors measured the DR spectrum of polystyrene powder, but then placed a clear polystyrene window of known thickness over the sample and remeasured the spectrum. From the increase in the intensity of the polystyrene bands, it was possible to show that the effective path-length through the powder was 1 mm (±~50%). Yet, the more intense the band measured, the shorter was the path-length calculated (although the authors did not recognize the fact that the path-length varied inversely with the absorptivity). The group then devised a way to correlate the effective path-length with the sampling volume, by using a random walk model to estimate the volume sampled by a typical photon (which they called a 'voxel'). It was calculated that the average path-length – that is, the sampling radius from which 68% (one standard deviation) of the measured intensity imaged onto a single detector pixel originates – was between 30 and 50 μm. Moreover, it is this distance – which is well over an order of magnitude greater than the diffraction limit – that determines the spatial resolu-

tion of NIR imaging measurements made in DR mode. As the spatial resolution of NIR hyperspectral imaging measurements of scattering samples (e.g., pharmaceutical tablets) is far larger than the diffraction limit, it is clear that NIR DR imaging is best used to characterize samples with a particle size that is far larger than the diffraction limit.

An alternative approach for NIR hyperspectral imaging to that described above is to use a Fourier transform NIR (FT-NIR) spectrometer. As the design of FT-NIR microspectrometers is more similar to that of instruments for mid-IR hyperspectral imaging than the dispersive instruments described above, they will be described later (see Section 1.6).

1.5
Raman Hyperspectral Imaging

Both, Raman mapping and imaging involve the use of CCD array detectors. In mapping, the spectrum of a point of the sample is dispersed across the detector, and the sample is moved when each spectrum has been measured. In Raman imaging, on the other hand, the image of the sample at a single wavelength is focused on the detector and the wavelength is changed after each measurement. Raman imaging methods can be broadly classified as either line imaging or wide-field source illumination approaches [60]. In the line approach, a cylindrical lens or a Powell lens is employed to distribute the laser beam in one direction across the sample. The Powell lens (which is a combination of a cylindrical lens and a prism) may be visualized as a prism with a small radius at one edge, which operates as a cylindrical lens with its radius of curvature decreasing from center to edge. The effect is a monotonic decrease in beam divergence from center to edge, so that the generated line has a near-uniform intensity along its length [61]. The laser line dimension is oriented parallel to the direction of the entrance slit of a polychromator, so that the spectrum is dispersed in the short direction of the CCD. This approach reduces the duration of the experiment by $\sqrt{n}$, where n is the number of image pixels, assuming that the laser power per pixel is kept constant. The spatial resolution parallel to the laser line is the convolution of the microscope magnification by the pixel size, while in the perpendicular direction it is equal to the width of the laser line convolved by the scanning precision of the instrument. As a result, the resolution in one dimension is frequently greater than in the second direction.

In global (wide-field) imaging, the entire sample field-of-view is illuminated by defocusing the laser. The scattered radiation is usually first passed through a notch filter or a long-pass filter to remove the Rayleigh-scattered radiation, and then through a device that blocks all but one wavelength region. This device may be a monochromator, a dichroic filter, an acousto-optic tunable filter or a liquid crystal tunable filter, with the latter being generally favored. The wide-field approach is generally favored over line-scan imaging when high-fidelity images at a limited number of wavenumbers are desired. In wide-field imaging, the spatial resolution

is determined by the convolution of diffraction, the CCD pixel size and the microscope magnification at the focal plane of the CCD.

Surprisingly, global laser illumination leads to sample heating degradation at much lower laser intensities than point illumination, because of the inefficiency in conducting heat away from a surface sheet rather than a point. For steady-state measurements at a given total laser power (in W), the optical damage threshold for a given material scales as the square root of the illuminated area (rather than linearly with the area). Thus, the laser intensity (in W m^{-2}) required to damage a sample is higher for a point illumination than for line illumination, which is in turn higher than for area illumination. There is still an advantage to distributing power over a wider area; it is just that this so-called 'power distribution advantage' is not as great as was previously assumed [62].

As noted in Section 1.3, confocal microscope designs have been used in several Raman microspectrometers that allow sample mapping by moving the sample between the measurement of each spectrum. However, confocal microscopy cannot be used for wide-field Raman imaging as the entire region of the sample of interest must be illuminated, and clearly the 'light source pinhole' (see Figure 1.12) in confocal microscopes does not allow this. For hyperspectral Raman imaging, the high image quality attained by the use of confocal optics and mapping is sacrificed somewhat for data acquisition speed. However, this approach is only fast if an image is to be acquired at a single wavelength; for the acquisition of full spectra, it can be very slow.

One of the first Raman imaging spectrometers to be produced in the USA was designed and fabricated by Levin's group at the U.S. National Institutes of Health (NIH) [63]. The wavelengths for this instrument were controlled by a TeO$_2$ AOTF. The instrument produced high-fidelity, large-format images with a theoretical spatial resolution of about 1 μm, although because of dispersion by the TeO$_2$ crystal the finite spectral bandwidth of the AOTF resulted in a slight smearing of the output image along one axis. This degradation, which is given by the internal beam spread in the crystal, $\Delta\theta_{di}$, could be estimated from the approximate relationship reported by Suhre *et al.* [64]:

$$\frac{\Delta\theta_{di}}{\Delta\lambda} = \left(\frac{\Delta n}{n_0\lambda_0}\right)(\sin 4\theta_1 + \sin 2\theta_1)^{1/2} \tag{1.10}$$

where $\Delta\lambda$ is the passband (2 nm), λ_0 is the center wavelength (700 nm), Δn is the difference in refractive index of TeO$_2$ for the ordinary and extraordinary rays at λ_0 (0.138), n_0 is the refractive index of TeO$_2$ for the ordinary ray (2.177), and θ_1 is the angle between the incident beam and the optical axis of the crystal (22.5°); the values for the AOTF used by Goldstein *et al.* are given in parentheses. These values give an external beam spread, $\Delta\theta_{di}$, of 0.13 mrad (0.0037°); this value may be compared with the diffracted beam spread of 0.19 mrad caused by the 7 mm^2 aperture presented to the AOTF entrance pupil. In total, these values would lead one to predict that the image resolution along one axis would be degraded by about a factor of 2.5 on passage through the AOTF. For each AOTF passband frequency,

the image on the CCD will be shifted slightly because of dispersion by the crystal, and software correction is needed if the visual and Raman images are to be correlated.

In the instrument described by Goldstein *et al.* [63], the 647.1 nm beam from a krypton ion laser was delivered to the sample by an infinity-corrected microscope objective using an epi-illumination scheme. For this, light from the rear housing was passed down a horizontal shaft and then reflected down through the objective to the sample. The 180° back-scattered light was returned to the objective and then to the spectrometer. Wavelength selection was accomplished by an AOTF that could provide either random or continuous wavelength selection. The epi-illumination scheme was seen to preserve the linear polarization of the incident laser beam. Because the AOTF is polarization-sensitive, a half-wave plate was used to rotate the plane of polarization by 180° in order to preserve the AOTF output. The collimated output from the AOTF was first imaged by a tube lens, and then by a projection lens onto a liquid-nitrogen-cooled silicon CCD array. One, or occasionally two, holographic notch filters were placed in front of the detector to eliminate stray radiation from the Rayleigh line. These filters transmitted between 75 and 80% of the Raman emission beyond $75\,cm^{-1}$ of the Rayleigh line.

In order to minimize the data acquisition time, the overall magnification of this system was made as small as possible, consistent with the spatial resolution desired. As the image is sampled by the discrete pixels of the CCD camera, the Nyquist sampling criterion must be obeyed to avoid the generation of artifacts. There is an explicit relationship describing how the number of counts per pixel depends on the optical design. It is known from Equation 1.3 that the radius of the Airy disk r is equal to $0.61\lambda/NA$. If the size of the CCD pixel is p, then the Nyquist sampling criterion requires that the overall magnification, M, satisfies the condition that $Mr > 2p$. Goldstein *et al.* designed their system such that $Mr = 2.3p$; in other words, the smallest resolvable feature was sampled by at least two pixels [63]. It should be noted that this rule of thumb is equally applicable to imaging spectrometers, where the spatial resolution of the measurement should be spread over at least two pixels.

The instrument reported by Goldstein *et al.* is shown diagrammatically in Figure 1.22. Also shown (in Figure 1.23a) is the Raman image of 1 μm-diameter polystyrene beads, obtained by recording the signal at $1000\,cm^{-1}$ from one of the pixels. Figure 1.23b shows the spectrum measured from one of the pixels in the region of this band. Note that its FWHH band is at least $25\,cm^{-1}$, whereas the true FWHH of this band is less than $10\,cm^{-1}$, thereby demonstrating the trade-off between magnification, image quality, spectral resolution and data acquisition time in Raman mapping. A similar system explicitly designed for *in vivo* tissue diagnostics has been described by Vo-Dinh *et al.* [65].

ChemIcon, Corp. (now ChemImage, Corp.) market a Raman imaging spectrometer that shares some of the features of the NIH instrument reported by Goldstein *et al.* but, nonetheless, has some significant differences. First and foremost, wavelength selection is accomplished through the use of an LCTF rather than an AOTF. The spectral bandpass of this instrument is $9\,cm^{-1}$, and it has the capability of
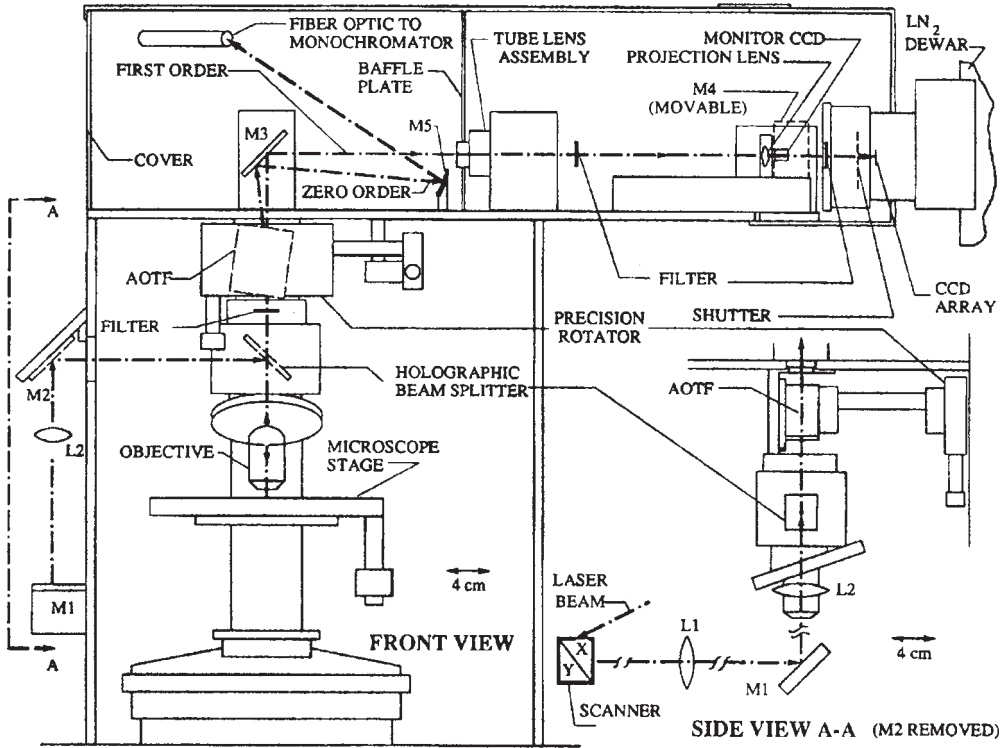
Figure 1.22 Schematic diagram of the Raman imaging microscope reported by Goldstein *et al.*. Reproduced with permission from Ref. [63].
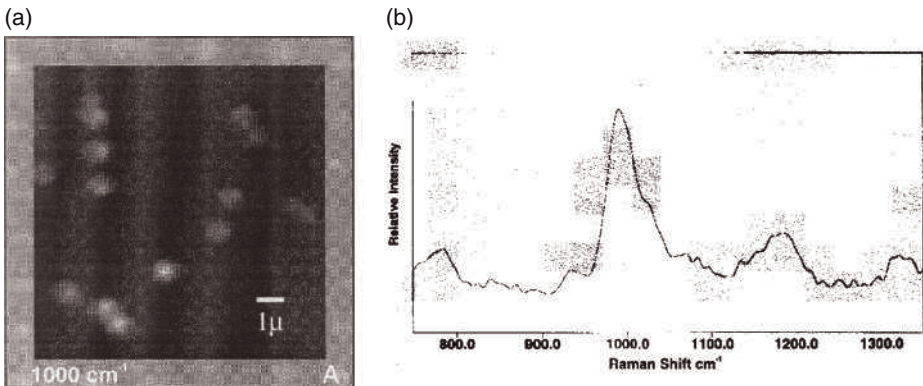
Figure 1.23 (a) Image of 1 μm-diameter polystyrene spheres acquired using the instrument shown in Figure 1.21 by holding the AOTF at 1000 cm^{-1}; (b) Spectrum from one pixel of the CCD. Reproduced with permission from Ref. [63].

being tuned at finer increments. It is also claimed that a spectral resolving power of better than $0.1\,\mathrm{cm^{-1}}$ has been consistently achieved, although this term probably refers to the accuracy to which the center wavenumber of the LCTF bandpass may be set, as the FWHH of the passband of an LCTF is never as small as $0.1\,\mathrm{cm^{-1}}$. The Raman microscope sold by Renishaw, Inc. may also be used in the imaging mode, by holding the monochromator at a certain wavelength for each time increment. However, the Renishaw instruments are mainly used in the Raman microscopy and mapping modes.

1.6
Mid-Infrared Hyperspectral Imaging

1.6.1
Spectrometers Based on Two-Dimensional Array Detectors

The first true chemical imaging microspectrometer was reported by Levin's group at NIH and Marcott's group at Procter and Gamble [66], who used a Bio-Rad (now Varian[2]) FTS 6000 step-scan FT-IR spectrometer equipped with a UMA-500 microscope. In their earliest instrument, the single-element detector mounted in the microscope was replaced by an indium antimonide (InSb) FPA detector with 64×64 elements imaging an average spatial area of $500 \times 500\,\mu\mathrm{m}$. A CaF_2 lens was used to focus the sample area onto the FPA detector. As InSb has a cut-off of $1800\,\mathrm{cm^{-1}}$, the fingerprint region of the mid-IR spectrum could not be measured with this instrument.

A short time later, Levin's group modified step-scan FT-IR spectrometer to operate with a mid-IR MCT FPA detector. Unlike most MCT detectors used in FT-IR spectrometers, which operate in the photoconductive (PC) mode, the pixels of MCT FPA detectors operate in the photovoltaic (PV) mode. As noted in Section 1.2.2, the cut-off wavenumber of narrow-band PC MCT detectors is about $750\,\mathrm{cm^{-1}}$. The PV detector elements used in MCT FPA detectors have the same high sensitivity as narrow-band PC MCT detectors, but the cut-off wavenumber is higher, at about $850\,\mathrm{cm^{-1}}$.

The first commercial instrument employing the concepts developed by Levin's group was designed by Bio-Rad and marketed as the *Stingray* in 1995. This instrument is shown schematically in Figure 1.24. In order to maintain the image

2) Like several other corporations in the field, the company now doing business as Varian has undergone several name changes. It was first known as Digilab, Inc. Founded in 1969, Digilab developed the first FT-IR spectrometer of the modern era, that is the first with He–Ne laser referencing, the use of a pyroelectric (TGS) detector and the first under minicomputer control. Digilab was purchased by Bio-Rad in 1978. In 2001, Bio-Rad sold the company to a group of private investors, who renamed the company Digilab LLC. The group sold Digilab to Varian in 2004. During each of these manifestations, this organization made many of the innovations that have led to the remarkable popularity of FT-IR spectroscopy today. In this chapter, the name of the company will be given as it was when the work was reported.

Microscope
(UMA 500)

MCT 64x64 Array

FPA Detector
(Santa Barbara)

FT

Sample

Step-Scan Bench
(FTS 6000)

Bio-Rad Stingray

Spectral Resolution : 2 to 8 cm^{-1}
Spatial Resolution : ~ 8 μm
Collection Time : 100 s to 2 Hrs.

OH band at ~3400 cm^{-1}
0.0 ████ 0.3

CN band at 2227 cm^{-1}
0.2 ████ 0.7
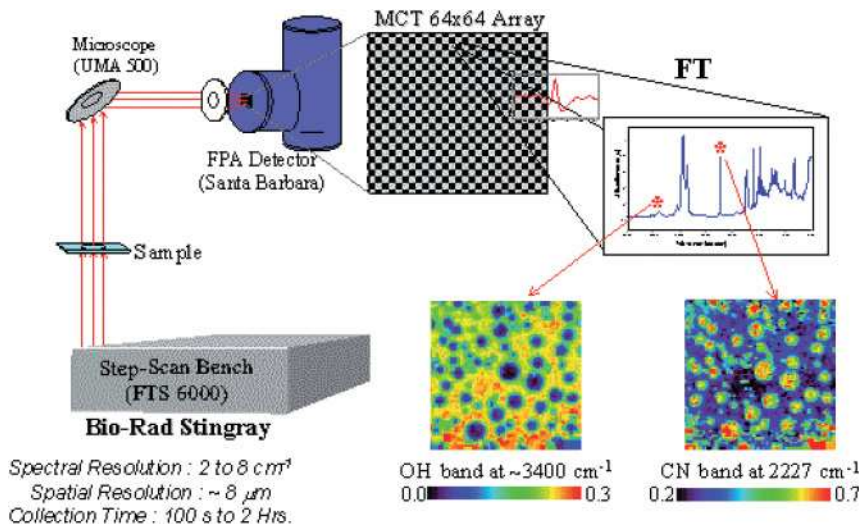
Figure 1.24 Schematic diagram of the Bio-Rad Stingray hyperspectral imaging spectrometer. Illustration courtesy of Varian Corporation.

quality, a ZnSe lens was used to focus the sample image onto a MCT FPA detector, rather than the Cassegrain system used in most microscopes. The instrument is equipped with a germanium long-pass filter to block visible and short-wave NIR radiation, and hence to prevent detector pixel saturation and improve the SNR. A lightly sanded KRS-5 plate placed in the beam path before the condenser further improves the spatial homogeneity in the camera field-of-view, and also prevents the detector elements in the center of the array from saturating.

These first attempts during the mid 1990s at true mid-IR FPA imaging using a 2-D MCT FPA detector were based on the detectors mounted in military heat-seeking missiles, and the spectrometers that resulted are now termed 'first-generation' instruments. As the detectors used in such instruments were not designed specifically for spectroscopic imaging, they had a number of limitations, one being a tendency for pixels to 'delaminate' and separate from the substrate. As these first-generation detectors were designed essentially for 'one use' applications, they were unable to cope with the thermal stresses of repeated heating–cooling cycles associated with liquid nitrogen cooling.

Another major limitation arose from the need to employ a step-scan interferometer. This necessity arose from the relatively slow read-out rates of these first-generation FPAs, which were of the order of only a few hundred Hertz. The read-out rate (or *frame rate*) of a FPA detector determines the type of interferometer that must be used for FT-IR imaging, as the FPA cannot be triggered (for data transfer) any faster than its maximum read-out (frame rate) speed. As the first-generation FPAs were only capable of frame rates in the hundreds of Hz, and rapid-scanning interferometers required a faster frame rate, the use of step-scan
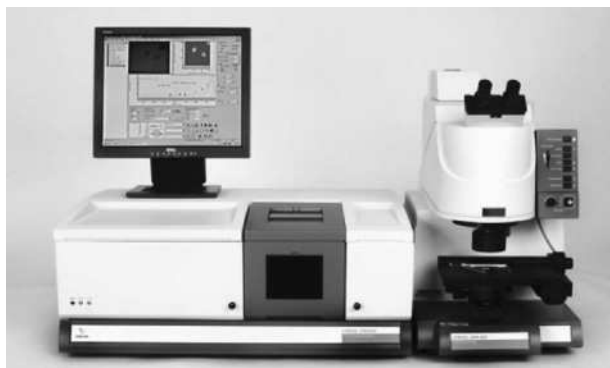
Figure 1.25 The first commercial rapid-scanning FPA chemical imaging system, introduced in 2001 by Digilab (now Varian Corporation).

interferometers – where the movable mirror of the interferometer could be held a given optical path difference for several seconds – was mandated.

In 1999, Snively *et al.* described the first report of the use of a rapid-scan interferometer in conjunction with a small first-generation focal-plane array for spectroscopic imaging [67]. In an attempt to design a mid-IR chemical imaging system designed specifically for spectroscopic applications, Digilab, together with the FPA supplier, developed and marketed the first commercial mid-IR 'rapid-scan' imaging systems in 2001, with the launch of the 'second-generation' FPA, designed specifically for spectroscopic chemical imaging (see Figure 1.25). These second-generation FPAs had frame rates which were an order of magnitude faster than their first-generation counterparts, such that the standard laboratory-type rapid-scanning FT-IR spectrometer could now be used for chemical imaging, with a significantly increased affordability yet reduced complexity. This, in turn, led to an increased use and application of mid-IR imaging spectrometers.

In addition to pioneering the developments in FPA detectors designed specifically for fast mid-IR hyperspectral imaging, Digilab redesigned their microscope to launch the first instrument designed specifically to cater for the unique requirements of FPA-based imaging. Such improvements included a wider and more uniform illumination field of view (FOV) of up to $700 \times 700 \, \mu m$, removing the need for any diffusers, the removal of refractive focusing optics and the introduction of optical zoom capabilities for changing the pixel size at the sample plane from 5.5 to 11 μm (with a corresponding increase in FOV). Despite the availability of 'rapid-scan' FPA mid-IR chemical imaging systems since 2001, it often still thought that mid-IR hyperspectral imaging spectrometers require step scanning, this being a legacy from the original first-generation, military-based FPAs of the mid 1990s.

Generally speaking, the larger the array, the slower the read-out frame rates of the FPA. The frame rates of today's second-generation FPAs range from several kHz for the smaller 16×16 and 32×32 FPAs, to just over 1 kHz for the largest

commercially available (128 × 128) FPAs. The ability to operate these FPAs at rapid scan speeds depends on the frequency at which the spectrometer triggers the FPA. The sampling of signals from FPAs is similar to that for a standard detector such as DTGS, whereby the detector response is recorded as a function of opd to provide an interferogram. For FPAs operated in PV mode, the FPA response (for each pixel) is triggered by the interferometer. At each trigger, the pixel response is read out in 'snapshot' mode, whereby all pixels are read out simultaneously, processed and transferred to the data system to provide for an interferogram datum point for each pixel in the FPA at each opd. The triggering rate must, of course, be less than the maximum frame rate of the FPA; for a 64 × 64 FPA, the maximum frame rate is 3.77 kHz. Because of the discrete speed settings available on most commercial FT-IR spectrometers, for a spectral range of 7900 cm^{-1} (the Nyquist wavenumber for a He–Ne laser-referenced system with an undersampling ratio of 2), the fastest scan speed that can currently be used to collect data from a 64 × 64 FPA is 2.5 kHz. The use of an undersampling ratio of 2 allows for the data to be collected without any aliasing into the mid-IR spectral region (<4000 cm^{-1}).

The data collection (interferometer) speed can be increased up to 5 kHz, by further undersampling the interferogram. An undersampling ratio of 4 (whereby the FPA is triggered for data read-out at every fourth He–Ne laser zero crossing; that is, every second wavelength of the HeNe interferogram) provides for a Nyquist wavenumber of 3950 cm^{-1}. However, in order to prevent spectral artifacts caused by aliasing from appearing in the spectrum, a low-pass filter must be mounted in the optical path to prevent radiation with wavenumbers above 3950 cm^{-1} from reaching the FPA detector. The insertion of such a filter has the added benefit of limiting detector saturation by preventing light from outside the spectral region of interest from reaching the detector, hence allowing longer integration times to be utilized for an increased SNR. The increase in interferometer scan speed to 5 kHz still means that the FPA is being triggered at 2.5 kHz, as now the triggering at every fourth zero crossing instead of every second zero crossing means that the interferometer scan speed can be increased twofold to 5 kHz. As the FPA is in fact still being triggered at 2.5 kHz, the actual frame period is hence the reciprocal of the frame rate at 0.40 ms. With typical integration times of 0.01 to 0.05 ms for high-throughput systems, it is clear that the FPA is typically integrating for only a fraction of the fully available frame period. This is a result of the high sensitivity of the MCT material requiring only a short integration time. Despite such advances in FPA design – and in particular of the electronics – the frame rates are still relatively slow. An ideal design would have the maximum probable integration time matched to the frame period. For example, assuming that a maximum integration period of 0.05 ms is required and the frame period is designed to match, this would result in a frame rate of 20 kHz. Although no commercially available FPA has such high frame rates, the technological advances observed in modern electronics indicates that these will be achievable in the foreseeable future.

For imaging measurements using a step-scan FT-IR spectrometer, the interferometer mirror is held at a constant position (usually at the zero-crossing of the laser interferogram) while the signal from each pixel is recorded by the ADC. This

process may be repeated several times at the same sampling position to allow *frame co-addition*, whereby the signals from all pixels are averaged several times before the interferometer mirror is stepped to the next sampling position. In practice, although frame co-addition works well until about 20 frames have been averaged, further averaging does not lead to any great improvement in the SNR. When the signal from each pixel has been averaged the required number of times, the interferometer mirror is stepped forward to the next sampling position, and this process is continued until sufficient data points have been measured to achieve the desired spectral resolution. Snively and Koenig showed that N successive images could also be signal averaged for the expected improvement in SNR of $\sqrt{N}$ [68]. When all the data have been acquired, the interferograms are converted to single-beam spectra, ratioed against the corresponding single-beam background spectrum, and converted to absorbance.

By analogy with Equation 1.2, Sniveley and Koenig showed that the SNR on the baseline of spectra measured with an imaging FT-IR spectrometer is given by:

$$\text{SNR} = \frac{0.12\pi A\left\{1 - \sqrt{1 - (NA)^2}\right\} U_{\tilde{v}}(T)\Delta\tilde{v}D^*\sqrt{t}}{A_D^{1/2}} \tag{1.11}$$

where NA is the numerical aperture and A is the area of the sample imaged onto the pixel. All the other parameters have the same meaning as in Equation 1.2 [68]. The factor of 0.12 is analogous to the efficiency term ξ in Equation 1.2. Sniveley and Koenig used this equation to compare the performance of FT-IR imaging and single-detector microspectrometers and found that, for measurements near the diffraction limit, the performance of imaging spectrometers should be higher than that of standard FT-IR microspectrometers if it is assumed that the D^* of the detectors and the area of the sample imaged onto the pixel are the same in both types of instruments. (In practice, the D^* of PV-MCT detectors is slightly higher than that of PC detectors for signals modulated at frequencies greater than 1 kHz, although the difference is small.) The biggest advantage of the imaging spectrometers is in the A_D term for array detectors. Whereas, most FT-IR microscopes are equipped with 250 μm detectors, the pixel size in most FPAs is 40 μm, which leads to an advantage in $\sqrt{A_D}$ by a factor of ~2.5 for the imaging spectrometer for measurements made close to the diffraction limit of spatial resolution.

However, the benefit in SNR of an imaging system over a single point system when close to the diffraction limit is much greater than a factor of 2.5. The probable reason for the significantly greater performance of the imaging spectrometers is that Equation 1.11 fails to account for the sample aperture (and its resulting degradation in étendue) when a spectrometer is operated close to the diffraction limit. Because they do not require an aperture, each entire pixel is fully illuminated in imaging systems. Consider the case of a measurement made at close to a diffraction limit of, say, ~10 μm (therefore with a 10 μm aperture). For a spectrometer with a single-element 250 μm detector, only 0.16% of the detector surface is illuminated, with the remaining 99.84% contributing only noise. When this factor is taken into account, together with the 2.5-fold improvement predicted by Equation
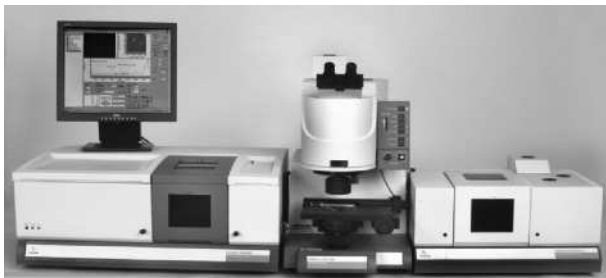
Figure 1.26 The 'Large Sampling Accessory' by Varian, provides for FPA chemical imaging at a 1:1 magnification for the analysis of 'macro' samples. Illustration courtesy of Varian Corporation.

1.11, imaging spectrometry recorded close to the diffraction limit provides for SNR benefits of many orders of magnitude!

Although chemical imaging is typically performed with a microscope, it need not be limited to microscopes and samples in the micro domain. In 1998, Digilab released the 'Large Sampling' (LS) accessory; this consisted of an external sample compartment unit in which the FPA detector could be mounted and transferred as required between the microscope and the LS (see Figure 1.26). The LS accessory is mounted either directly off the FT-IR spectrometer or off the microscope via 'pass-through' optics that allow the IR beam to bypass the internal optics of the microscope. Under this configuration, the overall magnification is 1:1, so that the pixel size at the sample plane now matches that of the native FPA pixel size at $40 \times 40\,\mu m$. Therefore, with a 128×128 FPA, sample areas of up to $5.1 \times 5.1\,mm$ can be imaged at once.

1.6.2
Spectrometers Based on Hybrid Linear Array Detectors

An alternative approach to hyperspectral imaging, namely a hybrid of imaging and mapping, was reported in 2001 by PerkinElmer (PE) as the *Spectrum Spotlight*. This instrument is an imaging FT-IR spectrometer that incorporates a linear array of 16 photoconductive narrow-band MCT detectors interfaced to a relatively inexpensive rapid-scanning interferometer. Although this detector is commonly (and perhaps for the sake of simplicity) often referred to as a 1×16 linear array detector, the pixels are in fact arranged in a 2×8 format. As the cut-off for the narrow-band PC-MCT detectors used in this spectrometer is about $720\,cm^{-1}$, the spectral range of the instrument is at least $130\,cm^{-1}$ wider than that of the PV MCT FPA detectors incorporated into most other hyperspectral imaging FT-IR spectrometers. The signals from each of the 16 detectors in the linear array are digitized simultaneously with separate ADCs. The sample is mounted on a computer-controlled stage that can be rapidly repositioned to allow the spectra from an adjacent region to be

measured once the spectral data from a given stage position have been acquired. The spectra are then quilted together to produce the image. This process is repeated until the entire spatial region of interest has been covered. In addition to this linear detector array, a single 100 μm medium-band MCT detector is mounted in the same Dewar flask, that allows individual spectra to be acquired over a wider range than the spectra measured with the array. A similar instrument is now available from Thermo Fisher Corporation that consists of a 28-pixel linear array arranged in a 2×14 pixel format.

Much confusion exists as to the advantages and disadvantages of linear-array versus FPA-based imaging systems, and detailed analysis and comparison is beyond the scope of this chapter. However, Bhargava *et al.* proposed a useful metric to aid in comparing the performance of two imaging systems that can be conveniently applied to the comparison of these two systems [69]. The figure of merit defined is the pixels per minute 'pixpm', and compares the performance of two imaging systems relative to each other for a specified SNR at defined spectral and spatial resolutions. The ratio of the pixpm values of two instruments is given by:

$$ R_{21} = \frac{n_2}{n_1} \left(\frac{t_1}{t_2} \right) \left(\frac{SNR_2}{SNR_1} \right)^2 \tag{1.12} $$

where R_{21} is the ratio of the pixpm of system 2 to system 1, n_i is the number of pixels collected over the defined sample measurement area, t_i is the time required to collect the image (of either 1 scan or to achieve the required SNR) and SNR_i is the average SNR achieved over the sample measurement area. Hence, the relative performance is linearly related to the time and number of pixels collected and to the square of the SNR.

Let us assume the sample area to be measured is moderate in size (say, 700×700 μm), and is to be collected at high spatial resolution and 4 cm^{-1} spectral resolution at a SNR of 200. Based on the manufacturers' typical specifications, if all other parameters are kept equal, we have:

	System 2 ($i = 2$)	System 1 ($i = 1$)
	64×64 FPA (5.5 μm projected pixel size)	16-element linear array (6.25 μm projected pixel size)
n_i (number for a pixels collected for a 700×700 μm sample area)	16 384 (four tiles)	12 544 (784 line scans)
t_i	5 min (32 scans co-added)	150 min (16 scans co-added)
SNR	200	200

Based on the above comparison, the FPA imaging system is 39-fold better, under the specified conditions, despite requiring twice as many scans (32 versus 16). This result can be rationalized by considering the massive multichannel advantage of a 64×64 FPA (4096 detectors) over a 16-element linear array. For example, the FPA has 256 times as many detectors collecting data simultaneously compared to the linear array. To cover the same $700 \times 700\,\mu m$ area, the 64×64 FPA, with its $5.5\,\mu m$ pixel size requires a four-tile mosaic, whereas the 16-element linear array in its high spatial resolution mode of $6.25\,\mu m$, requires 784 separate line scans. Thus, even though the time during which a given interferogram can be acquired with the linear array is shorter than when an FPA is used, the FPA-based spectrometer required a total of 128 (4×32) scans while the instrument that incorporated the linear array required 12 544 (16×784) scans. Thus, the acquisition of almost 100-fold more scans results in a significantly slower overall time of collection when the linear array is used. The smaller pixel size of the FPA system ($5.5\,\mu m$) compared to the linear array ($6.25\,\mu m$) results in more pixels being collected for the same sample measurement area which, according to Equation 1.12, further increases the advantage of the FPA-based instrument.

Although the differences between FPAs and linear arrays are not always of this magnitude, they are usually in favor of the FPA-based imaging system. In fact, when employing even larger FPAs, such as the 128×128 FPA, the differences are even larger. Linear array systems are, however, generally at their most efficient when operated at relatively low spatial and spectral resolutions (e.g., $25\,\mu m$ and $16\,cm^{-1}$, respectively) and with only a few co-added scans, where the synchronization of interferometer step and stage travel is most accurately achieved.

1.6.3
Sampling

Imaging can be accomplished by using any of the approaches used in mid-IR mapping, namely transmission, external reflection and attenuated total reflection. In some instruments, the microscope objective can be changed to permit operation at either high or low magnification. The key to any imaging measurement is that the sample should be accurately located at a beam focus so that it can be exactly re-imaged on the array detector. The first applications of mid-IR imaging were performed in the transmission mode, with a few examples of reflection spectroscopy. Imaging by ATR took longer to be reported, even though ATR imaging is by no means a new concept. For example, in his 1967 book *Internal Reflection Spectroscopy*, Harrick showed the visible ATR image of a fingerprint recorded photographically [70].

Despite Digilab (now Varian) having been granted a patent on ATR imaging in 2000 [71], this does not seem to have stopped others from employing this technique, using spectrometers from other manufacturers. Sommer *et al.* [72] used an ATR accessory with a germanium IRE mounted in the external beam of a Stingray spectrometer/microscope. By using the edge profile test (as discussed in Section 1.2.6), the group demonstrated a spatial resolution of about $8\,\mu m$ in the fingerprint
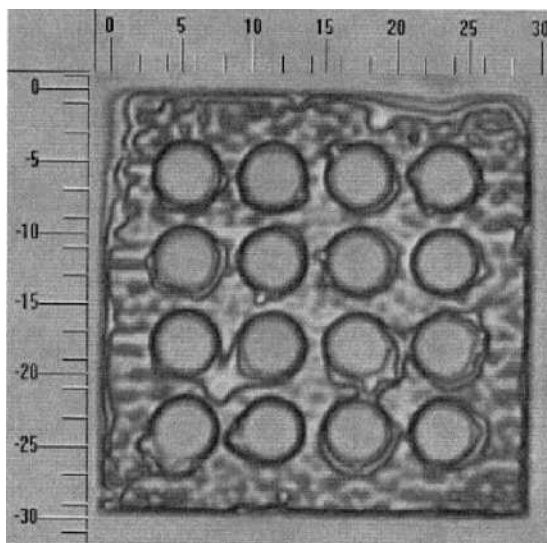
Figure 1.27 Visible image of the patterned PMMA film on a silicon wafer, captured with a 100× objective. The scales on the image are in micrometers. Reproduced with permission from Ref. [73].

region, and claimed also to have shown that the 4× magnification factor associated with the germanium internal reflection element was realized. However, a 4× reduction of the diffraction limit for a microscope with a *NA* of 0.6 should have meant that the spatial resolution was improved to 2.5 μm, and this was not explicitly demonstrated. More recently, Chan and Kazarian reported a detailed study of ATR imaging using a patterned film of PMMA on a silicon substrate [73]; the visible image showed circles of the polymer that were 4 μm in diameter with a separation of 2 μm (see Figure 1.27). Micro-ATR imaging with a germanium IRE ($n = 2.4$) showed that the PMMA circles were resolved when the spectrum was integrated between 1753 and 1672 cm^{-1} (average wavelength, $\lambda_{ave} = 5.8$ μm), but the image tended to wash out at longer wavelengths as the diffraction limit was approached (see Figure 1.28).

Perhaps the most detailed investigation into the resolution of ATR imaging instruments was presented by Everall, who first calculated the edge profile by convolving the image at 1600 cm^{-1} of the interface between the two polymers with the Airy disk, taking into account the 10 μm size of the pixels in the FPA MCT detector [74]. Everall then measured absorbance at 1600 cm^{-1} in each spectrum in the hyperspectral ATR image of a laminate of an acrylonitrile-butadiene-styrene (ABS) polymer in the region of the interface, using a Stingray imaging spectrometer equipped with a diamond ATR element. The fit was remarkably accurate, as shown in Figure 1.29.

Everall also demonstrated the problems of quantitative ATR imaging when trying to measure the image of a sample containing hard spheres with a diameter

10μm

(a)   (b)
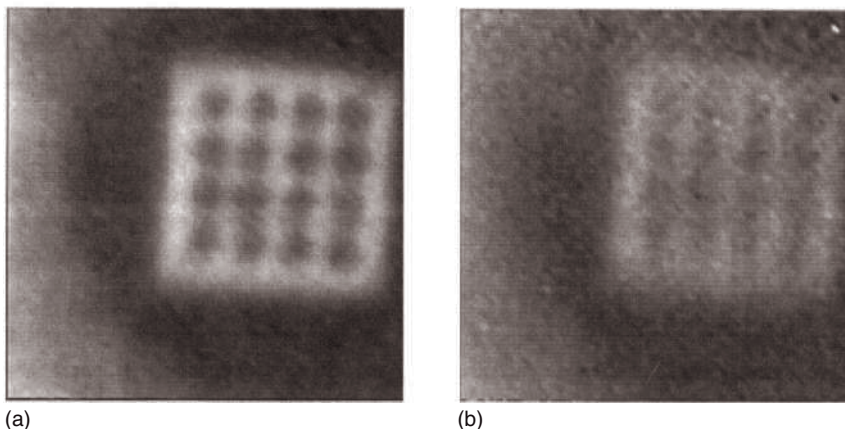
Figure 1.28 Micro-ATR images of the PMMA film on a silicon wafer shown in Figure 1.24 obtained by integrating between (a) 1753 and 1672 cm^{-1} ($\lambda_{ave} = 5.8\,\mu m$) and (b) 1179 and 1090 cm^{-1} ($\lambda_{ave} = 8.8\,\mu m$). Reproduced with permission from Ref. [73].
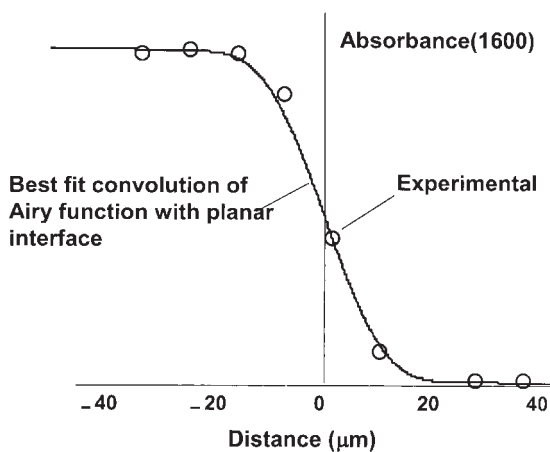
Figure 1.29 Calculated and experimental variation of the 1600 cm^{-1} band of polyurethane as a function of distance from the interface of a polyurethane-ABS laminate. Illustration courtesy of Dr Neil Everall, Measurement Science Group, Intertek Corporation.

equal to or smaller than the depth of penetration. It was shown that a shallow penetration, combined with the finite spatial resolution of an imaging spectrometer, renders ATR insensitive to hard spherical particles with domain sizes ranging between 10 and 150 μm. For large spheres, the shallow penetration depth underestimates the diameter whereas, for small spheres the finite spatial resolution overestimates the diameter due to blurring, causing the apparent size insensitivity of the technique for spheres. Everall's conclusions were equally valid for other irregular inclusions, while flat or 'platey' domains should yield more accurate results. Everall further showed that the compression of soft particles increased their apparent size, albeit in a noncontrolled fashion, and stressed that ATR imaging is nonetheless a valuable technique for assessing variations in the surface composition of polymer samples. It was suggested that, by sectioning the samples, a more accurate picture of the near-surface composition could be obtained.

Everall also measured the images of polystyrene spheres of several diameters using a 1450 cm^{-1} (6.9 μm) band of polystyrene [74], and showed that transmission spectroscopy gave far better estimates of sphere diameter than did ATR imaging. The error in estimating the sphere diameter was approximately 10% when the diameter was ≥50 μm, whereas with ATR imaging the estimated particle diameter was considerably less than the actual diameter. However, when the sphere diameter was ≤10 μm, their apparent diameter as measured by transmission imaging was approximately equal to the diffraction limit (20 μm).

Image-preserving ATR accessories can be mounted in the Varian LS accessory for 'Macro ATR Imaging'. In 2007, Specac – in partnership with and exclusive to Varian (under Varian's 'ATR imaging' patent [71] – released an imaging-specific version of their well-known 'Golden Gate' single-reflection diamond ATR that differed from the standard version by its patented 'image-preserving' optical design [75]. This is necessary if the spatial relationships of the image are to be preserved whilst being propagated through the IRE. The FOV with this accessory may be as large as 640 × 640 μm when used with a 64 × 64 FPA.

Another image-preserving ATR accessory that has been used in conjunction with 'macro imaging' is the Harrick FastIR, which consists of a simple inverted ZnSe prism such as that shown in Figure 1.9a. As the IRE is fabricated from ZnSe rather than diamond, this accessory is less robust, but does offer the advantage of having a considerably larger FOV of up to ~10 × 6 mm when used with a 128 × 128 FPA. These accessories open up a whole new avenue of research, as now one can combine the already proven and well-established benefits of ATR accessories such as limited or no sample preparation with the information-rich content afforded by FPA chemical imaging.

In another Digilab patent [76], a 'side port' adaptor directs the beam that would otherwise enter the objective (in reflection mode), via a 45° flat mirror toward the front of the instrument into an objective now facing outwards. In such a configuration, the sample size is no longer limited by the working distance of the objective (typically ~24 mm). Thus, large samples may be placed in front of the outward-facing objective for measurement (see Figure 1.30). In such a configuration, only the external reflection or ATR modes of sampling are possible. This mode of
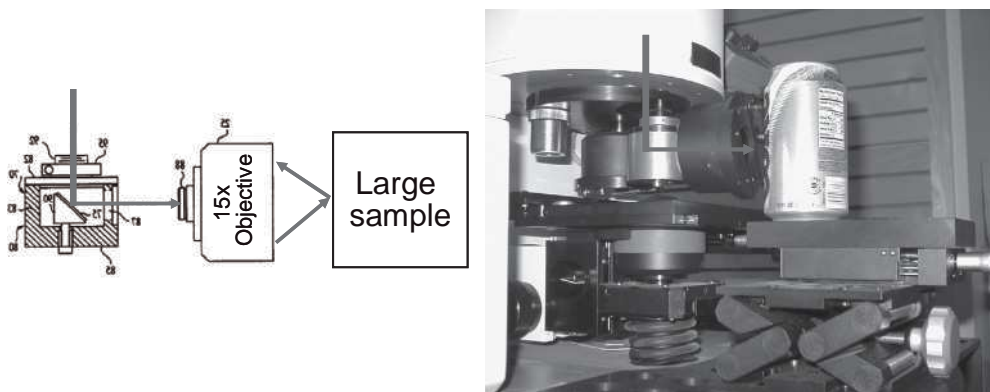
Figure 1.30 Varian's patented side-port adaptor and objective, allowing for the measurement of samples that are too large to be accommodated under the objective's standard 24-mm working distance. Illustration courtesy of Varian Corporation.

measurement makes it conceivably possible for large objects such as complete vehicle bumper bars to be stood on the floor and held in contact with the micro ATR accessory on the outward-facing side port objective.

In summary, ATR imaging has a number of advantages over transmission or external reflection imaging for studying surfaces that do not have spherical or irregular inclusions, not the least of which is the absence of artifacts caused by Mie scattering. Sample preparation is much easier and the diffraction-limited spatial resolution that can be obtained is less than can be obtained by transmission imaging, by a factor equal to the refractive index of the IRE. However, because the depth of penetration is low, the peak absorbance of even quite strong bands can be rather weak, especially if a germanium or silicon IRE is used. Finally, as noted above, if the sample contains spherical or irregular particles, they may not be adequately interrogated by the evanescent wave, making them appear smaller than they actually are. In an interesting example of 'what goes around, comes around', Kazarian's group recently published hyperspectral imaging data of human fingerprints in which trace quantities of drugs of abuse could be detected in a few of the spectra [77]. The science of imaging has certainly come a long way since Harrick's original ATR photograph of a fingerprint.

1.7
Mapping with Pulsed Terahertz Radiation

Vibrational spectroscopy covers the spectral region from about $0.75\,\mu m$ ($\sim 13\,500\,cm^{-1}$) to $1000\,\mu m$ ($10\,cm^{-1}$). To this point, we have covered the NIR (0.75 to $2.5\,\mu m$ or $\sim 13\,500$ to $4000\,cm^{-1}$) and mid-IR (2.5 to $25\,\mu m$ or 4000 to $400\,cm^{-1}$) regions. The final region that will be discussed in this chapter is the far-IR (25 to

1000 µm or 400 to 10 cm^{-1}). Many different types of transition are seen in the far-IR region of the spectrum; these include intramolecular stretching modes involving heavy atoms, skeletal bending modes involving the entire molecules, torsional modes, ring puckering vibrations of small-ring molecules, intermolecular vibrations of hydrogen-bonded molecules and charge-transfer complexes and lattice bands (or phonon modes) [78]. Until only a few years ago, far-IR spectra were difficult to measure and rarely used for chemical analysis. This state of affairs was a result of the fact that the radiative energy emitted by sources of continuous far-IR radiation, such as a Globar or high-pressure mercury lamp, is far lower than the corresponding energy emitted by mid-IR sources. The measurement of far-IR spectra using such sources is slow, even with a FT spectrometer.

In about 2003, a completely new way of generating far-IR radiation was developed such that far-IR spectra could be measured faster and at a higher sensitivity than before [79, 80]. As a result, there has been a renewed interest in this spectral region. In order to distinguish the 'old way' of measuring far-IR spectra from this 'new way', the new technology has been termed terahertz spectroscopy, since the wavenumber region from 1.2 to 130 cm^{-1} corresponds to the frequency region from 0.05 to 4 THz (1 THz = 1×10^{12} Hz).

The source for terahertz spectroscopy is an ultra-short-pulsed laser (usually Ti : Sapphire) that emits a stream of pulses of NIR radiation at ~80 MHz, with each pulse lasting for about 70 fs. The laser pulses are focused on a photoconductive switch (sometimes known as an 'Auston switch') which is a small semiconductor crystal (often GaAs) on which two planar metal electrodes support a large electric field across its surface [81]. The design of these metal electrodes is that of an antenna. The pulses of NIR radiation cause electron-hole pairs to be generated at the surface of the semiconductor, thereby changing the conductance and effectively closing the switch. With a carefully designed antenna, the electron-hole pairs are accelerated by a DC electric field applied across the device, leading to a rapid change in the current density. The changing dipole produces a THz transient in the antenna that is radiated into free space; the resultant effect is the emission of short bursts of broadband coherent terahertz radiation with each laser pulse. The long-wavelength radiation that is generated by this technique can then be collected using a silicon lens.

A small fraction of the NIR laser pulse is also used in the detection process. This radiation is focused onto a second semiconductor device where, once again, electron-hole pairs are generated at the surface. On this device, however, the electric field that is created by the coincident pulses of terahertz radiation induces a measurable photocurrent. The femtosecond laser pulse effectively acts as an optical gate, which is only open for the lifetime of the electron-hole pairs in the semiconductor (<200 fs.) By sweeping the time delay between the arrival of the femtosecond laser pulse and the terahertz pulse, a waveform comprising the terahertz signal as a function of time can be constructed (see Figure 1.31). The Fourier transform of this signal yields the single-beam spectrum, as shown in Figure 1.32.

An operating system of an instrument that is based on this principle, manufactured by TeraView Ltd. (Cambridge, UK), is shown in Figure 1.33 [82]. This
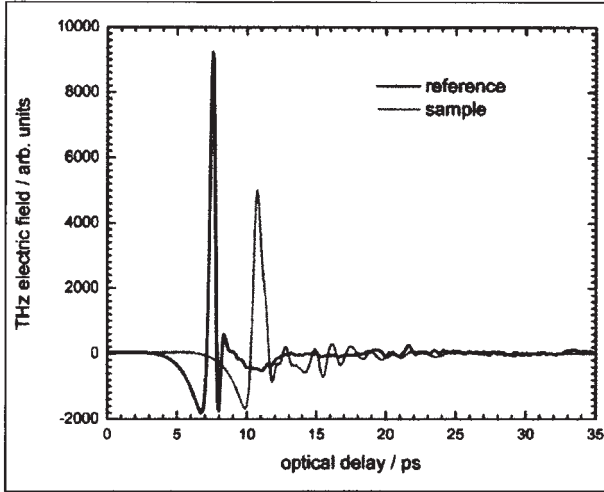
Figure 1.31 The terahertz electric field recorded as a function of time for the background (left centerburst) and when the beam passes through a 4 mm-thick silicon sample (right centerburst). Reproduced with permission from Ref. [79].
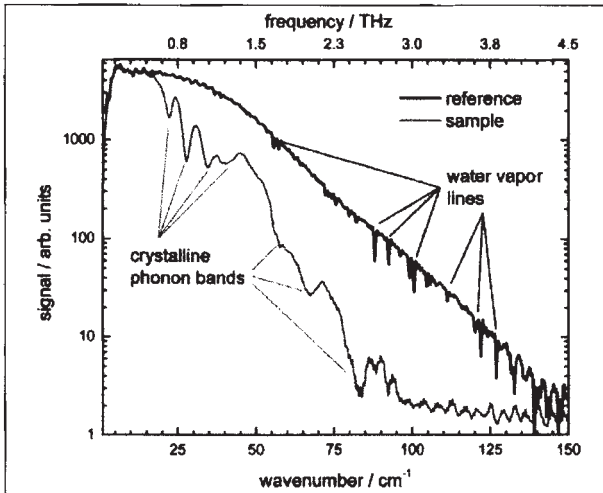
Figure 1.32 Fourier transforms of the two time domain waveforms shown in Figure 1.31. The signal is plotted on a logarithmic scale to show the dynamic range of the instrument. Pure rotation lines due to water vapor are seen on the background spectrum (above). The sample spectrum (below) is that of crystalline silicon. Reproduced with permission from Ref. [79].
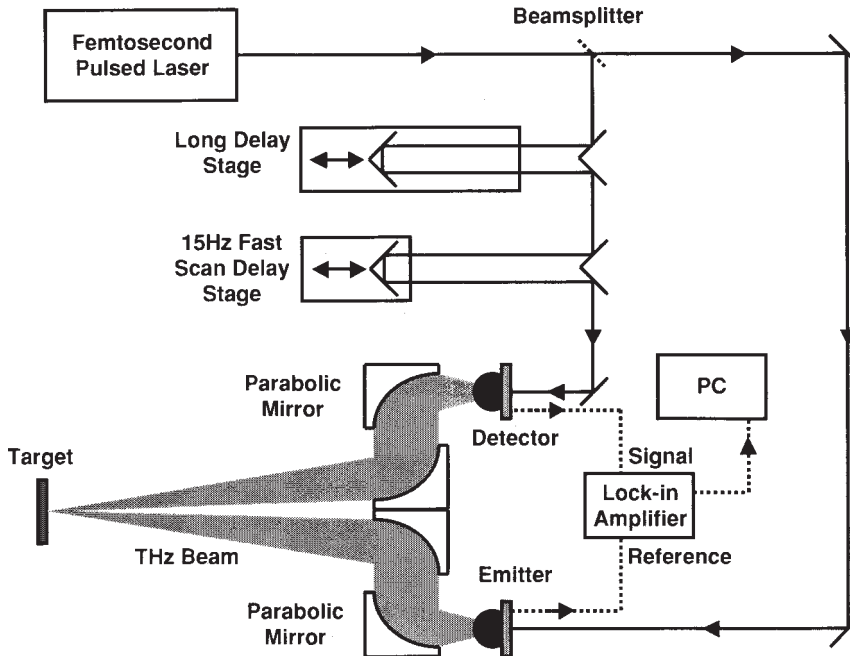
Figure 1.33 Schematic representation of a terahertz spectrometer. Reproduced with permission from Ref. [82].

spectrometer generates pulsed broadband terahertz radiation in the range of 0.05 to 4 THz (1.4 to 130 cm^{-1}). Measurements on this instrument can be recorded in two modes: (i) a rapid-scan mode, where the optical time delay is generated by mirrors that move rapidly and continuously and for which the maximum resolution is 1 cm^{-1}; and (ii) a step-scan mode where the time delay is generated by a cube-corner retroreflector the position of which is controlled by a stepper motor, where the maximum resolution is 0.1 cm^{-1}. The rapid-scanning delay line allows both the delay position and the output of the lock-in amplifier to be digitized and re-interpolated to obtain the THz field as a function of optical delay in real time.

Terahertz radiation has the major advantage that, because the wavelengths are so long, scattering is minimized. Thus, it is often possible to measure a THz transmission spectrum through a pharmaceutical tablet or cardboard packaging material. However, the absorption spectrum of water contains a very strong, broadband centered at 5.6 THz (17.9 cm^{-1}) which has been assigned to the resonant stretching of the hydrogen bond between the water molecules (although the present author believes that that mode should be observed at considerably higher frequency and the 5.6 THz band is more likely to be due to a bending or torsional mode of the hydrogen bond.) In any event, the high absorption of water in the THz region makes it possible to accomplish whole-body imaging [83], to observe the contrast between muscle and adipose tissue [84] and also between tumor and normal tissue [85].
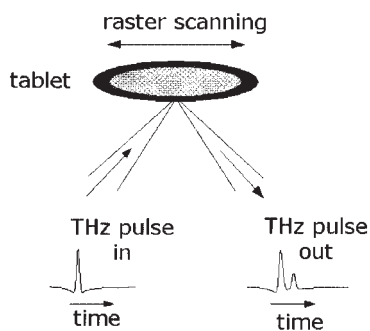
Figure 1.34 Schematic diagram of the experimental arrangement to examine the coating of a pharmaceutical tablet. Reproduced with permission from Ref. [86].

The spatial resolution in the x and y dimensions is determined by the diffraction limit (see Equation 1.3). Since λ is between ~70 and 700 μm, the resolution in these directions is far worse than for NIR or mid-IR microspectroscopy. On the other hand, significantly better resolution in the z direction may be obtained, since the THz pulse duration of <200 fs produces an axial resolution of 30 μm. The 3-D structure of the coating of pharmaceutical tablets has been studied by Fitzgerald *et al.* [86]. When the instrument is operated in the reflection mode, a reflected THz signal occurs whenever there is a change in boundary conditions; that is, the refractive index of two adjacent layers changes. This results in multiple pulses being returned to the detector, as shown schematically in Figure 1.34. Measurements of this type can be made in two ways: (i) one mode allows for a rapid single-point measurement of the coating thickness; alternatively (ii) multipoint measurements can be made by rastering the sample to allow false color maps of the uniformity of different layers to be produced.

An example of the time domain waveforms at several points on ibuprofen tablets from two different manufacturers is shown in Figure 1.35. The lower trace is for a tablet that has a single coating, whereas the upper trace is for a tablet with multiple coatings. By knowing the refractive index of each layer, its thickness can be calculated.

1.8
Summary

Powerful instruments for mapping and hyperspectral imaging in the NIR, mid-IR and far-IR regions, and by Raman spectroscopy, are now commercially available. Although instruments for imaging were initially expensive – frequently costing more than US$ 200 000 – the price tag continues to fall; for example, with the advent of rapid-scanning FPA imaging systems, the cost of mid-IR imaging
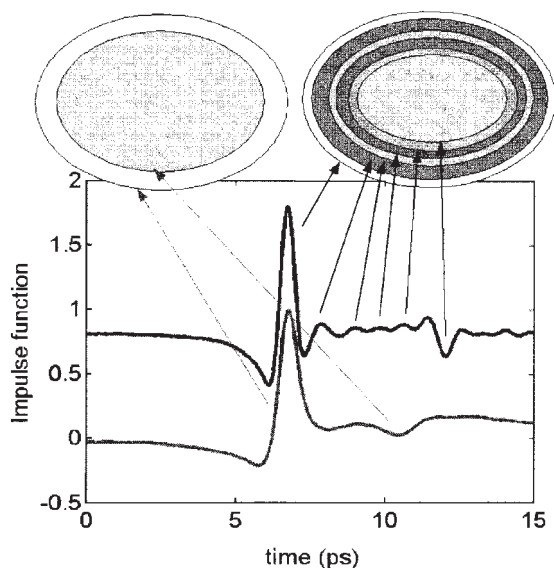
Figure 1.35 Example of depth profiling by terahertz spectroscopy. Pulses arise from interfaces between the coating layers, as illustrated by the schematic illustrations of the tablets. The lower trace is for the sample on the left, and the upper trace for the sample on the right. Reproduced with permission from Ref. [86].

spectrometers now starts from US$ 150 000. Instruments used for mapping measurements, where the spectra of single points on the sample are measured sequentially and the position of the sample is changed after each measurement, are less expensive than imaging spectrometers, but the measurements are much more time-consuming and the spectra, when measured with high spatial resolution, typically have a decreased SNR. The hybrid linear array mapping approach, although much faster than single-point mapping and with an increased SNR and spatial resolution, is still several-fold less efficient in terms of speed (time), SNR and spatial resolution than contemporary rapid-scanning, FPA-based chemical imaging systems. With NIR instruments, a similar comparison cannot be made, as most imaging measurements are made by changing the wavelength with an LCTF, and mapping NIR microspectrometers are rarely encountered. The situation is less definitive for Raman spectrometry, as mapping instruments are both sensitive and fast, especially with the development of electron-multiplying CCDs. In summary, it can certainly be said that hyperspectral imaging spectrometers are today revolutionizing the way in which vibrational spectroscopy is used, especially with respect to the analysis of pharmaceutical products and for medical diagnosis.

References

1 Lester, D.S., Kidder, L.H., Levin, I.W. and Lewis, E.N. (1998) *Cell. Mol. Biol.*, **44**, 29–38.

2 Lewis, E.N., Gorbach, A.M., Marcott, C. and Levin, I.W. (1996) *Appl. Spectrosc.*, **50**, 263–9.

3 Romeo, M.J., Dukor, R.K. and Diem, M. (2008) Introduction to spectral imaging, and applications to diagnosis of lymph nodes, in *Vibrational Spectroscopy for Medical Diagnosis* (eds M. Diem, P.R. Griffiths and J.M. Chalmers), John Wiley & Sons, Ltd, Chichester, UK, pp. 1–26.

4 Šašić, S. and Clark, D.A. (2006) *Appl. Spectrosc.*, **60**, 494–502.

5 Burch, C.R. (1947) *Phys. Soc. [London]*, **59**, 41–8.

6 Barer, R. and Cole, A.R.H. (1949) *Nature [London]*, **163**, 198–201.

7 Gore, R.C. (1949) *Science*, **110**, 710–11.

8 Blout, E.R., Bird, G.R. and Grey, D.S. (1950) *J. Opt. Soc. Am.*, **40**, 304–13.

9 Wood, D.L. (1950) *Rev. Sci. Instrum.*, **21**, 764–6.

10 Norris, K.P. (1954) *J. Sci. Instrum.*, **31**, 284–7.

11 Perkin-Elmer Instrument News (1951) Vol. 4, No. 4.

12 Rafferty, D.W. and Virnelson, R.C. (1997) *Spectroscopy*, **12** (5), 42–4.

13 Merklin, G.T. and Griffiths, P.R. (1997) *J. Chem. Phys. B*, **101**, 7408–13.

14 Griffiths, P.R. and de Haseth, J.A. (2007) *Fourier Transform Infrared Spectrometry*, 2nd edn, Wiley Interscience, Hoboken, NJ, pp. 277–81.

15 Griffiths, P.R. and de Haseth, J.A. (2007) *Fourier Transform Infrared Spectrometry*, 2nd edn, Wiley Interscience, Hoboken, NJ, pp. 161–8.

16 Williams, G.P. (2001) Synchrotron and free electron laser sources of infrared radiation, in *Handbook of Vibrational Spectroscopy*, Vol. 1 (eds J.M. Chalmers and P.R. Griffiths), John Wiley & Sons, Ltd, Chichester, UK, pp. 341–8.

17 Steiner, G., Sablinskas, V., Kitsche, M. and Salzer, R. (2006) *Anal. Chem.*, **78**, 2487–93.

18 Griffiths, P. R. and de Haseth, J.A. (2007) *Fourier Transform Infrared Spectrometry*, 2nd edn, Wiley Interscience, Hoboken, NJ, pp. 282–92.

19 Dumas, P. and Tobin, M.J. (2003) *Spectrosc. Eur.*, **15** (6), 17–23.

20 Levenson, E., Lerch, P. and Martin, M.C. (2006) *Infrared Phys. Technol.*, **49**, 45–52.

21 Miller, L.M. and Smith, R.J. (2005) *Vib. Spectrosc.*, **38**, 237–40.

22 Miller, L.M. and Dumas, P. (2006) *Biochim. Biophys. Acta*, **1758**, 846–57.

23 Dumas, P., Jamin, N., Teillaud, J.L., Miller, L.M. and Beccard, B.B. (2004) *Faraday Discuss.*, **126**, 289–302, discussion 303–11.

24 Everall, N., Lapham, J., Adar, F., Whitley, A., Lee, E. and Mamedov, S. (2007) *Appl. Spectrosc.*, **61**, 251–9.

25 Sommer, A.J. and Katon, J.E. (1991) *Appl. Spectrosc.*, **45**, 1633–40.

26 Smith, A.L. (1958) *Appl. Spectrosc.*, **12**, 153–9.

27 Romeo, M.J., Mohlenhoff, B. and Diem, M. (2006) *Vib. Spectrosc.*, **42**, 9–14.

28 Romeo, M.J., Boydston-White, S., Matthäus, C., Miljković, M., Bird, B., Chernenko, T., Lasch, P. and Diem, M. (2008) Infrared and Raman micro-spectroscopic studies of individual human cells, in *Vibrational Spectroscopy for Medical Diagnosis* (eds M. Diem. P.R. Griffiths and J.M. Chalmers), John Wiley & Sons, Ltd, Chichester, UK, pp. 27–70.

29 Mie, G. (1908) *Ann. Phys. (Leipzig)*, **25**, 377–452.

30 Walstra, P. (1964) *Phys. Br. J. Appl.*, **15**, 1545–52.

31 Hirschfeld, T. and Chase, B. (1986) *Appl. Spectrosc.*, **40**, 133–7.

32 Chase, D.B. and Rabolt, J.F. (1994) *Fourier Transform Raman Spectroscopy: From Concept to Experiment*, Academic Press, San Diego, CA.

33 McCreery, R.L. (2000) *Raman Spectroscopy for Chemical Analysis*, John Wiley & Sons, Inc., New York.

34 Sommer, A.J. and Katon, J.E. (1991) *Appl. Spectrosc.*, **45**, 527–34.

35 Delhaye, M. and Migeon, M. (1966) *Comptes Rendues Acad. Sci. Paris*, **262** (702-705), 1513–16.

36 Delhaye, M. and Dhamelincourt, P. (1975) *J. Raman Spectrosc.*, **3**, 33–43.

37 LaPlant, F. and Ben-Amotz, D. (1995) *Rev. Sci. Instrum.*, **66**, 3537–44.

38 Hollricher, O. and Ibach, W. (2007) Raman technology for today's spectroscopists. *Spectroscopy Supplement*, **June**, 38–43.

39 Cai, T.T., Zhang, D. and Ben-Amotz, D. (2001) *Appl. Spectrosc.*, **55**, 1124–30.

40 Savitzky, A. and Golay, M.C.E. (1964) *Anal. Chem.*, **36**, 1627–39.

41 Adar, F., Lee, E., Mamedov, S. and Whitley, A. (2006) *Spectroscopy Supplement: Raman*, **June**, 38–43.

42 Everall, N.J. (2007) Pittcon Conference and Expo, 2007, Chicago, IL, Paper 1820–5.

43 Macdonald, A.M. and Vaughan, A.S. (2007) *J. Raman Spectrosc.*, **38**, 584–92.

44 Pettinger, B. (2006) *Top. Appl. Phys.*, **103**, 217–40.

45 Zhang, W., Yeo, B.S., Schmid, T. and Zenobi, R. (2007) *J. Phys. Chem. C*, **111**, 1733–8.

46 Yeo, B.-S., Zhang, W., Vannier, C. and Zenobi, R. (2006) *Appl. Spectrosc.*, **60**, 1142–7.

47 Yeo, B.-S., Schmid, T., Zhang, W. and Zenobi, R. (2007) *Anal. Bioanal. Chem.*, **387**, 2655–62.

48 Hayazawa, N., Watanabe, H., Saito, Y. and Kawata, S. (2006) *J. Chem. Phys.*, **125**, 244706/1–244706/7.

49 Neugebauer, U., Roesch, P., Schmitt, M., Popp, J., Julien, C., Rasmussen, A., Budich, C. and Deckert, V. (2006) *Chem. Phys. Chem.*, **7**, 1428–30.

50 Roy, D., Wang, J. and Welland, M.E. (2006) *Faraday Discuss.*, **132**, 215–25.

51 Abrahamsson, C., Johansson, J., Andersson-Engels, S., Svanberg, S. and Folestad, S. (2005) *Anal. Chem.*, **77**, 1055–105.

52 Abrahamsson, C., Lowgren, A., Stromdahl, B., Svensson, T., Andersson-Engels, S., Johansson, J. and Folestad, S. (2005) *Appl. Spectrosc.*, **59**, 1381–7.

53 Chauchard, F., Roger, J.M., Bellon-Maurel, V., Abrahamsson, C., Andersson-Engels, S. and Svanberg, S. (2005) *Appl. Spectrosc.*, **59**, 1229–35.

54 Johansson, J., Folestad, S., Josefson, M., Sparen, A., Abrahamsson, C., Andersson-Engels, S. and Svanberg, S. (2002) *Appl. Spectrosc.*, **56**, 725–31.

55 Tsuchikawa, S. and Tsutsumi, S. (2002) *Appl. Spectrosc.*, **56**, 869–76.

56 Delphy, D.T., Cope, M., van der Zee, P., Arridge, S., Wray, S. and Wyatt, J. (1988) *Phys. Med. Biol.*, **33**, 1433–42.

57 Long, W. and Burns, D. (1997) *Anal. Chim. Acta*, **348**, 553–63.

58 Averett, L.A. and Griffiths, P.R. (2008) *Appl. Spectrosc.*, **62**, 377–82; 383–88.

59 Hudak, S.J., Haber, K., Sando, G., Kidder, L.H. and Lewis, E.N. (2007) *NIR News*, **18** (6), 68.

60 Treado, P. J. and Nelson, M.P. (2001) Raman imaging, in *Handbook of Vibrational Spectroscopy*, Vol. 2 (eds J.M. Chalmers and P.R. Griffiths), John Wiley

& Sons, Ltd, Chichester, UK, pp. 1429–59.

61 Christensen, K.A. and Morris, M.D. (1998) *Appl. Spectrosc.*, 1145–8.

62 Zhang, D., Hanna, J.D., Jiang, Y. and Ben-Amotz, D. (2001) *Appl. Spectrosc.*, **55**, 61–5.

63 Goldstein, S.R., Kidder, L.H., Herne, T.M., Levin, I.W. and Lewis, E.N. (1996) *J. Microsc.*, **184**, 35–45.

64 Suhre, D.R., Gottlieb, M., Taylor, L.H. and Melamed, N.T. (1992) *Opt. Eng.*, **31**, 2118–23.

65 Vo-Dinh, T., Stokes, D.L., Wabuyele, M.B., Martin, M.E., Soon, J.M., Jafannathan, R., Michaud, E., Lee, R.J. and Pan, X. (2004) *IEEE Eng. Med. Biol. Mag.*, Sept/Oct, 40–9.

66 Lewis, E.N., Treado, P.J., Reeder, R.C., Story, G.M., Dowrey, A.E., Marcott, C. and Levin, I.W. (1995) *Anal. Chem.*, **67**, 3377–81.

67 Snively, C.M., Katzenberger, S., Oskarsdottir, G. and Lauterbach, J. (1999) *Opt. Lett.*, **24**, 1841–3.

68 Snively, C.M. and Koenig, J.L. (1999) *Appl. Spectrosc.*, **53**, 170–7.

69 Bhargava, R. and Levin, I.W. (2005) Fourier transform mid-infrared spectroscopic imaging, Ch. 1 in *Spectrochemical Analysis Using Infrared Multichannel Detectors* (eds R. Bhargava and I.W. Levin), Blackwell Publishing Ltd, Oxford, UK, pp. 1–24.

70 Harrick, N.J. (1967) *Internal Reflection Spectroscopy*, John Wiley & Sons, Inc., New York.

71 Burka, E.M. and Curbelo, R. (2000) US Patent No. 6,141,1000.

72 Sommer, A.J., Tisinger, L.G., Marcott, C. and Story, G.M. (2001) *Appl. Spectrosc.*, **55**, 252–6.

73 Chan, L.A. and Kazarian, S.G. (2003) *Appl. Spectrosc.*, **53**, 381–9.

74 N.J. Everall (2007) ATR Imaging. Meeting of the Infrared and Raman Discussion Group, Sheffield, UK, April 2007.

75 Thomson, G.A. and Poulter, G. (2007) GB Patent No. 6,661,573.

76 Davis, J.R. (2003) US Patent No. 6,661,573.

77 Ricci, C., Bleay, S. and Kazarian, S.G. (2007) *Anal. Chem.*, **79**, 5771–6.

78 Griffiths, P.R. (2001) Far infrared spectroscopy, in *Handbook of Vibrational Spectroscopy*, Vol. 1 (eds J.M. Chalmers and P.R. Griffiths), John Wiley & Sons, Ltd, Chichester, UK, pp. 229–39.

79 Taday, P.F. and Newnham, D.A. (2004) *Spectrosc. Eur.*, **16** (5), 20–4.

80 Pickwell, E. and Wallace, V.P. (2006) *J. Phys. Appl. Phys.*, **39**, R301–10.

81 Auston, D.H., Cheung, K.P., Valdmanis, J.A. and Kleinman, D.A. (1984) *Phys. Rev. Lett.*, **53**, 1555–8.

82 Baker, C., Tribe, W.R., Cole, B.E. and Kemp, M.C. (2005) Developments in people screening using terahertz technology in optics and photonics for counterterrorism and crime fighting (eds T.P. Donaldson and C. Lewis), Proceedings, Optics and Photonics for Counterterrorism and Crime Fighting, SPIE, Bellingham, WA 2005, Vol. 5616, pp. 61–8.

83 Siegel, P.H. (2004) *IEEE Trans. Microw. Theory Tech.*, **52**, 1538–47.

84 Fitzgerald, A.J., Berry, E., Zinv'ev, N.N., Homer-Vanniasinkam, S., Miles, R.E. and Smith, M.A. (2003) *J. Biol. Phys.*, **129**, 123–8.

85 Pickwell, E., Fitzgerald, A.J., Cole, B.E., Pye, R.J., Ha, T., Pepper, M. and Wallace, V.P. (2005) *J. Biomed. Opt.*, **10**, 064021.

86 Fitzgerald, A.J., Cole, B.E. and Taday, P.F. (2005) *J. Pharm. Sci.*, **94**, 177–83.

2
Chemometric Tools for Image Analysis

Anna de Juan, Marcel Maeder, Thomas Hancewicz, Ludovic Duponchel, and Romà Tauler

2.1
Introduction

Hyperspectral images are measurements which include information not only of high quality, but also in high quantity. As the spectral output from an image provides a massive data set, there is a clear need to identify those tools that are capable of handling such measurements and extracting any interpretable knowledge. Before the analysis of an image is attempted, two main questions should be asked: (i) What are the chemical and mathematical properties of the measurement?; and (ii) What is the objective of the analysis? The answer to the first question will delimit the families of methods that potentially can be used, and also help in the design of new algorithms that may take into account the specificities linked to the image's nature. Setting the objective of the analysis will highlight the specific algorithm to be used, taking into account the input information available and the desired outcome.

The use of chemometric tools in image analysis is crucial in order to take advantage of the full measurement; this is opposed to the 'classical approach', where only pieces of information from the whole image are taken in order to provide easily visualizable, but partial representations. Image analysis is a field which is undergoing constant development in chemometrics and where although some solid knowledge has been already built, new working possibilities continue to emerge. In recent years, much effort has been devoted to exploring the spectral and spatial information contained in an image (known under the general denomination of multivariate image analysis, MIA) and to assigning the pixels of an image to different groups, according to the similarity of their spectral features (image segmentation). Whilst within these areas a number of excellent reviews and tutorials have been published [1–4] and improvements to the existing methodologies continue to appear, less-explored topics include the use of regression or calibration methods to relate the information of the image to properties, such as concentrations. As in classical spectroscopy, this area is particularly relevant in the near-infrared (NIR) images of food and/or pharmaceutical products. Multivariate resolution methods

are among the most recent tools incorporated into the field of image analysis, and these have proven to be most easily adapted to the nature of these measurements. Indeed, resolution methods can provide the pure spectra and distribution maps of the image constituents from sole raw image measurements.

When considering the diversity of existing and in-progress methodologies for image analysis, it would be far too ambitious and unrealistic to attempt to explain all of these in a single book chapter. Instead, we will focus here on a general description of hyperspectral measurements, and on some recent aspects of image analysis that although having received less attention in the available literature, may be of particular interest for infrared and Raman images.

Both, Raman and infrared spectroscopies provide information that is rich in fine spectral features, thereby providing excellent structural information and the possibility to differentiate among image constituents based on their distinct 'spectral fingerprints'. It is for this reason that resolution techniques, aimed at recovering the real pure spectra and distribution maps of the chemical components from a raw image, might benefit from the highest spectral definitions of Raman and infrared spectroscopic images. The adequacy of resolution methods to the nature of the Raman and IR measurement and the smaller amount of literature about these kind of chemometric methodologies for image analysis justifies that a large part of the chapter will be devoted to this field. While other methodologies will be described briefly, the reader will also be directed towards other literature sources that will provide further information on the subject, should this be required.

2.2
Hyperspectral Images: The Measurement

Hyperspectral images represent a particular type of measurement that contains both spatial and spectral–and thus chemical–information about a sample. The sample is physically preserved and compartmented into small surface or volume areas, referred to as 'pixels' or 'voxels', respectively. Each of these small portions of the sample is represented by a spectrum. Information on the chemical composition can then be extracted through an examination of the spectra and an interpretation of their bands, or by confrontation with a spectra library. Information on the constituent distribution is consequently obtained from the pixel-to-pixel spectral variation.

It is important, therefore, to take into account the spectral and spatial information contained in an image, because this duality conforms the singularity of this type of measurement as opposed to other bulk sample spectroscopic measurements. Data analysis tools should also take this spatial/spectral character into account if the maximum information is to be extracted from the raw data.

2.2.1
The Data Set and the Underlying Model

Hyperspectral images are often displayed as data cubes, where two dimensions are the pixel coordinates (x and y) and the third dimension is the spectral one. In

the following, the spectral dimension (wavelength/wavenumber) will be generally termed as the 'channel'. When dealing with a multilayer image, we should imagine a hypercube with three spatial directions (the x-, y- and z-voxel coordinates) and the spectral direction.

While this representation is very faithful to the nature of the measurement, it is also important to consider the underlying chemical (mathematical) model of the measurement, as knowledge of the model will allow selection of the data tools that adapt best to it.

It is tempting to associate the visual three-dimensional (3-D) or four-dimensional (4-D) representation of monolayer or multilayer images with equally dimensioned data arrays. This would force us to seek chemometric tools capable of handling tensors or higher-order data sets. Fortunately, the mathematical description of the variation of the data within an image is much simpler, and only needs the use of data tables that adequately represent the underlying bilinear chemical model of any spectroscopic measurement, that is the Beer–Lambert law.

It is well known that the spectrum of any pixel is represented by the concentration-weighted sum of the contributions of the pure spectra of the image constituents. These concentration weights vary from pixel to pixel, depending on the pixel composition, but the pure spectra of the constituents are the same along the whole image. These chemical ideas can be expressed mathematically by a bilinear model. First, we should unfold the image cube into a data table that contains all pixels one under the other (see Figure 2.1). This data table contains the raw image measurement and can be decomposed into the product of a matrix of pure spectra by
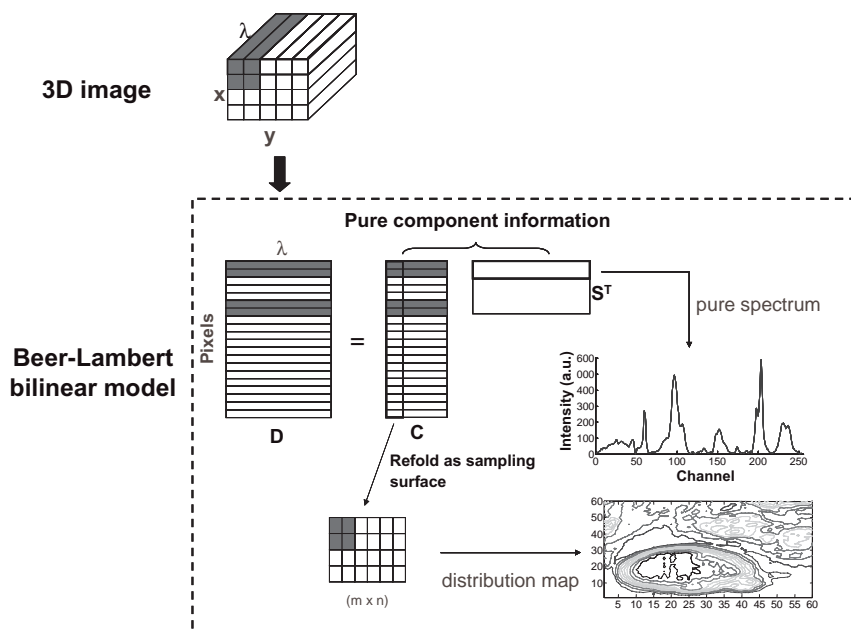
Figure 2.1 The underlying Beer–Lambert law (bilinear) model of hyperspectral images.

the concentration weights of these pure components in each pixel. In matrix form, the expression reminds us clearly of the Beer–Lambert law:

$$\mathbf{D} = \mathbf{CS^T} + \mathbf{E} \qquad (2.1)$$

The matrix $\mathbf{S^T}$ contains the pure spectra of the image constituents, and matrix $\mathbf{C}$ the concentration values of these constituents in each pixel. As we work with real measurements, $\mathbf{E}$ contains the experimental error due to signal variation, and not to the signal provided by the chemical compounds. By taking a row of the $\mathbf{C}$ matrix, information on the chemical composition of the related pixel can be obtained, whereas by taking a column the pixel-to-pixel variation of the concentration of a particular image constituent can be seen. Then, by folding back each $\mathbf{C}$ column to recover the original two-dimensional (2-D) or 3-D image configuration, the distribution map of each particular image constituent can be obtained.

There are important consequences linked to the bilinear image model, the positive points being linked to the simplicity of the mathematical model. There are many well-known chemometric tools that function to decompose the raw data into bilinear models and which, therefore, may be potentially suitable for image analysis. The negative aspect here is the decrease in the image dimensionality–that is, from the original 2-D or 3-D spatial dimensions into a single pixel direction, which implies that the concept of pixel neighborhood is lost and we should find additional ways of incorporating this spatial information into the classical bilinear analysis tools.

Today, a wealth of methods and algorithms is available that we can use to deal with images. As will be seen in the following sections, the selection is largely influenced by the goal of the analysis. For example, we may simply want to explore the image, and may be more interested in spatial or spectral information. Alternatively, we may try to segment the image into groups of similar pixels, or establish a quantitative model between the image measurement and some independent information, such as concentrations. We may even try to recover the underlying bilinear model of pure constituents from the raw measurement. Clearly, it is very important to select the right tool for the right purpose since, although we will encounter much progress in the adaptation of existing chemometric tools to the particular features of an image data set, we can also derive a host of information simply by using the available methodology.

2.3
Image Preprocessing

Although hyperspectral images contain a lot of information, the quality of the raw measurements is often affected by noise or by instrumental variations that hamper the analysis. Typical problems encountered in image measurements are the high noise level, the presence of intense and irregularly shaped baseline contributions or the existence of anomalous pixel spectra (dead pixels or outliers) that may influ-

ence the results of the image analyzed. It is for this reason that an effective pre-processing system can significantly improve the results obtained from any image data analysis tool. When the quality of the signal has been ensured, additional data pretreatments or image compression may be necessary, depending on the data analysis to be carried out.

2.3.1
Signal Preprocessing

2.3.1.1 De-noising

In recent years, many methods have been designed to de-noise spectroscopic data sets, all of which can be applied to hyperspectral images [5, 6]. Some of these methods rely on smoothing procedures, whether by averaging or fitting neighbor-ing spectral channels to a polynomial function (such as the Savitzky–Golay approach [7]), or on mathematical signal filtering (Fourier transform-based filters or wavelet-based filters [8, 9]). When applying any of these methodologies, it is vital that none of the relevant features of the data set is removed together with the noise [10, 11]. Other methods, such as principal component analysis (PCA) decom-pose the original data set into a bilinear model of latent variables [5, 12], a small number of which relate to chemical variation, and the rest to noise. The reproduc-tion of a data set, taking only the model with the relevant components, is also a good method of denoising. An appreciation of the de-noising effect of PCA on the spectra of a Raman emulsion image is shown in Figure 2.2b (more detailed infor-mation on the PCA method can be found in Section 2.4.2).

2.3.1.2 Baseline Correction

This is a commonly used preprocessing in image analysis that works better if it is performed after image denoising. In this way, the baseline is better defined and can, as a consequence, be better subtracted. Again, a typical baseline correction,
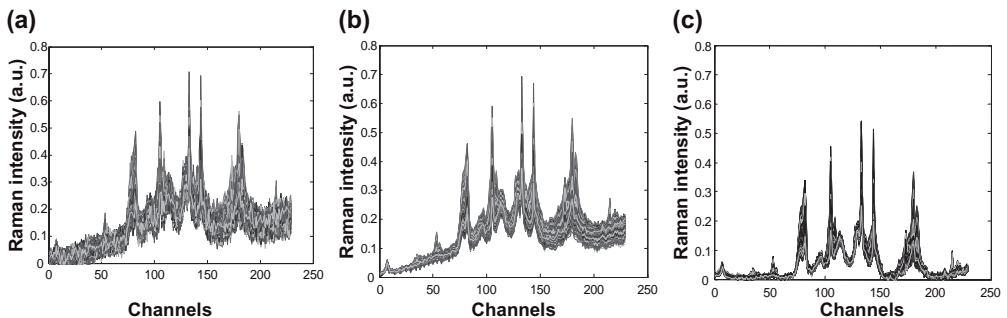
Figure 2.2 (a) Raw spectra of a Raman emulsion layer image; (b) Spectra after de-noising by principal component analysis (PCA); (c) Spectra after de-noising and baseline correction by asymmetric least squares.

based on linear models or on more complex mathematical functions, can be performed [6, 13]. Other strategies, such as working with derivative spectra instead of the raw spectra, help to eliminate instrumental variations such as offsets or linear baselines that are unrelated to the chemical composition of the image. Recently, more sophisticated baseline correction methods have been reported that are capable of handling irregularly shaped baselines changing from pixel to pixel; asymmetric least-squares (AsLS) is a good example of these new methodologies [14]. The AsLS method is based on a recursive fitting of the whole spectrum with a baseline. In the first fitting step, all channels are used, with part of the spectrum above the fitting line and part below. The spectral channels above the fitting line – that is, those channels where there is an absorption band – are downweighted in the next fitting step. After a small number of fitting cycles, no more variation occurs and the fitted baseline obtained is used to correct the spectrum. Depending on the shape of the baseline, the two parameters – one linked to the smoothness of the fit and one to the penalty imposed on the positive residuals (channels above the fitted baseline) – can be adjusted. This type of correction is particularly useful in spectra, such as Raman and infrared, where the baseline is smoother and has a significantly lower frequency than the spectral features. The baseline correction effect by AsLS on de-noised emulsion data is shown in Figure 2.2c.

2.3.1.3 Detection and Suppression of Anomalous Pixels or Anomalous Spectral Readings

Because of diverse instrumental artifacts, some of the pixels may show unexpected spectral readings (e.g., spikes)or present completely abnormal spectra (dead pixels) [15]. The presence of these very different measurements can distort the results obtained from image analysis, and these should be detected and eliminated/ corrected. One easy method of detecting unexpectedly high or low results may be by using thresholding methodologies that can highlight spectral readings (or complete spectra) that are well below or above a representative reference value (spectrum). Median values for spectral readings or median spectra taken from regions of interest (ROI) in the image can be used as references for this detection. For this purpose, mean values are not recommended because they can be significantly modified by the influence of any abnormal measurements [15]. Anomalous readings – for example, spikes – can be replaced by interpolated values obtained by taking the readings of normal neighboring spectral channels for this purpose. Likewise, dead pixels can be replaced by interpolated spectra, taking as reference the normal neighboring pixels.

2.3.2
Data Pretreatments

When the signal preprocessing is finished, additional pretreatments can be carried out to enhance certain properties of the image data set. Again, the spectra in an image can be subjected to any data pretreatment used in traditional spectroscopic data sets, with the choice depending on the spectral structure and the goal of the

data analysis. To give some examples, derivatives can be carried out to stress subtle differences in spectral features among spectra. Spectra normalization may represent an option when the focus is on comparing the shapes of the pixel spectra independently from their global intensity, for example for pixel classification purposes. Centering or scaling of spectral channels may also be options in quantitative regression methods. In contrast, keeping the original spectra intensity may be relevant in resolution methods. Further information regarding the effect of the main data set pretreatment on the results of the data analysis is available elsewhere [1, 5, 6, 13, 15–17].

2.3.3
Image Compression

Very often, the large size of raw images results in unreasonable computation times. Depending on the size of the image, and on the intensity of computation of the data analysis tool selected, the original image should be compressed. Compression can be performed on the spectral and/or on the spatial dimension. The simplest compression is to bin the image as much as needed so as to reach the desired data set size. The term 'binning' means to add the readings in an interval of neighboring spectral channels to form a single measurement (spectral binning), or likewise to add the spectra of neighboring pixels (binning in the pixel direction) to obtain a single spectrum. Which direction (spatial/spectral) should be binned will depend on the resolution of the image, and on which type of information is preferred. Although the binned image will enclose the information in all spectral channels or pixels, it will suffer a loss of spatial and/or spectral resolution. However, most images can be significantly reduced in this way without losing any relevant information. Compressed representations of the image that retain all of the information in the spectral channels can be obtained by using other methods, such as PCA. In this case, the original spectral channels are replaced by a small number of variables (principal components), which are linear combinations of the original ones and express the image information very efficiently [1].

A simple way of accelerating the computing time is based on the selection of a reduced number of pixels or spectral channels, according to different criteria. This is the case if feature selection is performed in the spectral direction, or if the analysis is performed on a representative pixel subset. Many methodologies are available for this purpose, some of which rely on the straight selection of the purest pixels or the purest spectral channels, such as SIMPLISMA [18–20]; others are based on more exhaustive search strategies, such as genetic algorithms [21–23]. A selection can also be made on spectral channels that have been previously transformed, as in wavelet-transformed data [8, 24, 25]. Representative pixel subsets can also be obtained by using sampling methodologies, taking into account the same strategies as are followed in chemical sampling [1]. If the compression performed does retain the relevant information on the original image, then no matter which methodology is used no deterioration will occur in the quality of the image analysis results.

2.4
Exploratory Image Analysis

Independent of the final objective of image analysis, it is always worth exploring the image in both spatial and spectral directions to obtain a first insight into the most relevant spectral features, or on any peculiarities linked to the component distribution.

2.4.1
Classical Image Representations

Some traditional approaches to exploring an image are carried out by sacrificing much of the information in order to obtain visual plots that can be easily interpreted with minimal or even zero computation effort. For example, the distribution map of a constituent can be displayed by taking a slice of the image on a particularly relevant wavenumber. This implies that many spectral channels carrying information are ignored and that the utilized wavenumber is assumed to have selective information for that particular component. However, such an assumption is only reliable when all the constituents of the image (and their pure spectra) are perfectly known. Even in this case, it may happen that a particular component does not have any selective wavenumber and, therefore, a map derived using a single mixed spectral channel will be a distortion of the real situation. It should also be taken into account that images from natural or complex samples may contain unknown components, so that assuming the presence of selective spectral channels without any solid evidence could provide incorrect distribution maps.

Another classical representation of images is the global intensity plot. This graph is obtained by adding up the readings of all spectral channels in a pixel spectrum. In this way, each pixel is represented by a single number related to the total spectral intensity measured. These plots allow for the observation of certain spatial features in the image, but do not provide any information about the chemical composition of the image, because all of the spectral information is collapsed into a single numerical value. At most, they provide a first approximation of the physical characteristics of the image. It would also be a mistake to associate these intensity measurements with concentrations, as the composition among pixels is variable and the intensity can also be affected by slight pathlength changes among pixels. Figure 2.3a shows the global intensity plot and Figure 2.3b a distribution map based on a single spectral channel for a monolayer emulsion image.

2.4.2
Multivariate Image Analysis (MIA) and Principal Component Analysis (PCA)

In contrast to classical approaches, MIA uses all of the information contained in the original image in the spatial and spectral directions, and provides simple ways of visualizing the image while preserving the relevant original information [1,
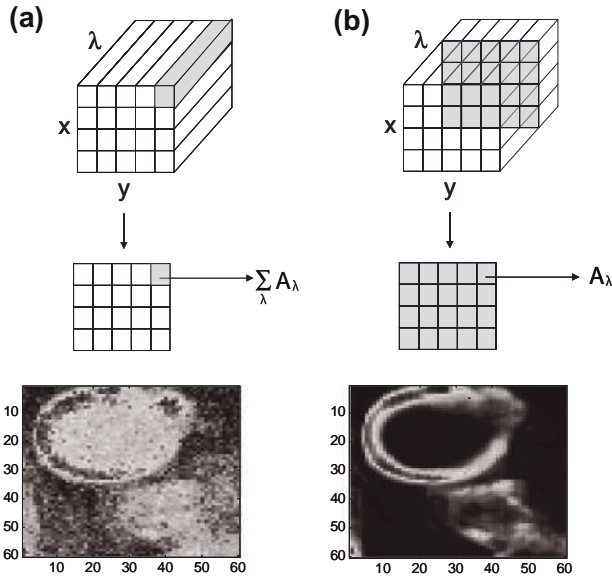
Figure 2.3 Classical visualizations of a Raman emulsion layer hyperspectral image. (a) Global intensity plot; (b) Distribution map derived from a single wavenumber.

26–29]. Very often, the expression MIA is linked to PCA, although many other methodologies could respond to this general denomination. The early and widespread use of PCA to analyze images is easily understood when considering the inner properties of this methodology. PCA is a chemometric method that decomposes a data table into a bilinear model of latent variables, the so-called 'principal components', according to the expression:

$$\mathbf{D} = \mathbf{TP}^{\mathbf{T}} + \mathbf{E} \tag{2.2}$$

where $\mathbf{T}$ are the scores, $\mathbf{P}^{\mathbf{T}}$ the loadings, and $\mathbf{E}$ accounts for the experimental error. Note that $\mathbf{D}$ must be rearranged, as shown in Figure 2.1. The principal components are linear combinations of the original variables, and are calculated so that they express the maximum variance contained in the data set in decreasing order of importance and there is null correlation among them [5, 12, 16]. In the context of image analysis, this means that even though an image can have hundreds or thousands of spectral channels, the relevant information in all these channels is contained in a very small number of principal components. This is due to the repeated information among spectral channels in the original image. Therefore, although a number of principal components equal to the number of spectral channels is calculated, only the first few describe spectral variations linked to the chemical composition of the image, while the remainder account for noise-related signal contributions.

It is worth noting the identical form of the PCA model and the Beer–Lambert law in matrix form, $\mathbf{D} = \mathbf{CS}^T + \mathbf{E}$. If the chemical model of an image only needs as many pure spectra as image constituents to reproduce any pixel spectrum, it should not be surprising that the number of principal components needed to describe an image data set is equal to the number of chemical constituents of the image. Indeed, the rows in the loadings matrix ($\mathbf{P}^T$) could be interpreted as abstract pure spectra and the columns in the scores matrix ($\mathbf{T}$) can also be folded back to form abstract distribution maps (as with the stretched concentration profiles in $\mathbf{C}$ in Figure 2.1). It is also illustrative to compare the real pure spectra and distribution maps of an image with the analogous loadings and scores representations, respectively.

Figure 2.4 shows a comparison of the results obtained from the PCA and real chemical models for a Raman emulsion image [30]. The latter image is formed by four constituents related to the drop phase, the interphase, an additive and the off-drop phase. The two models (real and PCA) resemble each other when considering general trends; for example, the 'score maps' are reminiscent of the real distribution maps, although the information seems to be more mixed, and the most salient spectral features in the real spectra can also be found in the different
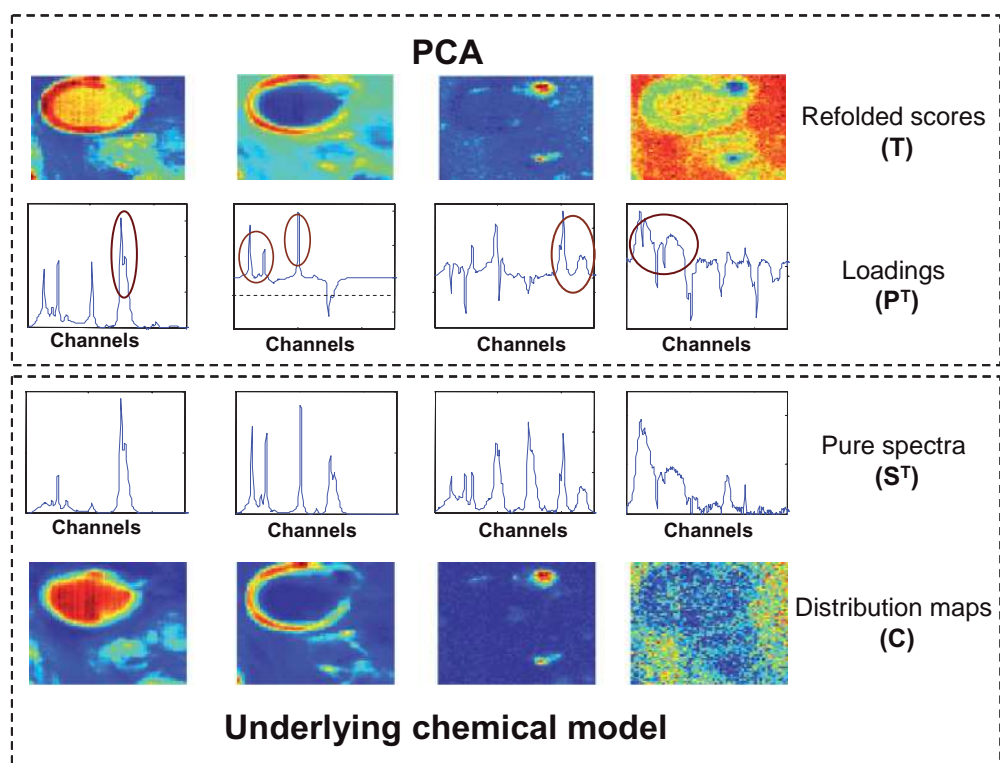
Figure 2.4 PCA model and real chemical Beer–Lambert model for a Raman emulsion image.

'loading spectra' (see the circled bands in Figure 2.4). There are relevant differences that should be taken into account, however. When comparing the pure spectra and the loadings, the first striking difference is the lack of any chemical meaning of the loadings, with negative bands (below the dashed line) nonexistent in the original Raman spectra. Likewise, we find negative values in the score distribution maps (color scale not shown), unacceptable for real concentrations. This stems from the fact that the principal components are calculated to maintain a null correlation among them; that is, the different 'loadings spectra' are completely uncorrelated. However, the real spectra of constituents hardly ever obey this condition, and it is for this reason that a principal component cannot be directly associated with a real chemical compound because the mathematical properties and chemical meaning of both are essentially different.

Nevertheless, performing PCA on an image data set is always useful because, often, the *a priori* information available is very scarce. When considering the loading plots, high absolute values will mark relevant spectral features for the image description. The score distribution maps will also provide insight as to which zones of the image are most related to the features detected in the related loadings. It is worth stressing here that PCA allows for a drastic decrease in the dimensionality of the original image data, preserving all of the relevant information enclosed in the abstract principal components. This strategy is very different from picking a few spectral channels for visualization, when all of the information outside the selected channels is thrown away. In PCA, all wavenumbers are represented under the different PC combinations, so that the image scores and loadings represent an excellent first approach to visualize an image in a space of small dimensions, without losing the richness of information of the original measurement.

It is interesting to examine a complementary aspect linked to the PCA compressed representation of an image. In a PCA model, a pixel is no longer represented by a full spectrum, but rather by a small number of score values that provide complete information about its chemical composition. Thus, pixels of similar composition in an image are expected to have similar score values. This idea has been used for image segmentation purposes, by using the score values instead of the full pixel spectrum as input information for the suitable segmentation algorithms. A simpler visual way to detect pixel clusters without the need of further calculation is through the observation of scatter plots of pixel scores. In these 2-D plots, two principal components are taken as the axes and each pixel is represented by a dot located according to the related score coordinates. Different scatter plots can be produced using different combination pairs of principal components. In scatter plots, the similar pixels cluster together in the displayed PC space. MIA software often allows for the creation of 'pixel masks' enclosing pixel clusters in scatter plots that afterwards are located spatially in the original image [31]. These masks can be created by a visual inspection of the score plots, enclosing groups of close pixels, or they may be automated with the help of auxiliary chemometric tools [32]. Figure 2.5 shows this procedure on the emulsion example. In this figure, the scatter score plot of PC3 versus PC2 is displayed (each pixel is a dot in this

(a)

The PC's viewed as a composite RGB image   Score space

Associations: Red = T_1 Green = T_2 Blue = T_3

(b)
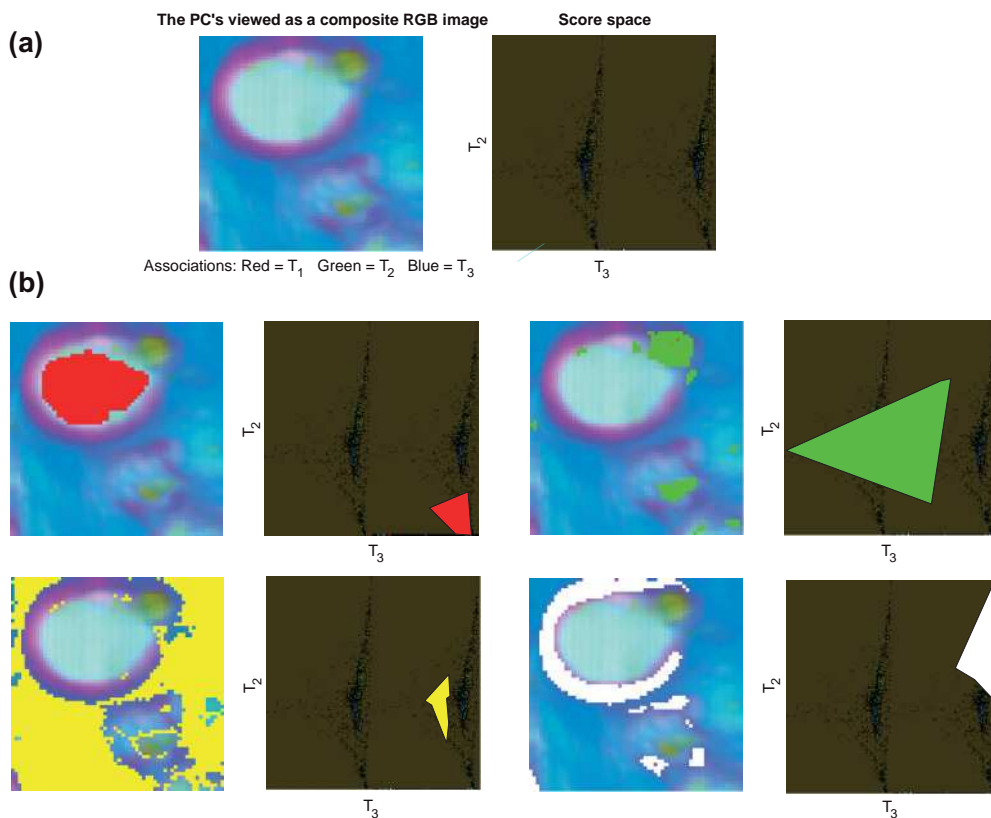
Figure 2.5 (a) Left: RGB plot of the score images related to PC1, PC2 and PC3. Right: Scatter score plot of PC3 versus PC2; (b) Pixel masks in scatter score plot and location of mask pixels in the Raman monolayer emulsion image.

plot; see Figure 2.5a, right plot). Figure 2.5b shows how the different masks in this scatter plot (drawn by visual inspection and marked in different colors) group those pixels with similar score values, which belong to the different image constituents in the sample (drop, additive, interphase and off-drop phase). The plots at the left of the masked score plots display the location of the pixels in the mask on the original 2-D spatial image representation.

In the approach presented, the shape of the pixel spectra is the driving force to detect structures or similarities among pixels. Recent improvements in MIA software incorporate explicit information on the spatial location of the pixels to assist with any interpretation of the image information [25].

Similarly to PCA, other methods exist that represent the image raw data in a space of smaller dimensionality, aiming to retain all relevant information. Some of these project the image in a small space according to different criteria, such as statistical independence in independent component analysis (ICA) [33], or are based on properties linked to data topology [34].

2.5
Quantitative Image Information: Multivariate Image Regression (MIR)

Although images are mainly focused on providing information on the chemical composition of the sample and the compound distribution, there are possibilities to use them for quantitative purposes if reference information is available. The methodologies in this field have been often referred to as multivariate image regression (MIR), although the denomination of MIR extends, in a more general way, to the relationship that may be established between an image and any related property to be predicted, or also among images [35–40]. MIR includes multivariate calibration methods used in spectroscopic data sets that have been adapted to investigations with images [5, 6, 16]. As in other chemical data examples, the most commonly used algorithm is partial least squares (PLS) [41], which functions by building an inverse calibration model, $\mathbf{Y} = \mathbf{XB}$ between a matrix of spectra ($\mathbf{X}$) and a matrix with the properties to be predicted ($\mathbf{Y}$); that is, concentration values in a quantitation context. Instead of working with the original variables in matrices $\mathbf{X}$ and $\mathbf{Y}$, PLS encloses the information of these original variables in a small number of latent variables that are calculated so that they capture the maximum covariance between $\mathbf{X}$ and $\mathbf{Y}$. The same caution used in building a PLS model for spectrometer data, for example the selection of the number of latent variables, internal and external validation, should be taken into account when the method is used with image data sets [5, 6, 16].

The main difference between using calibration methods for spectrometer data and images is that, in the first case, there is a reference concentration value per spectrum, whereas for images, the single concentration value relates to thousands of pixel spectra. Besides, the reference concentration value refers to the bulk sample and, in an image, there may be pixel-to-pixel variations of concentration for a particular compound. Therefore, strategies should be found that retain the validity of the relationship between the bulk concentration value and the spectral information in the image. It should also be taken into account that, because of instrumental reasons, the relationship between the spectrum intensity and the concentration may vary from pixel to pixel. Some studies recommend specific types of image preprocessing to account for these nonchemical differences [42].

The ideal situation to use calibration methods in images would be to have reference concentration information for each pixel. In this instance, a number of calibration models equal to the number of pixels would be built. By keeping the same experimental conditions in the image recording process, very accurate and precise results could then be obtained, although this is a very uncommon situation. Usually, there is a tendency to have only one quantitative value of the sample per image. From now on, only the scenario where a number of images is available with a single concentration value per image will be considered. The particularities linked to calibration for image data sets are linked to the strategy used to build the calibration model and to the information obtained in the prediction step.

In order to establish the calibration model, the available information is a set of calibration images and related concentration values. Due to the pixel-to-pixel

heterogeneity, a model built selecting a pixel spectrum per image would be neither representative nor reliable. A good approach to seek representivity has been proposed by Geladi [15], and consists of taking the median spectrum obtained from a ROI in the image as the representative spectrum of the image. The ROI should be large and contain many pixels in order to provide a median spectrum that is representative of the bulk concentration of the sample. The median spectrum is not a real measured spectrum, but rather is constructed by taking the median value of all spectral readings at each of the spectral channels measured. Median instead of mean spectra are preferred so as to avoid the influence of extreme spectral readings (from anomalous pixels or spectral channels) in the spectrum used to build the calibration model. Median spectra obtained from replicate images taken from the same sample can be used to be related to the same concentration value (see Figure 2.6 to see the scheme followed in the calibration step).

When the calibration model has been obtained, the validation is performed by applying the calibration model (the **B** matrix) to median spectra obtained from a set of validation images, for which the reference concentration value is known. As in any other calibration procedure, the predictions obtained can be used to evaluate
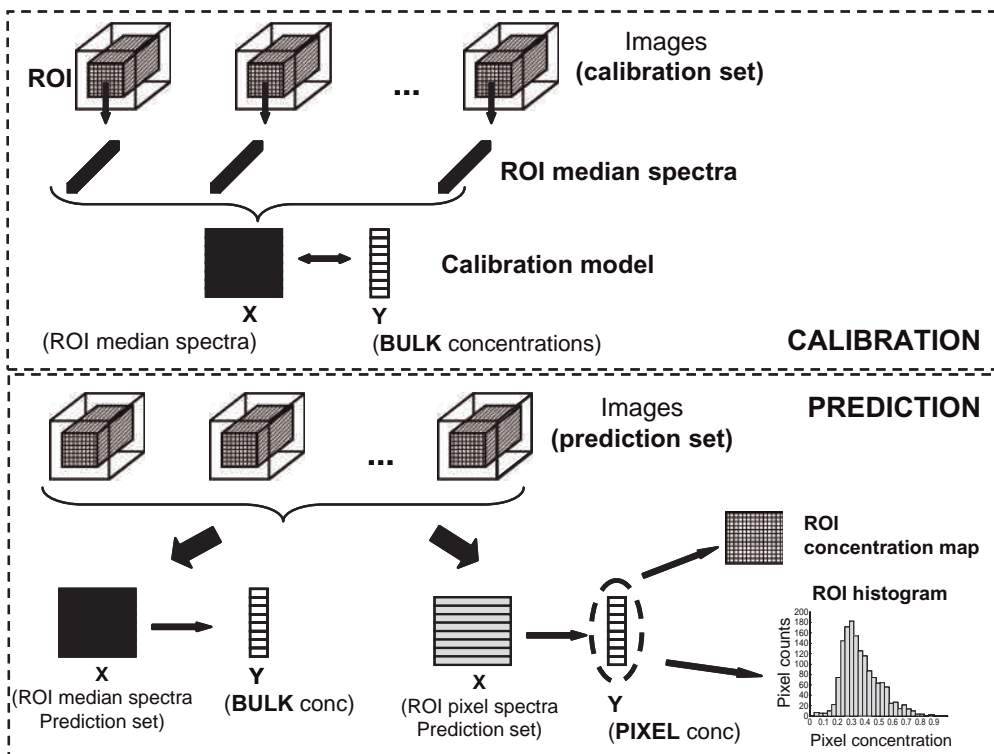
Figure 2.6 Strategies of calibration and prediction in multivariate image regression.

the accuracy and the precision of the bulk concentration estimates by examining the bias and the root mean square error in prediction (RMSEP).

$$\text{bias} = \sum_i (c_i - \hat{c}_i) \tag{2.3}$$

$$\text{RMSEP} = \sqrt{\frac{\sum_i (c_i - \hat{c}_i)^2}{ns}} \tag{2.4}$$

where c_i is the real reference concentration value for the ith sample, $\hat{c}_1$ the predicted concentration by the calibration model, and ns the number of samples. When the model has been validated, it can be used to predict bulk concentration values in unknown images.

So far, what has been presented does not differ much from the calibration models obtained with classical spectrometer data. However, the information obtained is greatly increased if we take into account the real nature of the image and use all of the available information – that is, all of the ROI pixel spectra – in the prediction step. When this is done, we obtain as many predicted concentration values as pixels in the image. The pixel concentration values obtained can be used in a straightforward way to display a distribution map of real concentrations, keeping the original spatial structure of the image (see Figure 2.6). This allows concentration information to be obtained in a local context, and also shows the homogeneity of compound distribution along the scanned image.

For statistical purposes, a histogram representation may be preferred, where the x-axis shows the concentration predicted values and the y-axis the pixel counts [15]. This histogram may provide information on the characteristics of the sample and also on the quality of the calibration model. As with the sample characteristics, the homogeneity of compound distribution can be easily seen by considering the width of the distribution obtained (the narrower the width, the more homogeneous the sample), while the presence of outlying pixels can be detected at the most extreme values of the histogram. The quality of the calibration model can be assessed in different ways. For example, a shift between the central value of the histogram and the reference concentration value of the calibration sample can detect the presence of a bias due to a bad selection of the number of components to be included in the model, or for other reasons. The width of the histogram is also indicative of the precision of the calibration model. Although the heterogeneity of the scanned sample will always be the main factor defining the width of the histogram, it may be interesting to determine whether the application of data pretreatments oriented to reduce instrumental variations of the measurements will also result in a decrease in histogram width. Recently, statistical diagnostics have been proposed that seek the correct balance between the histogram width and the shift between the center of the histogram and the reference concentration values to select the correct number of components in the calibration model.

It is relevant at this point to stress that calibration using hyperspectral images can provide results comparable to those given by spectrometer data, when median

spectra are used to predict bulk sample concentrations [43]. Moreover, when all the pixel spectra are included in the prediction step, the images provide much more detailed information regarding the complexity of the sample, highlighting aspects related to purity and heterogeneity that would never be known from a single spectroscopic measurement per sample.

2.6
Image Segmentation

One of the goals of image analysis is to identify groups of similar pixels in an image; that is, pixels with similar spectra and, therefore, similar composition and chemical or biological properties [4]. This operation is referred to as image segmentation, and can be used for different purposes, for example to separate zones in biomedical samples that may be later assigned to certain pathologies [44] or, simply, to obtain an insight into the variation of chemical composition along the surface scanned [45]. While many tools aimed at performing image segmentation are available, the main differences among them are linked to the *a priori* knowledge used in the segmentation process and to the definition of class membership for a particular pixel. The traditional implementation of the parent chemometric tools compares the spectral shape of the different pixels, as if they were completely independent from one another. Recently, some of these methodologies have been adapted to incorporate the spatial information linked to pixel neighborhood, and this has resulted in a better clustering performance for image data sets [25, 46].

2.6.1
Unsupervised and Supervised Segmentation Methods

These two families of methodologies can be distinguished according to the previous knowledge about the pixel classes used in the segmentation process. Unsupervised methods do not rely on any *a priori* knowledge, and take the whole unknown image to seek pixel clusters or classes, whereas supervised methods use previous knowledge of the pixel classes that need to be defined. That is, the class models are generated with well-identified pixels and are afterwards applied for class assignment of unknown pixels [5, 6, 47, 48].

Unsupervised methods assign pixels into the same cluster when their spectra are similar enough. The similarity can be evaluated with many different measures, depending on the algorithm at hand. As seen in Section 2.4, PCA is a good unsupervised segmentation method when the information in the scores scatter plot is used for this purpose (cf. Figure 2.5). In this case, the clusters are defined from a visual inspection of the scatter plots, creating masks that enclose pixels which group together in the PC space [1, 31]. A good point in the use of PCA for clustering is that, not only clusters can be obtained but, from the complementary information in the loading plots, it is also possible to detect which spectral features are linked to the different groups detected.

Other classical unsupervised cluster analysis methods rely on using mathematical indicators, such as distances, to quantify the similarity among pixel spectra. Thus, each pixel can be viewed as a point in the space of original wavenumbers or on other spaces, for example PC space. The coordinates of a pixel can be the spectral readings at the different wavenumbers (in the original image space) or the scores (in the PC space). Similar pixels should be close in the reference space and, therefore, distance measurements, such as Euclidean distance ($\wp$), can be used to assess this proximity:

$$\wp(x_i, x_j) = \sqrt{\sum_{l=1}^{d}(x_{il} - x_{jl})^2} \tag{2.5}$$

where x_i and x_j are two pixels and d is the total number of variables (wavenumbers, scores, etc.) defining the pixel coordinates. The distances can also be calculated from a pixel to the centroid of a cluster or between cluster centroids, and can be defined differently from a mathematical point of view [4, 47, 48]. The main distinction in *modus operandi* among unsupervised clustering methods based on distance measures is between agglomerative methods and partitional methods that attempt to optimize a clustering scheme with a predetermined number of clusters. Other methods using other concepts, such as density-based functions, will not be described here, although details may be found elsewhere [1, 49].

Agglomerative or hierarchical methods begin by considering each pixel as an individual class, after which the two most similar pixels are linked to constitute a new class. In each step, the number of classes decreases by one by merging the two closest clusters or a cluster with the closest pixel, until all pixels eventually form a single class. With these methods, it is possible to examine the clustering arrangements with different numbers of groups and to select a scheme that may be more easily interpretable. The drawback here is the intensive computation required, because new distances are calculated between pixels and clusters at each agglomerative step. This makes image compression a necessary preprocessing step, for example by using the scores as pixel coordinates or compressed images by spectral feature selection instead of the original full spectra. Although these methods provide very robust clustering schemes, the nested clusters result in a loss of flexibility of the clustering process. Single linkage, average linkage or Ward's method are among this family of algorithms [50–52].

Partitional methods function by optimizing a single clustering scheme with a preselected number of clusters [47, 48]. These methods generally begin with an initial set of centroid pixels, with the remainder of the pixels assembling around the closest centroid. Iterative cycles can be carried out, thus modifying the centroids every time to achieve a major degree of compactness in the clusters, or to improve a different optimization criterion. An index of compactness (E) can be defined as follows:

$$E = \sum_{j=1}^{g} \sum_{i} u_{ij} \wp(x_i, \omega_j) \tag{2.6}$$
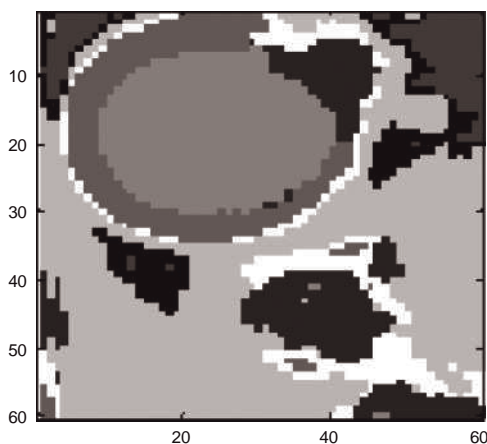
Figure 2.7 Results of image segmentation by the K-nearest neighbor method (hard clustering approach) for a Raman emulsion image.

where g is the number of clusters, ω_j the centroid of the jth cluster and u_{ij} defines the class membership of pixel i in cluster j (1 for presence, 0 for absence) [4].

These partitional methods are both fast and flexible, because they do not nest clusters; that is, the clustering schemes with five and six groups can be completely different. However, the selection of the number of clusters is not easy and, often, different results can be obtained depending on the starting point (centroids) of the clustering process. A good selection of the centroids is crucial to ensure good results and stable clustering schemes. Figure 2.7 shows the results of a partition clustering method on the emulsion image. As can be seen, pixels in some distinct zones in the image, such as the center of the drop, the interphase and the additive location (see Figure 2.4) are clustered together. There are other clusters more difficult to be interpreted. Unlike PCA, the remainder of the unsupervised clustering methods do not provide explicit information about the spectral features linked to the different classes, although the spectral information is the driving force for the clustering process.

Supervised segmentation methods operates by defining the different pixel classes beforehand with a series of well-identified pixels. Each different class is described by a model, and these models are used to assign unknown pixels to the predefined classes. Self-interactive modeling class analogy (SIMCA) [53–55] or PLS-discriminant analysis (PLS-DA) [56–58] are among the algorithms of this family. For example, PLS-DA functions by building class membership models by relating reference pixel spectra (**X**) to class membership information (**Y**), using the PLS algorithm. The class membership information is coded in a binary manner, assigning a value of '1' to a pixel in the class and a value of '0' to a pixel out of the class. Reference pixels in and out of the classes can be selected either by applying class membership masks in the image score scatter plots [59, 60], or by using results from unsupervised segmentation methods. When the discrimination model has been built it can be used to predict class membership values for

unknown pixels. As the **Y** predicted values for unknown pixels will hardly ever be 1 or 0, a threshold value between 0 and 1 is established that marks the membership of a pixel to a class. If the predicted class membership value is above the threshold, the pixel is in the class; if below, it is out of the class. So far, the methods described are based on linear models; other nonlinear methods, such as Artificial Neural Networks or Support Vector Machines, can also be used for the same purpose.

Although supervised and unsupervised methods have been in the past well-separated families, a number of hybrid approaches have appeared that combine both unsupervised and supervised classifiers for image segmentation purposes [61].

2.6.2
Hard and Fuzzy Segmentation Approaches

This distinction refers to the concept of class membership used in the segmentation method. In hard clustering methods, a pixel belongs to a single class, whereas in fuzzy clustering schemes, a pixel can have different probabilities to belong to several classes; that is, it has a fractional degree of membership for all clusters [4, 62, 63]. Recalling the index of compactness shown above, a hard clustering approach would only allow for degrees of class membership, u_{ij}, equal to 0 (pixel out of the class) or 1 (pixel in the class), whereas fuzzy approaches would allow for intermediate values between 0 and 1 for each pixel in the different classes.

In hard clustering schemes, the clusters are perfectly separated among them, whereas in fuzzy clustering a cluster overlap is allowed. Some fuzziness indices are based on the distances to the different clusters from a particular pixel. The fractional degree of membership of the pixel to the clusters will then be defined according to the distance that separates the pixel from the different clusters (a higher degree if the pixel is closer; a lower degree if it is further away).

Several factors can be considered to decide which segmentation modality is more suitable. On the one hand, hard clustering schemes provide a clear definition of the image groups, which may be more desirable when a clear segmentation scheme is needed. However, assuming the existence of perfectly defined classes with no overlap with each other implies that the pixel spectra of each class have a very well-defined and uniform spectral shape. This would be the case if pixels in each class were to be formed by a single chemical compound, or if regions that were well separated had a very homogeneous composition. This may not occur in many real images, where many pixel spectra reflect the signal contribution of several compounds overlapping on the image space. In heterogeneous images or images where interfacing zones of compounds may exist, a fuzzy clustering approach may be more appropriate to describe the real nature of the image. The more relaxed definition of class membership of fuzzy schemes accounts for this situation.

All of the methods and strategies presented in this section have a common characteristic, namely that the grouping schemes are obtained using only spectral information – that is, spectral similarity among pixels. This is a consequence of the original goal of the cluster analysis methods, oriented to find groups in spectra

collected from independent samples. In image analysis, pixels are not independent from each other, and it can be reasonably assumed that neighboring pixels are more likely to be similar than pixels that are far away from each other in the image. Therefore, the spatial position of a pixel in the image serves as potentially relevant information to be taken into account for image segmentation purposes [4, 46].

Recently, a number of modifications of the classical methods have appeared that incorporate the spatial distance among pixels as an additional criterion in the clustering schemes. Thus, similarity measures based on spectral distances, such as $\wp$, can be weighted incorporating pixel neighboring information; for example, the Euclidean distance can be redefined as:

$$\tilde{\wp}(x_i, \varpi_j) = \wp(x_i, \varpi_j) \cdot w(x_i, \partial_i, \varpi_j) \tag{2.7}$$

or:

$$\tilde{\wp}(x_i, \varpi_j) = \wp(x_i, \varpi_j) + w(x_i, \partial_i, \varpi_j) \tag{2.8}$$

where the term $w(x_i, \partial_i, \varpi_j)$ is the weight accounting for the neighborhood information between a pixel and a cluster, which can be defined in different ways. ∂_i is the symbol of the term that accounts for the neighborhood concept. When the pixel is close to a group, the weight term becomes small and, so, the considered distance for clustering, $\tilde{\wp}(x_i, \varpi_j)$. This strategy favors the incorporation of neighboring pixels into a group to the detriment of distant pixels, with larger weight terms. The incorporation of spatial information can also be performed out of the clustering process, as a preprocessing or postprocessing step [46].

There are many benefits which derive from the inclusion of spatial information into segmentation approaches. First, distant outlying pixels are not incorporated in clusters, the noise effect is minimized, and the general clustering scheme is smoothed. Another relevant improvement concerns the differentiation of spatially distant clusters that may be defined by similar spectral features. By adding the spatial-related weight term, the distances between far pixels are enhanced and cluster merging is hindered. The inclusion of spatial information has also been found useful in supervised segmentation methods, which do not use the concept of distance. The spatial information is incorporated in different ways in these types of algorithm [25, 64].

2.7
Image Resolution

2.7.1
The Image Resolution Concept: Monolayer and Multilayer Image Analysis

The resolution of hyperspectral images is focused on recovering the true underlying spectroscopic model from the raw recorded image. Thus, the goal is to know

the spatial (distribution map) and chemical (pure spectrum) information about each particular image constituent [65–67]. Resolution methods decompose the original raw image into the Beer–Lambert bilinear model, $\mathbf{D} = \mathbf{CS^T} + \mathbf{E}$, where $\mathbf{D}$ is the raw image, $\mathbf{S^T}$ is the matrix of pure spectra and $\mathbf{C}$ are the stretched concentration profiles. To do so, as shown in Section 2.2 (see Figure 2.1), the original 2-D or 3-D images should be unfolded into a data table with the spectra of all pixels one under the other. The spatial structure of the image is then recovered after the resolution process by folding back the stretched concentration profiles into the higher dimensional spatial ordering.

It is important to stress that resolution can be applied to one or more images together. Multi-image analysis finds an application whenever there is a multilayer image from a single sample or a series of images with related chemical composition – for example, groups of pills or the same sample imaged as a function of time, temperature or any other variable [65]. In these cases, the bilinear model is retained and, with it, the spectral consistency among different images. This means that the same image constituent has always associated the same pure spectrum in all the images simultaneously analyzed.

2.7.2
Spatial and Spectral Exploration

Resolution methods do not need *a priori* knowledge to perform the bilinear decomposition of the image, although when this information is available it can be included to obtain more accurate and chemically meaningful results. There are some aspects that might be of help in resolving an image. First, many resolution methods require a first guess of either the concentration profiles or the spectra of the pure constituents to begin an iterative search of the true underlying profiles. Knowing that this information is enclosed in the original measurement, some methods exist which are focused on finding the 'purest' spectral channels or pixels in the raw hyperspectral image [20, 68] – that is, the most dissimilar among them. The rows related to the purest pixels will provide good approximations of the pure spectra sought, whereas the columns linked to the purest spectral channels will allow for building approximate distribution maps of the pure constituents.

SIMPLISMA is one of the main methodologies used for this purpose and, as stated before, can be used to identify either the purest pixels or the purest spectral channels in an image [18]. If the focus is on finding the purest pixels, a purity index, p_i, will be calculated per each pixel spectrum as:

$$p_i = \frac{s_i}{m_i + f_i} \tag{2.9}$$

where s_i is the standard deviation of the elements in the pixel spectrum, m_i the mean and f_i an offset factor that accounts for the noise percentage in the data. The inclusion of this noise offset prevents the selection of background or noise pixels. The first spectrum selected is the one with highest purity. Once the first spectrum

is selected, the rest of spectra are normalized and a purity index is recalculated for each of them, as $p'_i = w_i p_i$, where w_i is a weighting factor that takes into consideration the dissimilarity of the pixel under analysis with the purest pixel previously selected (the more dissimilar the spectrum, the larger the weight). The second pixel selected will be the one with largest recalculated purity, p'_i. The sequence of purity recalculation (according to new weights based on the dissimilarity with all previously selected pixels) and new pixel selection will continue until a number of pixel spectra equal to the number of image constituents has been obtained. No previous knowledge on the number of image constituents is needed as the process can be stopped when the last purest spectrum selected is very similar in shape to a previously selected spectrum. Working in the pixel direction, the purest spectra of the image are obtained [19, 20]. Likewise, the selection can be made to identify the purest spectral channels and, as a consequence, the purest distribution maps can be derived.

Figure 2.8 shows an example of SIMPLISMA applied in the pixel and in the spectral direction to an emulsion image with four compounds (a drop, an
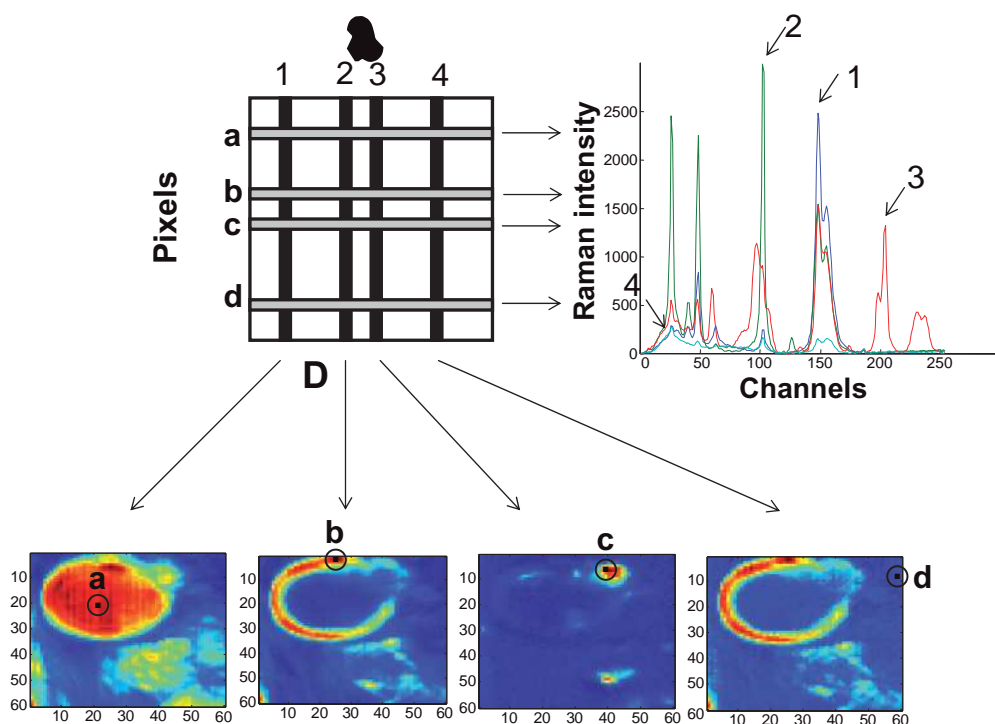
Figure 2.8 SIMPLISMA analysis on a Raman emulsion image. Representation of the spectra of the purest pixels (right plot) and the distribution map related to the purest spectral channels (bottom plot). Letters and numbers in both plots mark the location of purest pixels and purest spectral channels, respectively.

interphase, an additive, and an off-drop constituent). Here, a, b, c and d are the purest pixels selected in the image and provide the plotted spectra on the right-hand side, where 1, 2, 3 and 4 are the purest spectral channels that, once refolded, provide the distribution maps at the bottom of the figure. The pixels selected (a–d) are located in image zones clearly linked to the nature of the four constituents described and, therefore, it can be well imagined that their spectra will be very close (if not identical) to the real pure spectra sought. However, when considering the location of the four spectral channels selected (1–4), it can be easily understood why channels 1–3 produce reasonable distribution maps for the drop, interphase and additive constituents, but channel 4 fails to give a good map for the off-drop phase. Channel 4, despite being the most representative for the off-drop phase, has signal contributions from the remainder of the components, and therefore produces an unacceptable map for this component. These results stress two main points: (i) that SIMPLISMA often provides better results when applied in the pixel direction, because the possibilities to find selective pixels are often higher than to find selective spectral channels; and (ii) the straightforward association of SIM-PLISMA spectra and distribution maps with the real analogous profiles is a dangerous practice and may not always lead to the correct results.

Linked to the importance of the presence of selective pixels or spectral channels, and exploring the variation of the degree of compound overlap along the surface/volume scanned, there is another possibility to obtain information for future resolution purposes. As noted above, PCA for the whole image provides information on the total number of constituents of the data set. This information is derived from a global image analysis, and does not mean that all constituents are present in all pixels. To go to a local scale, PCA analyses should be performed on small areas of the data set (a pixel and its surrounding neighbors in the two or three spatial dimensions) until the whole image is PCA-scanned.

Fixed-size image window-evolving factor analysis (FSIW-EFA) is an evolution of the local rank algorithm Fixed Size Moving Window-EFA [69], which was designed particularly for the study of local pixel complexity in images [70]. To do so, two main concepts must be taken into account: (i) the need to divide the image into small areas to obtain local information; and (ii) the need to preserve the 2-D or 3-D spatial image structures, thus building the small areas by taking one pixel and all its surrounding neighbors.

Thus, FSIW-EFA can be used to perform local PCAs in the whole image by moving small windows around each individual pixel area. Each window is formed by a particular pixel and all of its neighbors in the two or three spatial dimensions of the image (see Figure 2.9a). The number of pixels in the window is a compromise between the smallest possible to preserve the spatial resolution of the image, and the total number of compounds in the image to allow for rank values representing all possible situations of compound overlap in the image. The singular values obtained in these local analyses are displayed together in singular value plots, where the spatial structure of the image is preserved (see Figure 2.9b for the emulsion example). In these plots, large values (in warm colors) represent significant contributions to the signal, related to the presence of chemical constituents, whereas small values (in cold colors) describe the experimental noise.
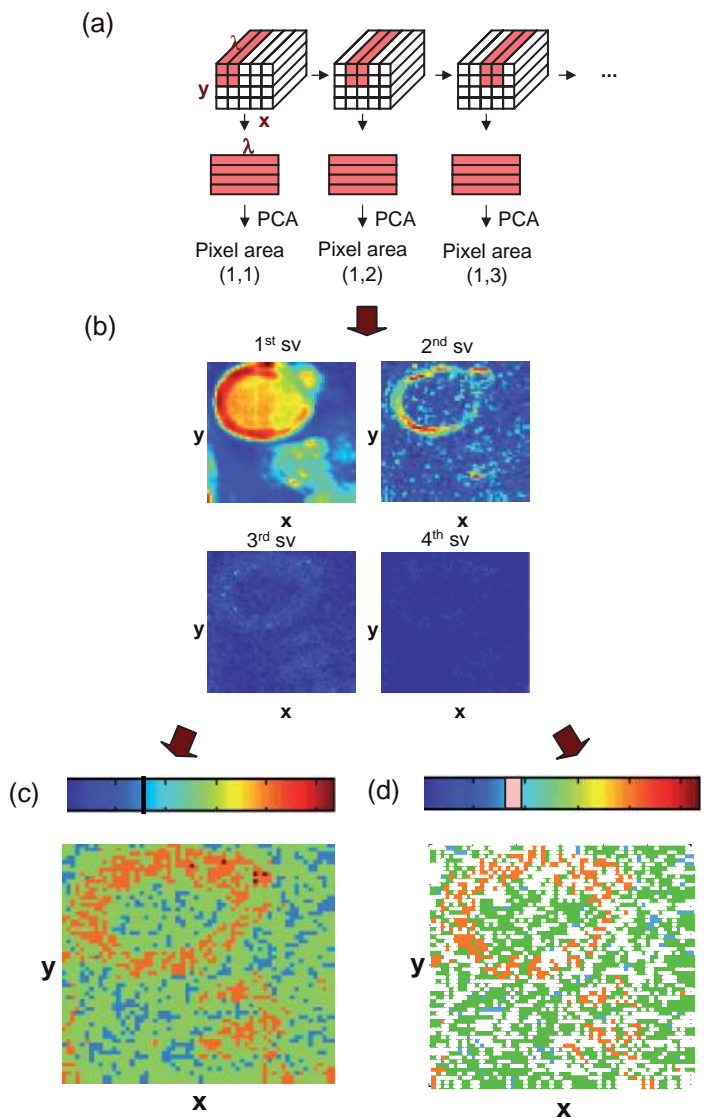
Figure 2.9 FSIW-EFA *modus operandi* (monolayer Raman emulsion image). (a) Construction of pixel windows; (b) Singular value plots of local PCA analyses; (c) Complete local rank map; (d) Partial local rank map. Blue pixels (rank 1), green pixels (rank 2), orange pixels (rank 3), deep red pixels (rank 4).

Local rank maps are derived from the singular value plots by displaying the number of significant singular values in each pixel area. A threshold value or a threshold band is set to mark the limit between significant and noise-related singular values (see the original reference for more detail regarding threshold selection [70]). Depending on the threshold selection and on the information sought, it is possible to distinguish between complete local rank maps (Figure 2.9c) and partial local rank maps (Figure 2.9d). The complete local rank maps display how many singular values are above a preset threshold value for each pixel in the image; that is, they show how many compounds overlap in each pixel. The complete local rank maps provide a good indication of which zones of the image have a lower or higher composition complexity. As expected for the emulsion example, those zones with higher local rank values appear in the interphase zones of the drop and in other potential zones of compound overlap.

The partial local rank maps are constructed by using a threshold band to separate significant from nonsignificant singular values. The use of a threshold band, which is as wide as needed, is meant to account for the threshold-dependence on the estimation of the pixel local rank. For some pixels, the local rank will remain invariant in the highest and lowest boundary of the threshold band, whereas for some others different rank values will be obtained when the lowest or the highest boundary of the threshold band are taken as a reference. Pixels that preserve an invariant rank along the threshold band offer robust local rank information, whereas pixels that do not have less-reliable local rank estimates. Partial local rank maps only display the pixels with a 'robust' local rank estimation. Although this representation has some 'void' pixels, it is the adequate representation to ensure the reliable detection of selective pixels or pixels with low complexity for resolution purposes.

As with its parent algorithm, the local character of the PCA analyses performed by FSIW-EFA is particularly suitable in the detection of very minor compounds in the image (impurities) that could pass unnoticed in a global PCA analysis. This aspect has been particularly useful for the analysis of impurities in images of pharmaceutical formulations. For this type of sample, FSIW-EFA has also provided relevant information on pill heterogeneity [65].

FSIW-EFA can also be used in multilayer images, taking into account the 3-D neighborhood of the voxels to build the small windows to be PCA-scanned [70]. In this context, a number of local rank maps equal to the number of layers in the image is obtained. It is important to note that the information in the local rank map of a particular layer has been obtained taking into consideration the pixels of that layer and those in the neighboring layers in the depth direction.

2.7.3
The Resolution Process: Initial Estimates and Constraints

The resolution of data sets into their underlying bilinear models can be performed with algorithms based on very diverse backgrounds [71, 72]. Some of these algorithms rely essentially on the inner mathematical structure of the data set, and

were conceived for data sets with an inherent order in the evolution of concentration profiles, such as processes. Image data sets lack this order in the concentration direction; that is, the pixel-to-pixel variation of composition seldom follows a smooth evolution along the whole image and, if it were to exist, it would be artificially truncated because the pixel data table does not preserve the spatial structure of the original measurement. This is the reason why the best algorithms for resolution of images are those whose performance is not affected by the lack of pattern in the concentration direction.

Multivariate curve resolution-alternating least squares (MCR-ALS) is an algorithm that fits the requirements for image resolution [71, 73–75]. MCR-ALS is an iterative method that performs the decomposition into the bilinear model $D = CS^T$ by means of an alternating least squares optimization of the matrices C and S^T according to the following steps:

1. Determination of the number of compounds in the raw image, D.
2. Generation of initial estimates (e.g., S^T-type matrix).
3. Given D and S^T, calculation of C under constraints.
4. Given D and C, calculation of S^T under constraints.
5. Reproduction of D from the product of C and S^T.
6. Go to step 3 until convergence is achieved.

The number of image constituents can either be known beforehand, or be determined by PCA on the whole image. The alternating optimization should always start by using the original measurement, D, and an initial guess of either the C or the S^T matrices. Typically, in images, the initial estimate is a matrix S^T, formed by pixel spectra picked up from the image according to previous knowledge (from pixels in areas of interest) or as a result of applying chemometric tools for purest pixel selection, such as SIMPLISMA [18]. Spectral initial estimates are more common because some of the image constituents (and, consequently, their spectra) may be known; alternatively, when this is not the case it is more likely to find selective pixels and, as a consequence, good spectral estimates, than selective spectral channels.

The alternating least-squares procedure in steps 4 and 5 involves the operations $C = DS(S^TS)^{-1}$ and $S^T = (C^TC)^{-1}C^TD$, respectively. The end of the iterative process takes place when the reproduction of the original image from the product of the resolved concentration profiles and spectra has enough quality and there is no significant variation among the results of consecutive cycles. The quality in the data reproduction can be estimated through the lack of fit, expressed as:

$$\text{lack of fit (\%)} = 100 \times \sqrt{\frac{\sum (d_{ij}^* - d_{ij})^2}{\sum d_{ij}^2}} \tag{2.10}$$

where d_{ij} is an element on the image data table and d_{ij}^* is the reproduced element by the MCR-ALS model. Different criteria can be adopted to mark the end of the optimization process; for example, the comparison between consecutive cycles of

the percentage of data fit variation or the dissimilarity of the concentration profiles and spectra recovered. Alternatively, the iterative process can also be stopped after a preselected number of cycles has been exceeded.

The way to incorporate previous knowledge about the images in MCR-ALS is through the use of constraints. These can be defined as chemical or mathematical properties that the concentration profiles or spectra should fulfill [71, 73]. During the iterative process, the calculated concentration profiles and spectra are modified so that they obey the preselected conditions. The application of constraints is optional, and should be performed according to the natural characteristics of the data set. Flexibility is also a relevant issue and, therefore, concentration profiles and spectra can obey different constraints and, within the $\mathbf{C}$ or $\mathbf{S}^T$ matrices, constraints can be applied profile-wise or even element-wise. Constraints play a double role in resolution methods: on the one hand, they ensure the chemical meaning of the recovered distribution maps and spectra, while on the other hand they greatly decrease the ambiguity in the resolved profiles.

The concept of ambiguity in curve resolution is linked to the fact that many $\mathbf{CS}^T$ products can reproduce the original data set with the same optimal fit – that is, many sets of concentration profiles and spectra can be potentially valid to describe the data. In mathematical notation, the bilinear model can be written as:

$$\mathbf{D} = \mathbf{CS}^T + \mathbf{E} \tag{2.10}$$

Or, in an equivalent form, as:

$$\mathbf{D} = \mathbf{CTT}^{-1}\mathbf{S}^T = \mathbf{C}'\mathbf{S}'^T \tag{2.11}$$

where $\mathbf{C}' = \mathbf{CT}$ and $\mathbf{S}'^T = \mathbf{T}^{-1}\mathbf{S}^T$, and there may be infinite $\mathbf{T}$ matrices (solutions). One way of reducing the uncertainty in the resolution results is by limiting the possible solutions to those that fulfill the preset constraints. Thus, the more efficient constraints are, the better defined are the resolution results.

In image analysis, non-negativity is the most commonly used constraint. Indeed, the concentration of any constituent in the image, as well as the spectroscopic infrared or Raman readings are, by nature, positive. As a consequence, elements in both $\mathbf{C}$ and $\mathbf{S}^T$ profiles should, by nature, be positive [65–67, 76–79].

Although many reports are available regarding constraints in curve resolution methods, the majority describe constraints linked to process profiles, such as unimodality (only one maximum per concentration profile) or closure (mass balance in reaction systems). These process-related constraints are not applicable to image concentration profiles, due to the above-mentioned lack of pattern in this direction of the data set. Instead, other types of information are used. One fairly intuitive possibility is to include knowledge of the identity (and pure spectrum) of certain image constituents, and when this is the case these spectral shapes are fixed in the $\mathbf{S}^T$ matrix during the iterative resolution process. In doing so, the possible combinations for spectral shapes of unknown constituents decrease and the recovery of the correct distribution map for the known component is ensured.

So far, not many constraints have been linked specifically to image resolution, although some attempts have involved the introduction of information derived from cluster analysis in the modeling of concentration profiles [80] and the use of a smoothing constraint on a local basis for the concentration of each pixel and the immediate neighbors [81]. However, particular attention should be paid to the adaptation of the so-called *local rank constraints* for image analysis [82]. These constraints, which include the well-known condition of selectivity, have long been used in resolution, and are among the most efficient to aid in the accurate definition of concentration profiles and spectra [73].

In the context of image analysis, the local rank of a pixel generally indicates how many constituents overlap within it. If it is lower than the global rank of the image, this means that some image constituents are absent from that particular pixel. The extreme and most relevant local rank constraint is selectivity; when a pixel is selective – that is, only a particular image constituent is present – the pure spectrum for this constituent can be straightforwardly derived. Likewise, when a spectral channel is selective, the distribution map of the related component can be directly obtained. Selectivity is introduced by forcing the absent constituents to present null or extremely low concentration values or spectral readings in the selective pixels in $\mathbf{C}$ or in the selective spectral channels in $\mathbf{S}^T$, respectively. Milder local rank constraints can be set when the rank of a pixel is lower than the total by setting only some of the image constituents to be absent. Local rank constraints have been proven to be the most efficient at reducing the ambiguity in resolution results. When there is selectivity for all components, or when some local rank conditions are fulfilled [83], then ambiguity is completely suppressed from the resolved profiles.

The introduction of local rank constraints in image analysis requires one to determine the number and identity of the missing components in the pixels to be constrained. When recalling the flexibility in the introduction of constraints, it is important to stress that not all the pixels need to be constrained. Thus, pixels with an ambiguous estimation of the local rank, or a dubious identification of the missing components, should be left unconstrained.

An exploratory analysis performed by FSIW-EFA provides an estimate of the number of components in each pixel. For resolution purposes, only those pixels in the partial local rank map will be potentially constrained, because these are the pixels for which a robust estimation of the number of missing components can be obtained. However, the FSIW-EFA information is not sufficient to identify which components are absent from the constrained pixels. For identification purposes, the local rank information should be combined with reference spectral information, the ideal reference being the pure spectra of the constituents, although in most images not all of these are known. For the image components with no pure spectrum available, the reference taken is an approximation of this pure spectrum. These approximate pure spectra can be obtained by pure variable selection methods, or they may be the result of a simpler MCR-ALS analysis where only non-negativity constraints have been applied.

Thus, to set the local rank constraints, the two necessary inputs are: (i) a partial local rank map, with the rank of pixels that can be potentially constrained (see Figure 2.10a); and (ii) a pure spectrum (or good estimate) per each constituent (see Figure 2.10b).

The incorporation of local rank constraints in any pixel *I* starts by estimating the number of missing components as follows:

$$\text{no. of missing components } (i) = \text{image total rank} - \text{local rank pixel } (i)$$

For example, in the emulsion (four compounds), for a pixel of rank three, we should look for one missing component. The way to identify this component passes through the calculation of the correlation coefficient between the raw pixel spectrum and each of the reference spectra for the different image constituents. The constituent with the lowest correlation coefficient with the pixel spectrum will likely be the one missing in this pixel. This procedure is carried out individually for each of the pixels that can be potentially constrained. At this point, we need to consider that the identification of the missing components may not always be conclusive enough. To prevent the introduction of misidentifications, a first step consists of seeing the natural correlation between the spectra used as reference (see the matrix below for the emulsion example).

$$
\begin{array}{c c}
 & \begin{array}{cccc} A & B & C & D \end{array} \\
\begin{array}{c} A \\ B \\ C \\ D \end{array} &
\left(\begin{array}{cccc}
1 & 0.58 & 0.75 & 0.52 \\
0.58 & 1 & 0.66 & 0.67 \\
0.75 & 0.66 & 1 & 0.61 \\
0.52 & 0.67 & 0.61 & 1
\end{array}\right)
\end{array}
$$

Thus, the absence of a particular component in a pixel will not be confirmed unless the correlation coefficient between the pixel spectrum and the reference spectrum of that component is equal or smaller than the largest element in the correlation matrix for that particular component. In this concrete example, A cannot be considered a missing component if the correlation coefficient obtained with the pixel spectrum is larger than 0.75. The highest acceptable correlation coefficients to consider B, C and D missing will be 0.67, 0.75 and 0.67, respectively. Therefore, even a pixel with a well-defined rank will not be constrained unless a reliable identification of the missing components is achieved. In this example, only 1177 pixels have been constrained, even though the number of pixels in the partial local rank map is 1934. The total number of pixels in the image is 3600. The double-check, in terms of local rank by taking only the pixels in the partial local rank map and, in terms of identification taking only the identifications that match the natural correlation of the spectral components, prevents the introduction of erroneous information in the resolution process.

The information accepted in terms of rank and compound identification (see Figure 2.10c) is translated into a 'mask' matrix, sized as **C** (no. of pixels × no. of

(a)

(b)

(c)

A absent

B absent

C absent

D absent

(d)

	A	**B**	**C**	**D**
Pixel (1,1)	0		0	0
Pixel (1,2)		0	0	
.				
.				
.		0		
Pixel (m,n)		0	0	0

Selective pixels
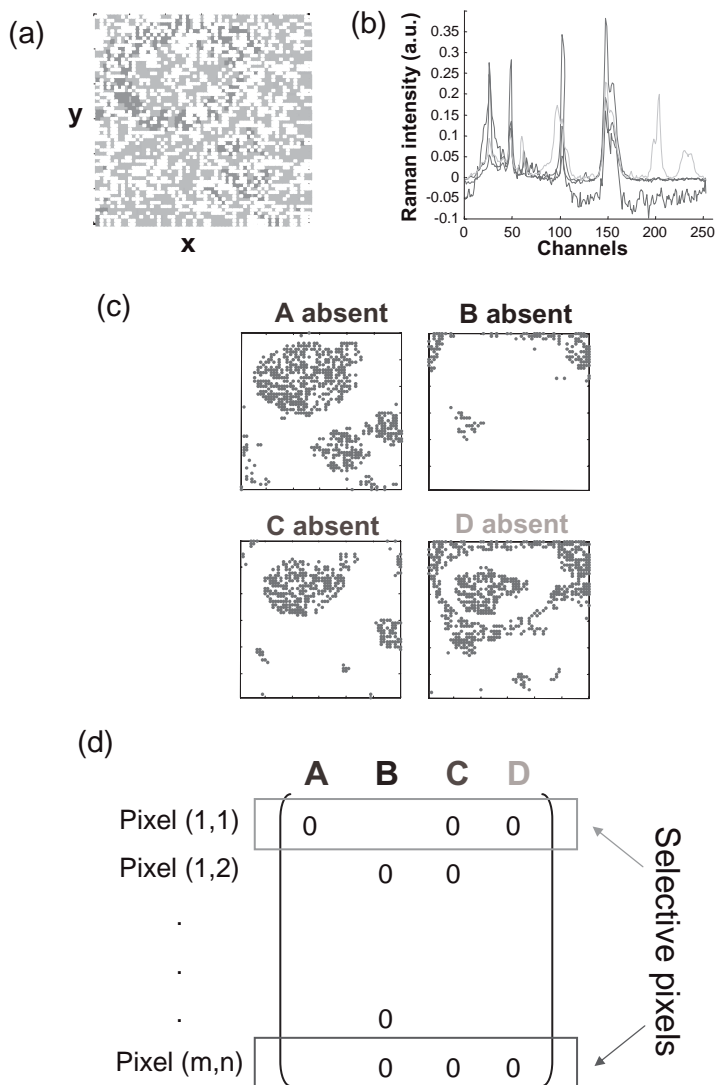
Figure 2.10 Procedure followed to incorporate local rank constraints in resolution (monolayer emulsion example). (a) Partial local rank map; (b) Reference spectral information (from SIMPLISMA); (c) Pixel masks for absence of constituents in image; (d) Transfer of information in (c) to a local rank information matrix.

components), that will be used to introduce the local rank constraints in the resolution process (see Figure 2.10d). This constraint can be applied by keeping null values in the concentration elements of the missing components in the constrained pixels (equality constraint), although in practice better results are obtained

if these missing components are set to have a concentration value equal or smaller than a very small predefined value.

The consequences of introducing local rank information are a better definition of the distribution maps and pure spectra of the components and a decrease in the ambiguity linked to the resolution results [82].

2.7.4
Resolution on Compressed Images

A typical problem in image analysis is the size of the data set. As a consequence, the computational effort required for resolution is highly increased. When images are too large, or when several images are analyzed together, *compression* may represent a reasonable preprocessing step. Compression can be performed either in the spectral or in the pixel direction. the 'golden rule' being that the relevant information on the compressed direction should be kept. If this is the case, then the resolution of compressed images will allow recovery of the full C and S^T matrices, with one derived directly from the resolution results (linked to the uncompressed direction) and the other from postprocessing, with a single least-squares step.

Figure 2.11 illustrates this two-step procedure for compressed data sets in the spectral (right) and spatial (left) directions. Taking as an example the compression in the spectral direction, resolution is first carried out on the compressed data set, D_{comp}, where all pixels are preserved and the number of spectral channels is
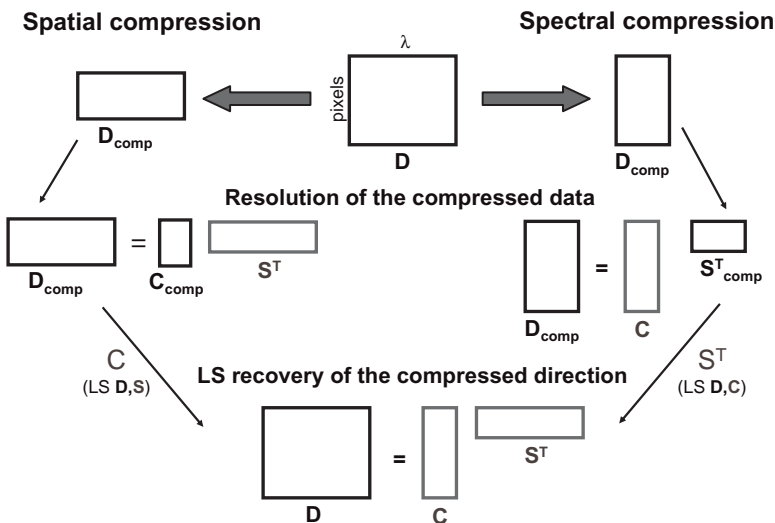
Figure 2.11 Resolution of images compressed in the spectral direction and in the spatial direction. Recovery of full C and S^T matrices.

reduced. The decomposition into the bilinear model, $\mathbf{D}_{comp} = \mathbf{CS}_{comp}^T$, gives the full concentration matrix, $\mathbf{C}$, and a matrix of resolved compressed spectra, $\mathbf{S}_{comp}^T$. If the information contained in the spectral channels is representative from the image, then the distribution maps recovered (from the $\mathbf{C}$ matrix) are the true ones. As a consequence, the bilinear model of the original measurement $\mathbf{D} = \mathbf{CS}^T$ can be used as a base to recover the missing full matrix, $\mathbf{S}^T$, from the single least-squares step $\mathbf{S}^T = (\mathbf{C}^T\mathbf{C})^{-1}\mathbf{C}^T\mathbf{D}$, where $\mathbf{D}$ is the original uncompressed image and $\mathbf{C}$ has been obtained from the resolution on the compressed data set.

As for many other methods of image analysis, binning in the spectral or in the pixel direction is an option. Actually, the spectral resolution in most images is rather high, and a significant compression of spectral channels can be performed without losing quality in the resolution results, neither in the data fit nor in the profiles recovered. Likewise, the same strategy can be applied in the pixel direction. Figure 2.12 shows the results of the resolution of the full emulsion image (center) and of a binned image in the spectral direction (left). The compression allowed passing from the original 253 channels to 16, without any loss of relevant information. It is interesting to note that the resolved compressed spectra, $\mathbf{S}_{comp}^T$, maintain the main features of the full spectra in $\mathbf{S}^T$. Other universal compression methods would consist of selecting alternating spectral channels (one of several), or of
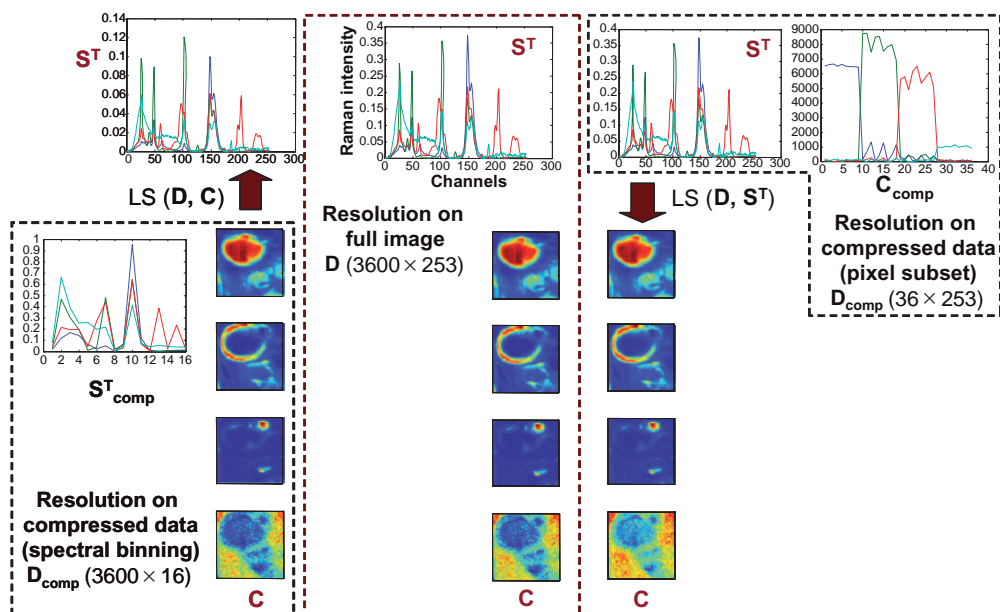
Figure 2.12 Left: Resolution results after image compression by binning in the spectral direction. Center: Resolution results from full image analysis. Right: Resolution results after image compression in the pixel direction by taking a pixel subset around SIMPLISMA purest selected pixels.

sampling pixels from the image so that all zones scanned were properly represented [1].

However, we can envision compression procedures more oriented to the resolution of the image into the pure components. With this way of thinking, the information to be kept should be representative and as unmixed as possible. The perfect and maximum compression would consist of taking a selective spectral channel or a selective pixel per image constituent. This would be the smallest amount of representative information needed to resolve the image. This ideal situation is hardly ever found in practice, but approximations based on this idea can be proposed. Thus, compression in the spectral direction can be performed by taking the spectral channels selected with pure variable approaches and small bands around them. These channels are selective or, if not, they are the purest ones in the image and contain the best available information per each image constituent. Likewise, the purest selection could be carried out in the pixel direction, keeping the purest pixels and their closest neighbors in the two- or three spatial directions. Another option to select the simplest pixels would be based on the local rank information provided by FSIW-EFA. In this case, the pixels with lowest rank (one or two) could be selected as the compressed subset to perform the resolution analysis. Figure 2.12 (right) shows the results of a compressed image in the pixel direction, where only 36 pixels of the original 3600 have been selected. These pixels are the four selected by SIMPLISMA (see a, b, c and d in Figure 2.8) and their eight immediate surrounding neighbors. As can be seen in the compressed concentration matrix, $\mathbf{C_{comp}}$, the recovered concentration profiles show the separate blocks related to each type of pixel (drop, interphase, additive and off-drop constituent). As these pixels are close to being selective, the recovered full $\mathbf{S^T}$ matrix is correct, and so are the full distribution maps derived from the single least-squares performed after resolution.

2.7.5
Resolution and Available Library Spectra

The resolution of images can be performed even if null knowledge of the image constituents is available. In some cases, however, partial information may be available on the identity of constituents, and this can be incorporated into the resolution process by forcing the pure spectrum of a certain constituent to maintain a known shape. A different case is formed by certain families of images, for example biomedical images, for which a spectra library with the most commonly found constituents may be available Libraries of spectra are often large, and there is a need for screening methodologies to identify candidates that may be present in a measured image. Hence, methodologies have been designed to perform this task, without the need of a previous resolution of the image, such as Target Factor Analysis [84, 85]. Unfortunately, the information obtained by this and other screening methods is only related to the presence or absence of a potential constituent in the image. Hence, it is not possible to know whether unidentified compounds, different from those reported in the library, might also exist. Consequently,

distribution maps cannot be directly derived using only the accepted library spectra.

A good alternative to performing this screening can be carried out as a postprocessing step in image resolution. To illustrate this possibility, we present an example of a kidney calculus image. Figure 2.13a shows the resolution of this image into three image constituents, with their related pure spectra and distribution maps. A library of Raman spectra is available with the spectra of the most common inorganic compounds present in this type of biomedical sample [86].

If the resolution results lacked ambiguity, the resolved spectra would be identical to some library spectra but, even if this is were not the case, the resolved profiles would be very close to the true ones. Despite the degree of ambiguity in the resolution results, the matrix $\mathbf{S}^T$ always allows for a good reproduction of the spectral variation in the raw image data set, either by using the real pure spectra of the constituents or linear combinations of them. From a geometrical point of view, this means that the resolved spectra in matrix $\mathbf{S}^T$ always span the spectral space of the image, and the library spectra related to the image constituents should belong to this space. Therefore, the screening is performed by projecting the spectrum of the potential library candidate onto the space defined by $\mathbf{S}^T$ (see Figure 2.13b for a schematic view of the projection process). To perform this projection, a transformation vector, $\mathbf{r}_i$, is calculated that relates the library spectrum to be checked, $\mathbf{t}_i$, to the space $\mathbf{S}^T$ as follows:

$$\mathbf{t}_i = \mathbf{S}^T \mathbf{r}_i \tag{2.12}$$

$$\mathbf{r}_i = \left(\mathbf{S}\mathbf{S}^T\right)^{-1}\mathbf{S}\mathbf{t}_i \tag{2.13}$$

Subsequently, the projection of the library spectrum onto $\mathbf{S}^T$ is obtained as:

$$\mathbf{t}_o = \mathbf{S}^T \mathbf{r}_i \tag{2.14}$$

When the library spectrum, $\mathbf{t}_i$, and its projection onto the $\mathbf{S}^T$ space, $\mathbf{t}_o$, are identical or very similar, the candidate is a constituent present in the image. When the distance among them, e_i, is large (the original spectrum is far away from the $\mathbf{S}^T$ space), the potential candidate is absent. Figure 2.13b shows the plot of e_i for all the library spectra of the calculus example. As can be seen, five library candidates show e_i values significantly lower than the rest of spectra, and these may be potential constituents of the analyzed sample. From these results, two constituents were unambiguously identified as whewellite and weddellite because of the excellent agreement with two of the pure spectra obtained during the resolution process (note the clear overlap between the library spectra, in red, and the resolved spectra, in black, in Figure 2.13c). As a second step (not shown), these library spectra were fixed in a new resolution analysis and the identification of the third image constituent (dahllite) could be carried out.

In general, this resolution postprocessing identification step has certain advantages over the classical TFA process. Basically, the library spectra accepted from
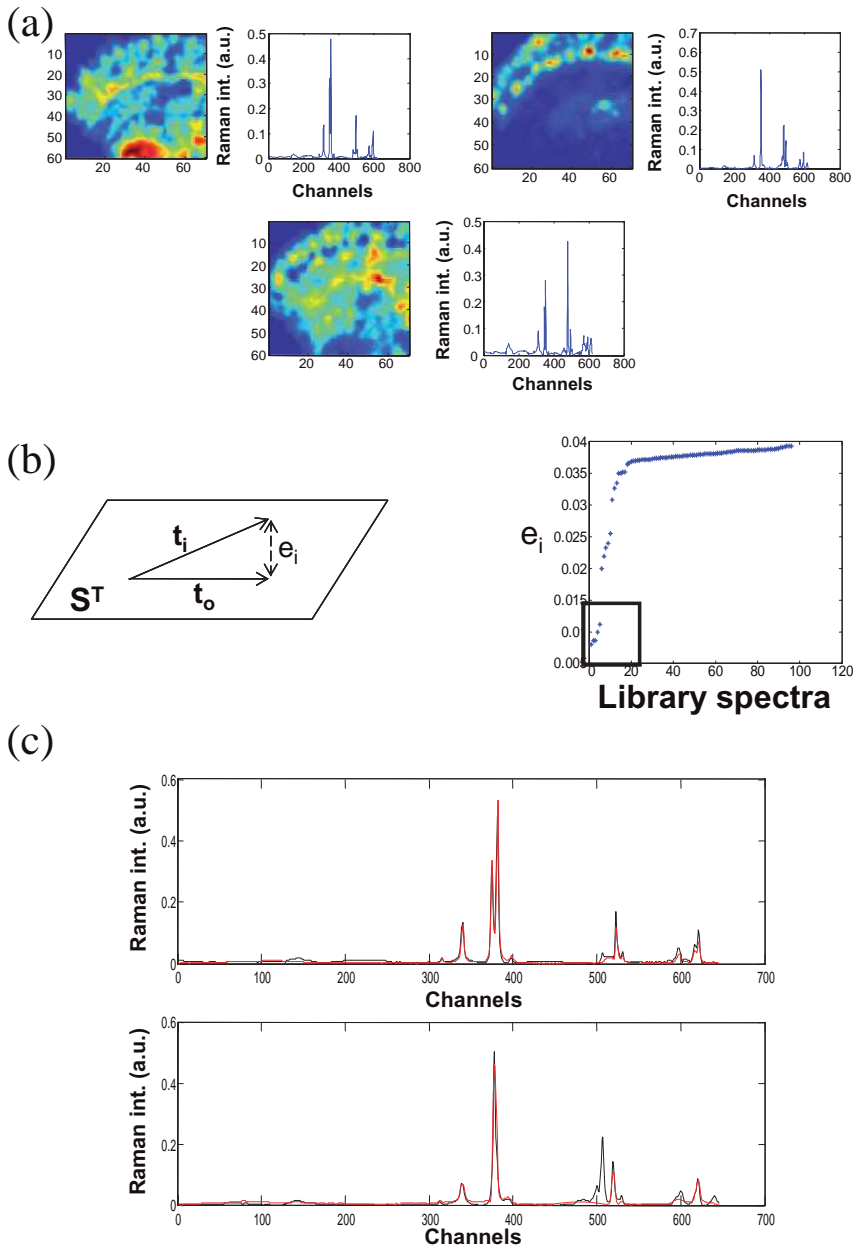
Figure 2.13 (a) Resolution results for a kidney calculus, distribution maps and related pure spectra; (b) Image constituent screening by projection of library spectra, t_i, onto resolved spectra space, S^T; (c) Clear straightforward identification of two of the accepted candidates as calculi constituents (black spectra: resolved spectra from MCR-ALS; red spectra: library spectra).

the projection approach can pass through a second identification check by visual comparison with the resolved spectra in $\mathbf{S}^T$. In contrast to TFA, which defines the image space through abstract score profiles, the pure spectra in $\mathbf{S}^T$ are chemically meaningful and a straight association can be made between accepted candidates/ resolved spectra. In addition, the resolution provides complete information concerning the image (distribution maps and pure spectra) and, in case any components from the library might also be present in the image, their pure spectra and distribution maps would also be obtained. As shown in the calculus example, following an initial identification step the library spectra of the confirmed components can be fixed in a new resolution process, not only to improve the results but also to help in the modeling (or eventual identification) of unknown components.

2.7.6
Multilayer and Multi-Image Resolution

As mentioned in Section 2.7.1, resolution can be applied simultaneously to several images. The most obvious application is to image layers from the same sample, scanned at different depths. Another particular example would be formed by images related to process monitoring of the same sample (as a function of time or temperature). However, this multi-image analysis can also be extended to independent samples that share image constituents in common, an example being several pills from a production line [65]. Clearly, multi-image analysis is based on the bilinear model based on the Beer–Lambert law (see Figure 2.14). Thus, the pixel spectra of all images are organized in a data table $\mathbf{D}$, where a block (or submatrix) belongs to a particular image. The decomposition $\mathbf{D} = \mathbf{CS}^T$ provides a single matrix $\mathbf{S}^T$ of pure spectra, valid for all the images analyzed, and a matrix $\mathbf{C}$, formed by as many submatrices as images in the data set. The profiles in each of these submatrices can be refolded conveniently to recover the related distribution maps of each image.
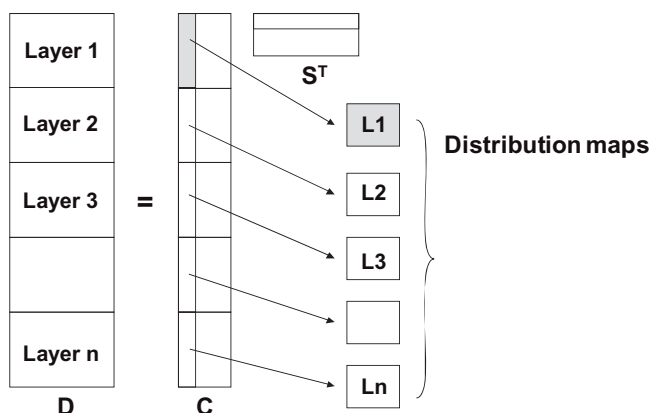
Figure 2.14 Bilinear model for a multi-image resolution analysis.

There are some important issues linked to the bilinear nature of multi-image analysis. First, the fact of obtaining a single S^T matrix for all images ensures spectral consistency of the resolution – that is, the same constituent will always be associated with the same pure spectrum in all analyzed images. Second, the stretched matrix of concentration profiles respects the natural difference of shape of the distribution maps among images.

Another relevant advantage derives from the complementary information in the different images, which helps towards a global improvement of resolution results [74]. Clear examples of the benefits of multi-image analysis occur when differences in concentration level of constituents or in compound overlap are encountered among images. In these situations, the minor constituents in one image are more easily resolved when analyzed with another image where these compounds are present in major proportions. Likewise, images with a high compound overlap are better resolved when analyzed with images with more unmixed information.

The *modus operandi* of multi-image resolution by MCR-ALS is essentially identical to the analysis of a single image, with the addition that the concentration submatrices linked to the different images can be constrained in different ways, if needed. Other types of information, such as the presence/absence of certain constituents in some images, may be incorporated as an additional constraint. Based on the results obtained in multi-image analysis, approximate quantitative information of the constituents among layers may also be gathered.

Two examples of multi-image analysis are briefly detailed here to illustrate some of the issues mentioned above. The spectral consistency problem is clearly shown in a multilayer emulsion example. From a chemical point of view, the fact that a certain image constituent should have the same pure spectrum in all image layers coming from a single sample is obvious, but this aspect is often overlooked when applying multivariate resolution methods, or is taken for granted when performing individual analyses of several layers of the same image. The spectral consistency among individual layer analyses would exist if all components had selectivity in all image layers or, at least, were unambiguously represented. In practice, however, this very rarely happens and the automatic assumption of this consistency among individual image analyses is overtly dangerous.

Figure 2.15a shows the distribution maps of some emulsion layers from individual image analysis and the large differences among the resolved pure spectra for the top and bottom layers. Figure 2.15b confirms the decreasing similarity (expressed as the correlation coefficient) between the spectra resolved on the top layer (taken as reference) and those resolved in the rest of the layers as the depth increases. Although the distribution maps could seem interpretable, the difference between the pure spectra of the different constituents clearly increases with depth and, as a matter of fact, this is a chemically unacceptable result.

Figure 2.16a shows the distribution maps and pure spectra for the multilayer image analysis. Although, the visual difference in distribution maps between individual and multi-image resolution may seem small, there is only a single set of pure spectra, representative of the whole sample. Figure 2.16b shows the
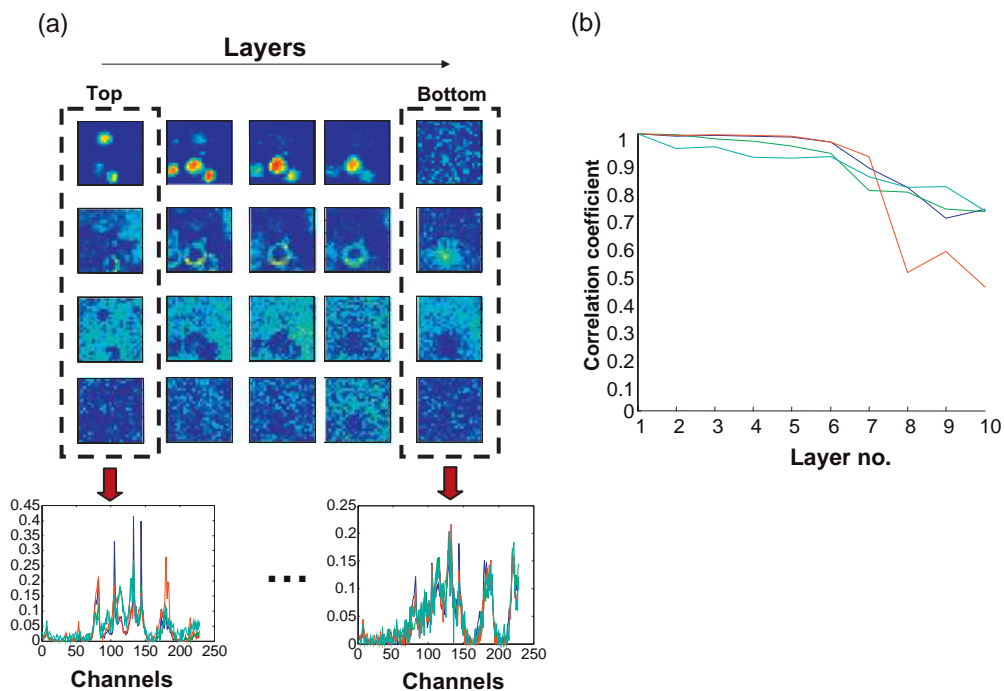
Figure 2.15 Resolution analysis of individual image layer analysis on a multilayer emulsion image. (a) Distribution maps of some emulsion layers and resolved pure spectra from top and bottom layer obtained by individual layer resolution; (b) Correlation coefficient plot among resolved spectra on the top and subsequent emulsion layers.

percentage of signal contribution of the different constituents in the image to the overall signal measured along the layers, sc_i, defined as:

$$sc_i\ (\%) = 100 \times \frac{\sum c_i s_i^T}{\sum CS^T} \tag{2.15}$$

Here, the subindex i refers to each individual constituent, and an sc_i value is calculated for each constituent in each of the layers. $c_i s_i^T$ and CS^T are the signal contribution of the ith component and the global signal within a layer image, respectively.

The signal contribution plot helps to understand the reasons for the spectral inconsistency linked to the individual image analysis, coming from the large difference in representativity of the image constituents in the different layers. Thus, three compounds have a very minor signal in the deepest layers and, as a consequence, the resolved spectra obtained from the individual analyses of these layers are of poor quality and differ significantly from the spectra obtained from the top

(a)

(b)
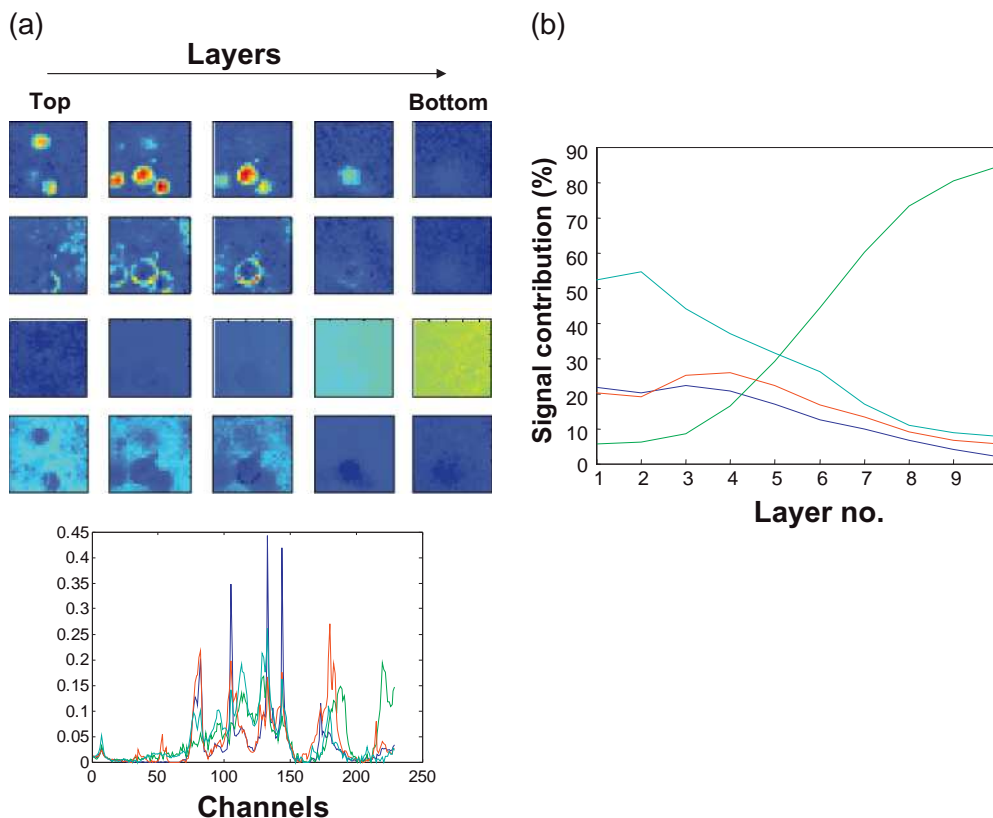
Figure 2.16 (a) Pure spectra and some distribution maps coming from global multilayer resolution analysis; (b) Plot of the signal contribution (in percentage) from the different constituents in the different layers.

layers, where the contribution of these compounds to the overall signal is dominant. The opposite happens when the most dominant compound in the deepest layers is almost absent from the top layer, and this justifies the differences in the resolved spectra among layers for this compound. Only the joint resolution of all layers in the image can provide a good quality description of all compounds in the sample, this being driven by the information in the most superficial layers to define three of the compounds, and by the information in the deepest layers to describe the fourth.

Another example of the gain in resolution quality from the complementary information among different images is seen in the analysis of a series of pills with different percentages of excipient and active principle ingredient (API) of 0, 20, 40, 60 and 80% [65]. The different proportions of compounds in the pills ensure a good recovery of the pure spectra, and also of the distribution maps of all compounds, even when one of them is present in only a small proportion. It should

be noted that commercial pills are designed to have a fixed composition, although for data analysis purposes it is a good practice to analyze the target pills with other samples where the information about the target compounds has been designed differently. In this case, attention should be paid to the presence of a pure excipient pill which, by lacking any pharmacological interest, provides an excellent means of introducing selective information on one of the compounds of the samples.

Although these pills were supposed to be formed by two constituents, a FSIW-EFA analysis detected the presence of a third compound (impurity) in some cases [65]. According to the theoretical composition of the pill and to the local rank analysis, information on the presence/absence of constituents in the different images could be introduced in the multi-image resolution process. From the pure spectra resolved and the distribution maps in Figure 2.17, the positive influence of the pill with the largest amount of impurity was noticeable when this compound was modeled in pills where it was present in very few pixels only.
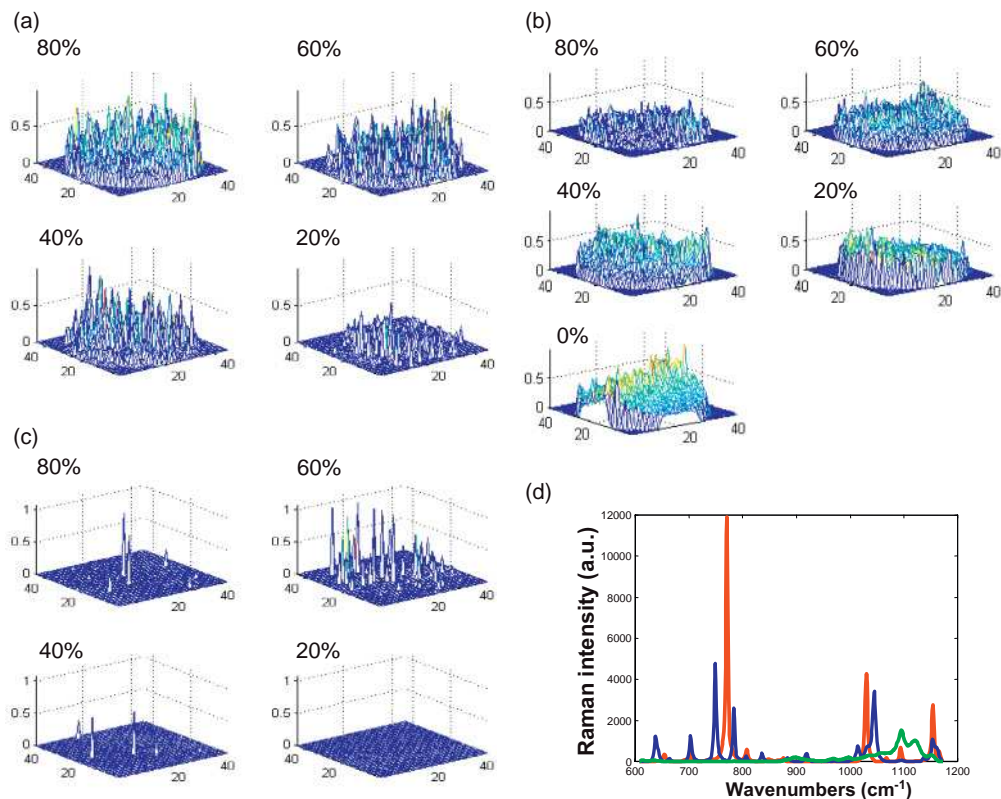
Figure 2.17 Distribution maps (a–c) and pure spectra (d) obtained in the multi-image resolution of pills ranging in percentage of API from 0 to 80%.

A positive consequence of multi-image analysis is the recovery of quantitative information. At this point, it should be taken into account that quantitation from images measured in reflection is never as accurate and precise as from images measured in transmission. The more representative the surface scanned is from the rest of the sample, then the more reliable the quantitative information will be. When referring to quantitative information, it is possible to differentiate between within-image and between-image quantitation.

Within-image quantitation is more correctly described as the signal contribution of a certain constituent to the overall signal, as shown in the emulsion example (see Figure 2.18a). The figures sc_i (%) given in this way should not be associated in straightforward manner with the compound concentrations, due to the various absorptivities of the different compounds in the image.

Between-image quantitation is the concept specifically linked to multi-image analysis. This quantitation is performed separately for each compound, and consists of estimating the relative concentration of a particular compound in the different images. To do this, the stretched concentration profile is taken and the 'concentration' value for each layer obtained as the sum of all elements in the concentration profile linked to a particular image, (c_{in} in Figure 2.18b). When the images have different sizes or a different number of background pixels (e.g.,
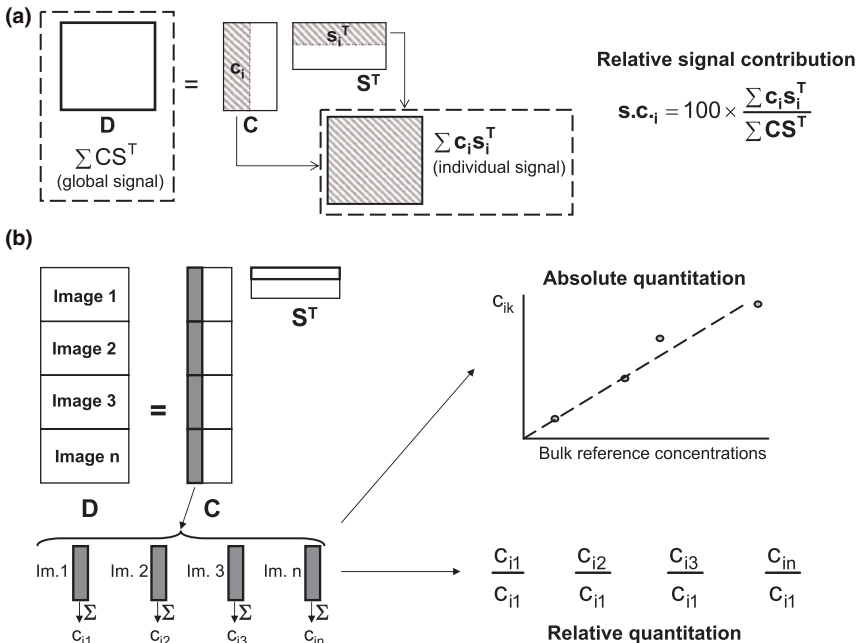
Figure 2.18 (a) Scheme followed to obtain within-image 'quantitative' information (% of signal contribution); (b) Scheme followed to obtain between-image quantitative information in image analysis.

in pills), this concentration value can be weighted according to the number of pill (nonbackground) pixels [65]. When reference values of concentration exist for some images, such as the percentages of API or excipient in the pills, they can be used to build calibration lines (r^2 >0.95 is obtained for the excipient and the API compound in the presented pill example). Otherwise, the information obtained is the relative concentration of a constituent among images. Although, it should be remembered that this quantitation has no analytical value, it does provide a gross estimation of the concentration in the different samples. As this quantitation is conducted individually and independently for each compound, the relative differences of absorptivity among image constituents do not suppose any problem.

Multi-image analysis is certainly one of the most interesting aspects of image resolution, and offers many possibilities yet to be explored. One essential point will be to pass beyond the individual analysis of the image of interest and to complement the information contained in this image with designed images of particular compositions (selective images or 'standard' images of known pure or mixed composition). The possibility of recovering approximately quantitative information should open a new field in the monitoring of processes through a series of images, as not only variations in the identity of compounds present and on their physical distribution in a sample would be obtained, but quantitative information among images would also indicate the evolution of profiles as a function of the process control variable.

Although, until now, our discussions have been limited to the analysis of images monitored using the same instrument, it would be extremely useful when designing methodologies to combine images obtained from the same sample but using different spectroscopic techniques (e.g., Raman/infrared). In doing this, the complementary spectral information obtained would help to differentiate more clearly between similar compounds, much in the way that multimodal imaging is carried out in the biomedical sciences. The ability to apply this strategy should lead to the identification of preprocessing procedures envisioned at matching image contours and balancing the different spatial resolution (pixel size) [87] of the coupled techniques. With such a clear challenge in mind, we shall surely witness major advances in this exciting field of image data treatment in the near future.

References

1 Geladi, P. and Grahn, H. (1996) *Multivariate Image Analysis in Chemistry and Related Areas: Chemometric Image Analysis*, John Wiley & Sons, Ltd, Chichester, UK.

2 Grahn, H.F. and Geladi, P. (2007) *Techniques and Applications of Hyperspectral Image Analysis*, John Wiley & Sons, Ltd.

3 Krooshof, P.W.T., Postma, G.J. Melssen, W.J. and Buydens L.M.C. (2009)

Evaluation of spectroscopic images, in *Biomedical Imaging: Principles and Applications* (ed. R. Salzer), John Wiley & Sons, Ltd (in press).

4 Tran, T.N., Wehrens, R. and Buydens, L.M.C. (2005) *Chemom. Intell. Lab. Syst.*, **77**, 3–17.

5 Massart, D.L., Vandeginste, B.G.M., Buydens, L.M.C., de Jong, S., Lewi, P.J. and Smeyers-Verbeke, J. (1997) Handbook of chemometrics and qualimetrics, in *Data*

Handling in Science and Technology, Vol. **20**, Elsevier.

6 Naes, T., Isaksson, T., Fearn, T., Davies, T. (2002) *Multivariate Calibration Classification*, NIR Publications, Chichester, UK.

7 Savitzky, A. and Golay, M. (1964) *Anal. Chem.*, **36**, 1627–39.

8 Walczak, B. (ed.) (2000) *Wavelets in Chemistry*, Elsevier, Amsterdam.

1 Ehrentreich, F. and Summchen, L. (2001) *Anal. Chem.*, **73**, 4364–73.

10 Steiner, J., Termonia, Y. and Deltour, J. (1972) *Anal. Chem.*, **44**, 1906–9.

11 Madden, H.H. (1978) *Anal. Chem.*, **50**, 1383–6.

12 Wold, S. (1975) Soft-modeling by latent variables: the non-linear iterative partial least squares (NIPALS) algorithm, in *Perspectives in Probability and Statistics* (ed. J. Garni), Academic Press, London, pp. 117–42.

13 Eriksson, L., Johansson, E., Kettaneh-Wold, N. and Wold, S. (2001) *Multi- and Megavariate Data Analysis*, Umetrics, Umeå.

14 Eilers, P. (2004) *Anal. Chem.*, **76**, 404–11.

15 Burger, J. and Geladi, P. (2006) *J. Chemom.*, **20**, 106–19.

16 Esbensen, K.H. (2000) *Multivariate Data Analysis – Practice*, 4th edn, Camo, Oslo.

17 Burger, J. and Geladi, P. (2007) *J. Near-Infrared Spectrosc.*, **15**, 29–37.

18 Windig, W. and Guilment, J. (1991) *Anal. Chem.*, **63**, 1425–32.

19 Gallagher, N.B., Shaver, J.M., Martin, E.B., Morris, J., Wise, B.M. and Windig, W. (2004) *Chemom. Intell. Lab. Syst.*, **73**, 105–17.

20 Batonneau, Y., Bremard, C., Laureyns, J., Merlin, J.C. and Windig, W. (2003) *J. Phys. Chem.*, **107**, 1502–13.

21 Leardi, R. (2003) *Nature-Inspired Methods in Chemometrics: Genetic Algorithms and Artificial Neural Networks, in Data Handling in Science and Technology*, Vol. **23**, Elsevier, Amsterdam.

22 Chtioui, Y., Bertrand, D. and Barba, D. (1998) *J. Sci. Food Agric.*, **76**, 77–86.

23 Wang, M., Zhou, X.B., King, R.W. and Wong, S.T.C. (2007) *BMC Bioinform.*, **8**, Article 32.

24 Ramos, P.M. and Ruisánchez, I. (2006) *Anal. Chim. Acta*, **558**, 274–82.

25 Liu, J.J. and McGregor, J.F. (2007) *Chemom. Intell. Lab. Syst.*, **85**, 119–30.

26 Esbensen, K. and Geladi. P. (1989) *Chemom. Intell. Lab. Syst.*, **7**, 67–86.

27 Geladi, P., Wold, S. and Esbensen, K.H. (1986) *Anal. Chim. Acta*, **191**, 473–80.

28 Bharati, M.H. and MacGregor, J.F. (1998) *Ind. Eng. Chem. Res.*, **37**, 4715–24.

29 Kohler, A., Bertrand, D., Martens, H., Hannesson, K., Kirschner, C. and Ofstad, R. (2007) *Anal. Bioanal. Chem.*, **389**, 1143–53.

30 Andrew, J.J., Browne, M.A., Clark, I.E., Hancewicz, T.M. and Millichope, A.J. (1998) *Appl. Spectrosc.*, **52**, 797–807.

31 Dunn, K.G. (2007) M.A.C.C. Multivariate Image Analysis (MACCMIA). Manual and Tutorial for Version 1.81. http://macc.mcmaster.ca (accessed 19 November 2008)

32 Liu, J.J., Bharati, M.H., Dunn, K.G. and MacGregor, J. (2005) *Chemom. Intell. Lab. Syst.*, **79**, 42–54.

33 de Edelenyi, F.S., Simonetti, A.W., Postma, G., Huo, R. and Buydens, L.M.C. (2005) *Anal. Chim. Acta*, **544**, 36–46.

34 Nattkemper, T.W. (2004) *J. Biomed. Inform.*, **37**, 380–91.

35 Geladi, P. and Esbensen, K. (1991) *J. Chemom.*, **5**, 97–111.

36 Esbensen, K.H., Geladi, P.L. and Grahn, H.F. (1992) *Chemom. Intell. Lab. Syst.*, **14**, 357–74.

37 Lied, T.T., Geladi, P. and Esbensen, K.H. (2000) *J. Chemom.*, **14**, 585–98.

38 Lied, T.T. and Esbensen, K.H. (2001) *Chemom. Intell. Lab. Syst.*, **58**, 213–26.

39 Yu, H.L. and MacGregor, J.F. (2003) *Chemom. Intell. Lab. Syst.*, **67**, 125–44.

40 Bharati, M.H., MacGregor, J.F. and Champagne, M. (2004) *Tappi J.*, **3**, 8–14.

41 Wold, S., Martens, H. and Wold, H. (1983) *Lecture Notes in Mathematics*, **973**, 286–93.

42 Burger, J. and Geladi, P. (2005) *J. Chemom.*, **19**, 355–63.

43 Burger, J. and Geladi, P. (2006) *Analyst*, **131**, 1152–60.

44 Wehrens, R., Simonetti, A.W. and Buydens, L.M.C. (2002) *J. Chemom.*, **16**, 274–82.

45 Lin, W.Q., Jiang, J.H., Yang, H.F., Ozaki, Y., Shen, G.L. and Yu, R.Q. (2006) *Anal. Chem.*, **78**, 6003–11.

46 Krooshof, P.W.T., Tran, T.N., Postma, G.J., Melsen, W.J. and Buydens, L.M.C. (2006) *Trends Anal. Chem.*, **25**, 1067–80.

47 Massart, D.L. and Kaufman, L. (1983) *The Interpretation of Analytical Chemical Data by the Use of Cluster Analysis*, John Wiley & Sons, Inc., New York.

48 Webb, S. (2002) *Statistical Pattern Recognition*, John Wiley & Sons, Ltd, Malvern, UK.

49 Sander, J., Ester, M., Kriegel, H.P. and Xu, X.W. (1998) *Data Mining Knowl. Discov.*, **2**, 169–94.

50 Sneath, P.H.A. (1957) *J. Gen. Microbiol.*, **17**, 201–26.

51 Lance, G.N. and Williams, W.T. (1967) *Comput. J.*, **9**, 373.

52 Ward, J.H. (1963) *J. Am. Stat. Assoc.*, **58**, 236.

53 Wold, S. (1976) *Pattern Recognit.*, **8**, 127–39.

54 Kohler, A., Skaga, A., Hjelme, G. and Skarpeid, H.J. (2002) *Comput. Electron. Agric.*, **36**, 3–16.

55 Krafft, C., Shapoval, L., Sobottka, S.B., Geiger, K.D., Schackert, G. and Salzer, R. (2006) *Biochim. Biophys. Acta – Biomembr.*, **1758**, 883–91.

56 Barker, M. and Rayens, W. (2003) *J. Chemom.*, **17**, 166–73.

57 Wold, S., Albano, C., Dunn, W.J., III, Edlund, U., Esbensen, K., Geladi, P., Hellberg, S., Johansson, E., Lindberg, W. and Sjostrom, M. (1984) *Chemometrics, Mathematics and Statistics in Chemistry* (ed. B.R. Kowalski), Kluwer Academic Publishers, Dordrecht, pp. 17–95.

58 Chevallier, S., Bertrand, D., Kohler, A.P. and Courcoux, P. (2006) *J. Chemom.*, **20**, 221–9.

59 Grahn, H., Szeverenyi, N., Roggenbuck, M.W. and Geladi, P. (1989) *Chemom. Intell. Lab. Syst.*, **7**, 87–93.

60 Geladi, P., Swerts, J. and Lindgren, F. (1994) *Chemom. Intell. Lab. Syst.*, **24**, 145–67.

61 Noordam, J.C., van den Broek, W.H.A.M., Geladi, P. and Buydens, L.M.C. (2005) *Chemom. Intell. Lab. Syst.*, **75**, 115–26.

62 Bezdek, J.C. (1981) *Pattern Recognition with Fuzzy Objective Function Algorithms*, Plenum, NY, US.

63 Teppola, P., Mujunen, S.P. and Minkkinen, P. (1999) *Chemom. Intell. Lab. Syst.*, **45**, 23–38.

64 Bharati, M.H., Liu, J.J. and MacGregor, J.F. (2004) *Chemom. Intell. Lab. Syst.*, **72**, 57–71.

65 de Juan, A., Tauler, R., Dyson, R., Marcolli, C., Rault, M. and Maeder, M. (2004) *Trends Anal. Chem.*, **23**, 70–9.

66 Wang, J.H., Hopke, P.K., Hancewicz, T.M. and Zhang, S.L.L. (2003) *Anal. Chim. Acta*, **476**, 93–109.

67 Duponchel, L., Elmi-Rayaleh, W., Ruckebusch, C. and Huvenne, J.P. (2003) *J. Chem. Inform. Comput. Sci.*, **43**, 2057–67.

68 Berman, M., Miiveri, H., Lagerstrom, R., Ernst, A., Dunne, R. and Huntington, J.F. (2004) *IEEE Trans. Geosci. Remote Sens.*, **42**, 2085–95.

69 Keller, H.R. and Massart, D.L. (1991) *Anal. Chim. Acta*, **246**, 379.

70 de Juan, A., Maeder, M., Hancewicz, T. and Tauler, R. (2005) *Chemom. Intell. Lab. Syst.*, **77**, 64–74.

71 de Juan, A. and Tauler, R. (2003) *Anal. Chim. Acta*, **500**, 195–210.

72 de Juan, A. and Tauler, R. (2006) *Crit. Rev. Anal. Chem.*, **36**, 163–76.

73 Tauler, R., Smilde, A.K. and Kowalski, B.R. (1995) *J. Chemom.*, **9**, 31–58.

74 Tauler, R. (1995) *Chemom. Intell. Lab. Syst.*, **30**, 133–46.

75 Jaumot, J., Gargallo, R., de Juan, A. and Tauler, R. (2005) *Chemom. Intell. Lab. Syst.*, **76**, 101–10.

76 Wentzell, P.D., Karakach, T.K., Roy, S., Martínez, M.J., Allen, C.P. and Werner-Washburne, M. (2006) *BMC Bioinform.*, **7**, Article 343.

77 Zhang, L., Henson, M.J. and Sekulic, S.S. (2005) *Anal. Chim. Acta*, **545**, 262–78.

78 Budevska, B.O., Sum, S.T. and Jones, T.J. (2003) *Appl. Spectrosc.*, **57**, 124–31.

79 Gallagher, N.B., Shaver, J.M., Martin, E.B., Morris, J., Wise, B.M. and Windig, W. (2004) *Chemom. Intell. Lab. Syst.*, **73**, 105–17.

80 Hancewicz, T.M. and Wang, J.H. (2005) *Chemom. Intell. Lab. Syst.*, **77**, 18–31.

81 Hancewicz, T.M., Wang, J-H., Pudney, P.D.A., and Zhang, S.L. (2004) Multivariate image resolution for spectroscopic image analysis, 228th ACS

National Meeting. Philadelphia, PA. August 22, Paper #15.

82 de Juan, A., Maeder, M., Hancewicz, T. and Tauler, R. (2008) *J. Chemom*, **22**, 291–8.

83 Manne, R. (1995) *Chemom. Intell. Lab. Syst.*, **27**, 89.

84 Malinowski, E.R. (2002) *Factor Analysis in Chemistry*, 3rd edn, John Wiley & Sons, Inc., New York.

85 McCue, M. and Malinowsk, E.R. (1981) *Anal. Chim. Acta – Comput. Tech. Opt.*, **5**, 125–36.

86 Dao, N.Q. and Daudon, M. (1997) *Infrared and Raman Spectra of Calculi*, Elsevier, Paris.

87 Duponchel, L., Milanfar, P., Ruckebusch, C. and Huvenne, J.P. (2008) *Anal. Chim. Acta*, **607**, 168–75.

Part Two   Biomedical Applications

3
Vibrational Spectroscopic Imaging of Soft Tissue

Christoph Krafft

3.1
Introduction

In general, biological tissue is a collection of cells that also includes the extracellular matrix (ECM). The cells of a particular tissue perform a similar function within an organism such that, in principle, all compartments of a multicellular organism – including the organs, structures and other components – can be assigned to a tissue class or are produced by a tissue type. The study of tissue is known as *histology* or, when in connection with disease, as *histopathology*. The classical tools for studying tissues include fixation, embedding in a wax block, the cutting of tissue sections, followed by their mounting on slides, staining and inspection using optical microscopy. More recent developments in electron microscopy, fluorescence microscopy and molecular biology have significantly increased our knowledge of the structure and function of tissues. Indeed, with these tools we can examine tissues both in health and in disease, thereby enabling a considerable refinement of clinical diagnosis. Unfortunately, all of these methods require substantial preparation procedures, the labeling of molecules, and interpretation of the information obtained by experts. Moreover, problems associated with label-based techniques may occur due to a limited accessibility of the label to the target, coupled with an inadequate binding specificity and a poor stability.

Following the development during the past decade of sensitive and rapid Fourier transform-infrared (FT-IR) and Raman spectrometry, vibrational spectroscopy appeared as a complementary tool for the assessment of tissues and their pathological changes. In general, more bands are observed in the vibrational spectra of tissues than in their optical spectra, because numerous vibrations of biomolecules can be excited simultaneously to produce a 'fingerprint-like' signature. Consequently, much more potential information regarding the biochemistry, composition and molecular structure of an underlying sample may be collected without the use of external labels, with minimal preparation, and without damaging the samples. The earliest of these studies were based on single spectra with a low lateral resolution. Hence, as the inherent inhomogeneity of tissue could not be

fully considered, a correlation between the histology and the vibrational spectra was only achieved for homogeneous sample regions. Major improvements resulted from the combination of vibrational spectroscopy with spatial information that opened wide perspectives in biomedical applications. These powerful imaging techniques enable the characterization of soft tissues with diffraction-limited lateral resolution. Spectroscopic near-field imaging can also be used to resolve details below the diffraction limit (as described in Chapter 2). Vibrational spectroscopic images can be analyzed using automatic procedures, thus enabling both high throughput and high reproducibility. Since such information is usually distributed over a wide spectral range, and the spectral variances between tissue types and pathological states are invariably small, multivariate algorithms are today more appropriate than univariate algorithms for such analyses. False color images produced by the segmentation and classification of vibrational spectroscopic images are directly comparable to the outcomes of standard histopathological staining protocols, and can also be interpreted by non-spectroscopists. Furthermore, these methods offer the possibility for optical biopsies in *in vivo* situations, using fiber-optic probes.

Four basic types of soft tissue are found in all vertebrates, including the human body and most invertebrates (but with some exceptions, such as fungi), namely the epithelium, connective tissue, muscle tissue and nervous tissue. (Details of vegetable fibers and tissues may be found in Chapter 10.) In this chapter we concentrate on the applications of Raman and FT-IR imaging to soft tissues, initially discussing the fundamental aspects of preparing soft tissues for vibrational spectroscopic imaging while excluding details of the instrumentation and data handling. Topics subsequently described include colon tissue (which contains epithelium, connective tissue and muscle tissue and nerve cells), brain tissue (which represents nervous tissue) and cervical tissue, which constitutes an example of carcinoma originating from the epithelium. Both, skin and ocular tissue are also included as dedicated instruments have been developed for the first *in vivo* applications of this technology.

3.1.1
Epithelium

The epithelium (the biological and medical collective term for covering and glandular tissues) is composed of layers of cells that line the outside and inside surfaces of organs. The outermost layer of the skin is composed of stratified squamous epithelial cells, while other epithelial cells line the insides of the respiratory, gastrointestinal, reproductive and urinary tracts, and also comprise the exocrine and endocrine glands. The functions of epithelial cells include secretion, absorption, protection, transcellular transport, sensation detection and selective permeability. The endothelium – the inner lining of blood and lymph vessels – is a specialized form of epithelium.

Epithelial cells are classified by their shape, stratification and specialization. The cell shape is subdivided into squamous, cuboidal, columnar and transitional:

- Squamous cells have an irregular, flattened shape. A one-cell layer of simple squamous epithelium forms the alveoli of the respiratory membrane and the endothelium, and provides a minimal barrier to diffusion. Other sites of squamous cells include the filtration tubules of the kidneys and the major cavities of the body. Squamous cells are relatively metabolically inactive, and are associated with the diffusion of water, electrolytes and other substances.

- Cuboidal cells have a shape similar to a cube, which means that their width is the same as their height.

- Columnar cells are longer than they are wide; the small intestine is a tubular organ lined with a simple columnar epithelium composed of a single layer of cells. Unicellular glands are scattered throughout this type of tissue and secrete mucus.

- Translational epithelium is found in organs that can stretch; examples include the urothelium that lines the bladder and ureter of mammals.

The stratification of epithelial cells is defined as either 'simple' – having a single layer of cells – or 'stratified' – having more than one layer. The stratified epithelium is usually composed of three layers, with cell division taking place in the basal cell layer (layer 1), after which the cells migrate and differentiate in the intermediate cell layer (layer 2) until they reach the superficial cell layer (layer 3).

Cell specializations include keratinized cells and ciliated cells. The keratinized epithelium contains the cytoskeletal protein keratin, and provides a tough impermeable barrier, mainly in the skin. Ciliated cells have apical plasma membrane extensions composed of microtubules and are capable of beating rhythmically so as to move mucus or other substances through a duct. Cilia are common in the respiratory system.

As the epithelium covers the surface of organs, it is generally exposed to the environment and hence is in contact with a wide range of potentially aggressive or harmful chemical and physical conditions that may induce the deregulation of cell division in the basal cell layer. Consequently, carcinomas of the epithelium are among the most common forms of cancer. Both, FT-IR and Raman imaging studies have been reported for the study of carcinomas of the skin [1], breast [2], colon [3], prostate [4], cervix uteri [5, 6], esophagus [7], bladder [8] and oral mucosa [9].

3.1.2
Connective Tissue and Extracellular Matrix

Connective tissue is a group of tissue types that differ significantly in form and function from each other, yet share common features in their development and structural organization. Connective tissue is involved in the structure and support of an organism, fills interspaces with ECM and generates (in the broadest sense) further specialized tissues such as blood, cartilage and bone, all of which are usually considered as connective tissues. However, because these specialized

connective tissues differ so substantially from the other tissues in this class, the term 'connective tissue proper' is commonly used to exclude those three. Connective tissue proper is classified into the following four groups:

- Areolar or loose connective tissue: this holds the organs and epithelia in place. It is separated from the epithelium by the basal membrane, and contains a variety of proteinaceous fibers, including collagen and elastin. It is also important in inflammation.

- Adipose tissue: this contains adipocytes which are used for cushioning, thermal insulation, lubrication and energy storage as fat.

- Dense or fibrous connective tissue: this forms ligaments and tendons. Its densely packed collagen fibers have great tensile strength.

- Reticular connective tissue: this is a network of reticular fibers made from fine collagen, type III. These fibers form a soft skeleton to support the lymphoid organs such as lymph nodes, bone marrow and spleen.

The ECM is defined as a collection of macromolecules outside the plasma membrane of cells in tissues and organs. The ECM is the main feature of connective tissue, although it is also found in epithelium, muscle and nervous tissue. Its functions include the shape-forming of tissues and organs, water storage, elasticity, stability and signal transduction. The dominant components of the ECM include various proteins, glycoproteins and polysaccharides. The largest group of proteins is the collagen family, which comprises 28 known members that are involved in the formation of various fibers. Carbohydrates form another large group, notably long-chain polysaccharides known as glycosaminoglycans. Except for hyaluronic acid, the carbohydrates associate with proteins to form proteoglycans.

Connective tissues have often been reported in Raman and FT-IR images as being located adjacent to the epithelium or to carcinomas. Disorders of cartilage [10], of the ECM in cardiac tissue [11] and of germinal centers in the lymphoid organ spleen [12] have each been studied using FT-IR imaging. Indeed, a Raman spectroscopic study was reported for sarcoma, a neoplastic process originating within the connective tissue [13]. Applications of vibrational spectroscopic imaging to bone (a member of the supportive connective tissue family and considered to be a 'hard tissue') are described in Chapter 4 of this book.

3.1.3
Muscle Tissue

Muscle is the contractile tissue of the body, its function being to produce force and cause motion, as well as either locomotion or movement within internal organs. Muscles are organized into fibers that are mainly composed of muscle cells which in turn contain myofibrils. The myofibrils contain sarcomeres that contain the filament-forming proteins actin, myosin and titin. Muscle tissue is further separated into three distinct categories:

- Skeletal or 'voluntary' muscle is anchored to bone and used to effect skeletal movement such as locomotion and maintenance of posture. Although such postural control is generally maintained as a subconscious reflex, the muscles responsible react to conscious control, like nonpostural muscles. The body of an average adult male human contains 40–50% skeletal muscle, while an average female contains 30–40%. Skeletal muscle is further subdivided into Type I (slow oxidative fibers), Type IIa (fast oxidative glycolytic fibers) and Type IIx (fast glycolytic fibers). These differ in composition, enzyme activity, contractile speed and color.

- Smooth or 'involuntary' muscle is found within the wall of organs and structures such as the esophagus, stomach, intestines, bronchi, uterus, urethra, bladder and blood vessels. Unlike skeletal muscle, smooth muscle is not under conscious control.

- Cardiac muscle is a specialized type of muscle found only within the heart. It is also considered to be an 'involuntary' muscle.

Within the context of muscle tissue, FT-IR and Raman imaging have each been applied more often to smooth muscle than to skeletal muscle. Both, FT-IR and Raman imaging of blood vessels were used to obtain chemical and spatial information about atherosclerosis [14–16]. Raman images of bronchial tissue containing not only cartilage and epithelium but also smooth muscle were reported [17]. Other FT-IR and Raman imaging studies on the esophagus, intestine and uterus concentrated rather on the epithelium than on smooth muscle, mainly because carcinomas arise in the epithelial tissues.

3.1.4
Nervous Tissue

Nervous tissues are composed of nerve cells (neurons) and glial cells, which in turn form the central nervous system (CNS) and peripheral nervous system (PNS). While the CNS comprises the brain and spinal cord, the PNS consists of all other nerves not lying within the CNS. The PNS transmits sensory stimuli to the CNS, and also transmits information to the muscles, glands and sensory organs. The CNS is responsible for the assessment of stimuli and any subsequent reactions, the development of thoughts and emotions, and the formation and storage of memories. The CNS can be subdivided into the gray and white matter: the gray matter is composed of unmyelinated neurons (neural cell bodies), while the white matter contains myelinated neurons (axons). Myelin is an electrically insulating phospholipid layer that surrounds the axons of many neurons. The neurons are connected to a complex network that processes and transmits cellular signals.

Glial cells in the human brain are smaller and more abundant than neurons, and are classified according to their structure and function into astrocytes, oligodendrocytes, microglia, ependymal cells, radial glia, Schwann cells and satellite cells. The main functions of glial cells are to surround neurons and hold them in place, to supply nutrients and oxygen to neurons, to insulate one neuron from

another, and to destroy pathogens and remove dead neurons. Glial cells retain the ability to undergo mitosis in adulthood, while neurons cannot. This view is based on a general deficiency of the mature nervous system to replace neurons after an insult or injury, while very often there is a profound proliferation of glia (called 'gliosis') near or at the stage of damage. However, there is also some recent evidence of neural stem cells in some regions of the mature nervous system being capable of generating new neurons. The CNS is enveloped by the meninges; these form a system of connective tissues that consist of the dura mater, the arachnoid mater and the pia mater. The arachnoid and pia mater are sometimes together called the leptomeninges. The primary function of the meninges is to protect the CNS.

Applications of IR and Raman imaging in the study of nervous tissue have been reported for Alzheimer's disease [18], Parkinson's disease [19], multiple sclerosis [20], scrapie infections [21] and brain tumors. Brain tumors can be categorized as either 'primary' tumors, originating from the brain cells, or 'secondary' tumors (also called brain metastases), originating from tumors outside the brain. As neurons have largely lost the ability to divide, most primary brain tumors are derived from glial cells. The wide field of neuro-oncological applications of FT-IR and Raman imaging was recently summarized [22], including details of primary brain tumors [23], tumors of the meninges ('meningeomas') [24], secondary brain tumors [25] and a murine brain tumor model [26].

3.2
Preparation of Soft Tissue for Vibrational Spectroscopic Imaging

3.2.1
General Preparation Strategies

Due to the high sensitivity of vibrational spectroscopy, accurate sample preparation procedures are essential in order to obtain reproducible results and to permit the transfer of results from one laboratory to another. One of the major advantages of both IR and Raman spectroscopy is that they require minimal or no preparation, which also makes them attractive for *in vivo* applications. However, depending on the experimental configuration and the origin of the tissue, samples must often be processed before image acquisition in order to fulfill the specific requirements of the spectroscopic method. As yet, standardized preparation procedures have not been defined. The effects of *ex vivo* handling procedures (drying, freezing, thawing and formalin fixation) on mammalian tissue [27], the effects of fixation on human bronchial tissue [28] and the efficacy of dewaxing agents on cervical tissue [29], have been described for Raman spectroscopy. Some general considerations are provided in the following sections.

To date, many of the studies on the vibrational spectroscopic imaging of soft tissues have been carried out on *ex vivo* specimens that were either snap-frozen at the time of collection or fixed using formalin, or transferred to an optimal

cutting temperature (OCT) medium or embedded in paraffin. Due to the time lapse between tissue excision and spectroscopic examination, such preservations are performed by many groups in order to maintain the biochemical state of the specimens. Fixation using a formaldehyde solution (formalin) preserves the tissue by preventing autolysis and stabilizing the tissue structure. Here, formaldehyde reacts with the amino groups of amino acids and promotes coagulation, but not the precipitation of proteins. Both, paraffin and OCT serve as support media; subsequently, thin tissue sections are cut using either a microtome (for paraffin-embedded tissue) or a cryotome (for snap-frozen tissue). A recently introduced femtosecond laser microtome (Rowiak, Hannover, Germany) offers an alternative procedure for slicing soft tissue in its native state, without freezing or embedding. The fixation of thin tissue sections by air-drying is also surprisingly effective. When the water content has been vaporized in a dry atmosphere, the proteins are precipitated to form an insoluble mass that is resistant to degradation. Spectral data collected from samples fixed in this way have revealed no apparent spectral changes when compared directly to those fixed with formalin [30].

Staining reagents such as hematoxylin for the cell nuclei and eosin for the cytoplasm, provide additional spectral contributions. Consequently, unstained tissue sections are normally prepared for IR and Raman spectroscopic studies, although opinion differs in this respect. When hematoxylin and eosin (H&E) – stained breast tissue sections were examined with FT-IR spectroscopy in the attenuated total reflection (ATR) mode (see Section 3.2.3), the spectral contributions of the staining reagents were found to be negligible [31]. Due to the nondestructive nature of these methods, tissue sections can be stained by H&E, or even by more specific stains after data acquisition, thus allowing both visual imaging and pathological examination. In order to pre-assess and select sampling areas before vibrational spectroscopic image acquisition, a parallel section can be prepared on standard glass slides, stained and inspected.

The process of paraffin-embedding requires fixation and sample dehydration before embedding and removal of the support medium by organic solvents after sectioning. The tissues are dehydrated by dipping in a graded series of ethanol/water mixtures, and then by bathing in xylene or benzene. However, a danger of this process is that the conformation of proteins and the structure of cells might be distorted, and the chemical composition of the sample is altered. For example, any hydrophobic constituents (e.g., tissue lipids) will also be partly dissolved by such solvent treatment. It is important to realize that, although each processing step might alter the chemical or molecular properties of the sample, those changes induced by the processing procedures may not be a cause for concern, as long as one protocol is strictly adopted throughout a study.

3.2.2
Vibrational Spectra of Reference Materials

The vibrational spectra of reference materials, notably the main components of soft tissue, are introduced in Figure 3.1. In the IR spectrum (trace A) of the all-beta
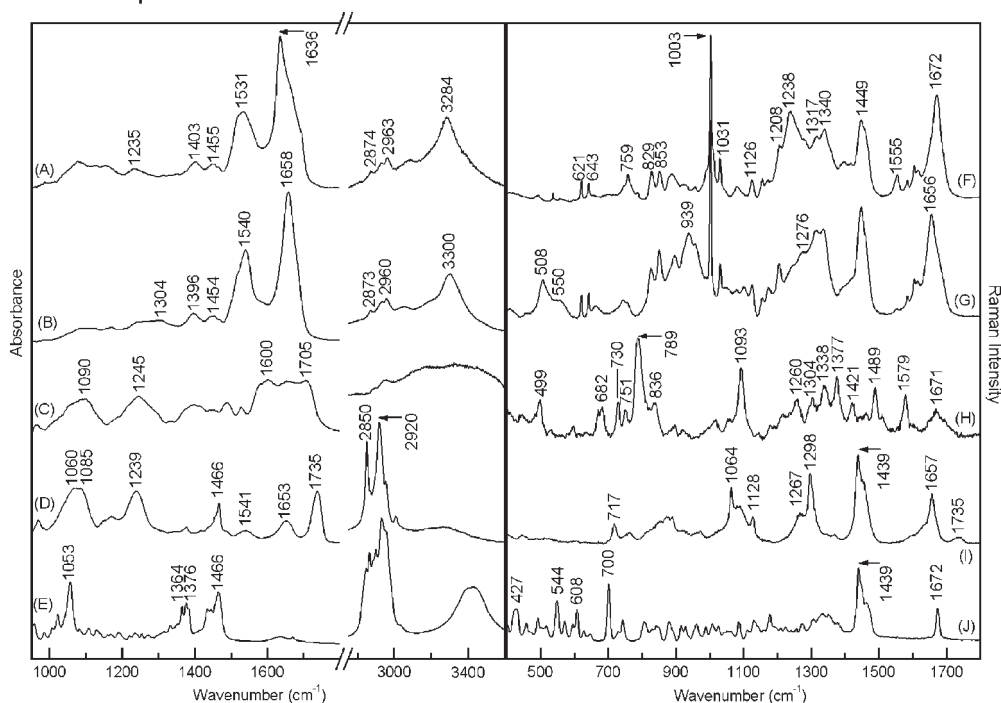
Figure 3.1 IR spectra from 950 to 1800 and from 2750 to 3600 cm^{-1} (A–E) and Raman spectra from 400 to 1800 cm^{-1} (F–J) of the protein concanavalin A (A, F), the protein bovine serum albumin (B, G), DNA from calf thymus (C, H), a lipid extract (D, I) and cholesterol (E, J). The wavenumber scale of the IR spectra in the interval 2750–3600 cm^{-1} is twofold compressed.

protein concanavalin A, IR bands due to the peptide backbone with β-sheet secondary structures are found at 3284 (amide A), 1636 (amide I), 1531 (amide II) and 1235 cm^{-1} (amide III). Bands at 1403 (COO$^-$) and 2963, 2874 and 1455 cm^{-1} (CH$_3$) are assigned to the amino acid side chains. These bands are located in the Raman spectrum (trace F) at similar positions at 1398 and 1449 cm^{-1}. The Raman amide I band is centered at 1672 cm^{-1} and the amide III band at 1238 cm^{-1}. The weak amide II band is not observed. Instead, other Raman bands of amino acids are identified at 759 and 1555 cm^{-1} for Trp; 621, 1003, 1031 and 1208 cm^{-1} for Phe; 643, 829 and 853 cm^{-1} for Tyr; 1126, 1317 and 1340 cm^{-1} (CH$_2$/CH$_3$) for aliphatic amino acids. The IR spectrum (trace B) and Raman spectrum (trace G) of the all-alpha protein bovine serum albumin show a number of differences. The amide bands are shifted due to the predominant α-helical secondary structures to 1304, 1540, 1658 and 3300 cm^{-1} (B) and to 1276 and 1656 cm^{-1} (F). Additional Raman bands are found at 939 cm^{-1} due to C—C vibrations of the α-helices and at 508 and 550 cm^{-1} due to S—S vibrations of the disulfide bridges. Other intensity differences

are caused by changes in primary and tertiary structures. The most intense bands in the IR spectrum of DNA (trace C) corresponds to vibrations of the nucleotides in the interval 1600 to 1705 cm^{-1} and to antisymmetric and symmetric vibrations of the phosphodioxy groups of the backbone at 1245 and 1090 cm^{-1}, respectively. The Raman spectrum of DNA (trace H) provides more information related to the nucleotides thymine (751, 1377, 1671 cm^{-1}), cytosine (789, 1260 cm^{-1}), adenine (730, 1304, 1338 cm^{-1}) and guanine (499, 682, 1489, 1579 cm^{-1}). Further bands are assigned to the phosphodiester group (836 cm^{-1}), phosphodioxy group (1093 cm^{-1}) and CH_2 group (1421 cm^{-1}) of the backbone.

The IR spectrum (trace D) of a brain lipid extract (Fluka No. 53282, Taufkirchen, Germany) in Figure 3.1 contains bands of phosphate groups of phospholipids (1085, 1239 cm^{-1}), ceramide groups of glycolipids (1541, 1653 cm^{-1}), C=O groups (1735 cm^{-1}), C—C groups (1060 cm^{-1}) and CH_2 groups (1466, 2850, 2920 cm^{-1}). The corresponding bands in the Raman spectrum (I) are at 1064 (C—C), 1085 (PO_2), 1439 (CH_2) and 1735 cm^{-1} (C=O). Additional Raman bands are assigned to the choline groups of hydrophilic lipid head groups (717 cm^{-1}) and to C=C groups in unsaturated fatty acid side chains (1267, 1657 cm^{-1}). There are numerous bands of the aromatic system of cholesterol with the most intensive IR bands at 1053, 1364, 1376 and 1466 cm^{-1} (trace E) and the most intensive Raman bands at 427, 544, 608, 700, 1439 and 1672 cm^{-1} (trace J). More comprehensive band assignments of biomolecules have been published in the *Handbook of Vibrational Spectroscopy* [32]. Taken together, these spectra demonstrate that they provide a sensitive fingerprint for each molecule, and that IR and Raman spectra complement each other to some extent.

3.2.3
Preparation for FT-IR Imaging

If FT-IR images are collected in transmission mode, the samples must be sufficiently thin and the substrates transparent to the wavelength range of the probing radiation in the mid-IR range, from 400 to 4000 cm^{-1}. In order to fulfill these conditions, tissue sections of typically 5 to 20 μm thickness are mounted on substrates made from materials such as CaF_2, BaF_2 or ZnSe. In particular, CaF_2 is a material with excellent spectral properties for the FT-IR imaging of soft tissue. In contrast to BaF_2, CaF_2 is almost insoluble in water and thus allows post-staining of the sections by H&E. Compared to ZnSe, the refractive index of CaF_2 is relatively low, so that the extent of optical fringing and chromatic aberrations introduced by the window material are reduced [33]. The disadvantages of CaF_2 are its high price (ca. €50; US$ 65 per slide) and a decreasing transmission towards zero for wavenumbers below 1000 cm^{-1}. Glass slides coated with a thin metal layer are also used as less-expensive substrates (ca. €1.5; US$ 2 per slide) for thin tissue sections (e. g., MirrIR slides by Kevley, Chesterland, OH, USA). Visible light penetrates these slides, thus allowing the tissue to be visually examined by light microscopy, whereas IR radiation is reflected by them, allowing IR spectroscopy in reflection–absorption mode. However, the IR spectra collected from these samples are often

affected by dispersion artifacts [34]. Thin tissue sections will dry rapidly under ambient conditions, and this improves the penetration of IR radiation in tissue because water strongly absorbs any IR radiation. The evaporation of water induces molecular changes in the tissue constituents of proteins, lipids and nucleic acids; the proteins may denature, lipids may crystallize (see Section 3.2.4) and nucleic acids may undergo a change from their natural B-conformation. FT-IR images can also be collected from nontransparent samples in back-scattered geometry using the ATR mode [35]. Here, samples are in contact with an ATR crystal prepared from an IR-transparent material of high refractive index. When the IR radiation strikes the ATR crystal at the correct angle of incidence, the radiation undergoes a total internal reflection such that, inside the ATR crystal a standing wave of radiation is established (called an evanescent wave) that penetrates a little beyond the surface. A sample which is in contact with the crystal can interact with the evanescent wave and absorb IR radiation, resulting in an IR spectrum. As the penetration of IR radiation is restricted to few micrometers (typically $0.5–3.5\,\mu m$), it is important to establish a close contact between the sample and the ATR crystal; this is sometimes difficult for a hydrated tissue, and might lead to destruction of the tissue sections.

The IR spectra (traces A–C) in Figure 3.2 demonstrate the effect of treating tissue sections with polar and nonpolar solvents. The IR spectrum (trace A) was obtained from a dried tissue section of a glioblastoma multiforme (GBM) brain tumor. Compared to the spectra in Figure 3.1, it is evident that this tissue is mainly composed of proteins and lipids. The IR spectrum (trace B) was acquired from a consecutive tissue section that had been treated for 10 min with a drop of toluol. The overlay of the normalized spectra indicates that lipid-associated bands at 1740,
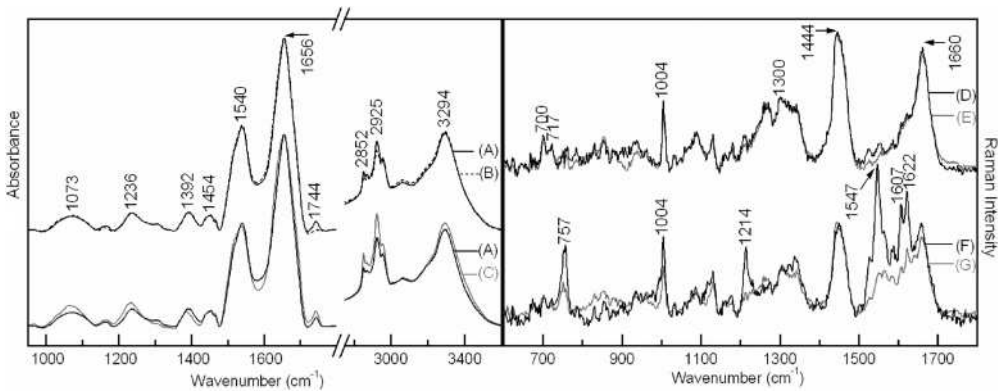
Figure 3.2 IR spectra from 950 to 1800 and from 2750 to 3600 cm^{-1} (A–C) and Raman spectra from 400 to 1800 cm^{-1} (D–G) of brain tissue. Untreated tissue section (A); tissue section after treatment with toluol (B) and tissue section after treatment with water (C); Native tumor tissue at 1 h (D) and 10 h (E) after surgery; Native tumor tissue with hemorrhage at 1 h (F) and 10 h (G) after surgery. The wavenumber scale of the IR spectra in the interval 2750–3600 cm^{-1} is twofold compressed.

2852 and 2925 cm^{-1} had decreased. The IR spectrum (trace C) was acquired from a consecutive tissue section that had been treated for 10 min with a drop of water. The overlay of the normalized spectra indicated that lipid-associated bands near 1070, 1230, 1740, 2852 and 2925 cm^{-1} had increased. In summary, the relative intensity ratios of lipid to protein bands decreased in the order (C) > (A) > (B), consistent with the removal of lipids by toluene and with the removal of proteins by water. Furthermore, the shapes of the amide bands changed, which was consistent with the secondary structure changes in proteins.

3.2.4
Preparation for Raman Imaging

Raman images of tissues are usually collected in a backscattering geometry using near infrared (NIR) radiation excitation between 700 and 850 nm. Then, most Stokes-shifted Raman bands are below 1100 nm which enables their sensitive detection by silicon-based NIR-optimized charge-coupled device (CCD) cameras. Within the visible wavelength range (400–700 nm), most tissues show a high absorbance, mainly due to hemoglobin which limits the penetration of the incident and scattered photons. Furthermore, a strong autofluorescence is usually excited using visible lasers which masks the inherently weak Raman signals. Alternatively, it is possible to use UV light at wavelengths below 270 nm to circumvent the fluorescence interference problem. Due to absorption of UV light by nucleotides and aromatic amino acids, their Raman signals are enhanced by a resonance effect. However, as the tissue penetration depth is only in the order of micrometers, care must be taken to avoid tissue damage when using UV light. Thin sections are mounted on substrates with low background signals. Upon 785 nm excitation, the CaF$_2$ or BaF$_2$ slides have a particularly low background, allowing also the collection of FT-IR images. The tissue can also be studied in its native state under *in vivo* conditions by using Raman spectroscopy, as water contributes only marginally to the Raman signals. The light penetration depends on factors such as the excitation wavelength, excitation intensity, sample composition and optical geometry. When using low-magnification objectives in combination with fiber-optic probes or with microscopes, the radiation might penetrate several hundreds of micrometers. (Methods used to collect spectral information from deeper layers are described in Chapter 7 of this book.) By using a confocal microscope with a high magnification/high numerical aperture objective, diffraction-limited lateral resolution can be achieved below 1 μm, while the depth of view is reduced to a few micrometers. As the laser must be accurately focused to optimally excite and collect the Raman signals, a fixed focus can only be applied for flat samples. For uneven samples, the focus must be adjusted before each measurement. Autofocus routines can be used for adjustment during Raman image acquisition in the mapping mode.

The Raman spectra (traces D–G) in Figure 3.2 demonstrate the effects of aging for a native specimen of a GBM brain tumor. Traces D and F represent two mean spectra of a Raman image which was acquired from the specimen just 1 h after surgery. The main spectral contributions of proteins are identified at 1004, 1450

and 1660 cm^{-1}, of lipids at 717, 1300 and 1440 cm^{-1}, and of cholesterol at 700 and 1440 cm^{-1}. Additional bands at 757, 1214, 1547, 1607 and 1622 cm^{-1} in spectrum (F) can be assigned to the hemoglobin of red blood cells [36]. These bands are enhanced by a resonance effect because the heme group partly absorbs the excitation radiation. The Raman spectra (traces E and G) represent two mean spectra of a Raman image which was acquired from the same specimen 10 h after surgery. An overlay of the Raman spectra (D) and (E) indicates that both spectra corresponding to tumor tissue are almost identical. However, an overlay of the Raman spectra (F) and (G) indicates differences in tumor tissue with a high blood cell content. The total and relative intensity changes point to a degradation and deoxygenation of the heme group. Further changes were observed after freezing and thawing; details of these findings have been reported earlier [37]. On drying the brain tissue sections, a crystallization of the hydrophobic components was induced; the Raman spectra of these crystals suggested that they contained almost pure cholesterol or cholesterol ester [38, 39]. Such an artifact can only be avoided if nondried tissue sections are studied. In summary, the effects of aging, freezing, subsequent thawing and drying must each be considered before results are transferred to spectra recorded under *in vivo* situations.

3.3
Applications to Soft Tissues

3.3.1
Colon Tissue

Colon tissue was selected as a model for the comparative analysis of soft tissue by FT-IR and Raman imaging at low and high lateral resolution, because it contains all four major tissue types such as muscle, connective tissue, epithelium and also nerve cells. The vibrational spectroscopic fingerprints of normal tissues and their distribution in control samples were determined. The compilation of such data is important before a method can be applied to pathological colon tissue such as colorectal adenocarcinoma, which is the third most common form of cancer and the second leading cause of death among cancer patients in the Western world. Colorectal adenocarcinomas originate from epithelial cells and are able to infiltrate the subjacent layers of colon and rectum.

A colon specimen was obtained with written parental consent from the colostomy site of a neonate with an anorectal malformation. The studied sample represented a fraction of the normal colon tissue. A tissue section of 20 μm thickness was prepared using a cryotome at temperatures between −18 and −22 °C. Figure 3.3 shows the photomicrograph of an unstained thin section of colon tissue (b), a FT-IR image (a) and a Raman image (c). The photomicrograph (e) shows a ganglion in the boxed area in (b) at 15-fold magnification. The FT-IR and Raman microscopic images of this area are included in panels (d) and (f), respectively.
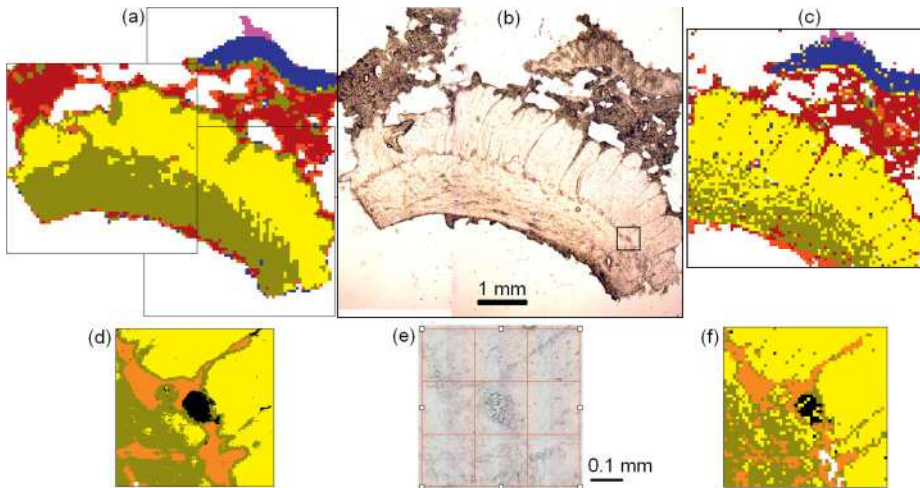
Figure 3.3 FT-IR images (a, d), photomicrographs (b, e) and Raman images (c, f) of a colon tissue section. The location of the sample area with a ganglion in the center (e) is indicated in (b) by a box. The color code represents the segmentation of spectra by a cluster analysis: mucus (magenta), mucosa (blue), submucosa (red, brown), circular muscle (yellow), longitudinal muscle (olive), fibrous septa (orange) and ganglion (black). Further details are presented in the text.

The images were acquired by a FT-IR imaging system coupled to a 64×64 focal plane array (FPA) detector (Bruker Optik GmbH, Ettlingen, Germany). The field of view in the macro chamber IMAC (Bruker) without magnification using a $4 \times 4 \, mm^2$ FPA detector was $4 \times 4 \, mm^2$. Because the size of the tissue section exceeded the field of view, three individual images were recorded and combined in Figure 3.3a. The field of view in the IR microscope (Hyperion; Bruker) with $15\times$ magnification using a $2.5 \times 2.5 \, mm^2$ FPA detector was reduced to $170 \times 170 \, \mu m^2$. A mosaic of 3×3 images was recorded and combined in Figure 3.3d. Although each pixel corresponded to an area of just $2.6 \times 2.6 \, \mu m^2$, the actual lateral resolution was limited by diffraction to $10 \, \mu m$ at $1500 \, cm^{-1}$ [40].

The Raman images were acquired using a Raman system that consisted of a 785 nm diode laser, a microscope, a notch filter, a spectrograph with a reflective grating and a CCD detector (Renishaw, Wotton-under-Edge, UK). By using a motorized sample stage, the spectra were sequentially registered from a pre-defined grid. The grating was moved during acquisition in order to access an extended spectral range from 600 to $1800 \, cm^{-1}$. The Raman image in Figure 3.3c contained 79×79 spectra at a step size of $62 \, \mu m$. The step size was selected in order to compare the data with the FT-IR image, where each pixel corresponded to an area of $62 \times 62 \, \mu m^2$. The laser of approximately 25 mW intensity was focused onto the sample by a $50\times$/NA 0.75 objective to a rectangular spot of approximately $2 \times 7 \, \mu m$. The Raman image (f) contained 53×52 spectra at a step size of $10 \, \mu m$.

A widely used multivariate method to segment vibrational spectroscopic images is *cluster analysis*. After preprocessing procedures, the spectra are grouped according to their similarity. The group or cluster memberships are color-coded for representation. Here, preprocessing encompassed the removal of low-intensity spectra, the subtraction of backgrounds, baselines and offsets, and also normalization. These procedures separate variances due to physical effects such as elastic light scattering and sample thickness from the chemical information. The algorithm k-means cluster analysis grouped the spectra into a predefined number of groups using a Euclidean distance metric. Removed spectra appear as white regions in the vibrational spectroscopic images; the details of which have been reported [41].

The resulting clusters in Figure 3.3a, c, d and f correspond to the gross architectural division of the colon tissue. The mucosa (blue) is the innermost, highly specialized layer of the gastrointestinal tract which is responsible for absorption and secretion, both of which are important processes in digestion. Some mucus (magenta) which has been secreted by epithelial glands is shown at the top of the image. A thin layer of muscle tissue (olive/yellow), termed the muscularis mucosae, is located between mucosa and submucosa (red/brown). The submucosa consists of a dense irregular layer of connective tissue, while below the submucosa can be seen a circular muscle layer (yellow) and a longitudinal muscle layer (olive). The serosa (red/brown), which belongs to the connective tissue class, is visible at the bottom of the image. The nerves and ganglia are the neurons of the enteric nervous system that controls the gastrointestinal tract, the ganglia often being inter-connected to form a complex system known as a plexus. A ganglion (black) of the myenteric plexus between the longitudinal and circular muscle layers and fibrous septa (orange), which surrounds the ganglion, can be resolved at higher magnification.

The cluster-averaged spectra of the six classes in Figure 3.4 reveal information about the underlying spectral properties. Calculating averages offers the advantages that pixel-to-pixel variations are reduced and the signal-to-noise ratios (SNRs) are improved. This was particular important for Raman spectra, which had a typical SNR of 34 under the applied experimental conditions. The SNR of a single spectrum could be increased by having a longer exposure time, although this would also increase the total acquisition time. As the current exposure times were already up to 27 h (Figure 3.3f) and 62 h (Figure 3.3c), a further increase was impracticable. Such a low SNR might contribute to the noisy appearance in the cluster assignments of the Raman images in Figure 3.3. As a consequence of the small clusters and low signal intensities for the ganglion (black) and for mucus (magenta), the averaged spectra (traces K and L) had lower SNRs than the spectra in traces G, H, I. Data acquisition by FT-IR imaging is much faster and yields higher quality spectra. For this, the typical acquisition times were between 1 and 5 min per FT-IR image, which consisted of 4096 individual spectra with a SNR between 500 (Figure 3.3a) and 1000 (Figure 3.3d). In spite of these differences, the cluster segmentations of the FT-IR and Raman images coincided well.
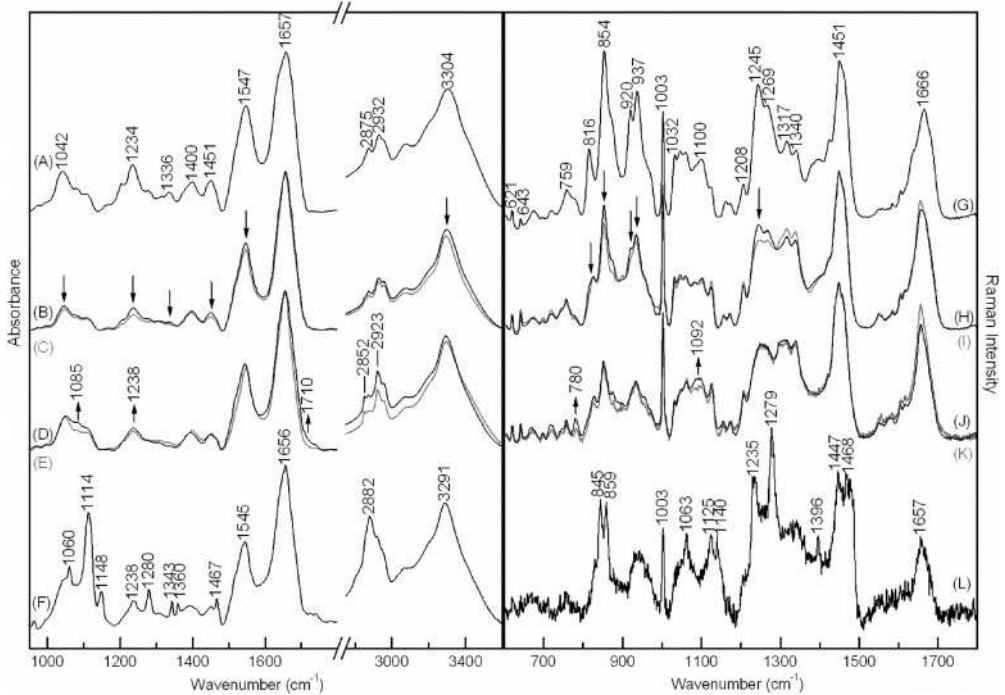
Figure 3.4 IR spectra from 950 to 1800 and from 2750 to 3600 cm^{-1} (A–F) and Raman spectra from 400 to 1800 cm^{-1} (G–L) represent the clusters of the images in Figure 3.3. Submucosa (A, G); longitudinal (B, H) and circular (C, I) muscle layers; ganglion (D, J); mucosa (E, K) and mucus (F, L). The wavenumber scale of the IR spectra in the interval 2750–3600 cm^{-1} is twofold compressed.

The IR spectra in Figure 3.4 are normalized to equal intensities of the amide I band near 1657 cm^{-1} and the Raman spectra to equal intensities of the CH$_2$/CH$_3$ bands near 1451 cm^{-1}. Compared to the previous spectra of the reference material in Figure 3.1, and of brain tumors in Figure 3.2, the IR and Raman spectra of submucosa contained additional spectral contributions, most evident at 1042, 1234, 1336, 1451 and 1547 cm^{-1} (A) and at 759, 816, 854, 920, 937 and 1245 cm^{-1} (G). These bands could be assigned to collagen, which is a major component in connective tissue. Collagen has an unusual amino acid composition with a high content of hydroxyproline, proline and glycine, and a special coiled-coil triple-helix secondary structure. The reduced intensities of collagen-associated bands constituted the main difference between submucosa (A, G) and muscle tissue and between longitudinal muscle layer (B, H) and circular muscle layer (C, I). As smooth muscle tissue often must be stretched, elasticity is an important attribute; consequently, smooth muscle cells secrete a complex ECM that includes collagen. The detection of a relatively small decrease in collagen bands in circular versus

longitudinal muscle requires spectra of high SNR; this is the case for the IR spectra, but not for the Raman spectra before averaging, as stated above. This result was consistent with some overlap between the yellow and olive clusters in the Raman images of Figure 3.3c and f. The collagen-associated bands further decreased in the Raman spectra of mucosa (J) and of the ganglion (K). More intense Raman bands at 780 and 1092 cm^{-1} pointed to a higher DNA content in mucosa, an observation which was confirmed by the more intense IR bands at 1085, 1238 and 1710 cm^{-1} in spectrum (D) than in (E), that were assigned to DNA phosphate groups and to carbonyl groups of nucleotides, respectively. More intense IR bands at 2852 and 2923 cm^{-1} compared with the IR spectra (A–D) indicated that more intense lipid bands also contributed to the bands near 1051, 1085 and 1238 cm^{-1}. Due to the overlap of spectral contributions from lipids, DNA and collagen in the interval 1000 to 1300 cm^{-1}, it is difficult to obtain this information from the IR spectra alone, and the Raman spectra provided complementary information about the DNA and collagen contents. The IR (F) and Raman (L) spectra of mucus are markedly different from the previous spectra, with additional IR bands being found at 1060, 1114, 1148, 1238, 1280, 1343, 1360, 1467 and 2882 cm^{-1}, and additional Raman bands at 845, 859, 1063, 1125, 1140, 1235, 1279, 1396 and 1468 cm^{-1}. These spectral signatures were consistent with carbohydrates and peptides. The main constituent of mucus is mucin, which is known to consist of highly glycosylated peptides. Furthermore, some bands pointed to the poly(ethyleneglycol) 4000 which was administered before surgery in order to flush through the gastrointestinal tract.

This example demonstrates that FT-IR and Raman imaging is capable of distinguishing between different tissue types in unstained tissue sections. A lower lateral resolution in the 60 μm range provided an overview over an extended area, while a higher lateral resolution in the 10 μm range allowed the identification of a single ganglion. As the diffraction-limited resolution of Raman imaging is less than 1 μm, it was shown recently that even subcellular features could be resolved in ganglia [41]. The underlying spectra revealed detailed information regarding the chemical composition, while the high DNA content in the mucosa indicated a high metabolic activity. Given that the mucosa is the outermost layer of the colon, and is therefore exposed to a variety of potentially carcinogenic substances, this explains why carcinogenesis occurs most often in the mucosa and the epithelial layer. The combined use of both modalities offers advantages over the isolated application of Raman and FT-IR imaging.

3.3.2
Brain Tissue and Brain Tumors

Brain tissue was selected for the comparative analysis of dried, thin-tissue sections by FT-IR imaging and nondried, native tissue by Raman imaging. Potential applications include the histopathological assessment of tissue sections to determine tumor type and grade, or the primary tumor of brain metastases and the intraoperative delineation of the tumor margins. The latter point is particularly important

in neurosurgery in order to maximize tumor removal with minimal neurological damage. Due to the large number of FT-IR images, classification models have been trained that could identify several nonpathological and pathological tissue types based on their IR spectroscopic fingerprint. Raman images of whole mouse brains have also been collected using a fiber-optic probe.

3.3.2.1 Whole Mouse Brains

An important step in the development of new diagnostic tools is their application to animal models. Figure 3.5 displays the photomicrograph of an unstained thin section of murine brain, a FT-IR image and a Raman image of the consecutive native tissue sample. The box indicates the approximate area which was analyzed by Raman imaging, while the color code represents the score plot of a principal component analysis (PCA) that constitutes another widely used multivariate method for the analysis of vibrational spectroscopic images. PCA is used to calculate the eigenvalues (scores) and eigenvectors (loadings) of the data matrix, with the loadings being orthogonal to each other. Whereas, the first principle components explain most of the variance within the data sets, the higher principle components are dominated by noise. The PCA was performed in the high wavenumber range from 2800 to $3000\,cm^{-1}$, which was previously suggested to distinguish between morphological structures in brain tissue [42]. The FT-IR image visualizes fiber tracts and cerebellar gyri in the cerebellum at the top, the mesencephalon in the middle part, the arachnoid cistern below the mesencephalon, and the ventricular wall within a ventricle of the left hemisphere. Distortion of the soft pristine brain tissue after transfer to the sample compartment was small, so that the Raman image coincides remarkably well with the FT-IR image. Larger structures such as the fiber tracts, the mesencephalon, the arachnoid cistern and the ventricle of the left hemisphere can also be identified. Finer structures such as the cerebellar gyri and the ventricular wall are not resolved, most likely because the Raman map was recorded at a larger step size.

The Raman image was acquired using a Raman system consisting of a 785 nm diode laser, a fiber-optic probe (Inphotonics, Norwood, MA, USA), a notch filter, a spectrograph with a transmissive holographic grating and a CCD detector (Kaiser Optical Systems, Ann Arbor, MI, USA). The specimen was placed onto a motorized stage, and the laser radiation was focused by the probe to a spot of 60 µm. The scattered light was then collected by the probe and the spectra were sequentially registered from a 30×91 grid at a step size of 120 µm. The grating covered the entire spectral region from 200 to $3550\,cm^{-1}$ without moving upon each exposure of the CCD. During data acquisition the specimen was covered by a CaF_2 window and sealed in a compartment in order to prevent the sample from drying.

The FT-IR image was acquired by a different FT-IR imaging system than described in Section 3.3.1. The applied system Spotlight 300 (PerkinElmer, Waltham MA, USA, cf. Chapter 1) was equipped with a small array of 16 detector elements, which were rapidly scanned over a predefined grid of 310×398 pixels. Each pixel corresponded to an area of $25 \times 25\,\mu m^2$, which enabled the resolution of smaller details in the FT-IR image (Figure 3.5a) than in the Raman image (Figure 3.5c).
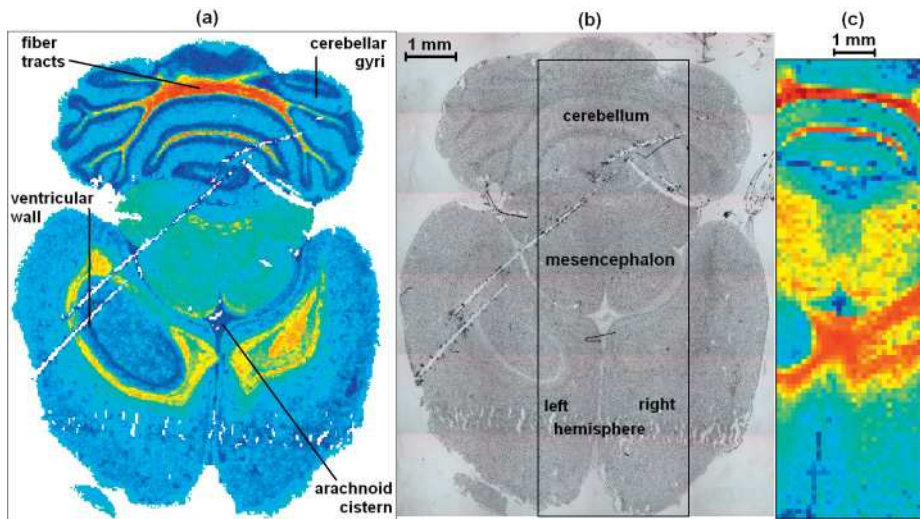
Figure 3.5 FT-IR image (a), photomicrograph (b) and Raman image (c) of a mouse brain tissue section. The approximate position of the Raman image is indicated in (b) by a box. The color codes represent the second principal component scores.
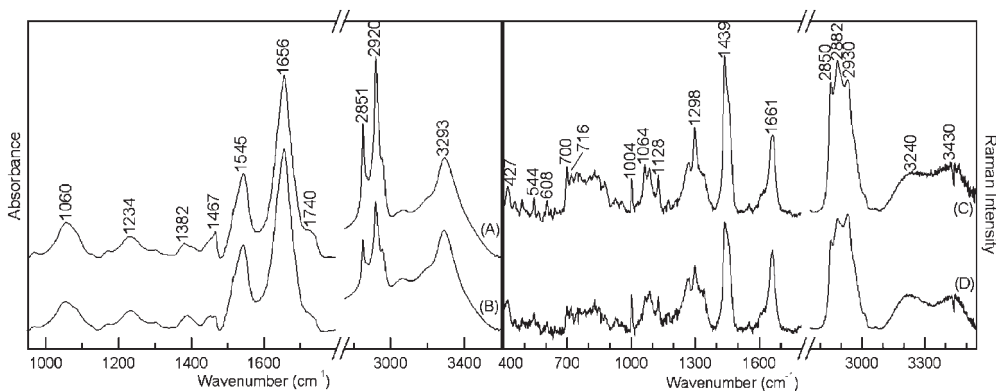
Figure 3.6 IR spectra from 950 to 1800 and from 2750 to 3600 cm^{-1} (A, B) of a mouse brain tissue section; Raman spectra from 400 to 1800 and from 2750 to 3550 cm^{-1} (C, D) of native mouse brain tissue. The wavenumber scale of the IR spectra in the interval 2750–3600 cm^{-1} is twofold compressed.

The IR and Raman spectra in Figure 3.6 were extracted from the images in Figure 3.5. These represent the fiber tracts (traces A and C) and the mesencephalon (traces B and D). The spectra contain more intense spectral contributions of lipids and cholesterol relative to the protein bands than the spectra of brain tumors in Figure 3.2. This is evident from the IR bands at 1060, 1234, 1382, 1467, 1740,

2851 and 2920 cm^{-1} and from the Raman bands at 427, 544, 608, 700, 716, 1064, 1298, 1439, 2850, 2882 and 2930 cm^{-1}. The Raman bands above 3100 cm^{-1} are assigned to water. The spectral contributions of proteins do not change significantly in the IR spectra (A, B) and Raman spectra (C, D). Further details of the vibrational spectroscopic imaging of mouse brains, and the detection of metastases from malignant melanomas in mouse brains, have recently been reported [26]. The possibility of inducing brain tumors in a small animal model opens the route to exciting studies for the application and optimization of acquisition techniques and data analysis algorithms for vibrational spectroscopic images.

3.3.2.2 Primary Brain Tumors

Normal human brain tissue contains 68–80% water, 10–11% proteins and 5–15% lipids, with higher lipid (15%) and lower water (68%) contents in the white matter, and lower lipid (5%) and higher water (80%) contents in the gray matter [43]. Most other tissues, such as muscle (4%), liver (3.1%) and lung (2.9%) contain lesser proportions of lipids. The high lipid content of brain tissue is a consequence of the fact that neurons and nerve cells are surrounded by a sheath of lipids. If a tissue of a lower lipid content is found within the brain, it might point to a different tissue type such as the dura mater, leptomeninges, hemorrhage or brain tumors. The dura mater and leptomeninges form the layers of the brain that encapsulate the meninges, and both have skin-like properties and high spectral contributions of collagen [24, 37, 38]. Another property of most brain cells, which distinguishes them from proliferating and dedifferentiated tumor cells, is that they are postmitotic; in other words, they do not undergo cell division and all of the cells are at the same stage of maturation. Brain tissue is a very soft tissue due to its high water content, yet this may even increase (to 90%) in patients with intracranial neoplasms and cerebrovascular pathologies [44].

Tumors that begin in the brain tissue are known as 'primary' brain tumors, and are classified according to the cell types from which they originate. Astrocytic gliomas, the most frequent primary brain tumors, originate from astrocytes, a special class of glial cells. The malignancy of these lesions has been classified by the World Health Organization (WHO) as grades I and II, both of which are benign, and grades III and IV, which are malignant tumors with a rapid and infiltrative growth pattern and a strong tendency to form metastases [45]. When more than 100 FT-IR images of human brain tissue and gliomas had been acquired, a supervised classification model was trained that distinguished six classes of: (i) normal tissue of regular cell density; tissue of (ii) low; (iii) intermediate and (iv) highly increased cell density; (v) hemorrhage and (vi) other tissues. The low, intermediate and highly increased cell density was found to correlate with astrocytoma grade II, astrocytoma grade III and GBM grade IV, respectively. The model was based on the algorithm linear discriminant analysis (LDA), which uses three band ratios as molecular descriptors. The key information here is the ratio of the lipid band at 2850 cm^{-1} and the protein band at 1655 cm^{-1}, which decreases with increasing malignancy. It has been reported that the model can assign single-spectra, FT-IR images which have been recorded with a single channel detector in the

sequential mode, and FT-IR images which were recorded with a FPA multichannel detector [46]. The class assignments are color-coded to visualize the results, while the selection of training data and the classification results were validated by a histopathological inspection of consecutive H&E-stained tissue sections. In a retrospective study, multiple brain tissue specimens from one patient were obtained under neuronavigation surveillance [47]. The LDA classification of FT-IR images was capable of distinguishing the central part of the tumor with high cell densities from the peripheral region with regular, low and intermediate cell densities. This success also enabled the application of FT-IR imaging as a complementary, *ex vivo* tool to monitor the progress of tumor extirpation. An example is shown in Figure 3.7 for ten tissue sections on CaF_2 slides obtained from a brain tumor patient with a multifocal GBM. The images were acquired using a FT-IR system coupled to a 64×64 FPA detector (Bruker, Ettlingen, Germany). The field of view in the macro chamber (IMAC; Bruker) was $4 \times 4 \, mm^2$ per image. The color-coded FT-IR images demonstrated the inhomogeneous nature of the tumor, and a diagnosis of GBM was unambiguously confirmed by FT-IR image (c), which was dominated by most malignant tissue of high cell density (red). Whereas the FT-IR images (d, h, i and j) also contained extended regions of high (red) and intermediate (orange) cell density, images (a, b, e, f and g) indicated mainly regular (green) and low cell densities (blue), which was consistent with low malignancies and a low number of tumor cells, respectively. It is important to note in the context of gliomas, that astrocytoma grades II and III could be used as descriptive terms to delineate the cellularity and morphological appearance of tumor areas, in analogy to the morphological parameters used for the WHO grading. However, they were not identical with the respective WHO classification. In a tumor which contained areas of
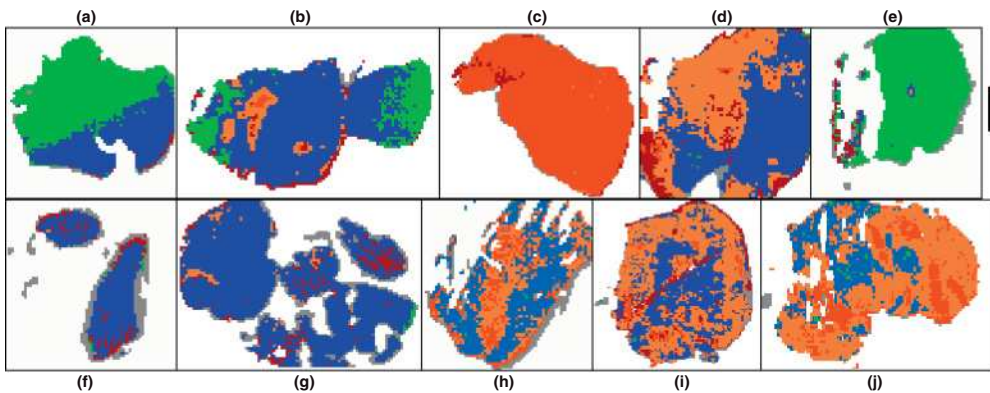
Figure 3.7 (a–k) FT-IR images of ten brain tissue sections obtained from a brain tumor patient with a multifocal glioblastoma multiforme. The color code represents the classification by a LDA model into six classes: regular (green), low increased (blue), intermediate (orange) and high (red) cell density, hemorrhage (brown) and other tissues (gray). The red and orange classes are characteristic of malignant brain tumors of the glioma type. Scale bar = 1 mm.

obvious malignancy (panel c), the areas of low cellularity with only a few tumor cells did not represent a benign tumor astrocytoma grade II. Despite the morphologically benign appearance, these tumor cells may retain their malignant potential, a fact which explains the strong tendency of GBMs to recur within a short period. The curing of a GBM is unlikely unless the tumor is eradicated completely; however, this also involves other approaches such as immunotherapy or vector-mediated gene therapy as adjuncts to surgery.

3.3.2.3 Secondary Brain Tumors

The term 'metastasis' refers to the spread of cancer. In 15–40% of all cancer patients, tumors that have started elsewhere in the body may spread to the brain to cause secondary brain tumors, known as 'brain metastases' [48]. Surprisingly, in up to 15% of all cases the primary tumor of brain metastases remains unknown, despite thorough investigations with standard screening techniques. While the failure to detect the primary tumor is usually due to its small size and lack of symptoms, this constitutes the main problem when selecting an organ-specific therapy. Lung cancer, which is known to cause thoracic symptoms at a fairly late stage of tumor development, is the most frequent site for brain metastases. Other frequent primary tumors include colorectal cancer, breast cancer, renal cell carcinoma and malignant melanoma. The concept of applying vibrational spectroscopy to identify the primary tumor is that metastatic tumor cells contain molecular information of the primary tumor. So, the fact that vibrational spectra can provide a 'molecular fingerprint' of the tissue type may enable its assignment by a supervised classification model. Two classification models have been introduced to distinguish between the white and gray matter of normal brain tissue, and between the brain metastases of renal cell carcinoma (RCC), lung cancer (LC), breast cancer (BC) and colorectal cancer (CC) [25, 49]. The first model was based on the LDA algorithm. Compared to the three molecular descriptors used for the classification of gliomas, the number of band ratios was increased to eight, since the differences between the tissue types were smaller. The second model was based on the algorithm soft independent modeling of class analogies (SIMCA), where the classes are defined by a set of principal components of training data. Following PCA, the test data were projected into the multidimensional data space of the training data and assigned to the class with the closest distance. Because ten principal components in the interval 950–1800 cm^{-1} were able to describe more variances, the SIMCA model tended to give better classification rates for three control specimens and 17 tumors than did the LDA model.

The color-coded classification results obtained, using the SIMCA and LDA models for five specimens, are shown in Figure 3.8. Four tissue sections were prepared on CaF_2 substrates from different brain metastases, while a normal brain specimen was obtained from an autopsy. The images were acquired using a FT-IR imaging system coupled to a 64×64 FPA detector (Bruker). The field of view in the macro chamber (IMAC) was $4 \times 4\,mm^2$, and the resolution of $62\,\mu m$ per pixel was sufficient to identify the molecular information of the main tissue classes.
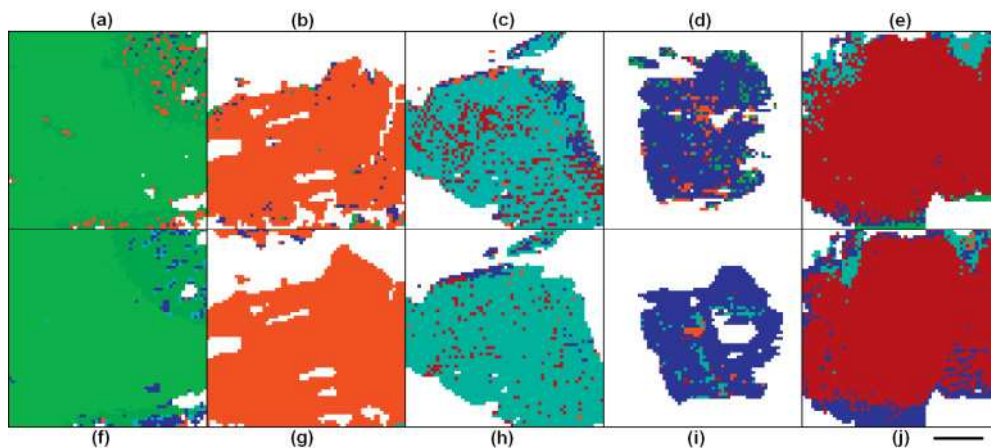
Figure 3.8 FT-IR images of brain tissue sections obtained from an autopsy (a, f) and four brain metastasis patients (b–e and g–j). The color codes represent the classification by a LDA model (a–e) and a SIMCA model (f–j). into six classes: white matter (green), gray matter (dark green), brain metastases of renal cell carcinoma (red), of colon cancer (cyan), of lung cancer (blue) and of breast cancer (brown). Scale bar = 1 mm.

The SIMCA model assigned 94.1% of the spectra from the normal sample in panel (a), while the LDA model assigned 95.4% of the spectra in panel (f) to white and gray matter. Incorrect assignments were observed mainly in the gray matter. Subsequently, 99.0% and 95.7% of the spectra from the RCC brain metastasis were assigned to RCC in panels (b, g) by the SIMCA and LDA models, respectively. A typical molecular property of renal cells is the expression and accumulation of glycogen, and these high correct classification rates were based on the detection of glycogen throughout FT-IR images of the brain metastasis. As glycogen is not present in significant amounts in normal brain tissue (nor in other brain metastases), this molecular marker is indicative of RCC. Although the molecular markers were less pronounced for the other brain metastases, the majority of spectra were always assigned to the correct primary tumor: 74.3% to CC (c), 86.3% to LC (d), 82.7% to BC (e), 90.2% to CC (h), 90.8% to LC (i) and 80.4% to BC (j). Besides model deficiencies, classification rates below 100% may occur for several reasons: (i) a fraction of normal tissue might be present; (ii) a tissue type which was not included in the model might exist; and (iii) the images might be affected by noise or physical effects that alter the spectral profile. In particular, incorrect classifications were observed at the tissue margins in panel (e), where the spectra were seen to have low intensities and SNRs. In addition, dispersion artifacts normally show a maximum intensity in IR spectra close to the tissue margins. These classification models can be optimized by acquiring additional training data, including more tissue classes, or by employing other algorithms such as artificial neural networks or support vector machines.

3.3.3
Cervix Uteri and Squamous Cell Carcinoma

Besides the colon, the tissues of the cervix uteri represent another application of FT-IR imaging to epithelial and connective tissues. In addition, the tissue section encompassed dysplasia, and carcinoma. In pathology, the term dysplasia refers to an abnormality in the maturation of cells within a tissue, and is often indicative of an early neoplastic process. In this section, we highlight the fact that FT-IR imaging is a high-throughput technique which can be used to acquire images from several extended regions with microscopic resolution in a relatively short time. Since such a large amount of data constitutes an analytical challenge, a processing procedure for data reduction must be introduced.

One field of research that has attracted much attention during the past decade has been the application of FT-IR and Raman spectroscopy in gynecological screening for cervical dysplasia and malignancies [50, 51]. Before breast cancer became the predominant cancer site among woman, cervical cancer was the most frequent neoplastic disease, although it is now estimated that screening programs and follow-up interventions have reduced its incidence by approximately 80% [52]. The currently accepted technique for diagnosing exfoliated cells is the Papanicolaou (Pap) smear test, where cells are collected from the cervical transformation zone and stained with the Pap stain. Despite its past success, cytological screening with the Pap smear test has its limitations, the most important being the high numbers of false-negative results. Thus, since the pioneering studies of Wong and coworkers during the early 1990s [53], the main objective has been to improve the diagnostic accuracy of the Pap smear by using FT-IR spectroscopy of the exfoliated cervical cells. The focal point of Raman spectroscopic research on cervical tissue has been the *in vivo* assessment of squamous dysplasia using fiber-optic probes [54]. Cervical tissue sections have also been studied by three groups using FT-IR imaging [5, 6, 55], with multiple adenocarcinoma tissue sections from a cervical biopsy being used as a model system to demonstrate the generation of three-dimensional FT-IR images [56] (these are described in more detail in Chapter 9).

Whereas, cervical samples were usually obtained by cone biopsy from patients diagnosed by cytology with high-grade cervical dysplasia or carcinoma, the specimen used in these studies [6] originated from a patient with a cervical carcinoma who had undergone a radical hysterectomy. A tissue section of the specimen was mounted on a CaF_2 slide and studied using FT-IR microscopic imaging in transmission mode. The FT-IR imaging system was coupled to a microscope equipped with a 64×64 FPA detector (Bruker). The field of view at 15× magnification using was $270 \times 270 \, \mu m^2$ per image, and each pixel corresponded to an area of $4.2 \times 4.2 \, \mu m^2$. Altogether, 122 FT-IR images totaling 499 712 IR spectra were recorded from seven areas representing cervical stroma, squamous epithelium, dysplasia and carcinoma. A dedicated strategy to segment this large data set (ca. 3 Gb) by cluster analysis was developed that was capable of identifying the main tissue types. The goal was to perform a hierarchical cluster analysis (HCA) over

the entire set of spectra, in order to fully characterize the range of spectral variations through all areas. An HCA on each individual area would provide a different clustering result, because some tissue types are not present in all FT-IR images. HCA has been reported to be the superior clustering algorithm for the segmentation of FT-IR images compared to fuzzy C-means (FCM) and k-means cluster analyses [3]. However, HCA has certain disadvantages, notably that it is difficult to visualize any relationship between large numbers of spectra in the resulting dendrogram, and also that long computation times are required to calculate the distance matrix ($n \times n$) for large wavenumber intervals and high number of spectra (n). Therefore, a cluster analysis using the FCM algorithm was applied as a pre-processing procedure to group the spectra into less than 100 clusters, such that each tissue type was represented by at least one cluster. The advantage of the FCM cluster analysis is that it can handle large data sets within relatively short computation times. This first cluster analysis reduced the number of spectra to a more manageable size for subsequent HCA, and also improved the SNR because each group was averaged over a certain set of IR spectra. The application to the current data set was further optimized by parallel computing, using several processors. The sequential cluster analysis approach combines the advantages of FCM and HCA so as to enlarge the tissue area to be characterized in one process by FT-IR imaging.

Two examples of such an analysis are shown in Figure 3.9, where photomicrographs of H&E-stained tissue sections are compared with FT-IR microscopic images of consecutive, unstained tissue sections. The deviations between each pair of tissue sections are small. The FT-IR image in Figure 3.9b is a mosaic of 4×4 individual images which is composed of 256×256 spectra, while the FT-IR image in panel (e) is a mosaic of 4×3 individual images which is composed on 256×192 spectra. The color codes represent the results of the sequential cluster analyses. In panels (b) and (e) the sequential cluster analyses were performed for all spectra in the spectral region from 950 to 1480 cm^{-1}. At the interface between stroma (pink) and the basal cell layer (red), a thin zone of mild inflammatory response (cyan) is visible (Figure 3.9b). Intermediate (light and dark orange) and superficial (brown) layers of epithelium are found at the right. The zone of severe inflammatory response (blue) broadens toward the dysplastic lesion (red) in the lower part. The red coloring indicates that this initial approach cannot yet distinguish the basal cell layer and the dysplastic lesion. Similarly, the dysplastic lesion in the top part of Figure 3.9e overlaps with the carcinoma in the lower part (both red). A blood vessel (green) in the middle part is surrounded by stroma (pink) and inflammatory infiltration (cyan, blue). A small fraction of mucus (yellow) is observed in the top right part. In order to separate the overlapping tissue types, the red cluster was subjected to a second cluster analysis in the interval 1420–1480 cm^{-1}. Figure 3.9c shows that the normal basal cell layer (yellow) can now be distinguished from dysplasia (orange), while Figure 3.9f shows that dysplasia (orange) can be distinguished from carcinoma (red). The blue cluster represents spectra of different tissue types. Overall, the distinction of normal basal cell layer from dysplasia and squamous cell carcinoma was much more difficult than of the different tissue
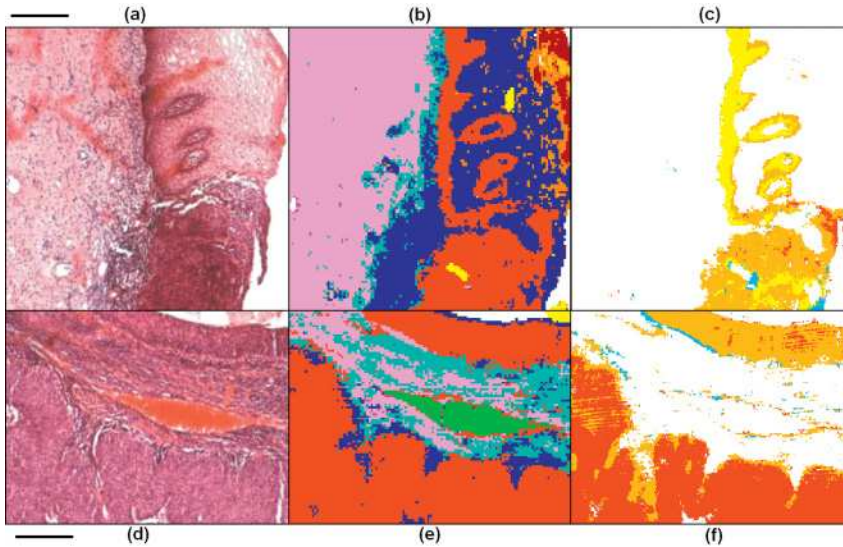
Figure 3.9 Photomicrographs of hematoxylin and eosin-stained tissue sections (a, d) and FT-IR microscopic images (b–c, e–f) of consecutive; unstained tissue sections obtained from a patient with squamous cell cervical carcinoma. Transition zone from normal epithelium to a dysplastic lesion (a–c) and carcinoma surrounded by cervical stroma containing blood vessels and inflammatory response (d–f). Color codes represent the segmentation of two sequential cluster analyses. Scale bars = 200 μm.

types, such as the cervical stroma or upper layers of the epithelium. The reason for such difficulties might be that normal and neoplastic basal cells enter the same cell cycle stages at approximately the same rate. The key difference is that neoplastic cells do not regulate this process, which is a hallmark of cancer [57]. As a consequence, the cytoplasm consists of similar composition and the nuclear-to-cytoplasm ratio is similar; this is also indicated by the darker H&E staining patterns of the respective tissue regions in Figure 3.9a and d.

The cluster averaged IR spectra of the main cervical tissue types are shown in Figure 3.10. The spectral variances in the amide I and II bands were small, and therefore the spectral interval 1480–1800 cm^{-1} did not improve the cluster segmentation and was omitted. Bands at 1026, 1080 and 1151 cm^{-1} in spectra (A–D) indicate a gradual increase in the glycogen level from the parabasal to the intermediate and to the superficial layers of the epithelium. This increase is consistent with an accumulation of glycogen on the maturation of epithelial cells. Bands at 1232, 1336, 1448 and 1538 cm^{-1} are more intense in the IR spectrum of cervical stroma (E) than in the other IR spectra. These bands were found earlier (see Figure 3.4, trace A) as indicative for collagen, which is typical for connective tissue. The spectra of inflammatory response (F, G) are similar to the spectra of stroma, which suggests that this inflammation pertains to stroma. The main difference is a band near 1069 cm^{-1} which gradually increases with the grade of inflammation. Spectral
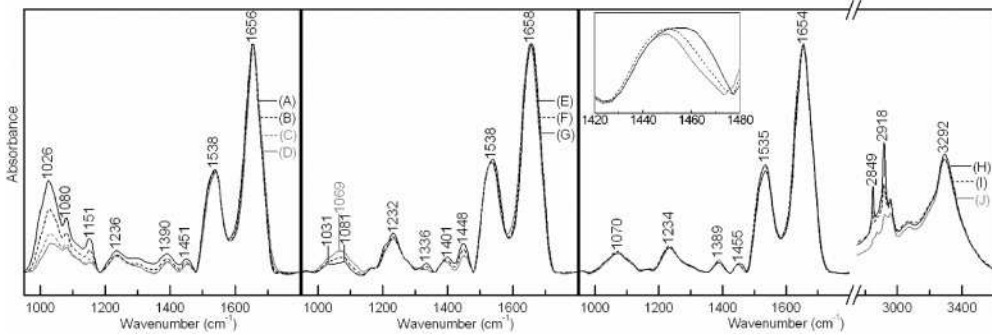
Figure 3.10 IR spectra from 950 to 1800 (A–J) and from 2750 to 3600 cm^{-1} (H–J) of a cervix uteri tissue section. Superficial (A); intermediate (B, C) and parabasal (D) cell layers of epithelium; cervical stroma (E); mild (F) and severe (G) inflammatory response; basal cell layer (H); dysplasia (I) and carcinoma (J). Spectra are normalized and baseline corrected for comparison. The wavenumber scale of the IR spectra in the interval 2750–3600 cm^{-1} is twofold compressed.

contributions near 1069 cm^{-1} are assigned to polymorphonuclear leukocytes (PMNs). The presence of PMNs in a cervical sample has been reported to be consistent with inflammatory conditions [58]. The IR spectra of the basal cell layer (H), dysplasia (I) and carcinoma (J) are very similar, which explains the observed overlap in one cluster in Figure 3.9b and e. The basal cell layer is the germ line for the epithelium. Upon cell division, basal cells generate cells that migrate to the surface and mature. Cancer cells originate from these progenitor cells, which makes the similarity plausible. The most significant spectral change in the interval 950–1480 cm^{-1} is the shift of the band at 1455 cm^{-1} towards 1448 cm^{-1}, with a concomitant intensity decrease as a function of malignancy (inset of Figure 3.10). A cluster analysis was able to differentiate these three tissue types using the spectral variances in the interval 1420–1480 cm^{-1}, as shown in Figure 3.9c and f. The bands in this interval are assigned to CH_2/CH_3 deformation vibrations. The CH_2/CH_3 stretching vibrations in the interval 2800–3000 cm^{-1} confirm the intensity decrease. The bands at 2849 and 2918 cm^{-1} are assigned to fatty acids side chains; these have maximum intensity for the basal cell layer, a medium intensity for dysplasia and a minimum intensity for carcinoma. A decrease of these bands with increasing malignancy was also observed in brain tumors (see Section 3.3.2). In view of the minimal spectral differences in the interval 950–1300 cm^{-1} in spectra (H, I, J), where bands due to the polar head groups of lipids are located, the pronounced differences of the CH_2 vibrations are unexpected. These studies utilized formalin-fixed, paraffin-embedded tissue because of its availability and relevance in the pathology laboratory. Fixation of the tissue specimen with formalin crosslinks proteins; then, during subsequent tissue dehydration with solvents (e.g., ethanol), paraffin embedding and deparaffinization of tissue sections with solvents (e.g., xylol), the unfixed fatty acids, lipids and their polar head groups are expected to be washed out. Spectral contributions due to incomplete removal of the paraffin

sectioning medium could be excluded because of the histopathologically confirmed correlation between the intensity of the CH_2 vibrations and the malignancy. Further experiments are required to study the effects of fixation, dehydration and deparaffinization on cervical tissue in more detail.

3.3.4
Skin

Skin offers unique possibilities for the application of vibrational spectroscopic imaging, because it is the largest human organ and its surface location makes it easily accessible. Applications to corneocyte biology, pharmacology and disease diagnosis have recently been reported. Two dedicated Raman instruments to measure the depth–concentration profiles of skin constituents (River Diagnostics, Rotterdam, Netherlands) and to determine the skin carotenoid level rapidly *in situ* (Pharmanex, Provo, UT, USA) are now commercially available. Human skin can be considered as a multilayered system which is divided into the stratum corneum, the epidermis and the dermis. The composition of these layers was assessed by FT-IR imaging using a vertical porcine skin section as an example [59]. The stratum corneum is the outermost layer and the main protective barrier against water loss, microorganisms and toxic agents. This thin (10–20 μm) superficial region has a biphasic structure consisting of anucleated, keratin-rich corneocytes embedded in a highly ordered, lamellar lipid network of ceramides, fatty acids and cholesterol. A major function of the underlying epidermis is to generate the stratum corneum. The principal cell of the epidermis is the keratinocyte, which differentiates as it migrates towards the stratum corneum. Terminally differentiated keratinocytes generate corneocytes. The thickness of the epidermis ranges from 40 μm on the eyelid to >1 mm on the palms. The dermis (0.4 to 4 mm thick) is the underlying layer of the epidermis, and dermis consists of tough connective tissue along with specialized structures. Approximately 75% of the dry weight of the dermis is comprised by collagen.

3.3.4.1   **Corneocyte Biology**
The maturation of corneocytes in healthy human stratum corneum was investigated using both FT-IR and Raman imaging [60]. During the differentiation of keratinocytes to corneocytes, a large insoluble protein called profilaggrin is converted to filaggrin. The processing of filaggrin includes proteolysis of the protein into its constituents amino acids, amino acids derivatives and salts. The resultant mixture, known as natural moisturizing factor (NMF), provides sufficient hydration to help keep the skin flexible and to facilitate various enzymatic reactions in the pathway that terminates with corneocyte desquamation. Corneocytes from different layers of the stratum corneum were collected from the same site of skin by sequential tape-stripping, a procedure which removes a layer of cells 0.5 μm thick. The most prominent difference in the spectra of FT-IR images, which were acquired from corneocytes in deeper layers, is the increased intensity in the band near 1400 cm^{-1}. The carboxylate symmetric stretching mode absorbs in this

spectral region, which is consistent with amino acid salts and ionized carboxylic acid derivatives in NMF. An NMF concentration profile was constructed from FT-IR images of individual corneocytes, and showed the relative NMF concentration to more than double within the outermost layers (5–6 μm). These results were in agreement with the outer layers sampled *in vivo* by a combination of confocal Raman imaging and confocal microscopy [61].

3.3.4.2 Pharmacology

Due to the strong absorption of IR radiation by water, the penetration depth in naturally hydrated skin is limited to a few micrometers. Therefore, in *in vivo* FT-IR experiments performed in the ATR mode, only the outermost layer of stratum corneum can be sampled. It was recently summarized how FT-IR imaging permits the monitoring of the effects of exogenous materials on stratum corneum lipid organization and protein structure [62]. Depth profiles of molecular concentration gradients and transdermal drug delivery can be obtained *in situ* by confocal Raman imaging in stratum corneum and epidermis up to a depth of 200 μm [63]. Prodrugs are often constructed to enhance transdermal delivery; once in the epidermis, the prodrug is converted to the active drug by endogenous enzymes or simple chemical hydrolysis. The prodrug 1-ethyloxycarbonyl-5-fluorouracil is known to enhance the transdermal delivery of 5-fluorouracil. When pig skin biopsies were treated with the prodrug, and the spatial distribution of both prodrug and drug determined with confocal Raman imaging [64], the permeation of both species was limited to the stratum corneum at 22°C, whereas both were distributed throughout the stratum corneum and viable epidermis at 34°C. Furthermore, a solid form of the drug was observed beneath the skin surface. The physical state (solution versus solid) could be identified in the Raman spectra. Evidently, an increased delivery of the prodrug at particular locations, and its conversion to the parent drug, resulted in a supersaturated solution from which the solid form precipitated.

3.3.4.3 Disease and Cancer Diagnosis

Skin cancer, which includes squamous cell carcinoma, malignant melanoma and basal cell carcinoma (BCC), is the cancer with the highest incidence worldwide. Hence, an understanding of the molecular, cellular and tissue changes that occur during skin carcinogenesis is central to cancer research in dermatology. As with many other tissues, vibrational spectroscopic imaging has been used to evaluate these changes (for a review, see Ref. [65]). A few studies are summarized here. As BCC is the most common cancer of the skin, 15 sections of BCC were sampled, and Raman images acquired and compared with histopathological results [66]. In this sample set, 100% sensitivity and 93% selectivity were demonstrated. Pigmented levi, which belong to benign skin lesions, were distinguished from malignant skin lesions in thin sections of biopsies by FT-IR imaging [67]. Melanoma is the most lethal form of skin cancer, and demonstrates a clinical diagnostic sensitivity in the order of 80% for trained dermatologists, but much worse for untrained medical personnel. The samples used in a Raman study included melanoma, pig-

mented nevi, basal cell carcinoma, seborrheic keratoses and normal skin [68]. The sensitivity and specificity of an artificial neural network classification for diagnosis of melanoma were 85% and 99%, respectively.

3.3.4.4 Raman Systems for Skin Studies

A Raman system was designed which can be applied noninvasively to record the depth–concentration profiles of living skin with a resolution of <5 μm (River Diagnostics, Rotterdam, Netherlands). Using laser excitation at 671 and 785 nm, a custom-built detection system and software tools, various parameters of the skin can be analyzed. Due to the limited penetration (of typically 20–40 μm), most studies are restricted to the stratum corneum. Applications include the determination of: (i) hydration of the skin; (ii) composition of the NMF; and (iii) the penetration of topically applied materials. This technique can be expected to experience growing use by skin scientists in the cosmetics, pharmaceutical and dermatological research fields.

Another commercially available Raman system can be used to determine carotenoid levels in the skin (Pharmanex, Provo, UT, USA). Carotenoids are known to be important in human health, with most of their health benefits being associated with action as antioxidants; that is, they protect cells and tissues from the effects of free radicals and reactive oxygen species. As carotenoids are insoluble in water, they are transported in blood by low-density lipoproteins (LDL). An increase in blood carotenoids is reflected in an increase of carotenoids in all organs of the body capable of taking up lipoproteins, including the skin. Thus, the direct measurement of carotenoids on skin can provide a good indication of the levels of carotenoids in the blood and other tissues, and hence indicate the body's overall antioxidant status. Due to the lack of any accepted noninvasive technology for the detection of carotenoids in living human tissue, resonance Raman spectroscopy was applied as a novel and rapid approach [69]. The Raman signals originating from single-bond and double-bond stretch vibrations of the pi-conjugated carbon backbone of carotenoids at 1159 and 1525 cm^{-1} are enhanced by a factor up to 100 000 under the correct conditions [70]. This instrument uses light-emitting diodes (LEDs) which are tuned to 471.3 and 473 nm in place of a laser. Although there is a large native fluorescence level in the skin upon Raman excitation with blue light, carotenoid levels can be measured over a very wide concentration range.

3.3.5
Ocular Tissue

Because Raman signals are typically weak, intense lasers in combination with sophisticated light collection must be used. Although intense laser radiation can potentially harm the delicate structures in the visual system, ocular tissue has been found to be a very suitable target for Raman spectroscopy for two reasons. First, the ocular media (cornea, lens and vitreous) generally have good optical clarity, which enables high penetration of laser excitation and optical detection of scattered

radiation. Second, the retina also contains the pigment carotenoid. Due to its two orders of magnitude higher abundance compared to skin, the excitation intensities can be reduced to light levels that are within established safety ranges. As no other biological molecules found in significant concentrations in human ocular tissues exhibit similar resonant enhancement with blue laser excitation, the *in vivo* carotenoid Raman spectra are remarkably free from confounding responses.

3.3.5.1 Macular Degeneration of the Retina

Age-related macular degeneration (AMD) is the leading cause of irreversible blindness in the elderly. Carotenoid macular pigments may provide protection against light-induced oxidative damage and lower the risk for this pathology. To explore the role of carotenoids in modifying the risk of AMD further, clinical studies to quantify their levels in the living human macula are impaired by the lack of appropriate instrumentation. Raman spectroscopy has been shown to assess the concentration and spatial distribution of carotenoids in the retina through undilated eyes, noninvasively, within a fraction of a second [71]. Ocular Raman instruments have been designed for this special application (Spectrotek LC, Salt Lake City, UT, USA; however, the company is no longer in business). A new generation of ocular resonance Raman scanners will incorporate wide-field imaging of macular carotenoid distributions [72].

3.3.5.2 Chemical Composition of the Vitreous and the Lens

Imaging the vitreous is a quest to view what is, by design, invisible. The combined use of techniques, including Raman spectroscopy, might provide a better imaging of vitreous for future investigational and clinical purposes. Raman spectroscopy was applied to image the vitreous in order to detect altered vitreous molecules such as glycated collagen and other proteins in diabetic vitreopathy [73]. Using filipin (which binds specifically to cholesterol) as an external Raman label, the distribution of cholesterol in a rat eye lens was determined using Raman spectroscopy [74]; here, the protein distribution was obtained by using intrinsic Raman protein bands. Numerous nonimaging Raman studies have been reported which demonstrate the high degree and long history of research activities in this field. A literature survey in Medline revealed more than 120 references.

3.4
Conclusions

The above examples, references and a recent review [75] together demonstrate that more FT-IR than Raman imaging studies of soft tissue have been reported to date, due mainly to the highly developed instrumentation for FT-IR imaging which is able to acquire high-quality images within minutes. The rapid acquisition of FT-IR images can complement histopathology as a tool to assess tissue sections, and FT-IR-based classification models have now been developed for prostate tissue [4], primary [23] and secondary brain tumors [25]. The latter models allow an on-site

analysis of cryostat sections accompanying neurosurgery that is performed to confirm initial diagnoses and to determine the tumor margins [47]. The size and location of tumors are usually determined using computed tomography (CT) or magnetic resonance imaging (MRI) before surgery, with such preoperative information being transferred during surgery by a neuronavigation system. However, the system accuracy is limited because the margins may deviate from the preoperative locations due to intraoperative brain shift or edema.

The acquisition of Raman images is usually more time-consuming, and the signal-to-noise ratio inferior. Nevertheless, Raman imaging offers advantages in terms of: (i) studying nondried, native tissue; (ii) the maximal, diffraction limited lateral resolution is higher; (iii) the spectral range can more easily be extended to lower wavenumbers; (iv) the technique can be coupled to fiber-optic probes; and (v) enhancement effects can be utilized. For example, the resonance Raman effect was used for the rapid and sensitive detection of carotenoids in skin [69] and retina [71], and also for melanin in brain metastases of malignant melanomas [26]. To date, almost all Raman images have been recorded using the sequential point mapping mode. In order to improve sample throughput in the future, faster and more sensitive Raman systems must be developed utilizing new sampling techniques such as line mapping or global imaging.

The complete assessment of an extended, inhomogeneous soft tissue sample exceeding $1 \, cm^2$ by vibrational microspectroscopic imaging with lateral resolutions below $10 \, \mu m$ requires the accumulation of more than $1\,000\,000$ spectra. Whereas, on the one hand, this is time-consuming when using currently available instruments (even FT-IR imaging systems), on the other hand the resulting large data set is difficult to analyze or classify using currently available computer equipment. Therefore, as yet, Raman and FT-IR microscopic imaging as a screening tool appears to be limited to smaller samples or smaller sampling areas. Such sampling areas require careful selection, using complementary tools such as the conventional staining of consecutive samples or using lower resolved vibrational spectroscopic images. Without this careful selection there is a great risk of missing important information, such as the detection of tumor cells outside the probed region.

Although in its early stages, one can be optimistic that vibrational spectroscopic imaging has the potential to become fully accepted as a diagnostic tool for soft tissues, with sufficient sensitivity and specificity for rapid and nondestructive *in vitro*, *ex vivo* and *in vivo* analyses.

References

1 Nijssen, A., Bakker Schut, T.C., Heule, F., Caspers, P.J., Hayes, D.P., Neumann, M.H.A. and Puppels, G.J. (2002) Discriminating basal cell carcinoma from its surrounding tissue by Raman spectroscopy. *J. Invest. Dermatol.*, **119**, 64–9.

2 Fabian, H., Thi, N.A.N., Eiden, M., Lasch, P., Schmidt, J. and Naumann, D. (2006) Diagnosing benign and malignant lesions in breast tissue sections by using IR microspectroscopy. *Biochim. Biophys. Acta*, **178**, 874–82.

3 Lasch, P., Haensch, W., Naumann, D. and Diem, M. (2004) Imaging of colorectal adenocarcinoma using FT-IR microspectroscopy and cluster analysis. *Biochim. Biophys. Acta*, **1688**, 176–86.

4 Fernandez, D.C., Bhargava, R., Hewitt, S.M. and Levin, I.W. (2005) Infrared spectroscopic imaging for histopathologic recognition. *Nat. Biotechnol.*, **23**, 469–74.

5 Wood, B.R., Chiriboga, L., Yee, H., Quinn, M.A., McNaughton, D. and Diem, M. (2004) Fourier transform infrared spectral mapping of the cervical transformation zone and dysplastic epithelium. *Gynecol. Oncol.*, **93**, 59–68.

6 Steller, W., Einenkel, J., Horn, L.C., Braumann, U.D., Binder, H., Salzer, R. and Krafft, C. (2006) Delimitation of squamous cell cervical carcinoma using infrared microspectroscopic imaging. *Anal. Bioanal. Chem.*, **384**, 145–54.

7 Shetty, G., Kendall, C., Shephard, N., Stone, N. and Barr, H. (2006) Raman spectroscopy: elucidation of biochemical changes in carcinogenesis of oesophagus. *Br. J. Cancer*, **94**, 1460–4.

8 de Jong, B.W.D., Bakker Schut, T.C., Maquelin, K., Van der Kwast, T., Bangma, C.H., Kok, D.J. and Puppels, G.J. (2006) Discrimination between nontumor bladder tissue and tumor by Raman spectroscopy. *Anal. Chem.*, **78**, 7761–9.

9 Schultz, C.P., Kerr, K.Z. and Mantsch, H.H. (1998) In situ infrared histopathology of keratinization in human oral/oropharyngeal squamous cell carcinoma. *Oncol. Res.*, **10**, 277–86.

10 Bi, X., Yang, X., Bostrom, M.P.G. and Camacho, N.P. (2006) Fourier transform infrared imaging spectroscopy investigations in the pathogenesis and repair of cartilage. *Biochim. Biophys. Acta*, **1758**, 934–41.

11 Gough, K.M., Zelinski, D., Wiens, R., Rak, M. and Dixon, I.M. (2003) Fourier transform infrared evaluation of microscopic scarring in the cardiomyopathic heart: effect of chronic AT1 suppression. *Anal. Biochem.*, **316**, 232–42.

12 Krafft, C., Salzer, R., Soff, G. and Meyer-Hermann, M. (2003) Identification of B and T cells in human spleen sections by infrared microspectroscopic imaging. *Cytometry A*, **64A**, 53–61.

13 Huang, Z., Lui, H., McLean, D.I., Korbelik, M. and Zeng, H. (2005) Raman spectroscopy in combination with background near-infrared autofluorescence enhances the in vivo assessment of malignant tissues. *Photochem. Photobiol.*, **81**, 1219–26.

14 Colley, C.S., Kazarian, S.G., Weinberg, P.D. and Lever, M.J. (2004) Spectroscopic imaging of arteries and atherosclerotic plaques. *Biopolymers*, **74**, 328–35.

15 van de Poll, S.W.E., Romer, T.J., Puppels, G.J. and van der Laarse, A. (2002) Imaging of atherosclerosis. Raman spectroscopy of atherosclerosis. *J. Cardiovasc. Risk*, **9**, 255–61.

16 Hsu, H.H.T., Camacho, N.C., Tawfik, O. and Sun, F. (2002) Induction of calcification in rabbit aortas by high cholesterol diets: roles of calcifiable vesicles in dystrophic calcification. *Atherosclerosis*, **161**, 85–94.

17 Koljenovic, S., Bakker Schut, T.C., van Meerbeeck, J.P., Maat, A.P., Burgers, S.A., Zondervan, P.E., Kros, J.M. and Puppels, G.J. (2004) Raman micro-spectroscopic mapping studies of human bronchial tissue. *J. Biomed. Opt.*, **9**, 1187–97.

18 Miller, L.M., Wang, Q., Telivala, T.P., Smith, R.J., Lanzirotti, A. and Miklossy, J. (2006) Synchrotron-based infrared and X-ray imaging shows focalized accumulation of Cu and Zn co-localized with β-amyloid deposits in Alzheimer's disease. *J. Struct. Biol.*, **155**, 30–7.

19 Szczerbowska-Boruchowska, M., Dumas, P., Kastyak, M.Z., Chwiej, J., Lankosz, M., Adamek, D. and Krygowska-Wajs, A. (2007) Biomolecular investigation of human substantia nigra in Parkinson's disease by synchrotron radiation Fourier transform infrared microspectroscopy. *Arch. Biochem. Biophys.*, **459**, 241–8.

20 LeVine, S.M. and Wetzel, D.L. (1998) Chemical analysis of multiple sclerosis Lesions by FT-IR microspectroscopy. *Free Radic. Biol. Med.*, **25**, 33–41.

21 Kretlow, A., Wang, Q., Kneipp, J., Lasch, P., Beekes, M., Miller, L. and Naumann, D. (2006) FT-IR-microspectroscopy of prion-infected nervous tissue. *Biochim. Biophys. Acta*, **1758**, 948–59.

22 Krafft, C. and Salzer, R. (2008) Neuro-oncological applications of infrared and Raman spectroscopy, in *Vibrational Spectroscopy for Medical Diagnosis* (eds M. Diem, J.M. Chalmers and P.R. Griffiths), John Wiley & Sons, Ltd, Chichester, pp. 231–59.

23 Krafft, C., Sobottka, S.B., Geiger, K.D., Schackert, G. and Salzer, R. (2007) Classification of malignant gliomas by infrared spectroscopic imaging and linear discriminant analysis. *Anal. Bioanal. Chem.*, **387**, 1669–77.

24 Koljenovic, S., Bakker Schut, T., Vincent, A., Kros, J.M. and Puppels, G.J. (2005) Detection of meningeoma in dura mater by Raman spectroscopy. *Anal. Chem.*, **77**, 7958–65.

25 Krafft, C., Shapoval, L., Sobottka, S.B., Geiger, K.D., Schackert, G. and Salzer, R. (2006) Identification of primary tumors of brain metastases by SIMCA classification of IR spectroscopic images. *Biochim. Biophys. Acta*, **1758**, 883–91.

26 Krafft, C., Kirsch, M., Beleites, C., Schackert, G. and Salzer, R. (2007) Methodology for fiber-optic Raman mapping and FT-IR imaging of metastases in mouse brains. *Anal. Bioanal. Chem.*, **389**, 133–1142.

27 Shim, M.G. and Wilson, B.C. (1996) The effects of ex vivo handling procedures on the near-infrared Raman spectra of normal mammalian tissues. *Photochem. Photobiol.*, **63**, 662–71.

28 Huang, Z., McWilliams, A., Lam, S., English, J., McLean, D.I., Lui, H. and Zeng, H. (2003) Effect of formalin fixation on the near-infrared Raman spectroscopy of normal and cancerous human bronchial tissues. *Int. J. Oncol.*, **23**, 649–55.

29 Faolain, E., Hunter, M.B., Byrne, J.M., Kelehan, P., Lambkin, H.A., Byrne, H.J. and Lyng, F.M. (2005) Raman spectroscopic evaluation of efficacy of current paraffin wax section dewaxing agents. *J. Histochem. Cytochem.*, **53**, 121–9.

30 Romeo, M., Mohlenhoff, B. and Diem, M. (2006) Infrared micro-spectroscopy of human cells: causes for the spectral variance of oral mucosa (buccal) cells. *Vib. Spectrosc.*, **42**, 9–14.

31 Dukor, R.K., Liebman, M.N. and Johnson, B.L. (1998) A new, non-destructive method for analysis of clinical samples with FT-IR microspectroscopy. Breast cancer tissue as an example. *Cell. Mol. Biol.*, **44**, 211–17.

32 Chalmers, J.M. and Griffiths, P.R. (eds) (2002) *Handbook of Vibrational Spectroscopy*, John Wiley & Sons, Ltd, Chichester.

33 Carr, G.L. (2001) Resolution limits for infrared microspectroscopy explored with synchrotron radiation. *Rev. Sci. Instrum.*, **72** (3), 1613–19.

34 Romeo, M. and Diem, M. (2005) Correction of dispersive line shape artifact observed in diffuse reflection infrared spectroscopy and absorption/reflection (transflection) infrared micro-spectroscopy. *Vib. Spectrosc.*, **38**, 129–32.

35 Kazarian, S.G. and Chan, K.L.A. (2006) Application of ATR-FT-IR spectroscopic imaging to biomedical samples. *Biochim. Biophys. Acta*, **1758**, 858–67.

36 Wood, B.R. and McNaughton, D. (2006) Resonance Raman spectroscopy in malaria research. *Expert Rev. Proteomics*, **3**, 525–44.

37 Krafft, C., Sobottka, S.B., Schackert, G. and Salzer, R. (2005) Near infrared Raman spectroscopic mapping of native brain tissue and intracranial tumors. *Analyst*, **130**, 1070–7.

38 Krafft, C., Sobottka, S.B., Schackert, G. and Salzer, R. (2006) Raman and infrared spectroscopic mapping of human primary intracranial tumors: a comparative study. *J. Raman Spectrosc.*, **37**, 367–75.

39 Koljenovic, S., Choo-Smith, L.-P., Bakker Schut, T.C., Kros, J.M., Puppels, H.J. and van den Berge, G.J. (2002) Discriminating vital tumor from necrotic tissue in human glioblastoma tissue samples by Raman spectroscopy. *Lab. Invest.*, **82**, 1265–77.

40 Lasch, P. and Naumann, D. (2006) Spatial resolution in infrared microspectroscopic imaging of tissues. *Biochim. Biophys. Acta*, **1758**, 814–29.

41 Krafft, C., Codrich, D., Pelizzo, G. and Sergo, V. (2008) Raman and FT-IR microscopic imaging of colon tissue: a comparative study. *J. Biophoton.*, **1**, 154–69.

42 Koljenovic, S., Bakker Schut, T.C., Wolthuis, R., de Jong, B., Santos, L., Caspers, P.J., Kros, J.M. and Puppels, G.J.

(2005) Tissue characterization using high wave number Raman spectroscopy. *J. Biomed. Optics*, **10**, 031116.

43 Agranoff, B.W. and Hajra, A.K. (1994) Lipids, in *Basic Neurochemistry* (eds G.J. Siegel, B.W. Agranoff, R.W. Albers and P.B. Molinoff), 5th edn, Raven Press, New York, pp. 97–116.

44 Yates, A.J., Thompson, D.K., Boesel, C.P., Albrightson, C. and Hart, R.W. (1979) Lipid composition of human neural tumor. *J. Lipid Res.*, **20**, 428–36.

45 Kleihues, P. and Cavenee, W.K. (2000) *Pathology and Genetics of Tumors of the Nervous System*, IARC Press, Lyon.

46 Krafft, C., Thümmler, K., Sobottka, S.B., Schackert, G. and Salzer, R. (2006) Classification of malignant gliomas by infrared spectroscopy and linear discriminant analysis. *Biopolymers*, **82**, 301–5.

47 Sobottka, S.B., Geiger, K.D., Salzer, R., Schackert, G. and Krafft, C. (2009) Infrared spectroscopic imaging as an intraoperative tool for defining tumor resectin margins in cerebral glioma surgery. *Anal. Bioanal. Chem.*, **393**, 187–95.

48 Polyzoidis, K.S., Miliaras, G. and Pavlidis, N. (2005) Brain metastasis of unknown primary: a diagnostic and therapeutic dilemma. *Cancer Treat. Rev.*, **31**, 247–55.

49 Krafft, C., Shapoval, L., Sobottka, S.B., Schackert, G. and Salzer, R. (2006) Identification of primary tumors of brain metastases by IR spectroscopic imaging and linear discriminant analysis. *Technol. Cancer Res. Treat.*, **5**, 291–8.

50 Dukor, R.K. (2002) Vibrational spectroscopy in the detection of cancer, in *Handbook of Vibrational Spectroscopy* (eds J.M. Chalmers and P.R. Griffiths), John Wiley & Sons, Ltd, Chichester, pp. 3335–61.

51 McNaughton, D., Bambery, K. and Wood, B.R. (2008) Cervical histo-pathology, in *Vibrational Spectroscopy for Medical Diagnosis* (eds M. Diem, J.M. Chalmers and P.R. Griffiths), John Wiley & Sons, Ltd, Chichester, pp. 187–202.

52 Roden, R. and Wu, T.C. (2006) How will HPV vaccines affect cervical cancer? *Nat. Rev. Cancer*, **6**, 753–63.

53 Wong, P.T.T., Lacelle, S., Sentermann, M. and Fung, F.K.M. (1995) Characterization of the exfoliated cells and tissues from the human endo- and ecto-cervix by FT-IR and ATR-FT-IR spectroscopy. *Biospectroscopy*, **1**, 357–64.

54 Utzinger, U., Heintzelman, D.L., Mahadevan-Jansen, A., Malpica, A., Follen, M. and Richards-Kortum, R. (2001) Near-infrared Raman spectroscopy for in vivo detection of cervical precancers. *Appl. Spectrosc.*, **55**, 955–9.

55 Chang, J.I., Huang, Y.B., Wu, P.C., Chen, C.C., Huang, S.C. and Tsai, Y.H. (2003) Characterization of human cervical precancerous tissue through the Fourier transform infrared microscopy with mapping method. *Gynecol. Oncol.*, **91**, 577–83.

56 Wood, B.R., Bambery, K.R., Evans, C.J., Quinn, M. and McNaughton, D. (2006) A three-dimensional multivariate image processing technique for the analysis of FT-IR spectroscopic images of multiple tissue section. *BMC Med. Imaging*, **6**, 12.

57 Hanahan, D. and Weinberg, R.A. (2000) The hallmarks of cancer. *Cell*, **100**, 57–70.

58 Chiriboga, L., Xie, P., Vigorita, V., Zarou, D., Zakim, D. and Diem, M. (1998) Infrared Spectroscopy of human tissue II. A comparative study of spectra of biopsies of cervical squamous epithelium and of exfoliated cervical cells. *Biospectroscopy*, **4**, 55–9.

59 Garidel, P. (2003) Insights in the biochemical composition of skin as investigated by micro infrared spectroscopic imaging. *Phys. Chem. Chem. Phys.*, **5**, 2673–9.

60 Zhang, G., Moore, D.J., Mendelsohn, R. and Flach, C.R. (2006) Vibrational microspectroscopy and imaging of molecular composition and structure during human corneocyte maturation. *J. Invest. Dermatol.*, **126**, 1088–94.

61 Caspers, P.J., Lucassen, G.W. and Puppels, G.J. (2003) Combined in vivo confocal Raman spectroscopy and confocal microscopy of human skin. *Biophys. J.*, **85**, 572–80.

62 Mendelsohn, R., Flach, C.R. and Moore, D.J. (2006) Determination of molecular conformation and permeation in skin via IR spectroscopy, microscopy and

imaging. *Biochim. Biophys. Acta*, **1758**, 923–33.

63 Caspers, P.J., Lucassen, G.W., Carter, E.A., Bruining, H.A. and Puppels, G.J. (2001) In vivo confocal Raman microspectroscopy of the skin: noninvasive determination of molecular concentration profiles. *J. Invest. Dermatol.*, **116**, 434–42.

64 Zhang, G., Moore, D.J., Sloan, K.B., Flach, C.R. and Mendelsohn, R. (2007) Imaging the prodrug-to-drug transformation of a 5-fluorouracil derivative in skin by confocal Raman microscopy. *J. Invest. Dermatol.*, **127**, 1205–9.

65 Eikje, N.S., Aizawa, K. and Ozaki, Y. (2005) Vibrational spectroscopy for molecular characterization and diagnosis of benign, premalignant and malignant skin tumors. *Biotechnol. Annu. Rev.*, **11**, 191–225.

66 Nijssen, A., Bakker Schut, T.C., Heule, F., Caspers, P.J., Hayes, D.P., Neumann, M.H.A. and Puppels, G.J. (2002) Discriminating basal cell carcinoma from its surrounding tissue by Raman spectroscopy. *J. Invest. Dermatol.*, **119**, 64–9.

67 Tfalyli, A., Piot, O., Durlach, A., Bernard, P. and Manfait, M. (2005) Discriminating nevus and melanoma on paraffin-embedded skin biopsies using FT-IR microspectroscopy. *Biochim. Biophys. Acta*, **1724**, 262–9.

68 Gniadecka, M., Philipsen, P.A., Sigurdsson, S., Wessel, S., Nielsen, O.F., Christensen, D.H., Hercogova, J., Rossen, K., Thomsen, H.K., Gniadecki, R., Hansen, L.K. and Wulf, H.C. (2004) Melanoma diagnosis by Raman spectroscopy and neural networks: structure alteration in proteins and lipids in intact cancer tissue. *J. Invest. Dermatol.*, **122**, 443–9.

69 Hata, T.R., Scholtz, T.A., Ermakov, I.V., McLane, R.W., Khachik, F. and Gellermann, W. (2000) Non-invasive Raman spectroscopic detection of carotenoids in human skin. *J. Invest. Dermatol.*, **115**, 441–8.

70 Koyama, Y. (1995) Resonance Raman spectroscopy, in *Carotenoids: Spectroscopy*, Vol. 1B (eds G. Britton, S. Liaaen-Jensen and H. Pfander), Birkhäuser, Basel, pp. 135–46.

71 Bernstein, P.S., Zhao, D.Y., Sharifzadeh, M., Ermakov, I.V. and Gellermann, W. (2004) Resonance Raman measurement of macular carotenoids in the living human eye. *Arch. Biochem. Biophys.*, **430**, 163–9.

72 Gellermann, W., Ermakov, I.V., McClane, R.W. and Bernstein, P.S. (2002) Raman imaging of human macular pigments. *Opt. Lett.*, **27**, 833–5.

73 Sebag, J. (2004) Seeing the invisible: the challenge of imaging vitreous. *J. Biomed. Opt.*, **9**, 38–46.

74 Sijtsema, N.M., Duindam, J.J., Puppels, G.J., Otto, C. and Greve, J. (1996) Imaging with extrinsic Raman labels. *Appl. Spectrosc.*, **50**, 545–51.

75 Krafft, C. and Sergo, V. (2006) Biomedical application of Raman and infrared spectroscopy to diagnose tissue. *Spectrosc. Int. J.*, **20**, 195–218.

4

Vibrational Spectroscopic Imaging of Hard Tissues

Michael D. Morris, Matthew V. Schulmerich, Kathryn A. Dooley, and Karen A. Esmonde-White

4.1
Infrared and Raman Spectroscopy of Bone

Chemical composition is an important contributor to bone quality, a term that encompasses the effects of architecture, composition and remodeling dynamics. An important advantage of infrared (IR) and Raman imaging in bone studies is that they allow the imaging of parameters that measure tissue quality and competence. These are usually measured as band height or band area ratios, and in some cases as band widths. Although measures of tissue properties are similar in both IR and Raman spectroscopy, the IR metrics have been validated with other techniques.

In the IR spectrum, the mineral:matrix ratio is a measure of the mineral content, and is calculated as the ratio of the integrated phosphate ν_1,ν_3 envelope (ca. 900–1200 cm^{-1}) to the collagen amide I envelope (ca. 1600–1700 cm^{-1}) [1]. This has been correlated with ash weight [2]. Similar metrics in Raman spectra use the phosphate ν_1 envelope alone [3] or the ratio of the phosphate ν_1 envelope to the amide I envelope. It should be noted that the amide envelope is sensitive to the state of collagen crosslinking [4] and, more generally, to changes in the hydrogen bonding in collagen fibrils. For example, in dentin equilibrated with alcohols or acetonitrile, the components of the amide I envelope shift to slightly different wavenumbers, and their intensities increase dramatically with the displacement of water [5]. Because of this, in our laboratory we prefer to use bands at 853 and 876 cm^{-1} as measures of collagen content [6, 7]. As such bands are predominantly due to hydroxyproline, they should be relatively insensitive to changes in the collagen secondary structure.

Crystallinity is a metric related to mineral maturity, and is a measure of mineral crystallite size, mineral maturity, and the amount of substitution into the apatitic lattice. Crystallinity increases when crystals are larger and more perfect (i.e., less substitution), and is directly proportional to the inverse width of the 002 reflection (c-axis reflection) in the powder X-ray diffraction pattern of bone mineral. Several features in the IR spectra of bone correlate with mineral crystallinity, including

the fractional area of the 1057 cm^{-1} and 1023 cm^{-1} components of the phosphate ν_1,ν_3 envelope [8]. More extensive Fourier transform-infrared (FT-IR) correlations in this same band system have been reported [9] and include the 1030 cm^{-1}:1020 cm^{-1} ratio [10]. The 1030 cm^{-1} band is a component of $PO_4^{-3}\nu_3$, while the 1020 cm^{-1} band has been attributed to HPO_4^{-2}. Similar correlations exist in components of the ν_4 (PO_4^{-3} bend) envelope [11]. All of these correlations should be usable in the Raman spectrum, provided that there are no other overlapping Raman bands. However, there has been less emphasis on crystallinity in the bone Raman literature, and only the width of the phosphate ν_1 band has been used as a measure of crystallinity.

The carbonate : phosphate ratio in the IR spectrum is calculated [10] from the area of the $CO_3^{-2}\nu_2$ components at 866 cm^{-1} (labile carbonate), 871 cm^{-1} (B-type carbonate), and 878 cm^{-1} (A-type carbonate) and the area of the $PO_4^{-3}\nu_1,\nu_3$ envelope. These correlations use earlier carbonate band assignments [12, 13].

Carbonate band assignment has been more difficult in Raman spectra because of near-overlap of the major carbonate ν_1 mode at 1070 cm^{-1} with a component of phosphate ν_3 at 1076 cm^{-1} in carbonated apatites [14]. These bands have earlier been reported as coincident [15], or have been assumed to be a single broad carbonate band [16]. Most investigators have used the ratio of the carbonate ν_1 band : phosphate ν_1 band as a measure of the carbonate : phosphate ratio. It is likely that, for a heavily carbonated mineral, this error is small, but for a lightly carbonated mineral the remeasurement or reinterpretation of some Raman spectroscopic data may be needed.

Collagen crosslinking is measured as changes in the amide I envelope [4]. The biochemical analysis of collagen model peptides showed that pyridinoline (Pyr) crosslinks resulted in a band at ca. 1660 cm^{-1} and dehydrodihydroxylysinonorleucine (de-DHLNL) crosslinks in a band at ca. 1690 cm^{-1}. It is known that the content of de-DHLNL crosslinks decreases with bone collagen maturity, while Pyr crosslink content increases [17], probably because the former matures into the latter [18]. Thus, the 1660 cm^{-1}:1690 cm^{-1} ratio is an indicator of matrix maturity. This metric was developed for IR spectroscopy, but it has also been used successfully in Raman spectroscopy [19, 20]. The same ratio has been used to indicate abnormal matrix crosslinking [21] and to infer rupture of crosslinks under mechanical load [19].

4.2
Infrared and Raman Imaging of Bone

4.2.1
Introduction

The development, aging, pathology, microstructure and compositional basis of the mechanical functioning of musculoskeletal tissue have been major application areas for vibrational spectroscopic imaging [16, 22]. For these applications, the

chemical composition and organization of bone components contribute greatly to the function of musculoskeletal tissue. Because bone is not homogeneous, a single IR or Raman spectrum offers limited information. Both IR and Raman imaging provide chemical composition information at a micron spatial scale, offering insight into the distribution of both mineral and organic matrix components. This information provides a more complete characterization of bone development, microstructure and aging because the chemical spatial variations contribute greatly to the structural integrity and ultimate biological function of bone.

As mentioned above, a common approach to spectroscopic imaging of musculoskeletal tissue is to use band height or area ratios, after background subtraction. The sources of background may include fluorescence or poly(methyl methacrylate) (PMMA) and epoxies if the specimens are fixed and embedded. Histological stains may also be a source of background, but their contribution is usually insignificant in IR imaging because the stain layer is usually thin compared to the probed thickness of the specimen. Unless very heavy staining is used, absorption by the stain does not result in thermal damage. For Raman imaging, stain fluorescence is not usually observed, because the deep red and near-infrared (NIR) excitation often lie well to the red of the absorption spectra of almost all stains. Crane and coworkers [23] have shown that the bands of hematoxylin and eosin, the most common stains, are not visible in Raman images.

In addition to the imaging parameters of band height : area ratios, there has also been a heavy reliance on the use of self-modeling curve resolution (SMCR) in Raman imaging, starting with the studies of Timlin [24] who showed that factor score images rather than Raman intensity images could be used. Even though the phenylalanine ring-breathing mode was misidentified as a HPO_4^{-2} band that is found at the same wavenumber, the ability of SMCR to extract and image spatially varying components was demonstrated.

While varimax rotation with a non-negativity constraint was used in our early investigations, we now employ band target entropy minimization (BTEM) [25] to extract Raman spectra and to generate score image contrast [26]. This technique allows the extraction of even minor components, provided that a band target – a region of the spectrum that uniquely identifies the component – can be identified either from the underlying spectra or, more commonly, from features in the first few eigenvectors of the spectra that comprise the image data set. Unlike varimax rotation, BTEM does not require extensive user intervention, and provides superior results for minor components. It should be noted that any data reduction procedure that begins with the extraction of principal components is based on the assumption that the data set consists of a small number of constituents, which contribute to the measured spectrum at any point in proportion to their composition at that point.

4.2.2
Imaging of Normal, Healthy Mineralized Tissue as a Function of Age

In this section, imaging studies performed on normal, healthy bone as a function of age are briefly reviewed, so as to provide a background to compare results from

tissue compromised by genetic modifications, external stresses or disease. Bone tissue of different ages is found in both osteonal and trabecular bone as a function of the remodeling process. Within an osteon (~200–250 μm in diameter), the youngest tissue is found at the center and the most mature at the edges. For trabecular bone, the youngest tissue is found at the edges of individual trabecula while the more mature tissue is located at the center.

In early FT-IR studies of osteonal and cortical bone [1, 10] it was shown that the mineral:matrix ratio and crystallinity increased from the center to the edge of an individual osteon [10], and from the periosteal region to the endosteal region of cortical bone [10]. A greater mineralization was found in more mature tissue, consistent with previous nonimaging studies [27–29]. For osteonal bone, a maximum in the mineral density was found ~50–60 μm from the osteon center [10] and, as with mineralization, a greater crystallinity (i.e., larger and more perfect crystals) was also found in older tissue. More recent FT-IR imaging has confirmed these results [11, 30, 31] and also allowed the examination of such compositions in greater detail [30]. The collagen crosslink ratio was also found to follow the same trends as the mineral:matrix ratio and crystallinity [32], while the carbonate: phosphate ratio and acid phosphate content were found to decrease away from the center of an osteon, with the most marked changes in acid phosphate occurring within 30 μm of the osteon [10, 11].

Similar results were found in trabecular bone, in which bone crystallinity decreased from the center to edge, indicating more mature mineral in the central, older tissue [10, 32]. Although the collagen crosslink ratio decreased from the center to the edge in newly forming trabeculae [4], this gradient was absent at older, resorbing trabecular surfaces [33]. As in osteonal tissue, the carbonate: phosphate ratio was highest in younger tissue at the edge of trabeculae, as shown in Figure 4.1 [32].

In interstitial tissue, SMCR has been used to generate images [34]. Two mineral factors were observed, one which corresponded to normal mineral and the other which contained a band at 952 cm^{-1}, which was interpreted as arising from amorphous calcium phosphate (ACP). Images of this factor showed that the ACP was located away from the edge of the osteon. The authors suggested that ACP might be found in regions susceptible to damage, or perhaps might have been the result of prior damage.

The use of polarized light to generate contrast between bone components provides information on the spatial distribution of bone components and their orientation. Kazanci *et al.* used Raman polarized imaging to examine the distribution of mineral and matrix constituents around osteons, and showed that the PO_4^{-3} ν_1 and amide I bands are highly orientation-dependent, whereas the amide III and PO_4^{-3} ν_2 and ν_4 are less orientation-dependent [35]. Orientation effects are nicely illustrated in Figure 4.2 [36]. The PO_4^{-3} ν_1:amide I ratio coincides with the orientation of the lamellae; the same lamellae have different contrasts, depending on the polarization of the excitation light and the orientation of the specimen.
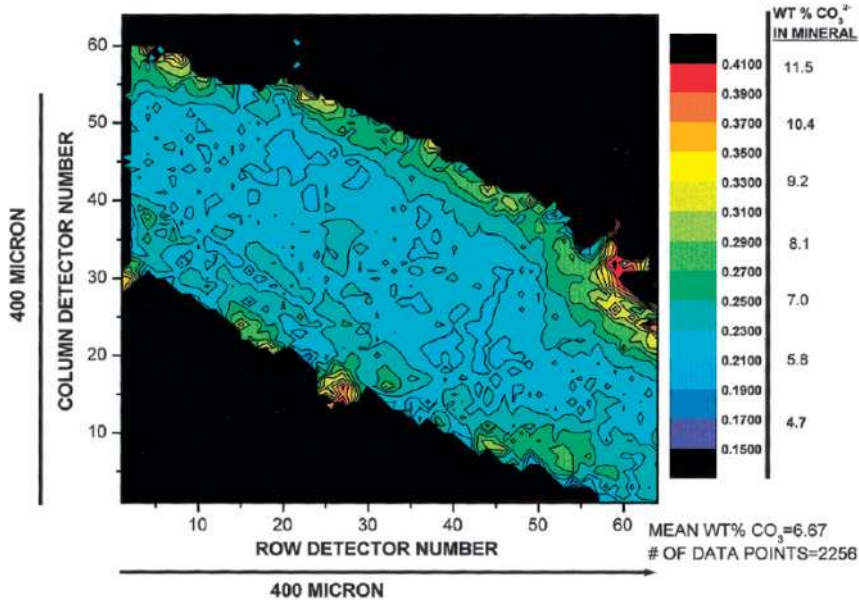
Figure 4.1 IR microscopic image of the carbonate ν_3 to phosphate ν_1 ratio in normal trabecular human iliac crest tissue. Reprinted with permission from Ref. [32].
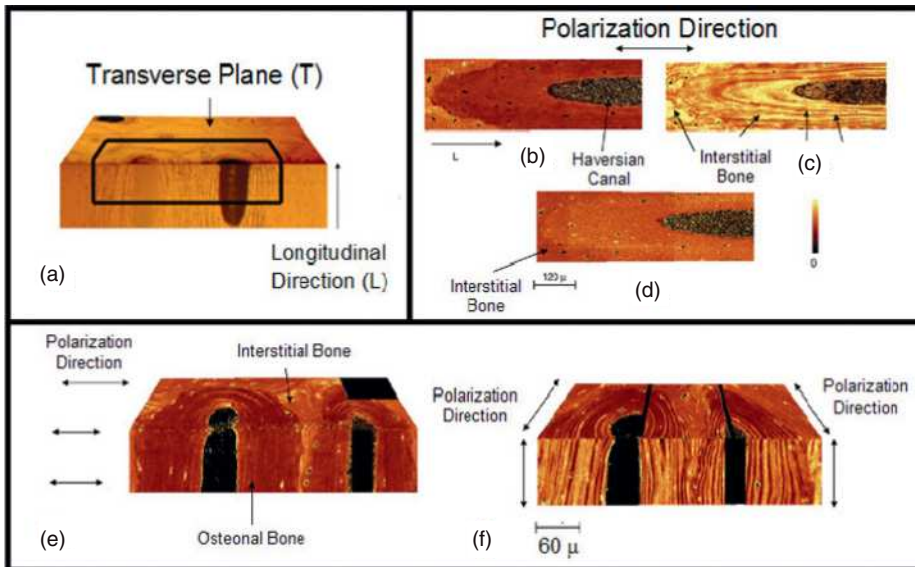

Figure 4.2 (a) Bone section under polarized light; the black line outlines where the Raman images were acquired. Polarized Raman images of (b) phosphate ν_2 : amide III; (c) phosphate ν_1 : amide I; and (d) carbonate : phosphate ν_2 band ratios at the interface between osteon and interstitial bone; (e, f) Three-dimensional view of phosphate ν_1 : amide I ratio for different polarization directions. Reprinted with permission from Ref. [36].

4.2.3
Adaptation of Bone Induced by Genetic Modifications

In bone studies, mice are often genetically modified so as to elucidate the role of a specific protein in the mineralization process. For example, Boskey *et al.* used IR imaging to compare the mineral content and crystallinity of the tibia and femur in osteopontin-deficient mice to wild-type controls at ages of 12 and 16 weeks [37]. An increase was observed in the mineral content and crystallinity of osteopontin-deficient mice in all sites, except for the periosteal bone (see Figure 4.3). Similar results were obtained for trabecular bone. The mineral differences apparent in the IR images were not observed with histological staining. The increases in mineral content and crystallinity were in agreement with the findings of other studies,
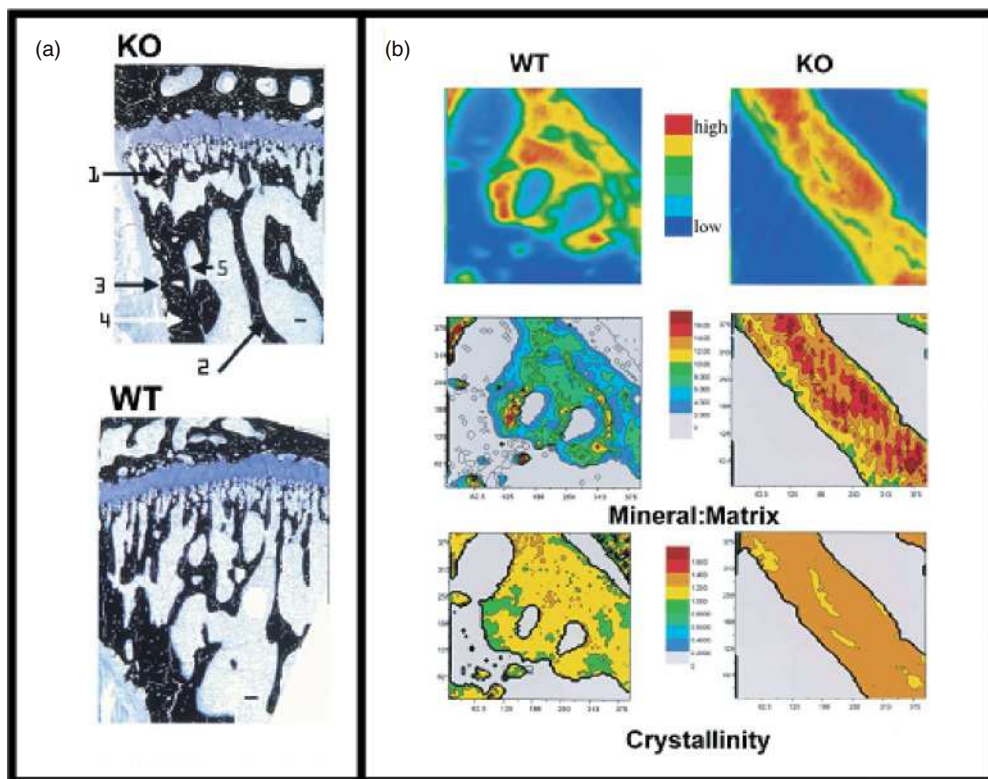
Figure 4.3 Tissue sections. (a) A 12-week-old mouse Von Kossa-stained for mineral and counterstained with toluidine blue for tissue morphology; (b) IR images of cortical bone at 16 weeks; the top panel shows the integrated area under the 900–1200 cm^{-1} phosphate envelope. The second and third panels illustrate the mineral to matrix ratios and crystallinity, respectively. Reprinted with permission from Ref. [37].

suggesting that osteopontin is an inhibitor of mineral formation and crystal growth [38–40].

Osteonectin-null mice have a lower number of osteoclasts and osteoblasts, as well as decreased bone formation and resorption [41]. Both, osteonectin-null mice and wild-type mice at 11, 17 and 36 weeks have been used for IR imaging experiments [41]. The osteonectin-null bone showed a significant increase in mineral content in newly formed periosteal bone, a decrease in mineral crystallinity for cortical bone, and an increase in collagen maturity in both cortical and trabecular bone. These data reflect the presence of both existing, older mineral that has not been reabsorbed, as well as a more mature collagen matrix that has aged without being degraded and replaced.

Additional studies utilizing IR imaging to characterize the skeletal phenotype for genetically engineered mice have examined the effect of transforming growth factor-β1 (TGF-β1) [42], dentin matrix protein-1 (dmp1) [43] and biglycan [44]. The TGF-β1-null specimens had reduced growth plates, less alkaline phosphatase activity, and reduced collagen maturity for all ages examined. No effect on mineral content or crystallinity was observed in trabecular bone, whereas in cortical bone and the secondary ossification center, the mineral content, crystallinity and collagen maturity was reduced. In another noteworthy IR imaging study, the role of dmp1 in mineralization was analyzed by comparing bone mineral and matrix properties in dmp1-null mice to those in heterozygous and wild-type controls [43]. The skeletal phenotype expressed a decreased mineral content and increased crystal size.

Morris and coworkers have investigated the early mineralization in mouse calvaria subjected to periodic loading to model craniosynostosis, a birth defect in which the calvarial sutures fuse prematurely. Here, Raman imaging was used to study the composition, relative amounts and locations of mineral and matrix components in murine fetal calvarial sections [45]; the results are summarized in Figure 4.4. The same mineral composition was found in the control and force-induced tissue. The addition of fibroblast growth factor-2 (fgf2) was found to increase the rate of mineralization, without causing any change in mineral composition [6, 46, 47], although the accelerating mineralization did result in a less-ordered mineral structure.

In a subsequent study, mineralization in cultured fetal murine calvarial sections was followed for up to 72 h [7]. Transient octacalcium phosphate (OCP) or OCP-like intermediates were observed and converted to carbonated apatite over periods of a few hours. When increased levels of OCP were found in sutures undergoing fgf2-induced accelerated mineralization, these results supported the transient precursor mineralization mechanism, which had been hypothesized but not previously observed [48, 49].

IR imaging has also been used to investigate mouse models of human disease, including Fabry disease (a lipid storage disease) [50] and skeletal disorders. Camacho *et al*. characterized bone mineralization in a mouse model of osteogenesis imperfecta (OI) after treatment with the bisphosphonate alendronate (ALN) [51]. The treatment of OI mouse models with ALN led to improved mechanical
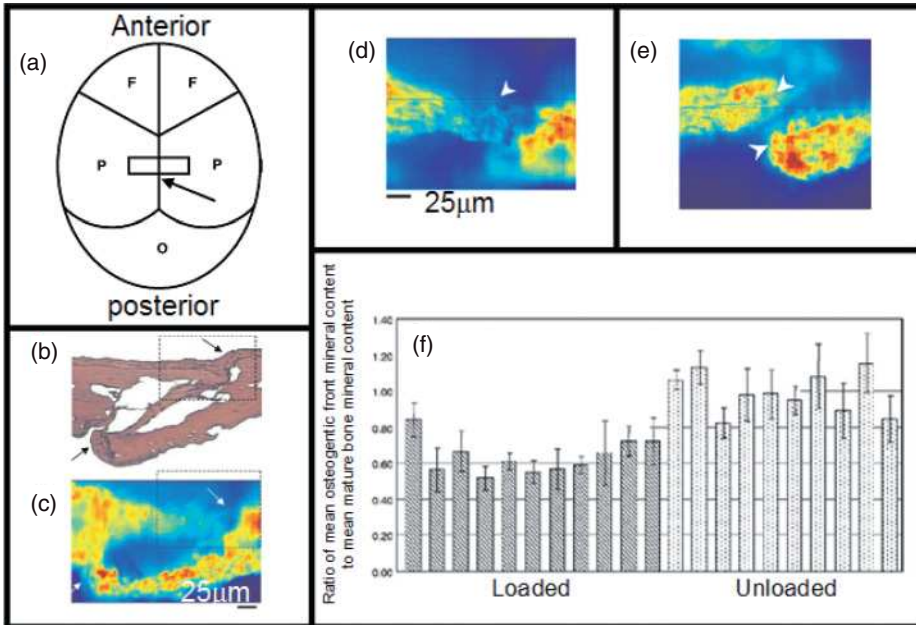
Figure 4.4 (a) Schematic of mouse calvaria; the arrow indicates the region from which the specimens were harvested; (b) H & E-stained section; the arrows indicate areas of increased collagen production and cell proliferation in the loaded specimen; (c) Mineral score image of loaded specimen; (d) Mineral score image of loaded specimen from the boxed region in panels (b) and (c); (e) Mineral score image of unloaded specimen; (f) Ratio of mean osteogenic front mineral content to mean mature bone mineral content. In the pseudo-color contrast, red indicates high mineral content and blue indicates low. Reprinted with permission from Ref. [45].

properties by increasing metaphyseal bone density and bone diameter, resulting in reduced fracture rates [52]. In this study, ALN treatment resulted in increased metaphyseal bone mineralization but was found not to improve mineral maturity. Although ALN treatment mechanically strengthens the bone, IR imaging has provided evidence that treatment neither rescues the phenotype nor normalizes the mineralization in OI mouse bone.

4.2.4
Adaptation of Bone in Response to External Stress

The first studies relating damage to bone chemistry focused on mineral changes that occurred near sites of mechanical deformation. Mineral phase transformations were observed in areas where microdamage and deformation/fracture were present [19, 53–55]. Timlin *et al.* used Raman imaging to investigate the relationship between bone mineral composition and microdamage in bovine bone [55]. Where no visible microdamage was present, only one 'normal' mineral factor with

a phosphate band at 959 cm^{-1} was found. In areas of visible microcracks, two mineral factors were observed, one representing 'normal' hydroxyapatite mineral and the other containing a high-frequency phosphate band at 963 cm^{-1} that is characteristic of stoichiometric (i.e., less-carbonated) hydroxyapatite. Images of each factor showed differences in their distribution at the crack tip. In regions of diffuse damage, a 'normal' mineral factor was found, in addition to one factor that contained a phosphate band at 961 cm^{-1}, a frequency which was slightly higher than for normal bone but not as high as for bone regions near a visible micro-crack. The score image of this factor showed not only a random distribution but also that diffuse damage was associated with smaller chemical changes than microcracking.

The results of subsequent studies confirmed that the abnormal mineral present in microdamaged bone was, in fact, a result of the damage and not a cause of it [19, 53]. Morris *et al.* used Raman imaging to investigate the effect of macroscopic fracture using femora from young and aged mice [53]. In undamaged four-month-old control tissue, only one 'normal' mineral factor was observed. However, after fracture the factor analysis identified two mineral factors: one similar to that observed prior to fracture, and another that contained a high-frequency phosphate band at 965 cm^{-1} but no carbonate band (typical of stoichiometric, uncarbonated apatite). These results were similar to those seen in the microdamage study, and consistent with phase transformation, a process that occurs in other crystalline materials such as ceramics as a means of adapting to an applied mechanical load. The score images showed a significant overlap between the two factors. However, in an 18-month-old mouse, only one 'normal' mineral factor was observed after fracture, either because aging might prevent mineral phase transformations, or because the damage did not propagate far enough to be observed.

In mechanically indented bovine bone, Raman imaging showed the presence of additional mineral species in the indented areas where compression had occurred, but not at the edge of the indent or in control areas [19]. The additional mineral factor was consistent with earlier results; however, the factor in the nanoindenta-tion studies usually contained a lower-frequency phosphate component rather than the higher-frequency component found in the fracture study. The addition of either a higher- or lower-frequency component is consistent with high-pressure studies on calcium hydroxyapatite, where the frequency of the phosphate v_1 band initially increases and then decreases with greater pressure [19]. Importantly, in both the indent and control areas, only one matrix factor was found. A second matrix factor was found at the edge of the indent where the shear forces were great. The spectral features of this factor were characteristic of the absence of mature Pyr crosslinks [4], and interpreted as a rupture of these crosslinks. No collagen damage was observed spectroscopically in the center of indents, and this was consistent with the known weakness of bone in shear mode, relative to compression.

Other studies have produced apparently conflicting results on the relationship between local composition and microcrack formation [56, 57]. In 2005, Akkus and coworkers used Raman microspectroscopy and human male femurs to examine

mineralization in the vicinity of microdamage. Mineralization was evaluated by calculating the intensity ratio of the phosphate v_1 band to the CH_2-scissoring band (~1450 cm^{-1}). Raman maps of this mineral:matrix ratio showed that the mineralization close to microcracks was greater than elsewhere, and that the mineralization was uniform in regions of microcracks and did not vary with distance from the crack. Statistical analysis showed that the average mineralization of areas near microcracks was consistently and significantly greater than the overall mineralization, suggesting that the formation of some microcracks may be composition-dependent.

However, with synchrotron IR imaging of canine vertebrae, no difference was observed in the mineralization ($v_4 PO_4^{-3}$ ~500–650 cm^{-1}):(amide II ~1510–1595 cm^{-1}) or crystallinity parameters between undamaged and microdamaged bone, showing that microdamaged areas were not overmineralized [57]. In addition, the carbonate:phosphate and carbonate:matrix ratios were significantly lower in the regions of microdamage, consistent with the results of previous studies where an additional phosphate band was attributed to a more stoichiometric, less-carbonated apatite species. The collagen crosslink ratio decreased in the vicinity of microdamage, as a result of broken crosslinks, and the acid phosphate content had also increased. As can be seen from Figure 4.5, all differences in composition had well-defined boundaries in the presence of microcracks, suggesting that these differences were an effect of microcrack formation. However, it is unclear whether the discrepancies between these studies reflect differences in the tissue, or in the methodology used by the research groups.

Pezzotti and coworkers monitored the spectral shift of Raman bands with mechanical loading to examine the *in situ* response of femoral and cortical bone to external stress [58, 59]. It has been proposed that collagen operates by a
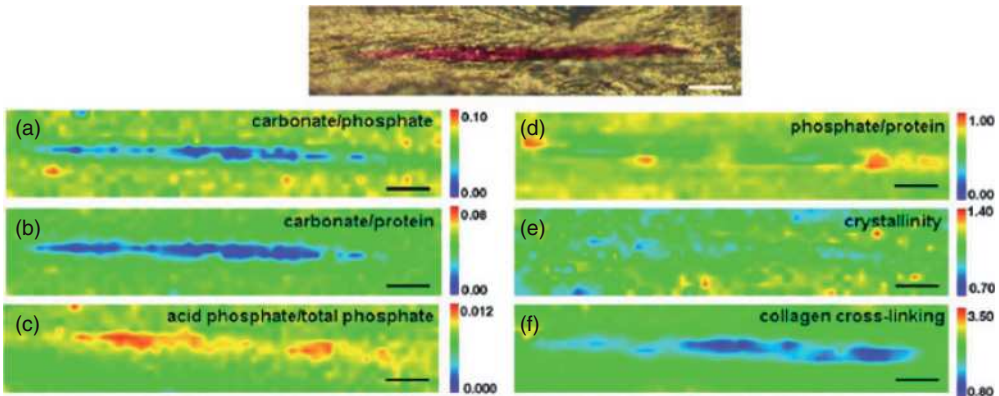
Figure 4.5 Top panel: Visible image of fuchsin-stained microcrack. Data were collected within the crack and surrounding area. (a–f) IR images of the same area illustrating: (a) the carbonate:phosphate ratio; (b) the carbonate:protein ratio; (c) the acid phosphate:total phosphate ratio; (d) the phosphate:protein ratio; (e) crystallinity; (f) collagen crosslinking. Scale bar = 25 μm. Reprinted with permission from Ref. [57].
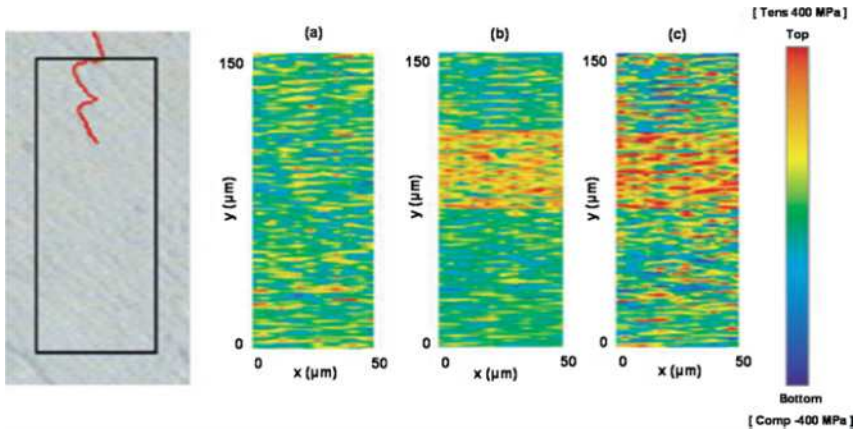
Figure 4.6 An optical micrograph and stress maps in bovine femoral bone near a fracture. The map in (a) was acquired at zero applied stress; and in (b) at critical stress for crack propagation. The net stress field was obtained by subtracting (a) from (b), as shown in (c). Reprinted with permission from Ref. [59].

crack-bridging mechanism during fracture initiation and propagation [60]. Tensile microstresses were quantitatively assessed for the first time by constructing microscopic stress maps from shifts of the phosphate ν_1 band. Figure 4.6 shows the stress maps in bovine femoral bone near a fracture. An area of high stress exists ahead of the crack tip, and subsequent micrographs showed that micro-cracks were present in this area of high stress [58]. Consistent with the crack-bridging mechanism, the stress field contained areas of stress relaxation and stress intensification, seen as the striped pattern in the maps.

A follow-up study highlighted the relationship between the composition and the redistribution of stress [58]. Cortical bone was loaded with external compression and tension, and the stress stored within the apatite crystals was assessed via the shift in phosphate ν_1 band in two regions: a collagen-rich area and an apatite-rich area. In the collagen-rich areas, stress was released under external tension, but localized stress intensification occurred under external compression (see Figure 4.7a). In apatite-rich areas, both tensile and compressive stresses were observed (see Figure 4.7b). Tensile stresses were intensified even under weak external compression, and a crisscross-like pattern was observed, suggesting a particular organization of the collagen fibrils.

4.2.5
Adaptation of Bone in Response to Osteoporosis

In an early FT-IR imaging study, compositional differences between iliac crest biopsies from untreated osteoporotic patients and normal controls were examined
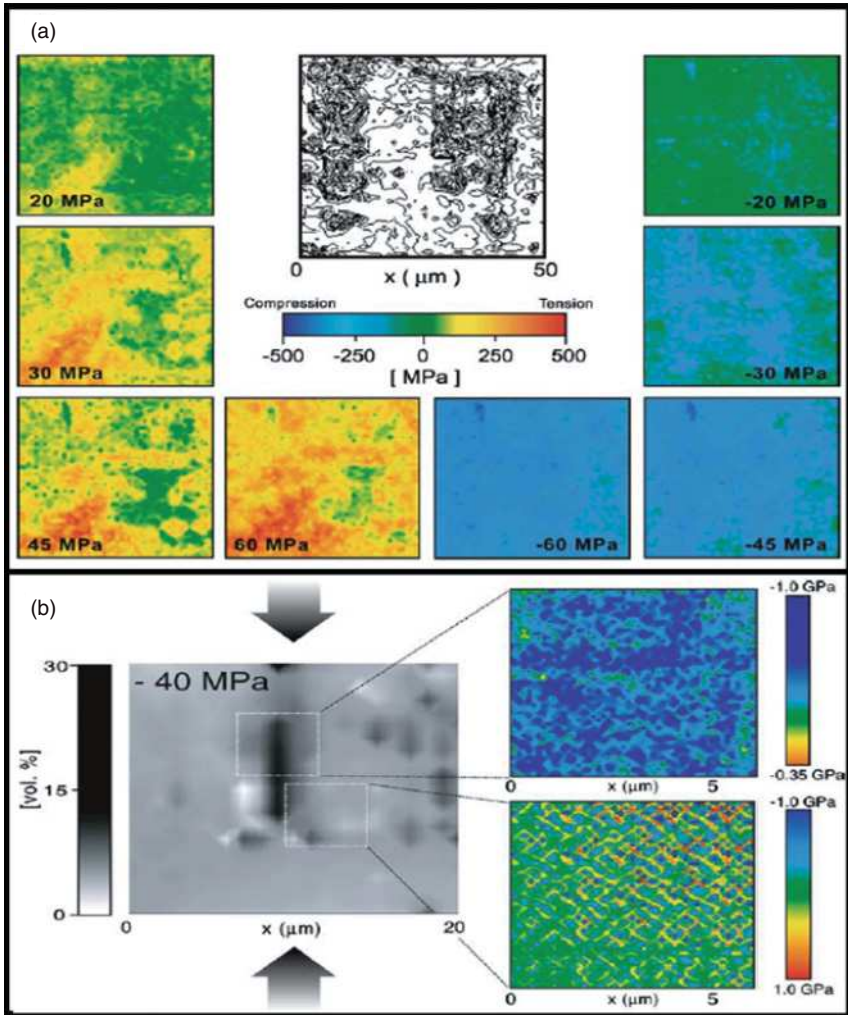
Figure 4.7 (a) The isovolumetric collagen fraction in bovine cortical bone is shown in the center, and maps of stress stored in the apatite crystals within this area are shown at the side. The values on each individual stress map indicate the remote uniaxial stress field applied to the specimen; (b) A map of the collagen volume fraction in cortical bone is shown on the left. Microscopic stress maps are shown on the right, including a map of an apatite-rich region (lower right). Reprinted with permission from Ref. [58].

[61]. No significant differences were found between osteoporotic and normal specimens in the mineral : matrix ratios of either cortical or osteonal bone. However, in younger osteonal and cortical tissue (defined as being within 20 μm of osteon center and 200 μm of periosteum, respectively), the crystallinity was significantly higher in osteoporotic bone, indicating that the mineral was more mature. Simi-

larly, the collagen crosslinks were shown to be more mature in osteonal, cortical and trabecular bone from untreated osteoporotic specimens [62].

More detailed FT-IR imaging of specimens from human iliac crest biopsies showed that mineralization in untreated osteoporotic trabecular bone samples was decreased by ~40% from the normal, and the mineral:matrix ratio was lower in the center of trabeculae (more mature tissue) than for controls [63]. The crystallinity ratio was also increased in osteoporotic specimens. Differences between the trabecular bone matrix of osteoporotic and normal bone have also emerged [64]. The spatial variation of crosslinks at bone-forming trabecular surfaces (within 50 μm) in patients with osteoporotic or multiple spontaneous fractures was significantly different from that in normal bone, and the collagen crosslink ratio was higher. It has been hypothesized that the matrix produced in osteoporosis might mature more quickly or undergo post-translational modifications for a longer time than normal bone matrix.

Ovariectomized (ovx) cynomolgus monkeys represent a common model for postmenopausal osteoporosis because they experience regular menstrual cycles, hormonal fluctuations and bone loss upon ovariectomy. Both, ovx monkeys and postmenopausal osteoporotic women showed similar modifications in trabecular mineral properties [65], specifically a decreased mineral:matrix ratio, increased crystallinity and increased carbonate content relative to controls. In addition, the spatial variation in the mineral:matrix ratio was the same in humans and monkeys.

In contrast to trabecular bone, in the cortical bone of ovx monkeys the mineral content was significantly increased in endosteal regions, while the crystallinity and collagen crosslink ratio remained constant in both periosteal and endosteal tissue [66]. Because these parameters displayed different trends in cortical and trabecular bone, the compositional adaptations may be site-specific.

Imaging can also be used to examine the effects of therapy. Several treatments for osteoporosis exist, and can be grouped as having either antiresorptive or anabolic effects. *Antiresorptive agents* suppress osteoclast activity, whereas *anabolic agents* increase bone formation. In general, imaging studies carried out using the antiresorptives of estrogen [64, 67], hormonal replacement therapy [68] and bisphosphonate [69] demonstrate an increased mineral:matrix ratio, crystallinity and collagen crosslink ratio, consistent with the suppression of osteoclast activity and the prevalence of more mature bone. One bisphosphonate study examined the effects of three- and five-year risedronate treatment on trabecular bone [70]. As can be seen from the images in Figure 4.8, patients receiving placebo for three years showed a significant increase in crystallinity and collagen crosslink ratio when compared to baseline values, which was consistent with previously discussed imaging studies on untreated osteoporotic trabecular bone [63]. Those patients who received risedronate for three or five years retained baseline values for both the crystallinity and crosslink ratio. These risedronate treatment results were in conflict with the increased crystallinity and crosslink ratio reported for the aforementioned antiresorptive treatments. In order to explore this discrepancy, a more spatially detailed analysis was performed within the first 50 μm of trabecular surfaces, at both
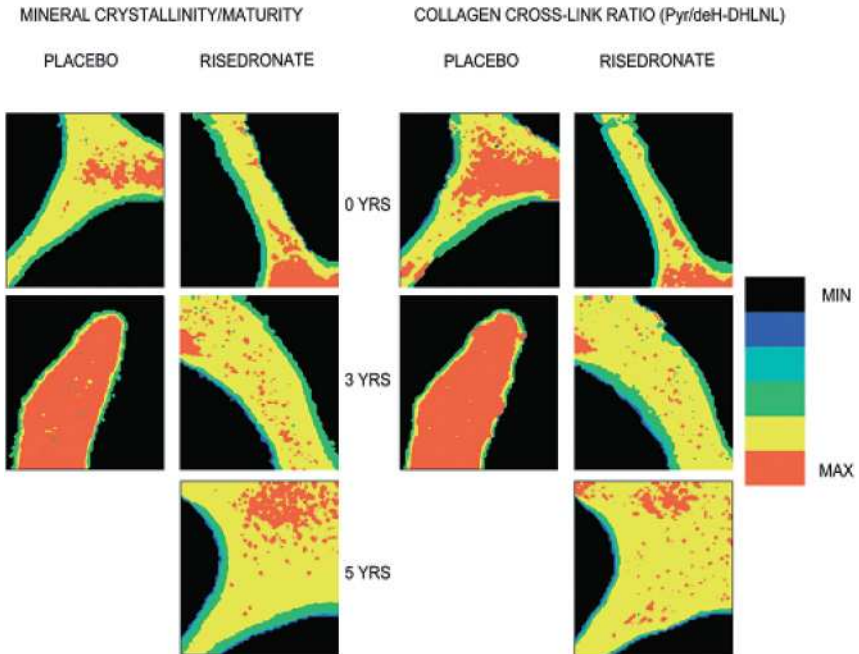
Figure 4.8 FT-IR images of trabecular bone from a placebo- and a risedronate-treated patient at baseline, and after three and five years of treatment. In placebo-treated patients, both mineral crystallinity and collagen crosslink ratio were significantly higher at three years compared to baseline. In risedronate-treated subjects, no significant differences in either parameter were found after three or five years. Reprinted with permission from Ref. [70].

formation and resorption sites. The bone-resorbing surfaces showed no significant changes in crystallinity or crosslink ratio as a function of either depth from the surface or risedronate treatment. However, at the bone-forming surfaces, risedronate treatment significantly lowered the crystallinity and crosslink ratio as a function of treatment duration. Even though risedronate is an antiresorptive agent, it was shown to have beneficial effects on bone-forming areas [70].

The anabolic agents parathyroid hormone (PTH) [66, 71] and nandrolone decanoate (ND) [72, 73] have both been shown to stimulate bone formation. PTH caused bone to exhibit compositional characteristics typically associated with younger bone, including a lower mineral:matrix ratio, crystallinity and crosslink ratio. In contrast, ND treatment restored those parameters affected by ovariectomy to the level of sham controls in cortical bone, but not in trabecular bone.

4.3
Infrared and Raman Spectroscopy of Cartilage

Cartilage tissue plays a significant role in the musculoskeletal system because of its proximity to bone, and its roles in long bone formation and in diseases such

as osteoarthritis. Three main types of cartilage have been identified, namely hyaline, elastic and fibrocartilage. Hyaline cartilage has been the focus of most vibrational spectroscopy studies because it is the type of cartilage that covers the ends of bones at joints (as articular cartilage), and also comprises the epiphyseal plates where the bones grow [74]. Articular cartilage is an avascular tissue located at the intersection of two bones, within the synovial joint. A thin layer of cartilage is attached to the joint surface of the patella, femur and tibia, and the cavity between and around the joint is filled with synovial fluid [75]. The primary function of articular cartilage is to minimize friction between bones during movement of the joints and to provide resistance to compression.

Cartilage contains mostly chondrocytes, proteoglycans and type II collagen; water is also a major component of cartilage, comprising 60–80% of its total weight. The most abundant proteoglycan in cartilage is aggrecan. Typically, proteoglycans consist of a hyaluronic acid (HA) backbone with core protein side chains that attach to sulfated glycosaminoglycans (GAGs), chondroitin sulfate and keratin sulfate. At physiological pH, the GAGs are negatively charged and highly hydrated.

Both the collagen fiber orientation and the overall composition of articular cartilage are heterogeneous in the axial direction, and thus contribute to the distinction of three zones of articular cartilage:

- The superficial zone contains the highest density of chondrocytes, with the type II collagen fibers being oriented parallel to the joint surface.

- In the tangential zone (or mid zone), the collagen fibers are not oriented preferentially.

- In the deep zone, type II collagen is ubiquitous and is oriented perpendicular to the cartilage surface. Although articular cartilage is unmineralized in its surface layers it contains a layer of calcified tissue adjacent to the subchondral bone.

In recent years many vibrational spectroscopic studies of macromolecular components of cartilage have been conducted, with GAG, sodium hyaluronate, chondroitin 6-sulfate and chondroitin 4-sulfate contents having been examined using both IR and Raman spectroscopy [76–81]. Both HA and chondroitin sulfate have been studied using FT-IR [82–85], while the dichroic properties of HA functional groups have been investigated using polarized IR spectroscopy [79, 80, 86]. Enzymatically digested HA was also examined using nuclear magnetic resonance (NMR), IR, Raman and visible spectroscopies [87]. Whilst the vibrational spectroscopic examination of type I collagen has been more extensive than that of type II collagen [88–93], the same methods can be used to examine type II collagen structures in tissue, to identify pathological tissues and to monitor fiber tension [94–101].

Studies such as those listed above provide a framework for assessing the pathological changes in cartilage tissue. For example, an IR examination of proteoglycans and GAGs present in a patient with Langer–Saldino achondrogenesis not only revealed a low sulfation of proteoglycan but also that levels of chondroitin 4-sulfate were decreased relative to those of chondroitin 6-sulfate [102].

4.4
Infrared and Raman Imaging of Cartilage

4.4.1
Unmineralized Cartilage Tissue

The imaging of type II collagen and proteoglycan in cartilage sections using FT-IR microscopy was first reported by Potter *et al.* [103]. For these studies, FT-IR images of normal bovine nasal cartilage, trypsin-treated bovine nasal cartilage and cartilage engineered in a hollow-fiber bioreactor (HFBR) were assayed for their sulfated GAG content. The pure-component spectra were found not to describe adequately the cartilage matrix because interactions between the cartilage matrix molecules had influenced the tissue spectra. The FT-IR images showed a spatial heterogeneity in the chondroitin sulfate distribution and also confirmed the loss of chondroitin sulfate in trypsin-digested cartilage. Images of engineered cartilage showed the penetration of type II collagen into the HFBR.

Camacho subsequently reported FT-IR microscopy and imaging on dehydrated bovine articular cartilage using polarized and unpolarized light [52]. The data of the FT-IR images were in agreement with histological data with regards to the distribution of type II collagen and aggrecan, which in turn validated FT-IR as a feasible method for identifying cartilage components and determining collagen fiber orientation, despite the great similarity between the spectra of type I and type II collagens and of many GAGs. Spectral markers for collagen orientation, proteoglycan content and type II collagen content were also reported, with differences in the proteoglycan and type II collagen content in each of the three layers of cartilage being reflected in their relative intensity variations. Polarized images highlighted the varying collagen orientation in each layer. The average fiber orientation, as observed by changes in the band area ratio of collagen's amide I:amide II envelopes, showed that the collagen orientation was more parallel to the adjacent bone surface in zones closer to the bone.

Another study in which orientation effects were examined used polarized FT-IR imaging to quantify collagen orientation in equine and human articular cartilage [104]. The FT-IR images quantified collagen orientation in each cartilage zone, from the area ratio of amide I : amide II. Importantly, the FT-IR images showed differences in collagen orientation that were not observed with polarized light microscopy; consequently, the authors suggested that these subtle changes in collagen orientation may either precede or accompany the early stages of osteoarthritis. Polarized FT-IR has also been used to generate anisotropy images to monitor the composition and orientation of type II collagen and proteoglycans in canine articular cartilage [105, 106].

The validity of using vibrational spectroscopy and imaging to assess damaged cartilage and early-stage osteoarthritis has been demonstrated [107]. A fiber-optic probe coupled to an attenuated total reflectance crystal in contact with articular cartilage was used to collect FT-IR spectra. Spectroscopically measured damage then correlated with Collins visual grading of cartilage damage. A further valida-

tion was carried out using cartilage exposure to high levels of the enzyme collagenase, which breaks down type II collagen (high levels of the enzyme in synovial fluid indicate cartilage damage) [108]. A review of FT-IR imaging and spectroscopy of cartilage reinforces the feasibility of this method for assessing collagen orientation and proteoglycan content in both normal and pathological cartilage [109].

The FT-IR imaging of chondroitin sulfate and type II collagen content in arthritic focal lesions was reported by David-Vaudey *et al.* [110]. Here, the FT-IR images were collected in the superficial, intermediate and deep cartilage zones from knee and hip cartilage sections from human patients exhibiting severe osteoarthritis. The distribution of chondroitin sulfate was calculated using the partial least squares and Euclidean distance method, as introduced by Potter *et al.* [103]. The FT-IR images revealed a heterogeneous chondroitin sulfate distribution, not only between cartilage zones but also within the territorial and inter-territorial matrices. The images also showed a significant decrease in superficial layer chondroitin sulfate content for severely osteoarthritic cartilage, and a variability in tangential zone collagen content. These FT-IR results correlated well with the Mankin scoring.

Crombie *et al.* employed a combination of histology, FT-IR imaging and immunofluorescence to determine if monoclonal antibodies (mAbs) to type II collagen penetrated into cartilage and were arthritogenic in nature [111]. The study results showed that the penetration of mAbs into cartilage tissue was associated with a loss of proteoglycan content and the denaturation of type II collagen, consistent with a collagenase-induced model of cartilage degradation. Figure 4.9 shows the loss of proteoglycan content, as measured by FT-IR images and toluidine blue staining. FT-IR spectra also highlighted collagen degradation associated with mAb penetration into cartilage, as indicated by a shift in the amide I band from $1666\,cm^{-1}$ in control mAb samples to $\sim 1639–1655\,cm^{-1}$ in arthritogenic mAb samples.

4.4.2
Mineralized Cartilage and Subchondral Bone

The role of subchondral bone has been examined in current models of osteoarthritis, on the basis that a common indication of osteoarthritis is a thickening of the subchondral bone plate. Both, radiography and imaging studies have shown alterations in bone architecture and chemistry, in addition to plate thickening [112–115]. However, it remains unclear if subchondral bone damage occurs before cartilage damage, or if bone tissue is altered to compensate for the cartilage damage. The pathological mineralization of subchondral bone, cartilage matrix vesicles and cartilage has been examined using Raman and synchrotron IR spectroscopy. The IR microscopy of subchondral bone was first reported in 1998 by Miller *et al.* [116], while the effects of age and defective type II collagen formation on murine subchondral bone were described by Dehring *et al.* [117]. In the latter study, subchondral bone specimens from normal mice and Del 1 (+/−) transgenic mice (a mouse model of early-onset osteoarthritis) were examined using Raman
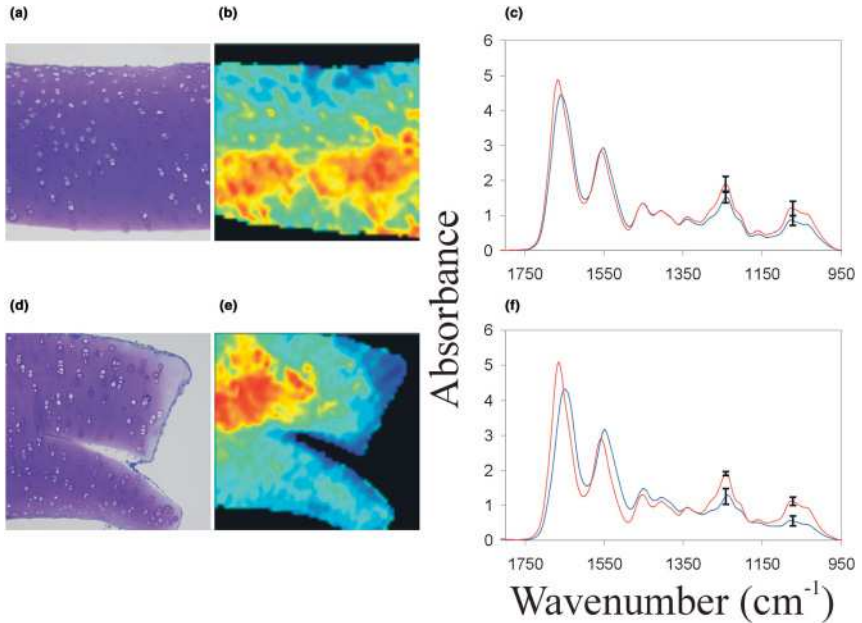
Figure 4.9 Effects of two arthritogenic monoclonal antibodies on cultured cartilage imaged by toluidine blue staining (a, d) and FT-IR of the proteoglycan spectral region 960–1175 cm^{-1} (b, e); High proteoglycan content regions in (b) and (e) are red, whereas low proteoglycan content is blue. A shift in the amide I envelope position showed denaturation of type II collagen (c, f) in spectra (c, f) taken from surfaces where arthritogenic mAbs had penetrated cartilage (blue spectra) compared to unaffected areas (red spectra). Reprinted with open access permissions from Ref. [111].

spectroscopy. While the results of these studies have been encouraging, no extensions to imaging have yet appeared.

4.4.3
Applications in Tissue Engineering

The early spectroscopic studies of cartilage allowed the establishment of methods for obtaining spectra, for identifying spectroscopic markers of tissue damage, and for developing software models of spectroscopic data. Moreover, these spectroscopic methods may be applied towards engineered bone and cartilage. Although, Boskey and Camacho have reviewed FT-IR imaging and microspectroscopic methods for the analysis of bone and cartilage [118], all of the studies reported to date for the examination of tissue-engineered cartilage have employed FT-IR.

When Camacho *et al.* studied genetically modified bovine chondrocytes using FT-IR imaging [52], they used previously identified markers for collagen orientation and proteoglycan content in cartilage. In this way, it was possible to examine the integration of engineered cartilage-like tissue into defect sites, and also to

evaluate the organization of the native cartilage. The images showed an increased proteoglycan production and a decrease in type II collagen, and also allowed a distinction to be made between the neo-tissue and host tissue. Surprisingly, the results showed an incomplete integration of neo-tissue, though the surrounding tissues in neo-tissue integration were not shown conclusively to play an active role. Based on these images, the authors suggested that cell-based repairs could not be achieved by simply placing an engineered tissue on top of a defective tissue.

FT-IR images to monitor quantitatively the proteoglycan content of nasal cartilage grown in a HFBR were reported by Potter *et al.* [103]. These authors showed that immature cartilage had developed after a three-week incubation period, and type II collagen was found to be present in the HFBR. A lower chondroitin sulfate content was found in bioengineered cartilage compared to native cartilage. Another study in which the growth of articular cartilage was monitored in a HFBR showed a significant increase in proteoglycan content at the center area and surface area of inflow tissue [119]. However, the estimated proteoglycan content did not correlate well with the biochemical assays of sulfated GAGs, due mainly to the small number of samples.

Cartilage spectroscopy and imaging present important challenges. The lack of an adequate *in vitro* model complicates proteoglycan quantification and the accurate interpretation of changes in the amide I envelope. In lieu of developing an *in vitro* model of cartilage using macromolecules, David-Vaudey has suggested the use of normal, nonarthritic cartilage as a suitable pure component spectrum [110]. The development of a model for the entire cartilage spectrum, without the use of pure-component spectra, holds much promise because it does not require user intervention. In addition, the incorporation of many (15+) factors into a least-squares model may be necessary to describe the interactions between collagen and proteoglycan molecules. Moreover, the incorporation of a parsimony measure to reduce noise contributions in model development may provide a better classification of osteoarthritic-related damage.

4.5
Conclusions

During recent years, vibrational spectroscopic imaging has matured into an important tool for the study of musculoskeletal tissues. Both IR and Raman spectroscopies contain signatures for the stages of development, for tissue disease and damage, and even for mechanical properties. Because the tissues are ordered, and their composition varies with their anatomic site, imaging has become an essential component of spectroscopic analysis. The application to bone has been especially fruitful because important details of the mineral composition and function are easily characterized when using IR and Raman spectroscopies, although these are difficult to obtain by other methods. The instrumentation for both FT-IR and Raman imaging will continue to evolve towards smaller, easier-to-use and faster systems. These advances will encourage an even more widespread use of

spectroscopy and spectroscopic imaging among basic research groups and clinicians in this important area of biomedical science.

References

1 Paschalis, E.P., Betts, F., DiCarlo, E., Mendelsohn, R. and Boskey, A.L. (1997) *Calcif. Tissue Int.*, **61**, 480.

2 Pienkowski, D., Doers, T.M., Monier-Faugere, M.-C., Geng, Z., Camacho, N.P., Boskey, A.L. and Malluche, H.H. (1997) *J. Bone Miner. Res.*, **12**, 1936.

3 Tarnowski, C.P., Ignelzi, M.A., Jr and Morris, M.D. (2002) *J. Bone Miner. Res.*, **17**, 1118.

4 Paschalis, E.P., Verdelis, K., Doty, S.B., Boskey, A.L., Mendelsohn, R. and Yamauchi, M. (2001) *J. Bone Miner. Res.*, **16**, 1821.

5 Nalla, R.K., Balooch, M., Ager, J.W., III, Kruzic, J.J., Kinney, J.H. and Ritchie, R.O. (2005) *Acta Biomater.*, **1**, 31.

6 Crane, N.J., Morris, M.D., Ignelzi, M.A., Jr and Yu, G.G. (2005) *J. Biomed. Opt.*, **10**, 031119.

7 Crane, N.J., Popescu, V., Morris, M.D., Steenhuis, P. and Ignelzi, M.A., Jr (2006) *Bone*, **39**, 434.

8 Pleshko, N., Boskey, A. and Mendelsohn, R. (1991) *Biophys. J.*, **80**, 786.

9 Gadaleta, S.J., Paschalis, E.P., Betts, F., Mendelsohn, R. and Boskey, A.L. (1996) *Calcif. Tissue Int.*, **58**, 9.

10 Paschalis, E.P., DiCarlo, E., Betts, F., Sherman, P., Mendelsohn, R. and Boskey, A.L. (1996) *Calcif. Tissue Int.*, **59**, 480.

11 Miller, L.M., Vairavamurthy, V., Chance, M.R., Mendelsohn, R., Paschalis, E.P., Betts, F. and Boskey, A.L. (2001) *Biochim. Biophys. Acta – Gen. Subj.*, **1527**, 11.

12 Rey, C., Renugopalakrishnan, V., Collins, B. and Glimcher, M.J. (1991) *Calcif. Tissue Int.*, **49**, 251.

13 El Feki, H., Rey, C. and Vignoles, M. (1991) *Calcif. Tissue Int.*, **49**, 269.

14 Awonusi, A., Morris, M. and Tecklenburg, M. (2007) *Calcif. Tissue Int.*, **81**, 46.

15 Penel, G., Leroy, G., Rey, C. and Bres, E. (1998) *Calcif. Tissue Int.*, **63**, 475.

16 Carden, A. and Morris, M.D. (2000) *J. Biomed. Opt.*, **5**, 259.

17 Otsubo, K., Katz, E.P., Mechanic, G.L. and Yamauchi, M. (1992) *Biochemistry*, **31**, 396.

18 Eyre, D.R., Paz, M.A. and Gallop, P.M. (1984) *Annu. Rev. Biochem.*, **53**, 717.

19 Carden, A., Rajachar, R.M., Morris, M.D. and Kohn, D.H. (2003) *Calcif. Tissue Int.*, **72**, 166.

20 Morris, M.D. and Finney, W.F. (2004) *Spectroscopy*, **18**, 155.

21 Blank, R.D., Baldini, T.H., Kaufman, M., Bailey, S., Gupta, R., Yershov, Y., Boskey, A.L., Coppersmith, S.N., Demant, P. and Paschalis, E.P. (2003) *Connect. Tissue Res.*, **44**, 134.

22 Boskey, A.L. and Mendelsohn, R. (2005) *Vib. Spectrosc.*, **38**, 107.

23 Crane, N.J., Gomez, L.E., Ignelzi, M.A., Jr and Morris, M.D. (2004) *Calcif. Tissue Int.*, **74**, 86.

24 Timlin, J.C., Carden, A., Morris, M.D., Bonadio, J.F., Hoffler, C.E., II, Kozloff, K.M. and Goldstein, S.A. (1999) *J. Biomed. Opt.*, **4**, 28.

25 Wee, C., Widjaja, E. and Garland, M. (2002) *Organometallics*, **21**, 1982.

26 Widjaja, E., Crane, N., Chen, T., Morris, M.D., Ignelzi, M.A., Jr and McCreadie, B. (2003) *Appl. Spectrosc.*, **57**, 1353.

27 Parfitt, A.M. (1976) *Metabolism*, **25**, 809.

28 Grynpas, M.D. and Holmyard, D. (1988) *Scanning Microsc.*, **2**, 1045.

29 Lukoschek, M., Schaffler, M.B., Burr, D.B., Boyd, R.D. and Radin, E.L. (1988) *J. Orthopaed. Res.*, **6**, 475.

30 Mendelsohn, R., Paschalis, E. and Boskey, A.L. (1999) *J. Biomed. Opt.*, **4**, 14.

31 Ou-Yang, H., Paschalis, E.P., Boskey, A.L. and Mendelsohn, R. (2002) *Appl. Spectrosc.*, **56**, 419.

32 Ou-Yang, H., Paschalis, E.P., Mayo, W.E., Boskey, A.L. and Mendelsohn, R. (2001) *J. Bone Miner. Res.*, **16**, 893.

33 Paschalis, E.P., Recker, R., DiCarlo, E., Doty, S.B., Atti, E. and Boskey, A.L. (2003) *J. Bone Miner. Res.*, **18**, 1942.

34 Carden, A., Timlin, J.A., Edwards, C.M., Morris, M.D., Hoffler, C.E., Kozloff, K. and Goldstein, S.A. (1999) *Biomedical Applications of Raman Spectroscopy*, Vol. 3608, 1st edn, SPIE, San Jose, CA, USA, p. 132.

35 Kazanci, M., Roschger, P., Paschalis, E.P., Klaushofer, K. and Fratzl, P. (2006) *J. Struct. Biol.*, **156**, 489.

36 Kazanci, M., Wagner, H.D., Manjubala, N.I., Gupta, H.S., Paschalis, E., Roschger, P. and Fratzl, P. (2007) *Bone*, **41**, 456.

37 Boskey, A.L., Spevak, L., Paschalis, E.P., Doty, S. and McKee, M.D. (2002) *Calcif. Tissue Int.*, **71**, 145.

38 Boskey, A.L., Maresca, M., Ullrich, W., Doty, S.B., Butler, W.T. and Prince, C.W. (1993) *Bone Miner.*, **22**, 147.

39 Hunter, G.K., Kyle, C.L. and Goldberg, H.A. (1994) *Biochem. J.*, **300**, 723.

40 Hunter, G.K., Hauschka, P.V., Poole, A.R., Rosenberg, L.C. and Goldberg, H.A. (1996) *Biochem. J.*, **317**, 59.

41 Boskey, A.L., Moore, D.J., Amling, M., Canalis, E. and Delany, A.M. (2003) *J. Bone Miner. Res.*, **18**, 1005.

42 Atti, E., Gomez, S., Wahl, S.M., Mendelsohn, R., Paschalis, E. and Boskey, A.L. (2002) *Bone*, **31**, 675.

43 Chrit, L., Hadjur, C., Morel, S., Sockalingum, G., Lebourdon, G., Leroy, F. and Manfait, M. (2005) *J. Biomed. Opt.*, **10**, 044007.

44 Boskey, A.L., Young, M.F., Kilts, T. and Verdelis, K. (2005) *Cells Tissues Organs*, **181**, 144.

45 Tarnowski, C.P. and Ignelzi, M.A., Jr, Wang, W., Taboas, J.M. Goldstein, S.A. and Morris, M.D. (2004) *J. Bone Miner. Res.*, **19**, 64.

46 Crane, N.J., Wang, W., Ignelzi, M.A. and Morris, M.D. (2003) *Proc. SPIE*, **4959**, 111.

47 Crane, N.J., Yu, G.G., Ignelzi, M.A., Jr and Morris, M.D. (2004) *Proc. SPIE*, **5321**, 242.

48 Grynpas, M.D. and Omelon, S. (2007) *Bone*, **41**, 162.

49 Weiner, S. and Wagner, H.D. (1998) *Annu. Rev. Mater. Sci.*, **28**, 271.

50 Faibish, D., Ott, S.M. and Boskey, A.L. (2006) *Clin. Orthop. Relat. Res.*, 28.

51 Camacho, N.P., Carroll, P. and Raggio, C.L. (2003) *Calcif. Tissue Int.*, **72**, 604.

52 Camacho, N.P., West, P., Torzilli, P.A. and Mendelsohn, R. (2001) *Biopolymers*, **62**, 1.

53 Morris, M.D., Carden, A., Rajachar, R.M. and Kohn, D.H. (2002) *Proc. SPIE*, **4614**, 47.

54 Golcuk, K., Mandair, G.S., Callender, A.F., Sahar, N., Kohn, D.H. and Morris, M.D. (2006) *Biochim. Biophys. Acta*, **1758**, 868.

55 Timlin, J., Carden, A., Morris, M.D., Rajachar, R.M. and Kohn, D.H. (2000) *Anal. Chem.*, **72**, 2229.

56 Wasserman, N.N., Yerramshetty, J.J. and Akkus, O.O. (2005) *Eur. J. Morphol.*, **42**, 43.

57 Ruppel, M.E., Burr, D.B. and Miller, L.M. (2006) *Bone*, **39**, 318.

58 Pezzotti, G. (2005) *Anal. Bioanal. Chem.*, **381**, 577.

59 Pezzotti, G. and Sakakura, S. (2003) *J. Biomed. Mater. Res.*, **65**A, 229.

60 Nalla, R.K., Kinney, J.H. and Ritchie, R.O. (2003) *Nat. Mater.*, **2**, 164.

61 Boskey, A.L., DiCarlo, E., Paschalis, E., West, P. and Mendelsohn, R. (2005) *Osteoporos. Int.*, **16**, 2031.

62 Paschalis, E.P., Ilg, A., Verdelis, K., Yamauchi, M., Mendelsohn, R. and Boskey, A.L. (1998) *Bone*, **23**, S342.

63 Paschalis, E.P., Shane, E., Lyritis, G., Skarantavos, G., Mendelsohn, R. and Boskey, A.L. (2004) *J. Bone Miner. Res.*, **19**, 2000.

64 Mendelsohn, R., Paschalis, E.P., Sherman, P.J. and Boskey, A.L. (2000) *Appl. Spectrosc.*, **54**, 1183.

65 Gadeleta, S.J., Boskey, A.L., Paschalis, E., Carlson, C., Menschik, F., Baldini, T., Peterson, M. and Rimnac, C.M. (2000) *Bone*, **27**, 541.

66 Paschalis, E.P., Burr, D.B., Mendelsohn, R., Hock, J.M. and Boskey, A.L. (2003) *J. Bone Miner. Res.*, **18**, 769.

67 Ouyang, H., Sherman, P.A.J., Paschalis, E.P., Boskey, A.L. and Mendelsohn, R. (2004) *Appl. Spectrosc.*, **58**, 1.

68 Paschalis, E.P., Boskey, A.L., Kassem, M. and Eriksen, E.F. (2003) *J. Bone Miner. Res.*, **18**, 955.

69 Monier-Faugere, M.-C., Geng, Z., Paschalis, E.P., Qi, Q., Arnala, I., Bauss, F., Boskey, A.L. and Malluche, H.H. (1999) *J. Bone Miner. Res.*, **14**, 1768.

70 Durchschlag, E., Paschalis, E.P., Zoehrer, R., Roschger, P., Fratzl, P., Recker, R., Phipps, R. and Klaushofer, K. (2006) *J. Bone Miner. Res.*, **21**, 1581.

71 Paschalis, E.P., Glass, E.V., Donley, D.W. and Eriksen, E.F. (2005) *J. Clin. Endocrinol. Metab.*, **90**, 4644.

72 Huang, R.Y., Miller, L.M., Carlson, C.S. and Chance, M.R. (2002) *Bone*, **30**, 492.

73 Huang, R.Y., Miller, L.M., Carlson, C.S. and Chance, M.R. (2003) *Bone*, **33**, 514.

74 Marieb, E.N. (1998) *Anatomy and Physiology*, 4th edn, HumanBenjamin/ Cummings Science Publishers, Menlo Park, CA.

75 Cohen, N.P., Foster, R.J. and Mow, V.C. (1998) *J. Orthopaed. Sports Phys. Ther.*, **28**, 203.

76 Bansil, R., Yannas, I.V. and Stanley, H.E. (1978) *Biochim. Biophys. Acta*, **541**, 535.

77 Barrett, T.W. and Peticolas, W.L. (1979) *J. Raman Spectrosc.*, **8**, 35.

78 Cabassi, F., Casu, B. and Perlin, A.S. (1978) *Carbohydr. Res.*, **63**, 1.

79 Cael, J.J., Isaac, D.H., Blackwell, J., Koenig, J.L., Atkins, E.D.T. and Sheehan, J.K. (1976) *Carbohydr. Res.*, **50**, 169.

80 Cael, J.J., Koenig, J.L. and Blackwell, J. (1974) *Carbohydr. Res.*, **32**, 79.

81 Gilli, R., Kacurakova, M., Mathlouthi, M., Navarini, L. and Paoletti, S. (1994) *Carbohydr. Res.*, **263**, 315.

82 Servaty, R., Schiller, J., Binder, H. and Arnold, K. (2001) *Int. J. Biol. Macromol.*, **28**, 121.

83 Haxaire, K., Maréchal, Y., Milas, M. and Rinaudo, M. (2003) *Biopolymers*, **72**, 10.

84 Haxaire, K., Maréchal, Y., Milas, M. and Rinaudo, M. (2003) *Biopolymers*, **72**, 149.

85 Maréchal, Y., Milas, M. and Rinaudo, M. (2003) *Biopolymers*, **72**, 162.

86 Quinn, F.R. and Bettelheim, F.A. (1963) *Biochim. Biophys. Acta*, **69**, 544.

87 Alkrad, J.A., Mrestani, Y., Stroehl, D., Wartewig, S. and Neubert, R. (2003) *J. Pharm. Biomed. Anal.*, **31**, 545.

88 Edwards, H.G.M. and Carter, E.A. (2001) *Biological Applications of Raman Spectroscopy*, Vol. **24**, Marcel Dekker Inc., New York.

89 Pelton, J.T. and McLean, L.R. (2000) *Anal. Biochem.*, **277**, 167.

90 Leikin, S., Parsegian, V.A., Yang, W.-H. and Walrafen, G.E. (1997) *Proc. Natl Acad. Sci. USA*, **94**, 11312.

91 Walrafen, G.E. and Chu, Y.-C. (2000) *Chem. Phys.*, **258**, 427.

92 Frushour, B.G. and Koenig, J.L. (1975) *Biopolymers*, **14**, 379.

93 Khajehpour, M., Dashnau, J.L. and Vanderkooi, J.M. (2006) *Anal. Biochem.*, **348**, 40.

94 Goheen, S.C., Lis, L.J. and Kauffman, J.W. (1978) *Biochim. Biophys. Acta*, **536**, 197.

95 Mizuno, A., Tsuji, M., Fujii, K., Kawauchi, K. and Ozaki, Y. (1994) *Jpn. J. Ophthalmol.*, **38**, 44.

96 Dehring, K.A., Smukler, A.R., Roessler, B.J. and Morris, M.D. (2006) *Appl. Spectrosc.*, **60**, 366.

97 Jackson, M., Choo, L.-P., Watson, P.H., Halliday, W.C. and Mantsch, H.H. (1995) *Biochim. Biophys. Acta – Mol. Basis Dis.*, **1270**, 1.

98 Frank, C.J., McCreery, R.L. and Redd, D.C.B. (1995) *Anal. Chem.*, **67**, 777.

99 Koljenovic, S., Bakker Schut, T.C., van Meerbeeck, J.P., Maat, A.P.W.M., Burgers, S.A., Zondervan, P.E., Kros, J.M. and Puppels, G.J. (2004) *J. Biomed. Opt.*, **9**, 1187.

100 Krafft, C., Sobottka, S.B., Schackert, G. and Salzer, R. (2006) *J. Raman Spectrosc.*, **37**, 367.

101 Wang, Y.N., Galiotis, C. and Bader, D.L. (2000) *J. Biomech.*, **33**, 483.

102 Feshchenko, S.P., Rebrin, I.A., Sokolnik, V.P., Sher, B.M., Sokolov, B.P., Kalinin, V.N. and Lazjuk, G.I. (1989) *Hum. Genet.*, **82**, 49.

103 Potter, K., Kidder, L.H., Levin, I.W., Lewis, E.N. and Spencer, R.G. (2001) *Arth. Rheum.*, **44**, 846.

104 Bi, X., Li, G., Doty, S.B. and Camacho, N.P. (2005) *Osteoarthritis Cartilage*, **13**, 1050.

105 Ramakrishnan, N., Xia, Y. and Bidthanapally, A. (2007) *Phys. Med. Biol.*, **52**, 4601.

106 Xia, Y., Ramakrishnan, N. and Bidthanapally, A. (2007) *Osteoarthritis Cartilage*, **15**, 780.

107 West, P.A., Bostrom, M.P.G., Torzilli, P.A. and Camacho, N.P. (2004) *Appl. Spectrosc.*, **58**.

108 Otterness, I.G., Bliven, M.L., Eskra, J.D., te Koppele, J.M., Stukenbrok, H.A. and Milici, A.-J. (2000) *Osteoarthritis Cartilage*, **8**, 366.

109 Bi, X., Yang, X., Bostrom, M.P.G. and Camacho, N.P. (2006) *Biochim. Biophys. Acta – Biomembr.*, **1758**, 934.

110 David-Vaudey, E., Burghardt, A., Keshari, K., Brouchet, A., Ries, M. and Majumdar, S. (2005) *Eur. Cells Mat.*, **10**, 51.

111 Crombie, D.E., Turer, M., Zuasti, B.B., Wood, B., McNaughton, D.,

Nandakumar, K.S., Holmdahl, R., Damme, M.-P.V. and Rowley, M.J. (2005) *Arth. Res. Ther.*, **7**, R927.

112 Matsui, H., Shimizu, M. and Tsuji, H. (1997) *Microsc. Res. Tech.*, **37**, 333.

113 Oegema, T.R., Carpenter, R.J., Hofmeister, F. and Thompson, R.C. (1997) *Microsc. Res. Tech.*, **37**, 324.

114 Burr, D.B. and Schaffler, M.B. (1997) *Microsc. Res. Tech.*, **37**, 343.

115 Tye, C.E., Rattray, K.R., Warner, K.J., Gordon, J.A.R., Sodek, J., Hunter, G.K. and Goldberg, H.A. (2003) *J. Biol. Chem.*, **278**, 7949.

116 Miller, L.M., Carlson, C.S., Carr, G.L. and Chance, M.R. (1998) *Cell. Mol. Biol. (Noisy le Grand)*, **44**, 117.

117 Dehring, K.A., Crane, N.J., Smukler, A.R., McHugh, J.B., Roessler, B.J. and Morris, M.D. (2006) *Appl. Spectrosc.*, **60**, 1134.

118 Boskey, A. and Camacho, N.P. (2007) *Biomaterials*, **28**, 2465.

119 Minwook, K., Xiaohong, B., Horton, W.E., Jr, Spencer, R.G. and Camacho, N.P. (2005) *J. Biomed. Opt.*, **10**, 031105.

5

Infrared and Raman Spectroscopy and Spectral Imaging of Individual Cells

Max Diem, Christian Matthäus, Tatyana Chernenko, Melissa J. Romeo, Miloš Miljković, Benjamin Bird, Jennifer Schubert, Kostas Papamarkakis, and Nora Laver

5.1
Introduction

Since the introduction of the first cytological cancer screening methods in 1941 by Papanicolaou ('Pap' for short) [1], these screening tests have been applied more than one billion times; in the US alone, more than 50 million cervical 'Pap' tests are carried out annually. This test originally consisted of the collection ('exfoliation') of cells, for example from the uterine cervix, with a brush or spatula, and smearing the cells from these collection devices onto a microscope slide (hence the colloquial term 'Pap smear' for cervical cancer screening). Subsequently, the cells were fixed and stained for microscopic interpretation. The severity of, and morbidity from, cervical cancer has been reduced by over an order of magnitude since the introduction of the Pap test. Furthermore, many other applications exist that use identical or similar methodology, an example being bladder cytology, in which cells isolated from urine are stained and examined using the same Pap stain.

Over the past two decades, new methods for preparing cytological samples of exfoliated cells have been developed, aimed at reducing the clumping of cells and improving the homogeneity of the cell deposits. This was achieved by removing the cells from the collection devices to form a suspension from which the cells–after suitable purification steps–are deposited onto slides. These methods, collectively referred to as 'liquid-based methods', produce a very homogeneous single layer of cells that increases the number and quality of cells available for visual inspection. Indeed, an entire branch of the medical device industry is targeted at this market, such that today fully automated instruments that can produce a dozen or so stained and fixed sample slides simultaneously are available and widely used in larger cytological laboratories.

Any further automation of cytology, however, has largely failed. During the early 1990s, several methods were developed and introduced that used automatic image analysis of cells to render a cytological diagnosis. However, none of these methods were widely used at the time of the writing of this review (2007), in part because all

the uncertainties of classical cytology are reflected in an automatic imaging system. These uncertainties of classical cytology result from the following aspects:

- The transition from a normal to a cancerous state of cells may proceed via a multistep sequence of events (atypia, dysplasia, neoplasia) that cannot be diagnosed with certainty from the cellar or nuclear morphology.

- The number of abnormal cells in a typical sample may be quite small, and may be masked by a majority of normal cells.

- The cytological diagnosis is inherently subjective, as it is made by visual inspection and comparison against data in the cytologist's memory.

These factors reduce the accuracy of cytological diagnoses (with respect to an independent 'gold standard', such as histopathology). Various values of the actual accuracy of the Pap test have been cited in the literature; these point to a value [2] of between 65 and 70%, with the majority of false diagnoses being false positives, which is in part due to the threat of litigation. The other source of disagreement is in the severity of a diagnosed abnormality. While it is unusual that a normal sample is diagnosed as cancer, or a cancerous sample is missed altogether, the classification as atypical, low-grade or high-grade squamous intraepithelial lesion (LGSIL and HGSIL, respectively) is extremely difficult, and accounts for many of the reported inaccuracies of the Pap test.

Thus, it would appear desirable to develop an automatic cytological procedure that could utilize quantitative, measured information as a basis for the diagnosis. Today, spectral methods – and particularly those based on vibrational spectroscopy – offer a promising venue for such an automatic procedure. Vibrational (infrared and Raman) spectroscopy is a method that not only provides 'fingerprint' sensitivity for the biochemical composition of a cell but also offers a 'snapshot' of the cell's physiological activity and state of health. In many reports, we and others have demonstrated [3–9] spectral differences between inactive cells, actively growing and mitotic cells, between different cell types within an organ, between those of different organs, and between cells of different states of health. In this chapter, we describe those methods that have been found to produce reliable spectra of individual squamous cells from the oral mucosa (buccal) and the uterine cervix, and urothelial cells from the bladder. In particular, the enormous variance observed for the spectra of individual cells will be explained, and methods introduced to deal with such spectral heterogeneity. These goals were achieved by employing a systematic approach towards samples with increased complexity: for example, the buccal samples contain almost exclusively mature squamous cells, whereas urine-borne cells consist predominantly of two cell types, namely squamous and urothelial cells. Cervical samples can contain various maturity states of squamous cells from the ectocervix, as well as glandular cells from the endocervix.

Earlier efforts to establish spectral cytology [10, 11] generally failed because the heterogeneity of samples was not understood, and measurements were attempted on cell pellets containing upwards of 1000 or 10000 cells. This was due in part to

the lack of sensitivity of infrared microscopes during the mid and late 1990s, and also to a lack of systematic groundwork to understand cellular spectroscopy.

In this chapter, we deal almost exclusively with the spectroscopy and spectral imaging of normal cells to establish their distribution, spectral databases and methodology, despite the overall aim of the research program being that of cancer detection and diagnosis. This approach differs greatly from earlier efforts [11], which were aimed squarely at cancer diagnosis but failed because the groundwork had not been properly established. Such information includes detailed methods of sample preparation and fixation, the discussion of artifacts and spectral variance, and methods to deal with these adverse effects. In addition, data preprocessing and the choice of diagnostic algorithms will be introduced.

5.2
Methods

5.2.1
Cell Collection and Culturing Methods

In the following sections, attention is focused on the spectroscopy of human (and some other mammalian) cells, most of which are healthy and of epithelial origin, the aim being to report the distribution and spectral patterns of normal cells of diagnostic significance. The current research program of the authors involves three common malignancies for which spectral screening procedures are being developed, namely oral, cervical and bladder cancer. For each of these diagnostic applications epithelial cells are readily available via oral scraping, gynecological examinations and urine samples. All cells utilized for these screening procedures were obtained with the approval of the Institutional Review Boards at the participating hospital (New England Medical Center-Tufts University) and Northeastern University. A common method for cell fixation and sample preparation is presented in Section 5.2.2.

5.2.1.1 Exfoliated Cells
Oral mucosa (buccal) cells were harvested from volunteer graduate and undergraduate students under a local Institutional Review Board protocol. To collect the cells, the inside of the cheek was gently swiped with a sterile polyester swab (it was estimated that one swipe would result in ca. 10^5–10^6 exfoliated cells). Exfoliated buccal cells are the most homogeneous samples reported in these studies; visual microscopic inspection indicated that >99% of the cells were large and squamous, with small, well-delineated nuclei and a large cytoplasmic area. Hence, they were ideally suited to establish the spectral variance of human cells. Due to digestive enzymes in saliva, the cells are completely devoid of glycogen, which normally is a major component of squamous cells. As the spectral contributions of glycogen mask the spectral region between 1000–1200 cm^{-1} (which contains the diagnostic phosphate vibrations [12]), the ability to analyze glycogen-free cells is invaluable.

Urine-borne cells were recovered using a membrane filtration technique. For this, the urine sample was passed through a nylon net filter held in a polypropylene holder (11 μm pore size, 47 mm diameter; Millipore, Billerica, MA, USA) [9]. The filter was then placed directly into a centrifuge tube containing 20 ml of fixative solution (*vide infra*). The cells were dislodged from the filter using a vortex mixer, and the resultant cell suspension allowed to stand for 20 min; this permitted fixation and further preservation of the cells. The filter was then removed, and the remaining specimen centrifuged ($600 \times g$ for 25 min) to concentrate the diagnostic cells. After being resuspended, the cells were prepared on 'low-emmissivity' (low-e) glass slides (*vide infra*) using the Cytospin method (see Section 5.2.2).

The two major cell types identified in the urine were urothelial cells (from the lining of the bladder) and mature squamous cells (from the distal end of the urethra). The presence or absence of glycogen in both cell types can be demonstrated spectroscopically.

The cervical cells were obtained via a routine gynecological examination, and stored on the collection devices in fixative until a satisfactory cytological reading was established (these samples otherwise would have been discarded). Consent to participate in this project was obtained from each patient. In all of the studies reported below, storage of the fixative was shown not to cause any spectral degeneration of the cells.

5.2.1.2 Cultured Cells

For adherent cell cultures, the following protocol for HeLa cells may serve as an example. Cervical adenocarcinoma (HeLa) cells (purchased from the American Tissue and Cell Culture Corp.; ATCC; Manhasset, VA, USA), cell line CCL-2, were seeded in 75 cm³ sterile plastic cell culture flasks (Fisher Scientific) at a concentration of approximately 2×10^4 cells cm^{-2}. Typically, the growth medium consisted of 20 ml Dulbecco's Modified Eagle's Medium (DMEM; ATCC), supplemented with 10% fetal bovine serum (FBS; ATCC). To prevent bacterial contamination, 2.5 μg ml^{-1} of amphotericin B (ATCC) and 100 IU ml^{-1} penicillin/streptomycin (ATCC) was added to the medium. The cells were incubated at 37 °C in an atmosphere containing 5% CO_2.

Cultured cells were used for the Raman studies reported in Section 5.3.2. For this, the cells were grown directly onto carefully cleaned and sterilized CaF$_2$ substrates, and then incubated for various times in a cell culture environment with the drug carrier systems reported below. Before spectroscopic data acquisition, the cells were formalin fixed and resuspended in buffer solution. Raman spectra of the exfoliated human cells were obtained from cells centrifuged (see Section 5.2.2) onto CaF$_2$ windows. The preparation of the drug delivery systems (deuterated liposomes) has been reported elsewhere [13].

When cells were grown directly onto substrates, carefully cleaned and sterilized windows (either CaF$_2$ or 'low-e' slides; *vide infra*) were deposited into the cell culture flasks, and a few milliliters of a suspension of trypsinized cells pipetted onto the substrates. After about two days, the cells were seen to grow on the substrate immersed in the medium. After a few division cycles, the cells had a totally

different morphology compared to the trypsinized cells (see below). The substrates were removed from the medium, and the cells fixed, washed and air-dried (see below). The final washing step was in deionized water to prevent salt crystals (from the balanced saline solution) forming on the cells during drying. To prevent cell lysis, the final drying step should be performed very quickly under a stream of dry, compressed air.

5.2.2
Sample Preparation

5.2.2.1   Sample Substrates

For the Raman microspectroscopic studies reported in Section 5.3.2, round CaF_2 windows of varying sizes were utilized. CaF_2 is also suitable as a substrate for infrared microspectroscopy (IR-MSP), although its high cost makes it impractical for routine cytological studies which require hundreds of sample slides. For all IR cytological studies, specially coated glass-slides were used in transflection mode; these so-called 'low-e' slides (Kevley Technologies, Chesterland, OH, USA) consist of Ag-coated glass where the coating is sufficiently thin as to be transparent in the visible region, but highly reflective in the IR region. Thus, any cell on these slides can be inspected using visual microscopy, while IR spectral data can be collected, in transflection, from the cells.

5.2.2.2   Fixation

Fixation is a major issue in spectral cytology. Exfoliated cells (e.g., oral mucosa cells) can be used unfixed after rapid drying and, once dry (ca. 1 min) will remain stable for many days (such stability was established by measuring spectra several days apart). Neither morphological nor spectroscopic changes could be observed as a function of storage time. Formalin-fixation, using 5–10% buffered aqueous formaldehyde for about 10 min, produces spectra that are indistinguishable from those of unfixed cells. This was demonstrated by analyzing the data sets of hundreds of fixed and unfixed spectra, using multivariate data analysis methods.

Today, however, most cytological procedures employ fixatives produced by the companies which produce the instrumentation for cytological sample preparation; examples include SurePath® (now known as BD Diagnostics-Tripath, Burlington, NC, USA) and Cytyc (Marlboro, MA, USA). When several different spectral cytology fixatives were tested, the fixation of individual exfoliated cells was shown to cause relatively small spectral changes, in contrast to earlier reports where there was a heavy dependence on fixation [14]. (These results are presented in Section 5.3.1.) As the present cytology procedures involved use of the SurePath method, a SurePath preservative fluid was used as fixative; this was an aqueous solution containing ca. 25% ethanol and a few percent of isopropanol and methanol.

5.2.2.3   Sample Deposition

In principle, it would appear quite straightforward to pipette a cell suspension onto a substrate and evaporate the solvent under mild vacuum or a stream of dry air.

However, this method generally produces poor samples, with the cells not spreading evenly but tending to clump. In addition, if isotonic saline is used to prevent cell lysis, then salt crystals will form around the cells, causing a substantial scattering of light. If pure water is used as solvent, the cells may lyse in the time required for the solvent to evaporate. Thus, exfoliated cells were deposited onto the low-e slides using the CytoSpin method [9], which was developed originally for cytological purposes. The aim of this deposition technique is to produce sparse monolayers of cells such that all cells are well separated from their nearest neighbors, as well as providing an unobstructed view (or measurement aperture) of each cell.

When using the CytoSpin technique (Thermo Shandon, Pittsburgh, PA, USA), approximately 0.5 ml of cell suspension (containing ca. 5×10^4 cells ml^{-1}) was placed into a special, conical funnel that was clamped against the sample substrate. A layer of wicking paper with a 5 mm-diameter hole is positioned between the funnel and the slide. The entire assembly was placed into a special centrifuge rotor and centrifuged at 800–1200 rpm for 20–300 s. In this process, the centrifugal force pressed the liquid onto the slides, where it was wicked away by the absorbent layer of paper, leaving the cells on the substrate. A typical sampling area of 5 mm diameter would contain approximately 10^3 cells, with the cells separated by a distance larger than the cell size.

5.2.3
Data Acquisition

5.2.3.1   Raman Spectroscopy and Raman Spectral Mapping

Raman data were collected using a Confocal Raman Microscope (Model CRM 2000; WITec, Inc., Ulm, Germany). Excitation (ca. 30 mW each at 488, 514.5 or 632.8 nm) is provided by air-cooled Ar ion or HeNe lasers (Models 05-LHP-928 and Model 532, respectively; Melles Griot). Exciting laser radiation is coupled into the Zeiss microscope through a wavelength-specific, single mode optical fiber, after which the incident laser beam is collimated via an achromatic lens and passed to a holographic band-pass filter, before being focused onto the sample through the microscope objective. A Nikon Fluor (60×/1.00 numerical aperture (NA); working distance (WD) = 2.0 mm) water immersion or a Nikon Plan (100×/0.90 NA, WD = 0.26 mm) objective was used in these studies.

The sample was located on a piezo-electrically driven microscope scan stage with X—Y resolution of approximately 3 nm and a repeatability of ±5 nm, and Z resolution of approximately 0.3 nm and ±2 nm repeatability. Raman backscattered radiation was collected through the microscope objective, and passed through a holographic edge filter to block any Rayleigh scattering and reflected laser light. Subsequently, the Raman scattered light was focused into a multimode optical fiber, which directed the light to the monochromator. The two optical fibers acted as pinholes for the confocal measurement. The Raman scattered light was dispersed by a 30 cm focal length monochromator and detected by a back-illuminated deep-depletion, 1024×128 pixel CCD camera operating at $-82\,°C$. The

spectral resolution varies significantly over the spectral range projected onto the CCD detector, and depends on the excitation wavelength and grating groove density. Most of the results reported were collected at an average spectral band pass of approximately 4 cm^{-1}. Raman spectral images were collected by moving the sample in a raster pattern, typically in 500 nm steps, through the focal point of the laser. Dwell times of between 300 to 500 ms per datum point were typically used.

5.2.3.2 Infrared Instrumentation

The IR spectra and spectral maps were collected using Perkin Elmer Spotlight 300 or 400 imaging infrared microspectrometers; these consisted of a Spectrum One Fourier transform infrared (FT-IR) spectrometer bench-coupled to a Model 300 or 400 IR microscope. These integrated imaging infrared microspectrometers incorporated a 16×1 element ($400\,\mu m \times 25\,\mu m$) HgCdTe (MCT) array detector and a single point, $100\,\mu m \times 100\,\mu m$ MCT detector mounted on the same Dewar. Both detectors were operated in photoconductive mode at liquid nitrogen temperature. The D* of each element in the array detector exceeded 4.5×10^{10} cm Hz$^{\frac{1}{2}}$ W^{-1}. The Cassegrain objective provided an image magnification of 6×, and had a NA of 0.58. The visual image collection via a CCD camera was completely integrated with the microscope stage motion and IR spectra data acquisition.

For single point measurements, individual cells were selected from the visually acquired sample image, as seen on the screen. For each cell position on the sample substrate, the aperture was selected to straddle the cell, and typically was $30\,\mu m \times 30\,\mu m$. The cell position and apertures were stored for each cell, and the data acquisition of all stored positions proceeded automatically. The microscope and optical bench were continuously purged with purified, dry air. In addition, the sample area in the focal plane of the microscope was enclosed in a purged sample chamber.

Following the spectroscopic data collection, the sample slides were stained using standard cytological protocols, using 'Pap' stain [1] within our own laboratory. Those cells examined in the analysis were then relocated on the slide, and visual images captured at high magnification (40×) to allow a cytological diagnosis.

5.2.4
Methods of Data Analysis

The earliest efforts to use spectroscopic methods for the diagnosis of disease used mostly a visual inspection of the spectra and simple band intensity ratios to correlate spectral features and histopathology. In contrast, the results presented here utilize supervised and unsupervised methods of multivariate statistics to maximize the spectral information used in the diagnostic process.

5.2.4.1 Data Pre-Processing

The raw data, in units of absorbance, were truncated to the most diagnostic wavenumber range, typically 800–1800 cm^{-1}, and corrected for a constant offset. The

IR data were converted to second derivatives, (d^2I/dv^2) and smoothed by a Savitzky–Golay [15] odd-point, sliding window. Individual spectra may be normalized (either min-max or vector normalization) to account for variations in sample thickness. Although derivatization decreases the signal-to-noise ratio (SNR) of the spectra, it offers a number of advantages. First and foremost, any sloping baselines are removed, and therefore the second-derivative spectra appear mostly with a totally flat baseline. Furthermore, second-derivative spectra exhibit collapsed band width with seemingly 'higher spectral resolution'. Indeed, Fourier self-deconvolution [16] (FSD) and second-derivative methods are offered in standard software packages as 'resolution-enhancing techniques'. Finally, it has been demonstrated recently that the distinction of bands consisting of one Gaussian/ Lorentzian envelope from those that contain more than one component is vastly enhanced by derivatization [9].

5.2.4.2 Principal Component Analysis (PCA)

Spectral data sets from individual cells were analyzed using PCA, a well-established multivariate data analysis method that is ideally suited to distinguish small, reoccurring spectral variations in large data sets containing uncorrelated variations. PCA was utilized at this time because it is a completely unsupervised method for establishing whether or not the spectra of cells are grouped into classes according to cell type, to donor identity or to disease, among other factors. For a more detailed description of PCA, the reader is referred to Chapter 2 of this book or to other reviews on chemometrics (e.g., Refs [9, 17]).

For PCA, the entire spectral data set, containing n spectra, is written as a matrix **S** in which each column represents one spectral vector S(v) of m intensity data points. The spectral vectors may be raw or smoothed intensities, or first or second derivatives.

The intensity correlation matrix **C** is constructed from the spectral matrix **S** according to

$$C = S \, S^T \tag{5.1}$$

where C is a $(m \cdot m)$ matrix, in which the off-diagonal terms C_{kl} are the correlation between intensity values at wavelengths v_k and v_l, summed over all spectra. Diagonalization of the correlation matrix yields the eigenvalues, which express the variance contained in each of the principal components, and the eigenvectors from which the 'principal components' Z can be constructed. These principal components are the original spectra expressed in a rotated coordinate system, based on the maximum variance of the original spectra. Subsequently, we may express each of the original spectra S(v) in terms of a linear combination of the new principal components (also known as 'loading vectors') where the 'scores', α, are given by the weighting coefficients in the linear expansion.

For spectral data sets of individual cells, it is found that a large fraction of the total spectral variance is contained in the first few 'loading vectors'. Typically, five to eight loading vectors contain more than 99% of the variance, such that the linear

combination can be truncated after the *p*th term, where *p* is the number of relevant loading vectors or principal components. Thus, the score matrix $\boldsymbol{\alpha}$, which determines how much each principal component contributes to each spectrum, will have the dimension $(p \cdot n)$. This method results in a much-reduced size of the data set, as all spectra are expressed in terms of a few (typically <10) basis functions and a 'score vector' of about *p* entries.

Similar spectra exhibit similar scores α, which may be used to discriminate, or group, spectra. This is accomplished by plotting the values α_i and α_j (i.e., the contribution of PC_i and PC_j to each spectrum) against each other, where each datapoint represents one spectrum. If grouping is observed, there are quantifiable and significant variations in the spectra, which can be used to construct discriminant algorithms for distinguishing cell types, the state of differentiation and maturation of cells, and disease. At this point, PCA can be introduced as an unsupervised, preliminary test to determine whether or not there are significant spectral differences.

5.2.4.3 Hierarchical Cluster Analysis (HCA)

HCA is a powerful method for data sorting based on local decision criteria. These criteria are based on finding the smallest 'distances' between items such as spectra, where the term 'distances' may imply Euclidean or Mahalanobis distances [17], or correlation coefficients. HCA is, *per se*, not an imaging method, but can be used to construct pseudocolor maps from hyperspectral data sets collected from cells or tissue sections [18].

In HCA, the spectral correlation matrix, **C**′ is calculated according to according to:

$$C' = S^T\, S \tag{5.2}$$

This matrix is of dimension $(n \cdot n)$, where *n* is the number of spectra in the data set, in which the off-diagonal terms C_{ij} are the correlation between spectra *i* and *j*, summed over all data points of the spectral vector $S(v_N)$. The correlation matrix is subsequently searched for the two most similar spectra coefficients – that is, two spectra *i* and *j* for which the correlation coefficient C_{ij} is closest to unity. Subsequently, these two spectra are merged into a new object, and the correlation coefficient of this new object and all other spectra is recalculated. The process of merging is repeated, but the items to be merged may be spectra, or spectra and merged objects. During the merging process, a membership list is kept that accounts for all individual spectra that are eventually merged into a cluster. We have used Ward's algorithm [19] for the process of merging of spectra, and the repeated calculation of the correlation matrix. When all of the spectra have been merged into a few clusters, color codes are assigned to each cluster, and the coordinates from which a spectrum was collected is indicated in this color. In this way, pseudocolor maps may be obtained that are based strictly on spectral similarities. Mean cluster spectra may be calculated that represent the chemical composition of all spectra in a cluster.

5.3
Results and Discussion

5.3.1
General Features of Infrared and Raman Spectra of Cells

In order to facilitate the discussion on Raman and IR spectra and spectral maps of human cells, we present here some characteristic spectral features of typical human cells. Although, depending on the cell type and special conditions, these spectra may vary to some extent, the information presented here is aimed at providing the reader with a survey of typical cellular spectral features.

A typical IR spectrum of an epithelial cell is shown in Figure 5.1, Trace A. One of the most prominent spectral features is the protein amide A vibration at approximately 3350 cm^{-1}, this being due mostly to the peptide linkage N—H stretching mode. Between 2800 and 3000 cm^{-1}, the C—H stretching vibrations of phospholipids, of protein side chains and of nucleic acid sugars and bases, are observed. Although this spectral region has been used less than the mid-IR spectral region
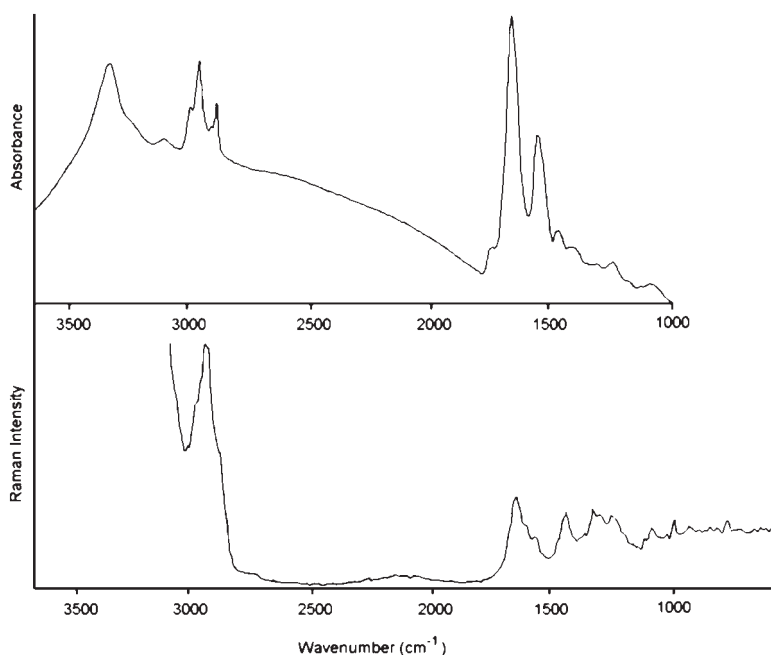
Figure 5.1 Infrared (top) and Raman spectra (bottom) of a typical cell, specifically a urothelial (bladder) cell. The infrared spectrum was taken of the entire cell, whereas the Raman spectrum was sampled at a small spot within the cytoplasm. Both spectra are presented in arbitrary intensity units, along the same wavenumber axis.

(*vide infra*), other authors have shown that the C—H stretching region may indeed be diagnostic for many cellular states and features.

The mid-IR region (1800–800 cm^{-1}) – also referred to as the 'fingerprint' region – contains the stretching vibration of the ester linkage of lipids at around 1740 cm^{-1}, and the most dominant spectral feature, the amide I protein vibration centered around 1655 cm^{-1}. This vibration is the exciton-coupled C=O stretching manifold, and consequently, is sensitive for both peptide and protein secondary structure. At approximately 1550 cm^{-1}, the quite strong amide II vibration is observed, which is due mostly to the peptide C—N stretching motion. At around 1450 and 1350 cm^{-1}, two broad, weak and relatively nondiagnostic peaks are observed, due to the C—H deformation modes and some carboxylic acid stretching modes. In the region of 1250 to 900 cm^{-1}, a number of significant bands occurs.

The peaks of varying intensity at about 1235 and 1085 cm^{-1} are due to the phosphate groups of DNA, RNA and some phospholipids. Within the context of this discussion, the biochemical nomenclature is used, where 'phosphate' refers to the phosphodiester linkage:

$$-O-PO_2^--O-$$

Here, the central phosphorus atom is surrounded approximately tetrahedrally by four oxygen atoms. The central phosphorus atom bears a negative charge that is countered in DNA by Na$^+$ ions, while the central PO_2^- group exhibits multiple bond character. The terms 'symmetric' and 'antisymmetric' phosphate stretching vibration refer to the vibrations of the central PO_2^- group, and are normal modes observed at about 1085 and 1235 cm^{-1}, respectively. The vibrations of the —O—P—O— moiety are referred to as the phosphodiester vibrations, which are less intense in the IR region, and occur around 800 and 830 cm^{-1}.

The antisymmetric phosphate vibration at 1235 cm^{-1} is partially overlapped by the lower component of the amide III vibration, a complex deformation mode of N—H and adjacent C—H groups which extends to about 1330 cm^{-1}. The phosphate region is frequently masked by carbohydrate vibrations, such as the prominent glycogen peaks shown in Figure 5.3 (this will be discussed later).

The Raman spectrum of a typical pixel from a cell is shown in Figure 5.1, lower trace. Since the probing laser beam is much smaller than the size of the cell, different pixels will exhibit different spectra; however, the lower trace shown in Figure 5.1 may serve as a representative cellular spectrum. The amide A region is very weak in all Raman spectra, but the C—H stretching region is the most prominent spectral feature in a nonresonant Raman spectrum, and may be of significant diagnostic value.

The amide I peak is relatively weak in the Raman spectrum, and the amide II peak is not observed. At the low-frequency side of the amide I peak, weak features of DNA and RNA may be observed for the nuclei and nucleoli. All cellular regions show distinct methyl and methylene deformation vibrations at about 1450 cm^{-1}, and broad, intense amide III vibrations between 1350 and 1220 cm^{-1}. At around 1000 cm^{-1}, the symmetric ring breathing mode of the aromatic phenyl alanine side

chain is observed in nearly all spectra. A number of characteristic DNA/RNA marker bands are observed (785, 1095 and 1575 cm^{-1}), and although some of these vibrations are quite weak, multivariate methods of analysis can detect their presence, and base image reconstruction decisions on their intensities.

5.3.2
Infrared Cytology

This section contains spectral results collected from entire individual cells, with the specific aim of differentiating between cell types that occur in samples of cells. The long-range goal of these studies has been the development of a completely automatic method to perform spectral cytology – that is, to analyze a sample of exfoliated cells (e.g., cervical cells obtained during the 'Pap' cervical cancer screening procedure) for the presence of abnormal cells.

Exfoliated human cells present an enormous variance in their spectral results, even for the most homogeneous samples of cells investigated to date. Thus, it has been necessary to establish the methodology to overcome such variance, and which has been reported previously [5, 20]. Here, we present a logical progression of sample complexity, from normal oral mucosa (buccal) cell samples (one cell type), through normal urinary cytology (two cell types) to normal cervical cytology, which involves at least four cell types.

5.3.2.1 Oral Mucosa Cells
Oral mucosa (buccal) cells have been used as one of the most easily obtainable exfoliated cell types from volunteer donors. The spectra collected from entire individual cells are used to introduce the possibility of using IR microspectral results to distinguish between cell types and to determine their state of health. In particular, the heterogeneity of observed spectra – and methods to overcome such problems – are discussed.

It has been reported [5, 9, 20] that the spectra of hundreds of buccal cells, collected from one volunteer, showed spectral variations that can be summarized as follows:

- There are large overall intensity variations in the overall amplitude of the spectra, by over a factor of 5 [9].
- Mie scattering contributions from the nuclei may contribute a broad undulating spectral background [5, 21].
- Distinct spectral variations in the low wavenumber region are observed for a small number of cells.

These features are now well understood, and methods to deal with them have been reported.

In spite of the apparent differences in the spectra observed for one cell type from one donor, PCA of the appropriately preprocessed data showed that there were no statistically significant spectral differences between the spectra observed for one normal donor. Similarly, when hundreds of cells from other normal donors were
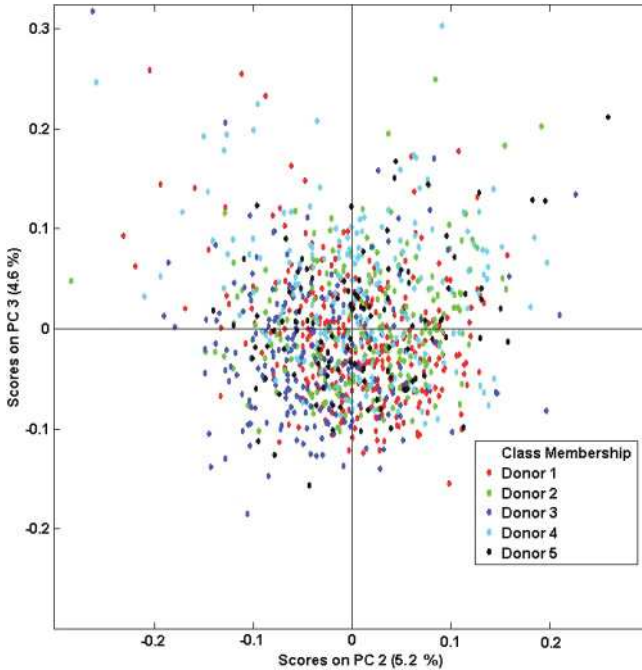
Figure 5.2 PCA 'scores plot' (PC2 versus PC 3) of the spectra of ca. 1000 oral mucosa (buccal) cells from five subjects. The distribution of scores around the coordinate origin suggests minimal person-to-person variation.

added to the data set, PCA produced a 'scores plot' that showed good scatter of the data, with barely any donor-to-donor variations. These early studies were carried out using formalin-fixed cells, but had to be repeated recently when new hospital procedures forced a change to SurePath fixation (*vide supra*). The new data sets from more donors, and using the novel fixation protocol, completely confirmed the original results (cf. Figure 5.2).

In our original studies [20], we proceeded to compare the human buccal cells to canine cervical cells, and found that IR spectroscopy/PCA could distinguish between the cell types. It was possible to explain this effect in terms of cell maturation, which was further confirmed recently for human cervical cells. Thus, we shall present the canine model in Section 5.3.2.3 along with the results from human cervical cells.

5.3.2.2 Human Urine-Borne Cells

The next application to be discussed is that of urine cytology, in which epithelial cells contained in urine are analyzed for abnormalities. Urine cytology is not carried out routinely in the US, even though urine samples are collected frequently and, in 2005, bladder cancer was the fifth most common cancer among males, and the eighth most common cancer among females. Presumably, routine urine

cytological screening is not carried out due to the overall low accuracy of cytology, and the lack of cytological laboratories available to cope with such a large workload.

Normal human urine contains both squamous cells from the distal urethra, and urothelial cells from the lining of the bladder. The former cell type may be further subdivided into glycogen-containing and glycogen-free squamous cells. Here, we aim to establish that IR spectral methods, followed by multivariate data analysis, can distinguish between these cells types. Our ultimate intention is to establish this methodology as a low-cost, automated test for bladder cancer.

Figure 5.3 shows photomicrographs of the three main types of epithelial cell identified in urine sediments after Pap staining. Here, Figure 5.3a is a glycogen-containing squamous cell, Figure 5.3b is a glycogen-free squamous cell, and Figure 5.3c is a urothelial cell. (Note: glycogen-free, in this context, implies that spectral contributions due to glycogen could not be detected in the IR spectra;
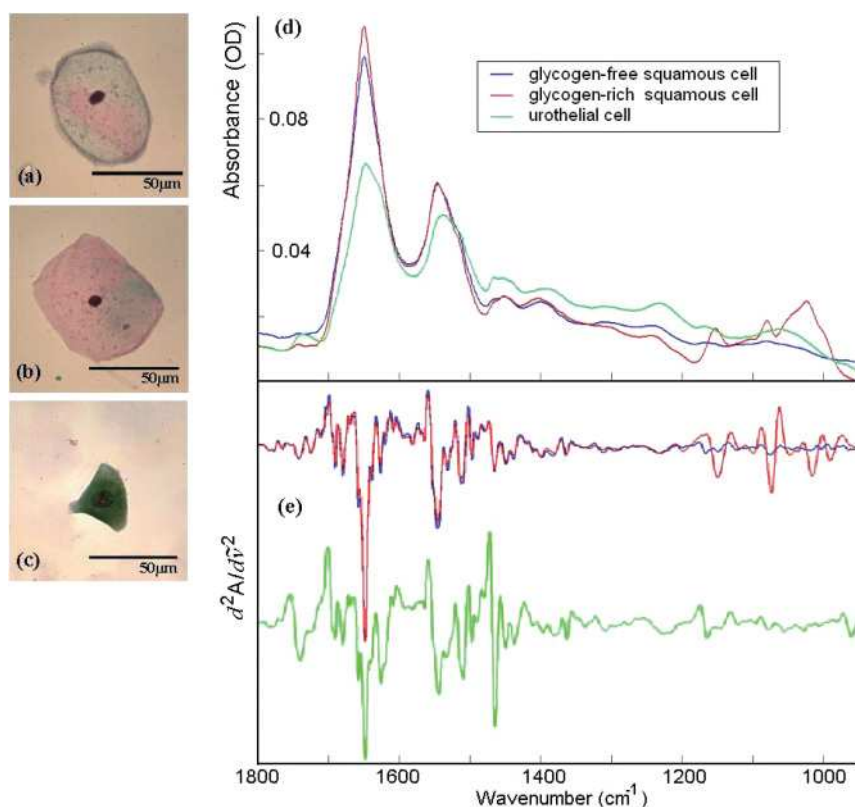
Figure 5.3 Urine cytology. (a–c) Photomicrographs of glycogen-containing, glycogen-free squamous cells, and a urothelial cell, respectively; (d) Vector-normalized IR spectra of cells shown in (a–c); (e) Second derivatives of spectra shown in (d).

special stains are used to visualize glycogen.) Both, glycogen-free and glycogen-containing squamous cells are from the distal end of the urethra, and constitute the majority of cells found in urine. They cannot be distinguished one from another by visual inspection, although it appears that the glycogen-free cells generally exhibit a smaller (more pyknotic) nucleus. Figure 5.3d shows vector-normalized absorbance spectra for the three cell types [22]. The glycogen-rich and glycogen-free cells differ by the presence of a strong, distinct set of carbohydrate peaks observed at about 1020, 1080 and 1130 cm^{-1}, whereas the spectra of the urothelial cells differ markedly from those of the squamous cells (*vide infra*).

Figure 5.3e shows the second-derivative spectra for the three cell types, where the red and blue profiles characterize the glycogen-rich and glycogen-free squamous cells, respectively. These two spectra are almost identical in the amide I/amide II region (1700–1450 cm^{-1}), and differ only in the 1200–1000 cm^{-1} region where the strong spectral bands characteristic for glycogen occur. The green profile describes the spectrum for the urothelial cells. There are several significant spectral differences between the squamous and the urothelial cells, among them the phospholipid marker band at 1738 cm^{-1}.

Spectra recorded from urothelial cells display particularly large absorbance intensities (this is not clear from Figure 5.3d, as the data are vector-normalized). This type of cell can range in size from 10 to 30 μm [23, 24] and typically feature one or more large nuclei. It has been demonstrated that this observed intensity difference for urothelial cells is caused mainly by an increased cell thickness (this point will be discussed in more detail in Section 5.3).

Squamous cells represent the vast majority of cells found in voided urine collected from healthy individuals, which contains very small numbers of transitional (urothelial) epithelial cells [24], an observation confirmed by our spectroscopic studies. For the squamous cells, a large variation in the overall amplitude of the spectra is observed, in accordance with previously discussed results for oral mucosa cells (see Section 5.3.2.1). Absorbance values recorded for the amide I band vary between 0.05 and 0.8 AU for the squamous cells. It is believed that these variations are largely due to deviations in both cell thickness and the nucleus : cytoplasm ratio within the spatial area sampled [5, 20].

Figure 5.4 presents results obtained from a PCA analysis of a fraction of the spectral data set that comprised both squamous and urothelial epithelial cells. The data have been projected onto the second (PC2) and third (PC3) principal component dimensions, where each dot represents an individual spectrum collected from a cell. As can be seen in the diagram, the main types of normal epithelial cell identified in the urine form three correlating clusters. The green cluster, representative of urothelial cells, displays a distinct separation from the squamous cells, and indicates a substantial spectral difference among these cells. Furthermore, the glycogen-rich (red) and glycogen-absent (blue) squamous cells are also clearly differentiated. These results are among the first ever to distinguish different cell types in exfoliated samples by completely automatic spectral methods at the level of individual cells, and constitute the groundwork for an eventual application of IR-MSP for the diagnosis of disease.
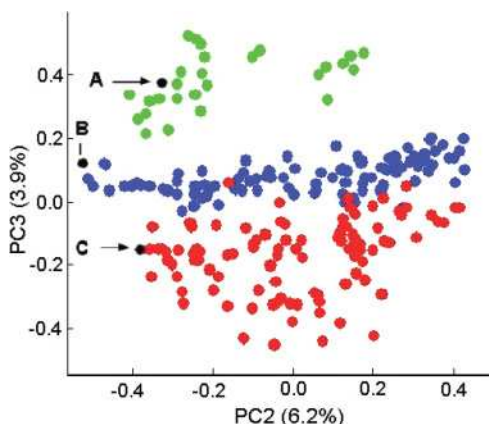
Figure 5.4 PCA 'scores plot' of urothelial and squamous cells from urine samples. The color code is the same as for Figure 5.3. The black dots marked A, B and C refer to the cells shown in Figure 5.5. See text for details.

Recently, we have also analyzed a number of cells spectrally that could not be classified cytologically. These cells often had a pale staining, appeared anucleated, and in some cases their cytoplasm was ruptured. There might be a variety of reasons for these degenerative changes, whether they be externally stimulated or induced internally. Nonetheless, conventional cytology requires both the nucleus to be clearly visible and the cytoplasm to be completely intact before a diagnosis can be made. Photomicrographs from three of 20 such cells are shown in Figure 5.5, where cell A appeared to have been ruptured, but displayed a dark blue-stained cytoplasm and a double nucleus that can sometimes be observed for urothelial cells. In contrast, cells B and C were much larger and had been stained pale red (indicative of a mature squamous cell), although both appeared to be anucleated and thus nondiagnostic.

To test whether these cells could be characterized using IR microspectroscopy, spectra from 20 nondiagnosable cells were introduced into the raw data set. A subsequent PCA classified all 20 spectra to belong clearly to one of the three cluster regions. The three cells are shown as black dots in the scores plot shown in Figure 5.4. Cell A was included in the green cluster of urothelial cells, while cells B and C were classified as squamous in origin. Thus, cells previously overlooked by cytologists due to bad staining or degenerative changes could be diagnosed using IR microspectroscopy. These initial results of the study show extreme promise, and consequently we are currently cataloguing the diagnosis of many thousands of recorded cell spectra to serve as input for supervised pattern recognition.

5.3.2.3 Human and Canine Cervical Cells

Previously, a number of studies were reported involving canine cervical cells [20] in which it was shown that mature and immature squamous cervical cells could
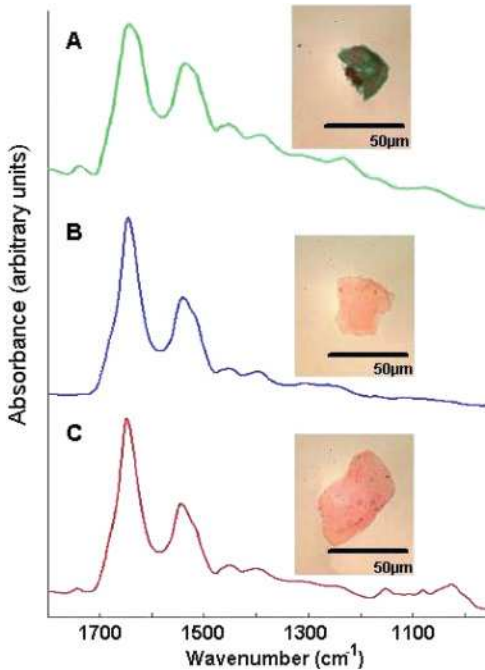
Figure 5.5 Urine-borne cells that could not be diagnosed via classical cytology due to incomplete cytoplasm (A) or poor staining (B,C), but that could be diagnosed easily via spectral cytology.

be differentiated using spectral cytology. The importance of this result may be understood from the viewpoint that, in human cervical cancer screening, the ectocervix and endocervix are scraped gently to remove squamous and glandular cervical cells from these two regions, respectively. The stratified squamous epithelium consists of four layers, namely the basal, parabasal, intermediate and superficial layers. In healthy squamous tissue, it is mostly cells from the outermost layer, the superficial layer, that are harvested during exfoliation, with only a small proportion of intermediate cells. In dysplasia, a higher proportion of immature cells extend through the squamous tissue layer, and consequently these will be contained among the exfoliated cells [25–27]. Thus, the distinction and detection of immature squamous cells is of prime importance for the envisioned spectral cervical cytology.

An initial indication of the ability to distinguish mature from immature cervical cells was derived from studies involving canine cervical cells. These cells were obtained from the cervices of spayed dogs by exfoliation with a small dental brush, fixed using a formalin fixation protocol, and then analyzed in the same manner as the oral mucosa and urine-borne cells described above. It was found cells obtained from that were in dogs in estrous during the spaying procedure clustered

differently from those of prepubescent and nonestrous dogs [20]. A visual inspection of the canine cervical cells indicated that the cells from estrous dogs were mature cervical cells, whereas those from nonestrous dogs were at the stage of development corresponding to immature cervical cells. This fact is well known among dog breeders, who establish the estrous cycles in bitches by the maturity of their cervical cells, which provide an indication of hormonal levels.

It is interesting to note that, whilst mature canine cervical cells could not be differentiated [20] from mature human buccal cells (which have a similar size and morphology), human and canine cervical cells may be very easily differentiated, as canine cells never accumulate glycogen whereas human cells are generally glycogen-rich.

The spectral patterns of human cervical cells may also depend on their degree of maturity. It is difficult to collect a sufficient number of immature cervical cells from normal women, as the majority of cells (see above) are mature superficial cells. However, in post-menopausal women who are not receiving hormone replacement therapy the reduced estrogen levels prevent complete maturation of the squamous cells, and consequently significantly more immature cells are found in the cervical exfoliates. This in turn has allowed studies to be conducted on the influence of hormone levels on the spectral properties of human cervical cells.

Fortunately, these cell types can be diagnosed relatively easily using classical cytological methods, thus affording an excellent means to correlate spectral and cytological results. Samples were prepared for spectral cytology (as described above), using cervical samples obtained from the New England Medical Center and stored in SurePath fixative. Alternatively, they were freshly prepared in the same fixative, by purification (filtration) and cytocentrifugation. As a consequence, thousands of cell spectra from normal and postmenopausal women were collected as described before, and the cells stained and subsequently imaged at high magnification for diagnosis. The results of this study are shown in Figure 5.6, where Figures 5.6a and b show the spectra and stained images of mature superficial and immature, intermediate cells from premenopausal women, respectively. The mature cell is seen to be rectangular in shape, with a very small, pyknotic nucleus, whereas the less mature cell in Figure 5.6b is smaller, with a larger nucleus, and more rounded in morphology. Figures 5.6c and d show similar cells from a postmenopausal woman, where the more mature cell is still angular in shape, but with a larger nucleus than the mature cell shown in Figure 5.6a. The even less mature cell shown in Figure 5.6d is smaller, with a more pronounced nucleus, and is even more spherical in shape.

Figures 5.6e and f show PCA score plots of the results from these cell samples. All PCA calculations were carried out in the amide I/II region (1800–1480 cm^{-1}) to reduce the influence of glycogen content of the individual cells. Although – as mentioned above – thousands of spectra have been collected to date, not all cell images have been analyzed. Nevertheless, the analyses of the spectra and cells analyzed so far show great promise. The distinction between superficial cells from postmenopausal women and those of premenopausal women was excellent. Moreover, the superficial (most mature) and intermediate cells from postmenopausal
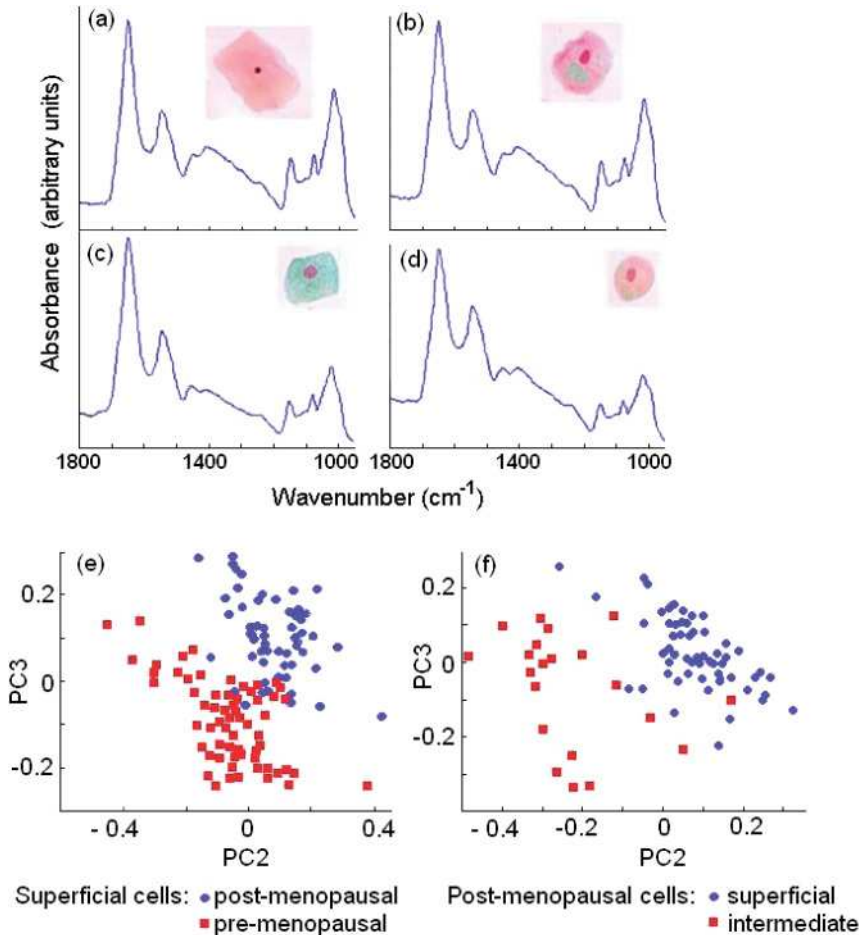
Figure 5.6 Spectra and distinction of human cervical cells. (a, b) Spectra and images of superficial and intermediate cell of premenopausal women, respectively; (c, d) Spectra and images of superficial and intermediate cell of a postmenopausal woman, respectively; (e) PCA 'scores plot' demonstrating the distinction of superficial cells from pre- and postmenopausal volunteers, respectively; (f) PCA 'scores plot' demonstrating distinction of superficial and intermediate cells from postmenopausal women.

women also showed a reasonable separation; in these cells, the most mature cells clustered quite tightly, whereas the more immature cells showed a larger variance, indicating them to be less homogeneous, and perhaps even less easy to diagnose on a visual basis.

It is also notable that the raw spectra shown in Figures 5.6a–d appeared very similar at first glance, with most variance contained in the glycogen region between the normal and the postmenopausal samples. However, the loading vectors showed significant differences in the amide I and amide II second-derivative band profiles

which were responsible for the distinctive power of the method. Thus, in the process of maturation of squamous cells from the intermediate to superficial stages, significant changes in protein composition must occur in a cell. A number of dysplastic cervical and cancerous bladder samples have been obtained recently, and are being investigated at the present time.

5.3.3
Results from Confocal Raman Microspectroscopy of Human Cells

5.3.3.1 Morphology and Subcellular Organization of Cells

Here, we will present the spectral maps of cells, with the aim of visualizing organelles and variations in chemical composition within a cell, as well as providing morphological information that will aid in the interpretation of IR spectral data. Figure 5.7 demonstrates the enormous power of multivariate analyses for image reconstruction based on Raman spectral hypercubes. These studies were carried out in collaboration with a medical research institute [28, 29], and involved the detection of the differentiation of living neuroblastoma cells. Figure 5.7a shows a univariate display of the integrated C—H stretching intensities of a cell in aqueous media. This panel shows only a rough shape of the cell, without any further information from within the cell. Figure 5.7b shows an image of the same cell constructed via HCA of the hyperspectral data set, where the gray areas depict the nucleus, and blue and red areas the more and less dense areas of the cytoplasm, respectively. The green perinuclear area exhibits quite different spectral patterns, as shown for one pixel in Figure 5.7c. The sharp peaks in this spectrum matched very well with a reference spectrum of noradrenaline, a small hormone that is known to be secreted by differentiating neuroblastoma cells [28, 29]. The HCA-based image provides much more detail than the univariate map, and may detect signals from components the presence of which is not known *a priori*.

Figure 5.8 shows results from a normal urothelial cell that have been included to contrast the morphology of such cells from that of mature squamous cells. In mature squamous cells, the cytoplasm was found to be is very thin [9] (typically 1–2 µm thick), with the nucleus somewhat thicker (3–5 µm). The short pathlength that such a cell presents to a probing IR beam can explain the low absorbance values observed in the cytoplasm of squamous cells (typically ca. 0.05 AU). Urothelial cells are significantly thicker, as demonstrated by the depth profile obtained via confocal Raman microspectroscopy. Figure 5.8a shows the visual image of a stained urothelial cell imaged (as described in Section 5.2.3.1) with a lateral spatial resolution of about 500 nm, using blue excitation (488 nm). Data (120 × 120 pixels) were collected at approximately 15 mW laser power at the sample, and the resulting data hypercube was subjected to hierarchical cluster analysis. A pseudocolor map, constructed from a hyperspectral Raman data cube via HCA (see Section 5.2.4.3), is shown in Figure 5.8b. This image shows two nuclei (normal urothelial cells often are binucleated) in blue color, and phospholipid-rich regions of the cytoplasm (red). The brightfield image of the stained cell barely shows the nuclei, which normally should stain dark blue when using Pap stain. However, it is not
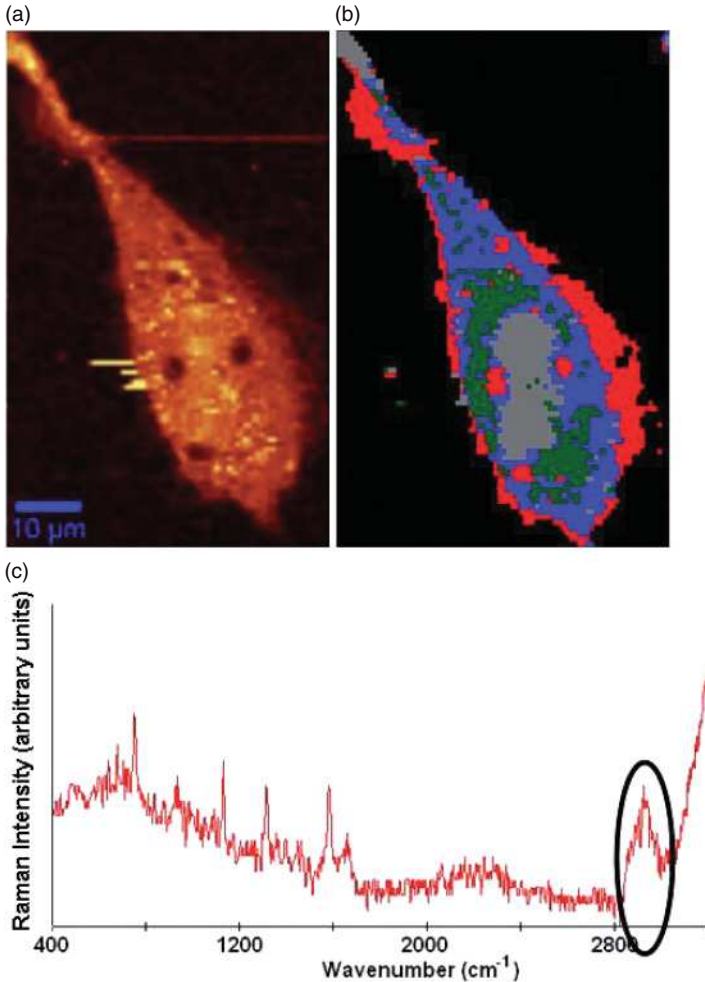
Figure 5.7 (a) Univariate (integrated C—H stretching intensity; see ellipse in panel c) Raman image of a neuroblastoma cell. The brighter hues indicate higher intensities; (b) HCA-based image of the same hyperspectral data set, showing the nucleus (gray), accumulations of noradrenaline (green) and dense (blue) and thin areas (red) of the cytoplasm. The three dark brown spots in panel (a) (colored red in panel b) indicate the holes burned by the laser. Scale bar in panel (a) = 10 μm.

uncommon that cells do not stain well in standard urine cytology (as discussed in Section 5.3.2.2); however, Raman spectral imaging would detect the nuclei, regardless of the cell's staining characteristics.

Figure 5.8c shows a confocal depth profile of the same urothelial cell, taken along the red dashed line in Figure 5.8b. This profile indicates that the cell is much thicker (ca. 8 μm) than a squamous cell, which explains its much higher IR absorbance. The Raman mean cluster spectra observed for the different regions are
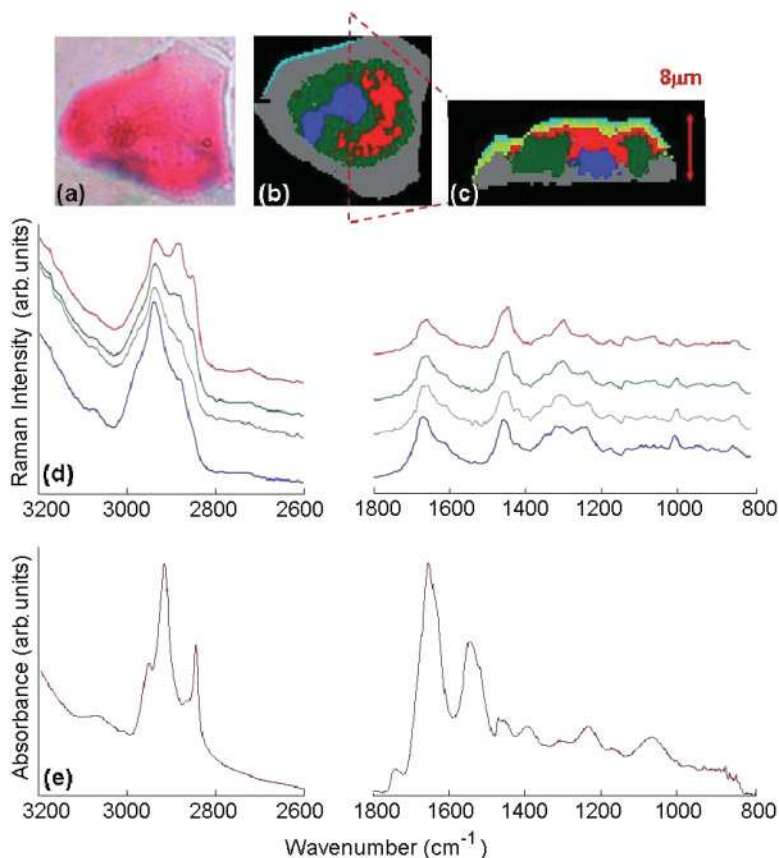
Figure 5.8 (a) Brightfield image (40×) of a stained urothelial cell; (b) Pseudocolor image, obtained from Raman hyperspectral data via HCA, of the cell shown in (a); (c) Confocal Raman depth profile of the same cell, collected along the dashed red line in (b); (d) Raman mean cluster spectra of the regions shown in the same color in (b) (see text for details); (e) IR spectrum of the entire cell.

shown in Figure 5.8d. Here, the blue trace is associated with the nucleus, the red trace is due to the phospholipid-rich region, and the gray and green traces are typical of spectra observed for cytoplasm. The spectra were surprisingly similar and, aside from obvious changes in the C—H stretching region of the lipid-rich trace, would not be amenable to visual interpretation. However, HCA is able to discriminate these spectra sufficiently to produce cluster maps of biological relevance. The IR spectrum of this cell (Figure 5.8e) shows significant lipid contributions at approximately $1740 \, \text{cm}^{-1}$, and distinct methylene stretching vibrations between 2800 and $3000 \, \text{cm}^{-1}$.

(a)   (b)   (c)
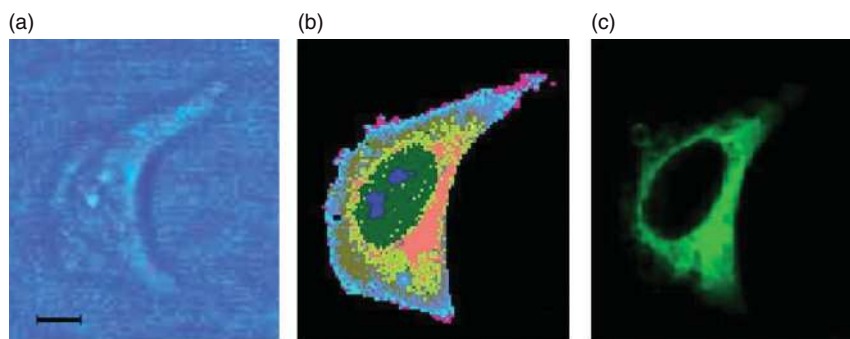
Figure 5.9 (a) Brightfield image of a HeLa cell, attached to a CaF$_2$ window, in buffer. Scale bar = 10 μm; (b) Raman spectral image, obtained via hierarchical cluster analysis (HCA) from a hyperspectral data cube collected at 500 nm spatial resolution (488 nm excitation, 15 mW laser power at sample, 500 ms dwell time); (c) Fluorescence image of the mitochondrial distribution in the same cell after Mitotracker staining. For details, see text.

Figure 5.9a shows a brightfield image of a HeLa cell attached to a CaF$_2$ substrate, collected in aqueous environment through a 60× water immersion object. Although the brightfield image reveals low contrast (as it was taken of a cell in an aqueous surrounding), the Raman image (Figure 5.9b) shows the nucleus, containing two nucleoli, and various regions of the cytoplasm in exquisite detail. The morphology of the cell is quite typical for a HeLa cell found in cell culture, where the cell exhibits spindle-like pseudopods and a large nucleus.

Immediately after Raman data acquisition, a fluorescent stain specific for mitochondria (Mitotracker Green FM; Invitrogen, Carlsbad, CA, USA) was added to the sample, without disturbing the optical settings of the instrument [30]. Fluorescence images were collected at about 20 min after stain addition, using the confocal Raman set-up described above (488 nm excitation, 1 mW laser power) and a dwell time of 0.2 s per datapoint. Figure 5.9c shows the fluorescence image of the HeLa cell stained after staining for mitochondrial distribution, where the bright green areas correspond to a high mitochondria content. The highest Mitotracker fluorescence intensity was observed in the perinuclear region. A comparison of Figure 5.9b and c reveals that the regions, from which significant fluorescence due to the Mitotracker stain is observed, colocalize very well with the salmon-colored and yellow regions of Figure 5.9b.

We have been found [30] that the mean cluster spectra obtained for nuclear, cytoplasmic and mitochondrial regions were too similar to interpret spectral changes reliably. All mean cluster spectra (nucleus, nucleolus, mitochondria-rich and remaining cytoplasm) are dominated by protein bands (the amide I vibration at 1655 cm^{-1}, the extended amide III region between 1270–1350 cm^{-1}, and the sharp phenylalanine ring stretching vibration at 1002 cm^{-1}), which is not surprising, given that the major component in all regions of the cell is protein. The nuclei and nucleoli exhibit a few, weak bands associated with nucleic acids (785, 1095

and 1575 cm^{-1}); although these bands are weak, they are sufficiently reproducible to be detected by HCA.

These results demonstrate that confocal Raman microspectroscopy, when coupled to image reconstruction methods such as HCA, can provide label-free methods for the visualization of intracellular components and processes. This subject will be elaborated further in the next section.

5.3.3.2 Visualization of Mitosis

Previously, it was shown that cellular nuclei could be distinguished from the cytoplasm, but that Raman signals due to DNA are barely visible. This suggests that HCA identifies the nucleus mostly by protein composition (the nuclear proteins differ from cytoplasmic proteins), rather than the actual DNA signal. However, it can be shown that, during certain stages of mitosis, the DNA is so condensed and exhibits such a strong signal that it can be observed relatively easily [31].

For most cell types, mitosis typically lasts for less than 1 h, and can be divided into prophase (chromosome condensation, growth of mitotic spindle and breakdown of nuclear envelope), metaphase (alignment of chromosomes along the 'equator' of the parent cell), anaphase (separation of chromosomes) and telophase (formation of new nuclear membrane around chromosomes). Finally, furrowing and division of the cell takes place during cytokinesis to yield two distinct daughter cells.

Figure 5.10 shows HeLa cells undergoing two of the stages of mitosis, metaphase and anaphase. Figures 5.10a and d show the cells after 4′-6-diamidino-2-phenylindole (DAPI) staining to visualize DNA/chromatin. Figures 5.10b and e show Raman maps of the nucleic acid band intensity at 785 cm^{-1}, normalized with respect to the protein peak, while Figures 5.10c and f depict the protein amide I intensity (1655 cm^{-1}). The protein intensity during mitosis is contributed largely by the microtubules and the dense histone-packed chromatin. Chromosomal condensation during metaphase and anaphase is manifested by a large intensity increase of the DNA-related peaks. The Raman chromatin (DNA) intensities correlate very well with the DAPI fluorescence of chromatin, but were obtained from the inherent Raman of cellular components, rather than from stains. The Raman images reveal the chromatin distribution for the metaphase and anaphase cells in detail [31]. In these stages, the highly condensed DNA produces the most prominent Raman signals.

5.3.3.3 Liposome Uptake into Cells

Apart from imaging subcellular features (as discussed above), Raman imaging may provide an opportunity to follow the uptake of molecules or assemblies into cells. One method of detecting the incorporation of molecules inside cells is to use deuterated compounds [32]. C—D stretching vibrations are shifted away from those of C—H groups by a factor of about the square root of the masses of H and D (a factor of 1.4). Consequently, C—D stretching vibrations will occur at about 2150 cm^{-1}, in a region devoid of any signals in the Raman spectra of cells and cellular components (see Figure 5.11c). The deuterium 'label' is invisible to the cell,

Fluorescence image of DAPI-stained chromatin   **DNA intensity**   **Protein intensity**

Metaphase
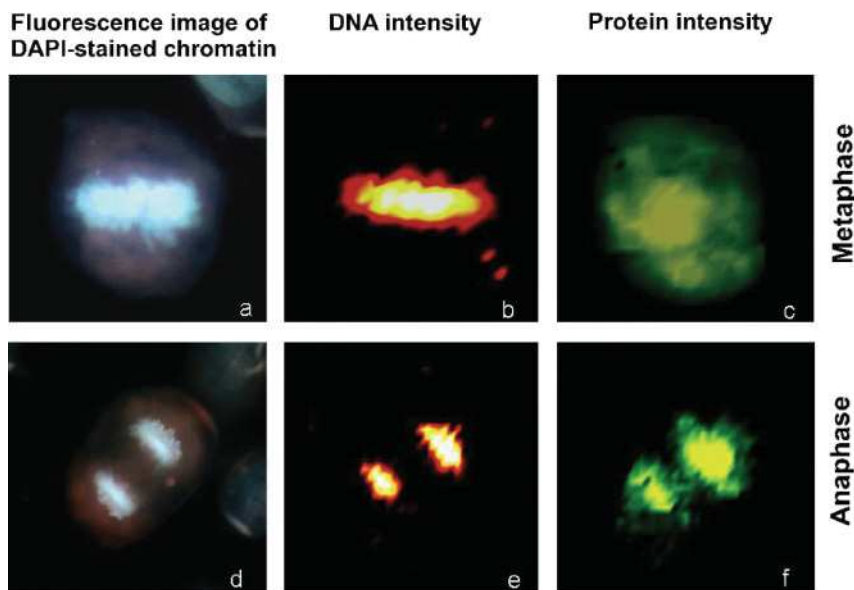
Anaphase

Figure 5.10 (a, d) Fluorescence images (using DAPI stain) of the chromatin distribution of HeLa cells in metaphase (a) and anaphase (d). The cell in (a) measures ca. 25 μm across; (b, e) Distribution of the Raman intensities of DNA-specific bands of the cells shown in (a) and (d); (c, f) Distribution of the Raman intensities of protein bands of the cells shown in (a) and (d).

as it occupies almost exactly the same volume, and acts chemically nearly identically to hydrogen.

This technique was used to investigate the cellular uptake and intracellular fate of lipid-based nanoparticles known as liposomes (Figure 5.11a). Liposomes are bilayer-based nanospheres with sizes that range from about 50 to 300 nm and currently are used for drug-delivery purposes [33], including intracellular drug and gene delivery [34, 35]. Many aspects related to the detailed mechanisms of the interaction of liposomes and cells remain unresolved, and this is especially true for the case of liposomal nanocarriers modified by cell-penetrating peptides, such as the HIV TAT (transcriptional activator-derived) peptide [33]. These carrier systems are currently considered to offer a very promising means of transferring various drugs, including protein and peptide drugs, into cells [36]. Here, we demonstrate the feasibility of Raman imaging to follow the uptake of TAT peptide-modified deuterated liposomes (TATp-LIP).

Deuterated liposomes were prepared from a dried lipid film cast from a chloroform solution of deuterated 1,2-distearoyl-*sn*-glycero-3-phosphocholine (DSPC-d_{70}; Avanti Polar Lipids, Inc., Alabaster, AL, USA; Figure 5.11b) [37, 38]. This film was hydrated and vortexed with HEPES-buffered saline (HBS), pH 7.4, at a DSPC concentration of 1.6 mM. The resulting liposomes were sized through double-stacked 200 nm pore size polycarbonate membranes (Nucleopore), after which the
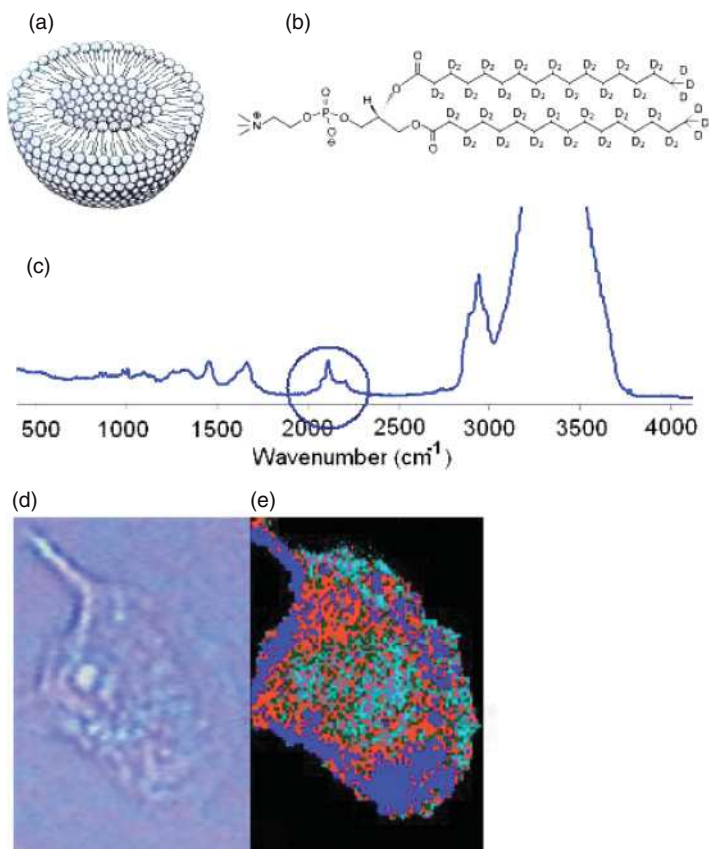
Figure 5.11 (a) Schematic drawing of a liposome; (b) Structure of DSPC-d_{70}; (c) Raman spectrum of cellular region rich in deuterated liposomes; (d) Brightfield image of cell in aqueous medium. The long dimension of the cell is ca. 40 µm; (e) HCA-based pseudocolor map of cell after liposome uptake. The dark blue areas denote regions of highly deuterated phospholipid concentration.

liposome size was determined using a Coulter N4 MD Submicron Particle Size Analyzer (Coulter Electronics). The preparation of TATp-liposomes was reported elsewhere [13].

Human breast adenocarcinoma MCF-7 cells were incubated for different time intervals with deuterated LIP and TATp-LIP at a lipid concentration of 2 mg ml^{-1}. After incubation, the cells were fixed in a phosphate-buffered formalin solution and subsequently washed and submerged in phosphate-buffered saline, to maintain the cell shape within the aqueous environment.

Figure 5.11d shows a microscopic image of an MCF-7 cell incubated with TATp-LIP for 6 h, while Figure 5.11e shows a pseudocolor map constructed from the hyperspectral data set using HCA. The cluster analysis is based mainly on the

detection of the C—D stretching vibrational signal, observed around 2150 cm^{-1}, and shown in Figure 5.11c. Large amounts of the deuterated phospholipids were found in the cell periphery.

The most important result of this study was that Raman microspectroscopy clearly allowed for the observation of lipid particle uptake by the cells. This uptake was enormously accelerated by TATp, thus confirming the results of previous experiments [36]. The uptake was clearly seen after only 3h for TATp-LIP, and after 12h for plain LIP. Although very small deuterated regions can be detected early in an uptake experiment, the aggregation or incorporation of deuterated phospholipids into other membrane structures occurs, and this results in contiguous regions of high deuterium content. To ascertain that the liposomes had been observed *within* the cytoplasm, and not simply adsorbed onto the cell surface, a depth profile (not shown) in the xz-direction was collected; the results did indeed indicate that the deuterated liposomes had penetrated the cell body. The spectral appearances of the C—D stretching region, with respect to band shapes and peak positions, did not change significantly upon uptake, indicating that the lipid side chains had not undergone any substantial conformational changes.

5.4
Conclusions

In this chapter we have presented the results from single cell Raman and infrared microscopic studies, demonstrating the exquisite sensitivity of vibrational spectroscopy to variations in spectral patterns that may be caused by spatial heterogeneity, cell maturation and differentiation, disease and other factors. It is believed that these techniques of will usher in a new era of biological and biomedical studies that rely on the spectral features of unstained cells collected by objective and reproducible measurements. These results may prove invaluable in diverse fields such as cytology and novel cancer screening applications, in cellular biology – including studies defining the uptake and effects of drugs into cells – and also in the identification and classification of microorganisms via spectral methods.

Acknowledgments

References

1 Papanicolaou, G.N. and Traunt, H.F. (1941) Smear diagnosis of carcinoma of the cervix. *Am. J. Obstet. Gynecol.*, **42** (2), 193–206.

2 Stohler, M.H. and Schiffman, M. (2001) Interobserver reproducibility of cervical cytologic and histologic interpretations. *JAMA*, **285** (11), 1500–5.

3 Chiriboga, L., Xie, P., Yee, H., Vigorita, V., Zarou, D., Zakim, D. and Diem, M. (1998) Infrared spectroscopy of human tissue. I. Differentiation and maturation of epithelial cells in the human cervix. *Biospectroscopy*, **4**, 47–53.

4 Diem, M., Romeo, M., Boydston-White, S., Miljkovic, M. and Matthaeus, C. (2004) A decade of vibrational micro-spectroscopy of human cells and tissue (1994–2004). *Analyst*, **129** (10), 880–5.

5 Romeo, M.J., Mohlenhoff, B. and Diem, M. (2006) Infrared microspectroscopy of human cells: causes for the spectral variance of oral mucosa (buccal) cells. *Vib. Spectrosc.*, **42**, 9–14.

6 Boydston-White, S., Romeo, M.J., Chernenko, T., Regina, A., Miljkovic, M. and Diem, M. (2006) Cell-cycle-dependent variations in FTIR micro-spectra of single proliferating HeLa cells: principal component and artificial neural network analysis. *Biochim. Biophys. Acta*, **1758** (7), 908–14.

7 Chan, J.W., Taylor, D.S., Zwerdling, T., Lane, S.M. and Ihara, K. (2006) Micro-Raman spectroscopy detects individual neoplastic and normal hematopoietic cells. *Biophys. J.*, **90**, 648–56.

8 Diem, M., Chiriboga, L., Lasch, P. and Pacifico, A. (2002) IR spectra and IR spectral maps of individual normal and cancerous cells. *Biopolymers*, **67** (4–5), 349–53.

9 Romeo, M.J., Bird, B., Boydston-White, S., Matthäus, C., Miljković, M., Chernenko, T. and Diem, M. (2008) Infrared and Raman microspectroscopic studies of individual human cells, in *Vibrational Spectroscopy for Medical Diagnosis* (eds M. Diem, J.M. Chalmers and P.R. Griffiths), John Wiley & Sons, Ltd, pp. 27–71.

10 Sindhuphak, R., Issaravanich, S.I., Udomprasertgul, V., Srisookho, P., Warakamin, S., Sindhuphak, S., Boonbundarlchai, R. and Dusitsin, N. (2003) A new approach for the detection of cervical cancer in Thai women. *Gynecol. Oncol.*, **90**, 10–14.

11 Wong, P., Wong, R., Caputo, T., Godwin, T. and Rigas, B. (1991) Infrared spectroscopy of exfoliated human cervical cells: evidence of extensive structural changes during carcinogenesis. *Proc. Natl Acad. Sci. USA*, **88**, 10988–92.

12 Lasch, P., Pacifico, A. and Diem, M. (2002) Spatially resolved IR microspectroscopy of single cells. *Biopolymers*, **67** (4–5), 335–8.

13 Matthäus, C., Kale, A., Chernenko, T., Torchilin, V. and Diem, M. (2008) New ways of imaging uptake and intracellular fate of liposomal drug carrier systems inside individual cells, based on Raman microscopy. *Mol. Pharm.*, **5** (2), 287–93.

14 Jackson, M. and Mantsch, H.H. (1995) The use and misuse of FTIR spectroscopy in the determination of protein structure. *Crit. Rev. Biochem. Mol. Biol.*, **30** (2), 95–120.

15 Savitzky, A. and Golay, M.J.E. (1964) Smoothing and differentiation of data by simplified least-squares procedures. *Anal. Chem.*, **36** (8), 1627–39.

16 Kauppinen, J.K., Moffatt, D.J., Mantsch, H.H. and Cameron, D.G. (1981) Fourier self-deconvolution: a method for resolving intrinsically overlapped bands. *Appl. Spectrosc.*, **35** (3), 271–6.

17 Adams, M.J. (2004) RSC Analytical Spectroscopy Monographs, in *Chemometrics in Analytical Spectroscopy*, 2nd edn (ed. N.W. Barnett), Royal Society of Chemistry, Cambridge.

18 Wood, B.R., Chiriboga, L., Yee, H., Quinn, M.A., McNaughton, D. and Diem, M. (2004) Fourier transform infrared (FTIR) spectral mapping of the cervical transformation zone, and dysplastic squamous epithelium. *Gynecol. Oncol.*, **93** (1), 59–68.

19 Ward, J.H. (1963) Hierarchical grouping to optimize an objective function. *J. Am. Stat. Assoc.*, **58** (301), 236–44.

20 Romeo, M., Mohlenhoff, B., Jennings, M. and Diem, M. (2006) Infrared micro-spectroscopic studies of epithelial cells. *Biochim. Biophys. Acta*, **1758** (7), 915–22.

21 Mohlenhoff, B., Romeo, M.J., Diem, M. and Wood, B.R. (2005) Mie-type scattering and non-Beer-Lambert absorption behavior of human cells in infrared microspectroscopy. *Biophys. J.*, **88** (5), 3635–40.

22 Bird, B., Romeo, M., Diem, M., Bedrossian, K., Laver, N. and Naber, S. (2008) Cytology by infrared micro-spectroscopy: automatic distinction of cell

types in urinary cytology. *Vib. Spectrosc.*, **48** (1), 101–6.

23 Rathert, P., Roth, S. and Soloway, M.S. (1991) *Urinary Cytology, Manual and Atlas*, 2nd edn, Springer Verlag, New York.

24 Brunzel, N.A. (1994) *Fundamentals of Urine and Body Fluid Analysis*, W. B. Saunders Company, Philadelphia.

25 Bibbo, M., Bartels, P.H., Chen, M., Harris, M.J., Truttman, B. and Wied, G.L. (1975) The numerical composition of cellular samples from the female reproductive tract. I. carcinoma in situ. *Acta Cytol.*, **19** (5), 438–47.

26 Bibbo, M., Bartels, P.H., Chen, M., Harris, M.J., Truttman, B. and Wied, G.L. (1976) The numerical composition of cellular samples from the female reproductive tract. II. Cases with invasive squamous carcinoma of the uterine cervix. *Acta Cytol.*, **20** (3), 249–54.

27 Bibbo, M., Bartels, P.H., Chen, M., Harris, M.J., Truttman, B. and Wied, G.L. (1976) The numerical composition of cellular samples from the female reproductive tract. III. Cases with mild and moderate dysplasia of the uterine cervix. *Acta Cytol.*, **20** (6), 565–72.

28 Scalfi-Happ, C., Jauss, A., Hollrichter, O., Fulda, S., Hauser, C., Steiner, R. and Rueck, A. (2007) Confocal Raman microscopy for investigation of the level of differentiation in living neuroblastoma tumor cells. Confocal, multiphoton, and nonlinear microscopic imaging III (eds T. Wilson and A. Periasamy), Proceedings of SPIE-OSA Biomedical Optics, Vol. 6630.

29 Scalfi-Happ, C., Jauss, A., Ibach, A., Hollrichter, O., Fulda, S., Hauser, C., Steiner, R. and Rueck, A. (2007) Confocal Raman microscopy as a diagnostic tool for investigation of living neuroblastoma tumour cells. *Med. Laser Appl.*, **22** (3), 157–64.

30 Matthäus, C., Chernenko, T., Newmark, J.A., Warner, C.M. and Diem, M. (2007) Label-free detection of mitochondrial distribution in cells by nonresonant Raman micro-spectroscopy. *Biophys. J.*, **93**, 668–73.

31 Matthäus, C., Boydston-White, S., Miljković, M., Romeo, M.J. and Diem, M. (2006) Raman and infrared microspectral imaging of mitotic cells. *Appl. Spectrosc.*, **60** (1), 1–8.

32 van Manen, H.J., Kraan, Y.M., Roos, D. and Otto, C. (2005) Single-cell Raman and fluorescence microscopy reveal the association of lipid bodies with phagosomes in leukocytes. *Proc. Natl Acad. Sci. USA*, **102** (29), 10159–64.

33 Gupta, B., Levchenko, T. and Torchilin, V.P. (2005) Intracellular delivery of large molecules and small particles by cell penetrating proteins and peptides. *Adv. Drug Deliv. Rev.*, **57**, 637–51.

34 Serpe, L., Guido, M., Canaparo, R., Muntoni, E., Cavalli, R., Panzanelli, P., Della, P., Bargoni, C., Mauro, A., Gasco, A., Eandi, M.R., Zara, M. and G.P. (2006) Intracellular accumulation and cytotoxicity of doxorubicin with different pharmaceutical formulations in human cancer cell lines. *J. Nanosci. Nanotechnol.*, **6** (9–10), 3062–9.

35 Rao, N.M. and Gopal, V. (2006) Cell biological and biophysical aspects of lipid-mediated gene delivery. *Biosci. Rep.*, **26** (4), 301–24.

36 Wadia, J.S. and Dowdy, S.F. (2005) Transmembrane delivery of protein and peptide drugs by TAT-mediated transduction in the treatment of cancer. *Adv. Drug Deliv. Rev.*, **57** (4), 579–96.

37 Dipali, S.R., Kulkarni, S.B. and Betageri, G.V. (1996) Comparative study of separation of non-encapsulated drugs from liposomes by different methods. *J. Pharm. Pharmacol.*, **48** (11), 1112–15.

38 Liang, W., Levchenko, T.S. and Torchilin, V.P. (2004) Encapsulation of ATP into liposomes by different methods: optimization of the procedure. *J. Microencapsul.*, **21**, 151–61.

6
3-D Imaging of Biomedical Samples

Don McNaughton, Bayden R. Wood, Timothy C. Cox, Jörg-Detlef Drenckhahn, and Keith R. Bambery

6.1
Introduction

Fourier transform infrared (FT-IR) microspectroscopy has been investigated for a number of years, and shown to be useful in the understanding, diagnosis and monitoring of a wide range of disease states. The major emphasis has been on cancers, including tumors of the cervix, breast, colon, liver, skin, lung and brain. Much of the progress made to date was outlined in a recent review that highlighted the current extent of the field [1]. Most of these cancer studies have focused on using single point spectroscopy, either with synchrotron IR sources [2] to approach diffraction-limited resolution, or in the laboratory with larger apertures. For tissue samples, point-to-point raster mapping, followed by chemometric manipulation to present the data as images, has been developed in an attempt to extend visible pathology into molecular-based pathology. Although this methodology has shown much promise, with an excellent correlation between the infrared images and those sections stained for pathology, the time involved in obtaining sufficient data is prohibitive [3]. However, with the advent of focal plane array (FPA) [4] and linear array-based imaging spectrometers capable of rapidly obtaining IR hyperspectral maps of thin tissue sections at close to diffraction-limited resolution, this data collection 'bottleneck' has been overcome. Today, these rapid spectroscopic imaging systems provide a basis for the further development of IR spectroscopy as a tool in the diagnosis and monitoring of pathological changes and disease progression in cells and tissue. The detailed contents of Chapters 3 and 4 of this book, when combined with the results of our studies on cervical cancer imaging [5], together outline the methodology and application of this two-dimensional (2-D) imaging approach, which at present is restricted to 4 to 8 µm-thick sections of tissue such that the extent and penetration of disease or tissue degeneration cannot easily be determined.

It follows that the acquisition of such information will require the ability to generate and manipulate three-dimensional (3-D) images of body parts or tissue sections, and indeed a number of powerful ways to achieve this have been devised.

Currently, the conventional methods for obtaining the contrast required for such 3-D imaging include computed tomography (CT), positron emission tomography (PET), magnetic resonance imaging (MRI) and 3-D ultrasound. In addition, X-ray-based techniques are becoming increasingly useful, especially when coupled with powerful coherent X-ray sources such as synchrotrons, where phase contrast- and diffraction-enhanced imaging provide remarkably clear and informative images [6, 7]. The fluorescence 3-D imaging of tissue sections is also currently undergoing development [8]. While each of these techniques provides contrast based on physical changes or on the introduction of markers, rather than on the existence of inherent molecular markers, vibrational spectroscopy-based techniques can supply direct information with regards to macromolecular composition in the image contrast. Hence, 3-D IR imaging would provide a useful and novel alternative, with the advantages of image contrast being based directly on the underlying macromolecular composition. Although the lack of penetration of mid-IR radiation into the tissues precludes any real-time imaging of whole samples, an alternative would be to build a composite from the 2-D images of adjacent sections of tissue, thus providing a method by which to gauge the extent and penetration of disease, and this may indeed be of clinical value. Moreover, such an approach has the advantage of not requiring a chemical or immunological staining protocol to provide biochemical information.

Unfortunately, the available knowledge in this area to date is extremely sparse, with only one report of 3-D imaging from IR having been presented by Wood *et al.* [9] on univariate and multivariate imaging of cervical sections, and another by Mendelsohn and coworkers [10], who constructed a 3-D univariate map of cortical bone based on the peak ratios from serial 2-D sections. In this chapter, while aiming to expand the current knowledge of the field, we outline the technique of 3-D IR image construction and highlight its achievements to date. But, more importantly, we also indicate the direction in which 3-D imaging is heading.

6.2
Methodologies

6.2.1
Sample Preparation and Spectroscopy

In these studies, fixed tissue samples were embedded in paraffin blocks and sliced using a microtome into 4 μm-thick sections. Although other groups, when preparing for 2-D imaging, have also used cryo-sectioning or fixation with glutaraldehyde, we find the standard protocols for pathology sectioning to be the most straightforward, provided that the paraffin is totally removed (otherwise, bands due to its presence are noted in the spectrum). The paraffin is removed by washing with xylene, the major drawback being the consequent removal of accessible lipid. Multiple adjacent sections are de-paraffinized and then mounted on Kevley 'low-e' IR reflective microscope slides and imaged with a Varian Stingray FT-IR micro-

scope system equipped with a 64×64 pixel HgCdTe liquid nitrogen-cooled FPA with a 15× Cassegrain objective. FT-IR hyperspectral data images were recorded in the range 4000–950 cm^{-1} at 6 cm^{-1} resolution, and with 16 scans co-added. For the adenocarcinoma tissue example described below and shown in Figures 6.1 and 6.2, step-motion control of the microscope stage was used to construct a 16-tile (4×4) FT-IR image mosaic from FPA recordings collected as 16-pixel aggregates. Thus, the lateral resolution obtained was approximately 22 μm per pixel aggregate. Each FT-IR image was therefore 2.0 mm^2 in area and with four 4 μm-thick adjacent sections, giving a total sampled volume of $1400 \times 1400 \times 16$ μm. A lateral resolution of 22 μm per pixel was used because this provided FT-IR images that covered an area of tissue large enough to encompass several examples of anatomically different tissue types within the sample. For the mouse heart section (five adjacent sections) and the chick face (16 sections), a similar procedure was used but with sufficient sample area selected to encompass each whole cross-section of the organ. In each case, occasional adjacent sections were mounted on glass slides and stained with the routine histopathology stain hematoxylin and eosin (H&E) for comparative light microscope examination. Hematoxylin has an affinity with nucleic acids, and eosin for the cellular cytoplasm.

6.2.2
Univariate and Multivariate Image Construction

Using a MATLAB routine developed by our group, simple 3-D univariate images can be derived by simply stacking sections color-coded for absorbance at a particular wavenumber (chemimages) vertically in a block. These blocks can then be cut vertically or horizontally to interrogate the tissue architecture. These crude 3-D images can be useful for determining the extent of pathological structure, however multivariate-based methods can provide additional information. The following discussion uses a four-section sample as an example of how the data can be treated, and the same general techniques have been applied to the other samples. For multivariate analysis, the four FT-IR images were stitched together side-by-side (or 'unfolded') using a MATLAB routine developed by our group [9], to produce a single large 2-D image frame which was then imported into Cytospec, a purpose-built spectroscopic imaging tool that includes preprocessing tools and univariate and multivariate imaging routines [11]. The absorbance was integrated over a large spectral region (1750–950 cm^{-1}) to assess sample thickness, using a routine in Cytospec; a spectrum was rejected if the determined integration value was higher or lower than a predefined threshold (1500 and 50 arbitrary units). This avoided inaccuracies from including too-thin portions of the samples with low absorbance, or those with too-high absorbance that suffered from a nonlinear detector response. Spectra that passed the thickness quality test were converted to second-derivative spectra using a Savitsky–Golay algorithm (13 smoothing points). Unsupervised Hierarchical Clustering Analysis (UHCA) is a rapid, nonsubjective analytical method for the identification of spectroscopically distinct anatomical features [3, 12]. UHCA (D values, Ward's algorithm) was performed to generate four clusters
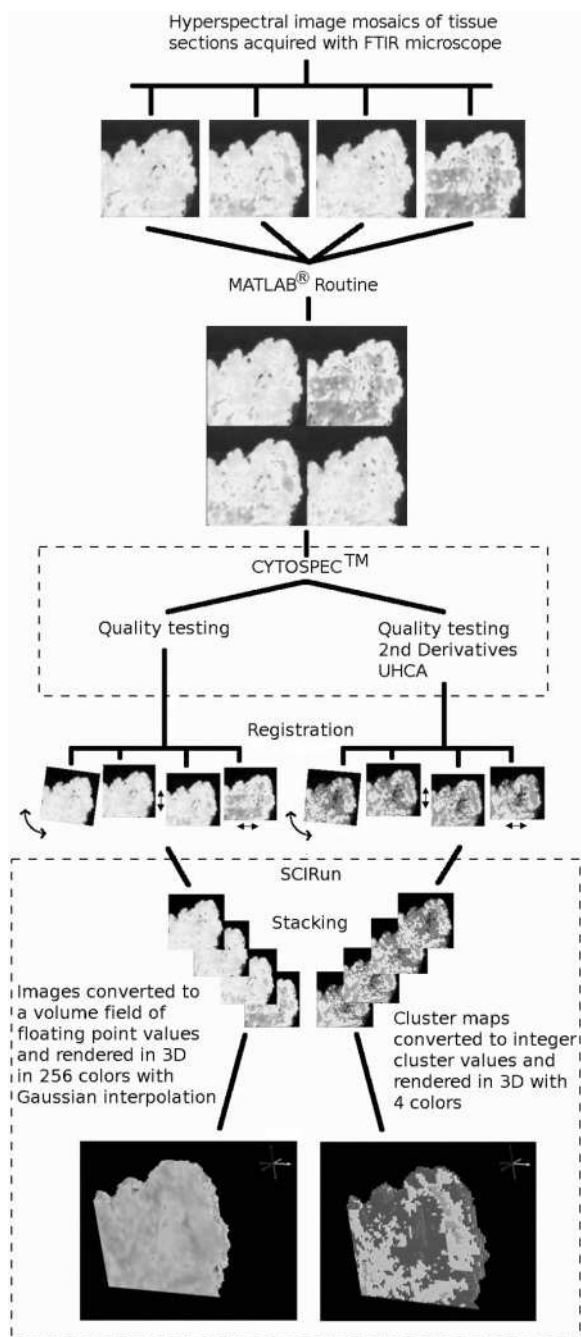
Figure 6.1 Schematic showing steps in the construction of 3-D FT-IR multivariate images.
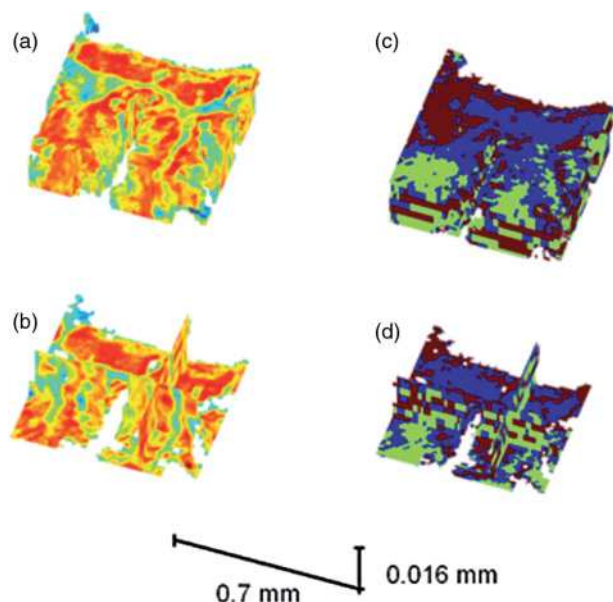
Figure 6.2 (a) Chemimage (amide I intensity) block constructed from four adjacent sections of monkey gut; (b) Sections through the block in (a); (c and d) UHCA-constructed block images of the same data.

from the second-derivative spectra over the 1272–950 cm^{-1} spectral window. The resultant cluster map was then reorganized (or 'back-folded') into the four individual 2-D cluster maps, each of which corresponded to one of the FT-IR images. These individual maps could then be stacked in the same fashion as the chemimages, using a MATLAB routine to provide images that can be sliced vertically or horizontally.

In order to generate more easily manipulated 3-D images, the four cluster maps were saved in an image file format with a unique false color assigned to each cluster and then aligned or 'registered' as separate floating layers of a single image in the GNU Image Manipulation Program (GIMP) [13]. This registration step is necessary because the sample orientation is not identical in both rotation and translation on each of the four acquired 2-D mosaic images. Proper pixel correspondence from one image to another was easily achieved using this manual approach, given the small number of image layers. The registered layers constituted a best fit because some slightly unequal distortion of the tissue matrix was observed, presumably caused by the sectioning and preparation processes. For this 3-D imaging technique, special care must be taken to ensure that the sections are not stretched or distorted when deposited onto the slides. For the cervical, heart and chick face samples, SCIRun [14] was used to generate the 3-D cluster images. The SCIRun software suite provides a graphical user interface for the rapid

development of 'networks' of instruction routines for the stacking and rendering of the input data. The registered images were loaded into SCIRun as a set of indexed integer values (one to four, corresponding to each cluster) and then 'stacked' into a scalar volume field of cluster values from which the 3-D cluster maps were rendered. 3-D univariate chemical maps depicting a single spectral feature were also generated. The spectra were first vector-normalized over the $1800–950\,cm^{-1}$ range, and the integrated absorbance under the band of interest then generated using a trapezoidal baseline function in Cytospec. The 3-D univariate maps were rendered from a scalar volume field of absorbance values generated from 2-D images stacked in SCIRun. The 3-D univariate maps were plotted with a 256 rainbow color palette using Gaussian interpolation between the data grid points to produce a smoothly varying color field. The 3-D cluster maps, on the other hand, were plotted in a palette of only four false colors and box-interpolated, with one false color corresponding to each cluster. Figure 6.1 depicts a schematic of the overall process from spectral acquisition to 3-D image reconstruction.

6.2.3
Artificial Neural Network Image Construction

The construction of UHCA images is a time-consuming and computer-intensive procedure for which a wide variety of alternative methods have been explored for its achievement. The most promising of these is the use of artificial neural networks (ANNs), which are computational models inspired by biological decision-making structures such as the brain. An ANN is a nonlinear adaptive-learning information processing system comprised of an interconnected network of functional computing elements that are usually referred to as 'neurons', after the cells of the nervous system and brain. ANNs have the ability to learn through adapting to accumulated knowledge of the classification question being posed. During learning, ANNs modify their own network topology by adjusting weights that act on the individual neuron's interconnections. In this way, ANNs mimic the strengthening and weakening of synaptic pathways, as occurs in the human brain during the learning process. Because ANNs are able to learn, they are a considered to be a supervised multivariate data analysis tool rather than an unsupervised multivariate classifier such as UHCA. ANNs are able to solve classification and pattern recognition problems from real nonlinear systems, where the statistical variation is not a simple sum of the information components or their multiples.

As noted below, in Section 6.3.2.1, in order to perform 3-D imaging using UHCA it is necessary to perform the analysis on the entire data set simultaneously. UHCA on a data set larger than 20 000 spectra is currently not feasible due to personal computer-addressable memory size limits and time constraints. Thus, to enable multivariate imaging beyond this limit, we have employed ANN for tissue type classification. However, prior to modeling the data set with ANN, UHCA may be gainfully employed to assess the range of spectral variation contained within individual 2-D images of selected tissue sections. Since UHCA is also very effective

for differentiating different anatomical and histopathological features in tissues, preprocessing with UHCA allows collections of spectra to be exported from each cluster, and these can then serve as input spectra for training and optimizing an ANN model [15].

The data preprocessing of FT-IR hyperspectral image data for ANN imaging essentially follows the same steps as described above for the UHCA multivariate image construction, except that the stitching, folding and back-folding steps are omitted. The 2-D FT-IR images from each tissue section are individually imported into CytoSpec, quality assessed for sample thickness, and then converted into second-derivative spectra as before. The members of a computationally manageable subset of these images are then individually processed with UHCA, and the resultant 2-D cluster maps compared with the H&E-stained sections. Sample spectra are extracted from those clusters that represent spectroscopically and anatomically distinct tissue types (i.e., unidentifiable and 'noise' clusters are rejected from further analysis at this point). These extracted spectra are then used to train an ANN model.

An ANN analysis was performed using the NeuroDeveloper 2.5b software [16]. Feed-forward neural networks were trained using the resilient back propagation (Rprop) algorithm. The NeuroDeveloper software allows development of networks that can solve multiclass classification problems, a necessary condition for generating ANN images when more than two classes of spectra are to be identified in the samples. The extracted spectra were split into two sets — a training set and a validation set — to monitor and stop the training before network overtraining occurred. During the training, the network layout was optimized by testing varying numbers of neurons in the input and hidden layers for the lowest training and validation data set errors.

CytoSpec software was employed to generate a 2-D ANN image for every tissue section calculated from the fully trained NeuroDeveloper ANN model. In the final step, the 2-D images are provided as inputs for the SCIRun software to render the completed 3-D ANN image.

6.3
Resultant 3-D Images

6.3.1
Chemimage and UHCA Stack Plots

Figure 6.2 shows a 3-D block image generated from four adjacent sections of monkey gut tissue. Figures 6.2a and b are chemimages where the color code is based on the absorbance value of the amide I band, with red (as usual) being the highest absorbance. In Figure 6.2a the gut villi can easily be seen projecting into the tissue block. Figure 6.2b shows how the stack plot can be cut both vertically and horizontally to show the internal tissue architecture. Figures 6.2c and d show stack plots based on a three- cluster UHCA, with the three clusters corresponding

to the epithelial cells, secretory cells and underlying connective tissue, respectively. The vertical and horizontal cuts in Figure 6.2d show how the cell structure within the sample varies with depth.

6.3.2
3-D Chemimage and UHCA Images

6.3.2.1 Cervical Adenocarcinoma

Figure 6.3 shows a H&E-stained 2-D cervical section exhibiting a relatively rare form of neoplasm known as villoglandular adenocarcinoma. The sample from which this section was taken serves as an ideal model for 3-D UHCA because it exhibits a variety of anatomical and histopathological features, including connective tissue, red blood cells, inflammatory exudate and glandular cells. The neoplasm is characterized by the presence of long villous fronds and papillae lined by columnar cells with intact cytoplasmic borders, and also displays minimal atypia [17]. Spherical clusters of cells with smooth intact communal cytoplasmic rings are also associated with this condition. Figure 6.4a depicts a chemical map generated from all four sections simultaneously by integrating the area under the band in the region associated mainly with phosphodiester contributions from nucleic acids (1275–1190 cm^{-1}). The chemical maps show a good correlation with morphology; however, specific correlations with anatomical and histopathological features cannot be gauged with this form of processing.

It is necessary to perform UHCA over the entire set of spectra collected to fully characterize the range of spectral variations through all the tissue sections. Performing separate UHCA on each individual tissue section would provide a different clustering result due to changes (though generally small) in the biochemical
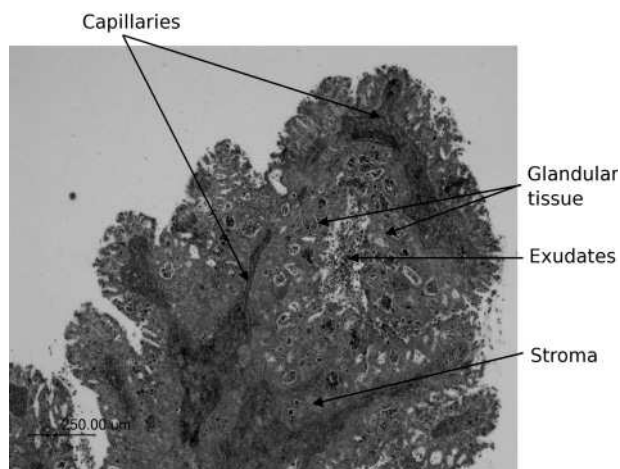
Figure 6.3 Light microscopy image of a labeled H&E-stained cervical section exhibiting villoglandular adenocarcinoma.
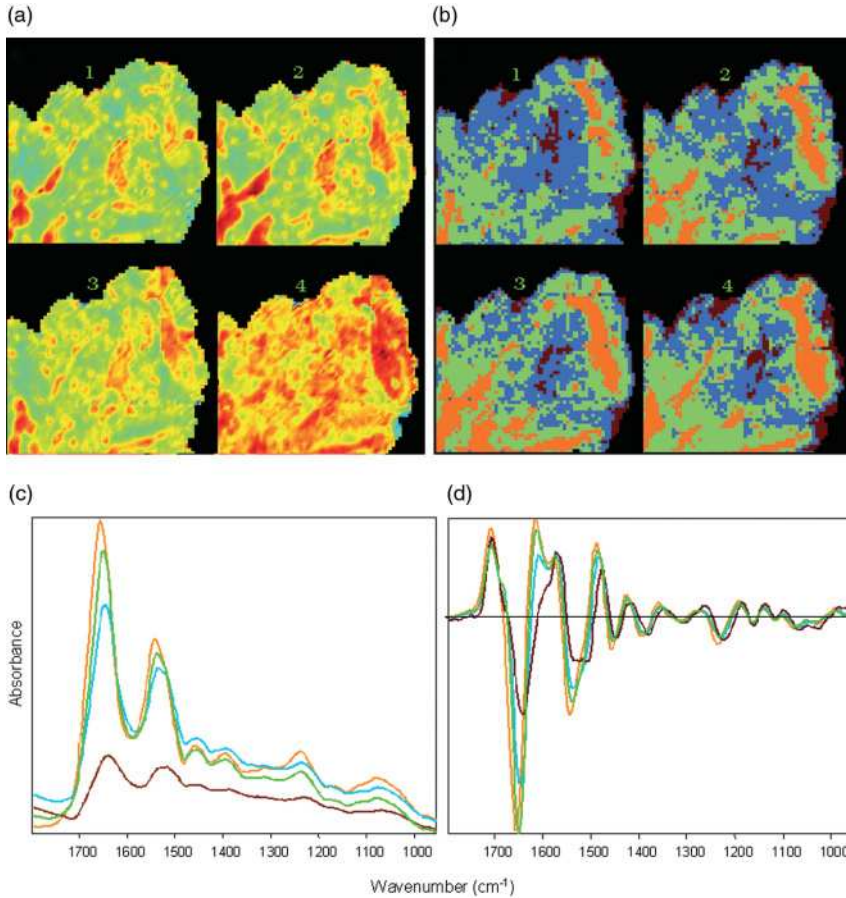
Figure 6.4 Hyperspectral FT-IR data processing performed simultaneously on four adjacent tissue sections from a cervical biopsy sample. The numbers 1 to 4 identify the individual sections in the figure. (a) A univariate chemical image obtained from the integrated area under the 1275–1190 cm^{-1} region after baseline subtraction; (b) A four-cluster map derived from analysis over the 1272–950 cm^{-1} spectral window. The cluster map false color scheme corresponds to brown for exudates, blue for inflamed glandular tissue, green for connective tissue and orange for blood-filled capillaries; (c) The four cluster average FTIR spectra are presented color-coded to match the clusters in panel (b); (d) The same four cluster spectra are presented but processed as second-derivative spectra.

composition between sections. For this reason, the images were 'stitched' together into a single frame to enable spectral preprocessing and UHCA was then performed in CytoSpec on all spectra from all images simultaneously. UHCA was performed on the 1272–950 cm^{-1} region on second-derivative, vector-normalized spectra simultaneously on four adjacent sections, and the resultant cluster maps are displayed in Figure 6.4b. The cluster maps show a general similarity, as might

be expected, and successfully highlight the major anatomical features. The orange cluster represents red blood cells embedded in the stromal matrix, the light green cluster is predominately stroma, and the brown is mainly lymphocyte exudates. The blue cluster is predominantly glandular tissue. In tissue sections 3 and 4 of Figure 6.4b there is an increase in the area of connective tissue (green cluster) relative to glandular tissue (blue cluster) when compared to sections 1 and 2; this indicates a penetration of the glandular tissue into the connective layer.

Figures 6.4c and d show the raw and second-derivative mean extracted spectra, color-coded in the same fashion as the clusters in Figure 6.4b. The maps and corresponding spectra are very similar for each section, indicating that the biochemistry between the adjacent sections is consistent. The spectra exhibit dramatic changes in the amide I mode, both in terms of band width and position. The peak center varies from approximately 1643 to $1659 \, cm^{-1}$; such variation is attributed to physical–chemical changes in the tissue matrix. Dramatic variation occurs in the areas of thin tissue and on the periphery of tissue sections, with the net result being a shifting of the amide I mode along with a concomitant increase in the amide II:amide I ratio. This effect is clearly observed in the mean extracted spectrum from the brown cluster, which shows the amide I mode appearing at $1643 \, cm^{-1}$ and an amide II:amide I ratio that is much greater for this spectrum when compared to the other spectra. Such strong distortions and shifts in band shape were recently addressed by Romeo *et al.* [18], who reported a method to correct for the 'dispersion artifact'. To minimize correlations with physical information, the analysis was carried out using the $1272–950 \, cm^{-1}$ region, which omits the proteinaceous range ($1720–1380 \, cm^{-1}$) that may be strongly distorted by the dispersion artifact. Spectra from lymphocyte exudates and glandular tissue are dominated by a band at $\sim 1240 \, cm^{-1}$ which is assigned to the anti-symmetric phosphodiester stretching vibration of nucleic acids. This band shows the most variation between all four mean extracted cluster spectra. The mean extracted spectrum from the stromal areas (light green) includes contributions from collagen vibrations, although the distinctive collagen triplet in the $1300–1200 \, cm^{-1}$ cannot be observed due to infiltration by red blood cells, lymphocyte exudates and glandular tissue into the connective layer.

The 3-D chemical image constructed from four adjacent sections and generated by integrating the area underneath the peaks in the $1272–950 \, cm^{-1}$ region is presented in Figure 6.5. In Figure 6.5a, the image is orientated to show the first section of the tissue block (section 1) while in Figure 6.5b the last section (section 4) is oriented towards the viewer. The darkest orange areas in section 1 (Figure 6.5a) correlate well with the stroma and glandular tissue, while the darkest orange area shown in section 4 (Figure 6.5b) is associated mainly with the stroma.

Figure 6.6 shows a 3-D UHCA map performed on the four sections simultaneously. The map shows excellent correlation with the anatomical and histopathological features indicated in Figure 6.3. The cluster colors are the same as those used in Figure 6.4b. The 3-D UHCA map enables one to visualize the extent of penetration of the anatomical features, and also the degree of variation from section to section (a movie of this section is available on the website in our

(a)　(b)

250 μm
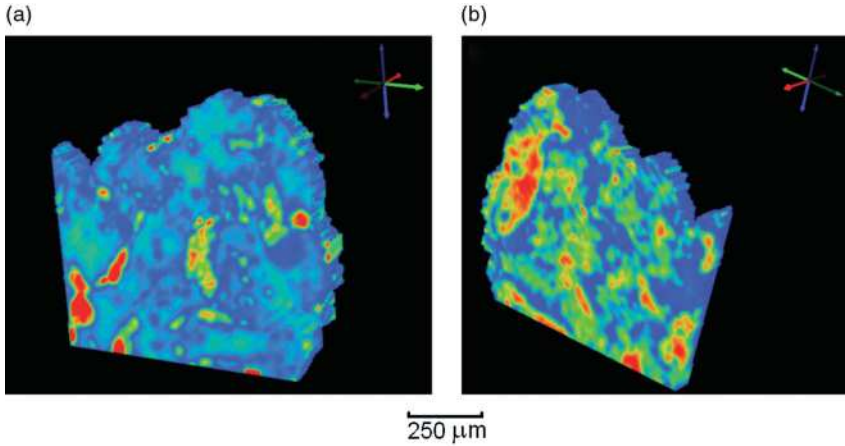
Figure 6.5 Two views of a 3-D univariate chemical map plotting integrated absorbance over the spectral region 1275–1190 cm^{-1}, after baseline correction. Red indicates areas of highest absorption, blue indicates areas of lowest absorption. The view is looking toward the section 1 side of the sampled volume in (a) and towards the section 4 side in (b).

(a)　(b)

250 μm
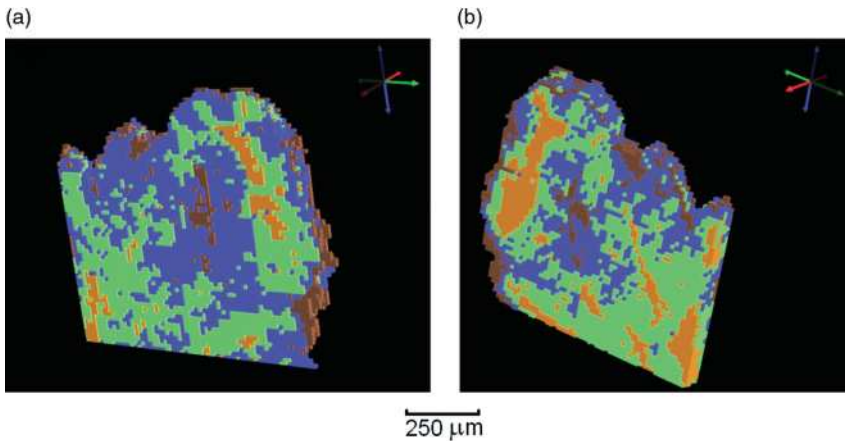
Figure 6.6 Two views of 3-D cluster maps for four clusters obtained from analysis in the 1272–950 cm^{-1} spectral region. In the cluster map false color scheme, brown corresponds to exudates, blue to inflamed glandular tissue, green to connective tissue, and orange to blood-filled capillaries (as in Figure 6.4b). The view is looking toward the section 1 side of the sampled volume in panel (a) and towards the section 4 side in panel (b).

Biomedical Central article [9]). Moreover, 3-D FT-IR multivariate processing enables the visualization of thick tissue sections that cannot normally be analyzed using conventional mid-IR spectroscopic techniques, due to the limited depth penetration of IR radiation. The thin sections (4 μm) required for use with the Kevley slides are less than the thickness of a single cervical cell; consequently, the

(a) (b)

250 µm
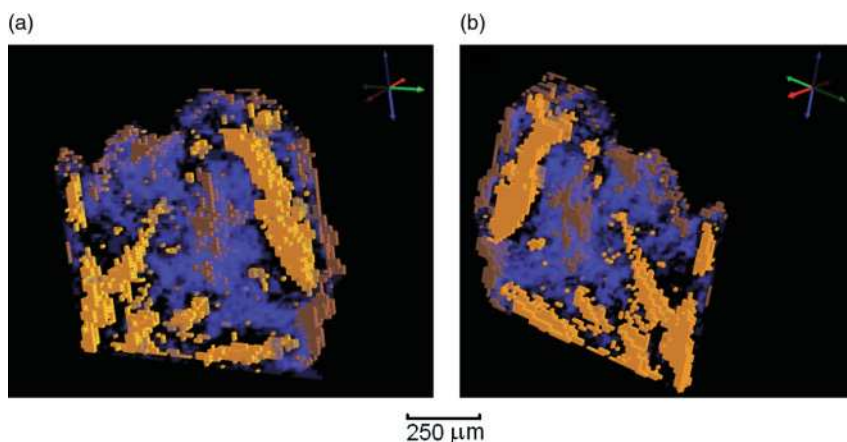
Figure 6.7 Two views of 3-D cluster maps identical to the maps in Figure 6.6, but with the stroma cluster removed from the plot and with glandular tissue now depicted in semi-transparent blue. The view is looking toward the section 1 side of the sampled volume in (a) and towards the section 4 side in (b).

use of multiple sections not only enables the analysis of whole cells but also minimizes the effects of orientation artifacts that can arise during tissue sectioning. Individual clusters can be studied by rendering the image in semi-transparent mode. Figure 6.7 is identical to Figure 6.6, but with the stroma cluster removed from the plot and with glandular tissue now depicted in semi-transparent blue. By making the image semi-transparent, it is possible to visualize clusters in the center of the 3-D FT-IR image and examine the shape and penetration of important anatomical and histopathological features (a movie of this section is available on the website in our Biomedical Central article [9]).

The time required to acquire and compile 3-D FT-IR univariate images is dependent on the following steps:

- Approximately 10 min to acquire each 2-D FT-IR image from each individual tissue section.

- A 2 min period to run the MATLAB stitching program.

- Registration of the images was performed 'by hand' in this study and was, consequently, quite time-consuming; however, it is envisioned that suitable software could be developed to automate the registration process, thereby reducing the time required for this to a few minutes.

- About 1 min is required for SCIRun to stack, interpolate and render a single 3-D image frame.

If a routine data-handling pipeline were to be developed, then it should allow a 3-D univariate image to be obtained in less than 1 h from commencement of

sample scanning on the FT-IR microscope stage. In approximately 1 h, SCIRun can additionally generate 3-D movies composed of a few hundred individual 3-D image frames. The production of 3-D UHCA cluster map images is, unfortunately, a significantly slower process, as UHCA is computationally intensive and requires a time of approximately 2 h (Pentium 4, 3.4 GHz, Hyper-Threading, 2 GB RAM) for the processing of four FT-IR images stitched together. The compilation of UHCA 2-D maps from large collections of tissue sections would be prohibitively slow for the current technique to have any value as a rapid diagnostic technique.

6.3.2.2 Adult Mouse Heart

The above-described information relating to cervical sections shows how the 3-D imaging can provide a powerful technique for examining the penetration of histopathological features. Hence, in order to demonstrate its power in examining an organ, we obtained a longitudinal section sample of an adult mouse heart. Research into the origins and prevention of heart disease requires a detailed understanding of the molecular chemistry of the heart tissue matrix. Heart tissue is comprised predominantly of cardiac muscle cells (cardiomyocytes) which contain the contractile assembly of sarcomere proteins and are also rich in mitochondria. The inner lining of the myocardium towards the lumen of the ventricles and atria is composed of a thin layer of endothelial cells – the endocardium – which are noncontractile cells with a low protein content. Similarly, the ventricles and atria are surrounded by the so-called epicardium, a sheet of epithelial cells separated from the myocardium by a thin layer of fibrotic tissue.

The sample was sectioned into five slices, after which FPA images were obtained in the same manner as described above, and 3-D chemimages constructed using SciRun. Figure 6.8a shows a static, full longitudinal section chemimage based on the integrated absorbance of the amide I peak; in Figures 6.8b and c the same image is rotated clockwise by 45° and 135°, respectively. The 3-D images show the basic anatomy of the adult mouse heart very well, with the major feature in the longitudinal section being the left ventricle (right-hand side of Figure 6.8a) composed of tissue with a high protein content (red). The right ventricle, parts of the right and left atria, and the base of the aorta are also discernible. Figures 6.8d–f show the same views, but with the weak amide I signals removed, whilst Figures 6.8g–i show views with only the strongest amide I signals remaining. It is apparent from these images that areas of high and low protein concentration can be spatially located within the mouse heart. Regions of low protein concentration (blue) correspond to areas of noncontracting cells, namely the endocardium and epicardium, as well as fibrotic tissue surrounding the aorta. In contrast, areas of high protein concentration (red) are associated with the contractile myocardial tissue. However, the myocardium is composed not only of cardiomyocytes but also contains various interstitial cell types such as fibroblasts, endothelial and smooth muscle cells of the myocardial vasculature and undifferentiated stem and progenitor cells. A preliminary UHCA failed to clearly distinguish between these different cell types, although a full analysis has not yet been carried out. However, the FT-IR 3-D imaging technique shows real potential as a method for investigating the
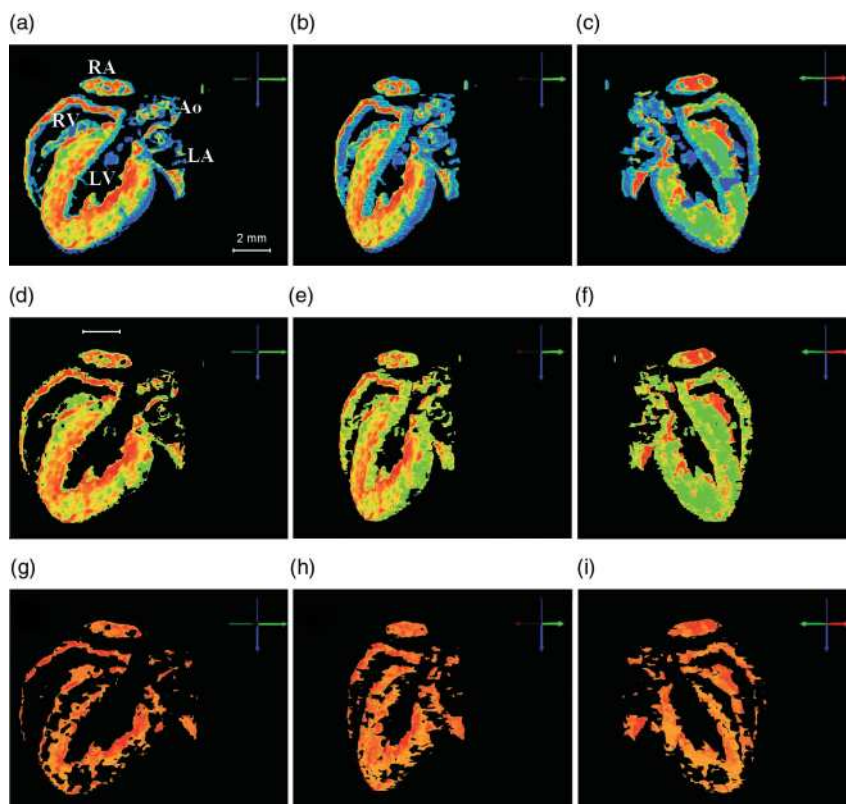
Figure 6.8 Nine views of 3-D chemimages based on the amide I peak, showing different protein concentrations within the adult mouse heart. (a) Full longitudinal section image (abbreviations: LV = left ventricle, RV = right ventricle, LA = left atrium, RA = right atrium, Ao = aorta); (b) Rotated clockwise by 45°; (c) Rotated 135°; (d–f) As for (a–c), but with the lowest protein absorbance values removed; (g–i) As for (a–c), but with only the highest protein absorbance values retained.

extent and/or severity of cardiac disease; it is also possible that even the progenitors of heart disease may be measured as changes in myocardial tissue composition. For example, myocardial fibrosis (i.e., the replacement of cardiomyocytes by fibrotic tissue) is a common pathological finding in various cardiac diseases, with the degree of fibrosis often correlating to the reduction in cardiac function. Furthermore, cardiac ischemia and myocardial infarction results in the loss of contractile tissue which is replaced by a fibrotic scar, the extent and localization of which significantly determines the resultant impairment of cardiac function. Therefore, a FT-IR-based 3-D reconstruction of the scar tissue might assist in the evaluation of cardiac performance following myocardial ischemia. Finally, metabolic diseases (e.g., mitochondrial dysfunction, glycogen storage diseases or cardiac deposition of pathological components) often first result in mild changes in the cardiac tissue matrix before causing more severe symptoms of cardiac dysfunction.

Hence, FT-IR might be valuable not only in the early diagnosis but also ultimately in the treatment of these deadly conditions, thus reducing morbidity rates.

6.3.2.3 3-D ANN Images

Figure 6.9a shows three views of an embryonic chick face (stained with ethidium bromide), with the images taken under a fluorescence dissecting microscope. For FT-IR imaging, 4 μm-thick microtome sections were obtained from an equivalent-age chick embryo. From a series of 16 sections, FT-IR hyperspectral 2-D images were collected using a PerkinElmer Spectrum Spotlight FT-IR microspectrometer at 4 cm^{-1} spectral resolution and a lateral resolution of 25 μm. Figure 6.9b shows a white-light micrograph of one of the sections which was FT-IR imaged (i.e., unstained). The labels identify the tissue types, including the maxillary processes
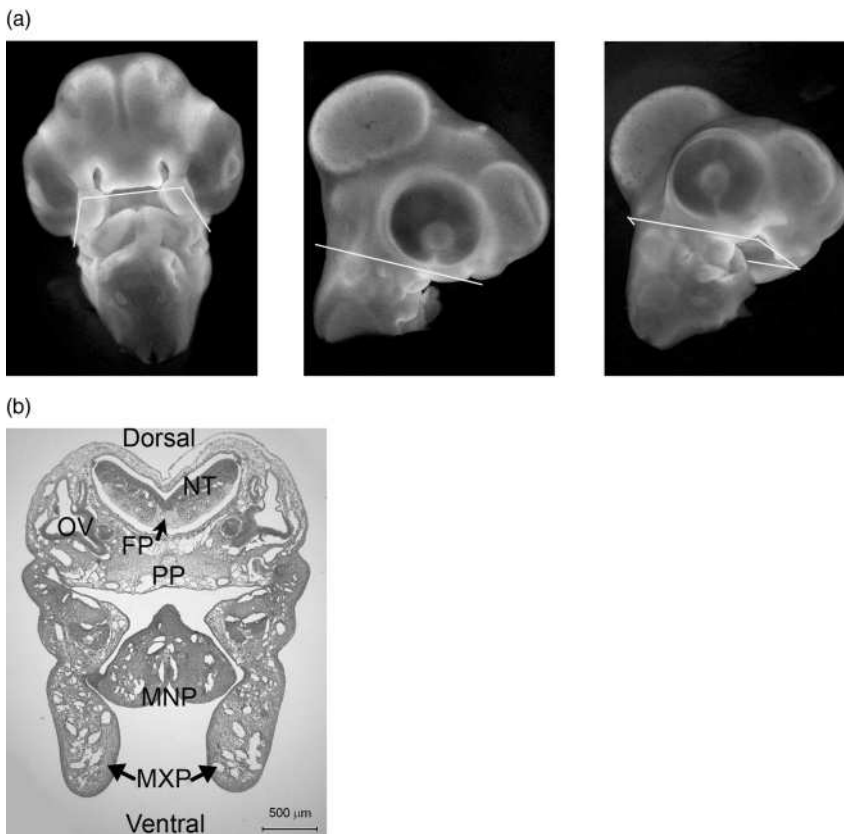
Figure 6.9 (a) Three views of an embryonic chick face (stage 27, 144 h) stained with ethidium bromide; the images were taken under a fluorescence dissecting microscope. The white lines in the image indicate, approximately, the plane of the sectioning; (b) White-light micrograph of 4 μm-thick unstained section from the chick face. MXP = maxillary processes, MNP = mandibular processes, NT = neural tube, OV = otic vesicle, PP = posterior palate, FP = floor plate.

that give rise to most of the upper jaw/ beak, the mandibular processes that give rise to lower jaw/beak, the posterior palate, the neural tube that gives rise to the central nervous system, and the otic vesicles, which are precursors of the ears.

Figures 6.10 and 6.11 show 3-D FT-IR images of an embryonic chick face constructed from the 16 sections. The image volume sampled was $2700 \times 3775 \times 64 \, \mu m^3$
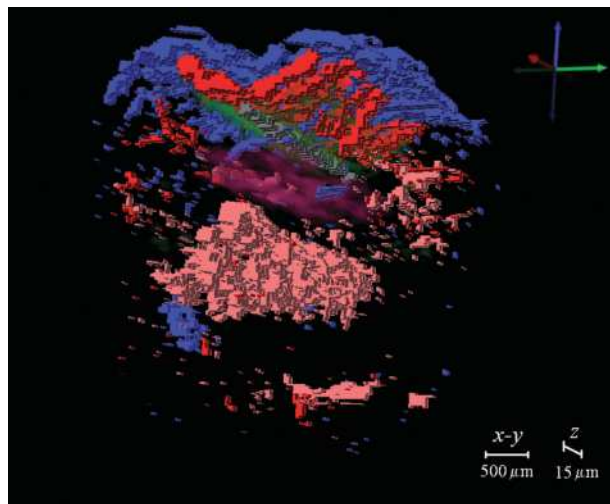
Figure 6.10 3-D ANN image of the embryonic chick face. Spectroscopically distinct anatomical features identified by combined UHCA and ANN analysis are plotted in five cluster colors. The maxillary processes that surround the bottom and sides of these features are removed for clarity.
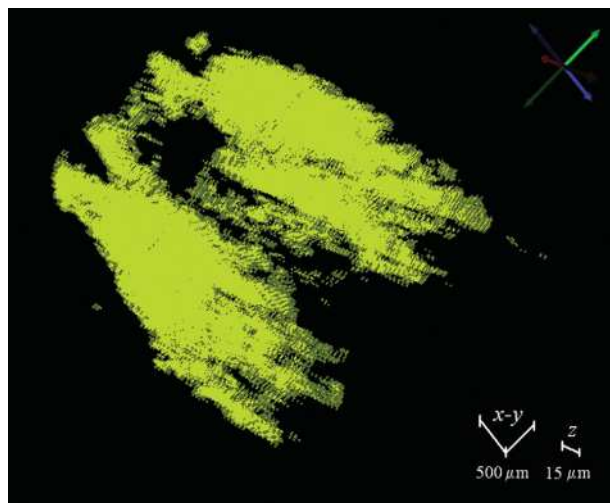
Figure 6.11 3-D ANN image of the embryonic chick face. This view shows only the outer cluster from the maxillary processes.

(x,y,z) and contained 265 088 spectra. Thus, the chick face data set was approximately 16-fold larger than that obtained for the cervical adenocarcinoma sample. As the number of spectra contained in this image was greater than can be processed with UHCA, an ANN model was used to perform the multivariate image analysis. UHCA was initially performed on four FT-IR hyperspectral images selected from the complete 16-image set to identify six spectroscopically distinct clusters. The spectra collected from these UHCA clusters were then used to train an ANN. After training, ANN 2-D image processing of all the sections was performed in CytoSpec, and validation of the ANN model performed by comparison with the UHCA imaging results. The final 3-D rendering of the ANN image was performed using the SCIRun software.

In Figures 6.10 and 6.11 the *z*-direction, which lies perpendicular to the sectioned faces, is in the direction represented by the red arrow in the red-green-blue axes indicator shown at the top right corner of the images. These images have a greatly exaggerated scale in the *z*-direction. The blue arrow indicates the dorsoventral axis, and the dorsal direction in Figure 6.10 is upwards. In Figure 6.10, the one UHCA/ANN cluster that was found to correspond with the maxillary processes has been removed so that the shapes of the more internal anatomical features can be traced through the sampled area of the chick face. The UHCA/ANN model has described the neural tube (not yet closed) as three identifiably distinct spectral clusters, shown in Figure 6.10 by the red, green and gray colors. For visual clarity, the green cluster has been rendered as semi-transparent. The spectroscopically identified gray cluster that can be seen penetrating all the way through the collected sections, parallel to the *z*-axis, is identified as the floor plate, a functionally defined part of the developing neural tube. Other anatomically identifiable UHCA/ANN spectral clusters are the posterior palate, presented as the semitransparent purple cluster. Figure 6.11 reverses the situation, and shows only the maxillary processes with the features internal to the face removed from the plot. Figure 6.11 also shows the face from a different vantage point; this view is rotated from that shown in Figure 6.10, as indicated by the new orientation of the axes indicator. In the SCIRun software the 3-D image can be freely rotated, and this ability provides the viewer with a clear impression of the shape of the various anatomical features, which is less apparent in the static images. In the foreground sections of Figure 6.11, the two maxillary processes can be seen as clearly separated tissues. However, in several background sections, it is possible to discern that tissue with essentially identical spectral properties approximates with the maxillary processes. This centrally located tissue is likely derived from the medial nasal process.

6.4
Conclusions

The coupling of vibrational spectroscopic imaging with 3-D multivariate processing greatly extends the capabilities of IR technology in medical diagnostics. From the perspective of the biomedical scientist, existing pathological and histochemical

protocols depend on sample morphology and visualization, and so the ability to maintain spatial integrity in three dimensions while assessing precise spectroscopic data intrinsic to a tissue sample represents an ideal combination. Three-dimensional multivariate processing, whether using chemimages, cluster images or ANN images in the case of larger samples, provides a new approach to visualizing tissue blocks, based on the underlying biochemical make-up of the tissue matrix. It is expected, therefore, that the above-described techniques, after further development, will in the near future achieve significant application in both biology and medicine.

Acknowledgments

References

1 Sabu, R.K. and Mordechai, S. (2005) *Future Oncol.*, **1**, 635–47.

2 Tobin, M.J., Chesters, M.A., Chalmers, J.M., Rutten, F.J.M., Fisher, S.E., Symonds, I.M., Hitchcock, A., Allibone, R. and Dias-Gunasekara, S. (2004) *Faraday Discuss.*, **126**, 27–39.

3 Wood, B.R., McNaughton, D., Chiriboga, L., Yee, H. and Diem, M. (2003) *Gynecol. Oncol.*, **93**, 59–68.

4 Lewis, E.N., Treado, P.J., Reeder, R.C., Story, G.M., Dowrey, A.E., Marcott, C. and Levin, I.W. (1995) *Anal. Chem.*, **67**, 3377–81.

5 McNaughton, D. and Wood, B.R. (2007) Applications of FTIR imaging in cancer research, Chap. 2 in *New Approaches in Biomedical Spectroscopy*, Vol. **963** (eds K. Kneipp, R. Aroca, H. Kneipp and E. Wentrup-Byrne), ACS Symposium Book Series, Oxford University Press, New York, pp. 14–29.

6 Socha, J.J., Westneat, M.W., Harrison, J.F., Waters, J.S., Lee, (2007) *W-K Biomedical Central*, 5.

7 Ritman, E.L. (2006) *Adv. X-Ray Anal.*, **49**, 1–12.

8 Zavattini, G., Vecchi, S., Mitchell, G., Weisser, U., Leahy, R.M., Pichler, B.J., Smith, D.J. and Cherry. S.R. (2006) *Phys. Med. Biol.*, **51** (8), 2029–43.

9 Wood, B.R., Bambery, K.R., Evans, C.J., Quinn, M.A., McNaughton, D. (2006) *BMC Med. Imaging*, **6**, 12

10 Ou-Yang, H., Paschalis, E.P., Boskey, A.L. and Mendelsohn, R. (2002) *Appl. Spectrosc.*, **56**, 419–22.

11 Lasch, P. (2005) CytoSpec 1.2 – an Application for FT-IR Spectroscopic imaging: see http://www.cytospec.com (accessed 27 November 2008).

12 Bambery, K.R., Wood, B.R., Quinn, M.A. and McNaughton, D. (2004) *Aust. J. Chem.*, **57**, 1139–43 and references therein.

13 Kimball, S., Mattis, P. *et al.* (2007) GNU Image Manipulation Program (GIMP), Free Software Foundation Boston, US. For details, see www.gimp.org/ (accessed 1 November 2007).

14 Scientific Computing and Imaging Institute (SCI) (2002) SCIRun: A Scientific Computing Problem Solving Environment, http://software.sci.utah. edu/scirun.html (accessed 1 November 2007).

15 Romeo, M.J., Dukor, R.K. and Diem, M. (2008) Introduction to spectral imaging with applications to lymph nodes, in *Vibrational Spectroscopy for Medical Diagnosis* (eds M. Diem, P.R. Griffiths, J.M. Chalmers), John Wiley & Sons, Ltd, Chichester, UK, pp. 1–26.

16 SynthonSoftware, © 2004.

17 Novotny, D.B. and Ferlisi, P. (1997) *Diag. Cytopath.*, **17**, 383–7.

18 Diem, M. and Romeo, M. (2005) *Vib. Spectrosc.*, **38**, 129–32.

Part Three   Agricultural Applications

7
FT-IR Microspectroscopic Imaging of Plant Material

David L. Wetzel

7.1
Introduction, Background and Perspective

7.1.1
Early Technology

Remote imaging (usual, thermal, or infrared) began move than nine decades ago, when artillery spotters in the era of trench warfare used balloons to view the terrain and the enemy forces. Their eyes served as image detectors, their brains as data processors and sketches as graphics, while a carrier pigeon transmitted the findings of their remote sensing to their own artillery battery. More recently, broadband channels of different wavelength ranges from high-flying aircraft or satellites employ sun-illuminated reflection to distinguish between bare soil and land covered by organic vegetation. The thermal images thus obtained reveal the emission of rays resulting from heat generated on the ground or of heat retained to a greater or lesser degree by different materials from the prior absorption of solar radiation.

Today, in the medical field, digital diagnostic images – including *computer tomography* (CT), *magnetic resonance imaging* (MRI), *positron emission tomography* (PET) and *ultrasound* – obtained at geographically remote clinics, and are then transmitted hundreds of kilometers via digital telephone lines with excellent image fidelity, to be read by an expert radiologist at another location. Likewise, imaging in light microscopy for histology has progressed from grayscale contrast to stains with chromophores or fluorophores that bind to a particular chemical species present in the tissue being examined. With vibrational spectroscopy – whether infrared, Raman, near IR or terahertz – staining is not required; rather, the intrinsic spectroscopic absorption properties provide a chemically selective image contrast. Today, chemical images from infrared microspectroscopy (IMS) reveal *what*, *how much* and *where*, various chemical species occur in nature and in manmade films, laminates, fibers or specimens from the materials or forensic sciences. IMS images obtained at different optical frequencies of the same wheat

(a)

1740 cm⁻¹ scutellum

(b)

1550 cm⁻¹ embryonic axis

(c)

1025 cm⁻¹ endosperm
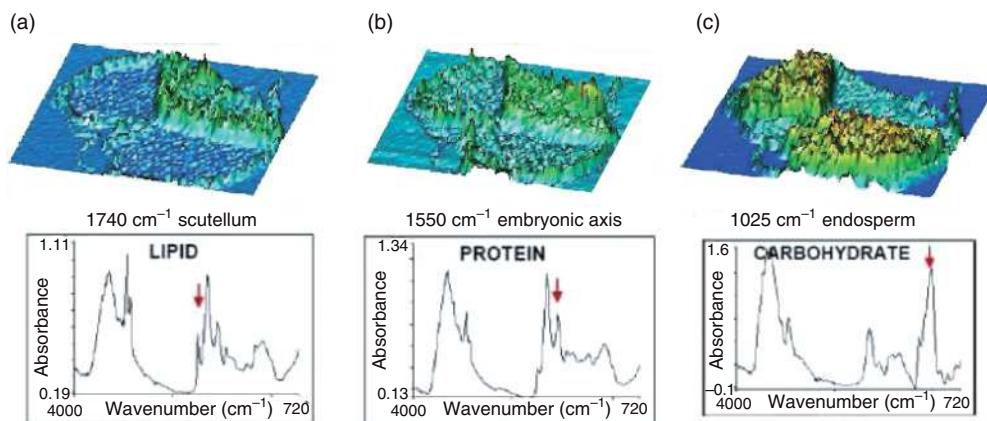
Figure 7.1 Chemical images of the same wheat kernel cross-section showing the population on the z-axis. (a) Lipid in the scutellum and aleurone cell walls; (b) Protein in the embryonic axis and aleurone cells; (c) Starch in the endosperm. The baseline-corrected band area maps of 1740, 1550 and 1025 cm⁻¹, respectively, result from bands marked in red on the lipid, protein and carbohydrate spectra extracted from the wheat kernel. Note: the section size is ca. $2000 \times 1000\,\mu m$. Reproduced with permission from Ref. [1]; © *Spectroscopy*.

kernel transverse section in Figure 7.1 show the locus and relative quantity of lipid, protein and carbohydrate in the different botanical parts [1]. The spectra from pixels high in each component have the absorption band identified for which the baseline corrected area was calculated to produce each corresponding chemical image.

Both, IMS and imaging, have developed rapidly since the introduction of the first research-grade infrared microscope in 1986. This instrument was equipped with front surface optics, remote projected image plane masks and a sensitive, dedicated detector with a small area to match the size of the microbeam passing through the specimen on the stage. Although the instrumentation for imaging is discussed in detail in Chapter 1 of this volume, and also in another monograph [2], a brief outline of the progression of microspectrometer development prior to the applications presented in this chapter should help readers to recognize the optics used for each application. Recently, in an editorial of *Applied Spectroscopy*, Peter Griffiths stated that 'By far and away the most significant development of a peripheral for FT-IR spectroscopy is the infrared microscope'.

7.1.2
Optical Advances

The IR-PLAN was patented in 1989 [3] and designed as an attachment for any commercial FT-IR instrument. Subsequently, other manufacturers provided similar peripheral microscopes for the same purpose with, in each case, an optical

interface being required. From that beginning, various IR microscope/IR spectrometer systems paired either by design or integrated systems have been used to enhance the optical efficiency to conserve the IR signal. The subsequent development of microprocessor-controlled motorized stages made raster scan mapping convenient, and multiple functional group maps (images) resulted from different baseline-corrected band areas, representative of various chemical species in the tissue being presented on the *z*-axis as a stacked contour map.

The enhanced spatial resolution which is enabled by the substitution of synchrotron radiation for a thermal (globar) source was a significant instrumental advance. The introduction of focal plane array (FPA) systems, initially InGaAs, for near-IR by Marcott and Lewis [4] occurred on 20 June 1994, while the subsequent development for mid-IR, using a mercury cadmium telluride (MCT) array by Lewis and Levine [5] at Bethesda, Maryland, resulted in very rapid image generation.

The instrument development cycle that began with a microscope accessory for an FT-IR spectrometer turned full circle with the production of a miniature interferometer accessory (the IlluminatIR™) for a research microscope. This latter development opened IMS to professional microscopists by adding a new, chemically selective dimension. Another small footprint-dedicated portable IMS used a diamond internal reflection element (IRE) to analyze solids or liquids on location. The internal reflection IMS is used in conjunction with a laptop computer that contains a spectral library; this set-up enables 'emergency first responders' or investigators to perform the onsite identification of unknown or potentially hazardous materials.

7.1.3
Early Imaging Applications

The vibrational spectroscopy of biological material has been a fruitful area of study and practical use for more than four decades, with biological products having been analyzed qualitatively with mid-IR systems, and quantitatively with near-IR. For mid-IR spectroscopy in most cases, homogenates or solid materials are analyzed on a macro scale in transmission as nujol mulls, or as KBr pellets or by diffuse reflection or reflection absorption techniques.

Remote sensing with relatively broad near-IR wavelength bands can provide a distinction between land covered with vegetation and bare earth from satellites, balloons and other high-altitude platforms. By using silicon photodiode cameras and filters, broad images resulted in the visible to very near-IR range up to 1050 nm. Thermal images were also obtained with InAs, InGaAs or InSb array cameras. In fact, many hundreds of reports have been made describing remote imaging for agriculture and botany. Likewise, laboratory-scale near-IR macro imaging, obtained in the silicon region, has been of great use in horticulture for the inspection of fruits, vegetables and leaves for surface defects, as well as for maturation or ripeness of the crop.

The commercial sorting of lemons on a massive scale was achieved as early as the 1980s by Sunkist. In this case, each lemon was inspected for spots on the skin

as it fell in a perfect spiral, using a near-IR camera system. In apples, a water core was detected with a handheld testing device designed for orchard use. More than a score of reports on bruised fruit (e.g., apples, pears) have dealt with the fact that any bruised flesh of the apple fills with water to a greater extent than does the other flesh within the same fruit [6], a fact which readily lent itself to macroimaging with an appropriate CCD camera. The use of a cut-off filter to remove wavelengths below 700 nm limits imaging from there to 1050 nm; however, with an interference filter the near-IR response of the water in the bruise can be distinguished from other absorbing species present in the fruit. Because the OH vibration is a very strong absorber, its combination and overtone bands that occur in the near infrared are relatively prominent.

7.1.4
Spatial Resolution

The spatial resolution of FT-IR microspectroscopy, without sacrificing spectral quality and resolution, makes imaging possible. Shortly after the introduction of the first research-quality IR microscope by Messerschmidt and Sting in 1986, Wetzel, Messerschmidt and Fulcher reported spectra obtained from wheat kernel transverse sections *in situ*, and compared them with flour milling fractions [7]. This was achieved with an accessory IR-PLAN microscope optically interfaced to a Nicolet interferometer bench. Subsequently, at the Agriculture Canada laboratory the same model IR-PLAN was interfaced to a Bomen Michelson IR 100 spectrometer such that, over the period of a year, transverse sections of wheat kernels, vanilla beans, peppercorns and soybeans were manually line-mapped to reveal any differences in microchemical structural characteristics between their different botanical parts [8].

The line maps clearly showed spectroscopic differences on a microscopic scale, with the cellulose and hemicellulose content of the pericarp layer of wheat readily apparent. The high lipid content of the pericarp was also revealed with prominent 2927 cm^{-1} CH$_2$ bands and carbonyl bands at 1740 cm^{-1}. Similarly, the aleurone cells and cell walls could be distinguished from adjacent endosperm and pericarp layers. Within the endosperm (which forms the larger part of the wheat kernel), a major compositional difference was documented between the subaleurone and a central endosperm; this was evidenced from the spectra by a high amide II:carbohydrate (1550:1025 cm^{-1}) band area ratio. Within another botanical part of the wheat, the germ, a microchemical structural difference was noted between the embryonic axis and the surrounding scutellum, with the former being high in protein and the latter containing considerable lipid.

As seen in Figure 7.2, the discoveries of these early studies formed the basis of subsequent research [8]. Meanwhile, Reffner [11] reported the organic functional group mapping of a transverse corn section from the outer part of the kernel into the endosperm. Instrumentation available at that stage of development consisted

(a)

(b)
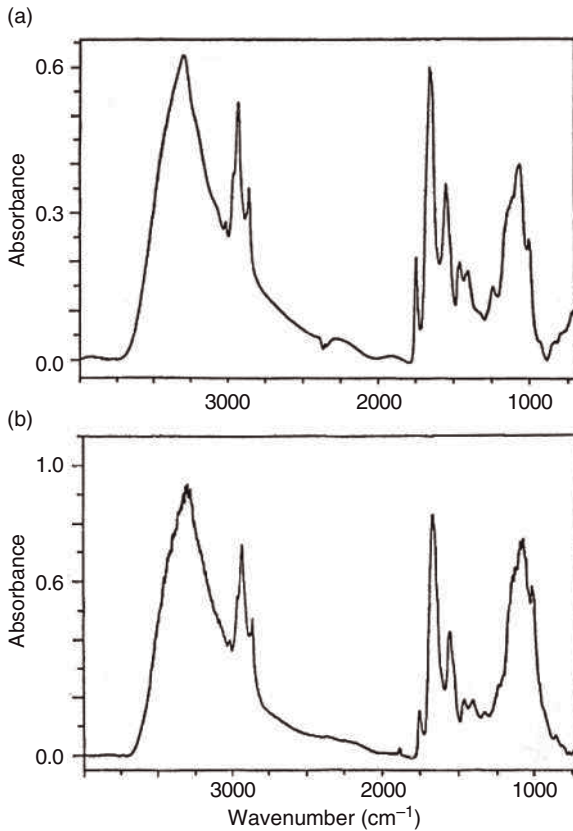
Figure 7.2 Synchrotron infrared microspectroscopy with $6 \times 6 \mu m$ confocal operation and truncation at low wavenumber due to diffraction showing: (a) The scutellum portion of the germ with high $1740 cm^{-1}$ lipid compared to $1650 cm^{-1}$ protein; (b) The embryonic axis portion of the germ with higher protein at $1650 cm^{-1}$ compared to lipid at $1740 cm^{-1}$. Reproduced with permission from Refs [9, 10]; © Elsevier and *Cellular and Molecular Biology*, respectively.

of an accessory IR microscope optically interfaced to an FT-IR spectrometer, and both mammalian and plant tissues were studied extensively using this system. Subsequently, line mapping and rectangular mapping were enhanced with the introduction of a microprocessor-controlled motorized stage and an optically integrated microscope/spectrometer system [9]. Another book chapter that includes confocal synchrotron IMS with $6 \times 6 \mu m$ image plane masking contains 125 figures with images and spectra of various seeds [12].

7.2
Application of IMS to Kernels and Seeds of Plants

7.2.1
Motive and First Applications of Spatially Resolved IMS

Revealing the chemical difference between the botanical parts of individual wheat kernels was the object of this author's immediate concern for using the first research quality accessory infrared microscope that was introduced in 1986, featured at that year's Eastern Analytical symposium and documented in a monograph that reported mostly forensic science, materials science, and potential medical applications [13]. The patent was subsequently issued to Messerschmidt and Sting [3]. The assumption that the quality factors of wheat (which is the primary cash crop of Kansas) may be revealed from a chemical microstructure led to a cooperative effort between the present author – a microscopist and expert in wheat morphology of Agriculture Canada – and the designer of the IR PLAN Spectra-Tech microscope. The first joint experiment involved milling identity-preserved hard red winter (HRW) wheat to produce physically separated fractions, at the Kansas State University (KSU) pilot flour mill. The spectra of these materials were compared with *in situ* microspectroscopically obtained spectra of individual botanical parts within 6–8 μm-thick frozen sections that had been thaw-mounted onto 13 mm-diameter BaF_2 windows. The transverse kernel sections representing HRW and soft red winter (SRW) wheat classes were sectioned and mounted, and the spectra collected were presented at the 1987 Detriot FACSS microspectroscopy symposium [7]. Other materials scanned included wheat gluten, wheat starch, wheat lipid and cellulose. Although the abstract for the Detriot symposium had referred to a motorized stage, a period of several months passed before Spectra-Tech produced such a stage that enabled what was referred to as 'mapping' the specimen to provide functional group images. Reffner demonstrated a single functional group line mapping of a corn transverse section which produced successive spectra capable of distinguishing between the pericarp and each layer from that outer portion of the seed into the central endosperm [11].

Subsequently, Reffner and Wetzel produced images from raster scans of a wheat section with a prototype of the Spectra-Tech IRμs. This was an integrated instrument that rigidly combined both an IR microscope and an FT-IR spectrometer with a dedicated small-element MCT detector that essentially matched the dimensions of the microbeam exiting the Schwartzchild/Cassegrainian condenser of the microscope. Yet, while processing the data to be presented at a 1980 international conference, a seemingly fatal flaw was revealed, in that spectra from pixels of starchy endosperm appeared with higher absorbance values in a protein functional group map than pixels known to be high in protein. Software was written to produce locally baseline-corrected band areas to negate any light-scattering effects that exceed – and thus obscure – the vibrational absorption in some cases [14].

Initially, it was exclusively plant materials, including sections of wheat kernels, soybeans, peppercorns, vanilla beans and individual starch granules, that were probed and manually line mapped. These early investigations were conducted using a Bomem-Michelson 100 FT-IR and an IR PLAN and interface on loan from Bomem and Spectra-Tech, respectively. The localized chemical compositional difference between botanical parts was first reported in 1989 by Wetzel and Fulcher [15]. Spectroscopic differences within the botanical parts endosperm (protein) and germ (lipid) were first observed from the manual line mapping of these tissues mounted on BaF_2, in transmission mode. Here, 100 µm-diameter confocal projected image plane masking was used in step sizes of 50 µm to obtain successive spectra within these botanical parts.

7.2.2
Mapping Tissue Sections

Use of the IRµs integrated instrument enabled line mapping across boundaries within plant tissue to observe differences in microchemical structure. This, after all, was the primary motivation for adapting FT-IR microspectroscopy to the investigative probing of plant material. Successive spectra taken across boundaries from pericarp, seed coat, outer cell wall, aleurone cells, inner aleurone cell wall, subaleurone endosperm, and finally the central endosperm, clearly demonstrated the chemical microstructural differences provided by nature. More surprisingly, these research laboratory revelations came about while IR microscope salesmen were using layered paint chips, ketchup bottles and photographic film cross-sections to demonstrate the power of spatial resolution in manmade laminates!

The period between the 1990s and the early 2000s was extremely fruitful for the imaging of plant material, particularly of kernels and seeds, with many of the studies being performed using a raster scanning procedure on a variety of instruments. At the Microbeam Molecular Spectroscopy Laboratory (MMSL) of KSU, the Spectra-Tech IRµs was used in a transmission mode with samples mounted on BaF_2, often in a compression cell with the specimen between two BaF_2 disks. Although the mapping procedures were lengthy, the compression cell kept the entire specimen in focus during the process. Mirrored microscope slides, and eventually IR-reflecting ('low-e') glass, were used for the reflection/absorption mode. This same model of instrument was the first to be installed on beamline U2b at the National Synchrotron Light Source (NSLS) at Brookhaven National Laboratory (BNL). In all cases for which maximum spatial resolution was needed, synchrotron IMS was carried out by the author and collaborators at that facility in several month-long summer residences and a 15-month sabbatical at NSLS. Each mapping procedure resulted in a number of different functional group images, during which time the various images were usually displayed as stacked contour maps. Emphasis was placed on transitions across boundaries between botanical parts in wheat, corn and a variety of other seeds. Some sketches of wheat and corn cross-sections are shown in Figure 7.3, where the rectangles superimposed on the sections show the regions mapped. A number of these reports

appeared in 1993 [9] and 1995 [12], and also in a 1993 article by Wetzel and Reffner [16]. Selected images were also included in a subsequent report in *Cellular and Molecular Biology*, in 1998 [17]. Selected stacked contour images from these early studies were also included as examples in a treatise chapter by Budevska, who also presented color graphic images of her FPA data. Aspects of color-highlighted protein, starch and other functional groups, for the identification of different botanical parts of the corn kernel, are discussed later in this chapter.

Rectangular x, y mapping was carried out in half-day periods or overnight, usually with the microtomed tissue sandwiched between BaF_2 windows to maintain focus of all parts of the targeted area to be mapped. Initially, functional group images were the result of interpolating skipped areas between spectra acquired when the stage step size was greater than the aperture dimension resulting from the image on the plane of the microscope stage. The images produced provided perspective with regards to the distribution of chemical species; however, the scientific contributions were dependent on acquiring excellent spectra. Images resulting from applying a mapping procedure were routinely used to locate areas of interest in a microscope field to be probed by the 'point and shoot' approach with adequate scans coadded to maximize the signal-to-noise ratio (SNR). The plant tissue effort benefited from parallel (1999) studies in forensic science [18], material science [19], and also extensive microspectroscopic investigations in cooperation with Steven LeVine, a neuroscientist at the University of Kansas Medical Center.

In parallel with the plant material research, mouse cerebrum sections revealed obvious differences between white matter, gray matter and basal ganglia. These data were obtained with the IRµs at the newly established MMSL at KSU. The control specimens showed a clear difference between the lipid-rich white matter and the protein-rich gray matter for the cerebrum of a normal mouse [20, 21]. However, for the corresponding brain tissue of a diseased mouse in which the white matter had not fully developed, there was little spectroscopic difference between the two regions of tissue [22]. In total, 16 scientists have operated at the KSU facility, which has hosted cooperative projects with Canadian, British and other American investigators, in addition to graduate students and faculty members from chemistry, biology and agriculture, as well as neuroscientists from the University of Kansas Medical Center. Elsewhere, other biological materials including medical specimens were under investigation in parallel, notably in laboratories at Hunter College, New York, the Russell Research Center, Athens, GA, and also in Australia, the United Kingdom and Japan.

7.2.3
Transitions across Botanical Parts

Mapping the transitions across boundaries between botanical parts in wheat and corn, shown as A–E on the wheat section (Figure 7.3a) and F–J on the corn kernel (Figure 7.3b), was accomplished in a raster scan procedure. This was achieved in a transmission mode between the time that the IRµs instrument was installed, and 1995. Spectra from each mapping experiment yielded functional group images

(a)   (b)
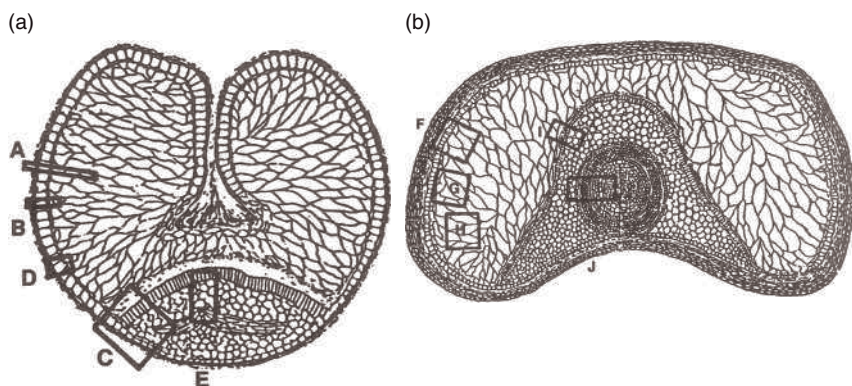
Figure 7.3 (a) Sketch of wheat kernel cross-section, showing from the outside towards the center: pericarp, aleurone cells, aleurone cell walls, endosperm, depleted layer and germ (scutellum and embryonic axis). The following regions of the kernel were studied: A = pericarp/endosperm; B = pericarp/subaleurone endosperm; C = corner of germ; D = single aleurone cell; E = endosperm/scutellum; (b) Cross-section (not to common scale) sketch of a corn kernel showing pericarp, aleurone cells, aleurone cell walls, endosperm, depleted layer, scutellum and embryo. The following regions of the kernel were studied: F = aleurone/endosperm; G = subaleurone/central endosperm; H = vitreous central endosperm; I = endosperm/root; J = scutellum/embryo (root). Reproduced with permission from Ref. [9]; © Elsevier.

for 3015, 2927, 1740 and 1469 cm^{-1}, representing C=C−H, CH$_2$ stretch, carbonyl and CH$_2$ bend useful in characterizing lipid deposition. The 3280, 1650 and 1550 cm^{-1} images provided relative amounts of protein in terms of the NH stretch, amide I and amide II. Imaging the 3300 cm^{-1} rounded OH stretching vibrational band was indicative of water or carbohydrate, as in the 1025 cm^{-1} band-imaged starch, and alternatively a carbohydrate band maximum at 1100 cm^{-1} accompanied by a trio of bands at 1420, 1370 and 1335 cm^{-1} plotted the locus of cellulose or hemicellulose structures. The 1250 cm^{-1} image showed phosphorous diesters or nucleic acids. The areas designated as 'B' in Figure 7.3a were chosen to exemplify the mapping procedure for this chapter. Starting in the pericarp, the mapping proceeded across the pigment layer, the outer cell wall, the aleurone cell, the inner cell wall, subaleurone endosperm, and finally into the central endosperm.

Figure 7.4a is the 1740 cm^{-1} stacked contour image of area 'B' in Figure 7.3a, showing the lipid present in the pericarp and cell walls, while Figure 7.4b is the 1550 cm^{-1} image showing the protein of the aleurone cells. Figure 7.4c from the 1025 cm^{-1} band area shows the starch of the endosperm inward from the aleurone layer. A corresponding set of images was produced for area 'F' of the corn kernel in Figure 7.3b. The transitions from subaleurone to central endosperm are produced from areas 'A' or 'G'; such transition within the endosperm was to document the results of early manual mapping. Similarly, the different parts within the germ were sampled from areas 'E' and 'J'.

(a)

(b)

(c)
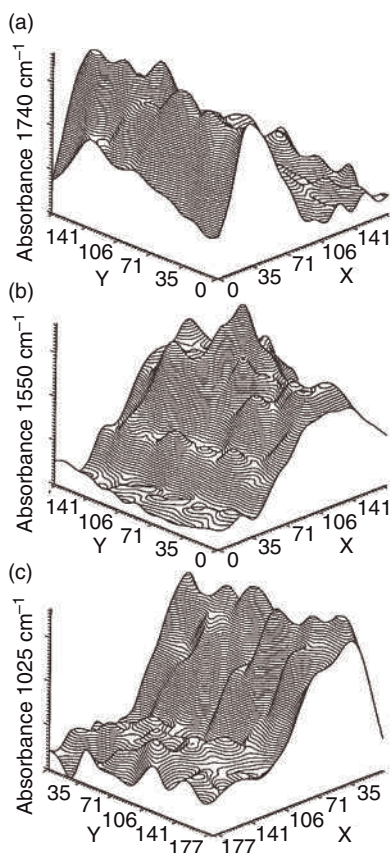
Figure 7.4 Stacked contour images of: (a) 1740 cm^{-1} for area B of Figure 7.3, showing the lipid present in the pericarp and cell walls; (b) 1550 cm^{-1} showing the protein of the aleurone cells and the ridge of endosperm behind; (c) 1025 cm^{-1} band area showing the starch of the endosperm inward from the aleurone layer. The units of the *x*- and *y*-axes are micrometers, and the z-axis band areas are in arbitrary units. Reproduced with permission from Ref. [9]; © Elsevier.

7.2.4
Imaging Single Cells

Imaging single aleurone cells with a typical size of 30 μm in wheat, corn and other grains proved to be a major achievement of the plant tissue IMS. Large algal cells (shown subsequently as chemical images), oral mucosa cells and cervical cells were analyzed and shown to be on the order of 100 μm in length. As early as 1992, a single cell was mapped at the author's laboratory with 6 × 7 μm confocal image plane masking on the Spectra-Tech IRμs. In this overnight procedure, the step size was equal to the aperture, so as to maximize the detail. The first single cell mapping was reported by Wetzel and Reffner [16]; the stacked contour plot of

(a)

(b)
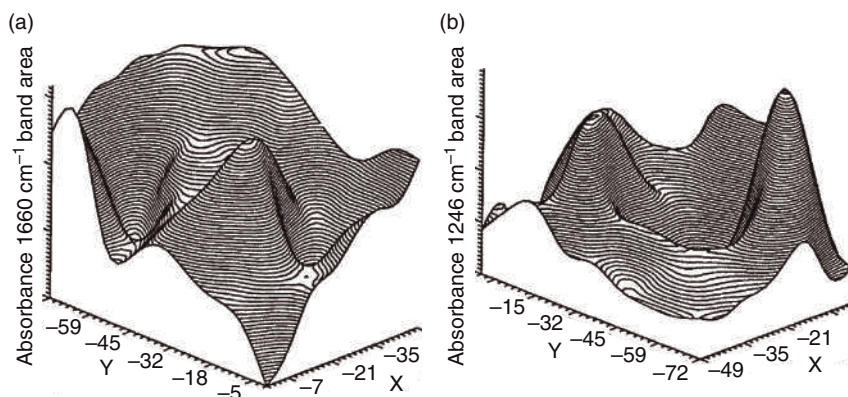
Figure 7.5 Raster scan mapping results at KSU 1992 with $6 \times 7\,\mu m$ confocal image plane masking and globar source. (a) Chemically distinct graphics of single cell and cell wall as stacked contour image of single wheat aleurone cell from $1650\,cm^{-1}$ baseline corrected band area; (b) Cell wall image from the $1246\,cm^{-1}$ band area. The units of the *x*- and *y*-axes are micrometers. Reproduced with permission from Ref. [16]; © *Cereal Foods World*.

Figure 7.5 shows the aleurone cell and part of the neighboring cell as a pyramid-shaped functional group stacked contour image of the amide II band at ca. $1550\,cm^{-1}$. The cell walls were also highlighted, using a frequency representative of that tissue; this was accomplished with 256 scans coadded using the built-in globar source.

Subsequently, with synchrotron IMS and confocal $6 \times 6\,\mu m$ image plane masking, a shaper functional group image of a row of cells and surrounding tissue were obtained. These images and a photomicrograph of the target are shown in Figure 7.6a. It should be noted that, in Figure 7.6b at $1550\,cm^{-1}$, images from synchrotron IMS, two intact cells and one broken cell were apparent. Likewise, in Figure 7.6c, rows of cell walls appeared in the $2927\,cm^{-1}$ CH_2 functional group map. Figure 7.6d of $1025\,cm^{-1}$ shows the appearance of starchy endosperm, as evidenced by the starch absorption [12, 17].

The next aleurone cell imaging was performed at Proctor and Gamble, using a 64×64 MCT focal plane array system assembled with a commercial MCT camera, an IR microscope and a step scan FT-IR spectrometer [23]. In Figure 7.7, two aleurone cells are shown with a red false color image for $1550\,cm^{-1}$. The cell walls are found in the $1740\,cm^{-1}$ image and the endosperm is identified by the carbohydrate image at $1025\,cm^{-1}$.

All of these small cell imaging studies were subsequently eclipsed by investigations of Jamin, Dumas and others, with synchrotron IMS of a single living cell undergoing mitosis [24]. Visualization of the two new nuclei shown in the lipid wavelength band area images in Figure 7.8 was made possible with confocal image plane masking at $3 \times 3\,\mu m$.

(a)

(b)

(c)

(d)
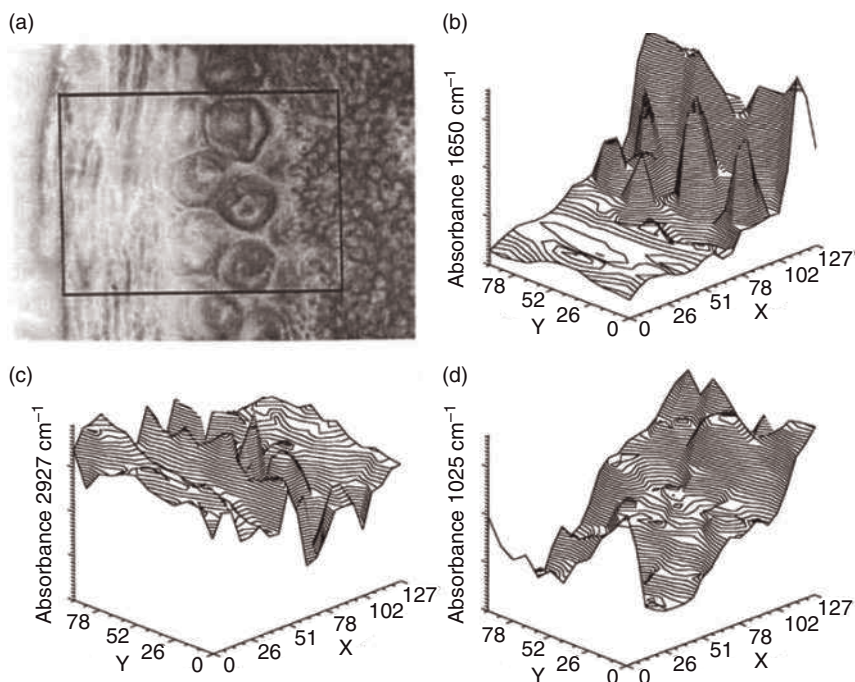
Figure 7.6 Synchrotron IMS images of corn aleurone. (a) Photomicrograph of aleurone cells (top broken, middle and bottom whole); (b) Cell image stacked contour plot of baseline corrected 1550 cm^{-1} band area, (lower left and right respectively). The cell wall images were based on the lipid content at 2927 cm^{-1} (c), and carbohydrate image at 1025 cm^{-1} (d) band area showing subaleurone endosperm. The units of the x- and y-axes are micrometers. Reproduced with permission from Refs [12, 17]; © Elsevier and *Cellular and Molecular Biology*, respectively.

(a)   (b)   (c)
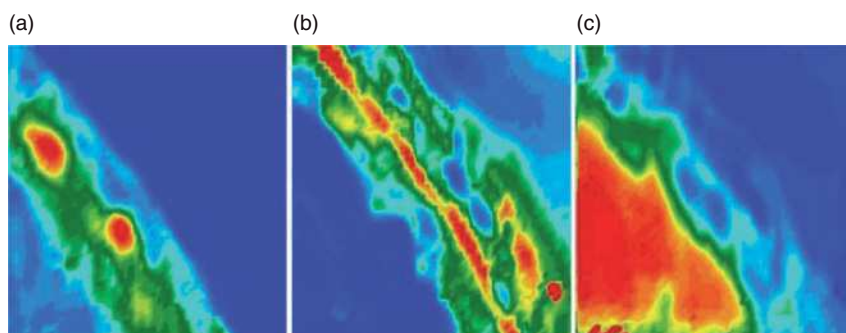
Figure 7.7 Focal plane array infrared images of the same cells as in Figure 7.6, cell walls and aleurone. (a) Aleurone cells highlighted by amide I at 1650 cm^{-1} band area; (b) Aleurone cell walls at 1040 cm^{-1} band area; (c) Endosperm 1025 cm^{-1} carbohydrate band area. The red areas indicate high absorbance values. The size of each image is ca. 250 × 250 μm. Reproduced with permission from Ref. [23]; © *Vibrational Spectroscopy*.
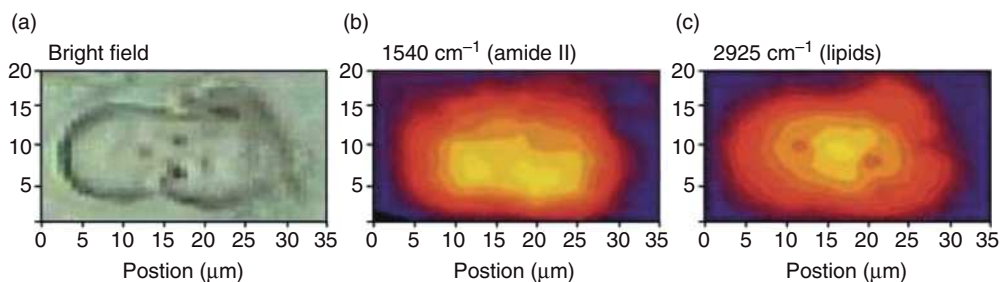
Figure 7.8 (a) Photomicrograph of a cell undergoing mitosis. (b, c) Chemical images of amide II band at 1540 cm^{-1} and the CH$_2$ stretch at 2925 cm^{-1}, respectively. Note the forming nuclei in panel (c). Reproduced with permission from Ref. [24]; © National Academy of Science, USA.
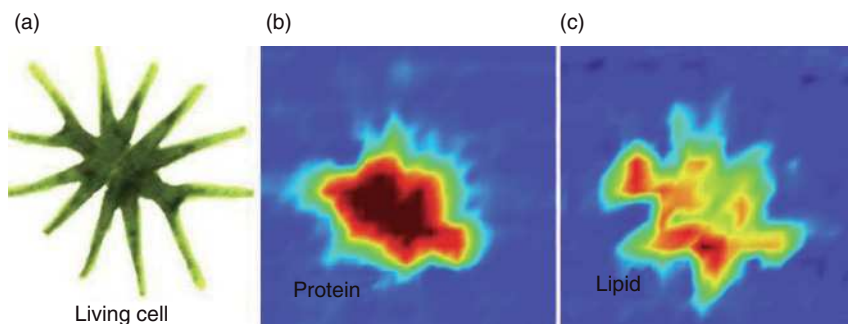
Figure 7.9 Green algal cell, *Micrasterias hardyi*. (a) Photomicrograph; (b) Chemical image from 1075 cm^{-1} baseline-adjusted band area, showing areas of protein concentration; (c) 1740 cm^{-1} image, showing area of lipid concentration. The red color indicates high absorbance values. The image sizes are 200 × 200 μm. Reproduced with permission from Ref. [25]; © *FEMS Microbiology Letters*.

Images of single algal cells from both marine Figure 7.9 and freshwater sources Figure 7.10 have been reported recently [25] and [26], respectively, in studies involving the influence of nutrients and their uptake by organisms in the algal colony.

7.2.5
Applying Synchrotron IMS to Kernels, Seeds and Other Tissues

While the first synchrotron IR microspectroscopy was performed at the NSLS of BNL during late 1992 [27, 28], in January 1993 the present author was able to access the temporary beamline set-up to obtain 6 × 6 μm confocal spectra of wheat cross-sections, including single cells in successive cell layers that form the bulls-eye pattern of the primary root (see Figure 7.11) [16]. The spectra in Figure 7.11
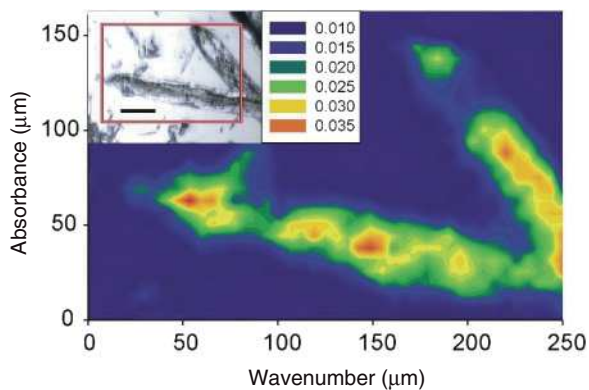
Figure 7.10 ^{15}N:^{14}N ratio of protein:amide II band in two *Cladophora glomerata* cells showing the subcellular distribution of ^{15}NO$_3$ incorporation. (ca. 150 μm diameter). Reproduced with permission from Ref. [26]; © *Vibrational Spectroscopy*.

(a)

(b)
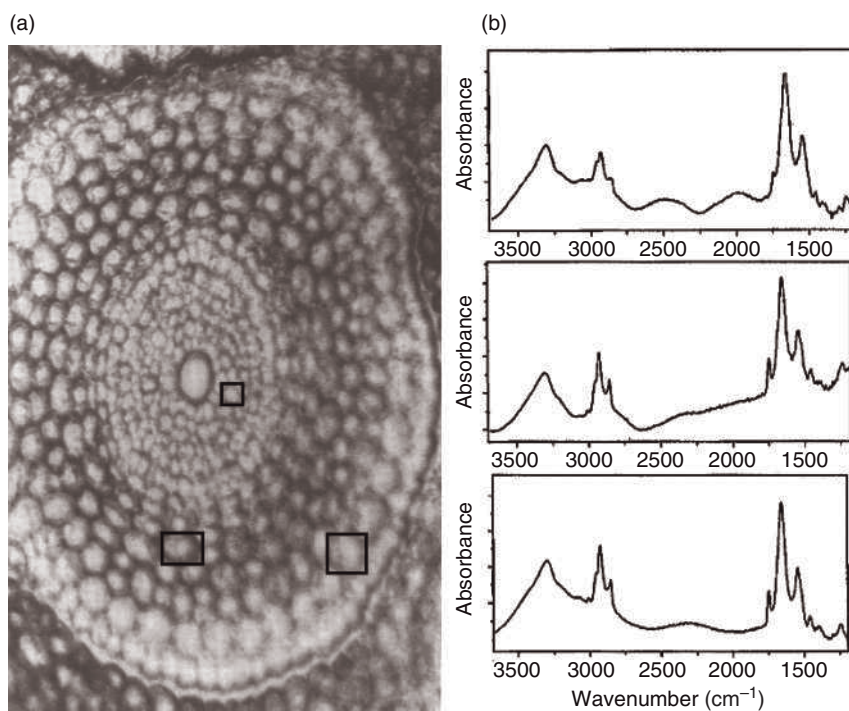
Figure 7.11 (a) Photomicrograph of the primary root of hard wheat, showing the surrounding colorhiza, the epidermis, cells of the cortex, cells of the central vascular cylinder and large cell at the core; (b) Single-cell spectra are from outer cell wall (top), mid (center) and inner cell rows (bottom). Reproduced with permission from Ref. [12]; © Elsevier.
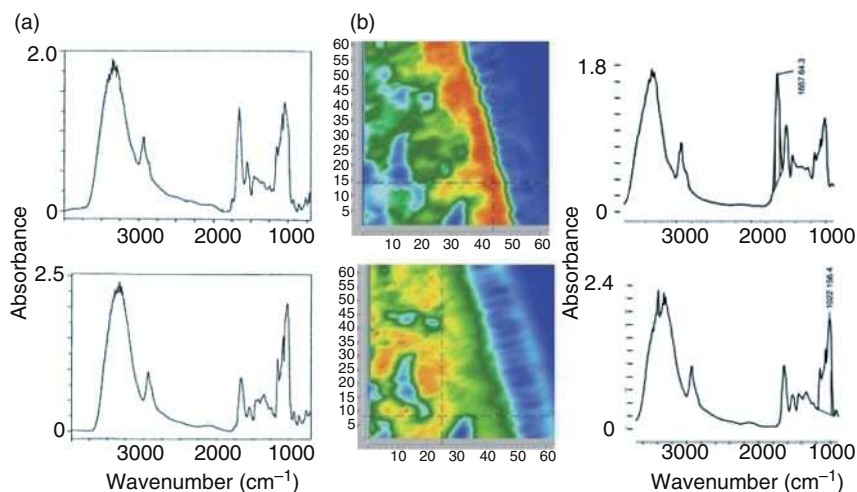
Figure 7.12 (a) Spectra of wheat subaleurone (top) and central 'starchy' endosperm (bottom), obtained in 1992, using the 'point-and-shoot' technique, from $12 \times 12\,\mu m$ confocal image plane masking [9]; (b) Focal plane array functional group images $1650\,cm^{-1}$ (top) and $1025\,cm^{-1}$ (bottom), highlighting the subaleurone and central endosperm, respectively [29]. The red color indicates high absorbance values. The spectra at the right-hand side are extracted from corresponding highlighted pixels (cross-hairs in images in the mid), showing differing protein:starch ratios within the wheat endosperm. These were measured in 2002 and support the earlier observations. Reproduced with permission from Refs [9] and [29]; © Elsevier and Wiley, respectively.

show the relative lipid content by row within the assembly. Subsequent synchro-tron experimental sessions with a three-person team operating around the clock produced maps and point probing with excellent spatial resolution. From the same target observed with a 15× objective that produced a $12 \times 12\,\mu m$ double aperture, readily produced a $6 \times 6\,\mu m$ spot size when the 32× objective mounted on the nosepiece was swung into place.

At the NSLS, sections of wheat, corn and other plant materials previously mapped using the conventional globar source at KSU were re-mapped with new similar sections so as to benefit from the increased spatial resolution. Con-sequently, more than 150 figures from the MMSL and NSLS were used to report the results of mapping across borders of different botanical parts in wheat and corn [12].

A subsequent chapter by Budevska showed extensive false color images of corn produced with the FPA imaging instrument in the agricultural division of Dupont [29]. Additionally, chemometric and imaging software was reported by the same authors [30].

The upper spectrum of Figure 7.12 was obtained from the red false color area of the subaleurone endosperm, and the lower spectrum from the orange false color portion of the central endosperm (note the relative amounts of protein and starch

at 1650 and 1025 cm^{-1}, respectively). These spectra were similar to those obtained with a thermal source shown on the left.

The nonplant synchrotron IR microspectroscopic analysis at the NSLS beamline included drug metabolites in hair [31], depth profiling of photodecomposition of polymer layers [19], and numerous mammalian tissue probings, including the brain tissue of rats that had consumed D_2O in their drinking water [10]. A summary of the plant material experience from BNL over a continuous 15-month period was reported in 1998 [17], and included the spectra of individual cells within a wheat primary root and the mapping of transitions between the botanical parts of wheat, safflower, oats, corn and barley.

7.2.6
Various Applications of IMS

A research project conducted at KSU included tracing the migration of water by tempering wheat with D_2O and mapping the OD absorption at 2500 cm^{-1}. This was accomplished using 20 µm-thick sections to measure this minor band area [32]. In these studies, the rate of water migration was measured for various different wheats, including classes of hard and soft wheat and various cultivars within those classes. Such variation is of particular interest in the flour milling industry, because the amount of water permitted in the wheat during storage is less than the optimum amount required to be present when milling takes place [32]. Thus, the achievement of an optimum, evenly distributed water content in wheat prior to milling is important for the efficiency of the milling process.

Other graduate research projects include the use of a polarizer after the beamsplitter, so as to obtain dichroism of wheat gluten films at positions of maximum stress, and also at positions of no stress. First, frozen gluten was microtomed to produce a film; a small hole placed in the film was then elongated to produce a stress gradient in space. Spectra with the polarizer parallel and perpendicular to the direction of stress were obtained along a line at various distances from the spot of maximum stress, outwards to the bulk of the film [33]. Parallel dichroism studies of polymer fibers for forensic purposes [34, 35] had a clear influence on these gluten dichroism studies since, although the sample preparation for mid-IR microspectroscopy of microtomed gluten was difficult, the mid-IR spectra led to use of the same mid-IR microspectrometer at higher frequencies between 4000 and 5800 cm^{-1}. In this way it was possible to obtain near-IR spectra in the region that included combination bands at 4865 and 4611 cm^{-1}. When these experiments were first performed (at the Shelton, CT facility of Spectra-Tech/Nicolet), the stock beamsplitter and source were exchanged for a quartz beamsplitter and a tungsten source. However, sufficient SNR was attained with the built-in globar source within the upper frequency limit of 5800 cm^{-1} imposed by the germanium coating on the KBr beamsplitter to produce excellent spectra. Because the attenuation of the beam was very large for one position of the polarizer, dichroic measurements were obtained at the higher transmitting angle of the polarizer, with dichroism

achieved by rotating the specimen under stress in a custom-fabricated stretching device (J.A. Reffner and D.L. Wetzel, unpublished results).

This investigative sequence, using a mid-IR instrument to measure near-IR spectra, resulted in the design and building of a dedicated near-IR instrument with programmable automated rotation of the specimen and digital stepwise elongation of the gluten film with a microprocessor-controlled stepping motor [36]. This was done to measure the strength of the wheat gluten, in terms of its resistance to molecular orientation in response to a fixed amount of work input that produced an eightfold elongation. The dedicated instrument employed a home-made acousto-optic tunable filter spectrometer with programmed electronic wavelength switching to obtain dichroic spectra at appropriate protein frequencies. Another project involved the mapping of isogenic wheat cultivars in the subaleurone to central endosperm part of the kernel; this was achieved by using a large number of sections to document the chemical microstructure of each [37].

7.2.7
Wheat Quality via IMS and Germination Study

Recent, ongoing studies with wheat have included determining the protein secondary structure, on behalf of the Kansas Agricultural Experiment Station wheat breeders. This approach to such an important aspect of hard wheat protein quality for bread making was first proposed by Piot, when confocal Raman microspectroscopy was used to reveal the relative populations of α-helix and β-sheet formations [38]. The same type of information was obtained using synchrotron IMS by Wetzel *et al.*, representing α-helix$:$$\beta$-sheet ratios of 1.5 to 2.2 for several mature hard wheats, and a ratio of approximately 1.0 for several mature soft wheats [39]. Subsequently, this technique was used as an ongoing project to rank the $\alpha$$:$$\beta$ ratios from 1.2 to 2.3 of hard wheat breeding lines, so as to enable the breeder to make an informed selection, thereby enhancing the breeding process. The results from multiple crop year experiments to determine the $\alpha$$:$$\beta$ ratios and wheat protein quality for end use were recently reported [40].

Another important issue in wheat breeding is to avoid the susceptibility of wheat to sprouting (germination), when in the field prior to harvest in years when high moisture conditions are encountered. By subjecting newly harvested breeding lines on moist blotter paper in a Petri dish for controlled periods of time, and applying a sensitive germination detection technique, differences between the various lines have been revealed by near-IR imaging [41, 42]. While nondestructive near-IR imaging has been developed for the routine testing of new breeding lines, a fundamental study of the chemical differences within the germ of the kernel before and after germination was conducted in the mid-IR region using synchrotron IMS [1]. Images at three wavelengths, highlighting the protein, lipid and carbohydrate, for one kernel that has not germinated and one that has germinated, are shown in Figure 7.13.

(a)

1740 cm^{-1} (carbonyl)   1550 cm^{-1} (amide II)   1025 cm^{-1} (carbohydrate)

(b)

1740 cm^{-1} (carbonyl)   1550 cm^{-1} (amide II)   1025 cm^{-1} (carbohydrate)
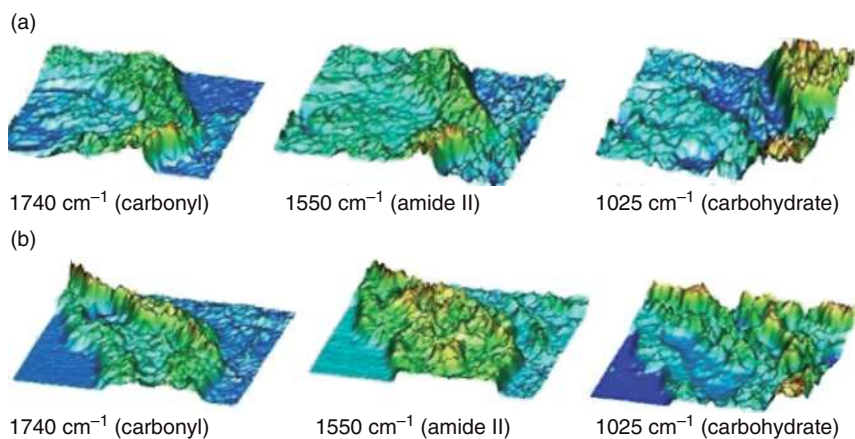
Figure 7.13 (a) Unsprouted kernel *x,y,z* chemical functional group maps of (left) scutellum (lipid), (center) embryonic axis (protein) and (right) endosperm (carbohydrate). All images are from the same imaging data cube; (b) Sprouted kernel *x,y,z* chemical functional group maps of (left) scutellum, (center) the developed proteinaceous embryo and (right) the endosperm next to the embryo, which is virtually void with respect to carbohydrate. The kernel length was ca. 4000–6000 μm. Reproduced with permission from Ref. [1]; © *Spectroscopy*.

Here, the germ in the upper right-hand portion of each image has two parts. In the extreme upper right portion is the embryonic axis, where new life develops after germination. In an arc around the embryo bordering on the endosperm is the scutellum. Whereas, the scutellum is sacrificed to provide nutrition and sustenance to the new life in the embryonic axis, it is observed that the high lipid content before germination is reduced significantly after germination. It is also noted from the protein images that the developing embryo has a much higher protein content than does the embryonic axis prior to germination. An extension of this experiment (see Figure 7.14) involved the mapping of a rectangular region in the scutellum for a number of ungerminated and germinated seeds.

A total of 48 000 spectra was recorded (28 000 sprouted, 20 000 unsprouted) and, by comparing the mean of the lipid : protein ratio in ungerminated and germinated seeds, a significant difference was noted, the average post-germination lipid content being only 80% of the original. Such information was utilized in recent near-IR procedures, where wavelengths between 1700 and 2400 nm revealed such chemical differences.

In the field of animal science, FT-IR microspectroscopy has been used to link animal feed performance (ruminant digestion) to localized chemical distributions within specific corn, barley and canola varieties [43, 44]. A potential solution for remediating chemicals encountered environmentally in contaminated soil is to grow plants capable of 'mining' such chemicals. As an example, sunflower stalks grown hydroponically were imaged by IMS to first locate, and then determine the relative uptake of, these materials [45]. The same group also reported selected
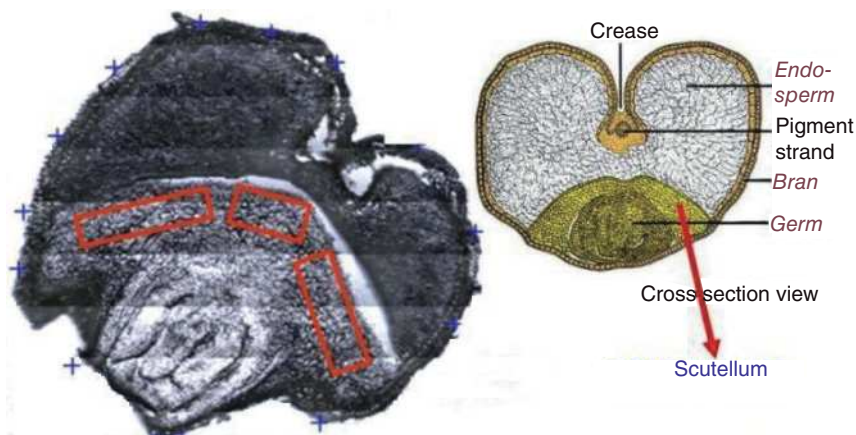
Figure 7.14 Photomicrograph of a wheat kernel transverse section, with mapped areas within the scutellum outlined in red. Note the corresponding botanical parts from the artist's sketch at the right (courtesy of Kansas Wheat Commission); the kernel dimensions were ca. $2000 \times 1000\,\mu m$. Adapted from Ref. [1]; © *Spectroscopy*.

articles on plant spectroscopy, including those prior to the introduction of the IR microscope [46].

7.2.8
Desiccation Study

Recently, IR microspectroscopy has been used to study protein secondary structures in isolated, immature maize embryos, to demonstrate their tolerance to rapid drying. A similar approach was also used to highlight the desiccation tolerance of developing maize embryos at various stages of growth, as a function of changes in their protein secondary structure that occur when they are dried at different stages of their development [47]. The deconvolved spectra of fresh maize embryos excised at 20 and 25 days after pollination differed slightly with regards to the non-α-helix population. The observation of such a difference was enhanced by using D_2O to hydrate samples excised at the same development stage; this avoided any distortion of the amide-I band due to the presence of H_2O. The rapid drying of immature embryos was seen to result in a proportionately lower α-helix content, and a higher contribution of β-sheet/turn stretches. This observation was especially prominent in embryonic axes at 20 days after pollination. However, when these embryos were flash-dried their β-sheet content remained unaffected, matching the profile of fresh embryos.

The IMS study showed an increased proportion in α-helix structure for both slow and mature drying. Thus, the acquisition of full desiccation tolerance is a gradual process that takes place during maturation, as suggested previously

(although at that time IMS was not available to reveal protein secondary structural changes). The rapid drying of embryos at 20 days after pollination led to a residual α-helix population and lost viability, whereas at 25 days after pollination some 74% of the embryos had germinated and the protein profile resembled that of fresh control embryos. However, with slow drying between 20–25 days after pollination, the α-helix content increased compared to fresh control embryos, and the survival rate from desiccation was high. These authors concluded that the slow drying of excised immature embryos led to an increased population of the α-helical protein secondary structure that coincided with an additional tolerance to desiccation stress.

7.3
Leaves

Leaves represent one of the most frequently quantitatively analyzed materials, from the early days of diffuse reflection near-IR instrumentation. In the past, tobacco leaves were analyzed for their nicotine, reducing sugars and moisture content on a routine basis, using a variety of near-IR instruments. Most of these analyses employed interference filter technology and chemometric relationships to effect the appropriate calculations. In this way, forage crops, including native grasses in pastures as well as hay, were analyzed for their feed value based on their protein, lipid and carbohydrate contents, and their digestibility. Recently, hay market auctions in the Pennsylvania dairyland have included loads of hay labeled with near-IR-determined nutrient values, so as to provide potential buyers with information that might concern the well-being of their dairy herds. Although the digestibility calibrations were based on data with a wide scatter, because of the poor precision and accuracy of animal experiments used for calibration, a large data base resulted in a useable regression line. Subsequently, the improved precision of near-IR in comparison with animal experiments made this approach both acceptable and practical.

Mid-IR microspectrometry data on parenchyma bundle sheath (PBS) transverse sections of grass leaf provide a molecular-based method for predicting eventual ruminant digestibility, for selection processes. Such a method is also useful for evaluating experimental crosses in a forage crop breeding program, the aim of which is to improve the digestibility of forage crops, thereby assisting in the conversion of plant protein into animal protein. In this way, large areas of rangeland considered unsuitable for tilling may be grazed with a greater efficiency towards the production of food. As an example, a forage network in North America was established by the United States Department of Agriculture that used near-IR to coordinate research towards the improvement of forage crops. The link between the chemical content of the leaf (PBS) and ruminant digestibility was established by biologist Aiben via microscopy experiments [48]. For this, sections of coastal Bermuda grass (CBG) and an experimental cultivar referred to as CBX, were placed on microscope slides with double-sided Scotch tape. A photomicrograph of each

section was taken before and after treatment with ruminant fluid, at the appropriate temperature for the animal. This results of this microscopic study revealed that, while other parts of the leaf section had been digested, the PBS remained undigested. Moreover, ruminant digestion was greater for the CBX than for the parent CBG, which was known to contain lignin with a high aromatic character.

The analysis of PBS in a cross-section of a grass leaf represented a major challenge to the spatial resolution of the microspectrometer. In 1989, early attempts using an accessory-type IR microscope attached to a conventional FT-IR instrument by way of an optical interface, proved to be unsatisfactory because the neighboring tissue was sampled accidentally and, consequently, the resultant spectra did not accurately represent the PBS. However, when the experiment was repeated using the Spectra-Tech IRμs integrated instrument, in which the spectrometer and microscope were built as a unit, the PBS alone could be probed. With an IRμs installed on NSLS Beamline U2b, the detailed mapping of the vascular bundle and its surrounding tissue was accomplished and the aromatic lignin localized.

The functional group images of the CBG shown in Figure 7.15 have been published previously [12, 17]. For this mapping IMS experiment, Aiken provided 6 μm-thick sections that were subsequently mounted between BaF_2 windows and mapped in transmission mode, using a raster scan process. Attention was focused on the aromatic character of the lignin, with a benzene ring absorption band at ca. 1508 cm^{-1}. The spatial resolution of IMS allows the *in situ* tissue imaging or probing of the PBS to obtain localized chemical imaging and analysis. Such an approach with experimental grasses can be substituted for animal digestion studies, with results having shown that such as technique could provide a means of screening various crosses at early stages of a forage-breeding program. Aiken *et al.* [49] independently reported the single point probing of PBS tissue in which a prominence of the 1508 cm^{-1} band was observed.

In 2005, Heraud *et al.* [50], while working with eucalyptus leaf transverse sections, provided a thorough study of the plant's epidermis, vascular bundle and mesophyl. Each of these botanical parts was characterized spectroscopically from an average of 40 spectra, together with chemometric assessments. The authors presented a useful tabulation of band assignments that referenced previously recorded original investigations. For lignin, in particular, five bands were identified that included 1595 and 1515 cm^{-1}; these were also identified from the spectra of the vascular bundle. The differentiation of protein secondary structures was also revealed between the other two fractions. For example, the amide I band maximum for the mesophyl band at 1658 cm^{-1} was indicative of the α-helix structure, whereas structures from the epidermis, where the amide I band appeared at 1630 cm^{-1}, provided evidence of a β-sheet protein secondary structure. This brief summary does not present the depth and breadth of these studies, however, and the reader is referred to the original article in which the advantages of imaging by synchrotron IMS to provide excellent spatial resolution are discussed. This was achieved with a NicPLAN equipped with a 15× Cassegrainian objective at the Advanced Light Source. A Varian Stingray 300, operated at 8 cm^{-1} resolution with a 64×64
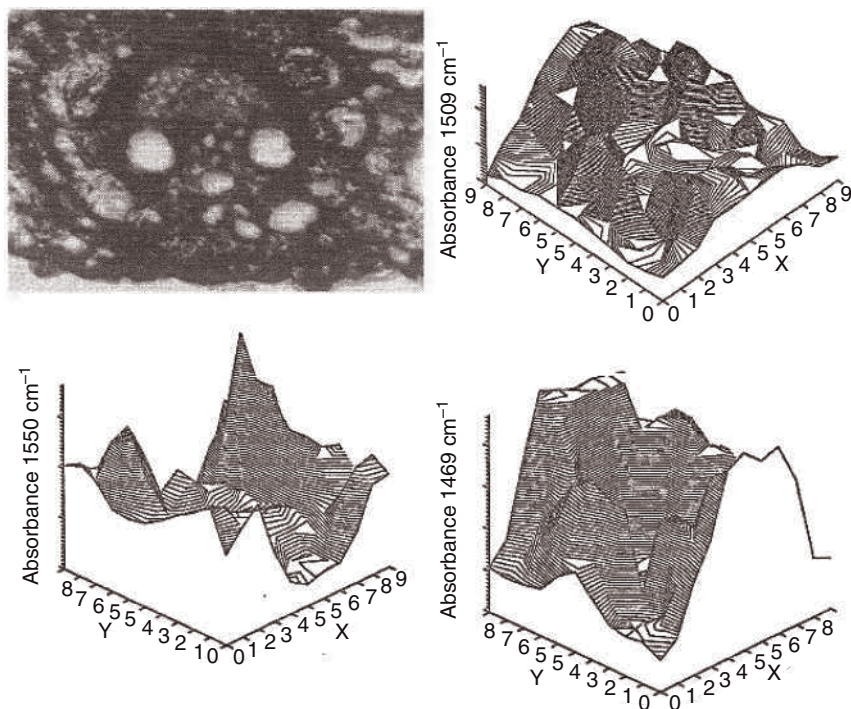
Figure 7.15 Forage digestibility prediction (leaf vascular bundle, shown in photomicrograph top left) analyzed for aromatic character of lignin in the parenchyma bundle sheath. The bundle sheath is less digestible if it is composed of lignin with a great amount of aromatic character. The 1509 cm^{-1} band area functional group map (top right) is indicative of aromatic character. Surrounding the sheath within the vascular bundle are the protein and lipid in the 1550 cm^{-1} and 1469 cm^{-1} band area images (lower left and right), respectively. The units of the *x*- and *y*-axes are micrometers ($\times 10^2$); the *z*-axis band areas are in arbitrary units. Reproduced with permission from Ref. [12]; © Elsevier.

focal plane array, also provided 4096 pixel images. Various spectroscopic features were identified in the epidermis, the vascular bundle and mesophyl, and band assignments were provided and discussed. The practicality of the IMS focal plane array instrument and the synchrotron IMS for data acquisition applicable to all similar studies of leaf materials, was also discussed.

Changes in wheat carbohydrate chemistry due to chemical enzymatic degradation were measured on a macro scale by internal reflection (attenuated total reflection; ATR) FT-IR spectroscopy from a spot size of $250 \times 250\,\mu m$ [51]. In this study, the absorption bands of sucrose, fructose, glucose, arabinose and galactose were identified, and spectra included for mahogany, huckleberry and oak, as well as for cellulose and cellophane. Both, principal component analysis (PCA) and plotting of PC1 versus PC2 enabled distinctions to be made between filter paper, cello-

phane, mahogany, huckleberry and oak. A table of band assignments was also included citing the original references.

7.4
Application of IMS to Stems and Cellulose Polymers

7.4.1
Structure and Lignification

The stems of plants represent the main sources of cellulose, hemicellulose and lignin. The structural function performed by the cellulose biopolymer enables the plant to stand upright alone, to expose the leaves to the sun and to support the weight of the fruit. The stems contain a vascular system that connects the exposed part of the plant to the nutrients and water via the roots. In the trunks of trees, cellulose is provided in the form of wood. Although remote spectroscopic sensing is used to survey the forest canopy, hard and soft woods are characterized in the laboratory by their infrared spectra, the details of which reveal the growing location (north or south), together with various compositional and varietal distinctions. Such findings, when first presented at the International Conference on Fourier Transform Spectroscopy in 1993, served as examples of what could be determined in wood by the use of spectroscopy [52]. Internal reflection techniques are often used on the surface of wood specimens, although very thin specimens obtained with a plane have been analyzed in transmission mode. The distribution and quantity of lignin throughout the specimen is of interest. The stems of small grains such as rice, wheat, oats and barley are potential sources of cellulosic ethanol, and for this particular end use the breeding of such plants with a reduced lignin content in their straw has been suggested.

During the late 1980s and early 1990s, while the present author and coworkers were using IMS to image and analyze brains and grains, McCann and colleagues, at the John Innes Centre for Plant Science Research in Norwich, United Kingdom (in cooperation with the Institute of Food Research in Norwich) were studying plant cell walls using IMS. In parallel with these activities, IMS was being used for biomedical research in areas of cancer, bone and cardiology; indeed, a thematic issue of *Cellular and Molecular Biology* [53] included multiple articles from several countries. In 1992, McCann *et al.* were the first to use IMS to examine plant cell walls [54]. For this, IMS was applied to the cell wall material at all stages of extraction and polymer purification, in the frequency range of 2000-900 cm^{-1}. At each step of extraction, when both the extracts (which contained pectins and xyloglucans) and the residue cell wall materials were examined, IMS was able to detect large conformational changes in pectin polymers on their removal from the cell wall and drying.

The spectra of extracted polymers via IMS were obtained by drying a droplet of extract on a BaF$_2$ window and selecting an area with an appropriate thickness from which to obtain the spectrum. The spectra of alkali-extracted polymers were alike,

and differed significantly from those of the pectins. Spectral subtraction between the successive extraction steps of onion cell wall material showed that distinct carbohydrate features were removed at each step. With polarizers aligned parallel and perpendicular to the long axis of the cell, dichroism studies showed the ester band, amide band, phenolic structure and carbohydrate band to be preferentially oriented transversely to the long axis of a carrot cell. These early IMS studies were performed with a 100 μm spot projected onto a BaF_2 disk, although subsequent investigations, where a greater spatial resolution was important, were conducted with smaller spot sizes. Some results of these experiments are detailed in Sections 7.4.2–7.4.4.

7.4.2
Application of Polarized IMS

The macromolecular orientation in dry and hydrated walls of single onion epidermal cells was studied using IMS [55] by group at Norwich, using polarizing radiation directed either parallel or perpendicular to the long axis of the cell. Dichroism was measured for a single onion cell under various hydration conditions on a Spectra-Tech IR-PLAN microscope stage, using a demountable humidity-controlled hydration cell with BaF_2 windows. Changes in the dichroism of the carbohydrate bands in the 1200–1000 cm^{-1} region were observed, while difference spectra (resulting from parallel polarized spectra minus perpendicular polarized spectra) were plotted for four distinct humidity conditions and compared to a spectrum of cellulose. Because an enhancement of the cellulose background vibration of the polymer chain at 1165, 1115 and 1070 cm^{-1} occurred with the parallel polarization, the authors concluded that cellulose in the epidermal cells was arranged parallel to the long axis of the cell.

7.4.3
Alteration of Cell Wall Architecture

Recently, McCann and coworkers reported the details of some extensive studies targeted at identifying and classifying cell wall phenotypes of mutants on a genome-wide scale [56]. For this, they studied the elongation of a maize coleoptile system for which the cell wall changes have been well characterized. Changes in cell wall architecture were studied during development in reference perturbation, environment or by mutation. Measurements were made at half-day intervals for the maturation study, in reflection/absorption mode, on gold mirror microscope slides with a Continuμm IR microspectrometer operating confocally. (These studies were a combined effort from the Department of Botany and Plant Pathology at Purdue University, IN, and the United Kingdom Cell and Developmental Biology research group.) Cell wall-related mutants in maize are currently being identified in a NSF-funded genomics project (http://cellwall.genomics.purdue.edu); two genes used in these studies are Robertson's *mutator* (*mu*) and Wisconsin 22 (W22). The well-characterized dynamics in cell wall composition that occur during elongation of the hybrid and the W22 maize coleoptiles were used to test the sensitivity of IR

spectra in detecting any defined differences in either monosaccharide or polysaccharide composition. Many subtle changes in band height and shape were seen to occur between the half-days of development, particularly in the carbohydrate fingerprint region involving bands at 1157, 1103, 1060 and 1030 cm^{-1}. A total of 36 IMS spectra was obtained from the cell walls of populations of coleoptiles for each half-day of elongation. Half-day differences in spectra and PCA were then used to account for the variance among a set of spectra.

The results of the PCA showed that three periods in the development of cell walls were defined, and those representing individual embryonic coleoptiles were generally well resolved from those of elongating and senescent days. The embryonic phase was represented by spectra pooled from 1- to 2-day specimens, while the elongation phase was represented by spectra from 3.5 to 4 days, and the senescent phase was represented by combining 5.5- and 6-day spectra. A spectral subtraction (elongating walls minus embryonic walls) revealed the characteristic bands of cellulose. In general, the positively correlated bands represented an increase in carbohydrate, while the negatively correlated bands at 1651, 1628 and 535 cm^{-1} indicated that the protein content of the embryonic walls was greater than that of the elongating walls.

Subtraction of the spectra of elongating walls from the senescent walls showed carbohydrate bands at 1157, 1068 and 1041 cm^{-1} that were relatively enriched. Negatively correlated bands at 1693, 1593 and 1515 cm^{-1} represented a higher content of aromatic compounds in the senescing walls. With the dynamic changes in cell wall composition documented by FT-IR spectra, the spectra were subjected to various multivariate statistical techniques to allow discrimination according to the stage of development, including PCA and ANN. The former technique discriminated 10 different growth stages, while the enhanced capacity of ANN was applied to all 12 growth stages to report on both class assignment, and on the probability of membership of each class for each spectrum. Both, a supervised approach with a genetic algorithm, Neuro-Shell 2, and an unsupervised Kohnen Lavine network were attempted [56].

When applying this procedure to the W22, only coleoptiles at maximum elongation rate could be clearly resolved as distinct classes. The authors predicted that the application of neural networks spectroscopic data into other multivariate measurements of phenotype would provide the framework for a systematic classification of cell wall phenotypes in response to numerous perturbations. In order to establish data for this massive effort, the triplicate average spectra from 36 to 60 inbred coleoptiles were averaged and used for digital subtraction. Baseline-corrected and area-normalized data sets of spectra were used in the chemometric analysis. The multivariate analysis involved PLS, PCA, linear discriminated analysis and Mahalanobis distance. Mahalanobis distance metrics were also applied to the PCA scores of original data. For neural networks, FT-IR spectra were analyzed by genetic and Kohonen algorithms, using a combination of NeuroShell2 and Classifier software (Wards systems group). For the genetic networks, a total of 432 spectra for hybrid maize belonging to 12 classes, each representing half-day growth intervals, was trained through 129 generations.

Synchrotron IMS was used by Raab and Vogel to study the role of *Arabidopsis* cell wall enzymes as susceptibility factors to the fungus *Erysiphe cichoracearum*, a causative agent of powdery mildew disease [57] that occurs in the leaf, stem and root tissues of some plants. For this, mutants of cell wall polysaccharides that lacked a particular biosynthetic enzyme were studied. Live plants were imaged in ecological experiments in small microcosms with a special cell constructed with ZnSe windows (this was referred to as a 'rhizobox'). Spatial resolution was an issue in relation to the root architecture effect of microbial symbioses on the quantity and quality of exudates. The leaf IR spectrum from *Arabidopsis* mutants lacking a particular gene was compared with leaf spectra of wild-type plants. When a detailed comparison of wild-type and *Arabidopsis* spectra was conducted in the 1200 to 950 cm^{-1} region, prominent absorption bands from 1159 to 962 cm^{-1} were assigned to various pectin-related species.

By studying the spectrum of the root in a transparent box, the proposal of studying the ecology of plant responses to different climates and soils was introduced. It has been suggested that the function of the roots is serve as a communication network in the soil. The authors [58] state that, during the life of the plant, as much as 15 % of the total fixed carbon will be diverted into sugars, proteins and other small molecules that are surrendered to the plant. The role of these exudates was discussed, the authors suggesting an interdisciplinary approach to the study of plants, soils and microbes in the field.

7.4.4
Flax Fibers

When Himmelsbach *et al.* used IMS to study flax stems [58], the microchemical structure of the flax stems was determined via an imaging procedure, with the individual domains within stems being identified where various chemical species were located and their spectra monitored. From these IR spectra it was possible to identify the different chemical species present, and to make band assignments, based on published data. Closely related studies performed by the same research group at their Athens facility involved microRaman spectroscopy. The inclusion of a microscopist (Akin) in the team allowed the plant morphology and chemical imaging to be combined in the same study. Subsequently, Akin and coworkers provided additional information on the dew-retted flax fibers; this was considered an important issue in the United States in anticipation of the reintroduction of flax as a cash crop to supply the textile industry. Morrison, Aiken and others described what occurs during the dew-retting of flax fibers [59].

Himmelsbach and colleagues continued to use IMS to produce maps of the distribution of chemical components in flax stem tissues by examining cross-sections of the flax cultivars, ariane and natasja. For this, the chemical composition was superimposed onto the anatomical structure from a photomicrograph, after which functional group maps were produced to indicate each component to the exclusion of others in the matrix by comparison of pure components. Waxes, which were indicated by a sharp shoulder at 2850 cm^{-1}, appeared primarily in the

cuticle and epidermal tissues. Pectin was observed based on the band at $1615\,cm^{-1}$ for the calcium salt form that was primarily detected in surrounding fiber bundles. Cellulose was mapped based on a $1335\,cm^{-1}$ band that showed the greatest intensity in fiber cells. Aromatic compounds were identified with a band at $1510\,cm^{-1}$, and were located primarily in the core tissue. Acetyl groups associated with hemi-cellulosic polysaccharides were indicated by a band at $1250\,cm^{-1}$ found within the fibers and the core tissues [59].

7.4.5
Biopolymer Structure

The protein secondary structure of silk fibroin [60] was studied with near-IR spectroscopy, using silk fibers that had been very carefully selected from naturally generated fibers. The isolation of individual fibers allowed the trapping from Nature of a protein with a particular secondary structure. A spider is able to generate different fibers for different uses, with each fiber having its own secondary structural composition. In the case of silk, an individual fiber may well have a particular composition secondary structure, and in this case it is possible to use near-IR spectra to perform a characterization. This is quite remarkable because the use of a relatively prominent amide-I band in the mid-IR represents a major challenge.

The subject of the secondary protein structure as a means of defining the performance characteristics of wheat endosperm – known as hardness – been explored over a seven year period [39, 40]. Another approach, taken by Baron *et al.*, involves the IMS imaging of the endosperm cell walls rather than of the protein found in the endosperm itself [61]. All of these authors performed the imaging *in situ*, following removal of the protein and starch, in order to study the compositional and architectural heterogeneity and, in relation to this, wheat hardness. In this case, the research was focused on kernel hardness rather than on endosperm hardness, as was the case with our studies. A further study of carbohydrate polymers by the same group involved the investigation of cereal arabinoxylans in relation to their structure and physico-chemical properties.

The technique of FT-IR internal ATR has been developed to the point that, today, ATR mirror lenses are available for an IR microscope. Furthermore, a newly developed, dedicated diamond internal reflection instrument, the IlluminatIR™ (Smith's Detection, Shelton, CT, USA) has now joined the ranks of microspectroscopy. This instrument incorporates a small, horizontally mounted diamond, on the surface of which is placed the material to be examined. In this way, the material is in optical contact with the diamond, and is held in place by a shaft pressing down from above. In this case, the radiation enters from beneath the instrument at an appropriate angle, and internally reflected rays are subsequently collected. The specimen is illuminated from beneath with a near-IR source that is detected and displayed on a video screen. With this optical arrangement, it is possible to locate a particular part of the material in the field of view and to interrogate it. Such an arrangement is particularly user friendly, and indeed it is mostly used by

nonspectroscopists. With modern-day developments in internal reflection, and the use of a diamond internal reflection element (IRE), a solid specimen such as a stem transverse section was easily analyzed in order to detect and measure the uptake of contaminants present in the soil (J.A. Reffner and D.L. Wetzel, 2001, unpublished results). Internal reflection has also been employed to detect *Fusarium* fungi on maize, this being a nondestructive testing system for the specific analysis of the surface of a material [62].

Cell walls have been analyzed during early grain development in rice by Gottlieb *et al.* [63], who paid particular attention to the cell wall at the (1-3) and on the (1-3, 1-4) position of the six-carbon units. In one study, conducted in 1990, Carpita *et al.* [64] collected IMS data with an image plane mask size of $25 \times 25 \mu m$, using a BioRad UMA 500 microscope interfaced to an FTS 1750 FT-IR spectrometer. The cell wall polysaccharides were studied and considered to be some of the most complex biopolymers yet found. The main concern of these authors was the structural and architectural changes in cell walls that appeared as a consequence of developmental regulation, environmental adaptation or genetic modification. Hence, a rapid method for screening large numbers of plants for cell wall phenotypes using IMS and PCA was developed.

IMS simultaneously reveals the type, distribution and relative abundance of chemical components within a particular system. A single spectrum contains information regarding the molecular structure and intermolecular interactions among individual sample components. Investigations in this area, including the detection of cell walls with altered compositions and the selection of mutant plants with altered cell wall compositions and architectures, is particularly useful because of the wide range of potential modifications and the possibility of uncovering novel genes that encode enzymes participating in biosynthetic pathways, wall assembly or modifications to polymers.

7.4.6
Cell Wall Alterations via Mutations

When pixelated imaging was employed in a transverse section of a three-day-old maize coleoptile [65], the $25 \times 25 \mu m$ pixilated images were produced in maps for $1720 \, cm^{-1}$ for phenolic esters, $1740 \, cm^{-1}$ for carbonyl, $1550 \, cm^{-1}$ for aromatics, and 1000, 1020, 1034 and $1090 \, cm^{-1}$ for various carbohydrate components. When PCA was carried out on an exploratory basis over the range of 1400 to $1200 \, cm^{-1}$, four bands (three of them cellulosic) were exhibited from potato tuber cortex from 20 wild-type tubers. On comparison of these spectra with those from 20 transgenic tubers, the latter were seen to have overexpressed a fungal galactanase associated with the apoplast. Transdifferentiation as a function of time from 30 min to 48 h was shown to involve both glucosyl transferase and cellulose synthase, and these developments were followed by galactosyl transferase and a cellulose synthase-like material, simultaneously with the addition of caffeic acid and *o*-methyltransferase. Such spectroscopically identified, genetically defined variations through mutant approaches or transgenic technologies offer an excellent opportunity to identify a broad range of structural and architectural alterations in cell walls.

7.4.7
Cell Wall Heterogeneity

Barron *et al.* [61] used IMS to study the architectural heterogeneity of endosperm cell walls. In order to obtain these cell walls, one endosperm was selected which was very soft, and other groups of endosperms that were very hard. Following removal of the endosperm, an analysis of the remaining cell walls revealed two distinct populations of endosperm cells that could be identified by spectral features related to the cell morphology and age. The main cell wall component responsible for the difference was the polysaccharide arabinoxylan, while the cell walls of the hard endosperm could be distinguished from those of the soft endosperm by their spectral features, in comparison with water-extractable arabinoxylan. In the central endosperm, structural differences within the polysaccharides are thought to contribute to the distinction between hard and soft cultivars. In the developing grain, a clear difference in the composition of the endosperm cell walls is observed 50 days after anthesis. These studies were conducted with a FPA Digilab instrument, where the nominal pixel size was $5\,\mu m^2$. The spectra were recorded in a internal reflection mode with an ATR Golden Gate accessory (Specac). Strictly speaking, these studies did not constitute *in situ* microspectroscopy because the cell walls were harvested from the endosperm prior to recording the spectra. However, this particular project and its results are interesting in relation to our own α-helix/β-sheet protein secondary structure found within the subaleurone endosperm and central endosperm of various hard wheats [39, 40]. Quantitation of the ratio of secondary protein structures was used in our studies to establish a ranking of the endosperm hardness trait. However, in carbohydrate microspectroscopy studies the cell wall was used as a matter of distinction by its architectural heterogeneity.

A combination of synchrotron IMS and immunolabeling techniques was used to study the biochemistry of aleurone cell walls at Synchrotron SOLEIL (France) [66]. A confocal operation with the synchrotron source led to a maximized spatial resolution. Such high spatial resolution and discrimination of various polysaccharides in cell walls enabled an estimation to be made of the localized relative population of β-glucan and arabinozylan. β-Glucan levels were found to be highest in the periclinal cell walls, close to the starchy endosperm, while the walls between cells were enriched with arabinozylan. When confocal imaging experiments were performed on both mature and early-stage kernel development, heterogeneity was seen to be greater prior to maturation.

7.4.8
Esters in Cell Walls

In studies conducted at Norwich by Sene and coworkers [67], a BioRad FTS-40 FT-IR instrument interfaced to a Spectra-Tech IR PLAN microscope was used, with sample areas of $100 \times 100\,\mu m$. The operation was conducted in transmission mode on BaF_2 windows, and the spot size used was compatible with areas of the single cell wall fragments of 0.1–0.2 μm thickness. Pectic polysaccharides extracted

from onion were examined, notably in the region of 1200 to 900 cm^{-1}. When operating with five plants that contained esters, the spectra showed the ester band to contain more than one type of ester. In both the cell walls and isolated polymers, the maximum ester band was between 1741 to 1730 cm^{-1}, indicating that the majority of wall esters were saturated alkyl esters. (Included in this reference is a table with assignments of the main bands of the IR and Raman spectra that had been imported from earlier published accounts.) Ester bands from cell walls in the onion and carrot were compared, and methyl esters of the D-galacturonic acid residues of pectin revealed. In this way, the spectra of the unextracted cell wall materials of onion, carrot, polypogon rice and sweet corn were obtained. These IR studies were backed up with Raman spectroscopy. The degree of esterification of the wall was compared to the extraction step used to obtain the sample.

7.5
Algae

Although algae has been the subject of biological investigation over time, since 1993 the application of FT-IR microspectroscopy [68] by groups from Australia, Italy, the UK and the US have involved the development of algal colonies and their response to available nutrients. This topic is not discussed here due to the limited space available; however, recently reported [25, 26] images of two single algal cells are shown in Figures 7.9 and 7.10.

7.6
Comments

Quoting John Reffner, 'Microscopy and spectroscopy are two of the oldest techniques used in the study of nature and combined, their value is greater than the sum of the two.' With this proposal I heartily agree. Indeed, array detection makes imaging more convenient and further enhances the contribution of IMS. Moreover, an acceleration of its use is expected to continue throughout the twenty-first century. **Come on in, the water is fine!**

References

1 Koc, H. and Wetzel, D.L. (2007) Imaging local chemical microstructure of germinated wheat with synchrotron infrared microspectroscopy. *Spectroscopy*, **22** (10), 24–32.

2 Wetzel, D.L. (2008) Biomedical Applications of Infrared Microspectroscopy and Imaging by Various Means, in *Biomedical Vibrational Spectroscopy* (eds P. Lasch and J. Kneipp), John Wiley & Sons, New York, pp. 39–78.

3 Messerschmidt, R.G. and Sting, D.W. (1989) Microscope having dual remote image masking. US Patent No. 4,877,960.

4 Lewis, E.N., Treado, P.S., Reeder, R.C., Story, G.M., Dowrey, A.E., Marcott, C. and Levin, I.W. (1995) Fourier-transform spectroscopic imaging using an infrared focal plane array detector. *Anal. Chem.*, **67**, 3577–387.

5 Lewis, E.N. and Levine, I.W. (1995) Real time, midinfrared spectroscopic imaging using Indium-Antimonide focal-plane array detection. *Appl. Spectrosc.*, **49** (5), 672–8.

6 Xing, J., Bravo, C., Moshou, D., Ramon, H. and DeBaerdemaeker, J. (2006) Bruise detection on golden delicious apples by vis/NIR spectroscopy. *Comput. Electr. Agric.*, **52**, 11–20.

7 Wetzel, D.L., Messerschmidt, R.G. and Fulcher, R.G. (1987) Chemical mapping of wheat kernels by FT-IR microspectroscopy, Federation of Analytical Chemistry and Spectroscopy Societies, 14th Annual Meeting, Detroit, MI, October 1987, Abstract No. 151, p. 70.

8 Wetzel, D.L. and Fulcher, R.G. (1990) Fourier transform infrared microspectrometry of food ingredients, in *Flavors and Off-Flavors* (ed. G. Charlambous), Elsevier Press, Amsterdam, pp. 485–510.

9 Wetzel, D.L. (1993) A molecular mapping of grain with a dedicated integrated Fourier transform infrared microspectrometer, in *Food Flavor, Ingredients and Composition* (ed. G. Charalambous), Elsevier Press, Amsterdam, pp. 679–728.

10 Wetzel, D.L., Slatkin, D.N. and LeVine, S.M. (1998) FT-IR microspectroscopy detection of metabolically deuterated compounds in the rat cerebellum: a novel approach for the study of brain metabolism. *Cell. Mol. Biol.*, **44** (1), 15–28.

11 Reffner, J.A. (1990) *Molecular Microspectral Mapping with the FT-IR Microscope* (EMAGMICRO89, London, September 1989), Institute of Physics Conference Series, No. 98, Chapter 13. IOP Publishing, London, pp. 559–69.

12 Wetzel, D.L. (1995) Microbeam molecular spectroscopy of biological samples, in *Food Flavors: Generation Analysis and Process Influence* (ed. G. Charlambous), Elsevier Press, Amsterdam, pp. 2108–39.

13 Messerschmidt, R.G. and Harthcock, M. (1988) *Infrared Microscopy: Theory and Applications*, Marcel Dekker, New York.

14 Wetzel, D.L. and Reffner, J.A. (1991) Compositional profile in grain thin sections by Fourier transform infrared microscopy. *International Cereal Chemistry Symposium, Vienna, Austria* (ed. R. Lasztity), ICC and Technical University of Budapest, Budapest, Hungary, p. 47.

15 Wetzel, D.L. and Fulcher, R.G. (1990) Fourier transform infrared microspectrometry of food ingredients, in *Flavors and Off-Flavors* (ed. G. Charalambous), Elsevier Press, Amsterdam, pp. 485–510.

16 Wetzel, D.L. and Reffner, J.A. (1993) Using spatially resolved Fourier transform infrared microbeam spectroscopy to examine the microstructure of wheat kernels. *Cereal Foods World*, **38** (1), 9–20.

17 Wetzel, D.L., Eilert, A.J., Pietrzak, L., Miller, S.S. and Sweat, J.A. (1998) Ultraspatially-resolved synchrotron infrared microspectroscopy of plant tissue *in situ*. *Cell. Mol. Biol.*, **44** (1), 145–67.

18 Cho, L.L., Reffner, J.A., Gatewood, B.M. and Wetzel, D.L. (1999) A new method for fiber comparison using polarized infrared

microspectroscopy. *J. Forensic Sci.*, **44** (2), 275–82.

19 Wetzel, D.L. and Carter, R.O., III (1998) Synchrotron powered FT-IR microspectroscopic incremental probing of photochemically degraded polymer films, in *Fourier Transform Spectroscopy* (ed. J.A. deHaseth), American Institute of Physics, Woodbury, New York, pp. 567–70.

20 Wetzel, D.L. and LeVine, S.M. (1992) Brain mapping with FT-IR microspectroscopy. *Proceedings of SPIE–Int. Soc. Opt. Eng.*, **1575**, 435.

21 Wetzel, D.L. and Levine, S.M. (1993) *In situ* FT-IR microspectroscopy and mapping of normal brain tissue. *Spectroscopy*, **8** (4), 40–5.

22 Levine, S.M., Wetzel, D.L. and Eilert, A.J. (1994) Neuropathology of twitcher mice: examination of histochemistry, immunohistochemistry, lectin histochemistry and Fourier transform infrared microspectroscopy. *Int. J. Dev. Neurosci.*, **12**, 275–88.

23 Reeder, C., Marcott, R.C., Sweat, J.A., Panzer, D.D. and Wetzel, D.L. (1999) FT-IR spectroscopy imaging microscopy of wheat kernels using a mercury-cadmium-telluride focal-plane array detector. *Vib. Spectrosc.*, **19**, 123–9.

24 Jamin, N., Dumas, P., Mincuit, J., Fridman, W.H., Teilland, J.L., Carr, G.L. and Williams, G.P. (1998) Highly resolved chemical imaging of living cells by using synchrotron infrared microspectrometry. *Proc. Natl Acad. Sci. USA*, **95** (9), 4837–40.

25 Heraud, P., Wood, B.R., Tobin, M.J., Beardall, J. and McNaughton, D. (2005) Mapping of nutrient-induced biochemical changes in living algal cells using synchrotron infrared microspectroscopy. *FEMS Microbiol. Lett.*, **249**, 219–25.

26 Murdock, J.N., Dodds, W.K. and Wetzel, D.L. (2008) Subcellular localized chemical imaging of benthic algal nutritional content via Hg Cd Te array FT-IR. *Vib. Spectrosc.*, **48**, 179–88.

27 Carr, G.L., Reffner, J.A. and Williams, G.P. (1995) Performance of an infrared microspectrometer at the NSLS. *Rev. Sci. Instrum.*, **66**, 1490–2.

28 Reffner, J.A., Carr, G.L., Sutton, S., Hemley, R.J. and Williams, G.P. (1994) Infrared microspectroscopy at the NSLS. *Synchrotron Radiat. News*, **7** (2), 30–7.

29 Budevska, B.O. (2002) Vibrational spectroscopy imaging of agricultural products, in *Handbook of Vibrational Spectroscopy*, Vol. **5** (eds J.M. Cholmers and P.R. Griffiths), John Wiley & Sons, Ltd, Chichester, UK, pp. 3720–32.

30 Budevska, B.O., Sum, S.T. and Jones, T.J. (2003) Application of multivariate curve resolution for analysis of FT-IR microspectroscopic images of *in situ* plant tissue. *Appl. Spectrosc.*, **57**, 2.

31 Wetzel, D.L. and Williams, G.P. (1998) Localized (5 mm) probing and detailed mapping of hair with synchrotron powered FT-IR microspectroscopy, in *Proceedings, 11th International Conference on Fourier Transform Spectroscopy, Athens, Georgia, August 1997* (eds J.A. deHaseth and R.A. Dluhy), American Institute of Physics, Woodbury, New York.

32 Sweat, J.A. (1995) Variations in tempering times for winter wheats by IR microspectroscopic tracking of D_2O. MS thesis, Kansas State University, Manhattan, KS.

33 Walchle, S.M. (1996) A potential sampling technique of wheat gluten for stress gradient measurement by infrared microspectroscopy. MS thesis, Kansas State University, Manhattan, KS.

34 Cho, L.L., Reffner, J.A., Gatewood, B.M. and Wetzel, D.L. (1999) A new method for fiber comparison using polarized infrared microspectroscopy. *J. Forensic Sci.*, **44** (2), 275–82.

35 Cho, L.L., Reffner, J.A. and Wetzel, D.L. (1999) Forensic classification of polyester fibers by infrared dichroic ratio pattern recognition. *J. Forensic Sci.*, **44** (2), 283–91.

36 Sweat, J.A. and Wetzel, D.L. (2001) Near infrared acousto-optic tunable filter based instrumentation for the measurement of dynamic spectra of polymers. *Rev. Sci. Instrum.*, **72** (4), 2153–8.

37 Panzer, D.D. (1999) Documenting the chemical microstructure in hard wheat varieties using infrared Microspectroscopy. MS thesis, Kansas State University, Manhattan, KS.

38 Piot, O., Autran, J.C. and Manfait, M.M. (2000) Spatial distribution of protein and phenolic constituents in wheat grain a probed by confocal Raman microspectroscopy. *J. Cereal Sci.*, **32**, 57–71.

39 Wetzel, D.L., Srivarin, P. and Finney, J.R. (2003) Revealing protein infrared spectral detail in a heterogeneous matrix dominated by starch. *Vib. Spectrosc.*, **31**, 109–14.

40 Bonwell, E.S., Fisher, T.L., Fritz, A.K. and Wetzel, D.L. (2008) Determination of endosperm protein secondary structure in hard wheat breeding lines using synchrotron infrared microspectroscopy. *Vib. Spectrosc.*, **48**, 76–81.

41 Smail, V.W., Fritz, A.K. and Wetzel, D.L. (2006) Chemical imaging of intact seeds with NIR focal plane array assists plant breeding. *Vib. Spectrosc.*, **42**, 215–22.

42 Koc, H., Smail, V.W. and Wetzel, D.L. (2008) Reliability of InGaAs focal plane array imaging of wheat germination at early stages. *J. Cereal Sci.*, **48**, 394–400.

43 Yu, P., Christensen, C.R., Christensen, D.A. and McKinnon, J.J. (2005) Ultrastructural-chemical makeup of yellow- and brown-seeded *Brassica canola* within cellular dimensions, explored with synchrotron reflection FT-IR microspectroscopy. *Can. J. Plant Sci.*, **85** (3), 533–41.

44 Yu, P., McKinnon, J.J., Christensen, C.R., Marinkovic, N.S. and Miller, L.M. (2003) Chemical imaging of microstructures of plant tissues within cellular dimensions using synchrotron infrared microspectroscopy. *J. Agric. Food Chem.*, **51**, 6062–7.

45 Dokken, K.M., Davis, L.C., Erickson, L.E., Castro-Diaz, S. and Marinkovic, N.S. (2005) Synchrotron Fourier transform infrared microspectroscopy: a new tool to monitor the fate of organic contaminants in plants. *Microchem. J.*, **81**, 86–91.

46 Dokken, K.M., Davis, L.C. and Marinkovic, N.S. (2005) Use of infrared microspectroscopy in plant growth and development. *Appl. Spectrosc. Rev.*, **40**, 301–26.

47 Wolkers, W.F., Bochicchio, A., Selvaggi, G., Hoekstra, A. and Folkert, A. (1998) Fourier transform infrared microspectroscopy detects changes in protein secondary structure associated with desiccation tolerance in developing maize embryos. *Plant Physiol.*, **116**, 1169–77.

48 Aiken, D.E. (1982) Section to slide technique for study of forage anatomy and digestion. *Crop Sci.*, **22**, 444–6.

49 Aiken, D.E., Himmelsbach, D.S., Carl, R.T., Hanna, W.W. and Barton, F.B., II (1993) Mid-infrared microspectroscopy to assess lignin in plant tissues related to digestibility. *Agron. J.*, **85**, 171–5.

50 Heraud, P., Caine, S., Sanson, G., Gleadow, R., Wood, B. and McNaughton, D. (2006) Focal plane array infrared imaging: a new way to analyse. *New Phytol.*, **173**, 216–25.

51 Marcella, M., Dighton, J. and Arbuckle, G.A. (2000) Characterization of plant carbohydrates and changes in leaf carbohydrate chemistry due to chemical and enzymatic degradation measured by microscopic ATR FT-IR spectroscopy. *Appl. Spectrosc.*, **54** (5), 681–6.

52 Faix, O., Bottcher, J.H. and Bertel, E. (1992) Using FT-IR Spectroscopy and FT-IR microscopy for examination of wood and wood tissues. *Proceedings of SPIE – Int. Soc. Opt. Eng.*, **1575**, 428–30.

53 Wetzel, D.L. and LeVine, S.M. (1998) Fourier transform infrared (FT-IR) microspectroscopy: a new molecular dimension for tissue or cellular imaging dimension for tissue or cellular imaging and *in situ* chemical analysis. *Cell. Mol. Biol.*, **44** (1), 1–280.

54 McCann, M.C., Hammouri, M., Wilson, R., Belton, P. and Roberts, K. (1992) Fourier transform infrared microspectroscopy is a new way to look at plant cell walls. *Plant Physiol.*, **100**, 1940–7.

55 Chen, L., Wilson, R.H. and McCann, M.C. (1997) Investigation of macromolecule orientation in dry and hydrated walls of single onion epidermal cells by FTIR microspectroscopy. *J. Mol. Struct.*, **408/409**, 257–60.

56 McCann, M.C., Defernez, M., Urbanowicz, B.R., Tewari, J.C., Langewisch, T., Olek, A., Wells, B., Wilson, R.H. and Carpita, N.C. (2007) Neural network analyses of infrared spectra for classifying cell wall

architectures. *Plant Physiol.*, **143**, 1314–26.

57 Raab, T.K. and Vogel, J.P. (2004) Ecological and agricultural applications of synchrotron IR microscopy. *Infrared Phys. Technol.*, **45**, 393–402.

58 Himmelsbach, D.S., Khalili, S. and Akin, D.E. (1998) FT-IR microspectroscopic imaging of flax (*Linum usitatissimum* L.) stems. *Cell. Mol. Biol.*, **44**, 99–108.

59 Morrison, W.H., III, Archibald, D.D., Sharma, H.S.S. and Akin, D.E. (2000) Chemical and physical characterization of water- and dew-retted flax fibers. *Ind. Crops Prod.*, **12**, 39–46.

60 Mo, C., Wu, P., Chen, X. and Shao, X. (2006) Near-infrared characterization on secondary structure of regenerated *Bombyx mori* silk fibroin. *Appl. Spectrosc.*, **60** (12), 1438–44.

61 Barron, C., Parker, M.L., Mills, E.N.C. and Rouau, X. (2005) FTIR imaging of wheat endosperm cell walls in situ reveals compositional and architectural heterogeneity related to grain hardness. *Planta*, **220**, 667–77.

62 Kos, G., Lohninger, H. and Krska, R. (2002) Fourier transform mid-infrared spectroscopy with attenuated total reflection (FT-IR/ATR) as a tool for the detection of *Fusarium* fungi on maize. *Vib. Spectrosc.*, **29**, 115–19.

63 Gottlieb, D.M., Schultz, B., Jacobsen, S.W. and Søndergaard, W. (2004) Multivariate approaches in plant science. *Phytochemistry*, **65**, 1531–154.

64 Carpita, N.C., Defernez, M., Findlay, K., Wells, B., Shoue, D.A., Catchpole, G., Wilson, R.H. and McCann, M.C. (2001) Cell wall architecture of elongating maize coleoptile. *Plant Physiol.*, **127**, 557–65.

65 McCann, M.C. and Caripta, N.C. (2005) Looking for cell wall mutants of *Arabidopsis thaliana*. *Plant Biosyst.*, **139**, 80–3.

66 Jamme, F., Robert, P., Bouchet, B., Saulnier, L., Dumas, P. and Guillon, F. (2008) Aleurone cell walls of wheat grain: high spatial resolution investigation using synchrotron infrared microspectroscopy. *Appl. Spectrosc.*, **62** (8), 895–900.

67 Sene, C.F.B., McCann, M.C., Wilson, R.H. and Grinter, R. (1994) Fourier transform Raman and Fourier transform infrared spectroscopy: an investigation of five higher plant cell walls and their components. *Plant Physiol.*, **106**, 1623–30.

68 Sekkal, M., Huvenne, J.P., Legrand, P., Sombret, B., Mollet, J.C., Mouradigivernaud, A. and Verdus, M.C. (1993) Direct structural identification of polysaccharides from red algae by FTIR microspectroscopy. 1. Localization of agar in *Gracilaria verrucosa* sections. *Mikrochim. Acta*, **112**, 1–10.

8
Near-Infrared Hyperspectral Imaging in Food and Agricultural Science

Véronique Bellon-Maurel and Janie Dubois

8.1
Introduction

8.1.1
A Brief History of Near-Infrared Spectral Imagers

Although imaging in the near-infrared (NIR) spectral range was first developed for remote sensing applications during the 1970s, major interest was not expressed in the NIR imaging of food products until the 1990s. By the start of the twenty-first century, however, the procedure had become generally accepted, driven by the availability of reliable NIR imaging systems for both on-line and laboratory purposes.

NIR imaging experiments create three-dimensional (3-D) images where two dimensions provide spatial information and one dimension provides spectral information. If the third dimension is restricted to a limited number of wavelength bands (typically between 3 and 10), a multispectral image is created; consequently, when the whole spectrum is scanned the image created is termed '*hyperspectral*' (Figure 8.1).

Optimizing the acquisition of this type of images has been a major challenge for the past 20 years, and two techniques have emerged and are now mainstream. The first method involves recording the images at each wavelength consecutively – that is, band-by-band – using either a filter wheel (for multispectral imaging only) or a tunable filter, generally an acousto-optic tunable filter (AOTF) or a liquid crystal tunable filter (LCTF), for hyperspectral imaging. The main advantage of these whole-image, single-band approaches is that the spatial resolution is very good and the entire image is acquired at once, thereby minimizing the presence of artifacts in the image. The downside is that inconsistencies may appear when the wavelength is changed, and if the optical device or the sample is not stabilized.

The second method of creating NIR images is to acquire one line of a sample at a time, projecting the spectral axis on the second dimension of the imaging
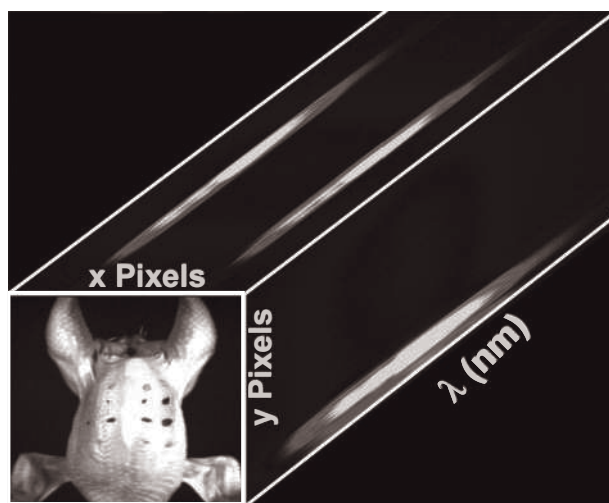
Figure 8.1 Hyperspectral image of poultry; the third dimension is the spectral one. Illustration courtesy of B. Park.

array (cf. Chapter 13 of this book). By sweeping along the sample line by line, it is possible to reconstruct the overall hyperspectral image of the sample. This technology, which has been widely used in remote sensing, is generally the one chosen for on-line cameras because the displacement of the sample on the conveyor belt is compatible with the need for relative repositioning of the sample below the array; the image is thereby acquired as the sample proceeds in front of the camera. The availability of prism-grating-prism (PGP) components designed for the 400–900 nm range during the late 1990s has boosted the design of line-by-line imagers. Such components are now also available in the 900–1700 nm range, with prototypes having also just been introduced for the 1000–2450 nm range [1]. The detectors are cameras, usually based on a silicon array for the short wavelength range (400–1000 nm), or on InGaAs, InSb or MCT arrays for longer wavelengths. There is a general agreement that the analogue/digital (A/D) converter must be at least 10 bits to yield valuable spectral information.

8.1.2
When Should NIR Hyperspectral Imaging be Used in Food and Agricultural Products?

Today, NIR imaging is increasingly investigated for the analysis of food. Applications range from on-line quality monitoring to the spatially resolved evaluation of structural and biochemical composition of various products [2]. The breadth of applications exploits both the broad wavelength range that is attributed to the NIR spectrometry and the facility and versatility with which applications can be developed, based on the simplicity of sampling. Although there are no rules that govern

where instrumentation may be most beneficial – that is, in the laboratory, at line or on-line – there has been a general trend to mount short-wavelength range instruments on-line, but to keep the imaging systems accessing the longer wavelength range in the laboratory. Many reasons have led to this inclination, the most important factors probably relating to cost and the type of information that is needed. This leads to two main types of use for NIR hyperspectral imagers:

- As a laboratory-based analytical technique, NIR imaging is an extension of NIR spectrometry. It accesses the same chemical information, but in a spatially resolved multispectral parallel approach. Laboratory devices are generally aimed at developing knowledge on product composition and at routine quality control. This calls on two main advantages of NIR hyperspectral imaging: (i) the capability of mapping chemical components; and (ii) the possibility of high-throughput analysis such as screening. In addition, NIR imaging enables acquisition with a small pixel size, and therefore can reduce considerably the limit of detection compared to that of traditional NIR spectrometry, as far as mixtures are dealt with. This opens very interesting paths in the detection of contaminants and small biochemical changes, as might be expected in genetically modified organisms (GMOs).

- As an on-line process monitoring technology, in the food plant NIR imaging appears more as an extension of vision and image analysis systems, when classical red/green/blue (RGB) vision systems fail. In-line devices are generally dedicated to detecting foreign bodies or anomalous areas (defects, etc.) which are not visible using RGB cameras.

Descriptions of these two 'families' of NIR hyperspectral imaging usage are provided in the following sections, together with example applications that illustrate today's state-of the art technologies and methodologies.

8.2
At the Laboratory Scale

Regardless of the final location of the analytical tool, all of these methods have originated in the laboratory. Hence, in order to avoid repetition we focus the discussion here on chemical imaging using vibrational spectroscopic principles – that is, the spectral range encompassing the combination, first, second and third overtone regions of the NIR spectrum. Beyond the third overtone, the spectral bands are broad and begin to overlap with fluorescence and visible bands. The short wavelength range is further discussed in Section 8.3, which details the on-line applications of these systems.

Here, we provide examples of various paths of development leading to NIR imaging methods that have been described for the analysis of corn. Although these examples focus on a single commodity, the approaches are universal and provide a good overview of possibilities for the development of NIR chemical imaging

methods in food science. The basic steps involved in determining optimal sampling, instrumentation and analytical parameters are presented, with particular emphasis placed on the practical aspects of the methods. Finally, we describe other areas, such as plant breeding and feed analysis, where laboratory NIR imaging systems are gaining, or already hold, important value in the food sector.

8.2.1
Factors to Consider in the Development of NIR Chemical Imaging Methods

The first question that must be answered before any development work can start is the objective of the method. For simplicity, we focus on three common and important goals: (i) the detection of contamination; (ii) the evaluation of economic value (grading); and (iii) understanding the biochemical and physiological changes. Each objective involves a number of different requirements. For example, the detection of contamination probably requires good chemical specificity, but also possibly a very large magnification if the contaminant is present at the microscopic scale. Grading is at the opposite end of the scale; here, speed is of the essence, some chemical specificity is needed, and a macroscale is often sufficient. Research-type methods aimed at characterizing subtle differences go beyond contaminant detection and sampling schemes, and often involve oversampling both on the spectral and spatial axes to gain a maximum amount of knowledge, regardless of the time penalty.

Once the objective has been established, the sampling options are appraised. The field of view required for the application, the type of measurement (transmission or diffuse reflection), the type and intensity of the NIR source, requirements for depth of field and spatial resolution must also be established.

The third step involves selecting the spectral range or bands that can access the desired information. As mentioned above, the width of the electromagnetic spectrum referred to as NIR is very large. For food applications, the reported NIR range expands somewhat beyond the traditional definition of the NIR, that is the 750–2500 nm range. The terms 'NIR chemical imaging' or NIR vibrational spectroscopic imaging specifically imply that the image contrast originates from the molecular vibrational transitions, as opposed to visible color or fluorescence, which originates from electronic transitions. Considering that NIR chemical imaging systems are perceived as better suited in laboratory settings and the lengthy discussion of shorter wavelength applications in the section discussing on-line application, the scope of this discussion is limited to NIR chemical imaging systems (i.e., 750–2500 nm).

Today, NIR spectroscopy is a staple in the food and agricultural analytical laboratory, and consequently tables of NIR bands arising from the chemical composition of foods are readily available (e.g., Ref. [3]). These may help to determine if a multispectral or hyperspectral imaging system suits the problem more economically and efficiently. However, it is really the scope of the problem, or question, at hand that ultimately guides the selection of the system. A hyperspectral imaging system is, by definition, a better option in a laboratory setting because it allows

access to the whole spectral range, providing the flexibility to explore large spectral regions, bands and/or specific wavelengths for optimal classification or quantification (cf. Chapter 2). Chemical specificity increases with wavelength, where the NIR bands arising from broad and weak overtone bands appear in the lower end of the range, while the sharper and more intense bands arising from combination bands typically show above 1800 nm. The *chemical specificity* required for a particular application is thereby a fundamental criterion for the selection of appropriate instrumentation.

The final step in the development of a method is to establish the requirements for speed versus the necessary specificity. In short, a method may perform better in terms of specificity if a broad spectral region is used in a comprehensive chemometric model, but the duration of data acquisition may not be suitable for the application. The opposite is also true, where a single- or dual-wavelength measurement may meet the ideal speed target, but fail in terms of specificity. Various instrumental platforms are available on the market, and it is imperative that a balance between these parameters be achieved for a method to ever reach deployment. For laboratory-based methods, specificity is often much more important than speed, reinforcing the need for a hyperspectral imaging system. If the instrument is to be used for quality control, then speed should be considered in the development of the method. It is important to bear in mind that speed and specificity are not mutually exclusive; indeed, they can often both be achieved if the method is properly targeted to the question at hand.

8.2.2
The Many Interests of Corn from a NIR Imaging Perspective

Corn is a great example of a food product that has generated broad chemical imaging interest. Early in the history of industrial applications of NIR spectroscopy, corn was placed in the NIR beam path to measure its moisture content [4]. A number of reports have described the determination of various constituent concentrations using NIR spectroscopy (e.g., Refs [4, 5]). Although the availability of the chemical information was clearly understood in these early advances, it was also established that the physical characteristics of the kernel, the fact that only a portion of the kernel is analyzed and the dilution of spectral information from minor components in the spectrum originating from the bulk components, played a large role in the errors of predictions obtained. When approaching the problem with a chemical imaging system, it is possible to investigate the chemical composition at all spatial positions on the kernel surface, thereby increasing the capability to detect and measure minor components. Appropriate data processing and calibrations can be devised to account for the spectral changes due to physical factors, such as baseline offsets resulting from density differences. For example, Cogdill and colleagues [6] used a custom NIR imaging system based on silicon CCD camera and an LCTF to measure individual corn kernels in the spectral range 750–1090 nm. The objective of these studies was to improve measurement accuracy by limiting the effect of sampling difficulties experienced with NIR

spectroscopy of individual kernels, where the spectrum is only representative of a portion of the kernel [7]. Placing the whole kernel in the field of view should improve the results by eliminating the variability associated with the position of the probe on the kernel. Although this experiment utilized an imaging system for data acquisition, the data were reduced to a single spectrum per kernel for processing. The signal-to-noise ratio (SNR) of the data, and the choices made in the data processing (especially discarding the spatial aspect of the data) limited the success of predicting moisture and oil content using this approach. Nevertheless, the authors foresaw interesting possibilities, and suggested that multiple models might be combined to predict constituent contents in the various regions of the kernel. This would also increase the intrinsic economic value of the results by expanding the method to measure the content of minor constituents, rather than limiting the focus on measurements of the major constituents. The results of these studies illustrate how an imaging approach differs from the traditional NIR spectroscopic measurement, and can greatly expand information that can be derived from the NIR spectra.

Another group approached the imaging of the whole corn kernel from a different angle, optimizing the use of the imaging array by selecting a magnification that allowed the simultaneous imaging of 25 kernels, while using sufficient pixels per kernel to differentiate the sections of each one [8]. Data acquisition was performed on a MatrixNIR commercial NIR chemical imaging system (Spectral Dimensions Inc., Olney, MD, USA) equipped with an InGaAs camera and fitted with optics providing a ~10×10 cm field of view. Diffuse reflectance images were acquired in the spectral range 950–1700 nm. Data processing was adapted for the two objectives of the paper: average spectra per kernel were computed and used in the prediction of oil content, while germ-specific average spectra were utilized to predict oleic acid content. The germ region was determined by various means, including computer-determined on the basis of spectral features corresponding to physical and chemical aspects of the kernel, and by visual inspection of the image by a qualified user. The root mean square error of cross-validation for the prediction of oleic acid was better when the spectral features were used to identify the germ. While the prediction accuracy for oil content did not match nuclear magnetic resonance (NMR) results or its speed, it was sufficient to allow sorting into high- and low-oil kernels. More valuable information was derived from the prediction of oleic acid because the results, although less accurate than achieved with the standard method, offered the distinctive advantage of being obtained nondestructively. Kernel orientation was reported as having a significant impact on the predicting ability for oleic acid because this fatty acid is present in the germ. The difference was due to the depth of penetration of NIR radiation in a diffuse reflectance measurement. When kernels are imaged on the endosperm side, little or no germ may interact with the incident radiation, while some (or even all) of the germ is sampled when the kernel is presented germ-side up. The speed of data acquisition, which may be increased further by the selection of a limited number of wavelengths required for the calibration, led to the imaging of all 25 kernels on both sides becoming a viable solution for this method.

In the two studies, the imaging systems were used to acquire data that were later reduced to either whole-kernel or section-specific average spectra. While the advantages in terms of simplicity of processing are obvious, these approaches clearly discard a tremendous amount of information related to the spatial localization of the chemical constituents and the corresponding heterogeneity of the individual spectra included in the image. In both cases, the objectives were to predict concentrations of specific components, or average values per kernel, both measurements being related to economic value and of special importance in plant breeding. Lewis and colleagues [9] presented a completely different approach to using NIR chemical imaging for accessing spatially resolved biochemical information in the corn kernel by examining the kernel in three dimensions. The same instrument as used in the second study mentioned above, the MatrixNIR, was used to acquire NIR chemical images of a single corn kernel over the spectral range 1100–1750 nm by utilizing a field of view of approximately 1×0.75 cm. The kernel was first imaged whole, after which a thin slice was shaved from the top and the kernel and it was imaged again; slices were then removed consecutively until the whole kernel had been imaged. Unsupervised data processing, namely principal component analysis (PCA; see Chapter 2), revealed significant spectral differences in the various regions of the kernel that allowed the clear classification of pixels as belonging to one of four specific structural elements of the kernel (Figure 8.2). Unlike traditional NIR imaging, this data set was volumetric in nature because the imaging array captured the two dimensions of the plane, and exposed sequential planes captured the third dimension. This analysis accesses completely novel information about the corn kernel (see also Chapter 7).
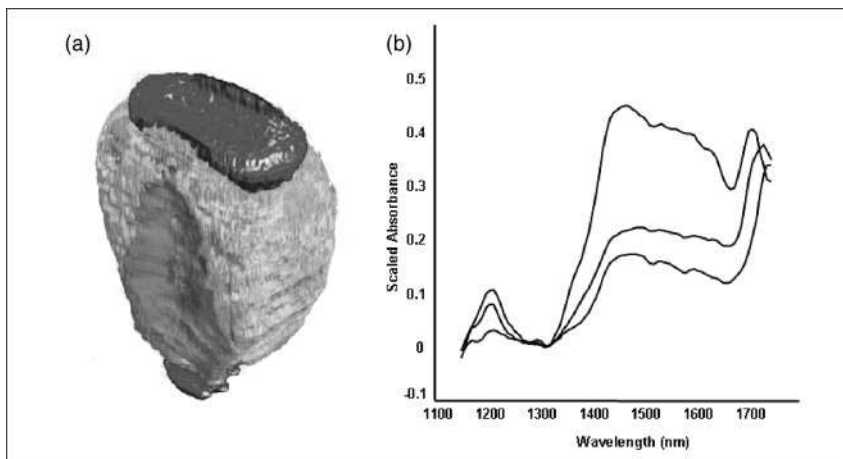
Figure 8.2 Three-dimensional NIR chemical imaging of a corn kernel. (a) False-color image based on the structures identified in the NIR imaging data set. Reprinted with permission from Ref. [9]; © 2007, John Wiley & Sons, Inc.; (b) NIR spectra extracted from selected structures highlighting the information content of the spectra.

This example illustrates a research application of NIR chemical imaging. Although the sampling time was not extravagant at a total of 80 min, the destructive nature of the analysis makes it incompatible with quality assurance-type methods. Despite the relatively short data acquisition time, the analysis accessed a large spectral range (i.e., it provided much chemical information) and spatially sampled the whole kernel – two factors that are important for laboratory methods used in plant breeding programs, for example. It is important to note also that fairly simple information was accessed with the data processing scheme selected, and that a wealth of additional details is contained in the spectral hypercube and could be extracted from the same data set.

While the level of detail accessed in this sampling scheme is excessive for a large number of applications, the availability of this information is important as it allows the selection of optimal parameters for the design of less laborious sampling, which can provide specific information in a manner that is suited for routine use.

8.2.3
Can NIR Chemical Imaging Replace Traditional Wet Chemistry?

Some of the difficulties experienced when developing spectroscopic techniques to replace traditional wet chemistry have related to the correlation of measurements, despite the intrinsic difference in their origin. Shenk and colleagues [3] discussed this issue in the context of NIR spectroscopy. For example, measurements of protein based on total nitrogen content are not directly equivalent to a spectroscopic approach that only probes the N—H bonds. Similarly, determining individual fatty acids from the fairly broad combination and even broader overtone bands found in the NIR region, is hardly related to the quantification of species isolated on the basis on chain length and level of saturation.

One of the most attractive roles of NIR chemical imaging is to use the chemical information, and its distribution in the image, to assess abundance as a primary method, rather than attempting to correlate all pixel spectra with a single value obtained using a traditional method. In order to mimic an average abundance measurement, the image must almost inevitably be averaged, thereby losing the spatial information. In a primary method, the presence and relative abundance of a species can be determined at every pixel of the image, and the total abundance estimation then relates to localized concentrations in relation to the volume occupied by a species. The classification of NIR spectra contained in NIR chemical images is a widespread approach in the determination of abundance and localization of ingredients in pharmaceutical products [10]. The same approach could be taken with food samples, where reference libraries for various chemical moieties of interest could be built from pure materials such as specific fatty acids or types of starch, and their localized abundance evaluated in a single plane or 3-D data set.

The three examples described above are clearly distinct in terms of the level of sophistication of image data acquisition, data processing and interpretation. Nevertheless, they all use spatially resolved NIR spectra for the identification of chemi-

cal species and their quantification, with or without relying on a reference method. They each represent a very different utilization of the technology, and all require some variations of basic instrumental characteristics and flexibility. For example, the first two applications imaged whole kernels; these measurements require a sufficient depth of field for all parts of the kernel surface to be in focus. However, the third example involved imaging flat surfaces created through careful sample preparation, and does not require a large depth of field. It does, however, require a precise sample positioning, although this can easily be overcome by using image correction routines (see Chapter 2). Moreover, a fast acquisition of a fairly large field of view of each plane with a reasonably small pixel size will keep the experiment within a time frame that avoids changes in the sample itself. This particular aspect of NIR imaging is not a concern in inert or stable products, such as many pharmaceutical ingredients and polymers, but it is important in food science, where samples may spoil or their chemical composition may change as a function of time over a period as short as a few hours.

8.2.4
Interest of NIR Chemical Imaging in Plant Breeding and GMOs

Plant breeding is a good candidate field for the development of analytical methods utilizing NIR chemical imaging, because it is a chemical analysis performed with a two-dimensional (2-D) spatial component. The products of genetic modifications are, by design, biochemical and/or physical changes in the plant. Hence, if the magnitude of the changes at the biochemical level matches the sensitivity of the system used for image acquisition, it is reasonable to expect that the results of the genetic modifications will be visible in the NIR image. The sensitivity, or limit of detection, depends on sample preparation, the acquisition procedure, and on the processing scheme applied to the data.

The instrument must provide a pixel size where the acquired spectrum is not averaging too-large a region. Of course, the pixel size required to avoid the dilution problem must be strictly related to the sample and the distribution of the biochemical changes. There is a greater probability of detecting the difference brought on by breeding if the biochemical modifications are localized. This means, on occasion, that a microscopic scale is required, while other sample types perform well with a macroscopic approach enabling a higher throughput. The choice of instrument must fit the question at hand, with the fields of view available and depth of field receiving special attention. For example, applications aimed at analyzing intact samples require a large depth of field to accommodate the irregular surface, and a reasonably large field of view to image a whole sample or multiple units at once. When the changes are expected to be detectable only in an experiment performed at the microscopic scale (with a magnification less than ca. 50 μm per pixel), the samples will almost inevitably need to be prepared in a manner that creates a flat surface to image.

Smail and colleagues [11] described the analysis of intact seeds using a Matrix-NIR, a focal plane array-based system operating in the spectral range 900–1700 nm,

to detect early germination in hard winter wheat varieties. Since the kernels were used whole and the objective was to develop a method for screening large numbers of seeds, the field of view was set to include 24 or 30 kernels. The authors estimated that 15 million spectra could be acquired in one day using this approach. Each kernel spans multiple pixels in this sampling scheme, representing well over 4000 kernels per day. In this report, NIR chemical imaging was successful at identifying kernels undergoing early sprouting, with a sensitivity greater than visual inspection or other tests such as the destructive alpha amylase and viscosity monitoring. The depth of penetration of IR radiation in this wavelength range produces a chemical image with features from both the outside and beneath the surface, thus enabling the detection of underlying sprouting structures.

Figure 8.3 illustrates the impact of the field of view selected to acquire different types of information on a particular sample. A large field of view provides a single image containing multiple wheat kernels (Figure 8.3a); as each pixel spectrum is a measure of a larger area of the sample ($125 \times 125 \, \mu m^2$ in this case), it is a good approach to investigate differences occurring on a larger scale. Figure 8.3b shows information obtained with a pixel magnification of about $40 \, \mu m$, where the various
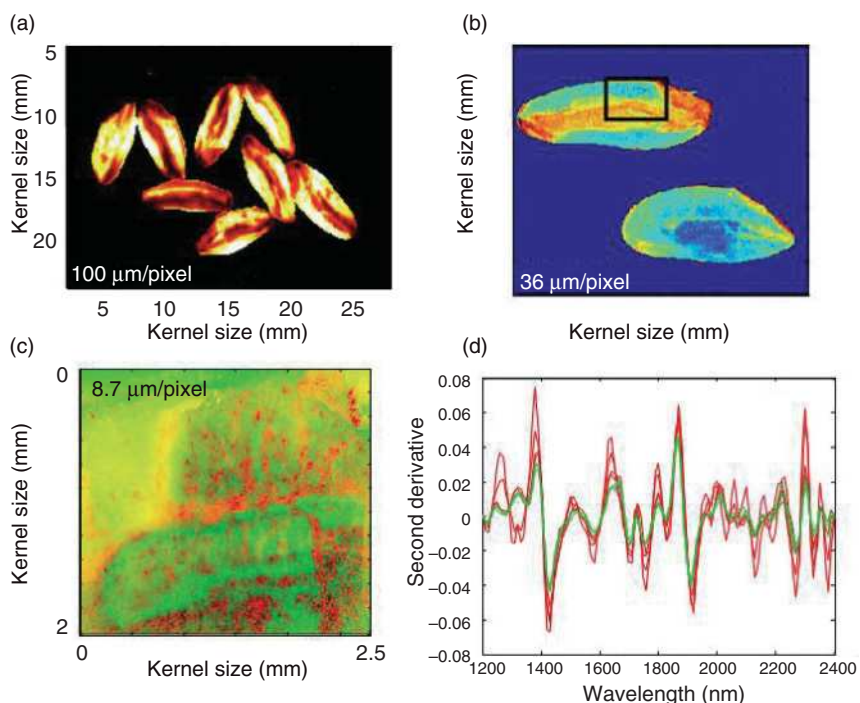
Figure 8.3 NIR chemical images of wheat kernels acquired at magnifications of: (a) $100 \, \mu m$ per pixel; (b) $36 \, \mu m$ per pixel; (c) $8.7 \, \mu m$ per pixel; (d) Second derivative spectra extracted from areas of image (c).

segments of the kernel are better defined than on the left. Finally, the image in Figure 8.3c represents a high-magnification acquisition, where a pixel magnification causing oversampling on the spatial axis (10 µm per pixel) [12]. The greater detail obtained with this approach provides access to the small-scale features of the kernel. The individual NIR spectra extracted from the image acquired at very high magnification (Figure 8.3d) illustrate the chemical differences that are measured.

Today, GMOs represent an example of biochemical modifications that may be measured using NIR chemical imaging. A study has been conducted to determine the suitability of this physical test for providing chemical information to detect GMO grains. The investigation is being conducted within the framework of the Co-Extra FP6 project (Nr 007158), studying Genetically Modified and non-Genetically Modified supply chains, their coexistence and traceability. The preliminary results have shown that GM soy and barley can indeed be differentiated from traditional grain by using NIR chemical imaging, using PCA scores of NIR (900–1700 nm) chemical imaging to detect differences between varieties. The GM and non-GM groups are fully separated in the training set, despite a wide variability of the spectra, a statistical challenge that is often faced in the analysis of biological samples.

8.2.5
Interest of NIR Chemical Imaging in Animal Feed

Recent problems associated with bovine spongiform encephalopathy and its apparent predecessor, scrapie, have brought about new demands for the analysis of animal feed. The challenges of analyzing feed are many-fold: the composition is variable, the food comes in various shapes and size ranges, and the components that are now considered contaminants are not biochemically very different from what is acceptable. Although it is expected that the level of distinction will in time need to reach the differentiation of species, this is not the case at present, when to discern mammalian from bird and fish is sufficient. Nevertheless, the demands on the methods are greater than expected for routine methods. Indeed, the level of detection required by current regulations in Europe is $1\,g\,kg^{-1}$ (0.1%), and performed at a speed that would enable the testing of large quantities. Hence, a variety of methodologies is being developed in parallel [13], among which NIR chemical imaging has shown much promise.

NIR microscopic mapping – that is, acquiring a single point at a time and moving this target point from one position on the sample to another – was investigated for this purpose. Although microscopy offers the type of spatial resolution required to detect low-level contaminants, the time required to collect data from all spatial positions in a sample make it impracticable for routine use. The use of an imaging system not only reduces the amount of time for data acquisition (cf. Chapter 1), but also has the benefit that the spectra are acquired from all neighboring pixels, which limits the risk of missing some contaminant particles by only performing 'spot checks' on a sample. These analyses have been described in detail [14, 15],

and are currently considered to show great promise, notably when a complementary data processing system is applied.

8.2.6
A Quick Look at Other Products

The examples discussed above clearly illustrate the breadth of the problems that can be tackled with NIR chemical imaging, and the innovative approaches leading to their solution. This sections is concluded with several examples demonstrating the flexibility of NIR chemical imaging to tackle samples of various shapes, sizes and chemical composition. Figure 8.4 shows a false-color image of a muesli cereal obtained by segmenting the image on the basis of spectral features that are well known for their use in the NIR spectroscopic analysis of food. The lipids, proteins and high-moisture content ingredients of the cereal can be easily distinguished using the NIR spectra, which might enable the use of these features to calculate ratios of ingredients, or to evaluate the integrity of each type of ingredient. An example might be the segments of a peanut showing a weak oil signature that is indicative of a deterioration problem. A two-step segmentation procedure could, for example, first identify the ingredient and then evaluate its quality. This image cube, containing the full spectra at each pixel, was acquired on a Sapphire chemical imaging system (Malvern Instruments Ltd, UK) in less than 3 min. A rapid method utilizing only the three wavelengths used to produce the image and two reference points would provide the same discrimination with an acquisition time of less than 10 s.
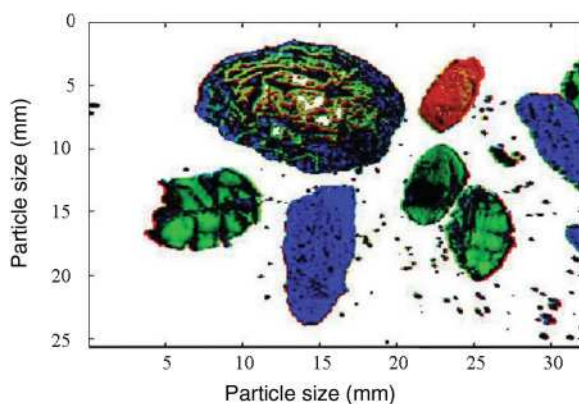
Figure 8.4 False-color image of muesli cereal based on the spectral intensity at three wavelengths in the NIR.
Red = 1720 nm (C—H first overtone); green = 1980 nm (OH combination); blue = 2150 nm (N—H + C—H combinations).

8.2.7
Conclusion: Laboratory-Based NIR Imaging

These many examples of applications of NIR chemical imaging in the laboratory environment and the various aspects of sampling, data acquisition and processing, must be borne in mind when approaching a new problem. With its chemical specificity, flexibility in spectral data selection, sample presentation options, fields-of-view and advanced mathematical processing now more user-friendly than ever, there is no doubt that NIR chemical imaging represents an invaluable tool for the analysis of food. Yet, many areas remain untouched, and there is much room for creative thought in the use of this technology to solve old and new problems alike. An additional advantage of this methodology is that it is amenable to both at-line and on-line measurements, under a variety of circumstances.

8.3
At the Industrial Scale

8.3.1
Introduction

8.3.1.1   **The Failure of RGB Systems in Food Quality Control**
In the food industry, numerous on-line controls are still made by human vision, especially for sorting bad-looking products or foreign bodies. This generates many problems: for example, human operators can miss defective items, the work is laborious and tedious, and the speed of the line is limited by the number of operators in charge of monitoring. Moreover, while visual sorting can be difficult for humans, cameras can perform the task easily and image analysis provide very accurate results. For example, the machine-vision sorting of size (diameter, length, etc.) or shape (roundness) can provide a much better performance than would be obtained with human vision. It is for this reason that, for many years, vision systems have attracted great attention for use in the food industry.

Despite all these advantages, vision systems are still relatively limited in the food industry, having been developed primarily for packaging operations because it is easier to handle manufactured items than very variable, highly heterogeneous biological products. The main problems associated with biological food products, when submitted to processing operations, is that they exist in a wide variety of states (liquid, solid, fragmented), shapes, colors and chemical compositions. They can also vary drastically with regards to origin, and even between the start and finish of the season! Food quality monitoring also encounters other issues such as chemical composition measurement, foreign body detection, nonconformity detection and grading.

Although technically and economically feasible artificial vision systems have been developed for the food industry, based on classic RGB video cameras, the

vision systems too often fail to detect defects or contaminants, for two main reasons:

- The colors of the objects to be discriminated are too similar; the three color components (red/green/blue or hue intensity saturation coordinates) are not sufficiently discriminative to identify differences between an object of interest and any surrounding objects. This problem is enhanced by a wide variability in color typical of biological products: variance of the colorimetric components inside an object may also be greater than the variance between this object and those to be removed. In that case, the solution is to seek other information, either in the visible spectrum or in the NIR spectrum. The NIR spectrum can provide information regarding the chemical composition and internal physical structure, and can be used to separate same-color objects of different composition.

- The scenes to be analyzed are too complex. Except for flat products (e.g., meat slices, fish, biscuits), the third dimension of food products may be relatively odd, with concave areas leading to shadowing and color changes. This is typically the case for the calyx cavity in fruits, which is generally 'seen' as a defect by classical RGB vision systems. Similar problems of misclassification due to concavities occur with chicken carcasses. The use of NIR imaging will allows these effects of shadowing and of depth of field to be reduced.

Consequently, within an industrial environment, hyperspectral NIR imaging has been used primarily to improve object detection previously carried out using RGB cameras and optical systems. Yet, the many other advantages of these systems make them highly suited to not only on-line analysis but also high-speed laboratory analyses for product grading.

8.3.1.2 How Did We Come to On-Line NIR Imaging?

The main driver for the introduction of NIR wavelengths into vision systems for on-line sorting has clearly been the dead-end of certain applications of classical RGB cameras. During the late 1980s, Cemagref, in Montpellier, France, built a vision system in which three CCD cameras could be equipped with three different filters. When equipped with only a red, a green and a NIR filter, this system was successful at differentiating between the stem-end/calyx and bruises on apples [16]. The hypothesis was that a NIR image could help to detect an object with a water content or an internal structure that differed from its surroundings and, based on this hypothesis, many other applications have been investigated.

An example of this occurred during the 1990s, when a NIR imager was developed for canning companies that could detect stone pieces in peach halves. In the canning plant, when the peaches are pitted automatically the stone may be broken by the saw of the stoner; a sorting step is then required to remove the residual stone pieces. The RGB cameras proved to be totally ineffective for this purpose as the stone contaminants were located in a concave area, generating shadows. When the task was performed manually it proved to be especially tedious as the colors of the stone and inner flesh were very similar. However, as the water content of
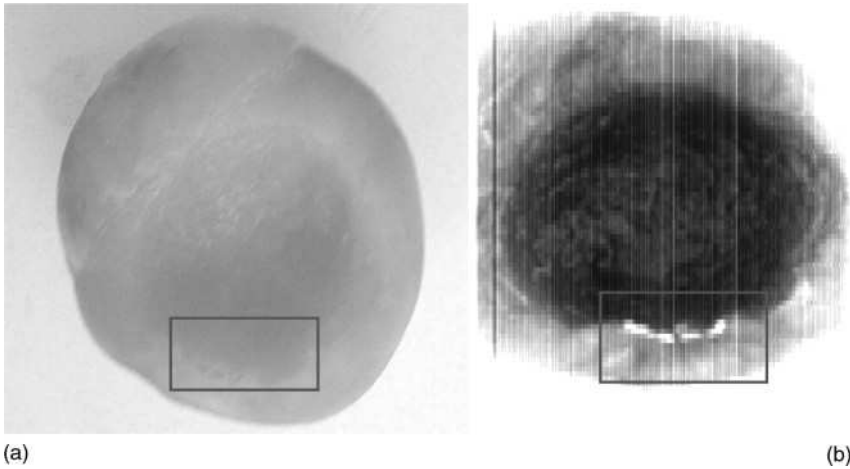
Figure 8.5 Detection of pieces of stone in peach halves (canning industry). (a) Visual image of the peach half; (b) NIR image of the same peach; the stone pieces are located inside the rectangle (white spots in the NIR image). Illustration courtesy of Gorretta, Cemagref.
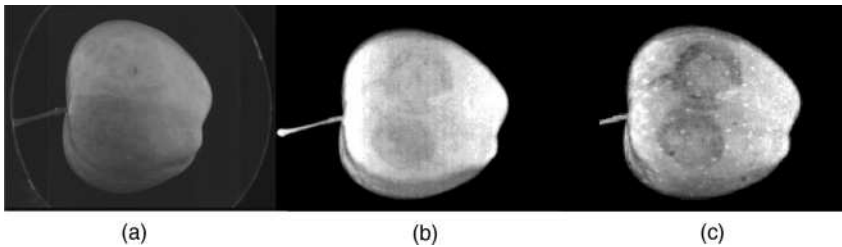
Figure 8.6 Detection of bruises on a Jonnagold apple. (a) Color image; (b) NIR image at 930 nm; (c) NIR image at 1200 nm revealing the two bruises. Illustration courtesy of C. Guizard, Cemagref.

the stone differed significantly from that of the flesh, Cemagref proposed the use of a basic NIR-imaging system based on the water absorption band. The flesh, with a high water content, absorbs NIR radiation, whereas the stone pieces do not, and hence a difference in the light colors of the image was apparent (Figure 8.5). Initially, the Cemagref device used an InGaAs camera (900–1700 nm; Sensors Unlimited, NJ, USA), and later a linear InGaAs array (Model G8160-256S, module C8161; Hamamatsu, Japan), the prototype of which was tested on-line. Custom image analysis software was subsequently developed to automatically detect the white (stone) spots of minimal area.

The same very basic one-band InGaAs camera system was also used in the ASTEQ project [17] to detect bruises on bicolored Jonnagold apples (Figure 8.6).

(a) (b)
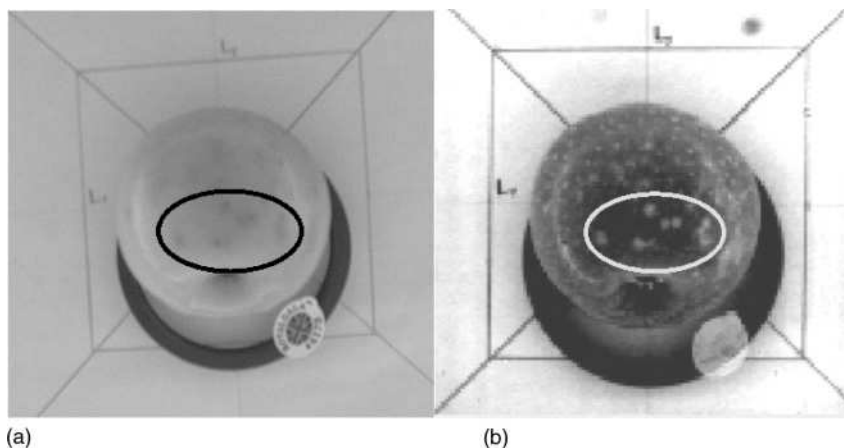
Figure 8.7 Bitter pit on a Golden Delicious apple. (a) RGB image; (b) NIR image. Illustration courtesy of C. Guizard, Cemagref.

When bruise causes damage to the internal structure of the apple flesh, the cells are destroyed and the cytoplasm invades the intercellular space; this leads to a change in diffusion and absorption coefficients, creating easily detected black spots.

Another, easily detected, example of structural changes in fruit tissue is that of bitter pit, which causes necrosis of the subsurface tissues in apples; this in turn creates a localized dehydration such that the bitter pit spot appears white when using a very simple, one-band (1200 nm) setting (Figure 8.7).

At the same time, during the 1990s, the manufacturers of sorting machines for grains, berries and small fruits began to include NIR lighting/imaging as a key for detecting foreign bodies and unwholesome products in high-speed sorting processes. For this, NIR lasers are used to illuminate the objects in a fall or on a sorting belt, while CCD cameras capture the images. The way in which the NIR light is scattered provides information concerning the presence of foreign bodies; for example, a lower scattering indicates problems such as foreign bodies or black spot.

In addition to differences in scattering, NIR lighting/imaging also allows advantage to be taken of more subtle chemical differences between objects, although in this case more sophisticated systems based on multispectral or hyperspectral imaging are required.

8.3.1.3 When Is NIR Imaging Worth Using in On-Line Settings?

Among the above-described advantages of NIR hyperspectral imaging in on-line settings, we can include the following:

- NIR imaging can be used to discriminate between same-color objects with different chemical compositions; among the properties of NIR this is the most exploited in on-line settings, to sort objects of diverse composition.

- NIR hyperspectral imaging can provide transmission images of commodities, due to the smaller absorption and diffusion coefficients in the NIR range (e.g., in apples [18]). With visible light, transmission is only possible through small and low-absorbing tissues, but with NIR light transmission can be carried out on thicker samples, such as an entire fruit. This allows the detection of internal defects, provided that they are sufficiently large.

- NIR imaging is capable of mapping areas of various chemical components in one sample; this property is largely used in laboratory studies, notably in the pharmaceutical industry, although examples are also found in the food industry, occasionally on-line.

- Even when used in reflection mode, NIR imaging will reveal much more information about the internal structure of products than will visible light. This is due to the fact that the diffusion coefficient is lower in NIR, and that the light is not altered by pigments at the surface of the commodity. This property is utilized to determine the physical traits of a sample, or to reveal beneath-skin defects.

- An appropriate combined use of molecular chemical information (NIR) and morphological measurements in macroscopic images (e.g., shape, optical texture, size) can enable the analysis of further complicated systems. This is particularly relevant when objects composed of different color-same compartments are being processed (e.g., meat slices), or when the product is composed of heterogeneous pieces within a bulk, such as animal feed.

Previously, these properties of NIR have been exploited not only by research groups but also by industrial teams to create new quality control systems for food processing and production. In the following sections, we describe a variety of examples of NIR imaging in the food industry, classified according to the industrial issues that they address.

8.3.2
External Contamination Detection by NIR Imaging

The main quality issue within the food industry is most definitely that of *safety* – keeping foods free from contamination and avoiding food-borne illness. The latter situation must be prevented by ensuring that processing is correctly carried out to avoid microbial development; these include respecting the time–temperature profiles during thermal treatment, and/or the hermetical sealing of cans or jars. However, food contamination also includes both macroscopic physical contamination (e.g., large foreign bodies) and microscopic contamination by small foreign bodies, microbes or hazardous chemicals (e.g., pesticide residues). Fortunately, food contamination can be detected by using NIR imaging much more accurately than when using RGB imaging and/or human sorting.

8.3.2.1 Foreign Bodies
'Surface' foreign bodies are, as their name indicates, present on the outer surface of the product, whereas embedded foreign bodies are 'hidden' inside the food

product; as a consequence, surface foreign bodies are much easier to detect. Foreign bodies may be either *intrinsic*, such as bone in an animal food product or stem or leaves in a vegetable food product, or *extrinsic*, such as metal, glass or insects. Foreign bodies may have a color which is similar to that of the commodity yet differ in its chemical composition and internal structure; in such a case NIR imaging will be more efficient than RGB imaging for foreign body detection.

Following the initial forays into foreign body detection using one-band systems described above, more sophisticated imaging systems based on multispectral imaging have now been proposed for this purpose. For example, BEST (Heverlee, Belgium) has proposed the use of sorters equipped with up to 12 lasers (some of which are in the NIR range) for sorting foreign bodies and unwholesome products in the bulk of small fruits, vegetables, grains, beans and tobacco leaves. For this, laser lines are projected consecutively onto the stream of objects and NIR multispectral images created by use of CCD cameras (Figure 8.8). The objects are sorted based on differences in scattering and in the absorbance spectrum. In the tobacco industry, for instance, the most frequently found foreign bodies include polypropylene strings, pieces of rubber and other plastic materials that are very similar to tobacco in color, but very different chemically.

Another solution to the problem, based on multispectral imaging, has been developed by Japan Tobacco (Tokyo, Japan) [19], by using three infrared bands in combination with an RGB camera. With this system, 78% of the targeted foreign
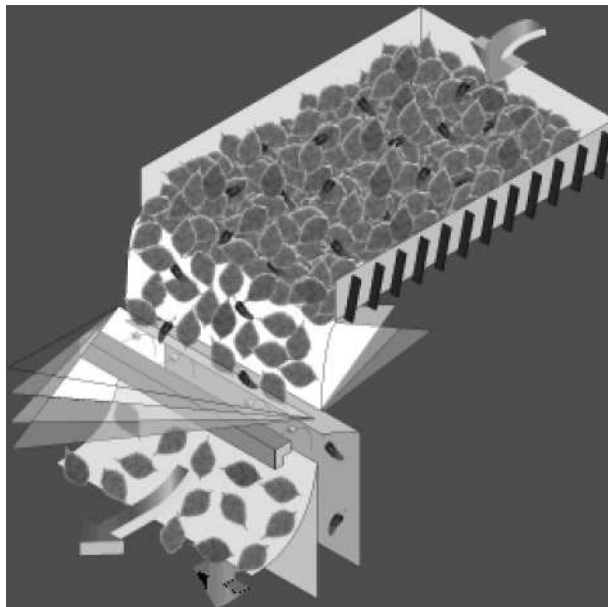
Figure 8.8 Sorting of tobacco leaves using laser lighting and CCD cameras for creating multispectral images. Illustration courtesy of BEST.

materials not recognized by the RGB system are correctly identified by the combined system, which is reported to provide a more than 98% recognition (based on weight) of foreign bodies.

The foreign body issue can be extended to that of small food product streams contaminated by abnormal individual units. For example, in grain streams it is necessary to detect any contamination by abnormal kernels and to remove these in order to maintain the level of contamination within regulatory limits. In particular, mold contamination is of great concern in the grain industry. As an example, *Fusarium* head blight (also called 'scab') produces mycotoxins (deoxynivalenol, DON) that become concentrated in (but are not limited to) the infected kernel. The Food and Drug Administration (FDA) specifies that the DON content of finished wheat products destined for human consumption should not exceed 1 ppm. Moreover, the monetary value of wheat may be reduced by 40% (or even more) if only 5% of the kernels are infected.

Currently, several groups are investigating the use of a visible-NIR hyperspectral imaging system to detect scab-damaged grains. For this, Delwiche and Kim [20] used a line-by-line hyperspectral camera composed of a ImSpector V9 monochromator and a 16-bit CCD camera (Specim, Oulu, Finland) in the 425–860 nm range to view wheat kernels positioned, crease-side down, in eight rows of eight kernels (four infected, four wholesome). The spatial resolution was 0.23 mm per pixel, and for each kernel a spectrum was computed by averaging the reflectance of all pixels; the kernels were then classified with regards to this spectrum. The misclassification error ranged from 2 to 17%, depending on the wheat variety. Polder *et al.* [21] studied the same problem, but worked in transmission mode and with two types of hyperspectral imager: one in the 400–900 nm (Vis-NIR) range (ImSpector V9 + 12 bit CCD camera), and one in the 900–1700 nm NIR range (ImSpector n17 + 8 bits InGaAs camera) (both from Specim). In both cases, preparing the transmission images would cause the sensor to be saturated at a place where there was no object, and to avoid this two strategies were employed. In the Vis-NIR range, polarized filters were used to block direct lighting from the source. However, in the NIR range the source was covered by a pinhole, on which the kernel was placed. The light was then scattered by the kernel and the image recoded. In both cases, imaging was necessary because the kernel presented saturated and conversely black areas which were removed by image analysis, but which would have biased a single spectrum. The conclusion of the study was that the NIR range was better suited than the Vis-NIR for detecting *Fusarium* in whole kernels, but that the set-up should be improved by incorporating NIR-sensitive polarization filters and using a higher dynamic range (12-bit) InGaAs camera.

8.3.2.2 Surface Liquid Contaminations

Contaminants include not only foreign bodies but also liquids or slurries that may be splashed onto the food products and create spots. For example, fecal contamination has caused food-borne diseases due to *Escherichia coli*, which in turn led to a thorough investigation of both apples and poultry. The first investigations into hyperspectral imaging as applied to fecal contamination were started at the USDA/

ARS Beltsville research center by Y.-R. Chen, R. Lu and B. Park [22], and later still by the teams of both Park and Lawrence at USDA Athens/GA, while Beltsville focused more on surface contaminants on apples.

The primary recommendation of the US FDA, to avoid cross-contamination in the washing pool of apples, is to remove any fruit which is contaminated with feces. Consequently, the research teams at the USDA Agricultural Research Service in Beltsville have been investigating the use of a NIR imager to detect cattle manure on apples. These studies were carried out using a home-made, line-by-line imaging system (known as the 'ISL imager') that comprised a PGP spectrograph imager (Specim) in the 350–950 nm range [22]. The aim was to use a hyperspectral system to identify optimal spectral bands for use in a multispectral detection scheme. First, the 450–850 nm spectral range was selected for its high SNR [23]. A PCA was then carried out that showed the most suitable wavelength bands to be the longest, suggesting that it was worthwhile examining wavelengths above 850 nm. In a second study [24], the investigated range was extended to 950 nm and the sensitivity to contaminant concentration evaluated. The average spectra were calculated in three types of regions of interest (ROI): uncontaminated, slightly, and importantly litter-contaminated apples. Whichever the apple variety or the skin color, the average reflectance intensities were seen to decrease from the uncontaminated to the importantly litter-contaminated apples. It was concluded that the 675–950 nm spectral range was best for developing a variety-stable calibration, thus highlighting the strength of NIR imaging in comparison to color imaging. In order to transfer the system on-line, a low-cost, dual-band system based on the 725 nm/811 nm band ratio was investigated. As these wavelengths are insensitive to the absorption from the pigments, the multispectral imaging system could potentially be used regardless of the cultivar. However, this system was shown to be unsatisfactory for detecting thin litter contamination on apples. Other spectral techniques, such as fluorescence imaging, were also investigated with the aim of overcoming this problem.

Poultry provides another, much more complex, example of litter-contaminated food product. The complexity is generated both by the odd shape of poultry carcasses, with several concave shaded areas (under the wings and the leg folds), by the heterogeneity of the skin color due to the relative transparency of the chicken skin, and by the various causes of safety hazards in chicken: here, not only litter contamination must be detected, but also cadaver, septicemia and tumor problems among others.

In Beltsville, several studies followed in quick succession, each based on the ISL hyperspectral imager with the aim of differentiating wholesome carcasses from cadaver, septicemia and tumor carcasses. In a preliminary study [22], the system was calibrated spectrally and tested on four classes of chicken carcass to determine the best discriminating spectral ranges; for this, 650–900 nm was selected based on qualitative observations. In a later study [25], a dual-wavelength camera was developed and tested.

The Athens hyperspectral system was similar to that produced by the Beltsville group, being composed of an Imspector PGP spectrograph and a CCD camera.
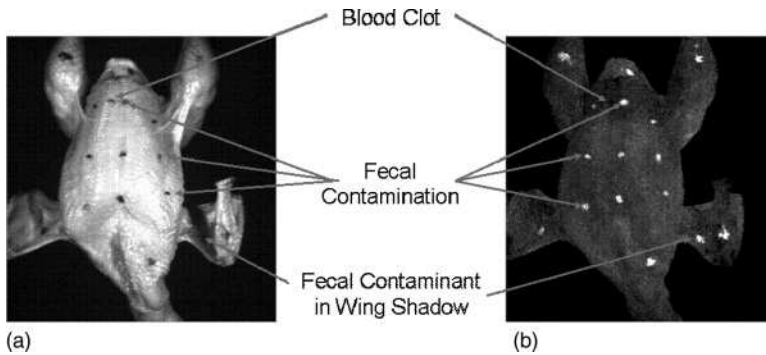
Figure 8.9 The utilization of multispectral machine vision to detect fecal contamination on poultry carcasses. (a) RGB image; (b) 565 nm/517 nm image ratio, in which the fecal contaminants are clearly highlighted. Illustration courtesy of USDA-ARS, Athens/GA, USA.

The system functioned in the 400–900 nm range, with a nominal resolution of 2.5 nm. The aim here was to define the specifications for a multispectral system based on a few wavelengths for a future on-line set-up in order to detect cecal, duodenal and colonic feces on wholesome chicken skin. In an initial study [26], the wavelength range of interest was investigated using a classical visible-NIR spectral analysis of the various objects to discriminate. Four wavelengths were extracted from the analysis of the loadings, namely 434, 517, 565 and 628 nm. (Note: in the following description, the hyperspectral image analysis relates only to these four spectral planes.) The shadows were removed by making ratio images, and the best performances were obtained with the 565 nm/517 nm ratio images (Figure 8.9). Here, not only were all of the contaminants revealed (including those hidden in the wing shadows), but blood clots – which are not actually contaminants – were also detected and correctly classified as 'wholesome'. In a later study [27], the hyperspectral image was used directly to determine the most significant wavelengths. ROIs were chosen at different locations representing various contaminations and various skin conditions (e.g., wings, thigh, breast). The average reflectance spectrum of each ROI was used for wavelength selection. The results of the study confirmed that the two-band ratio 565/517 was best suited; the prediction accuracy of surface contaminants was 96.2% and the number of false positives the lowest. A broad patent application has been filed covering a wide range of poultry and meat products [28]; it is planned to transfer this system to the poultry industry, to operate at 140 birds per minute, or more.

8.3.3
Surface and Subsurface Nonconformities

Whereas contamination corresponds to the addition of matter which is very different from the surface under investigation, other defects can be generated by

changes in the surface or subsurface optical properties of the product. In this respect, RGB cameras are generally efficient when the change occurs on a homogeneous surface, and is sufficiently contrasted with the background color. In all other cases, hyperspectral (and multispectral) imaging represents the only alternative for detecting defects.

Hyperspectral imaging is worthy of use for detecting two types of defect that are difficult to identify when using RGB cameras:

- Actual defects: that is, defects that would be recognized by a thorough human inspection, such as bruises and bitter pit; these are generally characterized not only by a change in the spectral absorption, but also mainly by a change in the light scattering due to water exchanges.

- Potential defects: that is, the 'defects' that are not yet detectable by human eye but which will turn into actual defects during processing; the spectral changes are small and are not accompanied by light scattering changes. These defects often relate to chilling injuries or to latent greening. In addition, hyperspectral imaging is used to differentiate between defects and shaded areas such as calyx/stem ends.

8.3.3.1 Human-Detectable Defects

'Actual defects' such as bruises or bitter pit encounter scattering coefficient changes, due to water movements in the tissues. As shown in Section 8.3.1 (see also Figures 8.6 and 8.7), these types of defect (bruise, bitter pit, necrosis) are relatively easily detected, with several research groups having successfully tackled the problem.

As an example, Xing and De Baerdemaeker [29] used a custom-built hyperspectral imager based on an ImSpector V10 imaging spectrograph (Specim), and proposed a two-step procedure for identifying bruises. First, the stem and calyx ends are identified by analyzing the general reflectance of the fruit (this is the first score image). Second, bruises are identified by searching indentations in the ring shape of the reflectance level lines. The classification levels obtained were as high as 85% for nonbruised apples, 77% for bruised apples, and 98% for the end-calyx group. The errors were the misclassification of bruised apples as stem-end/calyx (2.5%) and misclassification of stem-end when the latter was too close to the edge of the image. In this example, finally only six wavelengths (571, 608, 671, 709, 798, 867 nm) were deemed necessary for a successful discrimination.

Both, Mehl *et al.* [30] and Kleynen *et al.* [31] attempted to detect various defects on apples, including contaminations. Mehl *et al.* [30] used the ISL hyperspectral imaging system described above to detect defects ranging from rot to bruises, flyspecks, scabs, molds, black pox and other soil or fungal contaminations. The group showed that these defects could all be detected using either PCA applied to images acquired in the 682–900 nm range, or by a second-difference asymmetric method which used only three wavelengths (685, 722, 869 nm). However they did not deal with the issue of stem-end/calyx discrimination from defects. Kleynen *et al.* [31]

used a four-band multispectral system (Multispec Agro-imager; Optical Insight, Sante Fe, NM, USA) with filters at 450, 500, 750 and 800 nm to detect defects such as scald, hail damage, bruises, russets, scar tissues, frost damage and rot. The NIR bands were seen to be better suited than the RGB bands for detecting subsurface defects, based on the higher penetration power, whereas 450 nm was efficient enough to detect slight surface defects such as russet. The stem-end and calyx areas were removed by applying a template with a 90% recognition rate. In order to cope with the problem of stem end/calyx detection, Cheng [32] coupled a NIR monochromatic camera (700 nm) with a MIR camera (7.5–13 μm), because this last range was not sensitive to bruises but was affected by reflectance changes due to cavities.

Bruises were also investigated on other commodities such as tomatoes [33] and pickling cucumbers [34]. In the latter study [34], the interesting fact was that a longer-wavelength imager was used (900–1700 nm range); this was composed of an imaging spectrograph (ImSpector N17E; Specim) and an InGaAs camera (Model C4880-21; Hamamatsu); the greatest difference between safe and bruised tissues was observed in the 950–1350 nm range.

Another defect, which is more difficult to detect than bruises, is bitter pit; this appears as a subsurface necrosis of apple tissues, as spots of 2–5 mm diameter. Bitter pit appears as white spots in NIR images, as do old bruises showing dehydration (see Figure 8.7).

Nicolaï et al. [35] used an InGasAs camera (Sensors Unlimited) coupled with an Imspector spectrograph (Specim) to investigate apples translating under the camera. These authors showed a good separation between bitter pit pixels and wholesome pixels, even with only two latent variables in the PLS. It was concluded that, rather than spectral information, the total reflectance in the 900–1700 nm region was probably sufficient for detecting bitter pit. This was in full accordance with our own results (as shown in Figure 8.8).

8.3.3.2 Potential Defects: Chilling Injuries, Potential Greening Area

'Potential' defects are defects too slight to be detected by eye, but which may host chemical, and therefore spectral, changes. For example, chilling injuries are difficult to detect because the symptoms generally develop after the product has been placed in a warmer environment. On citrus, Menesatti et al. [36] used a 400–970 nm hyperspectral camera (Imspector v10 + Teli CCD camera) in reflectance mode to detect chilling injuries, 14 days before they were revealed visually; the detection was based on reflectance levels and reflectance ratios (610/680, 610/750 and 680/750 nm). When studying cucumbers, Cheng [32] used the ISL imager (450–950 nm) to show that cucumbers with severe and moderate chilling injury had a greater absorbance than wholesome fruit, above 700 nm. A performance rate of about 90% was achieved, and with a good robustness with regards to noise. In French fries, Noordam et al. [37] were able to detect latent greening defects that were invisible to the human eye or to a RGB camera by using a 430–900 nm hyperspectral camera composed of a spectrograph (ImSpectorV9; Specim) combined with a monochrome camera (model

PMI 1400EC; QImaging, Burnaby, Canada) and a support vector machine classifier (see Chapter 2).

In the applications described above (Sections 8.3.2 and 8.3.3), the contaminants were located on the surface or subsurface of the food product, or as separate bodies in a stream of other objects. Detection was mainly carried out on the basis of spectral absorption properties. Even more challenging is the detection of internal foreign bodies.

8.3.4
Detection of Internal Defects by Candling

The hyperspectral imaging of internal defects is based on a transmittance measurement, that is, candling the object with an IR source and analyzing the resultant image. NIR radiation is more suitable than the visible method for candling, because it is much less scattered. In biological samples, the reduced scattering coefficients decrease continuously from the visible range to the NIR range, as can been seen in Figure 8.10 [38]. Absorption has a lower influence because the absorption coefficients are about 10-fold (in slightly scattering media such as cartilage; see Figure 8.10) to 100-fold lower (in highly scattering media such as apples, as shown by Qin [18] or Chauchard *et al.* [39]) than scattering coefficients. Therefore, transmittance is much greater in the NIR range than in the visible range.

8.3.4.1 Internal Foreign Bodies

Internal foreign bodies (i.e., foreign bodies embedded into the food material) are a nightmare for food plant quality monitoring. Detection systems are generally based on analysis by X-rays, the absorbance of which depends on the atomic number and concentration of the material [40]. However, very often the X-rays are not sensitive to intrinsic foreign bodies such as stem, pits, skin pieces or hair,
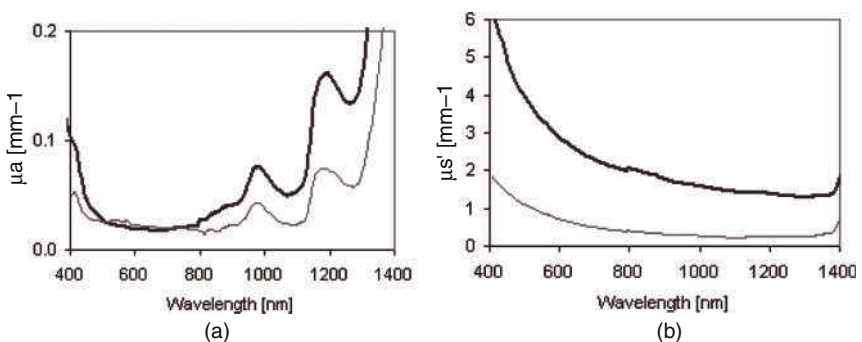
Figure 8.10 (a) Absorption μa coefficient and (b) reduced scattering $\mu s'$ coefficient of aural (light gray curve) and nasal septal (dark gray curve) cartilage samples as a function of the wavelength. Illustration courtesy of T.E. Milner, Center for Biomedical Engineering, University of Austin, TX, USA.

because the tissues are not significantly different in terms of their atomic number.

The detection of remaining pits in unpitted cherries [41] is an example of embedded foreign body detection. Qin and Lu used the same camera as for the feces-contaminated apple study, but this time the fruit were illuminated in transmission mode with a quartz halogen lamp irradiating through a 13 mm-diameter hole. The correctly unpitted cherries gave brighter images than those with a remaining pit. The best spectral range for separating the two classes of object ranked from 692 to 856 nm. Both, fruit size and defects had a major influence on the classification performance, whereas fruit orientation, color and post-bruising treatments had negligible effects. Last, but not least, the detection carried out using a ROI of the NIR image was twice as effective as that carried out on a single NIR spectrum detection, leading to an average error of 3%.

8.3.4.2 Internal Tissue Defects

Although less crucial than embedded foreign materials, internal defects are still very important from a commercial point of view, mainly because of the consumers' reaction to undetectable internal defects. Internal defects must have a large influence on the NIR signal in order to be detectable. Consequently, only defects of a large size, that generate a significant change in the scattering coefficient, will be detected. This is generally the case for defects leading to internal holes, such as mechanical damage in cucumbers.

Mechanical damage in cucumbers results in carpel separation and a hollow center. As the transmittance signal is very low, the spatial resolution is necessary to obtain a sensitive method. Hyperspectral imaging reduces mixing of the relevant signal from the unwholesome region with that of the wholesome region, and therefore increases the sensitivity. Ariana *et al.* [34] used a transmission visible/NIR hyperspectral imager developed at USDA/ARS at Michigan State University (450–950 nm) to detect internal defects in cucumbers. The set-up was composed of an imaging spectrograph (ImSpector) and a backlit CCD camera; a 150 W halogen light candled the cucumber with dual fiber-optic light lines. Three images were recorded for each cucumber by rotating it around its main axis and taking images 120° apart. The cucumbers were imaged before and after (2 h, 1, 2, 3 and 6 days) mechanical injuries were applied. Both, the average spectrum along the longitudinal line and standard deviation spectrum (of the pixels along that line) were recorded. As expected, transmission was greater for defective cucumbers with hollow hearts than for normal ones. The defective cucumbers also showed a greater standard deviation of transmittance levels, because the defect was not homogeneous along the longitudinal axis. Finally, a single-band image (at 800 nm) was found to be sufficient for this application, yielding a classification rate of about 90%. Further studies on pickling cucumbers showed a predictability of internal defects that reached 91.5%, based on a hyperspectral imaging method using the spectral range 700–1000 nm [42].

To date, no other studies related to the detection of deeply embedded defects such as vitreous melons, brown-hearted pears or frost-damaged citrus, have been

identified. Nonetheless, it would be worthwhile studying such defects which today, are only detectable by NMR and occasionally by X-ray analysis.

8.3.5
Measuring Internal Quality Traits

Due to its good diffusion in scattering media, NIR is better suited than the visible range to provide information concerning scattering properties across different media. Hence, NIR hyperspectral imaging is used to measure scattered light profiles, and to correlate them to scattering properties. Moreover, since the NIR range also provides chemical information, it is possible to 'kill two birds with one stone'–that is, to measure both the absorption and scattering coefficients of the absorbing medium.

For the first time, in 2007, Qin and Lu [43] used a NIR hyperspectral imager to determine the optical properties of turbid liquid foods. The system was that developed previously by USDA/ARS Michigan (16-bit camera coupled to an ImSpector spectrograph), and covered the 530–900 nm range. The coefficients μa and μs′ were calculated for model liquids, milk and fruit juices, using Farrel's model, which is a simplification of the radiation transfer equation (Boltzmann equation). Farrel's model computes the reflectance of a turbid medium in any point of a semi-infinite turbid material as a function of μa, μs′, the internal reflection coefficient (relative to the refractive index) and r, which is the distance from the incident point. The coefficients μa and μs′ were assessed by simulation and data assimilation, using 38 wavelengths with a 10 nm increment in the 530–900 nm range images. In this first study, the absorption coefficients were not used for predicting chemical values; rather, the milk fat content was deduced from the μs′ coefficient at 600 nm.

Renfu Lu's team has also applied hyperspectral NIR imaging to solid scattering media such as fruit [44]. These scattering properties are related to quality traits such as firmness, which in turn are linked to the structure of the fruit tissues, especially in peaches and apples. First, a very straightforward method is used for processing the reflectance image of apples, extracting three spectra for each fruit: the maximum reflectance spectrum (close to the incident point), the mean reflectance spectrum, and the standard deviation spectrum. The spectra are then fed into a neural network to predict both firmness and soluble solid content (SSC). The standard error of prediction ranges between 6 and 7.3 N cm^{-2} for firmness, and between 0.72 and 0.81 Brix for SSC. Later, a more accurate method was developed by Lu's team for analyzing reflectance images. Here, at each wavelength, the reflectance profile is modeled by a Lorentzian function, using two parameters, a and b; this gives rise to two spectra, for a and b, respectively, which are then used to predict firmness. In peaches, 10 to 11 wavelengths have been necessary to obtain a good prediction, $r^2 = 0.77$ and 0.58, for two varieties [45] whereas, in apples, the best predictions ($r^2 = 0.8$ and an error of prediction or SEP = 6.14 N) required 21 wavelengths [46].

8.3.6

Chemical Imaging Analysis of Heterogeneous Products and Heterogeneous Product Streams

When dealing with homogeneous products or product streams (liquid, slurry), NIR spectrometric devices are often sufficient to provide a good estimate of the chemical content. However, with heterogeneous products or solid product streams, imaging is necessary in order to avoid averaging among regions of different concentrations. This situation can be encountered in biological products in two cases:

- The chemical to be analyzed varies *gradually* or is not delineated by any membrane or organ. In that case, the chemical change is generally invisible and only detectable by NIR; NIR imaging is used to measure the concentration distribution of the component.

- The chemical of interest is embedded into a compartment of the product (e.g., lean/fat in meat products) or into one item of the stream. In this case, imaging is necessary to determine the ROI in which chemical analysis is carried out; NIR imaging is therefore initially used for image segmentation followed by *targeted chemical composition analysis*.

8.3.6.1 Gradual Chemical Changes: Mapping the Chemistry of a Sample
In issues dealing with chemical gradient mapping of biological products, the major challenge is to build an appropriate calibration. This difficulty is enhanced by the unavailability of reference materials. Examples of mapping chemical gradients at a macroscopic scale are generally found in fruit, wood and fish products.

8.3.6.1.1 **Fruit** One of the very first experiments was carried out in 1998 by Hart *et al.* [47], who mapped the SSC in kiwi fruit. For this, a NIR hyperspectral imager spanning the spectral range 650–1100 nm was used on a cut kiwi fruit. The crucial issue of the reference data was solved as follows: the SSC of plugs cut from thin slices of fruit were measured and related to the spectra collected on the same areas from which the plugs had been taken. A prediction error of 1.2° Brix (over a 4.7–14.1° Brix range) was obtained. Later, Tsuta *et al.* [48] built a 16-bit CCD camera system with band-pass filters at 846, 874, 902 and 930 nm to map the sugar content of half-cut melon. Cores measuring 25 mm in diameter were analyzed to calibrate the system. Long *et al.* [49] developed a low-cost multispectral system with an 8-bit CCD camera and five filters at 830, 850, 870, 905 and 930 nm to map sugar on half-cut melons. These authors concluded that it was necessary to average 23×23 pixel blocks to obtain a correct prediction ($r^2 = 0.98$ and standard error of cross-validation = 1.1° Brix) and that a 10-bit camera was required to increase the SNR.

Although these experiments are interesting from a scientific point of view, they do not directly address any practical grading issues. Peirs *et al.* [50] described an

application in which NIR hyperspectral imaging allowed the elimination of toxic product handling used in apple grading, namely iodine solution. The procedure entailed measuring the regression of starch in half-cut apples, to determine their maturity stage. Normally, the apple is stained with an iodine solution (which turns black in the presence of starch), and then analyzed using RGB or a black and white camera. The use of a NIR hyperspectral camera alleviated the need for the staining step, and allowed imaging of the continuous gradient of starch content instead of a binary (starch/nonstarch) response. In order to obtain a reasonably good evaluation of the starch/nonstarch areas, a threshold was applied to the first principal score image. However, the authors supposed that a multispectral camera might be sufficient to make this mapping, which would both reduce the price of the device and speed up the measurement time.

8.3.6.1.2 **Wood** Wood is the another vegetal commodity for which NIR hyperspectral imaging has attracted huge interest. The main issue here is being able to map the compression wood, which may cause problems as it provokes the future distortion of sawn wood. Hence, the mapping of compression wood on timber sections is of interest for both grading and research purposes, and to better understand compression wood elaboration factors. The chemical composition of compression wood differs from that of normal wood, in that the lignin content is higher. Several studies have been reported, using either hyperspectral or multispectral NIR imaging systems. The first method (dating back to 1941!) [51] for detecting compression wood involved candling the wood slices in the visible range: compression wood is opaque, whereas normal wood is translucent with regard to visible light. However, this method had certain limitations, and consequently methods based on NIR imaging were developed. For example, Nyström and Hagman [52] used a commercially available scanning system (IVP, Sweden) combined with a PGP spectrograph to create a real-time NIR imager. Whole-wood planks were scanned in reflectance mode in the 400–710 nm range, while the reference method for determining compression wood was based on scanning electron microscopy (SEM) and human judgment. The system was evaluated on a 4 m-long plank of Norway spruce, conveyed at $0.3 \, \text{m s}^{-1}$ with a resolution of 2 mm in the feeding direction. Both, PCA and PLS were carried out on pixels, and the real-time classification was correct in 11 of 14 cases.

Noordam *et al.* [53] used a multispectral imager composed of a PbS camera and a filter wheel (680, 740, 800, 840, 1010, 1110 nm) for viewing two wooden disks of pine and spruce wood (Figure 8.11). Based on PCA on single pixels, these authors were able to map three regions, namely bark wood, compression wood and normal wood.

8.3.6.1.3 **Fish** Among animal products, fish offers the best example of on-line chemical mapping, with a commercial system developed by SPECMOD (the Center for Bio-Spectroscopy and Data Modeling, Aas, Norway), together with Sintef ICT and the Norwegian company Qvision AS (Oslo, Norway). This industrial on-line visible/NIR spectroscopic imaging scanner has been used for mapping
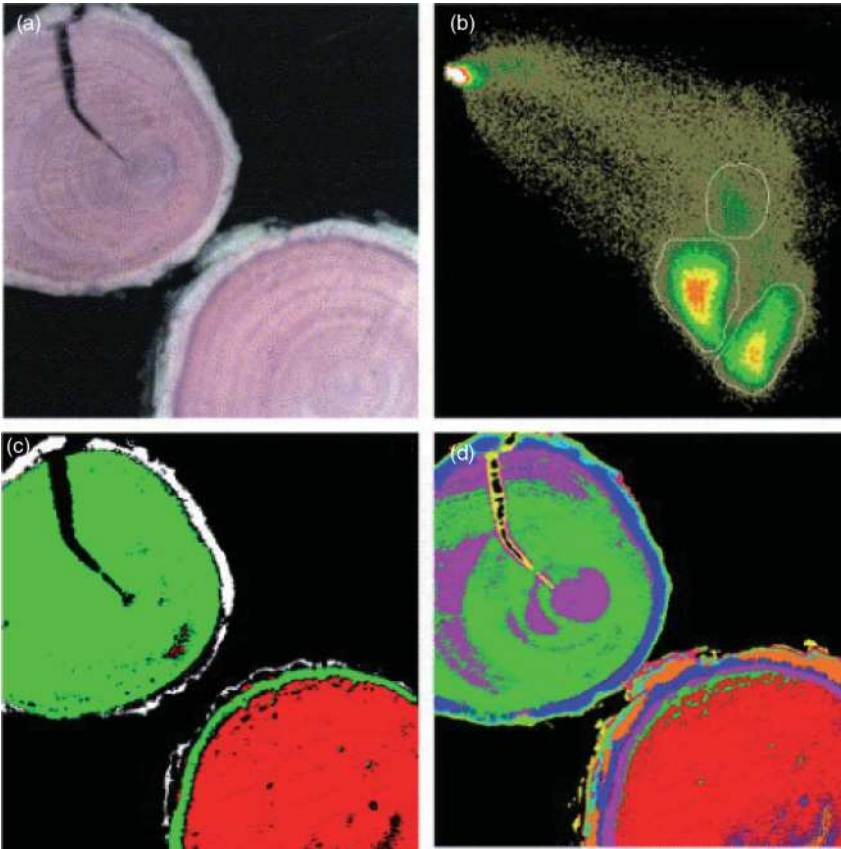
Figure 8.11 A multispectral wood image. (a) Pseudocolor image; (b) Score plot; (c) Multivariate image analysis (MIA) combined score image; (d) Feedback Multivariate Model Selection (FEMOS) nine-class segmented image. Illustration reproduced from Ref. [53].

the water content in salted cod (Figure 8.12) [54] and the fat and pigment contents in salmon fillet [55].

The system operates in transflectance mode, with a penetration depth of approximately 20–25 mm. The capacity of the system is about 60 fillets per second; at present, the system is being further developed for use in the meat industry.

8.3.6.2 Targeted Chemical Composition Analysis

The issue here is to use image analysis to identify the ROI; that is, the target where the chemical analysis must be carried out.

This is typically the case for streams of mixed items that require sorting, an example being in the recycling industries. Several reports [56, 57] and patents [58, 59] are related to on-line hyperspectral or multispectral imaging for the

(a)   (b)   (c)   (d)
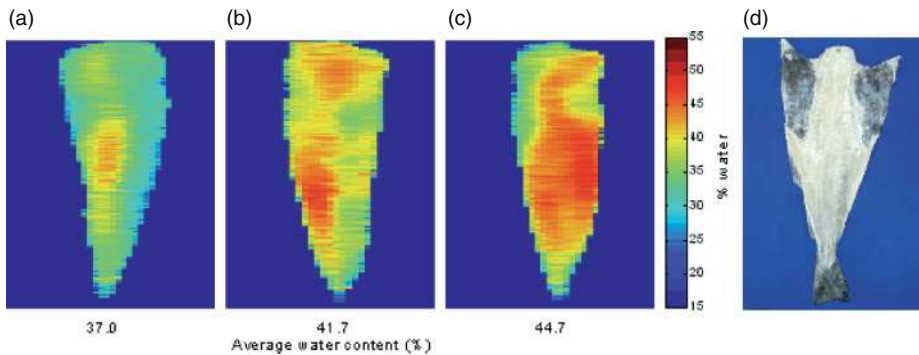
Figure 8.12 (a–c) Predicted water contents in dried and salted cod. (d) Image of a dried and salted cod for comparison. Illustration courtesy of SPECMOD, Aas, Norway.

identification and separation of various types of waste from each other, based on their NIR properties; including paper from cardboard, various types of plastic, and plastic film pieces in compost.

Images are either taken with a hyperspectral imaging system [56, 59] or are rebuilt from a whisk-broom scanning procedure [58]. In the latter case, a scanning mirror is made to rotate over the conveyor belt, perpendicular to the waste stream and, at each point in time, the reflectances at all wavelengths of interest are recorded. The typical velocity of the conveyor ranges from 2 to $3\,\mathrm{m\,s^{-1}}$.

Identifying a ROI is also relevant when a product is composed of various compartments of diverse compositions; here, meat slices are perhaps the best example. Hyperspectral images are first used to isolate the ROIs, and then to analyze their chemical compositions. For example, in pork quality studies [60, 61] spectral analyses are concentrated in the 'eye' of the loin area: the loin-eye ROI is segmented from fat or background, after which the spectra from this ROI are averaged for each sample. Following a PCA, the wavelengths with the highest weight are selected and fed into a neural network, the outputs of which are the four quality classes [60]. The classification with regard to quality has yielded a rate of 87% by use of this method.

8.3.7
Conclusion: On-Line Applications

The on-line applications of hyperspectral NIR imaging cover a wide range of issues, including the detection of foreign bodies and of contaminants (either exogenous or endogenous, internal or external), the identification for sorting, localized spectral analysis within a given ROI, and chemical mapping.

As in this situation the objects are moving, the hyperspectral images are easily created line-by-line. However, due to the high speed of the conveyor belt, huge amounts of data are collected and must be processed; consequently, companies endeavor to reduce the quantity of information, and hence often switch from

hyperspectral to multispectral imaging, either through software wavelength selection using the hyperspectral system, or by hardware modification geared towards multispectral imaging systems.

Until now, on-line applications have mainly been concerned with the very NIR and visible ranges (400–1000 nm), with systems composed of PGP spectrographs and CCD cameras of various dynamic ranges (from 10 to 16 bits). Few applications have been carried out on NIR longer wavelengths (i.e., in the 900–1700 nm range), due mainly due to the fact that cameras operating in this range have not only been developed more recently but are also more expensive and have lower SNRs. In the near future, it is expected that additional applications will be developed within this spectral range, thereby allowing those problems to be tackled that require the increased chemical specificity that is available with access to lower-order overtone bands and combination bands.

8.4
General Conclusions

Within 10 years of the first attempts to use NIR multispectral or hyperspectral imaging for food products, prodigious advances have been achieved such that NIR hyperspectral imaging is now commonly used in both laboratory and on-line applications. Yet, this outstanding technique continues to raise many questions that must be addressed before it is more widely accepted. Such questions relate not only to the hardware and data processing but also to specific issues related to NIR imaging.

8.4.1
Hardware Development

Hardware innovation incorporates extension of the spectral range towards longer wavelengths, as has been the case for linear diode arrays during the past 10 years. Whereas, long-wavelength (up to 2450 nm) NIR imagers based on solid-state tunable filters were first developed commercially in about 2003, line-mounted whisk-broom systems are very new devices for food applications, despite their long-term history in remote sensing. At the 13th International Conference on Near Infrared Spectroscopy, held in Umea, Sweden in 2007, Hyvärinen *et al.* [1] presented the details of a whisk-broom NIR imager in the 970–2450 nm range based on a PGP spectrograph and a MCT camera, as a novelty.

Today, major hopes are placed on the use of microelectromechanical systems (MEMS) for future NIR imaging schemes. In addition, individual submillimeter ($50 \times 50 \, \mu m^2$) modules that integrate an interferometer and a detector are becoming available [62] which, when arranged in arrays, will allow the design and construction of low-cost and robust hyperspectral imagers [63].

In parallel, the spatial encoding of signals with tools such as the Hadamard optical encoder represents an innovative means of gathering hyperspectral

information. The Hadamard spatial encoding of the sensor aperture consists of: (i) summing the spectra of some pixels at the scene, instead of recording the spectra of all pixels; and (ii) using the Hadamard transform to reconstruct the hyperspectral image. Recently, PlainSight Systems constructed a system based on this approach, where a digital mirror array (DMA) device realizes the Hadamard multiplexed imaging. As a consequence, some interesting results were reported by Mahalanobis and Muise [64], and more news of this development is expected to be heard in the very near future. Eventually, portable and even hand-held NIR imagers are expected to result from miniaturization and novel image-gathering schemes, for use either in the field or for raw material grading. It is not beyond consideration that novel concepts of overlaid projections of NIR-contrasted images onto the viewed scene [65] may represent some of the first improvements seen for hand-held imagers.

8.4.2
Data Processing

The availability of hyperspectral and multispectral imaging systems with large arrays has brought about new demands in terms of data processing capacity and the mathematics required to extract the important content from these large data sets. As spectral information in images greatly increases the amount of data to be processed, it is absolutely necessary to reduce the dimensionality of the data [66].

One route that has been explored to limit this challenge is that of data reduction, by acquiring fewer datum points. This can be achieved through either of the two dimensions – that is, spatial and spectral – by using less spatial resolution or moving towards multispectral imaging systems rather than hyperspectral approaches. Unfortunately, the main drawback of multispectral imaging is that, except for multispectral systems using hyperspectral components [67], the versatility is not preserved because the wavelengths are set. In contrast, hyperspectral imaging preserves the system versatility and, therefore, has a greater potential.

The other route to reduce the amount of data would be to develop dedicated image analysis software. The most important issue for hyperspectral image processing is to create efficient data processing methods based on all available information of the hypercube, based on both spectral and spatial information. For this, numerous creative approaches have been described [68–70], although the implementation of such new concepts has not yet been achieved in food science applications. Other imaging fields, such as magnetic resonance imaging (MRI) and remote sensing [71, 72] have moved towards novel processing schemes at an early stage, and offer good examples that may contribute to a broader deployment of NIR imaging for food analysis.

8.4.3
Calibration and Characterization of NIR Imaging Systems

Last, but not least, specific questions continue to arise regarding the characterization and calibration of spectral imagers. At present, there are no NIR imaging

standards that can be used to compare instruments, although a subcommittee (E13) of the American Society for Testing and Material (ASTM) is currently developing such a standard. Traditional NIR standards, such as NIST 1920a and NIST 2060, may be used to ensure wavelength accuracy, but provide no means of investigating spatial characterization. As the numerous NIR spectral imagers built for food applications (especially in the on-line domain) are in fact assemblies of individual components – each of which is susceptible to a number of possible sources of error such as noise, drift, nonlinear response of detectors, read-out errors, non-uniform illumination [73] – it is imperative that characterization routines and proper calibration and correction procedures be applied.

It is common practice to measure relative reflectance or transmittance values in global NIR imaging, using highly reflective materials (e.g., Spectralon or ceramics) as reference ($R_{Spectralon}$). Camera dark counts at every pixel (R_{dark}) are also measured and subtracted from the data, eventually to yield a relative reflectance value corresponding to ($R_{sample} - R_{dark})/(R_{Spectralon} - R_{dark}$), where R is the reflectance measured. Lawrence *et al.* [74] have proposed a three-step procedure to carry out calibration and corrections on a whisk-broom system. The geometric distortions are corrected by use of the geometric control point (GCP) calibration. The wavelength/pixel relationship is built using calibrating lamps and linear or quadratic models, and the relative reflectance value is calibrated with one standard 99% reflectance panel and a one-point correction (the dark).

Spectral calibration – that is, building up a relationship between pixels and wavelengths – represents another calibration issue of pushbroom and whisk-broom devices. By using PGPs as wavelength separators, Polder *et al.* [75] have focused on the issue of wavelength/pixel relationships on three devices covering the 400–1700 nm range. Here, a HgAr lamp is used for spectral calibration, and a third-order polynomial model provides an appropriate fit for the pixel to the wavelength mapping.

In order to create the most stable hyperspectral images, Burger and Geladi [73] proposed a two-step calibration procedure using 'external' and 'internal' Spectralon standards. Standards, termed 'external standards', imaged independently from the sample images, are used to cancel pixel-to-pixel variations due to camera inconsistencies and variations in sample illumination (as proposed by Lawrence *et al.* [74]). Standards recorded jointly to samples – that is, in the same image, termed 'internal standards' – are innovative and used to compensate for signal drift over time.

In addition to hardware characterization and calibration, analytical calibration (i.e., correspondence between spectral data and reference data) is, as in NIR spectrometry, *the* burning issue for biological products. One of the problems deals with the reference measurement, namely: How to take a sample for the reference measurement? This is, of course, very challenging for samples with gradient-like concentrations or for centimeter-scale samples (e.g., kernels). In the first case, the samples are punctured at various locations and submitted to reference analysis. In the second case, contrasted individuals (high and low concentrations) are chosen as reference samples. By using centimeter-large samples, another approach would be to build the calibration on images with regards to images built up using

other imaging technologies (e.g., fluorescence imaging) or moving toward classification approaches, which only require pure reference materials. These approaches alleviate the need for concentration calibration sets, which are difficult to obtain.

8.4.4
Concluding Remarks

NIR imaging in food science has broadened the way in which both NIR spectrometry and vision systems are used, and has therefore opened new opportunities for high-throughput analysis, reduced detection limits, chemical gradient mapping and improved object identification. We believe it is possible to go even further by extending the images to include other spectral information, such as combining NIR with fluorescence images, as proposed by Kim *et al.* [76]. Innovations in hardware, software control and data processing will surely pave the way for the development of additional analytical capabilities. Current on-line sorting mechanisms, based on size and color, will undoubtedly be augmented by additional sorting for quality and safety attributes of food products as a result.

References

1 Hyvärinen, T., Jussila, J., Karjalainen, H. and Jaskari, R. (2007) Proceedings of the 13th International Conference on Near Infrared Spectroscopy, Umeå, Sweden, 17–21 June.

2 Gowen, A.A., O'Donnell, C.P., Cullen, P.J., Downey, G. and Frias, J.M. (2007) *Trends Food Sci. Technol.*, **18** (12), 590–8.

3 Shenk, J.S., Workman, J.J., Westerhaus, M.O. (1992) *Handbook of Near Infrared Analysis* (eds D.A. Burns and E.W. Ciurczak), Marcel Dekker Inc., New York, Ch. 15, pp. 383–431.

4 Norris, K.H. and Hart J.R. (1965) Principles and Methods of Measuring Moisture in Liquids and Solids, Vol. **4**, *Proceedings, 1963 International Symposium on Humidity and Moistures*, Reinhold Publishing, New York, pp. 19–25.

5 Siska, J. and Hurburgh, C.R.J. (1994) *ASAE*, **37** (5), 1577–82.

6 Cogdill, R.P., Hurburgh, C.R. and Rippke, G.R. (2004) *Trans. ASAE*, **47** (1), 311–20.

7 Finney, E.E., Jr and Norris, K.H. (1978) *Trans. ASAE*, **41** (6), 1845–52.

8 Weinstock, B.A., Janni, J., Hagen, L. and Wright, S. (2006) *Appl. Spectrosc.*, **60** (1), 9–16.

9 Lewis, E.N., Dubois, J. and Kidder, L.H. (2007) *Near-Infrared Spectroscopy in Food Science and Technology* (eds Y. Ozaki, W.F. McClure and A.A. Christy), John Wiley & Sons, Inc., New Jersey, pp. 121–32.

10 Lewis, E.N., Schoppelrei, J.W., Lee, E. and Kidder, L.H. (2005) *Process Analytical Technology* (ed. K.A. Bakeev), Blackwell, pp. 187–225.

11 Smail, V.W., Fritz, A.K. and Wetzel, D.A. (2006) *Vib. Spectrosc.*, **42**, 215–21.

12 Hudak, S.J., Haber, K., Sando, G., Kidder, L.H. and Lewis, E.N. (2007) *NIR News*, **18** (6), 6–8.

13 von Raamsdonk, L.W.D., von Holst, C., Baeten, V., Berben, G., Boix, A. and de Jong, J. (2007) *Anim. Feed Sci. Technol*, **133**, 62–83.

14 Fernandez Pierna, J.A., Baeten, V. and Dardenne, P. (2006) *Chemom. Intell. Lab. Syst.*, **84** (1–2), 114–18.

15 De la Haba, M.J., Fernandez Pierna, J.A., Fumiere, O., Garrido-Varo, A., Guerrero, J.E., Perez-Marin, D.C., Dardenne, P. and

Baeten, V. (2007) *J. Near Infrared Spectrosc.*, **15** (2), 81–8.

16 Bellon, V., Rabatel, G. and Guizard, C. (1992) *Food Control*, **Jan**, 49–54.

17 Holm, F. (2003) *Food Quality Sensors, SMEs no. 4, FairFlow Europe*, INRA, Paris, France.

18 Qin, J. and Lu, R. (2007) ASABE Annual International Meeting, Minneapolis, MN, 17–20 June, Paper no. 073058.

19 Izumyia, T., Futamura, T. and Fukuchi, J. (2004) CORESTA Congress, Kyoto, Japan. October, 3–7.

20 Delwiche, S.R. and Kim, M.S. (2000) Proceedings SPIE, Biological Quality and Precision Agriculture, Conference II (eds J.A. DeShazer and G.E. Meyer), 4203, pp. 13–20.

21 Polder, G., Van der Heijden, G.W.A.M., Waalwijk, C. and Young, I.T. (2005) *Seed Sci. Technol.*, **33**, 655–68.

22 Lu, R. and Chen, Y.-R. (1998) SPIE Conference on Pathogen Detection and Remediation for Safe Eating, 3544, pp. 121–32.

23 Kim, M.S., Lefcourt, A.M., Chao, K., Chen, Y.R., Kim, I. and Chan, D.E. (2002) *Trans. ASAE*, **45** (6), 2027–37.

24 Liu, Y., Chen, Y.R., Kim, M.S., Chan, D.E. and Lefcourt, A.M. (2007) *J. Food Eng.*, **81**, 412–18.

25 Chao, K., Park, B., Chen, Y.R., Hruschka, W.R. and Wheaton, F.W. (2000) *J. Appl. Eng. Agric.*, **16** (5), 581–7.

26 Lawrence, K.W., Windham, W.R., Park, B. and Buhr, R.J. (2003) *J. Near Infrared Spectrosc.*, **11**, 269–81.

27 Park, B., Lawrence, K.C., Windham, W.R. and Smith, D.P. (2006) *J. Food Eng.*, **75**, 340–8.

28 Windham, W.R., Lawrence, K.C., Park, B., Martinez, L.A., Lanoue, M.A., Smith, D.A., Heitschmidt, J. and Poole, G.H. (2003) US Patent no. 6,587,575.

29 Xing, J. and De Baerdemaeker, J. (2005) *Postharvest Biol. Technol.*, **37**, 152–62.

30 Mehl, P.M., Chen, Y.R., Kim, M.S. and Chan, D.E. (2004) *J. Food Eng.*, **61** (1), 67–81.

31 Kleynen, O., Leemans, V. and Destaing, M.F. (2005) *J. Food Eng.*, **69** (1), 41–9.

32 Cheng, X. (2004) PhD thesis, University of Maryland, College Park (USA), https://drum.umd.edu/dspace/ bitstream/1903/2154/1/umi-umd-2133.pdf (accessed 19 August 2007).

33 Xing, J., Ngadi, M., Wang, N. and De Baerdemaeker, J. (2006) ASABE Annual Meeting, St Joseph, MI. Paper no. 063018.

34 Ariana, D.P., Lu, R. and Guyer, D.E. (2006) *Comput. Electron. Agric.*, **53**, 60–70.

35 Nicolaï, B.M., Lötze, E., Peirs, A., Scheerlinck, N. and Theron, K.I. (2006) *Postharvest Biol. Technol.*, **40**, 1–6.

36 Menesatti, P., Urbani, G. and Lanza, G. (2005) *Acta Hortic.*, **682**, 1347–54.

37 Noordam, J.C., van den Broek, W.H.A.M. and Buydens, L.M.C. (2005) *J. Sci. Food Agric.*, **85**, 2249–59.

38 Milner, T.E. (2002) Technologies at the Edge. *Biomedical Engineering Newsletter*, http://www.txcbme.org/Links/Newsletter%20Vol%202%20Issue%204.htm (accessed 8 September 2007).

39 Chauchard, F., Roger, J.M., Bellon-Maurel, V., Abrahamsson, C., Andersson Engels, S. and Svansberg, S. (2005) *Appl. Spectrosc.*, **59** (10), 1229–35.

40 Wallin, P. and Haycock, P. (1999) *Foreign Body Prevention, Detection and Control – A Practical Approach.* Blackie Academic & Professional, Thomson Science, London, UK.

41 Qin, J. and Lu, R. (2005) *Trans. ASAE*, **48** (5), 1963–70.

42 Ariana, D.P. and Lu, R. (2007) *Proc. ASABE*, **51** (2), 705–13.

43 Qin, J. and Lu, R. (2007) *Appl. Spectrosc.*, **61** (4), 388–96.

44 Lu, R. (2003) ASAE International Meeting, St Joseph, Michigan, Paper no. 036012.

45 Lu, R. and Peng, Y. (2006) *Biosyst. Eng.*, **93** (2), 161–71.

46 Peng, Y. and Lu, R. (2007) ASAE Annual Meeting, St Joseph, Michigan, Paper no. 076270.

47 Hart, D.A., Reno, C., Martinsen, P. and Schaare, P. (1998) *Postharvest Biol. Technol.*, **14** (3), 271–81.

48 Tsuta, M., Sugiyama, J. and Sagara, Y. (2002) *J. Agric. Food Chem.*, **50** (1), 48–52.

49 Long, R., Walsh, K.B. and Greensill, C.V. (2005) *J. Near Infrared Spectrosc.*, **13**, 177–86.

50 Peirs, A., Scheerlinck, N., De Baerdemaeker, J. and Nicolaï, B.M. (2003) *J. Near Infrared Spectrosc.*, **11**, 379–89.

51 Pillow, M. (1941) *J. Forest.*, **39**, 385–7.

52 Nyström, J. and Hagman, O. (1999) *J. Wood Sci.*, **45** (1), 30–7.

53 Noordam, J.C., Van den Broek, W.H.A.M., Geladi, P. and Buydens, L.M.C. (2005) *Chemom. Intell. Lab. Syst.*, **75** (2), 115–26.

54 Wold, J.P., Johansen, I.-R., Haugholt, K.H., Tschudi, J., Thielemann, J., Segtnan, V.H., Narum, B. and Wold, E. (2006) *J. Near Infrared Spectrosc.*, **14**, 59–66.

55 Segtnan, V. (2007) Proceedings of the 13th International Conference on Near Infrared Spectroscopy, Umeå, Sweden, 17–21 June.

56 Tatzer, P., Wolf, M. and Panner, T. (2005) *Real-Time Imaging*, **11**, 99–107.

57 Leitner, R., Mairer, H. and Kercek, A. (2003) *Real-Time Imaging*, **9** (4), 245–51.

58 Bourely, A. and Pellenc, R. (2004) US Patent 2004/0095571 A1.

59 Cowling, D. and Randall, P.N. (2007) US Patent 2007/0029232 A1.

60 Jun, Q., Ngadi, M., Wang, N., Gunenc, A., Monroy, M., Gariepy, C. and Prasher, S. (2007) *J. Food Eng.*, **3** (1), 1–12.

61 Qiao, J., Wang, N., Ngadi, M.O., Gunenc, A.M., Monroy, M., Gariepy, C. and Prasher, S.O. (2007) *Meat Sci.*, **76** (1), 1–8.

62 Bellon-Maurel, V. (2006) *NIRNews*, **17** (7), 14–8;23.

63 Stiebig, H., Knipp, D., Bhalotra, S.R., Kung, H.L. and Miller, D.A.B. (2005) *Sens. Actuators A*, **120** (1), 110–14.

64 Mahalanobis, A. and Muise, R. (2006) Information Optics: 5th International Workshop on Information Optics (WIO'06), AIP Conference Proceedings, 860, pp. 95–106.

65 Alsberg, B., Burger, J. and Skavhaug, A. (2007) Proceedings of the 13th International Conference on Near Infrared Spectroscopy, Umeå, Sweden, 17–21 June.

66 Carlsohn, M.F. (2006) *J. Real-Time Image Process.*, **1** (1), 25–32.

67 Vila, J., Calpe, J., Pla, F., Gómez, L., Connell, J., Marchant, J.A., Calleja, J., Mulqueen, M., Muñoz, J. and Klaren, C.A. (2005) *Real Time Imaging*, **11** (2), 85–98.

68 Noordam, J.C. and Van den Broek, W.H.A.M. (2002) *J. Chemom.*, **16**, 1–11.

69 De Juan, A., Maeder, M., Hancewicz, T. and Tauler, R. (2005) *Chemom. Intell. Lab. Syst.*, **77** (1–2), 64–74.

70 Burger, J. (2007) Proceedings of the 13th International Conference on Near Infrared Spectroscopy, Umeå, Sweden, 17–21 June.

71 Tran, T.N., Wehrens, R. and Buydens, L.M.C. (2005) *Chemom. Intell. Lab. Syst.*, **77** (1–2), 3–17.

72 Plaza, A., Benediktsson, J.A., Boardman, J., Brazile, J., Bruzzone, L., Camps-Valls, G., Chanussot, J., Fauvel, M., Gamba, P., Gualtieri, J.A., Marconcini, M., Tilton, J.C. and Trianni, G. (2007) Remote Sensing of Environment, in press, http://www.umbc.edu/rssipl/people/aplaza/Publications.htm (accessed 27 August 2008).

73 Burger, J. and Geladi, P. (2005) *J. Chemom.*, **19**, 355–63.

74 Lawrence, K.W., Park, B., Windham, W.R. and Mao, C. (2003) *Trans. ASAE*, **46** (2), 513–21.

75 Polder, G., Van der Heijden, G.W.A.M., Keizer, P. and Young, I.T. (2003) *J. Near Infrared Spectrosc.*, **11**, 193–210.

76 Kim, M.S., Chen, Y.-R., Cho, B.-K., Chao, K., Yang, C.C., Lefcourt, A.M. and Chan, D. (2007) *Sensing Instrumentation for Food Quality and Safety*, **1** (3), 151–9.

Part Four   Polymers and Pharmaceuticals

9

FT-IR and NIR Spectroscopic Imaging: Principles, Practical Aspects and Applications in Material and Pharmaceutical Sciences

Elke Wessel, Christian Vogel, Olga Kolomiets, Uwe Hoffmann, and Heinz W. Siesler

9.1
Introduction

Both, Fourier transform-infrared (FT-IR) and near-infrared (NIR) spectra of a multicomponent sample measured with a single-element detector, can provide information on the identity of the different components in the investigated sample area, but do not yield any information on their spatial separation. For many analytical problems, however, this is the crucial point of the investigation. In this respect, the development of focal plane array (FPA) detectors [1] for imaging measurements in the mid-IR and NIR has launched vibrational spectroscopy into a new era of analytical applications. Thus, several thousand spectra of laterally resolved sample positions can be measured simultaneously within a few minutes, thereby providing 'chemical images' of the investigated sample area. As a consequence, both FT-IR and NIR imaging techniques have over the past years proved to be powerful tools for a broad range of industrial and research applications. The experimental principles of operation, however, are different for the two imaging methods (see also Chapter 1). While FT-IR imaging is mainly operated in transmission mode or in attenuated total reflection (ATR) as a macro or, in combination with a microscope, as a micro technique, NIR imaging is almost exclusively applied in diffuse reflection in the macro mode. This can be explained in terms of the significantly higher absorptivities of the mid-IR absorption bands of fundamental vibrations compared to the NIR overtone and combination bands. The penetration depth of the ATR technique and the optimum sample thickness for mid-IR spectra lie in the range of a few microns, which corresponds approximately to the lateral resolution achievable with the FT-IR imaging technique. For NIR transmission spectra, sample thicknesses of up to millimeters are required, which are far beyond the theoretically feasible lateral resolution (in the μm-range) for the NIR wavelength region. Consequently, the focus of the two imaging techniques is in different fields of applications. While FT-IR imaging has mainly been applied for biomedical diagnostics and material (especially polymer)−analysis, NIR imaging has to date been used primarily for the quality control of food or agricultural products and for the analysis of solid pharmaceutical drug formulations.

The main research activities using a FPA detector for FT-IR imaging began in 1997, since when the group of Koenig, at Case Western Reserve University in Cleveland, USA, has made important contributions to this research area. In their first FT-IR imaging applications in the transmission mode (1996, 1998, 1999), the group studied the diffusion of liquid crystals into polymers. The diffusion process was analyzed in detail and quantitative results, such as diffusion coefficients, were derived [2–4].

FT-IR imaging was rapidly adopted in polymer research. For example, in 1998 Bhargava *et al.* reported their FT-IR imaging results of the interface of a phase-separated multicomponent polymeric system [5]. A subsequent report by Snively and Koenig in 1999 dealt with the examination of the homogeneity and the degree of orientation in semi-crystalline polymer systems, notably different poly(ethylene glycol) (PEG) systems [6].

Other examples from the research group of Koenig (2000–2002) include details of the dissolution behavior of polymers in different solvents (partly with the addition of nonsolvents) or a mixture of solvents. From these investigations, a nonuniform dissolution of the polymer at the interface could be observed for several solvent systems [7–11]. Further results of diffusion measurements were presented in 2002 by Rafferty and Koenig, and later in 2005 by Bobiak and Koenig [12, 13], in which the diffusion of nicotine into an ethylene–vinyl acetate copolymer was analyzed.

In 2002, Gupper *et al.* investigated polymer blends by using FT-IR imaging (ATR, transmission) in combination with Raman imaging and electron microscopy [14]. Later, Gupper *et al.* described the morphological characterization of polymer blends consisting of polyamide and poly(tetrafluorethylene) by using FT-IR mapping and electron microscopy [15]. The thermal oxidation of poly(isoprene) rubber with hot air (140 °C) as a function of time was investigated by Li and Koenig [16].

In an ATR imaging study, Kazarian and Chan described the behavior of polymer blends under high-pressure CO_2. Under these conditions and at 40 °C, initially homogeneous blends were seen to undergo a phase separation. By using this method, it was also possible to examine the influence of other gases on the material properties of polymers [17]. Likewise, in 2006, Kaun *et al.* demonstrated an FT-IR imaging system for the examination of a chemical reaction in a solution, and the time-resolved model reaction of formaldehyde and sulfite was also visualized [18].

Another field of application, especially for ATR imaging, is that of pharmaceutical formulations. Here, in 2003, Chan *et al.* reported the first results on macro and micro ATR imaging of pharmaceutical tablets by characterizing the spatial distribution of active ingredients and excipients [19]. Further examples in this field are described in Chapter 10 of this volume.

With the introduction of more economical, large-format (320×256 pixels) FPA detectors, NIR hyperspectral imaging was also developed into an important tool in selected industrial areas such as the evaluation of food quality (see Chapter 8) or in the pharmaceutical industry. Most likely, the delay in implementation of NIR

imaging relative to mid-IR and Raman imaging was based on the (largely unde-served) reputation of the inferior specificity of NIR compared to Raman and mid-IR spectroscopy. Yet, based on the much simpler and more rugged instrumentation for NIR chemical imaging, its rapid and nondestructive sampling, and also on the fact that in many cases *a priori* information on the investigated material is available (e.g., in pharmaceutical applications), the advantage of obtaining high-fidelity, spatially resolved pictures of the chemistry of the sample has eventually accelerated the practical application of this imaging technique. Typically, a NIR imaging ana-lyzer uses quartz halogen lamps as NIR sources, a device for wavelength discrimi-nation [e.g., a liquid crystal tunable filter (LCTF) or an acousto-optic tunable filter (AOTF)], and a large-format FPA detector which does not require cryogenic cooling. Additionally, working in the NIR permits the use of relatively simple refractive achromatic optics with long working distances. It must be pointed out however that, compared to mid-IR and Raman imaging, the diffraction-limited spatial resolution in the NIR region (~2 μm) cannot be exploited for two reasons:

- Due to the significantly lower (10–100-fold) absorptivities of overtone and com-bination bands compared to fundamental absorptions, the sample thickness for NIR transmission measurements must be several hundred micrometers.

- In diffuse reflection measurements of particulate materials, scattering effects also lead to maximum pathlengths of several hundred micrometers of the photons within the sample (see below and Chapter 1).

Apart from food industry (see Chapter 8), NIR chemical imaging has so far pri-marily been applied to qualitative and quantitative product characterization in the pharmaceutical industry. The ability to visualize and assess the compositional heterogeneity and structure of the end products is extremely important for both the development and manufacture of solid dosage forms [20]. Hence, NIR chemi-cal images have been used to determine authenticity, content uniformity, particle sizes and distribution of sample components, polymorph distributions, moisture content and location, contaminations, coating and layer thickness, as well as a host of other structural details [21–29].

9.2
Instrumentation for FT-IR and NIR Imaging

In the following sections the instrumentation used for the application examples described in this chapter will be discussed in some detail. Specifically, the basic instrumental features of the two imaging systems, different possible measure-ment modes and the occurrence of instrument-related and sample-related artifacts and misinterpretations will be outlined. Because NIR imaging instruments are simpler in design, these will be discussed first.

The application example outlined in detail in this chapter refers to diffuse-reflection NIR chemical imaging measurements of a pharmaceutical drug

formulation consisting of three active ingredients and two excipients. The main purpose of these investigations was to demonstrate that, from the imaging data not only qualitative information regarding the homogeneity of the component distribution but also quantitative data concerning the active ingredient content can be derived.

9.2.1
NIR Imaging

The NIR hyperspectral images presented later in the chapter were recorded on a MatrixNIR system (Malvern, formerly Spectral Dimensions, Olney, MD, USA) with four quartz-halogen lamps as NIR sources, a LCTF as monochromator, and a thermoelectrically cooled 256×320 InGaAs FPA detector covering 118 channels (960–1662 nm or 10417–6017 cm^{-1}) with a spectral resolution of 6 nm at 1600 nm (corresponding to 24 cm^{-1}). Figure 9.1a shows the instrument alongside an optical scheme of the system (Figure 9.1b). For high-throughput measurements the
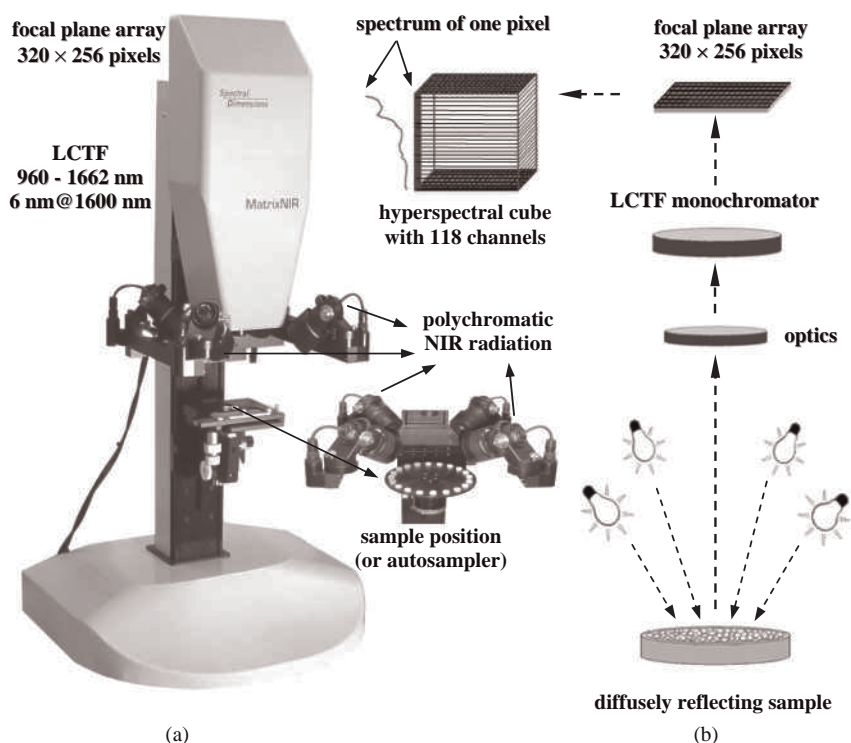
Figure 9.1 (a) The NIR imaging system; (b) The optical scheme of the instrument for diffuse-reflection measurements of a powder sample.

instrument can also be adapted with a programmable sample carousel which enables the sequential analysis of multiple samples.

The quantitative determination of the active ingredients is only part of the quality control requirements for a solid pharmaceutical drug formulation. At least as important is the homogeneous distribution of the active ingredients in the formulation. In this respect, the inherent advantage of imaging measurements comes into play and provides the relevant information. Because the majority of the NIR spectroscopic imaging measurements are made in diffuse reflection, the pathlength of NIR radiation in the sample for such measurements has become a fundamental area of debate [29–35].

Some possible schematic NIR radiation pathways in diffuse reflection measurements of a powder sample are outlined in Figure 9.2. The important issue with reference to the spatial resolution of imaging measurements is, on the one hand, the lateral extension of photons in the sample (Figure 9.2b, point 1) and, on the other hand, the maximum penetration depth of NIR radiation into the sample (Figure 9.2b, point 2).

The first question was addressed recently by E. N. Lewis *et al.* [36], whereby an effective pathlength of approximately $780\,\mu m$ at $1660\,nm$ ($6024\,cm^{-1}$), resulting in a sampling volume of a sphere with a diameter of $\sim 72\,\mu m$, was derived from theoretical calculations with a random walk model and transmission and diffuse

PDMS detection layer

(a)   (b)
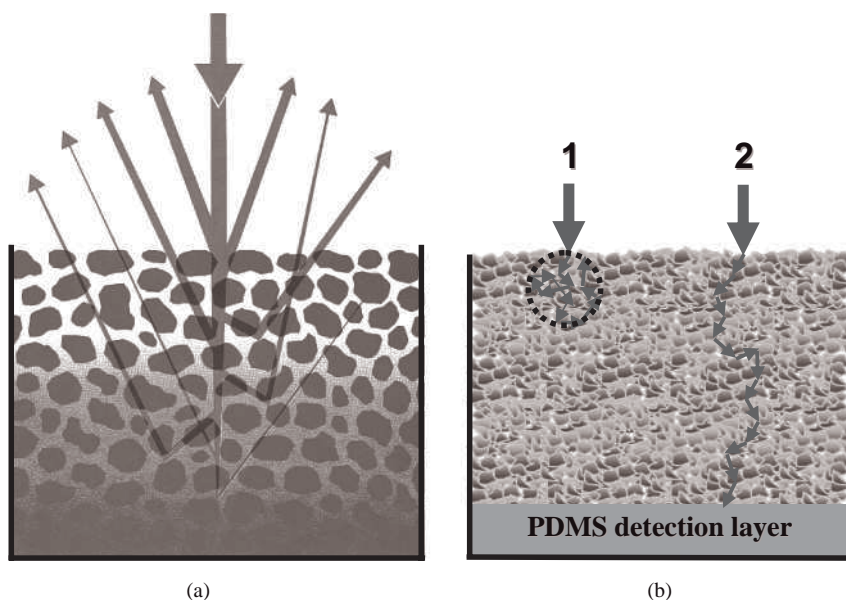
Figure 9.2 (a) Schematic pathways of NIR radiation in diffuse-reflection measurements of a powder sample; (b) Lateral extension (b, point 1) and maximum penetration depth (b, point 2) of NIR radiation in the powder sample (for details, see the text).

reflection measurements of an aspirin (acetylsalicylic acid; ASA) tablet. Furthermore, it has been concluded that, depending on the wavelength, approximately 70% of the photons exiting the sample at any given point in a diffuse reflection measurement will have interacted with a spherical region of a diameter between about 90 and 60 μm. The issue of maximum penetration depth has been addressed by Siesler *et al.* [68], using a somewhat different experimental approach (Figure 9.2b, point 2). Poly(dimethylsiloxane) (PDMS) films, containing 25 wt% silica particles, were stacked with layers of different thickness (100–900 μm) of the specified drug formulation. The spectra of these different two-layer drug formulation/PDMS stacks were then measured in diffuse reflection. The drug formulation used for these measurements had a composition of: ASA 18.1 wt%; ascorbic acid (ASC) 22.85 wt%; caffeine (CF) 19.05 wt%; and cellulose/starch (CE/ST, 1 : 3, w/w) 40 wt%.

PDMS has relatively sharp absorption bands in the NIR region that are not or only weakly superimposed by the broad absorption bands of the drug formulation. Thus, the polymer film can be used as a detection layer and the occurrence of signals in the PDMS-specific wavenumber regions are indicative of the penetration of NIR radiation through the drug formulation layer into the polymer film. With this experimental set-up, the decrease of the PDMS-specific absorption bands could be monitored in different wavenumber regions as a function of increasing drug formulation layer thickness to an intensity value <5% of the corresponding pure PDMS diffuse-reflection spectrum. These drug formulation layer thicknesses were taken as maximum penetration depth of the NIR radiation, and the following values estimated for selected wavenumber regions: ~300 μm for the 4000–4500 cm^{-1} region, ~400 μm for the 5300–6000 cm^{-1} region, ~550 μm for the 7000–7500 cm^{-1} region, and ~650 μm at 8440 cm^{-1}. Despite the different experimental approach, these values were relatively consistent with previous estimates [29]. Thus, in view of the diffraction-limited spatial resolution <3 μm in the NIR region (see Chapter 1), the NIR imaging technique is best used for the characterization of scattering samples with a particle size far larger than the diffraction limit.

9.2.2
FT-IR Imaging

The Bruker FT-IR imaging system (Bruker Optik GmbH, Ettlingen, Germany) used for the investigations described in this chapter is shown in Figure 9.3. The system consists of an IFS66/S step-scan/rapid-scan FT-IR spectrometer (left), which is connected to an IR microscope (Hyperion 3000) (center) and a macrochamber (IMAC) for the investigation of larger imaging areas. Depending on the type of measurement, the FPA detector can be connected either to the microscope or to the macrochamber.

The low-pass filter between the FT-IR spectrometer and the microscope restricts the high-wavenumber range beyond 3850 cm^{-1} in order to avoid artifacts due to Fourier fold-over.
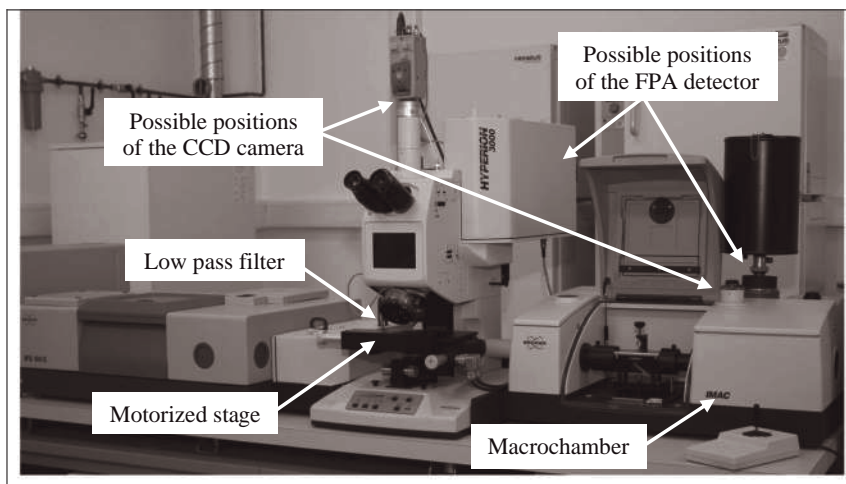
Figure 9.3 The Bruker FT-IR imaging system used for the investigations described in this chapter.

9.2.2.1 **Micro FT-IR Imaging**

For small samples, or in order to achieve a higher spatial resolution, the microscope is used which is specially designed for FT-IR measurements. In this case, a motorized mirror in the microscope enables a change between single-point measurements with a single-element detector and imaging measurements with the FPA detector. FT-IR images can be measured with different objectives in transmission, in reflection, or in the ATR mode. A computer-controlled motorized stage enables an exact positioning of the sample and a mapping with the single-element detector and also with the FPA detector. For transmission measurements, a well-aligned condenser focuses the IR radiation with maximum intensity on the sample. A live FPA image (see Section 9.2.2.3) is used to check the focus and facilitate the alignment.

For transmission and reflection measurements, a 15× objective with a numerical aperture (NA) of 0.4 and an imaging area or field of view (FOV) of $260 \times 260\,\mu m^2$ is used (see Table 9.1).

Micro ATR measurements in the reflection mode are performed using a special ATR objective with a Ge crystal. The tip has a diameter of $100\,\mu m$ and is shaped slightly convex in order to ensure an optimal contact between the ATR crystal and the sample. This is a 20× objective with a NA of 0.6 and a field of view of $50 \times 50\,\mu m^2$ (see Table 9.1).

The ATR crystal can be moved to different positions, as shown in Figure 9.4; a schematic diagram shows the ATR objective in two different configurations. For visual observation of the sample, the crystal is in the upper position (Figure 9.4a), while in the measuring mode the ATR crystal is in contact with the sample (Figure

Table 9.1 The objectives applied for the micro FT-IR imaging measurements and their corresponding instrumental parameters.

Objective

Type of measurement	Transmission/reflection	ATR (Ge-crystal)
Magnification	15×	20×
Numerical aperture	0.4	0.6
Imaging area	$260 \times 260\,\mu m^2$	$50 \times 50\,\mu m^2$
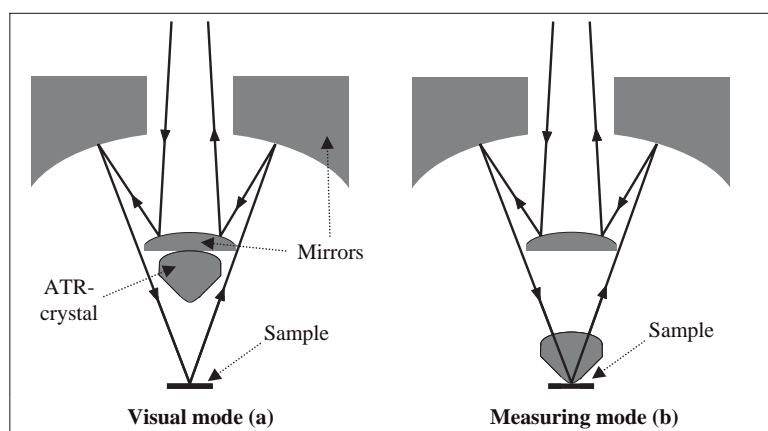
Figure 9.4 Schematic diagram showing the ATR objective in the two different measurement configurations. (a) Visual observation of the sample; (b) Measuring mode with contact of the ATR crystal and the sample.

9.4b). Five different pressure stages (0.5–8 N) are available in order to optimize the contact between the crystal and the sample.

9.2.2.2 Macro FT-IR Imaging
If a larger field of view is required, the macrochamber IMAC is used instead of the microscope. This consists of an optical and a sample compartment, with con-
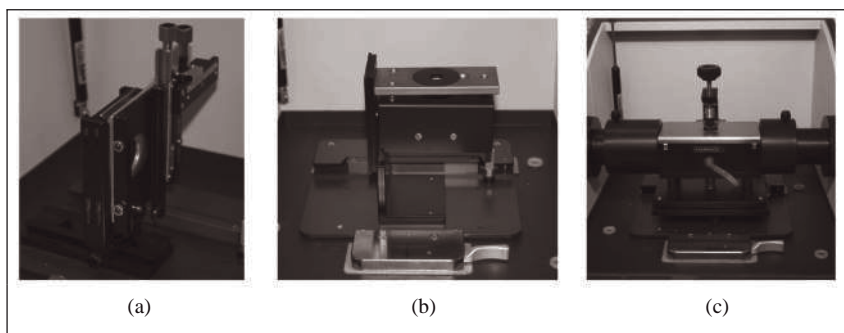
Figure 9.5 Available accessories for the imaging macrochamber. (a) Transmission (Bruker Optik GmbH, Ettlingen, Germany); (b) Reflection (Pike Technologies, Madison, USA); (c) ATR with a ZnSe crystal (Harrick Scientific Products Inc., New York, USA).

nections for the FPA detector and the CCD camera. Several other spectroscopic accessories may also be installed in the sample compartment.

The macrochamber enables measurements in transmission (with a manual x/y sample holder), in reflection and in the ATR mode. Some of the different accessories available are shown in Figure 9.5.

The imaging area for transmission and reflection measurements is consistent with the detector size ($3.9 \times 3.9 \, \text{mm}^2$). For ATR-measurements, the imaging area is $3.9 \times 5.5 \, \text{mm}^2$ because of the illumination geometry [37].

Usually, there is only one FPA detector available, and the position of the FPA detector must be interchanged between the microscope and the macrochamber.

9.2.2.3 Measurement of an FT-IR Image

While the imaging measurements were operated in the step-scan mode with the first-generation FPA detectors, the new-generation FPA detectors operate in a continuous rapid scan mode. Before the measurement, certain parameters – such as the frame rate, offset and gain – must be adjusted with assistance from the live FPA image and the oscilloscope image. Both images indicate if some pixels have a very low intensity, and if the illumination of the imaging area is not perfect and, if necessary, an adjustment must be performed.

Because of delamination, each detector has a few so-called 'bad' pixels which can be seen very clearly in the live FPA image. Their intensity and the signal-to-noise ratio (SNR) differ from those of other pixels. New FPA detectors must not have more than 3% 'bad' pixels. Similar to conventional single-element MCT detectors, the detector pixels function at low temperature, which can be attained by cooling with liquid nitrogen. During cooling, there is a thermal contraction of the detector pixels and, because the detector consists of layers of different materials (with different expansion coefficients), delamination can occur. However, the

imaging software allows these 'bad' pixels to be masked in order to avoid outliers in the IR image.

In order to minimize the number of cooling cycles guaranteed by the instrument manufacturer, special Dewar flasks with a prolonged holding time of up to about 50h (at −196 °C) can be used (note the black reservoir on the FPA detector in Figure 9.3).

9.2.2.4 Observation of a Penetration Depth Gradient in ATR FT-IR Spectroscopic Imaging Applications

In order to check the illumination uniformity of the ATR crystal of the FastIR accessory used in investigations with the macrochamber, a homogeneous liquid sample (paraffin oil, from Shell Deutschland Oil GmbH, Hamburg, Germany) was chosen because of its perfect contact with the ATR crystal [38]. However, despite this perfect contact, the integrated absorbance values for a particular band were not constant for the imaged area. Rather, an absorbance gradient in the z-direction of the image (the direction of the IR beam from source to detector) was observed in the image, for example, for the absorption bands at ca. 2920 and 1460 cm^{-1}, representing largely different penetration depths d_p of 0.64 and 1.28 μm [39, 40], respectively, for the nominal angle of incidence (45°) and refractive indices n(paraffin oil) = 1.4679 and n(ZnSe) = 2.4 (see Figure 9.6).

The quantitative evaluation of the integration results are listed in Table 9.2, there being a difference of approximately 16% between the highest and lowest absorbance values. The flat plateaus, observed in the absorbance values along the z-axis for low and high z-values (see Figure 9.6b and d), are also reflected in the bimodal histograms (see Figure 9.7) of frequency (number of pixels) versus integral absorbance plots with minima at intermediate absorbance values.

The explanation for the observed absorbance gradient is that the angle of incidence on the ZnSe reflection element is not exactly 45° for all IR rays, but varies between 45.6 and 44.3° (as calculated by Bruker Optik GmbH, using a ray-tracing technique) (Figure 9.8). This phenomenon is inherent to the construction of the accessory, and cannot be eliminated by alignment. As a consequence, the penetration depth and absorbance values increase in the z-direction. As shown in Figure 9.6, the phenomenon is most pronounced in the central region of the imaged area. No gradient can be observed across the width of the IR beam.

For homogeneous samples, it would be possible to correct this gradient mathematically. However, for heterogeneous samples, which are mostly analyzed with IR imaging, this is hardly possible due to the large influence of the different refractive indices, which would have to be taken into consideration.

The same artifact was observed for a solid sample. The example shown in Figure 9.9 demonstrates the ATR FT-IR images of the distribution of a release coat (poly(vinyl-stearylcarbamate; PVSC) on the polypropylene (PP) backing of an adhesive tape (tesa AG, Hamburg, Germany). Sample 1 has a heterogeneous distribution of PVSC (Figure 9.9a), whereas the release coat of sample 2 is homogeneously distributed (Figure 9.9d).
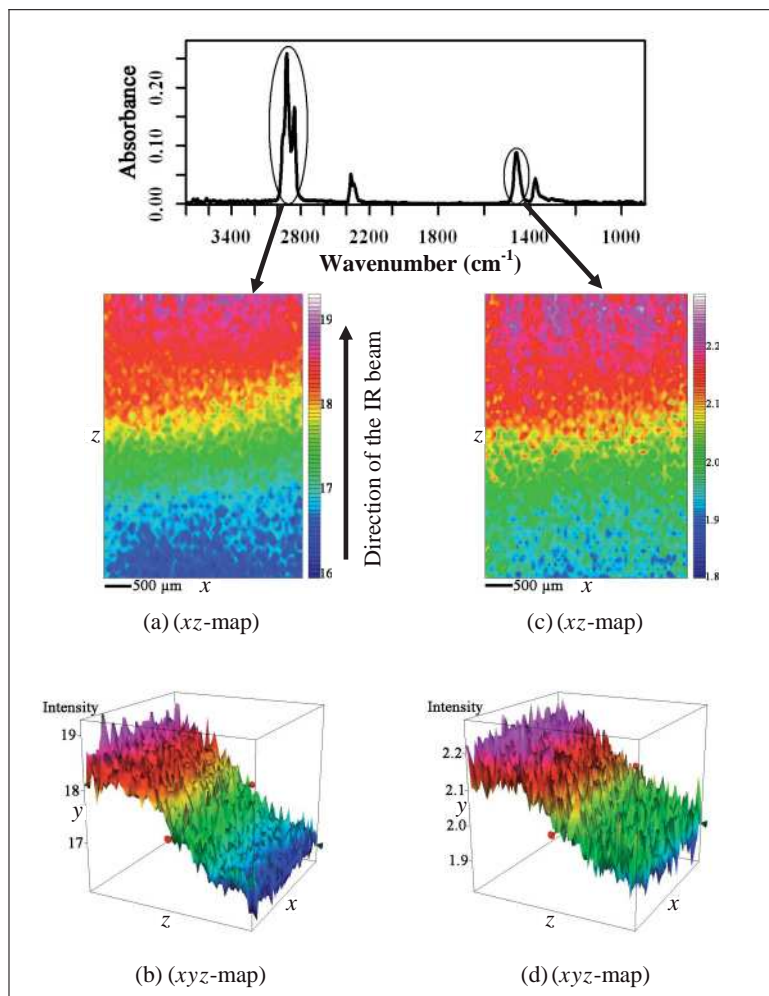
Figure 9.6 ATR FT-IR imaging results of paraffin oil for the $\nu(CH/CH_2/CH_3)$ absorption bands at 3000–2800 cm^{-1}. (a) 2-D; (b) 3-D and the $\delta(CH_2/CH_3)$ absorption bands at 1482–1425 cm^{-1} (c) 2-D; (d) 3-D. Reproduced with permission from Ref. [38]; © 2006, Society for Applied Spectroscopy.

Table 9.2 Integral absorbance of the ATR FT-IR imaging results of paraffin oil for the $\nu(CH/CH_2/CH_3)$ and $\delta(CH_2/CH_3)$ absorption bands.

Integral absorbance	$\nu(CH/CH_2/CH_3)$	$\delta(CH_2/CH_3)$
	(3000–2800 cm^{-1})	(1482–1425 cm^{-1})
Maximum value (approx.)	19.0	2.25
Minimum value (approx.)	16.2	1.88
Ratio (Max/Min value)	1.17	1.20
Percentage difference (%)	15	16
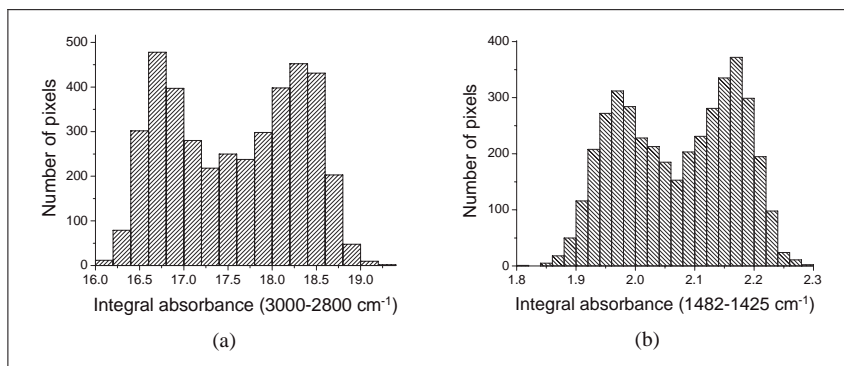
Figure 9.7 Histograms. (a) Number of pixels versus integral absorbance of the ATR FT-IR imaging measurements of paraffin oil for the $\nu(CH/CH_2/CH_3)$ absorption bands at 3000–2800 cm^{-1}; (b) $\delta(CH_2/CH_3)$ absorption bands at 1482–1425 cm^{-1}. Reproduced with permission from Ref. [38]; © 2006, Society for Applied Spectroscopy.
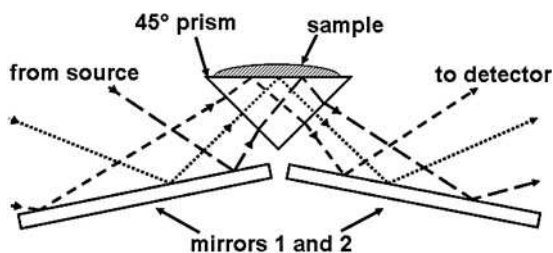
Figure 9.8 Schematic optical diagram of the ATR accessory FastIR, demonstrating the different angles of incidence on the interface of the sample and the ATR reflection element. Adapted from http://www.harricksci. com/accessories/H_fastir.cfm. The variably dashed rays have different angles of incidence, symbolizing the range from 45.6° to 44.3°. Reproduced with permission from Ref. [38]; © 2006, Society for Applied Spectroscopy.

However, it is difficult to differentiate clearly between the 'bad' (Figure 9.9a) and 'good' (Figure 9.9d) sample, because the instrumentally based absorbance gradient (as discussed above) is superimposed on the sample data and is also observable for a homogeneous distribution (Figure 9.9d). It is, therefore, not surprising that a gradient is also observed for the PP-backing only (Figure 9.9b, c, e and f). Thus, whenever possible, this penetration depth (absorbance) gradient should be taken into consideration for the interpretation of the results.

For heterogeneous samples this gradient does not become obvious in the imaging data. This is demonstrated in Figure 9.10, which shows a separation of the water and oil phases in an oil-in-water emulsion. Here, the absorbance gradient cannot be detected due to the large heterogeneity of the component distribution.
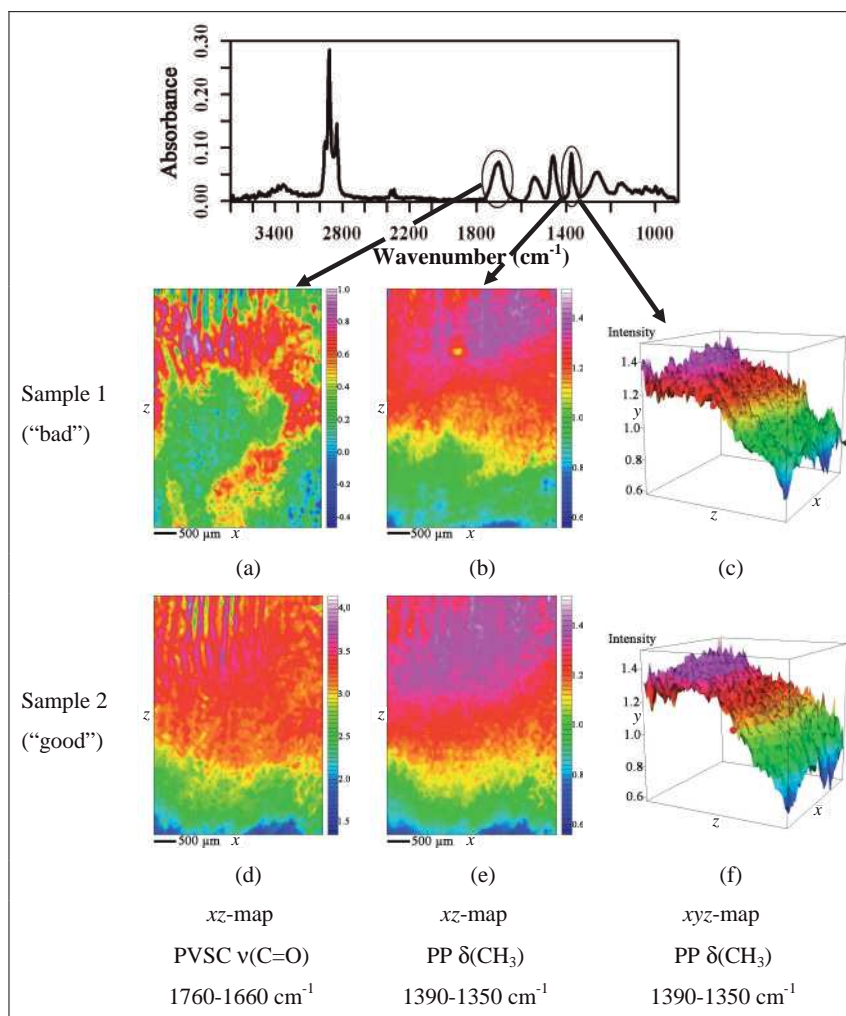
Figure 9.9 ATR FT-IR images of the distribution of a release coat (PVSC) on the PP-backing of an adhesive tape. Sample 1 ('bad') has a heterogeneous (a) and sample 2 ('good') a homogeneous (d) distribution of the release coat. The absorbance gradient observed for the original PP-backing is demonstrated in panels (b), (c), (e) and (f). Reproduced with permission from Ref. [38]; © 2006, Society for Applied Spectroscopy.

Generally, for a qualitative analysis of heterogeneous samples the results will hardly be influenced by this phenomenon. For quantitative analysis, however, the effect must be taken into account. By using another reflection element, for example, germanium with a higher refractive index (4.0 instead of 2.4 for ZnSe), the gradient would be much smaller (about one-third), because of the lower penetration depth under these experimental conditions.

9.2.2.5 **Influence of Pressure on ATR FT-IR Imaging Results**

With several polymer systems, ATR FT-IR microimaging measurements with a germanium ATR objective showed spectral differences in the area under observation, although the investigated film was completely homogeneous. This artifact, which is frequently observed for pressure-sensitive polymer systems, is demonstrated exemplarily for a poly(3-hydroxybutyrate-*co*-3-hydroxyhexanoate) (HHx = 12 mol%) film. Different image areas of $50 \times 50 \, \mu m^2$ of the polymer film were measured with the pressure stages 1, 2 and 3 by accumulating 10 scans in the spectral range from 3800 to 900 cm^{-1} with a spectral resolution of 8 cm^{-1} (Figure 9.11).

(a)(*xz*-map) (b)(*xz*-map)
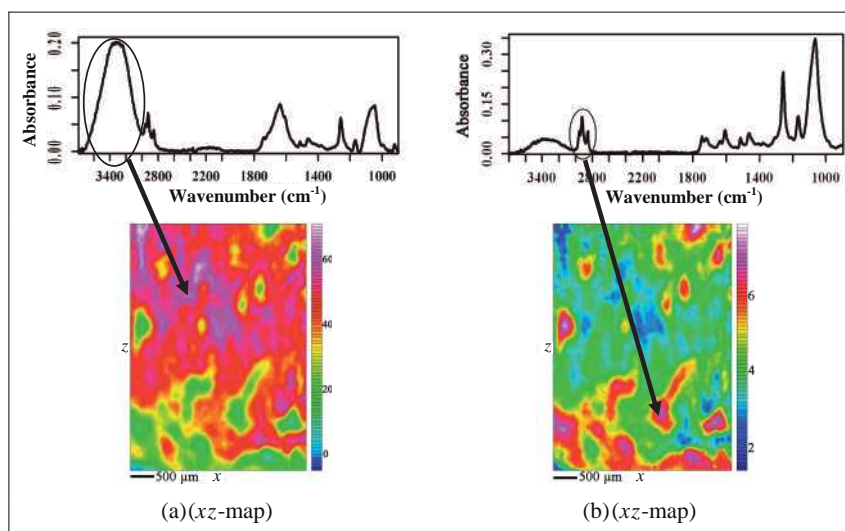
Figure 9.10 Phase separation of an oil-in-water emulsion. Integration of (a) the ν(OH) (3670–3015 cm^{-1}) and (b) the ν(CH/CH$_2$/CH$_3$) (3000–2800 cm^{-1}) absorption bands. Reproduced with permission from Ref. [38]; © 2006, Society for Applied Spectroscopy.

Pressure stage 1 Pressure stage 2 Pressure stage 3
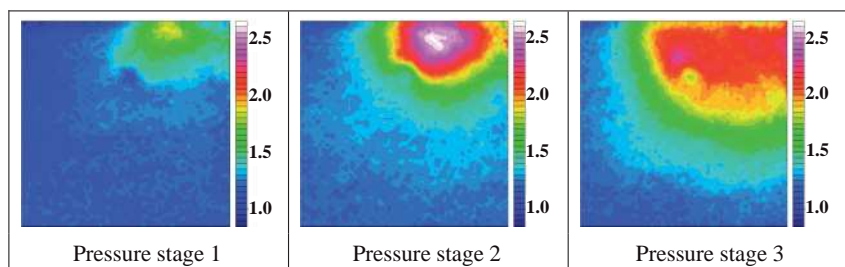
Figure 9.11 IR images of a poly(3-hydroxybutyrate-*co*-3-hydroxyhexanoate) film measured by ATR FT-IR imaging (Ge ATR objective) with the pressure stages 1–3 (evaluation of the left wing of the ν(C=O) band; see Figures 9.12 and 9.13).

The IR images of the analyzed sample areas were evaluated by integration of the left wing of the ν(C=O) absorption band, which is characteristic for the weakly hydrogen-bonded amorphous regions of this biopolymer (see Figures 9.12 and 9.13). In order to compare the colors of the IR images at different pressure stages, a standardized color scale was used which included the range from the lowest to the highest integral absorbance of the three measurements.

Although the sample was a homogeneous copolymer film, inhomogeneities were detected in the IR images with increasing pressure. Thus, the red areas in the right upper corner of the IR images (Figure 9.11) indicated a larger degree of amorphous content in the polymer film. However, this enrichment of amorphous regions is a consequence of the nonuniform contact pressure of the ATR crystal on the sample area, and is not due to the heterogeneity of the sample. Obviously, a higher pressure leads to destruction of the crystalline regions and an increase in the amorphous content of this pressure-sensitive biopolymer. The validity of this interpretation has been proved by repeated measurements of this copolymer film.

Figure 9.12 shows two spectra of the IR images measured with the pressure stage 3. The red spectrum corresponds to the red area in Figure 9.11, where the crystallinity has been reduced because of the higher contact pressure. Destruction of the crystallites is also accompanied by conformational changes of the polymer chains, because a comparison of the red and blue spectra clearly shows, that there are also significant changes of the spectrum in the fingerprint region. For an accentuation of the changes in the ν(C=O) absorption region, an enlarged section of this wavenumber region is shown in Figure 9.13. Here, the higher intensity of the left wing of the ν(C=O) absorption band of the red spectrum can be seen more clearly than in the spectra of Figure 9.12.
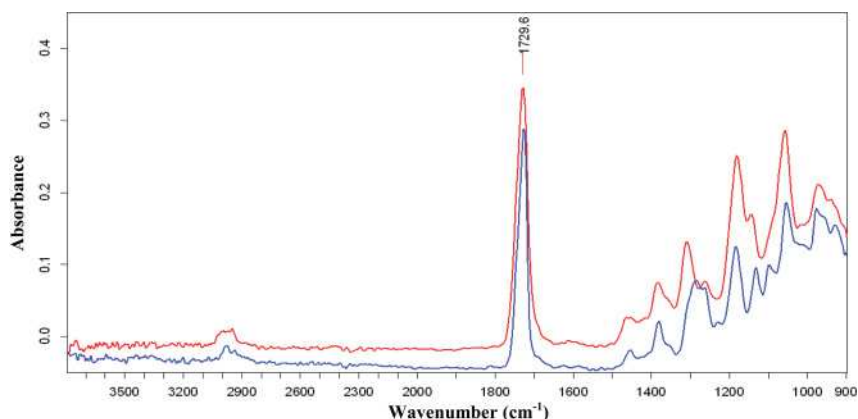
Figure 9.12 ATR FT-IR imaging spectra of the poly(3-hydroxybutyrate-*co*-3-hydroxyhexanoate) film measured with pressure stage 3 of the Ge ATR objective: comparison of two spectra of the 'red' (amorphous) and 'blue' (crystalline) regions.
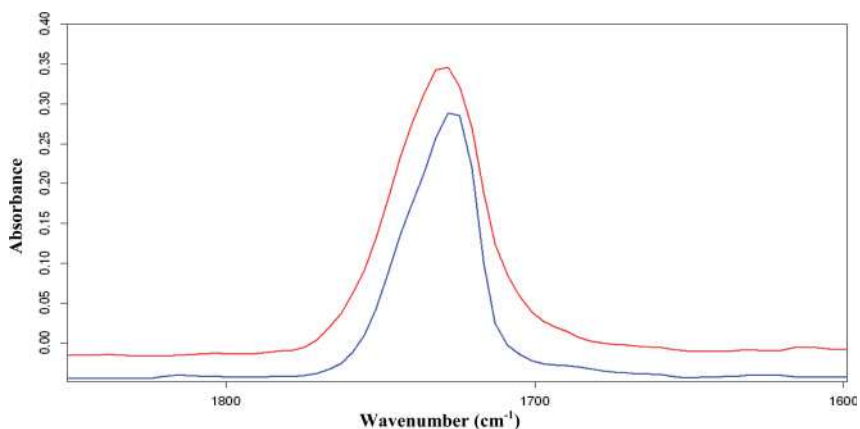
Figure 9.13 ν(C=O) absorption band of the ATR FT-IR imaging spectra of a poly(3-hydroxybutyrate-*co*-3-hydroxyhexanoate) film measured with pressure stage 3 of the Ge ATR objective: comparison of two spectra of the 'red' (amorphous) and 'blue' (crystalline) regions.

Similar effects have also been observed for films of the pressure-sensitive polymers poly(vinylidene fluoride) and poly(tetrafluoroethylene). Thus, repeated measurements of the investigated polymer are recommended in order to confirm this phenomenon and to avoid misinterpretations. For samples without conformation and state of order sensitive absorption bands, this phenomenon is not relevant.

9.2.2.6 Spatial Resolution of Micro FT-IR Imaging Measurements

For FT-IR imaging, a high spatial resolution is very important in order to visualize the distribution of different substances of a heterogeneous sample as precisely as possible. The size of the imaging area of, for example, a Ge ATR objective is $50 \times 50\,\mu m^2$. By using a FPA detector with 64×64 detector elements, an area of $0.78 \times 0.78\,\mu m^2$ can be allocated for each detector element. However, this does not mean that such a spatial resolution can be achieved, because this parameter is limited not only by the pixel size and magnification of the objective but also by the diffraction of the IR radiation (see Chapter 1, Section 1.2.4).

Chan and Kazarian were able to achieve a spatial resolution of 3–4 μm with micro ATR FT-IR imaging measurements with a Ge ATR crystal [37]. A recent report by Lasch and Naumann described the lateral resolution of FT-IR imaging measurements in transmission, whereby numerous results from measurements of a resolution target USAF 1951 and tissue samples with different imaging systems from different manufacturers and with different objectives were compared [41].

The theoretical definition of the spatial resolution requires a distance of $2r$ (where r is the Rayleigh criterion of resolution) in order to differentiate two adjacent points completely, and is limited by the wavelength of the IR radiation and the NA of the objective [42, 43] (see Chapter 1, Section 1.2.4).

The spatial resolution can be improved by evaluating absorption bands at high wavenumbers. Unfortunately, characteristic high-wavenumber absorption bands are not always available for the calculation of FT-IR images. However, by using a Ge ATR objective with a high NA, Sommer *et al.* and Chan and Kazarian were able to optimize the spatial resolution by a factor in the range of the refractive index of the Ge crystal ($n = 4$) [37, 44].

9.2.2.6.1 **The Test Systems** In order to demonstrate the spatial resolution achieved in practical measurements, two test sample systems were investigated by FT-IR imaging measurements in the ATR mode and in transmission. The sizes of the imaging areas were $50 \times 50 \, \mu m^2$ for the micro ATR FT-IR measurements (20× objective) and $260 \times 260 \, \mu m^2$ for the micro FT-IR transmission measurements (15× objective).

The first system involved a polymer laminate of polyethylene (PE) (25 μm) and polycarbonate (PC) (3 μm) films (both from Bayer AG, Germany). A portion of PC film (~1 cm^2) was positioned on top of a 2 cm^2 PE film, and the two were sandwiched between two aluminum foils, heated to 150 °C in a drying oven for 1 h and then compressed (10 bar pressure). The sample was then imaged at the sharp borderline of the PE/PC laminate and the single PE layer in the ATR mode ($50 \times 50 \, \mu m^2$) and in transmission ($260 \times 260 \, \mu m^2$).

The second system involved a poly(ethylene terephthalate) (PET) film, coated with a 3–4 nm aluminum layer. By using a semiconductor laser, grooves with a width and distance of 4.8 μm were written into the sample, in the form of a grid (tesa AG) and FT-IR/ATR imaging measurements performed within the area of the grid.

9.2.2.6.2 **Evaluation and Results** The IR images of the analyzed sample areas were calculated by integration of the specific absorption bands (see Table 9.3). The integral absorbances were converted into a color code (see color scale beside the IR images). The visible image of Figure 9.14 showed a sharp separation line between the PC/PE polymer laminate and the single PE layer. This separation line can also be seen in the IR images of Figure 9.14 for the evaluations of PC- and PE-specific absorption bands. The FT-IR/ATR spectra of the PE and PC areas are shown in Figure 9.15.

Table 9.3 Integration range for the image evaluation of the polymer samples.

Sample	Band assignment	Integration range (cm^{-1})
PC	ν(C=O)	1820–1740
PE	ν(CH$_2$)	2960–2820
PET	ν(C=O)	1750–1695

Visible image	IR image ν(C=O) PC	IR image ν(CH₂) PE
260 x 260 μm²	50 x 50 μm²	50 x 50 μm²
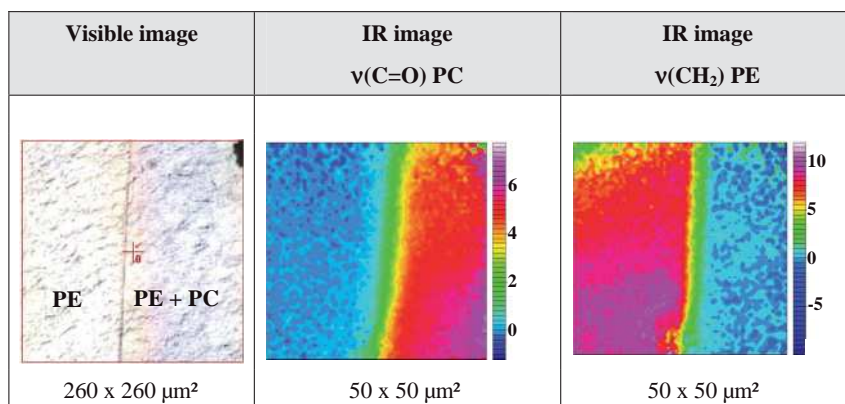
Figure 9.14 Visible image and FT-IR/ATR images of the borderline between PE and the PC/PE laminate ($50 \times 50\,\mu m^2$).
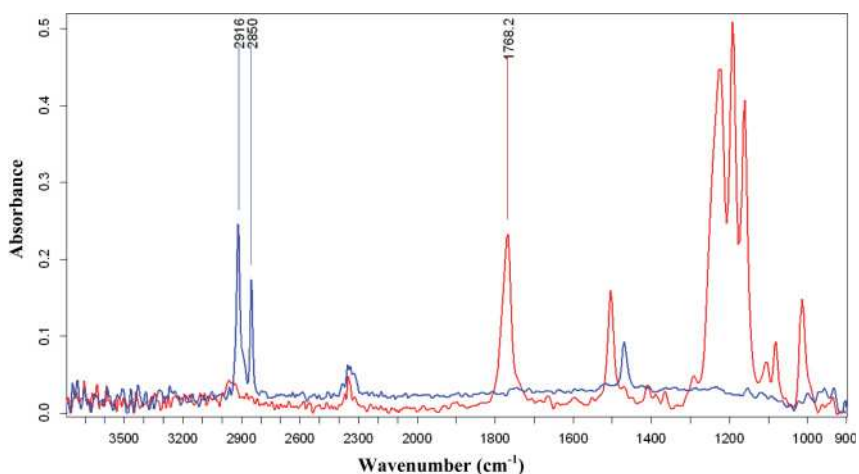
Figure 9.15 FT-IR/ATR spectra of the PE (blue) and PC (red) areas.

Figures 9.16 and 9.17 show graphs of the integral absorbance of PE and PC (FT-IR/ATR imaging measurement) and of PC (FT-IR imaging measurement in transmission) versus pixel number of a row (64 pixels) perpendicular to the PE/PC borderline between the laminate (PE/PC) and the single layer (PE) (50 μm and 260 μm, respectively). The integral absorbances used for the calculation of the spatial resolution at 95% and 5% of the maximum integral absorbance (100%) are marked.

According to Sommer *et al.*, the spatial resolution is the distance between 95% and 5% of the maximum integral absorbance (100%) [44]. The maximum integral absorbance was determined by averaging the maximum integral absorbances on the left and right sides of the border line, respectively (see marks in Figures 9.16
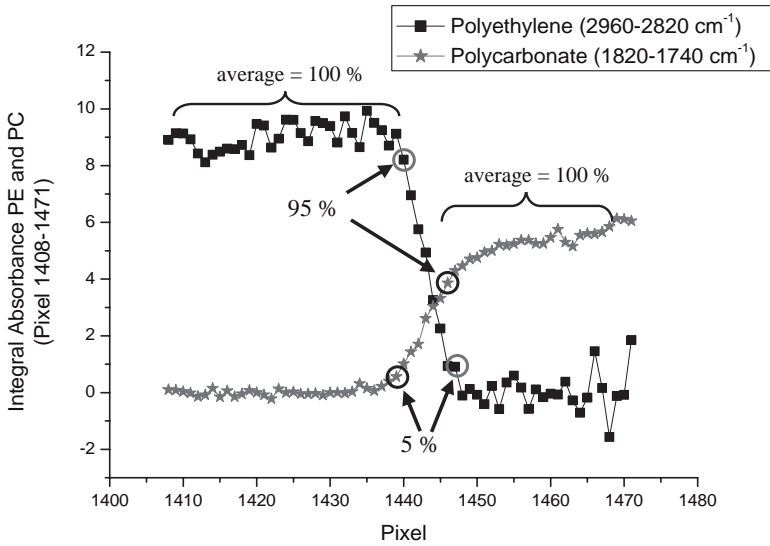
Figure 9.16 Graph of the integral absorbance of PE (black) and PC (grey) (FT-IR/ATR imaging measurement) versus pixel number of a row (64 pixel) perpendicular to the PE/PC borderline (50 μm, 0.78 μm per pixel). The integral absorbances at 95% and 5% of the maximum integral absorbance (100%) used for the calculation of the spatial resolution are marked.
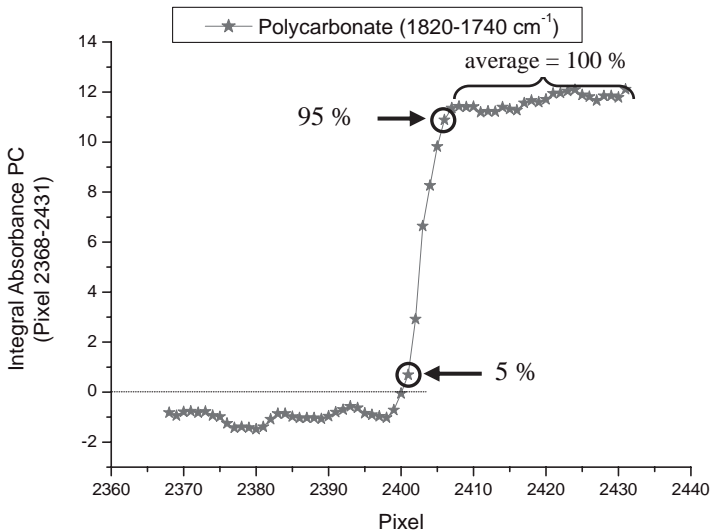
Figure 9.17 Graph of the integral absorbance of PC (FT-IR imaging measurement in transmission) versus pixel number of a row (64 pixel) perpendicular to the PE/PC borderline (260 μm, 4.06 μm per pixel). The integral absorbances at 95% and 5% of the maximum integral absorbance (100%) used for the calculation of the spatial resolution are marked.

and 9.17). The pixels with 95% and 5% of the maximum integral absorbance were then determined, and the distance (in μm) subsequently calculated from the number of pixels and the size of one pixel (ATR measurement: 50 μm/64 = 0.78 μm, transmission: 260 μm/64 = 4.06 μm). The results are summarized in Table 9.4. Thus, for the ATR measurement a spatial resolution of approximately 6 μm was achieved at 2880 and 1728 cm^{-1}; for the measurement in transmission, a spatial resolution of 20 μm at 1728 cm^{-1} was derived.

Figure 9.18 shows the visible image of the laser-induced grid on the aluminum-metallized PET film (the dark lines indicate the PET) and the corresponding FT-IR/ATR image based on the PET-specific ν(C=O) band. Figure 9.19 shows the FT-IR/ATR spectra of an exposed (irradiated) PET area (light gray) and of an aluminum-coated (non irradiated) area (dark gray); this spectrum clearly shows the dispersion-shaped features of a reflection spectrum.

Table 9.4 Results of the experimental determination of spatial resolution for the polymer laminate (PE/PC) and the laser-imprinted grid on an aluminum-metallized PET film.

	Wavenumber (cm^{-1})	Wavelength (μm)	Experimental *(and theoretical)* spatial resolution (μm)[a]	
			ATR	Transmission
PE	ca. 2880	3.5	5.5 (1.8)	—
PC	ca. 1768	5.7	6.3 (2.9)	20.3 (17.3)
PET	ca. 1716	5.8	4.0 (3.0)	—

a Values in parentheses are the theoretical (2*r*) values.

Visible image	FT-IR/ATR image ν(C=O) PET
Width of the grid: approx. 60 μm	50 x 50 μm²
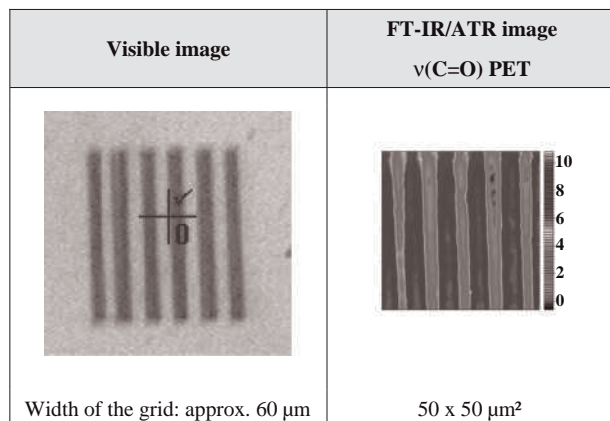
Figure 9.18 Visible image of a 60 μm-wide grid written by a laser into an aluminum-metallized PET film (dark lines = PET) and the corresponding ν(C=O) FT-IR/ATR image.

Figure 9.20 shows the integral absorbance of the n(C=O) band (PET) versus the pixels of a row perpendicular to the grid (50 μm). According to the method described above, a spatial resolution of approximately 4 μm could be derived with the 1716 cm^{-1} absorption band from this experiment.
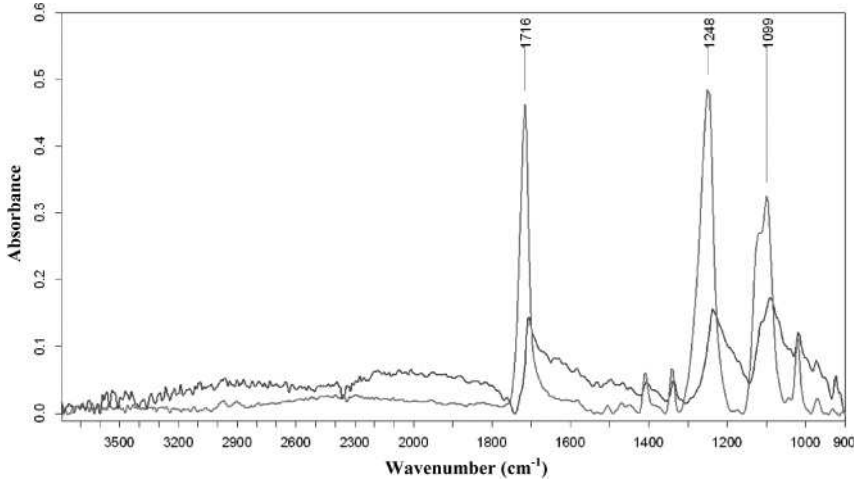
Figure 9.19 FT-IR/ATR spectra of an exposed (irradiated) PET area (light gray) and of an aluminum-coated (non-irradiated) layer (dark gray).
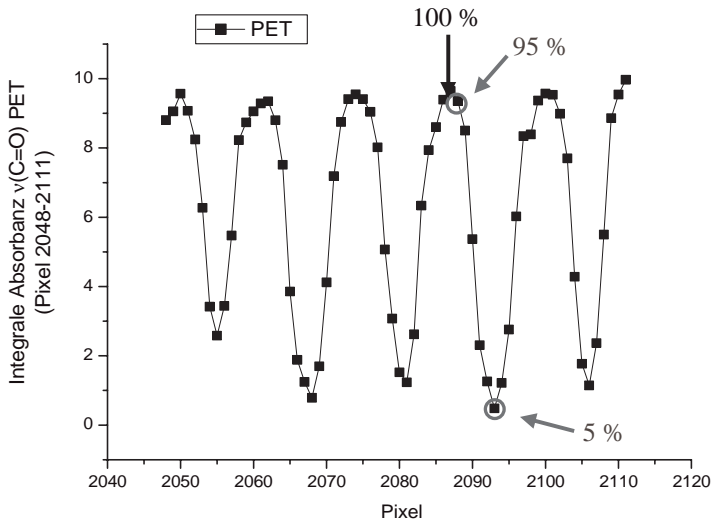
Figure 9.20 Graph of the integral absorbance of the ν(C=O) band (PET) versus the pixels of a row perpendicular to the grid (50 μm). The integral absorbances at 95% and 5% of the maximum integral absorbance (100%) which were used for the calculation of the spatial resolution are marked.

The results for the experimental determination of spatial resolution for the polymer laminate (PE/PC) and the laser-imprinted grid on the aluminum-coated PET film are summarized in Table 9.4. Whereas, a good agreement between the experimental and the theoretical ($2r$) values (in parentheses) was obtained for the transmission measurement and the aluminum-coated PET film, relatively large deviations were observed for the ATR FT-IR measurements and the theoretical values of the PE/PC laminate. This discrepancy can most likely be attributed to the thickness step along the borderline between the PC/PE dual layer and the PE monolayer film, and to the resultant nonoptimum contact of the polymer film and the reflection element in this area.

9.3
Applications of FT-IR Imaging for Polymer Research and Quality Control

One area of material science where FT-IR imaging has proved to be of extraordinary importance, in terms of scientific and practical aspects, is that of polymer analysis and polymer physics. In order to illustrate the broad range of applicability in these disciplines, we will now discuss some selected examples in detail, ranging from phase separation in biopolymer blends, the use of polarized radiation to produce anisotropy images of inhomogeneously deformed polymer films, and determination of the diffusion coefficient of D_2O in an aliphatic polyamide.

9.3.1
Investigation of Phase Separation in Biopolymer Blends

The blending of different polymers is a frequently used technique in industrial polymer production to optimize the material's properties. The biodegradable polymer poly(3-hydroxybutyrate) (PHB) [45, 46], for example, which can be produced by bacteria from renewable resources, has the disadvantage of being stiff and brittle. The mechanical properties of PHB, however, can be readily enhanced by blending with another biopolymer, poly(lactic acid) (PLA) [47]. In order to prepare the optimum blend, it must be noted that the miscibility of different polymers depends on their concentration, the temperature, and their structural characteristics [48].

Polymer blends of PHB and PLA have previously been analyzed with miscellaneous methods by several other groups [49–51]. In the following, the used of transmission FT-IR imaging will be demonstrated as an alternative approach towards a better understanding of the chemical and physical properties of these materials.

The FT-IR transmission spectra of the individual blend components PHB and PLA and of a PHB/PLA (50:50 wt%) blend film are shown in Figure 9.21a and b, respectively. In Figure 9.21a, only a limited number of absorption bands are detectable which are specific for the individual blend components PHB and PLA. For FT-IR imaging, primarily the nonoverlapped left and right wings of the intense
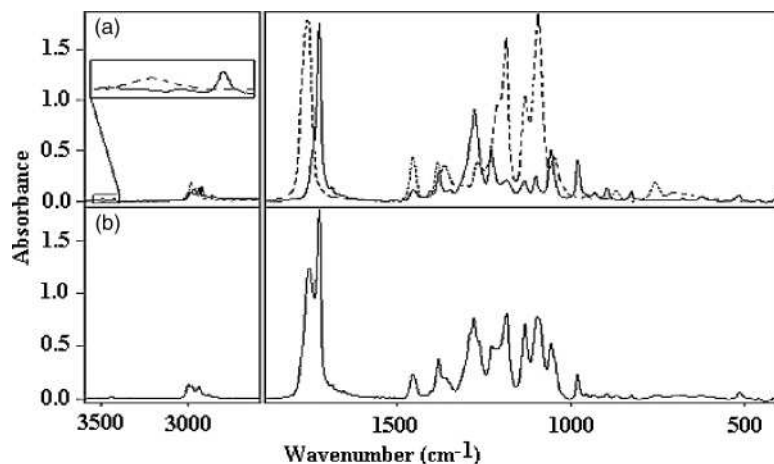
Figure 9.21 (a) FT-IR transmission spectra of a PHB (—) and a PLA (---) film (the inset shows the enlarged region of the $2 \times \nu$(C=O) absorption bands of PLA and PHB); (b) FT-IR transmission spectrum of a PHB/PLA (50 : 50 wt%) blend film. Reproduced with permission from Ref. [52]; © 2008, ACS Publications.

ν(C=O) absorption bands in the blends (Figure 9.21b) can be used to characterize PLA (1755 cm^{-1}) and PHB (1724 cm^{-1}), respectively.

The visible images and PHB- and PLA-specific FT-IR images of two polymer blends of PHB/PLA (50 : 50 wt% and 30 : 70 wt%) are shown in Figure 9.22. The polymers were blended by dissolving the components in the appropriate weight ratio in chloroform (p.a. grade), after which film samples of thickness of 7–10 μm were prepared by solution casting on surface-roughened microscope slides (to avoid interference fringes in the transmission spectra) and subsequent evaporation of the chloroform at 35 °C *in vacuo*. Areas (260×260 μm^2) of these polymer films were then analyzed in the transmission micro mode with the Bruker FT-IR imaging system (see Figure 9.3).

Figure 9.22a (left) shows the visual image of the PHB/PLA (50 : 50 wt%) blend with dark, circular islands embedded in a light matrix. To prepare the FT-IR contour plots, the PHB- and PLA-specific absorptions bands were integrated for all pixel spectra (PHB: 1720–1700 cm^{-1}; PLA: 1800–1770 cm^{-1}; baseline: 1880–1600 cm^{-1}). The FT-IR image based on the PHB-specific absorption band (Figure 9.22a, right) indicates a higher concentration of PHB in the islands (red-colored areas) which correlate with the darker areas in the visual image. On the other hand, the matrix has a higher concentration of PLA which can be derived from the red-colored areas in the PLA-specific image (Figure 9.22a, center). In contrast, within the available lateral resolution at this wavelength range (~20 μm), no phase separation could be observed in the FT-IR images of the PHB/PLA (30 : 70 wt%) blend film, nor in the visible image (Figure 9.22b).
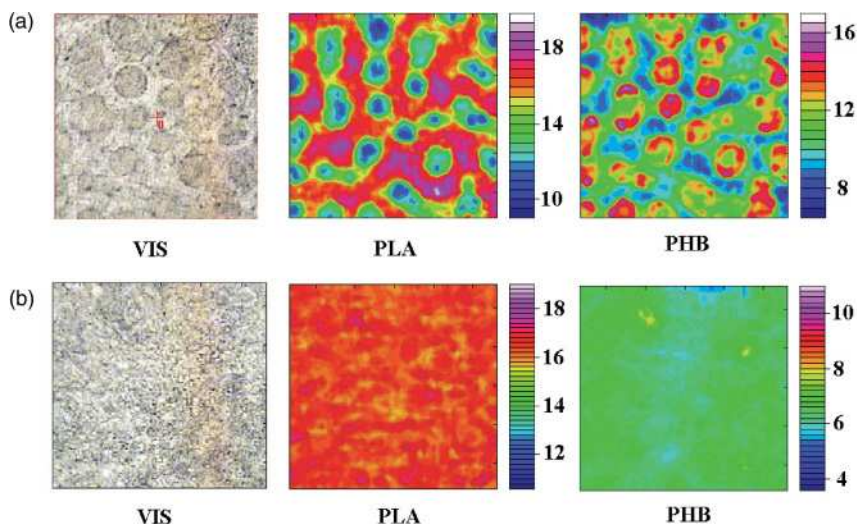
Figure 9.22 (a) Visual image (left), PLA-specific FT-IR image (center) and PHB-specific FT-IR image (right) of a PHB/PLA (50 : 50 wt%) blend; (b) Visual image (left), PLA-specific FT-IR image (center) and PHB-specific FT-IR image (right) of a PHB/PLA (30 : 70 wt%) blend. Reproduced with permission from Ref. [52]; © 2008, ACS Publications.

For a detailed compositional analysis of the blend phases, different PHB/PLA blends ranging from 15 : 85 wt% to 85 : 15 wt% were analyzed using FT-IR imaging. To compare these blends in terms of phase homogeneity and composition, the peak maxima of the PHB ν(C=O) band at $1723\,cm^{-1}$ and PLA ν(C=O) band at $1759\,cm^{-1}$, respectively, were determined for the spectra with the highest absorption intensities for PLA and PHB. The PHB_{max}/PLA_{max} intensity ratios were then mapped versus the concentration of PLA (wt%) (see Figure 9.23) for the different PHB/PLA blends. The data show clearly that the polymer blends with 15, 30, 60, 70 and 85 wt% PLA exhibit only small differences in the PHB_{max}/PLA_{max} intensity ratios for the PHB-rich and PLA-rich areas; such observations indicate that these blends are homogeneous one-phase polymer systems. The blends with 40 and 50 wt% PLA, on the other hand, show significant differences in the PHB_{max}/PLA_{max} intensity ratios of their PHB-rich and PLA-rich phases. Thus, the FT-IR images provide evidence that the blends are separated into two phases with different PHB/PLA compositions. These results were also confirmed with differential scanning calorimetry (DSC) measurements [52].

If a calibration line is drawn through the data points representing the miscible blends (15, 30, 60, 70 and 85 wt% PLA) in Figure 9.23, the compositions of the two phases in the phase-separated blends (40 and 50 wt% PLA) can be derived. In the PHB/PLA (50 : 50 wt%) blend, the PHB-rich phase has a concentration of 39 wt% PLA, while the PLA-rich phase contains 69 wt% PLA. For the PHB/PLA
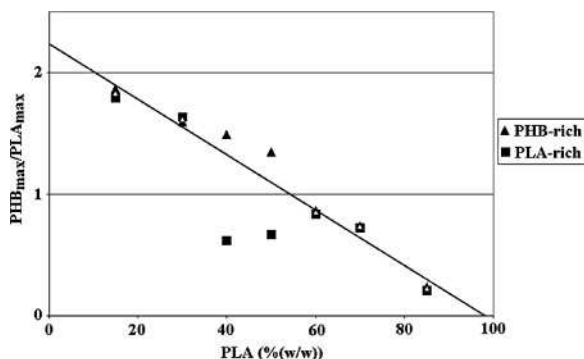
Figure 9.23 PHB_{max}/PLA_{max} ratio versus content of PLA for the PHB- and PLA-rich image areas of the different blend compositions (see text). Reproduced with permission from Ref. [52]; © 2008, ACS Publications.

(60:40 wt%) blend, 33 wt% and 71 wt% PLA were calculated for the PHB-rich and PLA-rich phases, respectively.

9.3.2
Imaging Anisotropic Materials with Polarized Radiation

9.3.2.1   Blends of PHB and PLA

Recently, FT-IR imaging was also applied to analyze phase-separated PHB/PLA blend films which had previously been oriented by uniaxial mechanical elongation [53]. For this purpose, a selected area of the polymer film was measured with radiation polarized parallel and perpendicular, respectively, to the drawing direction of the film sample. From these data, the orientation functions of the PHB and PLA polymer chains were calculated and images representing the anisotropy of the phase-separated regions with respect to the two polymer components were constructed. The first reports on the use of polarized radiation in combination with FT-IR imaging were made by Wilhelm *et al.* [54] and Koenig *et al.* [6].

The sample discussed here is a PHB/PLA blend (50:50 wt%) with an original thickness of 27 μm, that was elongated to 50% strain in a miniaturized, computer-controlled stretching machine with a drawing rate of 10% strain per minute. During elongation, the white areas with a length of up to about 800 μm ('islands'; see Figure 9.24a) developed, and for differentiation of the inhomogeneities therefore an imaging area of 3.9×3.9 mm^2 was used (as indicated by the square). Based on the absorption intensities of a reference film with known thickness, an image of the $\nu(C=O)$ structural absorbance $A_{0\ PHB+PLA}$ (see below) was calculated (Figure 9.24b) which represented the thickness variations of the analyzed film area. Thus, the white islands of the visible image (blue areas of the FT-IR image) were much thinner (thickness ~5 μm) compared to the darker matrix (red areas in the FT-IR image), which had a thickness of ~18 μm.
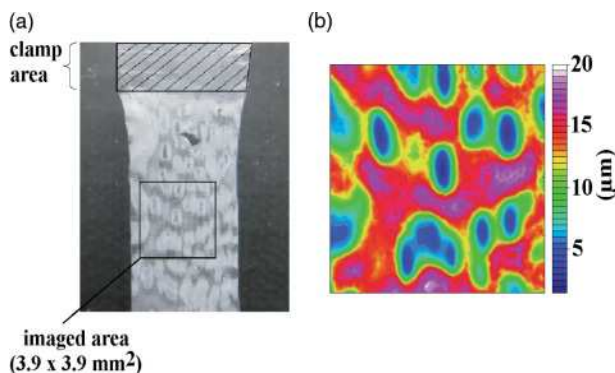
Figure 9.24 (a) Optical image and (b) FT-IR 'thickness image' $(3.9 \times 3.9\,\text{mm}^2)$ of the $\nu(\text{C}=\text{O})$ $A_{0\,\text{PHB+PLA}}$ of the 50% stretched PHB/PLA (50:50 wt%) blend film.

In polarization spectroscopy, the structural absorbance A_0 is frequently calculated from the band intensities measured with radiation polarized perpendicular $(A_\perp)$ and parallel $(A_\parallel)$, respectively, by Equation 9.1:

$$A_0 = \frac{2A_\perp + A_{II}}{3} \tag{9.1}$$

This intensity parameter eliminates the influence of anisotropy on the spectral data. In the present case, composition-specific images were calculated (Figures 9.25a and b) with the structural absorbance ratios $A_{0\text{PHB}}/A_{0\text{PLA}}$ and $A_{0\text{PLA}}/A_{0\text{PHB}}$ to eliminate the significant sample thickness inhomogeneities in the stretched polymer (see Figure 9.24b). The $\nu(\text{C}=\text{O})$ bands were evaluated with a baseline from 1880 to 1600 cm^{-1}, and the peak areas under the left wing (from 1779 to 1825 cm^{-1}) and under the right wing (from 1718 to 1691 cm^{-1}) were assumed to be characteristic for the PLA and PHB components, respectively. Figures 9.25a and b indicate that, here too, the islands are PHB-rich and the matrix has a higher PLA content.

In order to monitor the changes in chain orientation as a consequence of the mechanical treatment, the $\nu(\text{C}=\text{O})$ absorption bands of the PHB/PLA blend films were evaluated to calculate the orientation function $f_\perp$ (assuming a perpendicular transition moment of the $\nu(\text{C}=\text{O})$ absorption bands relative to the polymer chain direction) by:

$$f_\perp = -2\frac{R-1}{R+2} \tag{9.2}$$

where $R = A_\parallel/A_\perp$ is the dichroic ratio of the $\nu(\text{C}=\text{O})$ absorption bands evaluated from the polarization spectra. For more detailed experimental and theoretical
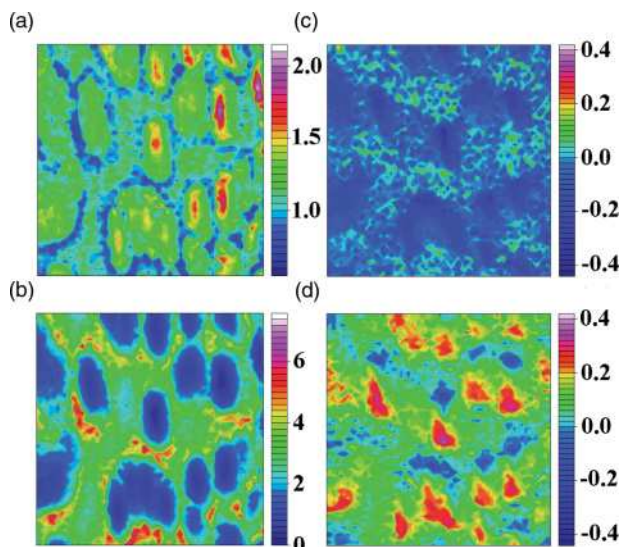
Figure 9.25 FT-IR images ($3.9 \times 3.9\,mm^2$) of (a) A_{0PHB}/A_{0PLA} and (b) A_{0PLA}/A_{0PHB}; Corresponding orientation function ($f_\perp$) images of (c) PHB and (d) PLA of the 50% stretched PHB/PLA (50:50wt%) blend film. For optimum comparison, the $f_\perp$ images (c) and (d) are shown with the same color scale. Reproduced with permission from Ref. [53]; © 2008, ACS Publications.

principles of FT-IR/FT-NIR polarization spectroscopy, the reader is referred to the relevant literature [55–57].

From the orientation function ($f_\perp$) images of the investigated sample area a negative orientation ($f_\perp \approx -0.4$) can be derived for the PHB chains in the 'islands' (Figure 9.25c), whereas the PLA orients positively in the same domains ($f_\perp \approx 0.3$) (Figure 9.25d). In the matrix, on the other hand, both PHB and PLA orient only very slightly positively ($f_\perp$ between 0 and 0.1) (Figures 9.25c and d). Thus, the two phases of the unstretched PHB/PLA (50:50wt%) blend film with uniform thickness respond completely differently to the applied mechanical stress: the PHB-rich phase is oriented to higher degrees and lower thickness with opposite orientation of the two polymer components (PHB negative, PLA positive), whereas the PLA-rich phase undergoes only a small elongation with low thickness reduction and very low positive orientation for both polymer components.

Figure 9.26a shows the FT-IR polarization spectra of the $3.9 \times 3.9\,mm^2$ area discussed above, but measured with a single-element detector. Thus, a perpendicular dichroism (corresponding to a preferential orientation of the polymer chains in the drawing direction) is observed for the $\nu(C=O)$ absorption of PLA and a parallel dichroism (corresponding to a negative chain orientation) for the $\nu(C=O)$ absorption of the PHB component. Figures 9.26b and c show the FT-IR imaging polarization spectra of pixels located in the matrix and in an 'island', respectively.
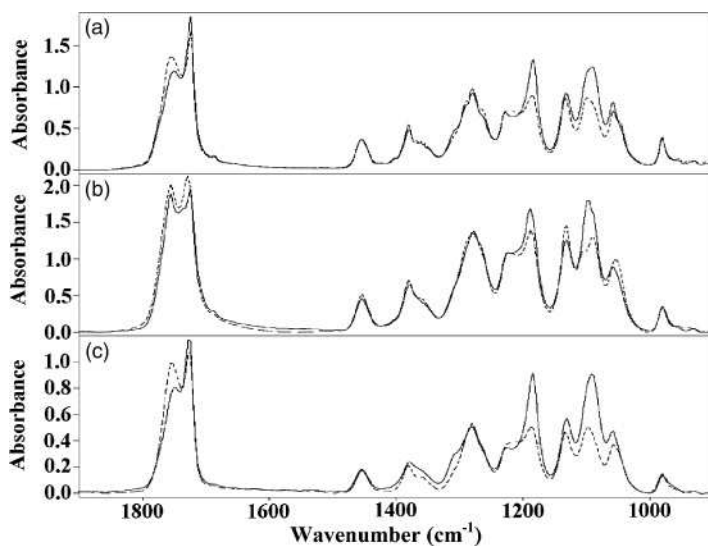
Figure 9.26 FT-IR polarization spectra (— parallel and ---- perpendicular to the strain direction) measured with a single-element detector of the whole area (a) and with one pixel in the matrix area (b) and 'island' area (c) of the 50% elongated PHB/PLA (50/50 wt%) blend film. Reproduced with permission from Ref. [53]; © 2008, ACS Publications.

In accordance with the discussion of Figures 9.25c and d, they reflect a slightly positive orientation for PHB and PLA in the matrix and an opposite orientation for the two polymer components (PHB negative, PLA positive) in the 'islands'. These figures clearly demonstrate that the polarization spectra recorded with a single-element detector cannot discriminate between the different orientation mechanisms in the phase-separated, anisotropic structure of this polymer blend.

For a non-phase-separated blend of PHB/PLA, the visual image of the elongated polymer appears homogeneous and has a uniform thickness [53]. This observation is also reflected in the images derived from the PHB- and PLA-specific absorption bands. Furthermore, the orientation function $f_\perp$ of the PHB and PLA absorption bands is, over the whole area, negative and positive, respectively.

9.3.2.2 Stress-Induced Phase Transformation in Poly(vinylidene fluoride)

Another example of the use of polarized radiation in imaging studies is the analysis of poly(vinylidene fluoride)(PVDF) films, which have been uniaxially elongated at different temperatures. Depending on the thermal, mechanical and electrical pretreatment, PVDF can exist in different modifications [59]. The crystal structure of the crumpled II(α) modification can be converted into the all-*trans* I(β) form by tensile stress below 140 °C (see Figure 9.27a). Figure 9.27b shows the stress–strain diagrams of PVDF films in the II(α) form which have been elongated to 400% strain at 100 and 150 °C. The observed decrease in stress upon elevation of the

experimental temperature to 150 °C demonstrates that the applied stress is too low to induce the conformational phase transition.

In order to monitor the transformation of the II(α) into the I(β) modification, the structural absorbance of the 975 cm^{-1} band ($\gamma_t(CH_2) + \nu_s(CF_2)$ vibration) $A_{0\ 975}$ has been used, because this band is characteristic for the II(α) form [60]. While the 975 cm^{-1} absorption band completely disappears in the film sample that has been elongated to 400% strain at 100 °C (Figure 9.28, top), this II(α) phase-specific band is retained during elongation of a film at 150 °C (Figure 9.28, bottom).
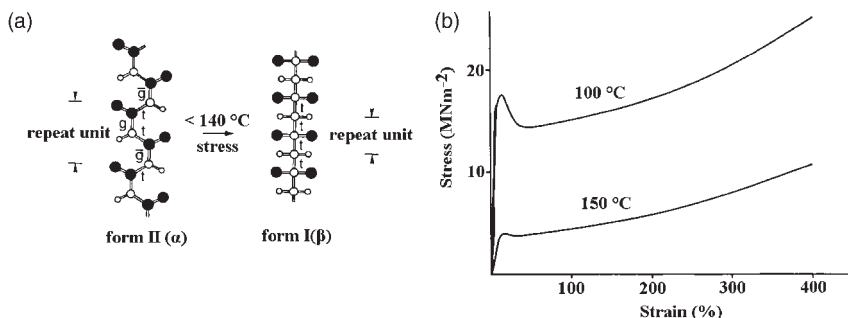
Figure 9.27 (a) Conformational changes occurring in the II(α) → I(β) transformation of PVDF; (b) Stress–strain diagrams of PVDF films elongated to 400% strain at 100 and 150 °C. Reproduced with permission from Ref. [58]; © 2008, Society for Applied Spectroscopy.
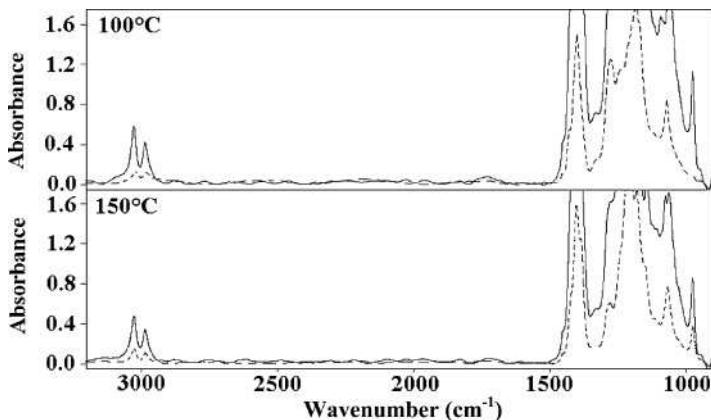
Figure 9.28 FT-IR imaging spectra measured in the clamp (—) and stretched (---) regions (top) and in the shoulder (—) and neck (---) regions (bottom) of PVDF samples elongated to 400% strain at 100 °C and to 100% strain at 150 °C, respectively. Reproduced with permission from Ref. [58]; © 2008, Society for Applied Spectroscopy.

The observed decrease in intensity is simply a consequence of the significant film thickness reduction in the elongated sample.

The optical image of the film sample which had been elongated to 400% strain at 100 °C is shown in Figure 9.29a. The imaging area of $3.9 \times 3.9 \, \text{mm}^2$ was selected at the borderline of the clamp area (undeformed material) and the neck region of the elongated part of the PVDF sample film (at elongations of 400% strain, the neck extended over the whole sample between the clamps). The FT-IR image evaluated with the $A_{0\,975}/A_{0\,\nu(CH)}$ (integration $A_{0\,975}$: 996–961 cm^{-1}; $A_{0\,\nu(CH)}$: 3060–2940 cm^{-1}) band ratio is displayed in Figure 9.29b, where the red and blue colors represent high and low values of this band ratio, respectively, corresponding to the extent of the stress-induced II(α) → I(β) transformation. The image shown in Figure 9.29c is based on the $f_\perp$ orientation function of the ν(CH) intensity (assuming a perpendicular transition moment). While the undeformed clamp area appears homogeneous in both the content of II(α) form (Figure 9.29b, top) and isotropy ($f_\perp \sim 0$) (Figure 9.29c, top), the neck region below the clamp area is quite inhomogeneous with reference to the extent of II(α) → I(β) transformation and anisotropy (variations of $f_\perp$ between 0.2 and about 0.5). Thus, the imaging technique offers the possibility of visualizing conformational as well as orientational inhomogeneities in this transition region.

The optical image of a PVDF film stretched to 100% strain at 150 °C is shown in Figure 9.30a. In contrast to the 400%-elongated sample, here the shoulder–neck region has not extended over the whole sample region between the clamps, and three different sample regions are observable in the visual image (Figure 9.30a): the undeformed clamp area (top), the (only very slightly oriented) shoulder region (center) and the deformed neck region (bottom).

Because of the experimental temperature of 150 °C no significant II(α) → I(β) transformation is expected during elongation in the neck region. This is confirmed by the $A_{0\,975}/A_{0\,\nu(CH)}$ image (Figure 9.30b) at the shoulder–neck border line. The
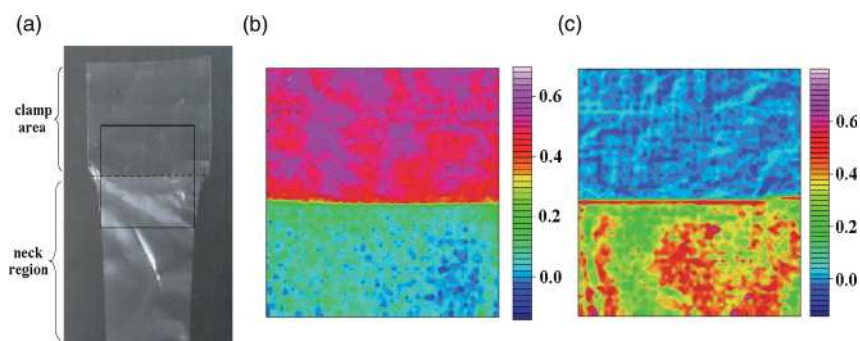
Figure 9.29 (a) Visual image; (b) $A_{0\,975}/A_{0\,\nu(CH)}$ image; and (c) $f_\perp(\nu(CH))$ image recorded of a $3.9 \times 3.9 \, \text{mm}^2$ area in the unstretched/stretched regions of a PVDF sample elongated to 400% strain at 100 °C. Reproduced with permission from Ref. [58]; © 2008, Society for Applied Spectroscopy.
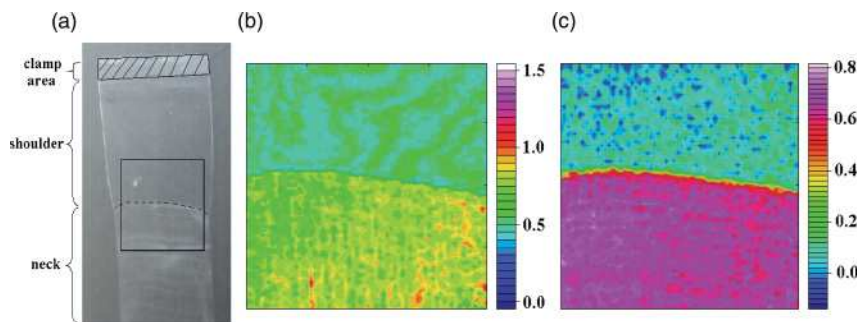
Figure 9.30 (a) Visual image; (b) $A_{0\,975}/A_{0\,\nu(CH)}$ image; and
(c) $f_\perp$ (975 cm^{-1}) image recorded of a $3.9 \times 3.9\,\text{mm}^2$ area in the
shoulder/neck region of a PVDF sample elongated to 100%
strain at 150 °C. Reproduced with permission from Ref. [58];
© 2008, Society for Applied Spectroscopy.

slight differences in the contour colors are mainly a consequence of the strong
intensity decrease of the $\nu(CH)$ reference band. In contrast to the conformational
similarity of the shoulder/neck regions (Figure 9.30b), a very strong difference
could be detected in the anisotropy of these regions, as represented by the orienta-
tion function ($f_\perp$) image obtained with the 975 cm^{-1} absorption band (Figure 9.30c).
Values of $f_\perp$ between 0 and 0.2 were obtained for the shoulder region, whereas the
neck region reflected $f_\perp$ values in the range 0.4–0.6.

9.3.3
Diffusion of D$_2$O into Polyamide 11

The diffusion of small molecules into polymeric materials is important for many
areas of application, such as food packaging and protective clothing. Polyamides
absorb small molecules such as water and alcohols, the process being accompa-
nied by a change in the melting temperature and glass transition temperature (T_g)
[61]; there is also a strong influence on the mechanical [62] and electrical properties
of the materials. Thus, measurement of the diffusion coefficient is crucial to both,
a better understanding of the material transport mechanism, and for the design
of materials with optimized permeation properties. Several types of diffusion
behavior have been identified [63]. Fickian (or case I) diffusion follows the second
law of Fick [64]:

$$\frac{\partial c}{\partial t} = D \frac{\partial^2 c}{\partial x^2} \tag{9.3}$$

where c is the concentration of the diffusant, D is the diffusion coefficient, t the
time and x the distance along the diffusion direction. In general, Fickian diffusion
is only observed in glassy systems when the diffusants are simple gases or solvents
with small molecular diameters or partial solvents at very low temperatures and

penetrant activities. At temperatures and penetrant activities where the polymer is swollen, transport is often controlled by a combination of polymer relaxation and Fickian diffusion mechanisms.

Case II transport occurs when the sorption is entirely controlled by stress-induced relaxations taking place at a sharp boundary separating an outer swollen shell, essentially at equilibrium penetrant concentration, from an unpenetrated glassy core. Ideally, this sharp boundary moves through the polymer at a constant velocity during case II transport. Super-case II transport occurs when the velocity of the case II sorption boundary is sufficiently slow so that a Fickian tail may develop ahead of the sorption discontinuity [63].

In the following it will be shown that FT-IR imaging spectroscopy is a unique tool to visualize and study the penetration of water molecules into a polyamide film. If D_2O is used as a diffusant instead of H_2O, the mobile NH-protons of the polyamide (in the present investigations, PA11) undergo a H/D-exchange in the accessible regions of the polymer. Most importantly, IR spectroscopy is a very convenient method to study this H/D-exchange by the observed isotope effects [65, 66]. Because the H/D-exchange is directly linked to the diffusion of D_2O into the polyamide, the FT-IR imaging technique can be applied to follow the diffusion process as a function of time and to monitor the lateral extension of the diffusion front. For this purpose, a $260 \times 260\ \mu m^2$ area at a $PA11/D_2O$ interface was monitored using FT-IR imaging spectroscopy. On the basis of the obtained FT-IR spectra, not only the type of diffusion but also the diffusion coefficient of D_2O into PA11 can be calculated [3, 12].

9.3.3.1 Experimental

For the FT-IR imaging transmission measurements, a small piece of a PA11 film (thickness ~10 μm) was sandwiched between two CaF_2 disks with different diameters (2 and 1.5 cm) and a thickness of 1 mm (see Figure 9.31). From DSC measurements, a T_g of 46 °C and a melting point of 180 °C with a melting enthalpy of 50 J g^{-1} – corresponding to a crystallinity of 23% ($\Delta H_{(100\% \text{ cryst. PA 11})} = 222$ J g^{-1}) – were determined for the PA 11 under investigation. In order to prepare a void-free stack of the CaF_2 windows and the PA11 film, the sandwich was heated to 250 °C on a heating plate, and at 1–2 min after melting of the PA11 film the heating plate was switched off and the polymer allowed to cool to room temperature under the pressure of a small metal cylinder (158 g). The spectrum recorded with this sample was then used as the reference (t_0 measurement). The D_2O was then carefully dropped onto the rim of the larger CaF_2 base plate and allowed to penetrate into the free space between the CaF_2 windows under capillary action. When this process was complete, excess D_2O was removed, the CaF_2 windows were sealed with vaseline to keep the D_2O between the capillary space, and the time-dependent measurements were started. As shown in the $260 \times 260\ \mu m^2$ image of the ν(NH) absorption band in Figure 9.31, this sample preparation provided a perfect boundary between the polymer and the D_2O diffusant. The FT-IR imaging spectra were recorded at 23 °C over a time period of 165.2 h. During the first day, the measurement intervals were initially 10 min, but these were reduced with progressing diffusion to 15 and

30 min. During the second day the measurement intervals were further reduced to 1–2 h, and from the third day onwards only one to two measurements per day were made. The spectra were baseline-corrected and the peak area of the ν(NH) absorption band was determined between 3380 and 3220 cm^{-1} for construction of the images. The ν(NH) band was the optimum signal for this purpose, because its short wavelength position (~3 μm) allowed the highest possible spatial resolution for the images to be obtained (see Section 9.2.2.6). For a consistent color code of the FT-IR images, the smallest and largest values of the absorbance were set 0 and 100%, respectively.

9.3.3.2 Results and Discussion

Figure 9.32 shows the FT-IR spectra of the PA11 film before and after deuteration for 8.2 h. The intensity of the ν(NH) absorption band at 3308 cm^{-1} decreased, and simultaneously two new absorption bands developed at 2469 and 2411 cm^{-1}. This band doublet was ascribed to Fermi resonance of the evolving ν(ND) band and the Amide II (1470 cm^{-1}) + Amide III (975 cm^{-1}) combination band of the deuterated PA11 [67]. Furthermore, a significant decrease in the Amide II band of the
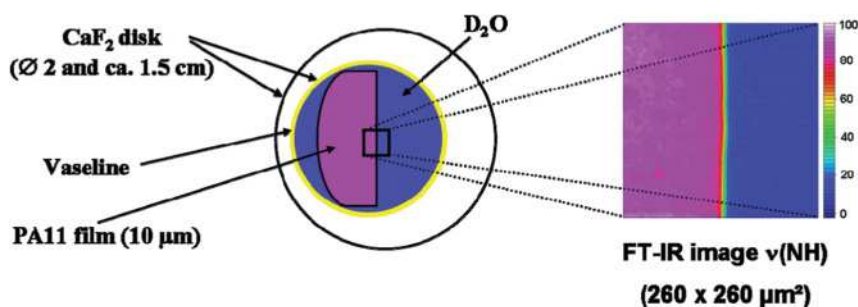
Figure 9.31 Sample preparation for FT-IR imaging studies of the diffusion of D$_2$O into PA11.
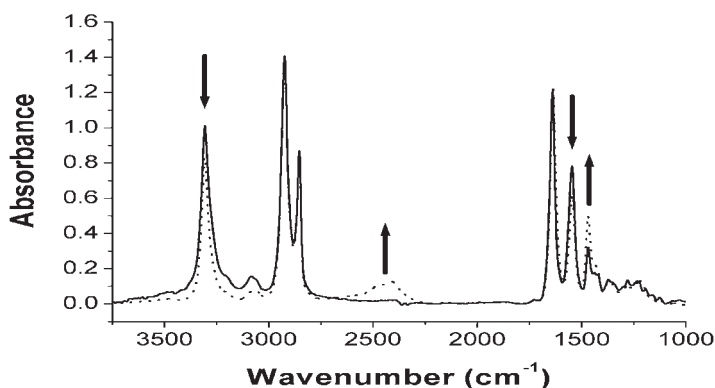
Figure 9.32 FT-IR spectra of PA11 before (——) and after 8.2 h (- - -) deuteration.

nondeuterated polymer at 1543 cm^{-1} and a concurrent increase of the analogous Amide II (ν(CN) + δ(ND)) band of the deuterated polymer at 1470 cm^{-1} was observed.

In Figure 9.33, the $260 \times 260\,\mu m^2$ FT-IR images of the ν(NH) band with the borderline between PA11 and D$_2$O are shown for three different deuteration times. On the left-hand side (magenta and red) the PA11 film, and on the right-hand side (blue) the D$_2$O are mapped. Initially ($t = 0$ min), no D$_2$O has diffused into the polymer film, and thus the PA11 part of the image is homogeneously magenta-colored. After 193 min, the deuteration front has progressed into the PA11 area, and this has led to a decrease in the ν(NH) absorbance with an accompanying change to a red color. With advancing deuteration time, the NH/ND exchange front moves further into the PA11 area such that, after 493 min (Figure 9.33, right) the front of the NH/ND exchange has reached the end of the measurement area. Continuing deuteration leads to a further fading of the red color on the PA11 side towards orange.

Figure 9.34 shows the three-dimensional (3-D) FT-IR images based on the ν(NH) absorption band for deuteration time $t = 0$ min and $t = 193$ min. At $t = 0$ min, no ND-functionalities have developed and the ν(NH) absorption intensity of the PA11 region provides a homogeneous color contour plane. At the borderline between PA11 and D$_2$O the intensity values decrease extremely sharply and become zero in the region of D$_2$O. After 193 min diffusion of D$_2$O into the PA11 film, the image of the PA11 area is no longer homogeneous, and a decrease in the integrated ν(NH) band intensity, starting at the diffusion front towards the PA11/D$_2$O borderline, can be observed as a result of the H/D exchange.

The percentage accessibility (Z(%)) of the PA11 film for deuterium exchange was calculated by the equation [66]:

$$Z(\%) = \frac{A_{t=0}(NH) - A_t(NH)}{A_{t=0}(NH)} \cdot 100\% \tag{9.4}$$

where $A_t(NH)$ and $A_{t=0}(NH)$ are the integral absorbance values measured at deuteration time t and $t = 0$ (before the start of the deuteration), respectively.
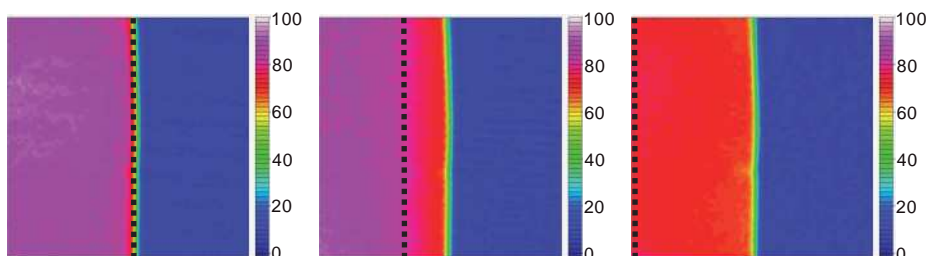
Figure 9.33 FT-IR images of the ν(NH) band representing the measurement area of $260 \times 260\,\mu m^2$ after 0 min (left), 193 min (center) and 493 min (right) deuteration. The dashed lines indicate the diffusion front.

For the calculation of accessibility as a function of the deuteration time, only the spectra of the pixels in a square area of $48.8 \times 48.8 \,\mu m^2$ (144 pixels) on the PA11 side, starting at the PA11/D$_2$O borderline, were used (see Figure 9.35). The average value of the integrated absorbance of the $\nu(NH)$ band for this area then corresponds to transmission spectra of a PA11 film where D$_2$O has access to a surface area of $48.8 \times 10 \,\mu m^2$. In Figure 9.36 the corresponding accessibility $Z(\%)$ is plotted versus deuteration time. As also observed in previous investigations [66], the accessibility of the PA11 film rises steeply initially and then levels off into a plateau after about 60 h of deuteration, with a maximum value of 28%. From the DSC measurements, an amorphous fraction (the regions which are normally expected to be accessible to diffusants) of approximately 77% was determined.
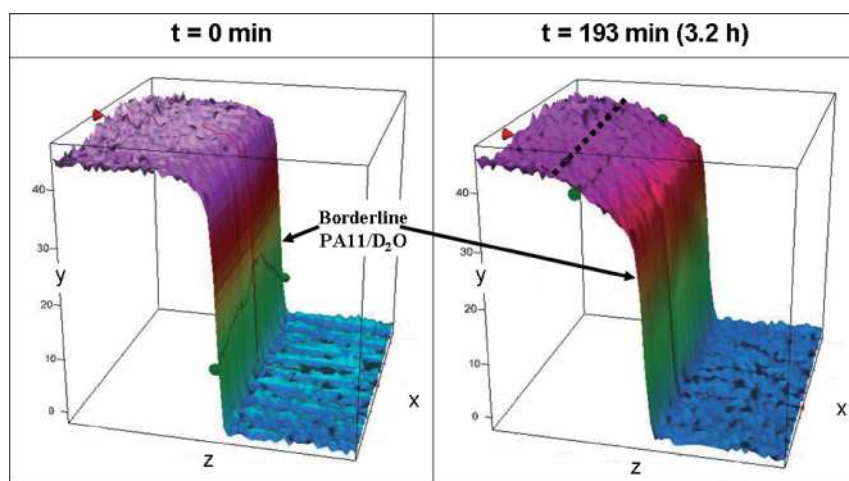
Figure 9.34 3-D FT-IR images based on the integrated $\nu(NH)$ absorbance (y-axis) for the measurement area (x- and z-axes, $260 \times 260 \,\mu m^2$) for deuteration time $t = 0$ min and 193 min. The dashed line indicates the NH/ND exchange front.
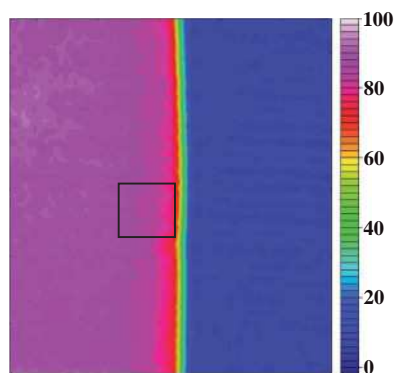
Figure 9.35 Image area used for the evaluation of the percentage accessibility $Z(\%)$ of the NH/ND isotope exchange (square area of $48.8 \times 48.8 \,\mu m^2$).
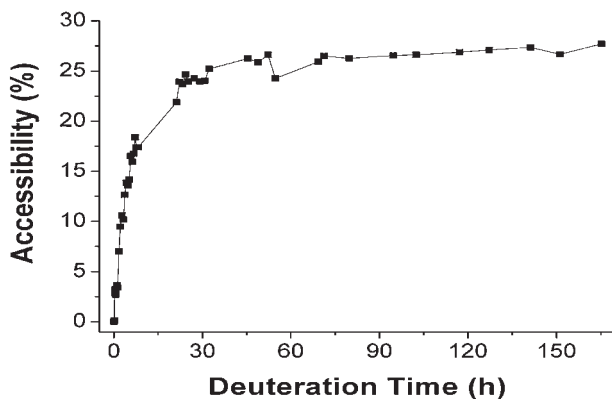
Figure 9.36 Accessibility of PA11 film for D₂O versus deuteration time at 23 °C.

This value is much larger than the maximum accessibility of 28% derived from Figure 9.36. This discrepancy can be partly attributed to the experimental temperature of 23 °C, which is significantly below the T_g value of 46 °C of PA11, since Wu *et al.* [66] identified an accessibility of 47% for the same polyamide at 50 °C. However, this result also shows, that the frequently used simple two-phase model of polymers is certainly not applicable, and intermediate states of order – which are not accessible for the penetration of D₂O – must be taken into account (see below).

For the determination of the type of diffusion, Snively and Koenig [3] have used the equation

$$d = At^{\alpha} \tag{9.5}$$

where d is the pathlength of the diffusion front (in the present investigations, the distance of the NH/ND exchange front to the PA11/D₂O borderline), A is a proportionality factor, t the time and α the diffusion exponent. The diffusion exponent is characteristic of the diffusion process, and can take on the values of 0.5 and 1.0 for the limiting cases of Fickian (case I) and case II diffusion, respectively. For an anomalous diffusion process the value is $0.5 < \alpha < 1.0$, and for the super-case II type α is > 1 [64]. The logarithmic form of Equation 9.5 is given in Equation 9.6, and allows the determination of the diffusion exponent α from the slope of a plot of log d (d measured in μm) versus log t (t measured in s).

$$\log d = \log A + \alpha \cdot \log t \tag{9.6}$$

In order to monitor the diffusion front, the spectra of pixels in five neighboring rows extending perpendicularly to the PA11/D₂O borderline into the PA11 area were evaluated. The fluctuations of the integral absorbance of the ν(NH) band was compensated by calculation of the average spectrum corresponding to the five neighboring pixels at the same distance from the PA11/D₂O phase separation. The

position of the diffusion front was defined as the distance from the PA11/D$_2$O borderline to the pixel column, where the first significant decrease in the ν(NH) band is detectable (see also Figure 9.34). From the plot of log d versus log t (Figure 9.37) a diffusion exponent α of 0.36 was derived which can be interpreted in terms of a Fickian-type diffusion.

Rafferty and Koenig [12] also calculated the diffusion coefficient from FT-IR imaging spectra. In a Fickian system, the position d of the penetrant front versus time can be described by the equation

$$d = kt^{1/2} \tag{9.7}$$

where t is time and k is a proportionality constant that is related to the square root of the diffusion coefficient D (see below). The average diffusion coefficient D can be calculated from the initial gradient of the sorption curve of a gravimetrically determined mass uptake [63, 66]. For this purpose, the values of M_t/M_{max} are plotted versus the square root of time according to Equation 9.8:

$$\frac{M_t}{M_{max}} = \frac{4}{\sqrt{\pi}} \cdot \sqrt{\frac{Dt}{l^2}} \tag{9.8}$$

where M_t is the mass uptake at time t, M_{max} is the mass uptake at saturation and l is the thickness of the film. For their FT-IR spectroscopic imaging measurements, Rafferty and Koenig [12] used the following equations:

$$d = \frac{4}{\sqrt{\pi}} \sqrt{Dt} \quad \text{with} \quad d = \frac{M_t}{M_{max}} \cdot l \tag{9.9}$$
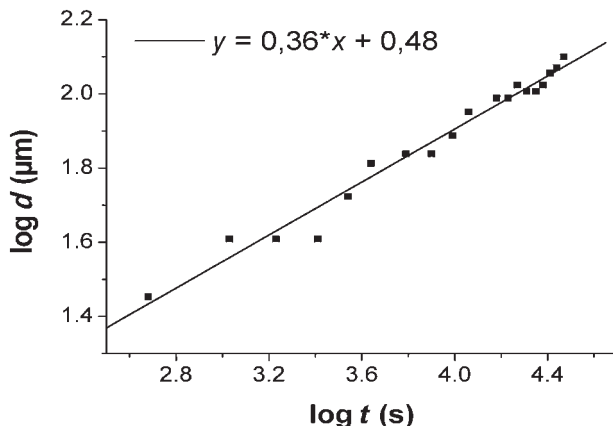
Figure 9.37 Plot of log d (distance of the D$_2$O penetrant front from the borderline PA11/D$_2$O in μm) versus log t (deuteration time in s).
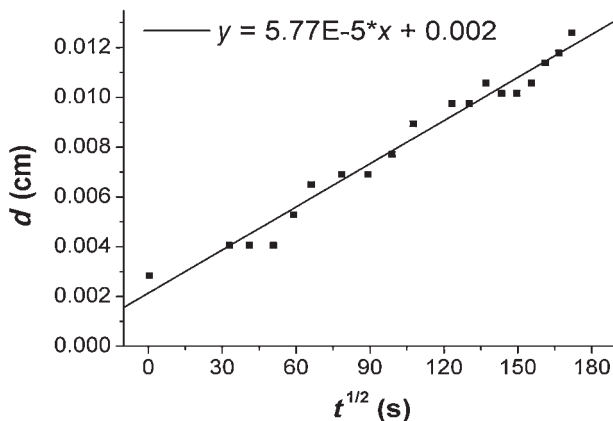
Figure 9.38 Plot of the distance *d* (in cm) of the D_2O penetrant front from the borderline (PA11/D_2O) versus the square root of the deuteration time *t* (in s).

By combining Equation 9.7 with Equation 9.9, the following relationship is obtained:

$$k = \frac{4}{\sqrt{\pi}} \sqrt{D} \qquad\qquad (9.10)$$

Thus, *D* can be calculated from the proportionality constant *k* by:

$$D = \left(\frac{k\sqrt{\pi}}{4}\right)^2 = \frac{k^2 \pi}{16} \qquad\qquad (9.11)$$

In Figure 9.38 the distance *d* (in cm) of the NH/ND exchange front to the borderline PA11/D_2O is plotted versus the square root of time *t* (in s). By linear regression, a proportionality constant *k* of 5.77×10^{-5} was derived, and finally a diffusion coefficient *D* of $6.54 \times 10^{-10}\,cm^2\,s^{-1}$ was calculated using Equation 9.11.

Thus, the FT-IR imaging technique allows the diffusion of D_2O into a PA11 film to be monitored via spectroscopic changes of the NH/ND isotope exchange in the FT-IR imaging spectra. Furthermore, the value of the diffusion exponent was close to a Fickian-type diffusion. Based on the assumption that the diffusion of D_2O and NH/ND exchange occur simultaneously, a diffusion coefficient of $6.54 \times 10^{-10}\,cm^2\,s^{-1}$ was calculated from the kinetic data of the H/D exchange for the first 8 h period.

9.3.4
Conclusions

The above-discussed examples demonstrate that FT-IR spectroscopic imaging can be applied in a multiplicity of applications for the characterization of polymers.

Thus, apart from the visualization of phase separation in polymer blends – including the quantitative determination of blend components – FT-IR imaging can provide a thickness map of the investigated sample area. By using polarized radiation, anisotropy images based on orientation function values can be constructed. And last, but not least, the potential of FT-IR imaging for time-resolved investigations of diffusion phenomena has been demonstrated. In conclusion, these examples show that a much more detailed picture of the chemical, physical and orientational properties of polymers, with reference to their lateral distribution, may be obtained from imaging studies.

9.4
NIR Imaging Spectroscopy for Quality Control of Pharmaceutical Drug Formulations

Although, NIR spectroscopic imaging was only introduced on a large scale following the initial development of FT-IR spectroscopic imaging, during the past few years it has achieved significant progress and proved to be extremely important in the field of agricultural (Chapter 7), food (Chapter 8) and especially pharmaceutical quality control [26, 29]. Because most of these applications are performed in diffuse-reflection mode, the recently discussed issues of the effective pathlength of NIR radiation into solid materials [36], together with previous studies relating to the penetration depth of NIR radiation [28, 30–35], demonstrate that further research is required in order to prove the representative nature of quantitative determinations by NIR imaging measurements.

In the application discussed below, the derivation of quantitative results from NIR spectroscopic imaging data of solid drug formulations is reported. In order to assess the validity of these procedures, however, the results will be compared to the compositional analysis of the same sample set by conservative NIR spectroscopic diffuse-reflection measurements with a single-element detector [68].

9.4.1
Quantitative Determination of Active Ingredients in a Pharmaceutical Drug Formulation

The solid drug formulations investigated comprised mixtures (in varying concentrations) of the three crystalline, active ingredients acetylsalicylic acid (ASA), ascorbic acid (ASC) and caffeine (CF), with the two amorphous excipients cellulose and starch in a fixed ratio and constant composition. A set of 48 samples was prepared by milling varying amounts of the active ingredients over a concentration range of 13.77 to 26.04 wt% with equal amounts (40 wt%) of a 1 : 3 (w/w) mixture of cellulose and starch for 5 min in a Retsch mill (type BMO; Retsch GmbH, Haan, Germany). By using scanning electron microscopy (SEM), the final particle size of the mixtures after milling was determined to range from 10 to 30 μm.

The NIR hyperspectral images were recorded on a MatrixNIR system (Malvern, formerly Spectral Dimensions, Olney, MD, USA) (see also Figure 9.1) with four

quartz-halogen lamps as NIR sources, a LCTF as monochromator and a thermo-electrically cooled 256×320 InGaAs FPA detector in 118 channels (960–1662 nm or 10 417–6017 cm^{-1}) with a spectral resolution of 6 nm at 1600 nm (corresponding to 24 cm^{-1}). Each channel was scanned 10 times using a 64 ms integration time. The image FOV was 50×62 mm^2 with approximately 200×200 µm^2 pixels, and the total image acquisition time was around 5 min. For the imaging measurements, the powder drug formulations were presented in a circular sample holder (FOSS, Hillerod, Denmark) with an outer diameter of about 40 mm and a sample layer thickness of 3 mm. In order to eliminate the shadow effects of the sample holder, a region of interest (ROI) with a radius of 80 pixels (ca. 16 mm) was chosen, resulting in a sample pixel count of ~20 000 points. All sample images were bracketed with sets of five images of Spectralon standard tiles with 2, 25, 50, 75 and 99% reflectance values (Labsphere Inc., North Sutton, NH, USA), and a second-order polynomial fit was used to create a transform function that translated the instrument counts to % reflectance. Finally, the reflectance data were transformed into log 1/R ('absorbance') spectra and a multiplicative signal correction (MSC) was applied as data pretreatment. Euclidian distances to a mean spectrum were computed and then thresholded to eliminate outlier pixels from each hyperspectral image (any pixel greater than five standard deviations was eliminated). This procedure typically left about 18 000 pixels with clean spectra for further data treatment.

From the total sample set (48 samples), 45 samples were used as calibration samples. The three samples excluded from the calibration set were selected on the basis of a representative variation of their active ingredient concentrations, and finally used as 'unknown test samples' to predict the content of their active ingredients. Partial least squares (PLS) models for each active ingredient were developed with the Unscrambler Software (version 9.6; CAMO Software AS, Oslo, Norway) from the MSC-pretreated median spectra of all pixels of each of the 45 calibration sample images. Based on these calibration models, the predictions of the active ingredient content for each pixel of the imaging data of the three test samples and their evaluation as histograms, contour plots and RGB plots was performed with Matlab v. 7.0.4 software (see below).

The conventional single-element detector NIR spectra were measured on a Bruker Vector 22N FT-NIR spectrometer (Bruker Optik GmbH) equipped with a tungsten-halogen light source, a quartz beam splitter, a thermoelectrically cooled InGaAs detector and a light-fiber-coupled diffuse-reflection probe. The data acquisition and manipulation was performed using OPUS software (version 4.0.24; Bruker Optik GmbH). A home-made sample cell consisting of a cylindrical brass cup of 37 mm height and an internal diameter of 10.25 mm in the top 7 mm (to fit the probe head with a 10.0 mm external diameter) and a bore hole with an internal diameter of 4.0 mm for the residual 30 mm height (corresponding to the light-fiber bundle diameter of the probe head) was used. The interior of the sample cup was sand-blasted and subsequently gold-coated. For each measurement, the 30/4 mm Ø volume of the sample cell was filled with the powder drug formulation and the probe head positioned on top of the sample in the 7/10.25 mm Ø opening

(Figure 9.39) [68]. Each sample was measured in duplicate (repacks) with a spectral resolution of $2\,cm^{-1}$, and 256 scans were accumulated. For the development of the calibration models, the mean spectra of the replicate measurements were used. To match the spectral resolution of these spectra to the imaging data ($24\,cm^{-1}$), the spectral resolution was mathematically reduced with the OPUS software in two data sets with $16\,cm^{-1}$ and $32\,cm^{-1}$, respectively. The spectral range between 9050 and 7450, 7100–5570 and 5300–4000 cm^{-1} was selected for quantitative evaluation and a MSC was applied. The data pretreatment and development of the PLS calibration models for each active ingredient (based on 45 of the 48 samples) was also performed with the Unscrambler Software for the data sets with 16 and $32\,cm^{-1}$ spectral resolution.

In Figure 9.40a the conservative NIR diffuse-reflection spectra (reduced to $32\,cm^{-1}$ spectral resolution) of the three test samples not contained in the calibration set are compared to typical single-pixel imaging spectra (Figure 9.40b). Apart from the limited wavenumber range of the imaging spectra, their SNR is much lower than for the conservative diffuse-reflection spectra. For the development of PLS models in the quantitative evaluation of active ingredient content, the median spectra calculated from all pixels of each image of the 45 calibration samples have been used. The improvement in SNR compared to the single-pixel spectra is demonstrated for the three test samples in Figure 9.40c. In Table 9.5, selected calibration/cross-validation parameters, including the correlation coefficient, random mean-square error of prediction (RMSEP) and number of factors, for the PLS
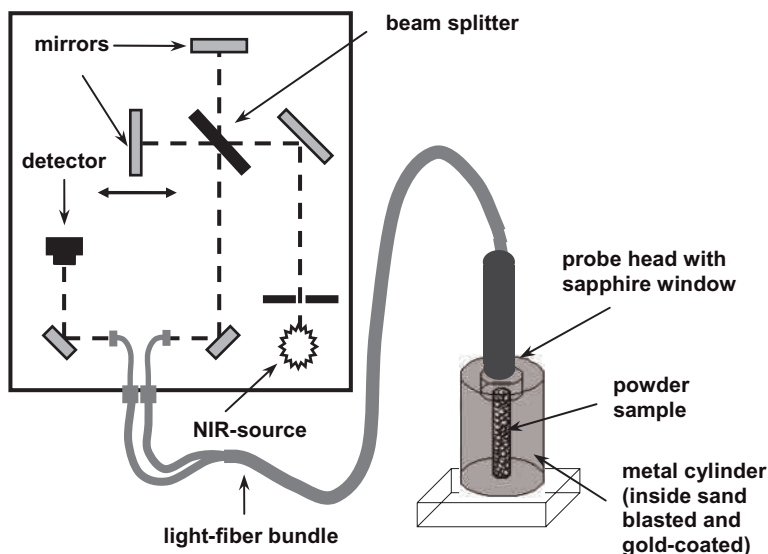
Figure 9.39 Schematic representation of the diffuse-reflection measurements with a single-element detector FT-NIR spectrometer. Reproduced with permission from Ref. [68]; © 2008, Society for Applied Spectroscopy.

(a)

(b)

(c)
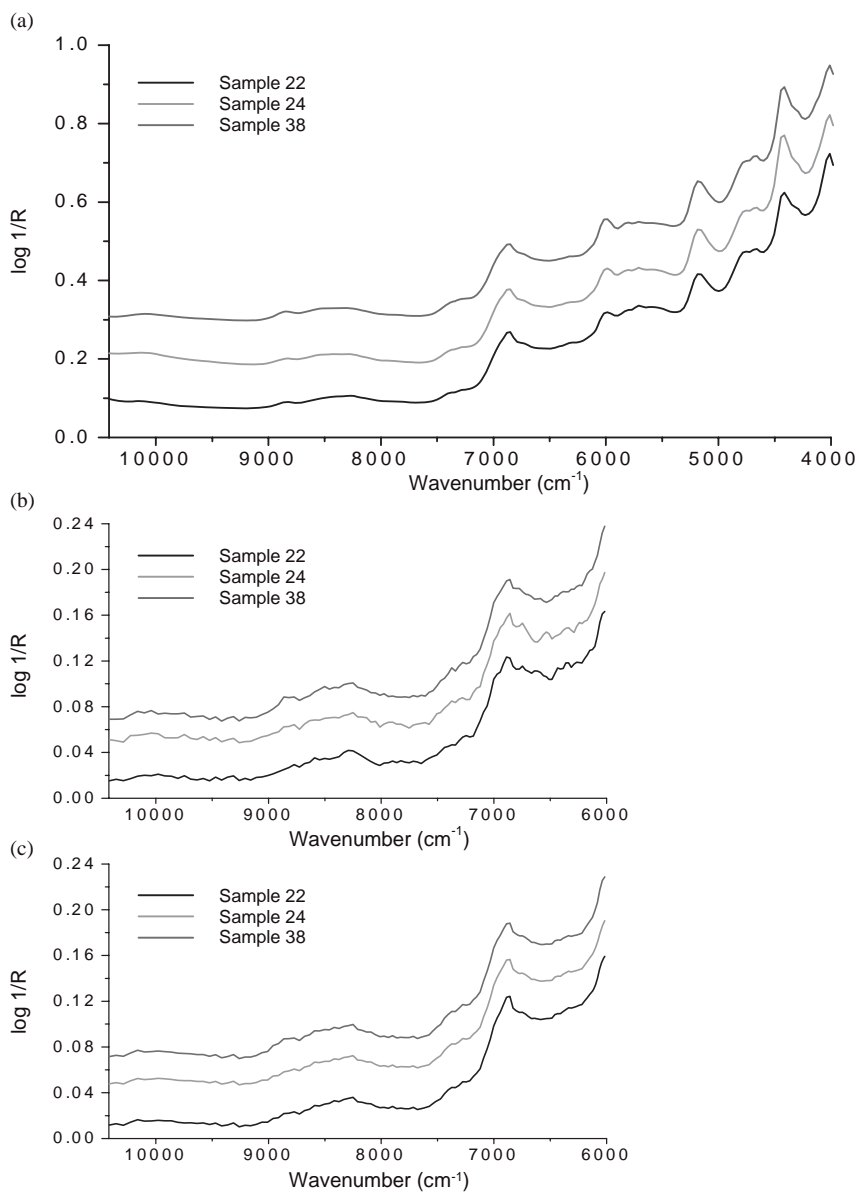
Figure 9.40 (a) NIR spectra of the three test samples measured in diffuse-reflection with a single-element detector; (b) NIR single-pixel imaging spectra of the three test samples; (c) NIR median imaging spectra of the three test samples. Reproduced with permission from Ref. [68]; © 2008, Society for Applied Spectroscopy.

Table 9.5 Calibration parameters of the PLS models for ASA, ASC and CF for the two measurement techniques.

Single-element detector (16 cm^{-1})

	RMSEP	Corr. coeff.	No. of factors
ASA	0.51	0.98	6
ASC	0.65	0.97	6
CF	0.51	0.99	2

Imaging median spectra (24 cm^{-1})

ASA	0.71	0.96	4
ASC	0.65	0.97	2
CF	1.03	0.95	4

Single-element detector (32 cm^{-1})

ASA	0.54	0.98	6
ASC	0.67	0.96	6
CF	0.52	0.99	2

models of the imaging median spectra of the 45 calibration samples are bracketed between the corresponding data for 32 and 16 cm^{-1} spectral resolution of the diffuse-reflection measurements with the single-element detector for ASA, ASC and CF. Despite the availability of a much smaller wavenumber region and the inferior SNR of the imaging median spectra (see Figures 9.40a and c), only slightly higher RMSEP values are obtained for the active ingredients. Based on these calibration models, the composition of the three test samples (samples 22, 24, 38) have then been predicted on the one hand from their conservative diffuse-reflection single-element detector spectra (with 16 and 32 cm^{-1} spectral resolution), and on the other hand from their ROI single-pixel spectra. This last-mentioned prediction step has been performed by applying the **B** matrix of the inverse calibration model, $\mathbf{Y} = \mathbf{XB}$ (where **X** is the matrix of the 45 median imaging calibration spectra and **Y** is the reference concentration matrix) to the ROI single-pixel spectra of the three test samples. When this is done, as many predicted concentration values as pixels in the images of the three test samples have been obtained (see Chapter 2). The individual pixel concentration values have then been used to display a distribution map where the *x*-axis shows the concentration predicted values and the *y*-axis the pixel counts (with the central value of the histogram representing the predicted concentration; see Figure 9.41a). The predicted concentrations for the three active ingredients of the three unknown samples are shown in Table 9.6, and reflect the comparable prediction capability of the single-pixel imaging data with reference to the single-element detector measurements.
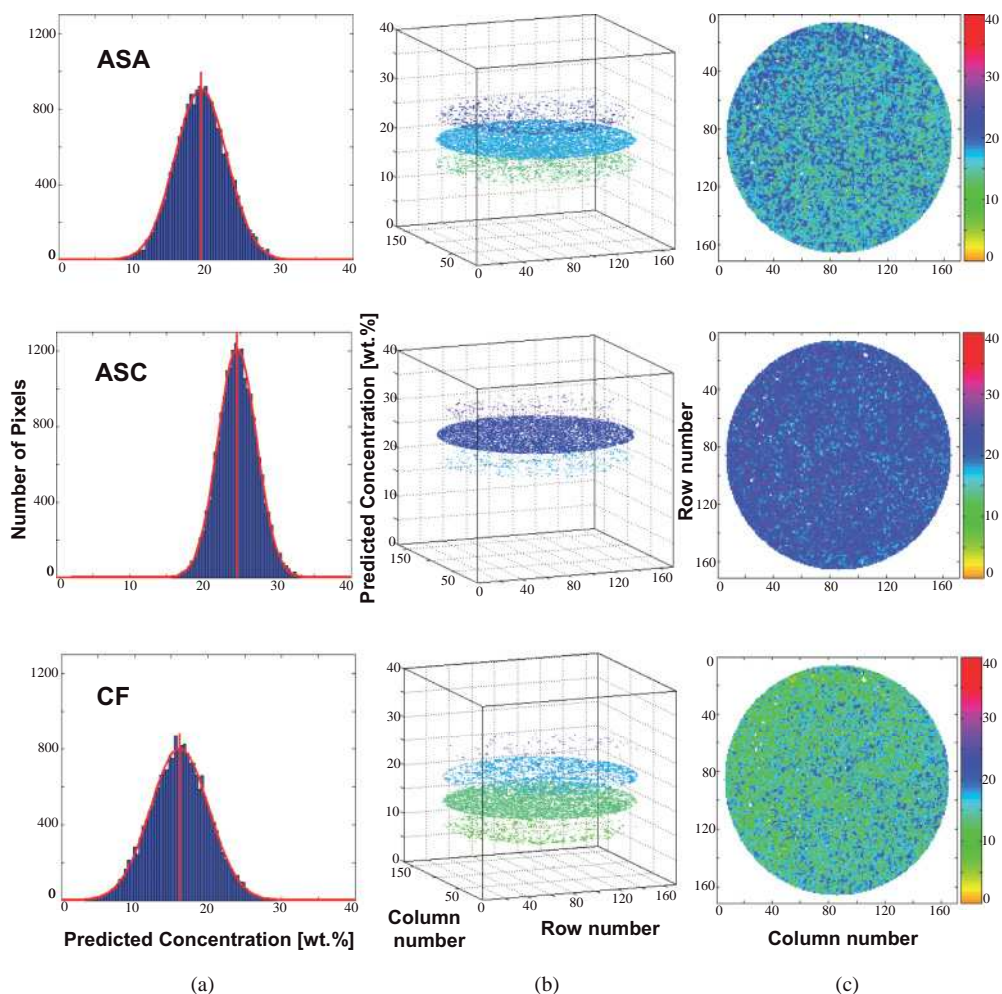
Figure 9.41 Typical imaging plots for test sample 22. (a) Pixel count/pixel concentration histograms for the three active ingredients; (b) 3-D contour plot in 5 wt% level intervals; (c) 2-D color image plot. Reproduced with permission from Ref. [68]; © 2008, Society for Applied Spectroscopy.

9.4.2
Spatial Distribution of the Active Ingredients in a Pharmaceutical Drug Formulation

The quantitative determination of the active ingredients forms only part of the quality control requirements for a pharmaceutical drug formulation. Equally important is the homogeneous distribution of the active ingredients in the formulation, and in this respect the inherent advantage of imaging measurements comes into play and provides the relevant information. As an example, in Figure 9.41 the

Table 9.6 Prediction results for the three test samples obtained from the diffuse-reflection single-detector measurements (for 16 and 32 cm^{-1} spectral resolution) and the single-pixel imaging spectra.

NIR Diffuse-reflection single-element detector spectroscopy

(Spectral resolution 16 cm^{-1}, spectral calibration range: 9050–7450, 7100–5570, 5300–4000 cm^{-1})

	Sample 22		Sample 24		Sample 38	
	Reference	**Prediction**	**Reference**	**Prediction**	**Reference**	**Prediction**
ASA	20.01	20.16	16.52	16.75	23.39	22.86
ASC	25.26	25.01	20.87	20.15	16.27	16.80
CF	14.73	15.05	22.61	22.57	20.34	20.28

NIR Diffuse-reflection imaging spectroscopy

(Spectral resolution 24 cm^{-1}, spectral calibration range: 10417–6017 cm^{-1})

	Sample 22		Sample 24		Sample 38	
	Reference	**Prediction**	**Reference**	**Prediction**	**Reference**	**Prediction**
ASA	20.01	19.35	16.52	16.41	23.39	22.91
ASC	25.26	24.57	20.87	21.17	16.27	16.16
CF	14.73	16.13	22.61	22.69	20.34	20.51

NIR Diffuse-reflection single-element detector spectroscopy

(Spectral resolution 32 cm^{-1}, spectral calibration range: 9050–7450, 7100–5570, 5300–4000 cm^{-1})

	Sample 22		Sample 24		Sample 38	
	Reference	**Prediction**	**Reference**	**Prediction**	**Reference**	**Prediction**
ASA	20.01	20.19	16.52	16.68	23.39	22.85
ASC	25.26	24.99	20.87	20.23	16.27	16.80
CF	14.73	15.05	22.61	22.56	20.34	20.31

width of the concentration distribution over all pixels and the lateral distribution of the three active ingredients over the imaged area of test sample 22 are shown in different representations:

- Histograms of the number of pixels versus concentration for the three active ingredients (Figure 9.41a). The bold vertical line represents the concentration predicted by the corresponding PLS model.

- 3-D color contour plots of the concentration (at 5 wt% level intervals) (Figure 9.41b).

- Two-dimensional color image contour plots of the imaged sample area (representing the top view of the 3-D color contour plots) (Figure 9.41c).

The histograms in Figure 9.41a show that CF has the lowest concentration uniformity over the imaged sample area compared to ASC and ASA (the same phenomenon has been detected for samples 24 and 38). This observation is in agreement with the larger particle size inhomogeneity of the original CF material (which was obviously not completely eliminated by milling) compared to ASC and ASA. Although, the heterogeneity of the imaged sample will always be the dominant factor, the broader width of the CF-histogram could also be partly indicative of the lower precision of the calibration model for this active ingredient (see also Table 9.6). Figures 9.41b and c represent the lateral distributions of the different concentration levels of the three active ingredients over the imaged sample area.

The lateral distribution of all three active ingredients may be represented in one RGB image. As an example, Figure 9.42a shows the RGB images for the three test
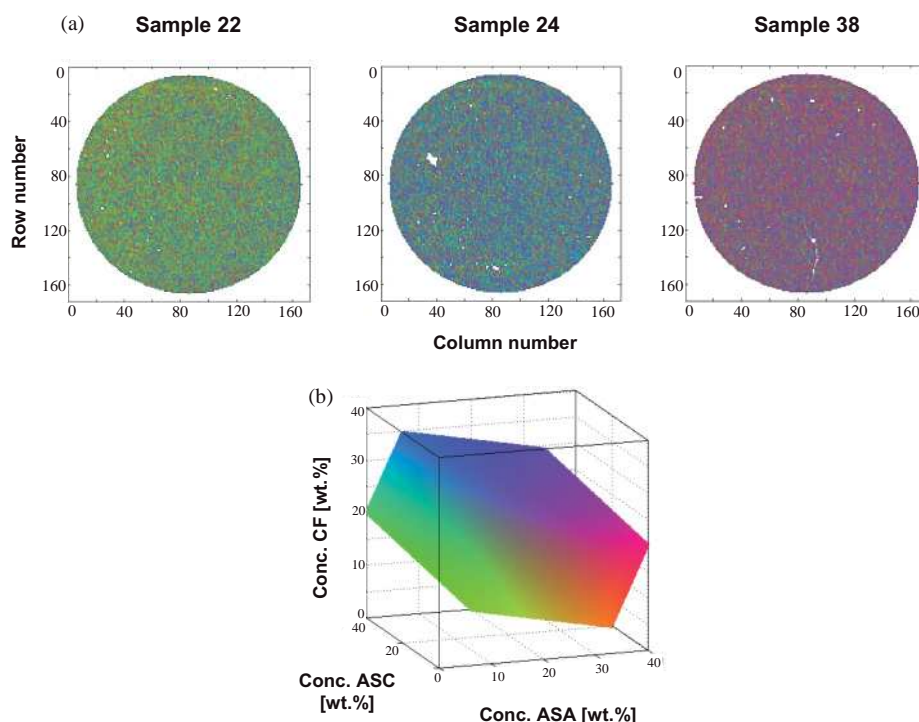
Figure 9.42 (a) RGB (red: ASA, green: ASC, blue: CF) plots for the three test samples; (b) The corresponding color scale. Reproduced with permission from Ref. [68]; © 2008, Society for Applied Spectroscopy.

samples 22, 24 and 38, based on the RGB scale included in Figure 9.42b (the white areas in the RGB images correspond to pixels of which the spectra had been identified as outliers). On the one hand, the different compositions of the three 'unknown' test formulations can be clearly visually discriminated by the tint of their RGB images, and on the other hand the spatial distribution of the active ingredients becomes available from these data.

9.4.3
Conclusions

Notwithstanding the comparatively large penetration depth and effective pathlength of NIR radiation into particulate matter (see Section 9.2.1), and the limited wavenumber range and low SNR of NIR imaging spectra, this technique provides a powerful approach to combine the quantitative investigations of multicomponent systems with the acquisition of information with regards to the spatial distribution of components in the investigated samples. Thus, PLS calibration models based on NIR imaging spectra have yielded results that were comparable to those of calibration models of single-element detector diffuse-reflection spectra for the prediction of the active ingredient content.

References

1 Lewis, E.N., Treado, P.J., Reeder, R.C., Story, G.M., Dowrey, A.E., Marcott, C. and Levin, I.W. (1995) *Anal. Chem.*, **67**, 3377–81.

2 Challa, S.R., Wang, S.-Q. and Koenig, J.L. (1996) *Appl. Spectrosc.*, **50**, 1339–44.

3 Snively, C.M. and Koenig, J.L. (1998) *Macromolecules*, **31**, 3753–5.

4 Snively, C.M. and Koenig, J.L. (1999) *J. Polym. Sci. Part B: Polym. Phys.*, **37**, 2261–8.

5 Bhargava, R., Wang, S.-Q. and Koenig, J.L. (1998) *Appl. Spectrosc.*, **52**, 323–8.

6 Snively, C.M. and Koenig, J.L. (1999) *J. Polym. Sci. Part B: Polym. Phys.*, **37**, 2353–9.

7 Ribar, T., Bhargava, R. and Koenig, J.L. (2000) *Macromolecules*, **33**, 8842–9.

8 Ribar, T. and Koenig, J.L. (2001) *Macromolecules*, **34**, 8340–6.

9 Miller-Chou, B.A. and Koenig, J.L. (2002) *Macromolecules*, **35**, 440–4.

10 González-Benito, J. and Koenig, J.L. (2002) *Macromolecules*, **35**, 7361–7.

11 Koenig, J. (2002) *Adv. Mater.*, **14**, 457–60.

12 Rafferty, D.W. and Koenig, J.L. (2002) *J. Control. Release*, **83**, 29–39.

13 Bobiak, J.P. and Koenig, J.L. (2005) *J. Control. Release*, **106**, 329–38.

14 Gupper, A., Wilhelm, P., Schmied, M., Kazarian, S.G., Chan, K.L.A. and Reûner, J. (2002) *Appl. Spectrosc.*, **56**, 1515–23.

15 Gupper, A., Wilhelm, P., Kothleitner, G., Eichhorn, K.-J. and Pompe, G. (2004) *Macromol. Symp.*, **205**, 171–80.

16 Li, G.L. and Koenig, J.L. (2002) *Appl. Spectrosc.*, **56**, 1390–6.

17 Kazarian, S.G. and Chan, K.L.A. (2004) *Macromolecules*, **37**, 579–84.

18 Kaun, N., Vellekoop, M.J. and Lendl, B. (2006) *Appl. Spectrosc.*, **60**, 1273–8.

19 Chan, K.L., Hammond, S.V. and Kazarian, S.G. (2003) *Anal. Chem.*, **75**, 2140–6.

20 Clarke, F.C., Jamieson, M.J., Clark, D.A., Hammond, S.V., Jee, R.D. and Moffat, A.C. (2001) *Anal. Chem.*, **73**, 2213–20.

21 Lewis, E.N., Carroll, J.E. and Clarke, F.C. (2001) *NIR News*, **12**, 16–18.

22 Lyon, R.C., Jefferson, E.H., Ellison, C.D., Buhse, L.F., Spener, J.A., Nasr, M.M. and

Hussain, A.S. (2003) *Am. Pharm. Rev.*, **6**, 62–70.

23 Lyon, R.C., Lester, D.S., Lewis, E.N., Lee, E., Yu, L.X., Jefferson, E.H. and Hussain, A.S. (2002) *AAPS Pharm. Sci. Tech.*, **3**, 17.

24 Clarke, F.C. (2004) *Vib. Spectrosc.*, **34**, 25–35.

25 Clarke, F. and Hammond, S.V. (2003) *Eur. Pharm. Rev.*, **8**, 41–50.

26 Lewis, E.N., Schoppelrei, J.W., Lee, E. and Kidder, L.H. (2005) NIR chemical imaging as a process analytical tool, in *Process Analytical Technology* (ed. K. Bakeev), Blackwell Publ. Ltd., Oxford, pp. 187–225.

27 Shah, R.B., Tawakkul, M.A. and Khan, M.A. (2007) *J. Pharm. Sci.*, **96**, 1356–65.

28 Clarke, F.C., Hammond, S.V., Jee, R.D. and Moffat, A.C. (2002) *Appl. Spectrosc.*, **56**, 1475–83.

29 Lewis, E.N., Kidder, L.H., Lee, E. and Haber, K.S. (2005) Near-infrared spectral imaging with focal plane array detectors, in *Spectrochemical Analysis Using Infrared Multichannel Detector* (eds R. Bhargava and I.W. Levin), Blackwell Publ. Ltd., Oxford, pp. 25–55.

30 Olinger, J.M. and Griffiths, P.R. (1992) Theory of diffuse reflectance in the NIR region, in *Handbook of Near-Infrared Analysis* (eds D.A. Burns and E.W. Ciurczak), Marcel Dekker, New York, p. 28.

31 Berntsson, O., Danielsson, L.-G. and Folestad, S. (1998) *Anal. Chim. Acta*, **364**, 243–51.

32 Andersson, M., Josefson, M., Langkilde, F.W. and Wahlund, K.-G. (1999) *J. Pharm. Biomed. Anal.*, **20**, 27–37.

33 MacDonald, B.F. and Preeble, K.A. (1993) *J. Pharm. Biomed. Anal.*, **11**, 1077–85.

34 Haanstra, W.G., Hansen, W., Huys, M.J.G., Kip, B.J., Palmen, P., Roulmen, J., Snieder, M., van der Weerdhof, T., Weidemann, S. and Wortel, V.A.L. (1998) *Appl. Spectrosc.*, **52**, 863–8.

35 Berntsson, O., Burger, T., Folestad, S., Danielsson, L.-G., Kuhn, J. and Fricke, J. (1999) *Anal. Chem.*, **71**, 617–23.

36 Hudak, S.J., Haber, K., Sando, G., Kidder, L.H. and Lewis, E.N. (2007) *NIR News*, **18**, 6–8.

37 Chan, K.L.A. and Kazarian, S.G. (2003) *Appl. Spectrosc.*, **57**, 381–9.

38 Wessel, E., Heinsohn, G., Schmidt-Lewerkuehne, H., Wittern, K.-P., Rapp, C. and Siesler, H.W. (2006) *Appl. Spectrosc.*, **60**, 1488–92.

39 Harrick, N.J. (1967) *Internal Reflection Spectroscopy*, John Wiley & Sons, Inc., New York, p. 327.

40 Mirabella, F.M. (1993) *Practical Spectroscopy, 15: Internal Reflection Spectroscopy – Theory and Application* (ed. E.G. Brame), Marcel Dekker, Inc., New York, p. 374.

41 Lasch, P. and Naumann, D. (2006) *Biochim. Biophys. Acta*, **1758**, 814–29.

42 Hecht, E. (2001) *Optik*, 3. Aufl., Oldenburg Wissenschaftsverlag GmbH, München, 1040.

43 Nishikida, K. (2004) *Spatial Resolution in Infrared Microscopy and Imaging*, Thermo Electron Corporation, Application Note: 50717, Madison, pp. 1–5.

44 Sommer, A.J., Tisinger, L.G., Marcott, C. and Story, G.M. (2001) *Appl. Spectrosc.*, **55**, 252–6.

45 Hocking, P.J. and Marchessault, R.H. (1998) Polyhydroxyalkanoates, in *Biopolymers from Renewable Resources* (ed. D.L. Kaplan), Springer Verlag, Berlin, p. 220.

46 Doi, Y. and Steinbüchel, A. (2001) *Biopolymers, 3 b: Polyesters II – Properties and Chemical Synthesis*, Wiley-VCH Verlag GmbH, Weinheim, p. 480.

47 Auras, R., Harte, B. and Selke, S. (2004) *Macromol. Biosci.*, **4**, 835–64.

48 Coleman, M.M., Graf, J.F. and Painter, P.C. (1991) *Specific Interactions and the Miscibility of Polymer Blends*, Technomic Publ., Lancaster, p. 19.

49 Blümm, E. and Owen, A.J. (1995) *Polymer*, **36**, 4077–81.

50 Park, J.W., Doi, Y. and Iwata, T. (2004) *Biomacromolecules*, **5**, 1557–66.

51 Furukawa, T., Sato, H., Murakami, R., Zhang, J., Duan, Y.-X., Noda, I., Ochiai, S. and Ozaki, Y. (2005) *Macromolecules*, **38**, 6445–54.

52 Vogel, C., Wessel, E. and Siesler, H.W. (2008) *Biomacromolecules*, **9**, 523–7.

53 Vogel, C., Wessel, E. and Siesler, H.W. (2008) *Macromolecules*, **41**, 2975–7.

54 Chernev, B. and Wilhelm, P. (2006) *Monatsh. Chem.*, **137**, 963–7.

55 Siesler, H.W. (1984) Rheo-optical Fourier-transform infrared spectroscopy: vibrational spectra and mechanical properties of polymers, in *Advances in Polymer Science*, Springer Verlag, Berlin, Heidelberg, pp. 1–77.

56 Siesler, H.W., Hoffmann, G.G., Kolomiets, O., Pfeifer, F. and Zahedi, M. (2007) Variable-temperature rheo-optical Fourier-transform infrared spectroscopy of polymers, in *Vibrational Spectroscopy of Polymers: Principles and Practice* (eds N.J., Everall, J.M. Chalmers and P.R. Griffiths), John Wiley & Sons, Ltd, Chichester, pp. 313–47.

57 Dechant, J. (1972) *Ultrarotspektroskopische Untersuchungen an Polymeren*, Akademie Verlag, Berlin, p. 516.

58 Vogel, C., Wessel, E. and Siesler, H.W. (2008) *Appl. Spectrosc.*, **62**, 599–602.

59 Lando, J.B., Olf, H.G. and Peterlin, A. (1966) *J. Polym. Sci. A-1*, **4**, 941–51.

60 Enomoto, S., Kawai, Y. and Sugita, M. (1968) *J. Polym. Sci. A-2*, **6**, 861–9.

61 Batzer, H. and Kreibich, U. (1981) *Polymer Bull.*, **5**, 585–90.

62 Reimschuessel, H.K. (1978) *J. Polym. Sci. Polym. Chem. Ed.*, **16**, 1229–36.

63 Jacques, C.H.M., Hopfenberg, H.B. and Stannett, V. (1974) Super case II transport of organic vapors in glassy polymers, in *Permeability of Plastic Films and Coatings to Gases, Vapors and Liquids* (ed. H.B. Hopfenberg), Plenum Press, New York, p. 73.

64 Crank, J. (1975) *The Mathematics of Diffusion*, 2nd edn, Oxford University Press, New York, p. 414.

65 Mann, J. and Marrinan, H.J. (1956) *Trans. Faraday Soc.*, **52**, 481–7.

66 Wu, P. and Siesler, H.W. (1999) *Macromol. Symp.*, **143**, 323–36.

67 Cannon, C.G. (1960) *Spectrochim. Acta*, **16**, 302–19.

68 Kolomiets, O., Hoffmann, U., Geladi, P. and Siesler, H.W. (2008) *Appl. Spectrosc.*, **62**, 1200–8.

10

ATR-FT-IR Imaging for Pharmaceutical and Polymeric Materials: From Micro to Macro Approaches

Sergei G. Kazarian, K. L. Andrew Chan, and Feng H. Tay

10.1
Introduction

Novel approaches to Fourier transform-infrared (FT-IR) spectroscopic imaging are needed to fully utilize the power of this chemical imaging technique. In our group, we have developed a range of approaches and applications of FT-IR imaging in both attenuated total reflection (ATR) and transmission modes for a broad range of materials and chemical systems. It has been demonstrated that ATR-FT-IR imaging has the potential for greatly improved spatial resolution compared to conventional transmission microscopy, with the achieved resolution of FT-IR imaging being beyond the diffraction limit for IR light in air. As a consequence, this development opened up many new areas amenable to study, which were previously ruled out by the inadequate spatial resolution – for example, to study the distribution of a drug in a tablet, or to image the cross-section of a human hair without recourse to a synchrotron.

ATR imaging with visible light can be observed most easily if a glass of water is held in the hand, when the skin or finger print making contact with the glass can be observed through the surface of the water, while the remainder of the light is totally internally reflected. The area where the surface of the glass makes contact with the skin destroys the total reflection and forms an image of the finger print. An ATR image of a finger print has been demonstrated by Harrick [1], who obtained the ATR image by illuminating a prism with a finger pressed on the large surface and then focusing the light that had been internally reflected off the prism onto a photo film. The same principle described by Harrick has been applied using ATR-FT-IR spectroscopic imaging. Here, instead of shining visible light, and using a photo film to record the projected image, the IR light was shone through an interferometer, an IR transparent crystal, and onto a focal plane array (FPA) detector [2].

The applicability of ATR-FT-IR imaging ranges from micro ATR imaging using a microscope objective to the use of ATR accessories with focused or expanded optics, without need to use the microscope. The ATR crystal in a prism shape

provide much versatility in terms of sample preparation. Thus, the range of areas in the samples that could be measured simultaneously using FPA detectors and prism-shape ATR crystals was from $500 \times 700 \, \mu m^2$ to $1.6 \times 2.1 \, cm^2$ (see Section 10.2). The measured area with macro ATR imaging depends not only on the specific optics used in these ATR accessories but also on the size of the pixels in the array detector. Most currently available detectors have a pixel size of $40 \times 40 \, \mu m^2$ or $60 \times 60 \, \mu m^2$.

One of the main advantages of FT-IR spectroscopic imaging in the ATR mode is that it requires minimal or no sample preparation. The minimal penetration of IR light into the sample when using the ATR mode also allows one to image samples in contact with aqueous solutions, or materials containing a high water content. As with any technique, however, FT-IR imaging in the ATR mode has its limitations. In one of the first reports on the application of ATR-FT-IR imaging, a sample of a polymer blend [polyamide 6.6, poly(tetrafluoroethylene) and silicon oil] was analyzed using both FT-IR imaging in transmission and ATR modes, and the results were compared [3]. Moreover, these studies represented the first occasion that chemical images obtained by both FT-IR imaging and Raman microspectroscopy for the same samples had been compared. The chemical images were also compared to the results obtained with scanning electron microscopy (SEM), energy-dispersive X-ray spectrometry and microthermal imaging analysis. Remarkably, this direct comparison between four different imaging techniques resulted in an excellent agreement between them! The agreement between FT-IR images obtained by transmission and ATR was helped by the fact that the thickness of the polymer film was 5 μm. It was also highlighted in this report that, because of the limited penetration of the evanescent wave into the sample, the images obtained by the ATR-FT-IR method would only reflect the composition of the surface layer of the 1–3 μm-thick sample, depending on the type of ATR crystal employed, the angle of incidence and the wavelength of the light [3]. However, it was also noted that the small thickness of the probed layer in ATR imaging might also be advantageous. For example, imaging in transmission may average through the thickness of the sample, and microtoming of samples is usually required for thicknesses less than the domain size in order to ensure that imaging in transmission does not result in the production of spurious images [4]. The differences between the two FT-IR imaging modes (transmission and ATR), when discussed in more detail, were the advantages and limitations of the particular imaging mode in terms of spatial resolution, the image field of view (FOV) and possible artifacts [4]. Micro ATR imaging has the advantage of having a better spatial resolution [5–7], while the sample preparation is relatively simple (there is no need to microtome and polish).

There is a general belief that pressure must always be applied to a sample in order to obtain its FT-IR image in the ATR mode. Whilst it is important to ensure homogeneous contact between the sample and the ATR crystal, such that the image would not represent only the quality of the contact, there is often no need to apply pressure in this situation. Examples in macro ATR imaging include the swelling pharmaceutical tablets or biomedical tissues, whereby a good and repro-

ducible contact is achieved simply by placing the samples onto the surface of the ATR crystal. Clearly, special care should be taken to ensure that no excessive pressure is applied when working in micro ATR mode, where the use of an ATR microscope objective and a small contact area with the sample may result in significant pressures. However, modern IR microscopes can employ commercial or home-made pressure-monitoring devices to ensure that a controlled and reproducible contact is achieved in the micro ATR mode. The introduction of various macro ATR accessories has provided the opportunity to obtain chemical images with different fields of view, without recourse to using an IR microscope. In this chapter, we describe some general principles and applications of FT-IR imaging in the ATR mode, with the focus on new developments achieved primarily in our laboratory. While some applications in transmission are discussed, the main focus of the chapter is on FT-IR imaging in micro and macro ATR modes, and also to present some new, previously unreported, information.

10.2
The Versatility of ATR-FT-IR Imaging

Previously, it was difficult to obtain ATR-FT-IR images without the use of a FPA detector because, when using the mapping approach, the crystal is in contact with the sample during the measurement, such that the sample might be deformed and the distribution of different components in the mixture altered. Furthermore, if the crystal remains in contact with the sample during translation from one measuring location to another, smearing of the sample – or even its physical damage – might reduce the reliability of the ATR method for mapping. Yet, if the crystal is detached from the sample when moving from one measuring point to another, then the time required to acquire a single map will be extended and the multiple contacts between the crystal and sample might cause damage to the sample. As a consequence, Esaki *et al.* [8] have developed a new ATR crystal with a hexagonal shape that allows ATR mapping, but without the problems stated above. Here, the crystal is translated with the sample attached, while the size of the ATR map is limited only by the size of the crystal used (ca. $2 \times 7 \, mm^2$ map). As a specific ATR crystal is required [9] for this type of measurement, it is currently not as widely available as the hemispherical crystals. Lewis *et al.* [10] have demonstrated ATR mapping with a hemispherical germanium crystal on a photographic film laminate. Their study involved mapping an image by translating the ATR crystal together with the sample, such that there was no smearing of the sample. However, while this method eliminated any potential damages to the sample, it remained a relatively long process for mapping a relatively small area. Recently, this ATR mapping approach has been further developed by the use of a linear array detector rather than a single-element detector [11]. While this new development speeds up the mapping process to a point where it could rival the FPA approach [12], it also has some other advantages over the FPA detector, such as a more flexible imaging size (up to ca. $600 \, \mu m$ before significant optical aberration takes place) and a larger

spectral range in the lower wavenumber spectral region (down to $700\,cm^{-1}$). However, the inability to acquire all of the spectra at the same time would serve as a limitation when studying dynamic systems. The spatial resolution and depth of penetration of this approach is variable across the imaged area, however, the further optimization of the method is still in progress.

When using the FPA detector and a stationary ATR crystal, all spectral information across the whole imaging area is captured simultaneously [5]. The snap-shot feature of this FPA imaging approach enables the study of dynamic systems, such as drug dissolution [13, 14], parallel analysis of many samples in a high-throughput (HT) manner [15–18], studies of biopolymers and biomedical systems [19–23] and diffusion processes *in situ* [24–27]. FT-IR imaging in transmission has been used in many polymer applications [13, 28–31], with recent exciting applications including micro patterning reactions [32]. As there is no rastering with a fixed ATR crystal, the imaging area or FOV is defined by the size of the FPA and the optics. Patterson *et al.* [12] have shown that it is possible to combine FPA imaging and mapping methods by using the translating ATR crystal to image a larger area of the sample although, as with other mapping methods, this is limited to the study of static systems. Another approach to obtain flexibility in the imaging with different FOVs, without sacrificing the ability to study dynamic systems, is to employ different optical arrangements or to use different sizes of detector. With this option, the number of pixels measured per image and the FOV is defined by the number of pixels of the detector, the size of each pixel, and the optics used to project the image onto the detector. Today, a range of different sizes of FPA detectors is available commercially, from 32×32 to 256×256. While the earlier versions of the FPA detector had a pixel size of approximately $62\,\mu m$, with a relatively slow performance, the new-generation FPA detectors may have a pixel size of ca. $40\,\mu m$ and be up to 10-fold faster in operation. However, FPA detectors are often expensive, the choice of detector size is still limited, and switching between detectors requires an alignment procedure to be carried out which often is not preferable. It is, therefore, logical to obtain the flexibility in FOV by using different optical arrangements.

When considering a 64×64 new FPA (pixel size ca. $40\,\mu m$), and with no magnification, the FOV of the image would be approximately $2.6 \times 2.6\,mm^2$. In an IR microscope equipped with a $10\times$ Ge ATR objective, the magnification would be $40\times$, and hence the theoretical image size would be $65 \times 65\,\mu m^2$ (measured image size of $50 \times 50\,\mu m^2$ using the old FPA with a $20\times$ Ge ATR). Although the image size is relatively small, a high spatial resolution ($4\,\mu m$) can be achieved. It is important that this value of achieved spatial resolution is obtained using the stringent test of measuring the distance between the 5% to 95% points on an absorbance profile, obtained through a sharp interface between two materials with similar refractive indices [7], rather than artificial resolution markers that use reflective and transparent features. There is a small degree of flexibility in the FOV when using different objectives and FPA detectors, although the range would be rather small unless a rastering or mapping approach were to adapted (as discussed above). For imaging with a larger FOV using a stationary ATR crystal, the IR light
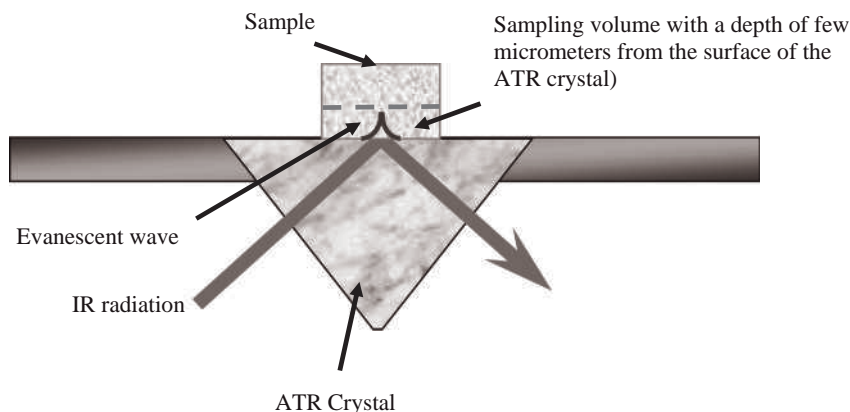
Figure 10.1 Schematic diagram of the optical arrangement using an inverted ATR prism.

is directed to a large sample compartment instead of to the IR microscope. This chamber allows different accessories to be used; specifically, ATR accessories with an inverted prism can be employed that make measurements more convenient for many applications. The optical arrangement using an inverted prism is shown schematically in Figure 10.1.

By using an inverted prism diamond ATR accessory, it has been shown that the FOV was approximately $500 \times 700\,\mu m^2$ (ca. 5× magnification) [7]. For the inverted prism ZnSe ATR accessory, which does not contain any lenses (e.g., Oil Analyzer; Specac, UK) [14], the FOV becomes approximately $2.6 \times 3.6\,mm$, with the change in the imaging aspect ratio being related to the geometry of the prism and the angle of incidence [7]. Other novel developments include a new diamond ATR accessory designed specifically for imaging applications, an inverted prism ZnSe ATR accessory with expanding lenses [33] and an accessory which allows ATR imaging with variable angles of incidence [34] (the applications of these are discussed later in the chapter). The different FOVs and spatial resolutions of the ATR accessories are summarized in Table 10.1.

10.2.1
Micro ATR Imaging

The main advantage of micro ATR imaging with the use of a microscope objective is the high spatial resolution images that can be achieved. The high refractive index of the ATR crystal used for this type of imaging (for a Ge crystal this is 4) greatly increases the numerical aperture of the system, and hence it is possible to achieve a spatial resolution beyond the diffraction limit of light in air when compared to transmission mode, where the Ge crystal is not used [6, 35]. High-spatial resolution FT-IR images up to the diffraction limit can also be obtained using a bright synchrotron source (cf. Chapter 13 and [36]). However, as these images are obtained

Table 10.1 Summary of the capabilities of different ATR-FT-IR imaging approaches.

	Large ZnSe	Variable angle ATR accessory	Medium ZnSe	Diamond ATR	Micro ATR with 10× Ge objective
Field of view/mm × mm[a]	15.4 × 21.5	~3.9 × 5.5	2.6 × 3.6	~0.5 × 0.7	0.064 × 0.064
Spatial resolution (estimated)	500	150	60	15–20	4
Combined with a UV detector	No	No	Yes	Yes	No
In situ compaction of samples	No	No	No	Yes	No
High-throughput applications (number of samples)	Yes (>100)	Yes (100)	Yes (50)[b]	Yes (10)[b]	No
Depth profiling	No	Yes	No	Yes	No

a Sizes quoted are obtained with new 64 × 64 FPA detector (40 µm pixel size).
b Only possible when using a microdroplet dispensing system.

by rastering, the method is usually relatively slow and lacks the capability to study dynamic systems, as spatial resolution is still limited by the diffraction of light traveling in air. The signal-to-noise ratio (SNR) of the spectra collected, on the other hand, is often better than for those spectra measured with FPA detectors, and may in fact be complementary to the latter approach. Measurements using the FPA detector in micro ATR mode can be achieved within a few minutes of acquisition time, and the SNR is often sufficient for most applications. With this advantage, micro ATR imaging enables the measurement of small features that were not previously attainable. The high resolving power also enhances the detection limits for heterogeneous materials [37]. Hence, micro ATR imaging has opened a range of new opportunities for the study of complex materials, polymer blends and pharmaceutical tablets, where the ROI is often in the micrometer scale [3, 7, 19, 38–42].

10.2.2
ATR-FT-IR Imaging with a Diamond Accessory

In ATR-FT-IR spectroscopy, the crystal used to create the internal reflection must be IR-transparent, while the refractive index must be relatively high to permit the measurement of a wide range of materials. One such widely used material is

diamond, the high integrity of which has proven to be a valuable property, as a high contact pressure between the sample and crystal may need to be applied in order to improve the reproducibility of the spectrum, without damaging the crystal [43, 44]. Such integrity also makes possible the study of polymer materials under high-pressure environments *in situ* [45–47]. Recently, a diamond ATR accessory, although not originally designed for imaging purposes, has been shown to be applicable for the acquisition of FT-IR images [4, 7, 48]. Further developments of this have led to the introduction of a new diamond ATR accessory, the Imaging Golden Gate (Specac, UK), which is designed specifically for imaging applications. The aspect ratio of the ATR images obtained using the original diamond ATR accessory had to be corrected by a factor of 1.4 due to the geometry of the ATR crystal and the angle of incidence of the IR source [7]. However, the new accessory incorporated a pair of zinc selenide/germanium lenses and a new mirror configuration patented by Specac [49], which supposedly corrects any optical aberrations and the aspect ratio of the images.

10.2.2.1 Comparison of 'New' and 'Old' Diamond ATR Accessories

The ATR-FT-IR images of poly(dimethyl siloxane) (PDMS) on a copper grid from the nonimaging diamond ATR accessory with the old FPA detector, and from the new imaging diamond ATR accessory with the new FPA detector, are shown in Figure 10.2. The images are generated based on the distribution of the absorbance of spectral bands at 1150–950 cm^{-1}. The visible image of the copper grid used is shown in Figure 10.2c, and the distance between each square is approximately 63 μm. Previously, Chan and Kazarian [7] reported the results of a similar experiment with the same imaging system, but using poly(vinyl acetate) (PVA) pressed onto the same copper grid; the size of the chemical image captured was shown to be approximately 820 μm × 1140 μm. However, with the imaging diamond ATR accessory and the new FPA detector, it could be seen that there were about nine squares in the *x*-direction and 8.4 squares in the *y*-direction; thus, the new imaged area was about 570 μm × 530 μm. The aspect ratio of the measured area was also shown to have improved, from 1 : 1.4 to 1 : 1.1. Moreover, the new image of the copper grid not only showed a greater magnification but also appeared to be sharper and a better resemblance to the 5× optical image of the grid.

It should be noted that the measured area differed from that specified by the manufacturer, of 650 μm × 650 μm. The aspect ratio and magnification of the measured area are largely dependent on the alignment of the system. In a typical IR macro imaging system, the ATR accessory is placed in the large sample compartment that can be adjusted along the path of the IR beam. In order to obtain a well-focused image, the two most important parameters are the position of the objective lens in the ATR accessory, and the image distance that can be taken as the path distance of the IR light from the objective lens to the FPA detector. Specific to this imaging system, the new ATR accessory was aligned slightly left of the default factory position, for which the imaging Golden Gate ATR accessory is designed, and this may help to explain the slight deviation from the ideal aspect ratio and increase in magnification.

(a)

(b)

(c)
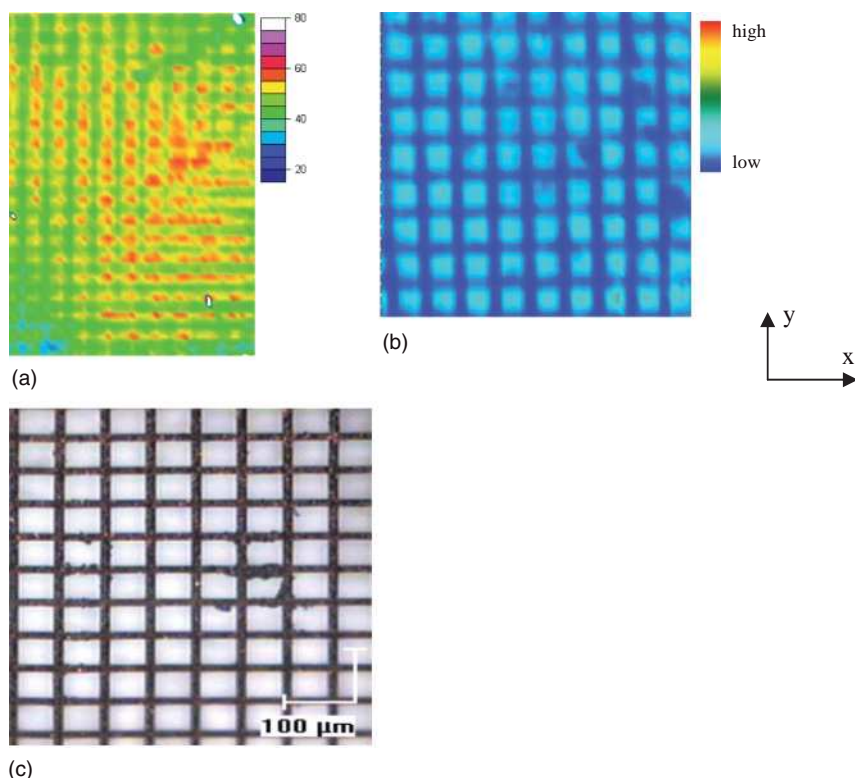
Figure 10.2 ATR-FT-IR images of a copper grid with a thick film of PDMS pressed behind and measured using (a) the ordinary and (b) the new imaging diamond ATR accessory; (c) the white light image of the copper grid measured with a 5× objective.

10.2.3
ATR-FT-IR Imaging with an Expanded Field of View

For studies where a larger FOV would be advantageous, a large ZnSe inverted prism with a set of expanded optics can be used. The design of these optics utilized expanding lenses and slightly concaved surfaces of the ZnSe crystal (except for the measurement surface) to increase the size of the FOV. [33] Hence, the area that could be measured in a single snapshot using this accessory would be approximately $15.4 \times 21.5 \, mm^2$; a schematic diagram of the accessory is shown in Figure 10.3.

The large measuring area of this imaging method enables the simultaneous measurement of many samples. This accessory has been used to measure the spectrum of over 100 samples in one single image acquisition, and the dissolution study of five different pharmaceutical formulations, simultaneously [33]. However,
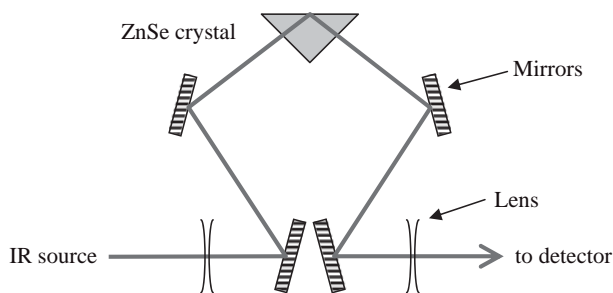
Figure 10.3 Schematics diagram showing the optics of the accessory which gives an expanded FOV.

with the expansion of the IR beam, the imaged pixel size will be increased, together with a decrease in the numerical aperture (NA) of the system. The spatial resolution is significantly lower compared to that of the nonexpanded ATR imaging method, which makes this approach unsuitable for imaging samples with smaller features, although it would provide an overall distribution over a larger area. A further discussion of this imaging method, as applied to HT usage, is provided later in the chapter.

10.2.4
ATR-FT-IR Imaging with Variable Angle of Incidence

Depth profiling of materials using variable-angle ATR spectroscopy is a well-established approach [50–53] that is based on the fact that the depth of penetration, d_p, is a function of the angle of incidence in an ATR measurement. The relationship between d_p, the wavelength of light, λ, the refractive indices of the ATR crystal and the sample (n_1 and n_2, respectively) and the angle of incidence, θ, is shown in Equation 10.1.

$$d_p = \frac{\lambda}{2\pi n_1 \left(\sin^2\theta - \left(\frac{n_2}{n_1} \right)^2 \right)^{0.5}} \tag{10.1}$$

A combination of variable-angle ATR spectroscopy with the FPA detector provided the possibility of obtaining three-dimensional (3-D) images with chemical information [34]. This experiment is made possible by using a macro sample chamber that has sufficient space for the variable angle of incidence ATR accessory, and the associated alignment procedure. In order to demonstrate this imaging approach, a thin film of poly(vinyl pyrrolidone) (PVP) was cast from a solvent on one half of the imaging FOV, followed by the pressing on top of a thick PDMS film [34]. ATR-FT-IR images at different angles of incidence were then captured; the results are shown in Figure 10.4, with the color scale normalized against the maximum PDMS absorbance observed in each image. These images show how

41°   45°   52°
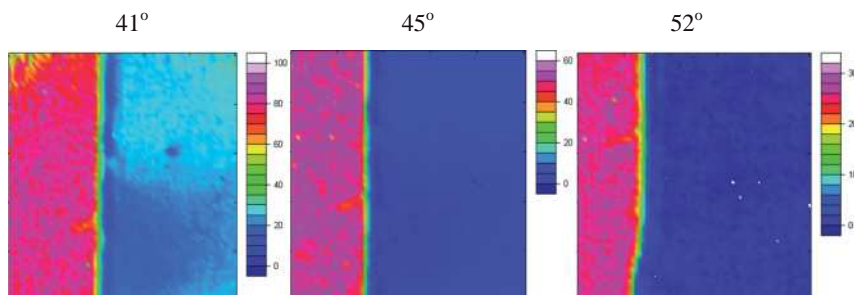
Figure 10.4 FT-IR images of a thin film of PVP covering half of the imaging area with a large piece of thick PDMS pressed on top.

the thick PDMS film is distributed in the measured area. It is clear that, when the thin film of PVP is not present, a strong PDMS absorbance can be observed (left-hand side of the image). However, at an angle of incidence of 52°, which corresponds to a depth of penetration, d_p, of approximately 1.3 μm, no PDMS could be observed on the side where the ATR crystal was covered by the thin film of PVP; this was shown by the zero absorbance of PDMS (represented as the dark blue on the color scale). At 45° ($d_p = 1.7$ μm), a small PDMS absorption (navy blue) could be seen through the PVP layer, while the PDMS absorption became stronger (light blue) when the angle of incidence decreased to 41° ($d_p = 2.3$ μm). This straightforward study showed clearly that information from different layers of the sample can be obtained simply by changing the angle of incidence, while the lateral distribution could be readily measured using the FPA detector. Moreover, this approach could be applied to study heterogeneity in both lateral and axial directions for those layers of samples adjacent to the surface of the ATR crystal.

It is important to note here that the variable-angle ATR accessory was originally designed for single point measurements, and therefore there is a scope to improve the quality of the images and optimize the image size from the optical design aspect. Nevertheless, a major potential clearly exists for the use of variable-angle ATR-FT-IR imaging with heterogeneous materials, notably biomedical materials such as skin [34].

10.2.5
Quantitative ATR-FT-IR Imaging

As with 'ordinary' ATR spectroscopy, ATR-FT-IR imaging results can be analyzed quantitatively, some recent examples including the study of tablet dissolution in water. In this case, the concentration profiles of hydroxylpropylmethylcellulose (HPMC) and niacinamide, at different stages of the dissolution process, were utilized to provide an understanding of the drug release mechanism [54]. Using this technique, it could be shown that the concentration profiles of different components could be obtained with the partial least squares (PLS) method. Here, with

concentration profiles readily measurable, it is possible to monitor other parameters, such as diffusion type (i.e., Fickian versus non-Fickian mechanism of diffusion). *In situ* ATR-FT-IR spectroscopic imaging has also been used to investigate the polymer interdiffusion of PVP and poly(ethylene glycol) (PEG), under high pressure CO_2 [55]. The diffusion mechanism of the system was described based on the spectroscopic imaging data, and it was found that CO_2 molecules dissolved in the polymeric system greatly enhanced the interdiffusion process. These two examples have shown that valuable information can be acquired via ATR-FT-IR spectroscopic imaging studies, thus providing an aid for the development of new mathematical models in the analysis of dynamic processes.

Quantitative analysis is made possible by employing the Beer–Lambert law; here, when the pathlength (l) of the sample is kept constant, the absorbance (A) at a wavenumber is proportional to the molar concentration (c) of the absorbing species (Equation 10.2). In this way, a calibration curve can be produced, either by measuring the absorbance of a number of samples of various known concentrations, or by identifying the molar absorptivity (ε) from reference sources and the pathlength in the measurement. For transmission measurements, the pathlength is usually equal to the thickness of the sample. In ATR measurements, this is to be taken as the effective pathlength, and can be calculated using Equation 10.3 for nonpolarized light [34].

$$A = \varepsilon l c \tag{10.2}$$

$$\frac{d_e}{\lambda} = \frac{\frac{n_2}{n_1}\cos\theta\left[3\sin^2\theta - 2\left(\frac{n_2}{n_1}\right)^2 + \left(\frac{n_2}{n_1}\right)^2\sin^2\theta\right]}{2\pi\left(1 - \left(\frac{n_2}{n_1}\right)^2\right)\left[\left(1 + \left(\frac{n_2}{n_1}\right)^2\right)\sin^2\theta - \left(\frac{n_2}{n_1}\right)^2\right]\left(\sin^2\theta - \left(\frac{n_2}{n_1}\right)^2\right)^{0.5}} \tag{10.3}$$

It is important to note that the measurement should operate at least a few degrees above the critical angle in order to avoid a strong dispersion of the refractive index effect to the spectrum.

It has been reported that an absorbance gradient was observed across an ATR-FT-IR spectroscopic image when measuring a homogeneous paraffin oil using a FastIR ATR accessory. The explanation for this phenomenon was that the angle of incidence (θ) was not uniform across the imaging plane [56]. Should the angle of incidence change across the imaging plane, the effective pathlength will be different, and hence the absorbance would not be the same, even if the concentration of the sample were uniform. Apparently, the alignment of the optics in the accessory is crucial to the occurrence of this absorbance gradient effect, and therefore it is important to ensure that the ATR accessories used in imaging studies are well aligned if quantitative results are important to the study.

To demonstrate that the gradient effect can be removed in an aligned system, similar experiments were performed by measuring a homogeneous sample of mineral oil (refractive index c 1.48), using both the ZnSe ATR accessory and the diamond ATR accessory (Supercritical Fluid Analyzer, Specac, UK). Both results

Table 10.2 Statistical summary of the integral absorbance of mineral oil at the 1480–1420 cm^{-1} band.

	ATR accessory	
	ZnSe	Diamond
Refractive Index	2.4	2.4
Included no. of pixels	4009	4035
Mean absorbance (a.u.)	2.1	3.5
Standard deviation (a.u.)	0.09	0.26
Upper limit (a.u.)	2.39	4.34
Lower limit (a.u.)	1.87	2.68
Excluded no. of pixels	87	61

showed a relatively homogeneous distribution of the integrated absorbance in the range of (1480–1420 cm^{-1}) over the whole imaged area (see Figures 10.5 and 10.6). For the ZnSe ATR accessory, the mean integrated absorbance was approximately 2.1 arbitrary units (a.u.) with a standard deviation of ±0.09 a.u., while for the diamond ATR accessory the mean integrated absorbance was approximately 3.5 ± 0.26 a.u. The remainder of the statistical results are summarized in Table 10.2. Notably, the ZnSe ATR accessory had a better SNR due to the intrinsic design of the equipment (a better throughput of energy). The difference in mean integrated absorbance could be explained by the difference in the average angle of incidence. It has been reported previously that the angle of incidence is not necessarily the same as the specification provided by the manufacturer [47]. Rather, it is very much dependent on the alignment of the spectrometer and the ATR accessory, which may of course vary from system to system. The findings presented in Figures 10.5 and 10.6 are important because they show that the acquisition of reliable quantitative imaging data is possible with the use of macro ATR accessories. But, the findings also highlight the fact that the *choice* of accessory and its *alignment* are crucial if such data are to be obtained in this way.

10.3
Applications of ATR-FT-IR Imaging in the Materials Sciences

10.3.1
Study of the Polymer/Carbon Fiber Interface

Micro-carbon fibers with a 5 μm diameter, embedded in a polymer matrix, have been manufactured as a composite product with improved mechanical properties that result from the synergy of the two materials. An understanding of interfacial properties in such materials is key to their design and manufacture. The
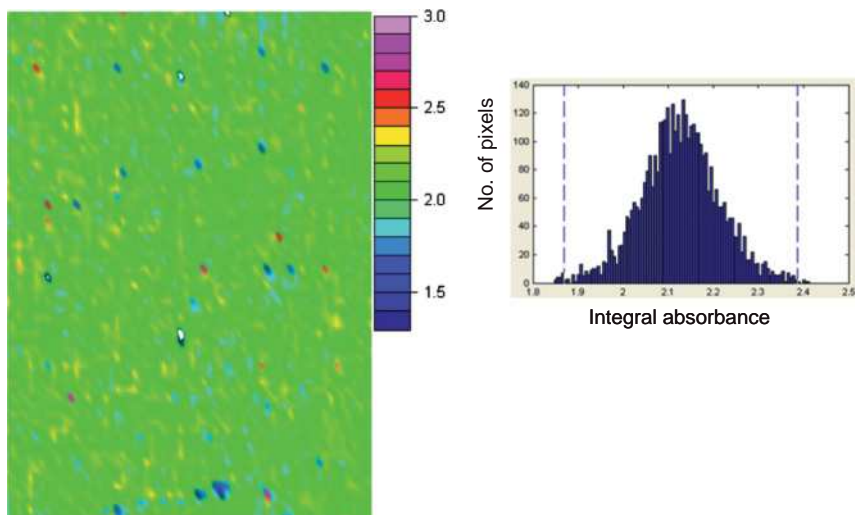
Figure 10.5 ATR-FT-IR image of mineral oil measured with a ZnSe ATR accessory showing the integrated absorbance at 1480–1420 cm^{-1}. The histogram showing the number of detector pixels for different values of the integrated absorbance at the same range for the ATR-FT-IR measurement.
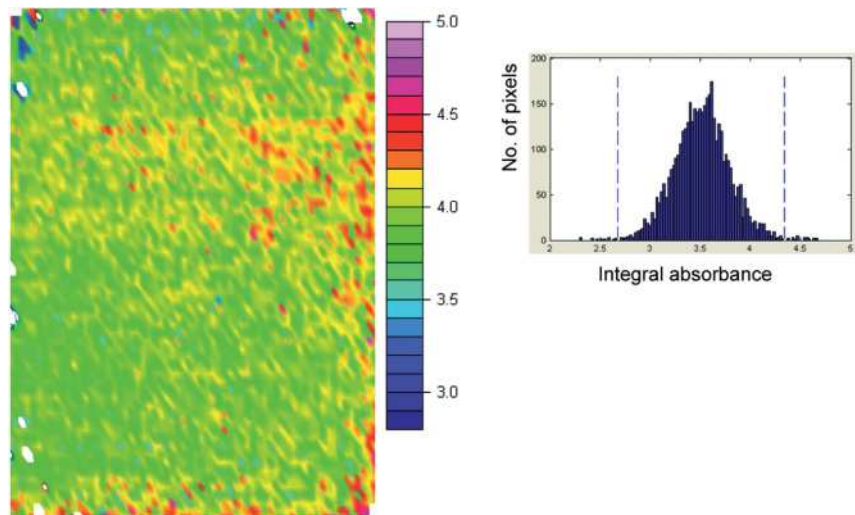
Figure 10.6 ATR-FT-IR image of mineral oil measured on a diamond ATR accessory showing the integrated absorbance at 1480–1420 cm^{-1}. The histogram showing the number of detector pixels for different values of the integrated absorbance at the same range for the ATR-FT-IR measurement.

measurement of IR spectra from the interfacial area between the micro-carbon fiber cross-sections can easily be obtained using a micro ATR imaging approach, with a microscope objective fitted with a Ge crystal. As the carbon fiber absorbs all wavelengths in the mid-IR region (it is a black body), the distribution of micro-fibers in the polymer matrix shown in Figure 10.7 can be observed by monitoring changes in absorbance in the 3500–3000 cm^{-1} spectral region, where the polymer matrix does not have any spectral bands. The size of the microfiber shown in the micro ATR-FT-IR image is approximately 5 μm, which is very similar to the actual fiber size and demonstrates the spatial resolving power of this imaging technique. The spectra extracted from the polymer matrix area close to the microfibers have been compared to those extracted from the bulk. The difference spectrum (not shown) has revealed that the spectra extracted near the fibers have an extra band at 1011 cm^{-1}. An image generated by plotting the integrated absorbance of this band across the imaged area is shown in Figure 10.7. The resultant image showed that the material in the polymer matrix that has this extra band appears to be distributed near the carbon fibers, although this is due to a specific manufacturing process (further details of which cannot be revealed here as the sample is proprietary). Nonetheless, it is important to note that this result can only be achieved by utilizing the high spatial resolution offered by micro ATR-FT-IR imaging. It is also important to note that the interfacial area between the fiber and the polymer matrix is very small, and thus the diffraction of light – which is also present in the ATR measurements – will affect the quality of the image (Figure 10.7b). Nevertheless, the consistency of its distribution with the distribution of fibers, coupled with an ability to extract its spectrum, is significant in our understanding of the design of these novel composite materials.

Carbon Fibre (3500-3000 cm^{-1})   Polymer near fibres (1032-944 cm^{-1})
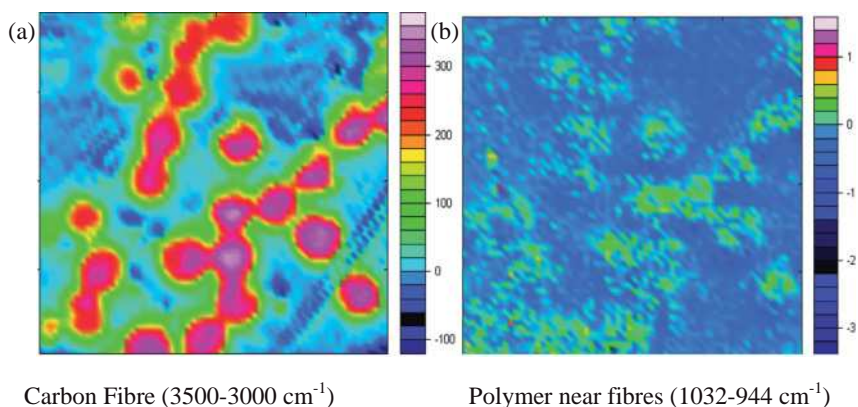
Figure 10.7 ATR-FT-IR images of the polymer matrix showing the distribution of (a) carbon fiber; (b) distribution of the absorbance of the band at 1011 cm^{-1}. Image size is 50 μm × 50 μm.

10.3.2
Polystyrene, Polyethylene Blend: The Effect of a Compatibilizer

The mixing of polymers is an important process in the polymer industry since, by combining the strength of different polymers through blending, new products with desirable physical properties can be produced [2]. FT-IR imaging with a micro ATR objective has been used to study the effect of a compatibilizer on the mixing of two immiscible polymers, namely polystyrene (PS) and low-density polyethylene (LDPE). The compatibilizer used in this study is a triblock copolymer of polystyrene-*b*-poly(ethylene-butylene)-*b*-polystyrene (SEBS). The blends are prepared by using a microextruder that allows small amounts of the materials to be blended [2]; this is an important point, as a major advantage of FT-IR imaging with the micro ATR objective is the minimal sample preparation. The sampling pathlength is independent of the sample thickness, such that there is no need to perform microtoming. The two polymers can easily be characterized by their specific absorption bands at 1492 cm^{-1} and 1450 cm^{-1} for PS, and the band at 1466 cm^{-1} for LDPE.

Two batches of PS/LDPE blend, one containing 5% SEBS and the other without compatibilizer, were produced. The FT-IR images of both blends were subsequently generated by plotting the distribution of the integrated absorbance of the corresponding spectral bands of each component with a carefully selected baseline; the integral values were then plotted across the imaged area. The results (see Figure 10.8) showed the image of PS distribution to be complementary to that of PE distribution, indicating that a good contact had been established between the sample and the Ge ATR crystal. In the absence of the compatibilizer, the blend exhibited a large segregation of the LDPE and PS, whereas the images of the blend with 5 wt% compatibilizer showed a more disperse-type structure. The PS domains, which ranged between 5 and 15 μm in size, were seen to be dispersed within the LDPE matrix. It is important to note here that the small PS domains could only be revealed with sufficient spatial resolving power, and that micro ATR-FT-IR imaging represented the most suitable method for imaging this type of sample [2].

10.4
Applications of ATR-FT-IR Imaging in the Pharmaceutical Sciences

10.4.1
Imaging of Compacted Tablets

The ATR-FT-IR method is particularly suitable for the spectroscopic analysis of pharmaceutical tablets, mainly due to the minimal sample preparation required and the possibility of obtaining quantitative chemical information from the sample. Such advantages are important with this type of sample, because it is difficult to microtome a tablet into the suitable thicknesses (usually <10 μm) that are often needed for transmission studies. The diffuse-reflection technique is also often very
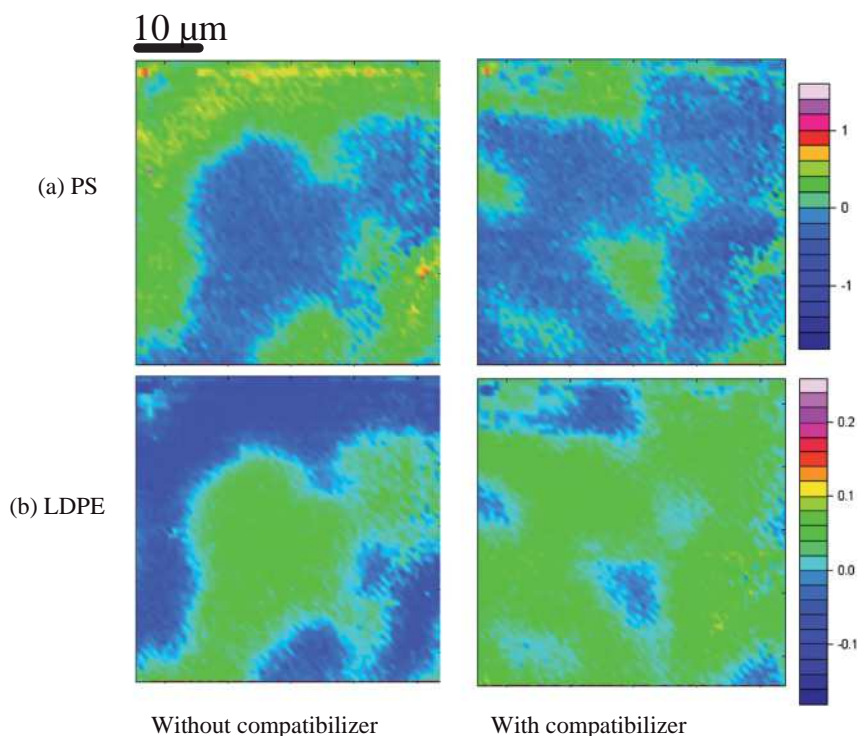
Figure 10.8 ATR-FT-IR images showing the distribution of the absorbance band of (a) PE and (b) LDPE with and without compatibilizer.

difficult to calibrate for quantitative analysis. Hence, ATR-FT-IR imaging has become a very useful tool for studying the distribution of different components within compacted tablets [35, 54, 57–61].

Typically, the contact area of the ATR crystal is circular, with a diameter in the order of 100 μm. Such an area is small enough to establish, very easily, a homogeneous and intimate contact between the ATR crystal and the tablet. To test the procedure, a model tablet containing approximately 3 wt% caffeine in a matrix of starch and hydroxypropylmethylcellulose (HPMC), in a ratio of about 4:6, was compacted and imaged using the micro ATR method; the results are shown in Figure 10.9. The distribution of starch complemented that of the HPMC, supporting the assumption that a good contact had been formed between the crystal and the tablet. The images using a micro ATR approach revealed in great detail how the different components were distributed in the tablet. For example, caffeine particles of less than a few micrometers could be easily detected, although the images were actually somewhat misleading as to the amount of starch and HPMC that existed in the tablet, due to the relatively small sampling volume used for the imaging measurements. Several images at different locations of the sample were

required in order to obtain results that were statistically significant, assuming that the determination of the amounts of each component was the objective of the study. Alternatively, a larger area of the sample could be measured by using different optical arrangements. In order to image with a larger FOV, the shape of the tablet is an important issue. Tablets manufactured in the pharmaceutical industry often have curved surfaces to avoid chipping during the various stages of processing and transportation, but this curvature limits the size of the image that can be recorded in a single measurement. Compressing the tablet, by applying pressure, may achieve a good contact over a larger surface area, without greatly altering the original distribution of the different components, but will risk fracturing the tablet during the measurements. Another approach would be to compact the tablet directly onto the measuring ATR crystal surface and to perform the measurements *in situ*; this approach is shown schematically in Figure 10.10.

The latter approach enables measurement of the compacted tablet during and after the process of compaction, and can be used to evaluate the effect of pressure on the distribution of the different components and the density of the tablet [60]. The *in situ* compaction study is only possible by using hard ATR crystals, due to the high compressive force used for tablet compaction. Consequently, diamond is the material of choice here, and use of the diamond ATR accessory to obtain ATR-FT-IR images of compacted tablets has been demonstrated previously [35]. ATR-FT-IR images of a model pharmaceutical formulation containing
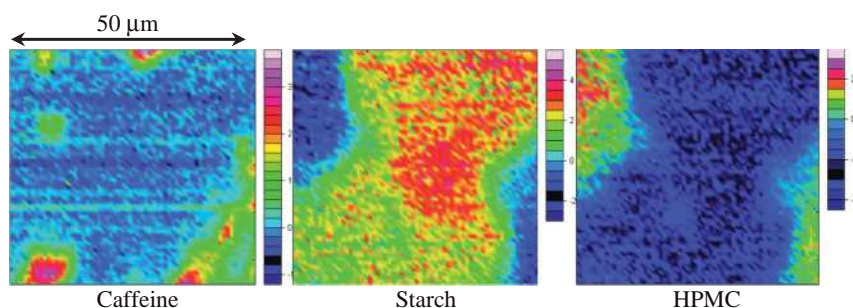
Figure 10.9 Micro ATR-FT-IR images of a tablet showing the distribution of caffeine, starch and HPMC.
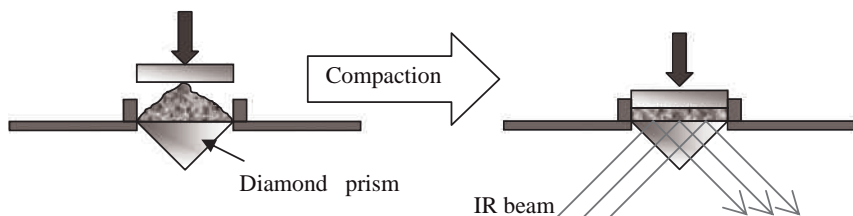
Figure 10.10 Schematic diagram showing the idea of in situ imaging of tablet compaction using a diamond ATR accessory.

820 μm
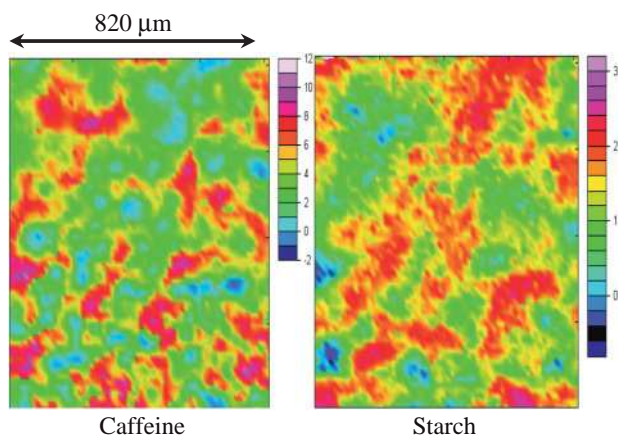
Caffeine   Starch

Figure 10.11 ATR-FT-IR images of a tablet with two components compacted directly on the surface of the diamond crystal in the ATR accessory.

approximately 56 wt% starch and 44 wt% caffeine, compacted and measured *in situ* on the diamond ATR accessory, are shown in Figure 10.11. The results showed that images with a larger FOV better represented the actual composition of the tablet.

10.4.2
ATR-FT-IR Imaging of Tablet Dissolution

An understanding of the mechanism of drug release from a pharmaceutical for-mulation is important for the safe and effective design of tablets and pharmaceuti-cal formulations. ATR-FT-IR spectroscopic imaging has been shown to be a valuable asset in such studies, and has allowed an insight to be gained into many processes, such as the polymorphism of drugs [14, 18, 62], polymer swelling [63], the effect of pH of the dissolution medium on drug release [59], the effect of drug loading and sample preparation methods [54, 64].

Apart from an ability to acquire thousands of IR spectra simultaneously within a matter of seconds, thus allowing dynamic systems to be studied for FT-IR imaging with the FPA detector [14, 22, 30], this type of study is not only made possible by the ATR approach but also allows the study of samples within an aqueous environment. To perform the same experiment using the transmission approach represents a major challenge, due to the very strong absorption of water in the mid-IR region. Previous attempts at transmission-mode measurements have required the use of deuterated water and a very thin spacer [65]. Hence, the ATR approach, with its advantage of a sample thickness that is independent of the pathlength and a small depth of penetration, allows the dissolution of pharmaceu-tical formulations (including tablets in water) to be studied much more easily [14].

This is achieved by visualizing the complex process of dissolution that leads to the distribution and morphological changes of the different components in the formulation, as a function of space and time. A large FOV would be favorable for this type of study as it would provide the opportunity to study dissolved substances at some distance from the original tablet. However, a good spatial resolution is also desirable in order to detect small changes in the tablet, or the formation of small crystallites [14, 62]. Subsequently, this led to the development of the applications of diamond ATR imaging and ZnSe ATR imaging for dissolution studies. These two approaches are complementary in terms of their different FOVs and spatial resolutions, as summarized in Table 10.1. A schematic representation of the dissolution set-up is shown in Figure 10.12.

One important aspect of this type of dissolution approach is that a good contact between the crystal surface and the sample is essential, not only for the imaging of the tablet or pharmaceutical formulation but also to ensure that water penetrates into the sample only from the side of the tablet. This is especially important when mathematical modeling of the dissolution process is compared with experimental data. When using the diamond ATR approach, the tablet is pressed onto the diamond, and hence the leakage of water between the diamond surface and the tablet is not expected [66].

An innovative approach to studying drug release, using a specially designed dissolution cell fitted onto a diamond ATR accessory and which allowed controlled compaction of the tablet and monitoring of the dissolution of the same tablet *in situ*, has been demonstrated previously [57]. When a ZnSe crystal was used for the imaging with a larger FOV, the softness of the crystal would not allow a high pressure to be applied. Formulations which are produced by dissolving the drug in a molten polymer matrix may be prepared directly onto the ZnSe crystal surface, provided that the polymer matrix has a low melting point. This approach has been successfully applied to study the dissolution of PEG-based formulations [14, 64]. For matrices with a higher melting point (e.g., HPMC), it has been shown that swelling of the polymer at the tablet edge upon contact with water prevented undesirable water ingress from the top or bottom of the tablet into the interfacial
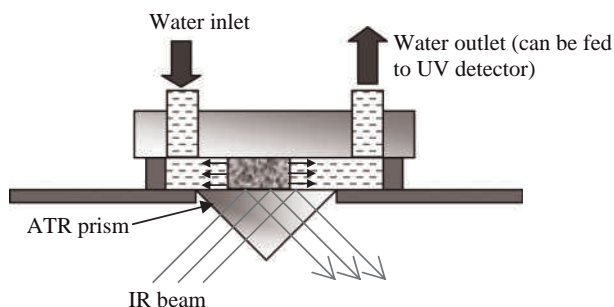
Figure 10.12 Schematic diagram of drug dissolution study using the ATR-FT-IR imaging approach.

area with the ATR crystal [63]. The important feature of both, the diamond and ZnSe ATR dissolution cells, was the introduction of flow around the tablet in the cell, as this helped to prevent saturation of the solution [54, 64]. The effluent stream may be examined using an external UV-visible detector, thereby obtaining results similar to those of standard dissolution tests reported in the United States Pharmacopeia (USP).

The results of a typical dissolution study for a model pharmaceutical formulation are shown in Figure 10.13. Here, PEG was used as the model carrier matrix, and nicotinamide as the model drug. The effect of different polymer molecular weights (PEG 35 000 and PEG 8000) on drug release from a 50% nicotinamide tablet was investigated using the ATR-FT-IR method, fitted with the medium-sized ZnSe ATR accessory [64]. Nicotinamide, which is highly water-soluble, would be released when the polymer dissolved, and consequently the release rate would be controlled by the polymer dissolution rate. The images showed that the total drug release time with PEG 35 000 as carrier was almost double that when PEG 8000
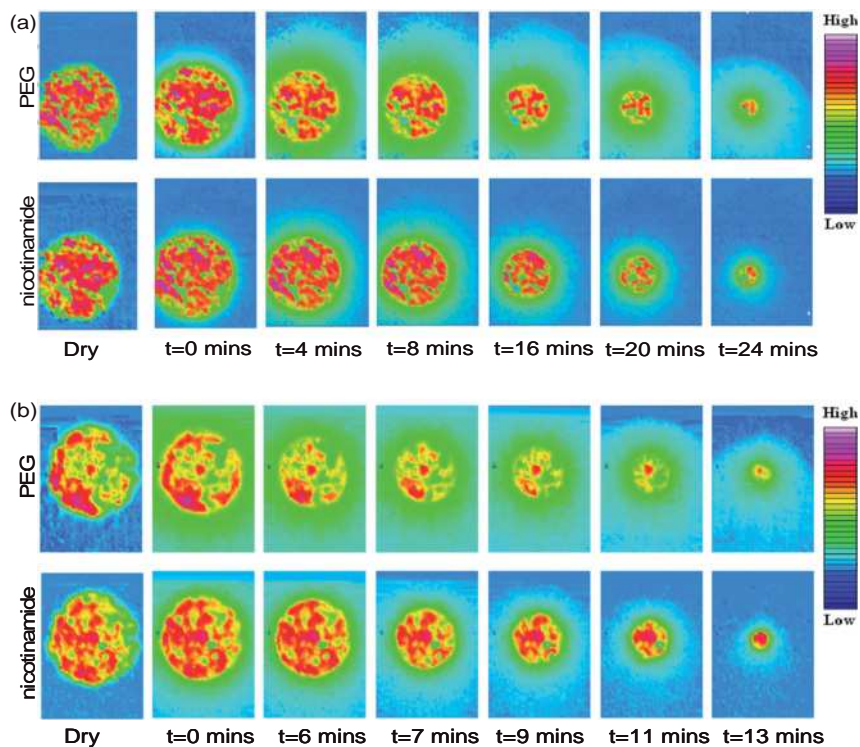
Figure 10.13 ATR-FT-IR images showing distribution of PEG (top row) and nicotinamide (bottom row) through dissolution as a function of time for 50% nicotinamide tablet with (a) PEG 35000 and (b) PEG 8000. Image size is circa $3.8 \times 5.3 \, mm^2$.

was used. On contacting the water, the polymer swelled but the polymer chains remained entangled, thus offering a degree of impedance to drug dissolution into the surrounding water. But, as water accumulated in the polymer, the chains disentangled and the polymer dissolved. The lower-molecular-weight PEG had a shorter polymer chain which could more easily disentangle and thus dissolve more rapidly. These results showed that, together with the chemical and spatial information provided by ATR-FT-IR spectroscopic imaging, complex processes that affect overall drug release could be better understood. The most recent applications of the diamond ATR accessory have included the simultaneous imaging of tablet dissolution with optical photography and ATR imaging [67] and combined ATR imaging and X-ray microtomography of compacted pharmaceutical tablets [61].

10.4.3
High-Throughput Studies with ATR-FT-IR Imaging

Recent research studies have demonstrated the possibility of applying chemical imaging in the ATR mode to the HT analysis of pharmaceutical formulations [18, 33, 68, 69]. It should be noted here that both FT-IR mapping [70, 71] and Raman spectroscopic mapping approaches may also be used in HT applications. However, the use of these mapping approaches means that measurements of all samples are not performed simultaneously – which is the key advantage of the FT-IR imaging approach. The mapping method would also not be suitable for the simultaneous analysis of many samples under a controlled environment. Thus, the use of ATR-FT-IR imaging would be superior to other mapping techniques when applied to HT analysis.

A major problem with the use of FT-IR imaging when studying many solid samples might be that of having to prepare many samples with small, but precise, thickness (thick samples would absorb too much IR light). Possible variations in the pathlength may also affect the quantitative data. Consequently, ATR-FT-IR imaging would represent a suitable approach in the HT arena as it provides a highly reproducible, small pathlength, and requires minimal sample preparation. Today, HT studies of the behavior of pharmaceutical formulations under different humidities are conducted not only to assist in the design of tablets in terms of their drug release, but also to identify ways of extending the shelf life of pharmaceuticals.

This was successfully achieved using a drop-on-demand device by preparing arrays of micro-drop samples directly on the surface of the ATR crystal. The development of macro ATR-FT-IR imaging has allowed the simultaneous study of more than 100 samples deposited on the surface of the ATR crystal, within a controlled environment. By using this approach, it has been possible to obtain 'chemical snapshots' from a spatially defined array of many different polymer/drug formulations, under identical conditions. This HT approach has provided information with regards to a specific weight fraction of nifedipine in PEG, which should not be exceeded in the formulation in order to avoid crystallization of the active agent [18]. This method provides a direct measurement of the material properties for

HT formulation design and optimization. The simultaneous response (water sorption, crystallization, etc.) of the array of formulations to environmental parameters was studied.

A novel ATR accessory with an expanded FOV has also been designed and applied to obtain, simultaneously, the IR spectra of more than 150 miniature samples. In principle, this approach enables the measurement of up to 1024 samples [33]. The introduction of this new accessory with an expanded FOV provided the opportunity of combining ATR-FT-IR spectroscopic imaging with a multichannel grid that allowed the simultaneous imaging of the dissolution of several different formulations. PEGs with different molecular weights, with or without the addition of ibuprofen, have been used as model pharmaceutical formulations, and chemical imaging of the simultaneous dissolution of five formulations of PEG/ibuprofen has been demonstrated. A direct comparison between these different formulations, under identical conditions, was made possible by using this imaging approach. The use of a PDMS grid to serve as sample support plate has also been realized; the illustration in Figure 10.14 shows a PDMS grid prepared for the simultaneous imaging of many liquid samples.

Despite the challenges of using FT-IR imaging in transmission for the HT analysis of pharmaceutical formulations, a novel approach which allowed macro FT-IR imaging in transmission of samples under a controlled environment has also been demonstrated [69, 72]. This approach required the construction of an optical accessory that enables the measurement of samples placed in a horizontal position in the macro chamber of the imaging system. This accessory expands the range of possible applications of macro FT-IR imaging in studies of samples under controlled environments. A combination of this new accessory with a controlled humidity cell provided the opportunity of obtaining chemical images of the large areas of samples under controlled humidity. In this study, the approach was
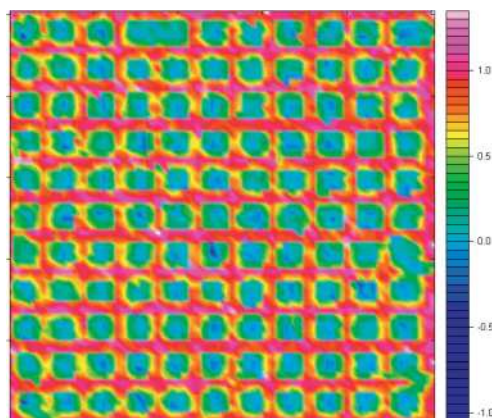
Figure 10.14 ATR-FT-IR image of the grid made of PDMS containing the wells for 121 samples. The red lines show the walls of the PDMS grid.

applied to study the effect of humidity on the polymorphic transitions of a thin film of amorphous nifedipine [72]. It has been shown that the exposure nifedipine to the experimental conditions for 4 h resulted in its transformation from an amorphous to a β-crystalline form, while further exposure (several hours) resulted in conversion of the β form to the α form. It has also been shown, using HT FT-IR transmission imaging, that the crystallization of a series of amorphous drugs could be monitored *in situ* simultaneously [69]; this was achieved using a 128×128 FPA IR detector rather than a 64×64 array detector. The effect of sample thickness on the analysis of the imaging results was addressed by using a different definition of the imaging criteria, based on the wavenumber position of characteristic vibrational bands rather than their absorbance, to create images. The thickness-independent images were obtained by plotting the distribution of the wavenumber corresponding to the peak maximum of the $\nu(N—H)$ vibrational mode, which is sensitive to formation of the various crystalline polymorphs of the studied drugs [69]. Such chemical images enable the spectra of different polymorphs to be extracted and analyzed independently, without the need for spectral subtraction.

Macro ATR-FT-IR approach included the imaging of many different pharmaceutical formulations under a controlled environment, as well as simultaneous studies of the dissolution of several formulations in separate microchannels [33]. With exciting research opportunities existing with the possible combination of microfluidics devices and chemical imaging (Figure 10.15), this approach could serve as a new microfluidics platform with a powerful chemical imaging detection method [73]. The use of chemical imaging offered by ATR-FT-IR imaging could allow the simultaneous analysis of fluid composition as a function of spatial position, to provide a better understanding of the dynamic properties of reactive systems. Both, chemical and quantitative analysis of dynamic systems will surely play important roles in the further development of microfluidics. Moreover, chemical imaging will enhance the ability to utilize very small amounts of materials and fluids for new technologies, because it is possible to obtain 'chemical snapshots' from microarrays of samples or multichannel microsystems [33] for rapid process
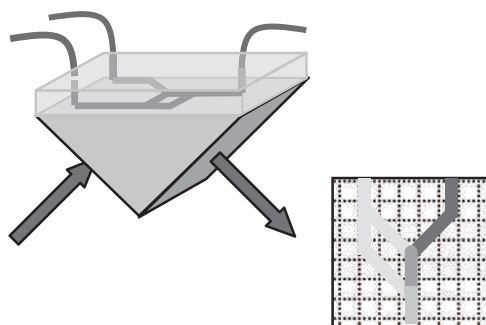
Figure 10.15 Schematic presentation of ATR imaging combined with a microfluidics device for multi-channel studies.

control and analysis. Separations using microfluidics are also set to benefit from *in situ* chemical imaging analysis with IR array detectors. This approach is also the first example of the application of spectroscopic imaging to microfluidics, and may broaden its future use in miniaturized HT devices [73].

Currently, most microfluidics devices are constructed from polymers, steel, glass or silicon. The devices made from silicon are relatively easy to fabricate, and have been used to analyze flow regions in microfluidics, although at present the chemical and physical processes in these devices are characterized using conventional optical microscopy. In combination with chemical imaging, this will surely open a range of new opportunities for the use of devices engineered from Si or Ge. As an example, Si-based microchemical systems have been recently developed by Jensen [74], with potential use in the chemical synthesis of nanoparticles or in the high-temperature conversion of hydrocarbons to hydrogen. The combination of such devices with ATR-FT-IR imaging will lead to opportunities for the development of a new technology for microreactors and process intensification with unprecedented chemical specificity. There is also clear potential for the application of this new approach to proteomics and drug discovery, notably in areas of protein separation and crystallization, and the advantages of FT-IR imaging in the ATR mode to analyze aqueous solutions will undoubtedly be explored in these applications [73].

10.5
ATR-FT-IR Imaging for Forensic Applications

10.5.1
Detection of Trace Materials

For a homogeneous sample, the detection limit of a system is defined by the SNR of the measurement. As a rule of thumb, the SNR should not be less than 3 if the signal corresponding to a particular substance is considered as being 'detected'. However, for a heterogeneous material the detection limit of a system, apart from being a function of the SNR, is also determined by the sample volume that is being measured. Thus, a small sample volume would enhance the signal and hence improve the detection limits; this situation is illustrated schematically in Figure 10.16.

Large sampling volume, concentration of dark grey dot (the signal) = area of dark grey dot/area of circle ~ 0

Small sampling volume, concentration of dark grey dot (the signal) = area of dark grey dot/area of circle = 1
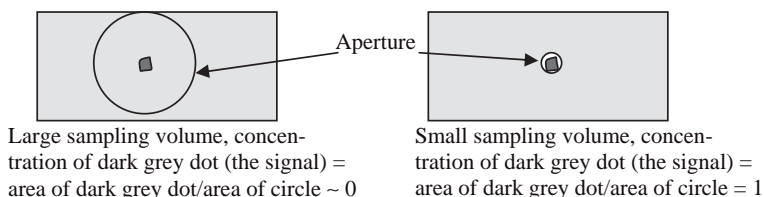
Figure 10.16 Schematic diagram demonstrating how the signal of the same sample may be enhanced by choosing a different sampling volume.

Although the signal is increased by decreasing the sampling volume, the chance of detection is decreased. The reduced aperture also restricts the amount of light reaching the detector, which increases the noise level in the measurement. Fast imaging methods without an aperture, such as the use of a FPA detector, will, therefore, provide the opportunity to improve the detection limits for heterogeneous materials, without long measurement times. A comparison of the detection limit between two FT-IR spectroscopic systems – one using a single-element detector and another using an FPA detector – has shown that, when applied to a heterogeneous sample, the FPA system has a significantly better detection limit than the single-element detector system [37]. This enhancement in detection limit when comparing single-element detectors to array detectors applies to all imaging methods, and is particularly important for the detection of trace materials in forensic investigations. The ease of sample preparation, together with the power of FT-IR spectroscopy in material characterization, has led ATR-FT-IR imaging becoming a valuable tool in many applications, notably in forensic studies [75, 76]. A clear example of this application is the detection of small particle residues left on the surface of a person's finger after they have handled some drug particles. The resultant images (see Figure 10.17) demonstrate the power of this imaging technique for detecting a single small particle of drug trapped between the ridges of the fingerprint. The size of this particle was estimated at a few hundred micrometers, while the spectrum extracted from the particle identified it as ibuprofen.

This approach was extended to combine the 'tape-lifting' method with ATR-FT-IR imaging when particles were collected from different surfaces, using adhesive tape [76]. The most recent exciting examples of the application of ATR-FT-IR imaging to samples of forensic interest have included the chemical imaging of latent fingerprint residues [75, 77] rather than imaging of the surface of a finger (as described above) or the imaging of developed fingermarks [78]. FT-IR imaging in reflection has also been applied to image latent fingermarks [79]. The chemical
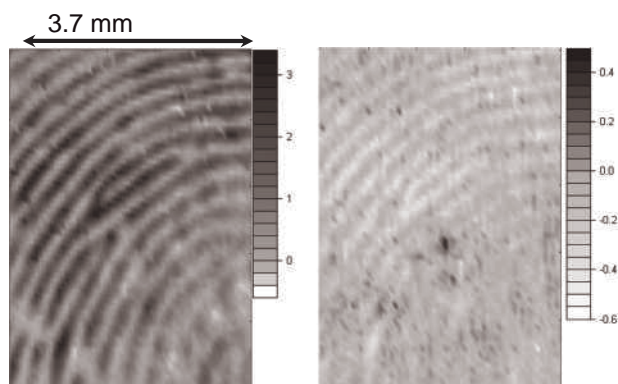
Figure 10.17 ATR-FT-IR image of the finger surface. The image on the left represents the protein distribution while the image on the right represents the ibuprofen distribution.

images of the fingerprints also provide valuable information to the forensic scientist regarding possible chemical changes that have occurred in fingerprint residues as a function of time [77]. Here, fingerprint residues left directly on the surface of the ATR crystal were analyzed with ATR-FT-IR imaging as a function of temperature; this is especially important for understanding the evolution of these residues at elevated temperatures [77].

10.5.2
Imaging of Counterfeit Tablets

The chemical imaging of pharmaceutical tablets is important not only in optimizing the production of specific pharmaceutical products, but also in differentiating between genuine and counterfeit products. Today, the prevention of counterfeit tablets is set to benefit from the chemical specificity of the FT-IR imaging approach, while in ATR mode it will offer a nondestructive approach for the study of such samples, without the need either to stain or to solubilize them. The counterfeiting of drugs and medicines presents a very serious threat to public health, an example being the spread of counterfeit artesunate antimalarial tablets, which is widespread in some countries. To prevent this situation, the counterfeit tablets must be identified and analyzed to determine their origin, and a combined ATR-FT-IR imaging and desorption electrospray-ionization linear ion-trap mass-spectrometry system was used recently in this role [41]. The nondestructive approach of ATR-FT-IR imaging has also been complemented with highly sensitive mass spectrometry, while micro ATR imaging with a high spatial resolution has been used not only to analyze localized area of counterfeit tablets but also to show that they contain undesirable contaminants [41]. Macro ATR-FT-IR imaging using a diamond accessory was also combined with spatially offset Raman spectroscopy to analyze bulk and surface compositions of counterfeit antimalarial tablets [80]. These investigations successfully combined the applications of ATR-FT-IR imaging with mass-spectrometry and Raman spectroscopy, and have demonstrated their potential for forensic investigations of counterfeit medicines [41, 80].

10.6
Conclusions and Outlook

In this chapter, we have presented some of the recent developments and applications of ATR-FT-IR imaging to pharmaceutical samples and polymeric materials. The use of both micro and macro modes in ATR-FT-IR imaging has been discussed. Imaging in the ATR mode may be very versatile, and offers imaging with different spatial resolution and different fields of view. It is important to remember that ATR imaging provides information only about that layer of the sample which is adjacent to the surface of the ATR crystal, and that the thickness of this layer may range from a fraction of a micrometer to several micrometers. However, the opportunity exists to obtain chemical images from layers of different thickness in

this range, by using an accessory with variable angles of incidence. This allows one to combine chemical imaging with depth profiling, which is important for heterogeneous structures, such as biomedical materials. The spatial resolution in the z-direction, which is perpendicular to the plane of the imaged area, is not limited by diffraction but rather is determined by the depth of penetration, which can be changed by variations in the angles of incidence. This has provided the opportunity of imaging nanostructures in the z-direction, which is important for nanocomposites and other materials. As demonstrated in this chapter, the main advantage of chemical imaging using FPA detectors lies in the study of dynamic systems, such as diffusion and dissolution. Thus, significant potential exists in the application of FT-IR imaging, and in particular of ATR-FT-IR imaging, to the HT analysis of many samples. ATR-FT-IR imaging within a controlled environment is beneficial for studying many samples, including pharmaceutical formulations, while systems containing water can easily be imaged by using the ATR mode. The most recent examples of such applications include research into tissue engineering, which is set to benefit hugely from the use of ATR-FT-IR imaging.

The enhanced spatial resolution of micro ATR-FT-IR imaging will benefit many areas of research, ranging from polymeric materials to biomedical and forensic sciences. Recent examples include the successful application of micro ATR imaging to study objects of cultural heritage [40, 81]. The development of applications of imaging with a single reflection diamond accessory will continue, due to an excellent combination of the achieved spatial resolution with a relatively large area that is imaged simultaneously. The examples of *in situ* imaging of tablet compaction and dissolution presented in this chapter show that significant potential exists for innovative experiments in imaging, without the need for a microscope using a diamond accessory. Further applications of ATR-FT-IR imaging will benefit from combinations with other imaging methods, such as optical photography in macro imaging [67], Raman microscopy and X-ray microtomography [61].

References

1 Harrick, N.J. (1976) *Internal Reflection Spectroscopy*, John Wiley & Sons, Inc., New York.

2 Kazarian, S.G. and Higgins, J.S. (2002) *Chem. Ind.*, May (10), 21–3.

3 Gupper, A., Wilhelm, P., Schmied, M., Kazarian, S.G., Chan, K.L.A. and Reussner, J. (2002) *Appl. Spectrosc.*, **56**, 1515–23.

4 Kazarian, S.G. and Chan, K.L.A. (2006) *Prog. Colloid Polym. Sci.*, **132**, 1–6.

5 Burka, E.M. and Curbelo, R. (2000) US Patent, 6141100, Imaging ATR spectrometer.

6 Sommer, A.J., Tisinger, L.G., Marcott, C. and Story, G.M. (2001) *Appl. Spectrosc.*, **55**, 252–6.

7 Chan, K.L.A. and Kazarian, S.G. (2003) *Appl. Spectrosc.*, **57**, 381–9.

8 Esaki, Y., Nakai, K. and Araga, T. (1993) *Bunseki Kagaku*, **42**, 127–32.

9 Esaki, Y., Yokokawa, K. and Araga, T. (1993) US patent 5216244.

10 Lewis, L.L. and Sommer, A.J. (2000) *Appl. Spectrosc.*, **54**, 324–30.

11 Patterson, B.M. and Havrilla, G.J. (2006) *Appl. Spectrosc.*, **60**, 1256–66.

12 Patterson, B.M., Havrilla, G.J., Marcott, C. and Story, G.M. (2007) *Appl. Spectrosc.*, **61**, 1147–52.

13 Koenig, J. (2002) *Adv. Mater.*, **14**, 457–60.

14 Kazarian, S.G. and Chan, K.L.A. (2003) *Macromolecules*, **36**, 9866–72.

15 Snively, C.M., Oskarsdottir, G. and Lauterbach, J. (2001) *Catal. Today*, **67**, 357–68.

16 Snively, C.M., Oskarsdottir, G. and Lauterbach, J. (2001) *Angew. Chem. Int. Ed.*, **40**, 3028–30.

17 Kubanek, P., Busch, O., Thomson, S., Schmidt, H.W. and Schuth, F. (2004) *J. Comb. Chem.*, **6**, 420–5.

18 Chan, K.L.A. and Kazarian, S.G. (2005) *J. Comb. Chem.*, **7**, 185–9.

19 Colley, C.S., Kazarian, S.G., Weinberg, P.D. and Lever, M.J. (2004) *Biopolymers*, **74**, 328–35.

20 Randle, W.L., Cha, J.M., Hwang, Y.S., Chan, K.L.A., Kazarian, S.G., Polak, J.M. and Mantalaris, A. (2007) *Tissue Eng.*, **13**, 2957–70.

21 Dehghani, F., Annabi, N., Valtchev, P., Mithieux, S.M., Weiss, A.S., Kazarian, S.G. and Tay, F.H. (2008) *Biomacromolecules*, **9**, 1100–5.

22 Kazarian, S.G. and Chan, K.L.A. (2006) *Biochim. Biophys. Acta*, **1758**, 858–67.

23 Steiner, G., Tunc, S., Maitz, M. and Salzer, R. (2007) *Anal. Chem.*, **79**, 1311–16.

24 Snively, C.M. and Koenig, J.L. (1999) *J. Polym. Sci. B. Polym. Phys.*, **37**, 2261–8.

25 Ribar, T., Bhargava, R. and Koenig, J.L. (2000) *Macromolecules*, **33**, 8842.

26 Gupper, A., Chan, K.L.A. and Kazarian, S.G. (2004) *Macromolecules*, **37**, 6498–503.

27 Gupper, A. and Kazarian, S.G. (2005) *Macromolecules*, **38**, 2327–32.

28 Artyushkova, K., Wall, B., Koenig, J.L. and Fulghum, J.E. (2001) *J. Vac. Sci. Technol. A*, **19**, 2791–9.

29 Bhargava, R., Wang, S.-Q. and Koenig, J.L. (2003) *Adv. Polym. Sci.*, **163**, 137–91.

30 Koenig, J.L. and Bobiak, J.P. (2007) *Macromol. Mater. Eng.*, **292**, 801–16.

31 Miller-Chou, B.A. and Koenig, J.L. (2003) *Prog. Polym. Sci.*, **28**, 1223–70.

32 Biswal, D. and Hilt, J.Z. (2006) *Polymer*, **47**, 7355–60.

33 Chan, K.L.A. and Kazarian, S.G. (2006) *Lab Chip.*, **6**, 864–70.

34 Chan, K.L.A. and Kazarian, S.G. (2007) *Appl. Spectrosc.*, **61**, 48–54.

35 Chan, K.L.A., Hammond, S.V. and Kazarian, S.G. (2003) *Anal. Chem.*, **75**, 2140–7.

36 Dumas, P., Jamin, N., Teillaud, J.L., Miller, L.M. and Beccard, B. (2004) *Faraday Discuss.*, **126**, 289–302.

37 Chan, K.L.A. and Kazarian, S.G. (2006) *Analyst*, **131**, 126–31.

38 Kazarian, S.G., Chan, K.L.A., Maquetb, V. and Boccaccini, A.R. (2004) *Biomaterials*, **25**, 3931–8.

39 Chan, K.L.A., Kazarian, S.G., Mavraki, A. and Williams, D.R. (2005) *Appl. Spectrosc.*, **59**, 149–55.

40 Ricci, C., Bloxham, S. and Kazarian, S.G. (2007) *J. Cultur. Herit.*, **8**, 387–95.

41 Ricci, C., Nyadong, L., Fernandez, F.M., Newton, P.N. and Kazarian, S.G. (2007) *Anal. Bioanal. Chem.*, **387**, 551–9.

42 Goodall, R.A., Hall, J., Sharer, R.J., Trazler, L., Rintoul, L. and Fredericks, P.M. (2008) *Appl. Spectrosc.*, **62**, 10–6.

43 Everall, N.J. and Bibby, A. (1997) *Appl. Spectrosc.*, **51**, 1083–91.

44 Kazarian, S.G., Brantley, N.H. and Eckert, C.A. (1999) *Vib. Spectrosc.*, **19**, 277–83.

45 Kazarian, S.G. and Martirosyan, G.G. (2002) *Int. J. Pharm.*, **232**, 81–90.

46 Kazarian, S.G., Flichy, N.M.B., Coombs, D. and Poulter, G. (2001) *Am. Lab.*, **33** (16), 44–9.

47 Flichy, N.M.B., Kazarian, S.G., Lawrence, C.J. and Briscoe, B.J. (2002) *J. Phys. Chem.*, **106**, 754–9.

48 Kazarian, S.G. and Chan, K.L.A. (2004) *Macromolecules*, **37**, 579–84.,

49 Thomson, G. and Poulter, G. (2006) US Patent 26,1274.

50 Ekgasit, S. and Ishida, H. (1997) *Appl. Spectrosc.*, **51**, 1488–95.

51 Fina, L.J. and Chen, G. (1991) *Vib. Spectrosc.*, **1**, 353–61.

52 Shick, R.A., Koenig, J.L. and Ishida, H. (1993) *Appl. Spectrosc.*, **47**, 1237–44.

53 Kirov, K.R. and Assender, H.E. (2004) *Macromolecules*, **37**, 894–904.,

54 van der Weerd, J. and Kazarian, S.G. (2004) *J. Control Release*, **98**, 295–305.

55 Fleming, O.S., Chan, K.L.A. and Kazarian, S.G. (2006) *Polymer*, **47**, 4649–58.

56 Wessel, E., Heinsohn, G., Schmidt-Lewer-Kuehne, H., Wittern, K.P., Rapp, C. and Siesler, H.W. (2006) *Appl. Spectrosc.*, **60**, 1488–92.

57 van der Weerd, J., Chan, K.L.A. and Kazarian, S.G. (2004) *Vib. Spectrosc.*, **35**, 9–13.

58 Chan, K.L.A., Elkhider, N. and Kazarian, S.G. (2005) *Chem. Eng. Res. Des.*, **83**, 1303–10.

59 van der Weerd, J. and Kazarian, S.G. (2005) *J. Pharm. Sci.*, **94**, 2096–109.

60 Elkhider, N., Chan, K.L.A. and Kazarian, S.G. (2007) *J. Pharm. Sci.*, **96**, 351–60.

61 Wray, P., Kimber, J., Chan, K.L.A. and Kazarian, S.G. (2008) *J. Pharm. Sci.*, **97**, 4269–77.

62 Chan, K.L.A. and Kazarian, S.G. (2004) *Mol. Pharm.*, **1**, 301–5.

63 van der Weerd, J. and Kazarian, S.G. (2004) *Appl. Spectrosc.*, **58**, 1413–19.

64 Kazarian, S.G., Kong, K.W.T., Bajomo, M., Van der Weerd, J. and Chan, K.L.A. (2005) *Food Bioprod. Process.*, **83**, 127–35.

65 Coutts-Lendon, C.A., Wright, N.A., Mieso, E.V. and Koenig, J.L. (2003) *J. Control Release*, **93**, 223–48.

66 van der Weerd, J. and Kazarian, S.G. (2007) *Techniques and Applications of Hyperspectral Image Analysis* (eds H.F. Grahn and P. Geladi), John Wiley & Sons, Ltd, Chichester, pp. 221–60.

67 Kazarian, S.G. and van der Weerd, J. (2008) *Pharm. Res.*, **25**, 853–60.

68 Chan, K.L.A. and Kazarian, S.G. (2006) *J. Comb. Chem.*, **8**, 26–31.

69 Chan, K.L.A., Kazarian, S.G., Vassou, D., Gionis, V. and Chryssikos, G.D. (2007) *Vib. Spectrosc.*, **43**, 221–6.

70 Fernandez, D.C., Bhargava, R., Hewitt, S.M. and Levin, I.W. (2005) *Nat. Biotechnol.*, **23**, 469–74.,

71 Bhargava, R., Fernandez, D.C., Hewitt, S.M. and Levin, I.W. (2006) *Biochim. Biophys. Acta*, **1758**, 830–45.

72 Chan, K.L.A. and Kazarian, S.G. (2006) *Vib. Spectrosc.*, **42**, 130–4.

73 Kazarian, S.G. (2007) *Anal. Bioanal. Chem.*, **388**, 529–32.

74 Jensen, K.F. (2006) *MRS Bull.*, **31**, 101–7.

75 Ricci, C., Bleay, S. and Kazarian, S.G. (2007) *Anal. Chem.*, **79**, 5771–6.

76 Ricci, C., Chan, K.L.A. and Kazarian, S.G. (2006) *Appl. Spectrosc.*, **60**, 1013–21.

77 Ricci, C., Phiriyavityopas, P., Curum, N., Chan, K.L.A., Jickells, S. and Kazarian, S.G. (2007) *Appl. Spectrosc.*, **61**, 514–22.

78 Tahtouh, M., Kalman, J.R., Roux, C., Lennard, C.I. and Reedy, B.J. (2005) *J. Forensic Sci.*, **50**, 64–72.

79 Crane, N.J., Bartick, E.G., Perlman, R.S. and Huffman, S. (2007) *J. Forensic Sci.*, **52**, 48–53.

80 Ricci, C., Eliasson, C., Macleod, N.A., Newton, P.N., Matousek, P. and Kazarian, S.G. (2007) *Anal. Bional. Chem.*, **389**, 1525–32.

81 Spring, M., Ricci, C., Peggie, D. and Kazarian, S.G. (2008) *Anal. Bioanal. Chem.*, **392**, 37–45.

11
Raman Spectral Imaging on Pharmaceutical Products

Eunah Lee

11.1
Overview

Applications of Raman hyperspectral imaging in pharmaceutical products are wide and various. For example, magnesium stearate is a very fine powder that is used as a lubricant in tablet formulation when typically, it is added at a low concentration and tends to spread very thinly. The spatial distribution of magnesium stearate can affect the dissolution rate [1, 2] of tablets, which is an important factor when determining the bioavailability of a formulation. Bulk analysis may not be able to detect the presence of magnesium stearate due to its low concentration; neither can it provide any information on spatial distribution. Likewise, low spatial resolution methods may be unable to detect magnesium stearate due to its small particle size. However, Raman hyperspectral imaging, with its high spatial resolution, is an excellent analytical tool by which to detect the presence and characterize the distribution of magnesium stearate in tablets.

Infrared (IR) hyperspectral imaging, of course, can provide valuable and complementary information to Raman hyperspectral imaging, especially with instruments that combine both Raman and IR microscopy while measuring the sample at the same location [3].

With the increasing popularity of hyperspectral imaging, more and more spectroscopic and spectrometric technologies now offer hyperspectral imaging capabilities. Multimodal hyperspectral imaging, combining complementary technologies, may bring us a step closer to the complete characterization of an unknown sample. Energy-dispersive X-ray fluorescence (EDXRF), which detects elements rather than molecules, is a good example of a complementary technology to molecular spectroscopy such as Raman and IR. For example, Raman hyperspectral imaging can be used to obtain magnesium stearate images, while EDXRF hyperspectral imaging will show magnesium images. When such images are obtained with independent technologies and measured separately, they will verify and confirm each other so as to heighten the credibility of the analysis results. An example of the comparison of Raman and EDXRF hyperspectral imaging is provided later in the chapter.

11.2
Hyperspectral Imaging

11.2.1
Terminologies

Hyperspectral imaging combines spectroscopy (*not* hyperspectroscopy) and microscopy. With continuous improvements in instrumentation, spectroscopy and microscopy aspects begin to mingle more. In fact, commercial instruments are now available that can routinely record three-dimensional (3-D) data, the image and spectral quality of which are comparable to spectroscopy-only or microscopy-only data. This 3-D data – two spatial axes and one spectral axis – is called the hypercube, and the method to record it is referred to as hyperspectral imaging to differentiate it from spectral imaging (cf. Chapter 1). However, the terms of spectral imaging and hyperspectral imaging are often used interchangeably.

Raman hyperspectral imaging uses the Raman microscope to obtain hypercubes, the spectra of which are Raman spectra, or Raman hypercubes. Although multiple hardware approaches are available for obtaining Raman hypercubes, Raman mapping using the point mapping method – that is, recording one spectrum at a time – is still the standard data collection method for Raman hyperspectral imaging. Other methods include Raman line scanning, Raman dual scanning or Raman global imaging [4]. Raman imaging is an abbreviated term of Raman hyperspectral imaging, and refers to any Raman mapping, scanning or imaging method that yields Raman hypercubes. A Raman map is a conventional term for the Raman hypercube, and is more often used. Raman images or Raman chemical images are data processing results of Raman hypercubes, and their contrast must reflect chemical differences, not simply optical or physical differences. The chemical contrast in Raman images or Raman chemical images must be verified with original Raman spectra from Raman hypercubes, and not just loadings, models or principal components.

In this chapter, Raman hyperspectral imaging was performed using the confocal dispersive Raman microscope. Raman maps were recorded in point mapping and dual-scanning modes, with results being given in Raman images, which show spatially resolved chemical information based on Raman spectral analysis and can be projected to further image analysis.

11.2.2
Advantages

The main attraction of hyperspectral imaging is to obtain 'the complete picture' of the sample. It has been reported that particle size or blending quality (spatial distribution characteristics) is as important to the performance of a pharmaceutical product as its chemical composition [5, 6]. Hence, by characterizing both the chemical and spatial composition of the sample, hyperspectral imaging can provide valuable insight that bridges the relationships between processing and perfor-

mance, thus playing an important role in PAT (processing analysis technology) and QbD (quality by design) initiatives.

A hypercube consists of numerous spectra, enabling unsupervised chemometric and statistical analysis. Under the right circumstances, this provides an alternative way to perform quantitative analysis, which requires no calibration set or model development.

Raman hyperspectral imaging inherits all the advantages of Raman spectroscopy, such as a high chemical specificity, high spatial resolution, wide sample ranges and minimum sample preparation. A confocal dispersive Raman microscope allows high resolution (this depends on the samples but better than $2\,\mu m$ under preferable conditions) depth profiling, enabling not only lateral but also axial and volumetric chemical imaging.

In the case of pharmaceutical samples, Raman spectroscopy is sensitive to crystallinity and polymorphism, both of which are important with regards to the bioavailability (and protection of the intellectual property) of active ingredients. With polarized Raman spectroscopy, the orientation and degree of crystalline of molecules are observed, which is important when studying polymers that are used as carriers, in coatings, and for containers. As Raman spectroscopy can be used to measure low-frequency bands ($<400\,cm^{-1}$), inorganic ingredients such as TiO_2 are easily detected. Raman scattering tends to be very effective for aromatic compounds (typical active ingredients), allowing the rapid measurement of active ingredients. Consequently, Raman hyperspectral imaging can be seen as an excellent tool for the molecular characterization for pharmaceutical applications.

11.2.3
Spectra versus Image

One often-neglected aspect of Raman maps is that, ironically, as they are composed of Raman spectra, the quality of the spectra directly affects the quality of the Raman image, while the speed of the spectral measurement affects the speed of Raman mapping.

11.2.3.1 Spectral Intensity and Speed

The intrinsic Raman scattering strengths of different molecules vary widely, easily more than an order of magnitude or more, from one material to the next. Therefore, the speed of mapping, ultimately, is determined by the sample. To demonstrate the impact of the intrinsic spectral intensity on the mapping speed, let us consider three materials of different Raman scattering strengths that require 10 ms, 100 ms and 1 s to achieve the same signal-to-noise ratio (SNR), respectively. The lengths of time to record a Raman map of 10 000 spectra at the same level of SNR for each sample are listed in Table 11.1.

Conversely, if one instrument is more sensitive than another, it will require a shorter acquisition time to achieve the required SNR for the same sample, and so will be faster in operation.

Table 11.1 Net acquisition time to record a Raman map of 10 000 spectra with samples of different Raman scattering strength.

Sample	Net acquisition time per spectrum	Net acquisition time of the map
Weak Raman scattering	1 s	10 000 s = 2 h 46 min 40 s
Medium Raman scattering	100 ms	1000 s = 16 min 40 s
Strong Raman scattering	10 ms	100 s = 1 min 40 s

11.2.3.2 SNR and Image Quality

The SNR in the Raman spectrum is directly correlated to the image quality (i.e., the sharpness of contrast in a chemical image), because the contrast in a chemical image is driven by the spectral differences which are, naturally, clearer in higher than in lower SNR data.

Three Raman maps were recorded on the same acetaminophen (paracetamol) crystal under the same experimental conditions, except for net acquisition times of 100 ms, 1 s and 2 s per spectrum, respectively, to achieve increasing SNR values. Raman images were created by mapping integrated intensities from 1310 to 1350 cm^{-1} of individual spectra (Figure 11.1). In each image, the intensity of the band is color-scaled to red, green or blue; the brighter the color, the higher the intensity. The colored areas, therefore, represent acetaminophen, while the black areas represent its absence. The histogram of each Raman image is created by plotting the integrated intensity versus the number of spectra.

Determining the quality of an image can be performed intuitively. For example, an image is deemed 'better' when sharper edges, smoother faces and more distinctive features can be seen. Qualitatively, as the SNR increases, the edges of crystals in Raman images become sharper and the surfaces smoother. A quantitative assessment of the quality of an image, on the other hand, can be achieved using histograms (further details on producing and interpreting histograms are provided later in the chapter).

All three histograms in Figure 11.1 show two separate populations representing spectra from the acetaminophen crystal and those from the background (denoted in Figure 11.1b). An image is 'good' when there is a separation between two populations, and 'better' when the distance between the two populations is greater. As the SNR increases, the separations between two populations increase, reflecting a heightened contrast in the images. In Figure 11.1a, the centers of the populations are at ~0 (low intensity, black area, background) and at ~43 (high-intensity, red area, acetaminophen). In Figure 11.1b, the center of population for acetaminophen (high-intensity, green area) increases to ~457, while the center of population for background (low-intensity, black area) stays the same. The same trend is maintained in Figure 11.1c, where the center of population for acetaminophen (high-intensity, red area) increases to 920. It is clear, therefore, that a high SNR directly translates to high image quality.

(a)

(b)

Spectra from back-
ground (black area)

Spectra from aceta-
minophen (green area)

(c)
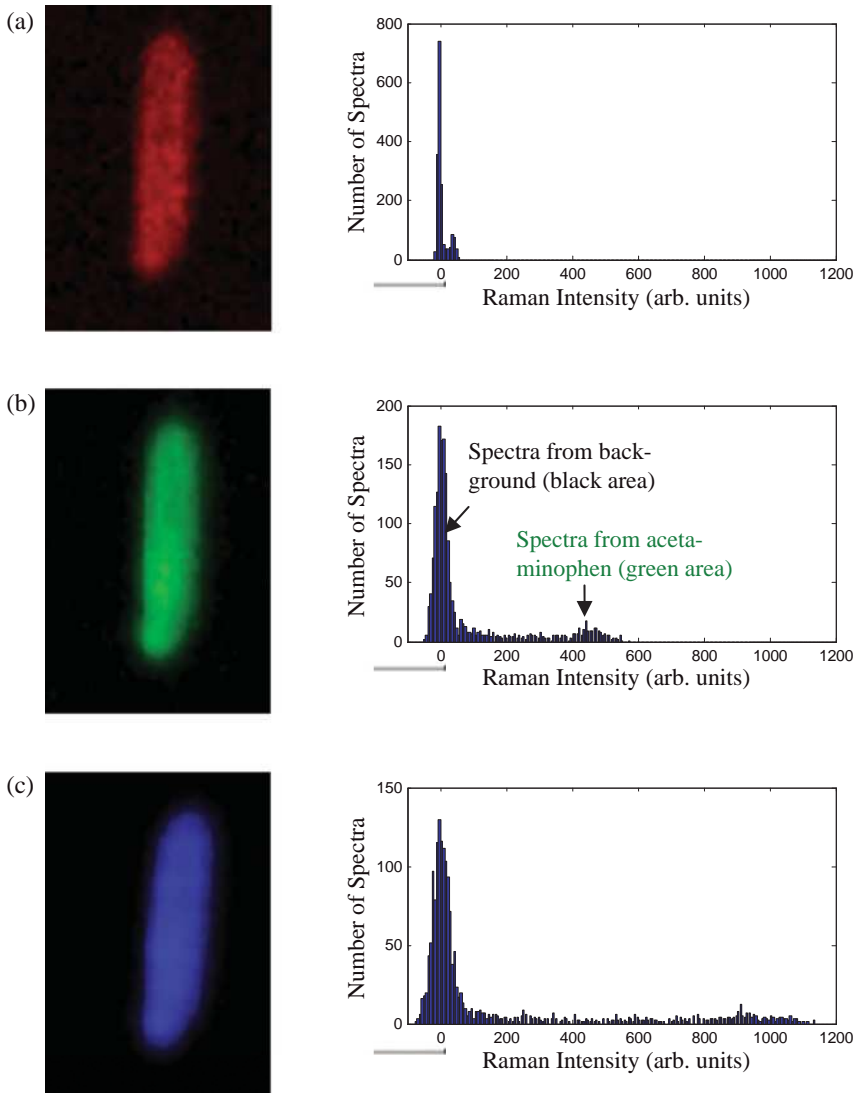
Figure 11.1 Raman images created as integrated intensity
maps (1310–1350 cm⁻¹) from Raman maps of an
acetaminophen crystal recorded at net acquisition times of
(a) 100 ms (red); (b) 1 s (green) and (c) 2 s (blue) per
spectrum Figure 11.2. The histogram of each Raman image
(*x*-axis, Raman intensity in arbitrary units; *y*-axis, number of
spectra) is displayed next to each Raman image.

11.2.3.3 **Spectral Resolution and Detection Limit**

In Raman hyperspectral imaging, the spectral resolution and spectral sampling frequency become factors in determining the detection limit. An example is shown in Figure 11.2. Here, two Raman maps were recorded from the same sample over the same area, using identical system configurations and experimental conditions, except for the grating choices (1800 and 300 grooves mm^{-1}, respectively) to achieve high and low spectral resolutions. Within the spectral range of 1525–1675 cm^{-1}, the Raman map collected with the 1800 grooves mm^{-1} grating has 0.98 cm^{-1} per datum point (an indicator for spectral resolution), whereas the Raman map collected with 300 grooves mm^{-1} grating has 8.5 cm^{-1} per datum point.

Spectra (baseline-corrected and normalized to unit area) from the same spot in high- and low-resolution maps are shown in Figure 11.2. The shoulder band at 1604 cm^{-1} is clearly visible in a spectrum from the high spectral resolution map, but not in a spectrum from the low spectral resolution map. Subsequent unsupervised chemometrics analysis (Modeling, LabSPEC 5; HORIBA Jobin Yvon Inc., Edison, NJ, USA) is performed to produce score images from each data set. As the low-resolution data set cannot distinguish the fourth element (pink areas), the numbers of factors employed were different.
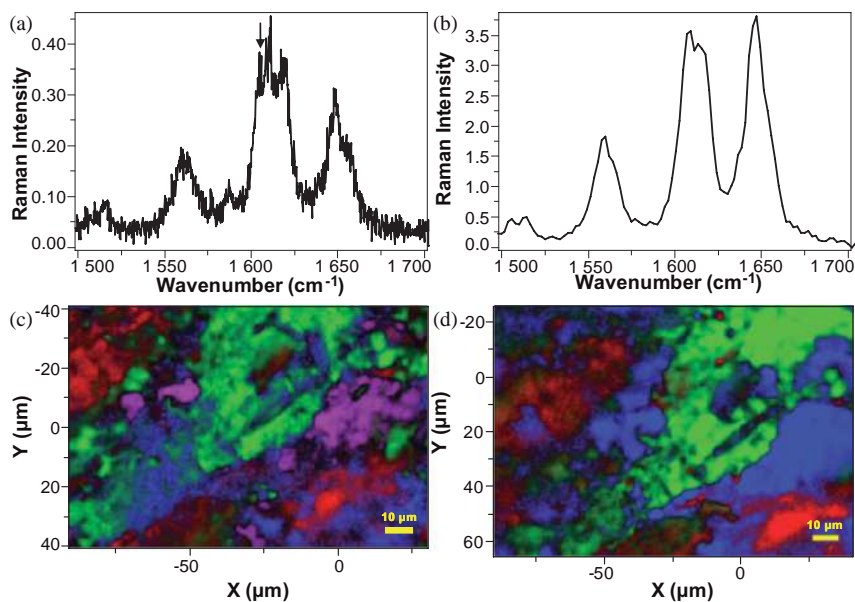
Figure 11.2 Raman spectra measured from the same spot.
(a) With high spectral resolution (grating: 1800 grooves mm^{-1}); (b) With low spectral resolution (grating: 300 grooves mm^{-1}); (c,d) Combined score images of (c) high spectral resolution Raman map with four factors and (d) low spectral resolution Raman map with three factors.

It is important to note that the contrast of an image alone cannot determine the authenticity of a chemical image. For example, Figure 11.2d appears to appear to be 'nicer' (clearer and cleaner interface between different colored areas) than Figure 11.2c. However, as Figure 11.2d fails to capture the fourth component, it is further from the real characteristic of the sample than Figure 11.2c, where all components are identified.

11.2.3.4 Instrumentation

The Raman spectral imaging data were collected with a confocal dispersive Raman microscope (LabRAM HR 800; HORIBA Jobin Yvon Inc.) using Point and DuoScan mapping modes. Data processing was performed with LabSPEC 5 (HORIBA Jobin Yvon Inc.) and ISys 4.1 (Malvern Instruments Ltd, UK). The EDXRF imaging data were collected with XGT-5000 and EMAX-scanning electron microscopy (SEM) (both from HORIBA, Kyoto, Japan).

11.2.4
An Example of Raman Hyperspectral Imaging Analysis: I

An example of Raman hyperspectral imaging analysis on a tablet of a prescription drug, the surface of which had been shaved flat with a razor blade, is shown in Figure 11.3. A multivariate analysis resulted from a Raman map of the tablet, with loadings and score images representing the spatial distributions of the active ingredient (green), calcium carbonate (red), microcrystalline cellulose (blue) and magnesium stearate (pink). The wavelength of the excitation laser was 785 nm, the grating 300 grooves mm^{-1} and the objective lens $50 \times$ [numerical aperture (NA) 0.55]. The mapped area was $70 \times 48 \mu m^2$, and the map was recorded in standard point mapping mode with $1 \mu m$ step, resulting in 3479 ($=71 \times 49$) spectra. The data were normalized to unit area and then subjected to the direct classical least-square algorithm to isolate the four ingredients.

11.3
Empirical Approach to Successful Raman Hyperspectral Imaging

The goal of Raman hyperspectral imaging analysis is to obtain chemical images which provide both chemical and spatial characterization of the sample. In an ideal world, each of the chemical components is identified and its distribution visualized; the analysis results then also provide the statistical and quantitative results.

11.3.1
Spectroscopy

A typical pharmaceutical sample contains both active and inactive ingredients that are combined into a form that can easily be delivered, such as tablets, injection solutions, transdermal patches or implants. Most often, the active ingredients have
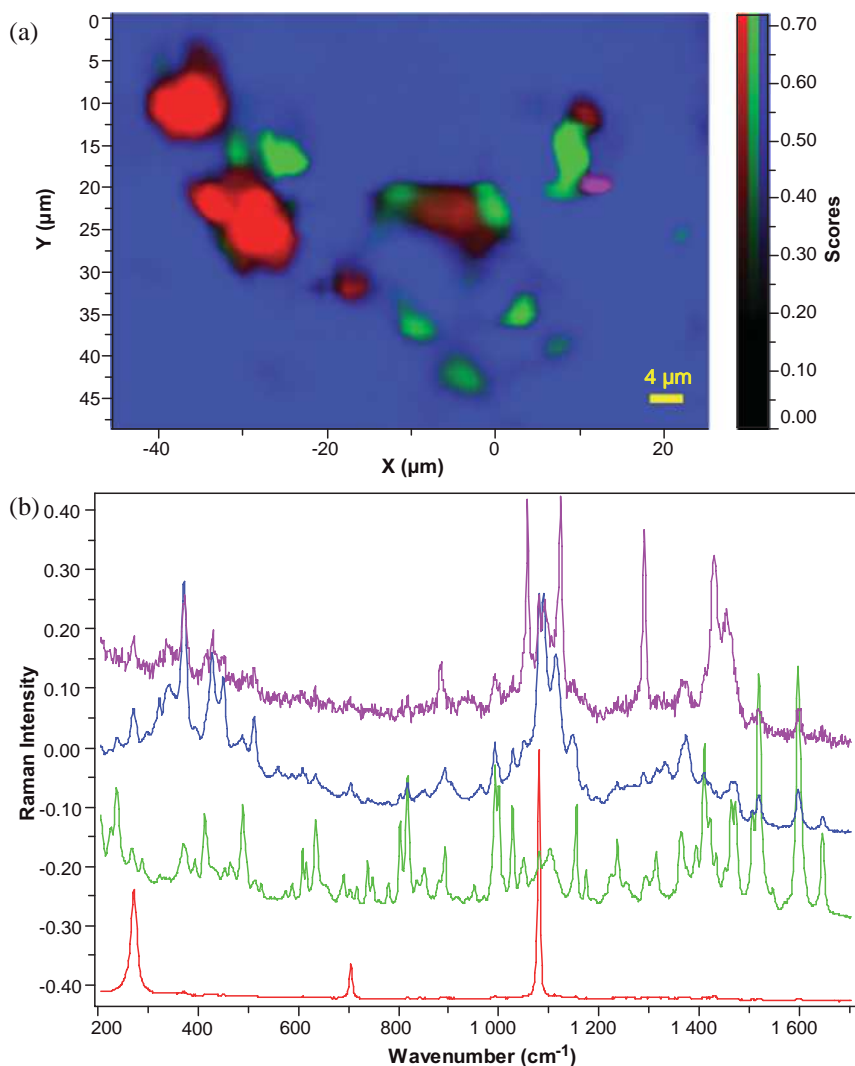
Figure 11.3 (a) Score images and (b) loadings that represent the spatial distributions of active ingredient (green), calcium carbonate (red), microcrystalline cellulose (blue) and magnesium stearate (pink).

aromatic groups (e.g., acetaminophen), while the inactive ingredients are generally sugars (e.g., cellulose, lactose), organic salts (e.g., magnesium stearate) or inorganic compounds (e.g., calcium carbonate). Compounds with aromatic groups show distinctive signatures in the Raman spectra (a strong band ~1000 cm^{-1} or ~1600 cm^{-1}, depending on numbers and locations of the substitutions) [7], which help to identify the active ingredients in the formulation. To distinguish inactive ingredients one from another is more complicated than for active ingredients,

because many different types of material (e.g., polymers, sugars, metal oxides, organic salts) are used for many different purposes, including binders, coatings, disintegrants and lubricants. Inorganic compounds tend to show fewer bands than organic compounds; in fact, they often show Raman bands in the low-frequency region ($<1000\,cm^{-1}$), and certainly none in the C—H stretching region (2700–3300$\,cm^{-1}$). The O—H stretching region ($>3500\,cm^{-1}$) is of interest because it may reflect the degree of hydration. The Raman scattering of polysaccharides tends to be weak, although it does vary a great deal depending on the state of the material (e.g., crystallinity and hydration). Some examples of Raman spectra are shown in Figure 11.4.

A few points are worthy of consideration here:

- It is ideal to measure reference Raman spectra of all ingredients in their pure forms, using the same conditions as the sample. Because Raman spectroscopy is sensitive not only to molecular structure but also to the local environment of molecules (degree of hydration and crystallinity, different isomers and polymorphic forms, long-chain polymers of different level of branches and saturations,
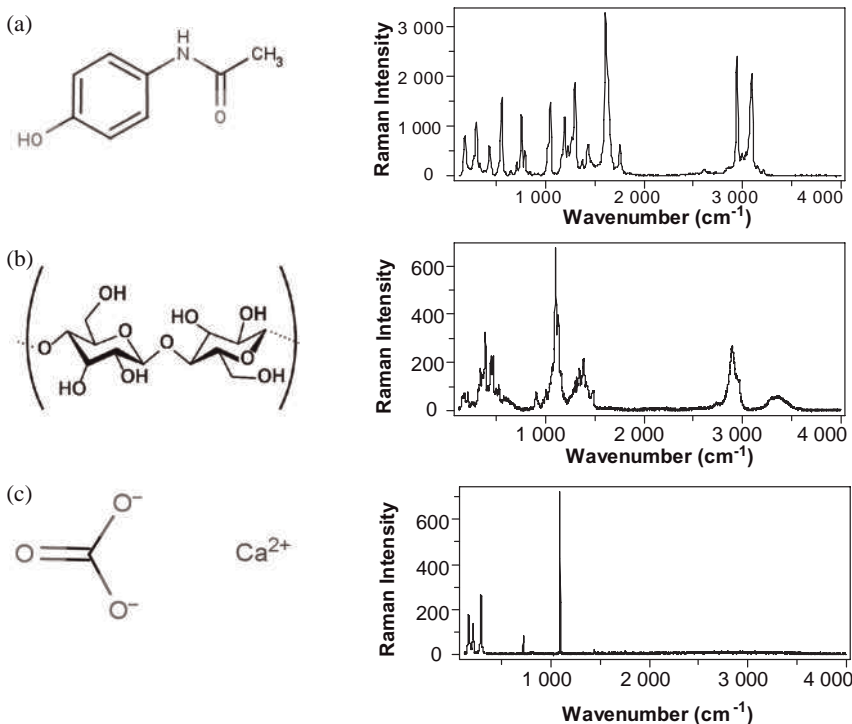
Figure 11.4 Molecular structures and Raman spectra of (a) acetaminophen, an active ingredient; (b) Cellulose, an organic inactive ingredient; (c) Calcium carbonate, an inorganic inactive ingredient.

etc.), it is best to measure, whenever possible, what actually was used in the sample.

- Most primary analysis methods, such as high-performance liquid chromatography (HPLC) yield contents (e.g., milligrams), while optical spectroscopy analysis methods, including Raman, yield concentrations (e.g., wt/wt%). The results of HPLC analyses require additional information (e.g., the weight of a tablet) in order to make the conversion, which must be recorded.

- The spectral resolution must be high enough to satisfy the sample requirements. Closely located Raman bands require a high spectral resolution to resolve them. A high spectral resolution configuration of a Raman microscope also provides a large number of datum points within a given spectral range, which is critical when measuring peak positions, band widths and band shapes of Raman bands.

- The exposure time – the length of time that the photons are accumulated on the detector before read out – must be long enough to achieve the proper SNR. Weak Raman scattering samples require longer exposure times to achieve the same SNR than do strong Raman scattering samples. As shown in Section 11.2, high-SNR data always produce better results than low-SNR data, under the identical circumstances. Reference spectra measured from the pure components can help to determine the requirements for spectral resolution and exposure time.

11.3.2
Mapping

In setting up a Raman map, there are three major parameters to consider: (i) the location (or center) of the map; (ii) the size of the mapped area; and (iii) the spacing between measurements (step size). An ideal map would be centered at the region of interest (ROI) but covering the whole region. The spacing between measurements would be smaller than the smallest object in the sample (ideally one fifth or less of the smallest). The question then is, how can the location and size of the ROI be determined without mapping? How can the size of the smallest object be determined? It might be possible to map the entire sample with the smallest step size available, but this could prove to be an impractical task – it would take too long and produce an unreasonably large file.

Survey mapping – that is, mapping a large area with a large step size – is, therefore, a very important step. From a survey map, it is possible to identify the ROI, to glimpse the chemical composition, and to obtain an approximation of the necessary step size. An example is shown in Figure 11.5, where a Raman map of an over-the-counter (OTC) analgesic tablet was measured over $800 \times 800\,\mu m^2$ at $100\,\mu m$ steps ($= 9 \times 9$ spectra). The number of spectra (81) was sufficiently small to perform a manual exploration for the different spectral species. There were at least three different chemical compounds. As this is a survey map, there are at least three different chemical compounds (perhaps more). Raman bands unique
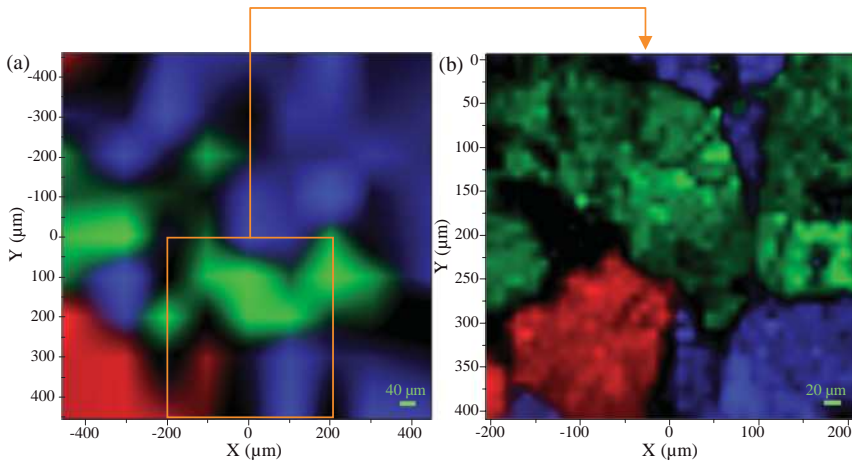
Figure 11.5 Raman images of an over-the-counter (OTC) analgesic tablet with: (a) 100 μm step over $800 \times 800\,\mu m^2$; and (b) 10 μm step over $400 \times 400\,\mu m^2$.
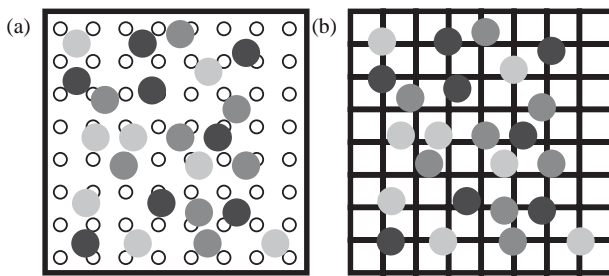
Figure 11.6 Schematic diagrams for (a) point mapping and (b) DuoScan mapping the same area at the same step size. The colored circles represent materials of interest. (a) Small circles represent laser focus; (b) Small squares represent pixels.

to each spectral species were selected and the Raman images created as intensity maps of these bands. A ROI where all three components were present is identified (marked with a rectangle). It appears that areas of each spectral species occupied are larger than 100 μm in diameter, 10 μm steps would provide sufficient sampling. A second Raman map of the rectangular marked area ($400 \times 400\,\mu m^2$) recorded at 10 μm steps ($41 \times 41 = 1681$ spectra) is shown in Figure 11.5b.

The point mapping method, however, may not be optimum for the survey mapping. The purpose of survey mapping is to map a large area quickly, with coarse steps. However, the laser spot size ($\sim\lambda_{excitation}/NA$), which determines the sampling area (or volume) of each measurement, is relatively small. When a large step size is used, many of the spaces between measurements are missed (Figure 11.6). A low-NA objective lens can be used for a large spot size, but it is still limited

to ~10 μm. More importantly, the use of a low-NA objective reduces the collection solid angle of scattering light, essentially reducing the sensitivity of the instrument. The exposure time to achieve an adequate SNR must then be increased, which in turn will slow down the mapping speed. The DuoScan mapping mode rasters the laser beam in two directions (*x*- and *y*-axes) over a predetermined area (a pixel), thus measuring a spectrum from the pixel area. Although the pixel size is still limited by the objective lens, it is considerably larger than the laser spot size. For example, the laser spot size is 1–2 μm in diameter when the excitation wavelength is 633 nm and NA of the objective lens is 0.55. The same lens could be used to measure a pixel as large as 30 μm, without sacrificing the sensitivity and speed. The largest pixel size to have been achieved to date has been 300 μm (with a 10× objective). A survey map with a large pixel and matching step size covers the entire mapping area without missing surface area. Whereas, the pixel spectrum will be more likely mixed (superposition of multiple spectral species) than the point spectrum, the latter will be more likely pure (single spectral species of one type or another) than the pixel spectrum.

11.3.3
Data Analysis: Spectroscopy

11.3.3.1 Unsupervised Analysis
Unsupervised analysis is performed when there are no other samples, information or data than the sample itself and the Raman map to be analyzed. When the sample is truly unknown, unsupervised analysis is the first (sometimes only) step in characterizing the sample. The objective of the analysis would be to determine the chemical and spatial compositions of the unknown sample.

Raman spectroscopy, compared to IR spectroscopy, is considered to be 'easy' spectroscopy. Often, it is possible to identify spectral features that are unique to each chemical component in the sample, and to use them for univariate analysis. When the number of spectra in a Raman map is small and the chemical composition of the sample is simple, then a univariate analysis is usually sufficient. The typical analysis strategy would be to pretreat the spectra (baseline correction, normalization, etc.), explore to identify any unique spectral features, and to create intensity maps of those features as Raman images. When differences between spectral species are reflected in peak shifts or band broadenings, the peak positions or bandwidths can also be mapped to create Raman images.

When a Raman map consists of a very large number of spectra, it is practically impossible to manually explore and identify all spectral species. On the other hand, a multivariate analysis will classify the individual spectra in a Raman map into groups, based on the systematic and significant variances between them. For a Raman map to have a healthy variance, it requires a sufficiently large number of spectra, and therefore multivariate analysis will become necessary and advantageous for a Raman map with a large number of spectra. In addition, when the sample is suspected of having a complex chemical composition, it becomes exceedingly difficult to identify, compare and isolate all of the spectral species. Yet, by

classifying the spectra into groups of relative homogeneity, a multivariate analysis can simplify the task – it is possible to examine one group at a time, for example.

When performing an unsupervised multivariate analysis it is important to remember that it is a numerical analysis based on the variance of the data set. Whenever the data set is manipulated, the results may change. Hence, it is imperative to verify the results with the original spectra to confirm the chemistry. Repetition is also a form of variance; when there is more repetition of a spectral species, the loading will seem smoother. Conversely, even if the SNRs of the original spectra are similar the loading of a spectral species of less repetition will seem noisier.

The Raman map given as an example in Figure 11.3 consists of 3479 spectra; here, there are numerous cellulose spectra compared to only a few magnesium stearate spectra. When the original Raman spectra are compared, however, they show a similar level of SNR. When the loadings were calculated using direct classical least square regression, the cellulose loading showed a better SNR than did that of magnesium stearate (Figure 11.7).

The next example of an OTC map was treated first using a direct classic least square (DCLS) method, and then with more sophisticated multivariate analysis methods. The tablet was mapped over $800 \times 800\,\mu m^2$ with $10\,\mu m$ steps. The data were baseline-corrected and normalized before being subjected to an unsupervised multivariate analysis. The first set of results was produced using univariate analysis (Figure 11.8a), when a manual exploration revealed three distinguishable and
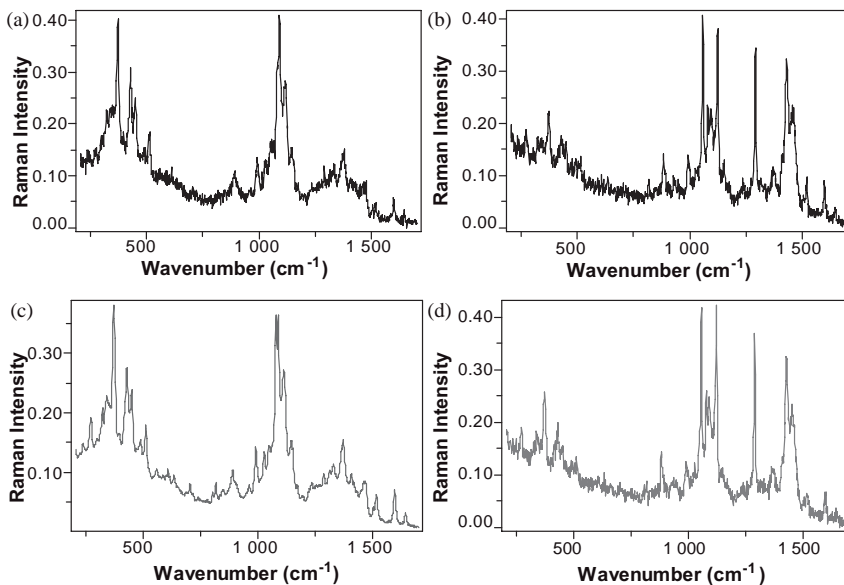
Figure 11.7 Raw single-point spectra of (a) cellulose and (b) magnesium stearate; (c,d) Loadings representing (c) cellulose and (d) magnesium stearate.
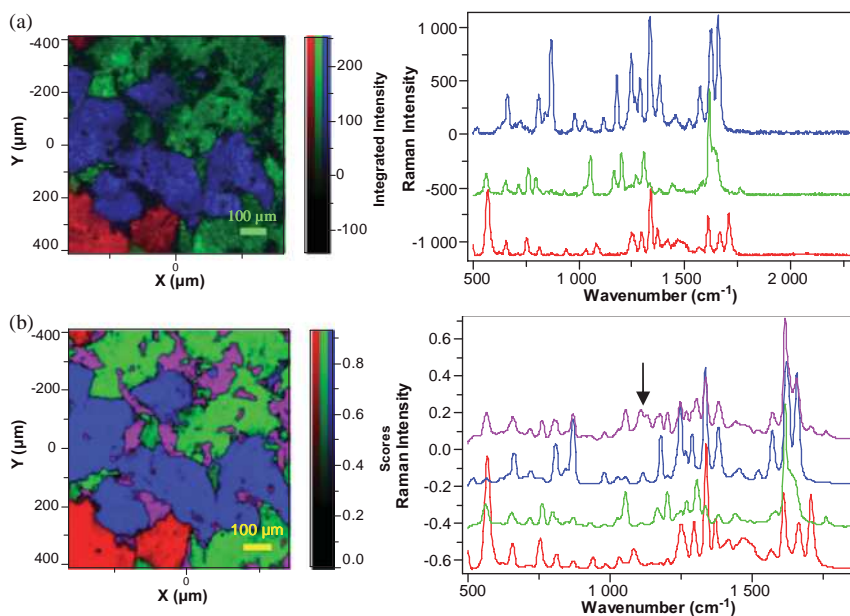
Figure 11.8 (a) Spectra and Raman images (integrated intensity maps) generated from a Raman map of an OTC analgesic tablet; (b) Loadings and Raman images (score images) of the same data, produced using DCLS. Note that the fourth loading (pink) is 'mixed', with unique spectral features (marked with an arrow) as well as those of other loadings.

recognizable spectra: caffeine, acetaminophen and aspirin. Raman bands at 568, 1181 and 1057 cm^{-1} were unique to each compound, respectively, and integrated intensity maps (red, 536–591 cm^{-1}; green, 1030–1077 cm^{-1}; blue, 1164–1197 cm^{-1}) were created. These were Raman images that showed the spatial distribution of the chemical components. Spectra from the high-intensity points were also shown.

Cellulose was shown to be present in the sample, but at a low concentration. The cellulose spectra were fewer and superimposed with spectral features from other elements, when detected at all. Thus, it was not easy either to isolate or to recognize the presence of cellulose while manually exploring the sample. DCLS regression (unsupervised mode, four factors) isolated cellulose loading (Figure 11.8b) showing the distinctive spectral signature of cellulose (the doublet at ~1110 cm^{-1}). However, the loading shows high-intensity spectral features of other components.

More sophisticated multivariate algorithms can separate the spectral features of cellulose to a better degree. A factor-based analysis (Factor Analysis, Isys 4.1; Malvern Instrument Ltd, UK) was applied (Figure 11.9) where, in the result the cellulose loading appeared almost pure.

Unsupervised analyses are often performed on unknown samples in order to obtain qualitative results. The results shown in Figure 11.9 can be considered the final results; here, the sample consisted of at least four chemical components – caffeine, acetaminophen, aspirin and cellulose – and their distributions were visualized in Raman images.

The large number of spectra in a hypercube provides yet another means of quantitative analysis via statistical analysis. For example, the spatial distribution image of caffeine (Figure 11.9b) is created with scores. The histogram (Figure 11.10a) of the image is then created by plotting scores (*x*-axis) versus the number of spectra (*y*-axis), and shows a clear distinction between two populations – one centering at high score (~5) for caffeine-rich and the other at low score (~0) for caffeine-poor. In the image, areas of more caffeine (high scores) are colored red, and those of less caffeine (low scores) in black. In the histogram, the population at high scores represent caffeine-rich points, and the population at low scores caffeine-poor regions. (Note that all assessments here are relative.) By classifying any spectra for which the scores are greater than 2.8 (threshold) as caffeine, the number caffeine spectra is 661; this is ~10% of 6561 total spectra. The label information on this product indicates the caffeine concentration (wt/wt%) as ~9.6%.
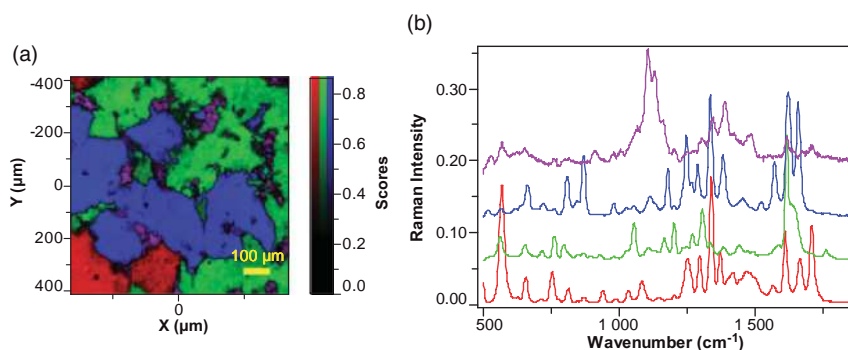
Figure 11.9 (a) Loadings and (b) score images from factor-based analysis.
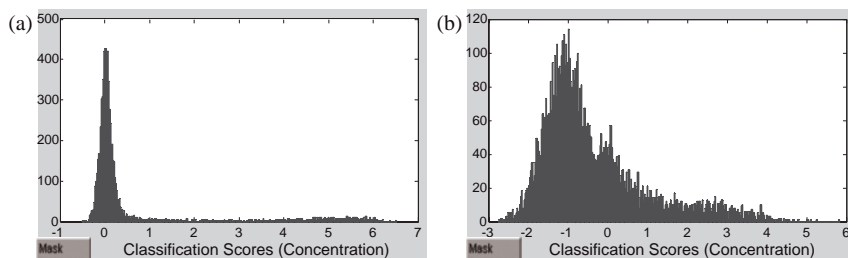
Figure 11.10 Histograms of (a) caffeine and (b) cellulose score images. The *x*-axis shows the score; the *y*-axis the number of spectra.

This is one of the best examples where all criteria for a good approximation (good spatial and spectral segregation between components, similar density of all components, etc.) are met, and demonstrates the potential usefulness of the approach.

Two other points should be considered when employing this approach to quantification. First, spatial segregation between the chemical components must be significant. For example, from individual spectra, it is known that caffeine-rich areas are mostly pure caffeine, while cellulose-rich areas are not pure cellulose. In other words, caffeine enjoys a good spatial segregation while cellulose does not. Classifying a group of spectra as caffeine spectra based on the histogram, therefore, is a good approximation. On the other hand, performing the same procedure for cellulose may not be as effective. However, high spatial resolution data will increase the chance of good spatial segregation in the Raman map for low-concentration or small-particle elements.

Second, the position of the threshold must be carefully considered. In the case of the caffeine image used here, the separation between two normal distribution curves is far and clear. Even if there was a degree of uncertainty in determining the threshold, the errors would be small. On the other hand, the histogram for cellulose (Figure 11.10b) does not show as a clear distinction and, depending on the threshold value–even if the difference were small–this may be a significant error in estimation. The histogram can be fitted with multiple normal distribution curves to help determine reproducibly the separation of one curve from another.

11.3.3.2 Supervised Analysis

Supervised analysis is performed when there additional information or data available, such as reference spectra, calibration samples and concentrations.

The simplest form of supervised analysis is to 'look for' a chemical component using a reference spectrum. For this, the most widely used methods include correlation coefficients, Euclidean distance and DCLS regression, in supervised model (using reference spectra).

When a supervised analysis is mentioned in the pharmaceutical industry, it often refers to a concentration prediction using a chemometric model. By nature, the objective of the analysis is not to identify the ingredients of the sample, as they are all known. Rather, the aim is to predict their concentrations in the sample.

The first step is to prepare a calibration set of samples, which contain the same ingredients as the target samples but in varying concentrations. A macro measurement is first performed to record a spectrum from each sample (Figure 11.11a), which are assumed to be homogeneous. The spectrum is a superposition of individual spectra of ingredients with the spectral contributions proportional to their concentrations. These spectra form the *training matrix*, while the concentrations of the calibration samples compose the *concentration matrix*. A chemometric model is then developed to correlate the training and concentration matrices.

The second step is to prepare a validation set of samples in the same way that the calibration set is prepared. The validation set is also measured in the same way as the calibration set. The model is then applied to the spectra of the validation
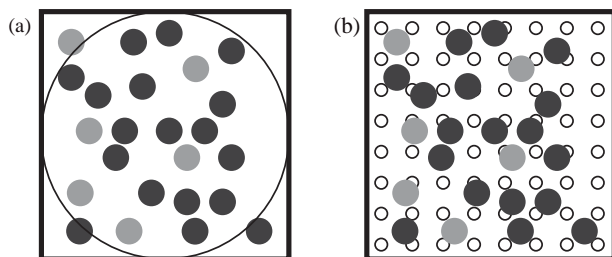
Figure 11.11 (a) Simulation of a macro measurement. A spectrum from a sample covering a large area (large circle); (b) Simulation of micro measurements. Multiple spectra from a sample each covering a small area (small circles).

set to predict the concentrations. The model is then adapted (different pretreatment, different number of factors, different algorithms, etc.) until the concentration prediction of the validation set is successful. The final model is then applied to the target sample to predict its concentration. This procedure works best when the underling assumptions are well met−a homogeneous sample and a large area measurement. Among commercial Raman instruments, the P^{h}AT system (Kaiser Optical Systems, Ann Arbor, MI, USA) was specifically developed for macro Raman measurements.

In Raman hyperspectral imaging, on the other hand, a single spectrum is often measured from a ≤1 μm spot. The Raman spectrum produced will more likely represent either pure A or pure B, rather than a mixture of spectra of A and B. The underling assumptions for the model development procedure described above break down and the procedure can no longer be used. An alternative approach was implemented in ISys (Malvern Instruments) to use a reference matrix, which is a collection of spectra measured from pure components, and a membership matrix (matrix elements have values of 0 or 1) in place of the training and concentration matrices. The same algorithms are applied then to develop chemometric models [8]. As the membership matrix has been used instead of the concentration matrix, the results are considered to be of relative abundance rather than of absolute concentrations. Samples of known chemical compositions can be used to validate the model and to calibrate the results from the relative abundance to the absolute concentrations. The samples are assumed to be heterogeneous, in fact the more heterogeneous the sample is, the better the method works.

11.3.4
Data Analysis: Raman Images

11.3.4.1   Statistical Analysis
A chemical image is an image where the gradient from brightness to darkness is associated with the abundance of a chemical component, thus providing chemical
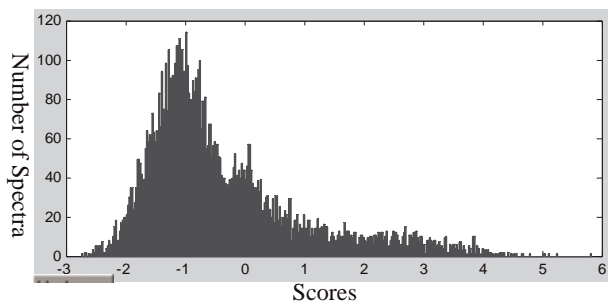
Figure 11.12 A histogram of a Raman image. Total number of spectra = 6561; mean score = −0.35; standard deviation of scores = 1.3; skew of scores = 1.3; kurtosis of scores = 1.4.

information in an image. In contrast, a Raman image is a chemical image for which the chemical information is based on Raman spectra. As a subject of a numerical analysis, on the other hand, a Raman image is simply a collection of numbers, each of which is associated with a level of abundance of a chemical component and a location of the sample. If the spatial association is removed, then a Raman image can be treated simply as a collection of numbers representative of the abundance of a chemical component. A histogram of a Raman image then can be created by plotting these numbers (intensities of a characteristic band, scores resulting from multivariate analysis, etc.) versus populations (the number of spectra or measurement points) (Figure 11.12).

The histogram provides both qualitative and quantitative characteristics of the Raman image. For example, the histogram of a Raman image of a pure compound or a completely homogeneous mixture would show a normal distribution. The mean value would be equivalent to the bulk measurement results. An increase in standard deviation, skew or kurtosis would indicate an increased deviation from the normal distribution, and in turn an increased sample heterogeneity. Conversely, the standard deviation, skew and kurtosis can be used to quantitatively assess the sample heterogeneity. For example, samples that are well blended would show a low heterogeneity. By comparing the standard deviation, skew and/or kurtosis it is possible to compare the blending quality in quantitative terms [5].

11.3.4.2 Morphological Analysis

When a number of adjacent spectra (or points or pixels) are classified as one chemical component, they can be termed as a domain. These could be particles, agglomerates or simply a continuous area of the same chemical component. However, when they form discrete areas, they are more likely to be from particles or agglomerates, and it is viable to determine their sizes and distributions. The Raman image (Figure 11.13, left) shows the spatial distribution of caffeine; the white areas are caffeine-rich. A binary image isolating these areas is created by assigning 1 to all points above a threshold, and 0 to all below. The threshold

value was determined based on the histogram of the Raman image. Various statistics can be drawn from the binary image (or classification image), such as the number of domains, mean size in areas and diameters, and distribution statistics. Table 11.2 shows the domain statistics of the image shown in Figure 11.13; here, the order of quadrants is from top to bottom, and then left to right. The percentage coverage is calculated by dividing the sum of the domain areas by the quadrant area.

Table 11.2 An example of domain statistics from the image in Figure 11.13.

Number of domains		13
Mean size in area (μm^2)		2.9×10^4
Mean size in diameter (μm)		170.0
Quadrant 1	No. of domains[a]	3
	Coverage (%)	4
Quadrant 2	No. of domains[a]	4
	Coverage (%)	3.8
Quadrant 3	No. of domains[a]	4
	Coverage (%)	3.3
Quadrant 4	No. of domains[a]	4
	Coverage (%)	12

a Count partial domains.
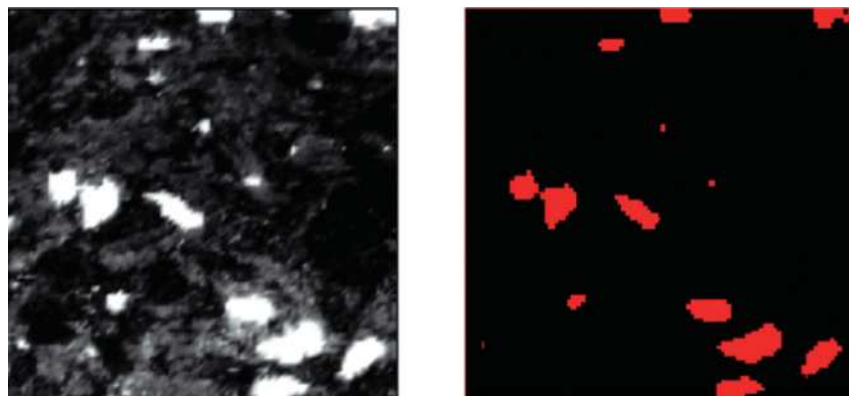
Figure 11.13 A Raman image and a binary image showing caffeine chemical domains in red.

11.3.5
An Example of Raman Hyperspectral Imaging Analysis: II

In this analysis, three Raman maps of an OTC analgesic tablet were mapped (Figure 11.14); the areas are caffeine-rich (red), aspirin-rich (green) and acetaminophen-rich (blue).

The Raman image in Figure 11.14b encompasses $7.4 \times 6.2 \, mm^2$, mapped with $75 \, \mu m$ steps; hence, a Raman spectrum is measured at every $75 \, \mu m$ in the mapping area. These data are excellent for assessing the overall characteristics of the sample and identifying the ROI.

The Raman image in Figure 11.14c encompasses $2.5 \times 2.5 \, mm^2$ and is mapped with $25 \, \mu m$ steps; this is the image investigated in Section 11.2.3.1 and Figure 11.13. These data are excellent for assessing the local domain statistics and identifying a domain of interest. The Raman image in Figure 11.14d encompasses
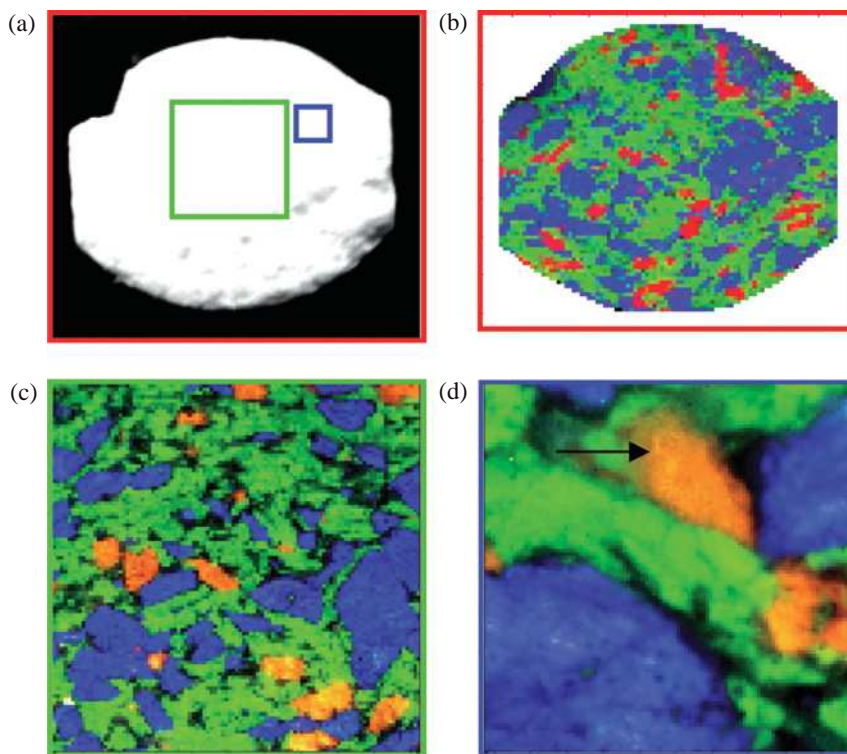
Figure 11.14 (a) A visual image of an OTC tablet, cross-sectioned; (b) Raman images of a large area of the tablet at a coarse grid (marked in red); (c) Intermediate area at intermediate grid (marked in green); (d) Small area at fine grid (marked in blue).

Table 11.3 Single domain characteristics of the domain marked with an arrow in Figure 11.14d.

Domain size (μm^2)	18 225
Orientation (°)^a	44.6
Major axis (μm)^b	222
Minor axis (μm)^c	107
Diameter (μm)	152

  a Angle between the major axis and the horizontal axis.
  b Length of the longest line within the domain.
  c Length of the line drawn perpendicular to and through the
     center of the major axis within the domain.

0.5×0.5 mm^2 and is mapped with 5 μm steps; these data are good for characterizing a single domain (Table 11.3).

11.4
Raman in Multimodal Hyperspectral Imaging

An OTC cold medicine tablet was mapped with Raman, X-ray/EDXRF and SEM/EDXRF. The ingredients were acetaminophen (325 mg), chlorpheniramine maleate (2 mg), dextromethorphan-HBr (10 mg), phenylephrine-HCl (5 mg), benzoic acid, carnauba wax, corn starch, D&C Yellow No. 10 Lake, FD&C Blue No. 1 Lake, hypromellose and magnesium stearate. The tablet weight was ~625 mg. The concentrations of active ingredients were 52.0% for acetaminophen, 0.3% for chlorpheniramine maleate, 1.6% for dextromethorphan and 0.8% for phenylephrine (totaling 54.7%). The molecular structures of the ingredients are shown in Figure 11.15.

A Raman map of the tablet was recorded over 500×500 μm^2 at 5 μm steps. The tablet contained four active ingredients. At first glance, all spectra showed features of acetaminophen. This is in accordance with the fact that the acetaminophen concentration was ~50% and its spectral features were likely to be present predominantly. However, a close inspection revealed that the relative intensities of the band at 853, the doublet at 1608 and 1615, and the doublet at 1645 and 1650 cm^{-1}, varied from spectrum to spectrum. Figure 11.16 shows four spectra individually identified to demonstrate the largest variance in relative intensities. The scores of the individual spectra were calculated using these spectra as loadings and the DCLS regression algorithm. The pink spectrum in Figure 11.16b is recognizable as that of acetaminophen, while the blue spectrum shows the highest intensity at 853 cm^{-1}, and is likely to represent phenylephrine (a secondary amine). It is reasonable to assume that the relative intensity variances in the red and green spectra are spectral contributions from the other two ingredients, chlorpheniramine maleate and dextromethorphan-Hbr. It is not easy to determine which spectral features belong to which component without reference spectra from pure

(a)   (b)   (c)

(d)   (e)   (f)
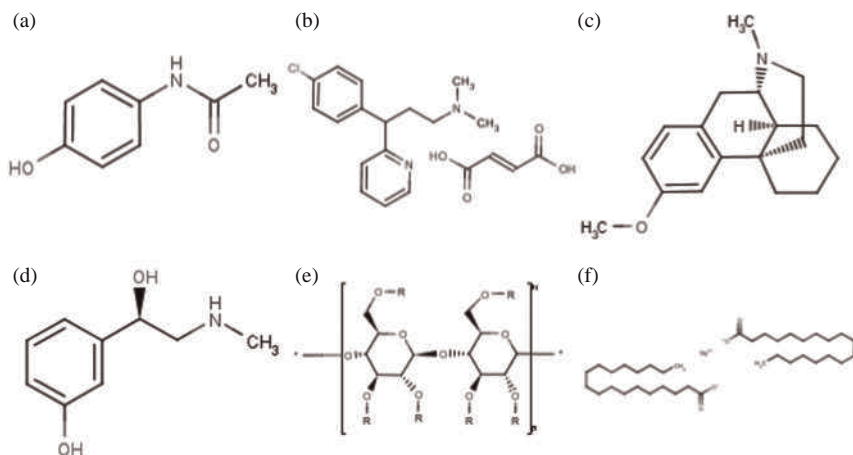
Figure 11.15 Molecular structures of (a) acetaminophen; (b) chlorpheniramine maleate; (c) dextromethorphan; (d) phenylephrine; (e) hypromellose; and (f) magnesium stearate.
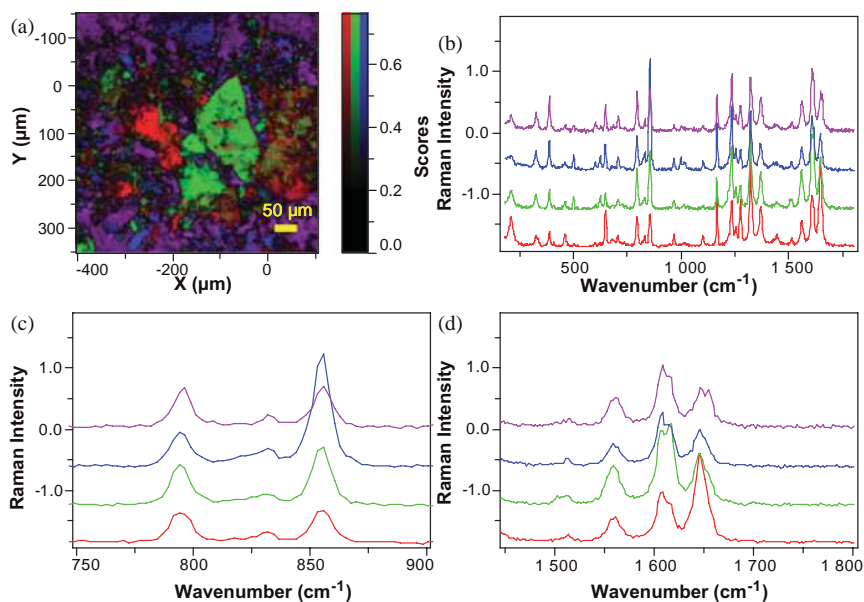
Figure 11.16 (a) Raman score image using (b) four individually identified spectra that are furthest from each other; Zoom-in of spectral ranges of (c) 750–900 and (d) 1450–1800 cm⁻¹.

components from the Raman spectra of this map. On the other hand, dextro-methorphan-Hbr is the only component that contains Br, which is very easily detected with the EDXRF analysis.

X-ray fluorescence (XRF) mapping was performed over $1024 \times 1024 \mu m^2$, measuring 256×256 points; the results are shown in Figure 11.17 (red spot marked with an arrow in 'Whole image'). The XRF images identified Mg, Si, Cl, Ca and Br, there being two Br images from the K and L lines. The L line was low energy (1.48 keV) from the surface, while the K line was high energy (~11.9 keV) from the entire depth. As the data measurement conditions were optimized for low-energy (15 KeV) bands, the L line image of Br was more reliable than the K line image in this case.

In comparison to Raman images, the Cl and Br images should correlate and confirm chlorpheniramine maleate and dextromethorphan-HBr. The Mg image should highlight the magnesium stearate distribution, which was not easy to isolate in Raman imaging. According to the ingredient list there was no Ca, but this might have been a component of the coloring material or a background artifact. SEM/EDXRF imaging (see below) was also unable to detect Ca, confirming the presence of a background artifact.

The magnesium image showed many small spots that may, or may not, have been Mg-rich. Based on the label information, magnesium was known to be present in the sample; however, if this had been an unknown sample then the image would have been of insufficient quality to determine the presence of magnesium.
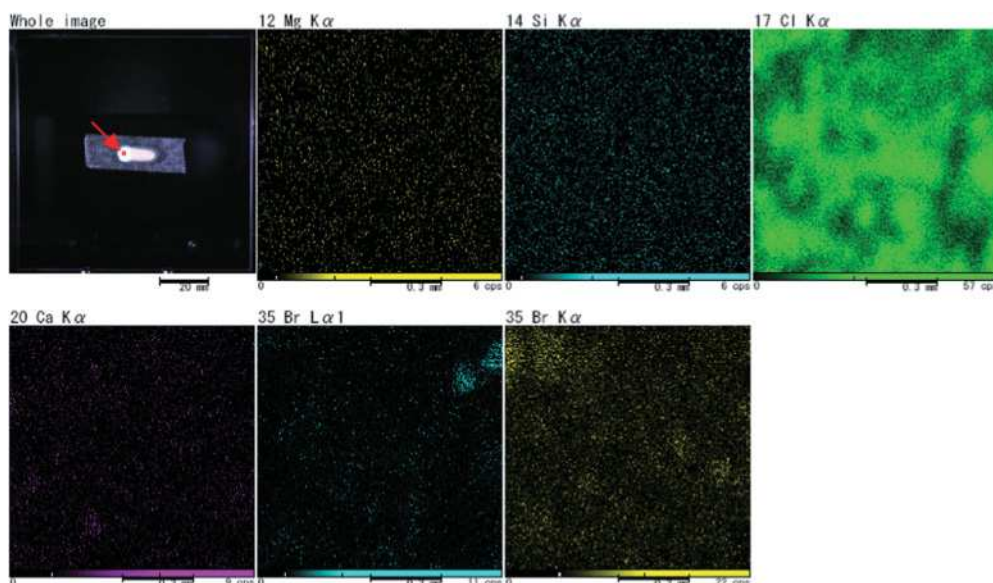
Figure 11.17 X-ray/EDXRF images for Mg, Si, Cl, Ca and Br.
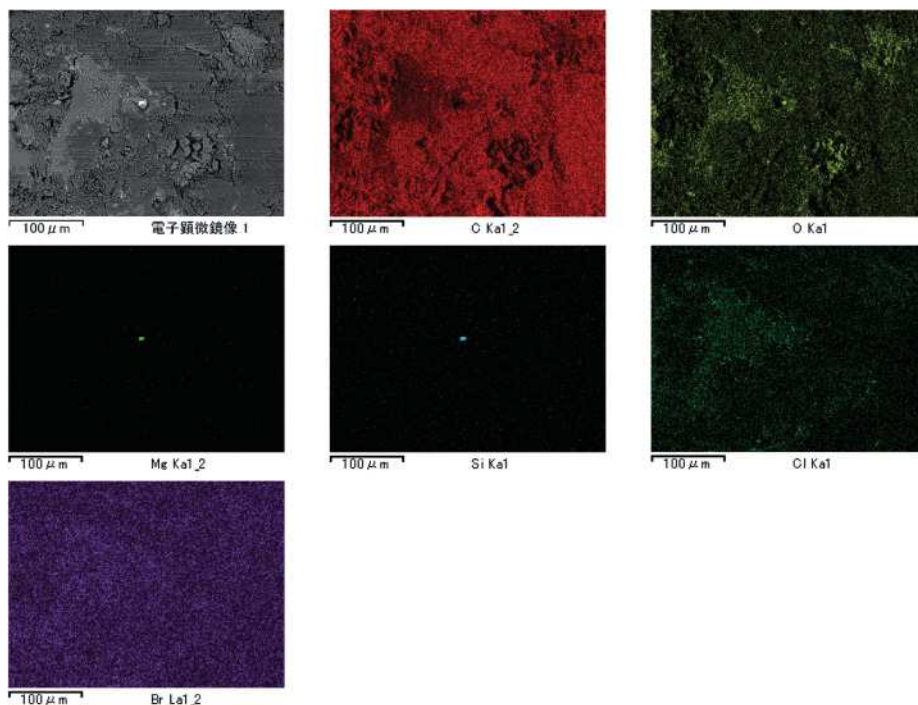
Figure 11.18 SEM/EDXRF images for C, O, Mg, Si, Cl and Br at 350×.

When the same sample was measured using SEM/EDXRF mapping, the map (Figure 11.18) was recorded over a $400 \times 400\,\mu m^2$ area at 350× magnification. The Mg map showed a distinctively sized Mg domain (~5 μm in diameter), and the Si map highlighted the same spot. The EDXRF spectrum (Figure 11.19) from this highlighted spot confirmed the coexistence of Mg and Si.

11.5
Conclusions

Raman hyperspectral imaging provides an excellent means of characterizing the chemical and spatial composition of pharmaceutical products. The most important point when performing successful Raman hyperspectral imaging is to understand the intertwined relationship between spectroscopy and imaging, as the spectral quality – and especially the spectral resolution and SNR – will have a direct impact on the spatial quality produced.

The underlying assumptions for multivariate analysis are different for macro- and microanalyses. While Raman hyperspectral imaging is preferred for microanalysis and heterogeneous samples, macroanalysis has been shown preferable for homogeneous samples. However, whichever approach is utilized the
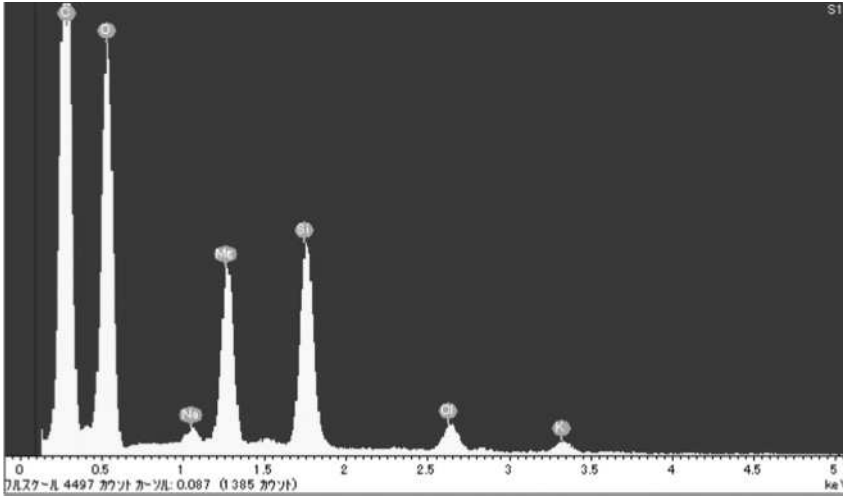
Figure 11.19 EDXRF spectrum of the highlighted spot in the Mg map of Figure 11.18.

multivariate analysis results must first be validated and verified with original spectra and chemistry.

Raman hyperspectral imaging data sets consist of many spectra, thus providing an additional means of extracting quantitative information by the use of statistics. The spectra can be classified into groups, with relative homogeneity being based on the spectral analysis, or with the scores being associated with individual spectra, based on spectral comparisons. The results obtained can then be assessed statistically to provide details of relative abundance, quantified heterogeneity and domain statistics.

In addition, EDXRF hyperspectral imaging can be employed to detect the elemental distribution of the sample, with the results being used to complement Raman hyperspectral imaging.

Acknowledgments

References

1 Iranloye, T.A. and Parrott, E.L. (1978) *J. Pharm. Sci.*, **67** (4), 535–9.

2 Chowhan, Z.T. and Chi, L.H. (1986) *J. Pharm. Sci.*, **75** (6), 542–5.

3 Adrian Knowles (2006), "FTIR microscope. html", http://www.jobinyvon.com/Raman/ FTIR-Microscope (accessed February 2009)

4 Delhaye, M. and Dhamelincourt, P. (1975) *J. Raman Spectrosc.*, **3**, 33–43.

5 Lyon, R.C., Lester, D.S., Lewis, E.N., Lee, E., Yu, L.X., Jefferson, E.H. and Hussain, A.S. (2002) *AAPS PharmSciTech.*, **3** (3), 17.

6 Lewis, E.N., Schoppelrei, J. and Lee, E. (2004) *Spectroscopy*, **19** (4), 26–36.

7 Chalmers, J.M. and Griffiths, P.R. (2002) *Handbook of Vibrational Spectroscopy*, Vol. **3**, John Wiley & Sons, Ltd, Chichester, UK, p. 1838.

8 Koehler, F., Haber, K. and Dubois, J., ISys 4 User's Manual (2006) Malvern Instrument Ltd, UK.

Part Five   Developments in Methodology

12
Deep, Noninvasive Raman Spectroscopy of Diffusely Scattering Media

Pavel Matousek

12.1
Introduction

In many analytical applications in biomedical and pharmaceutical sciences it is desirable to probe, noninvasively, the composition of deep layers of samples with high chemical specificity. Examples include the diagnosis of bone disease and breast cancer, as well as the noninvasive probing of pharmaceutical products in quality control applications and drug authentication.

Presently, the main chemically specific optical spectroscopic techniques used in these areas include near-infrared (NIR) absorption spectroscopy, mid-infrared (MIR) spectroscopy and Raman spectroscopies. Although, NIR is widely used in a number of these applications for its simplicity, it suffers from a limited chemical specificity [1, 2]. By comparison, both MIR and Raman spectroscopy offer a substantially higher degree of chemical specificity, but until now their use has been confined to probing only shallow layers of turbid media. In the case of MIR, this is due not only to the requirement for sample thinning or dilution in the case of bulk probing, but also an incompatibility with aqueous samples, as water strongly absorbs the MIR radiation. Raman spectroscopy, in contrast, does not suffer from these fundamental limitations, and thus holds a substantial potential to become a mainstream analytical tool in the areas concerned [2]. It should be noted that the applicability of this technique is limited to samples that do not exhibit strong fluorescence emission in the spectral region coincident with the Raman spectra, as this can easily swamp the relatively weak Raman signals. However, the problem of fluorescence can be significantly reduced by using NIR excitation away from the electronic absorption bands of most fluorescing species.

To date, the Raman method has been used with commercial Raman probes and microscopes, predominantly in the backscattering collection mode (see Figure 12.1), although in a number of specialist laboratories a 90° collection geometry is also used [1]. While the backscattering mode is used mainly for its instrumental simplicity and ease of use, this approach permits the effective depth discrimination of Raman signals in these media only at shallow depths [1]. Consequently, as
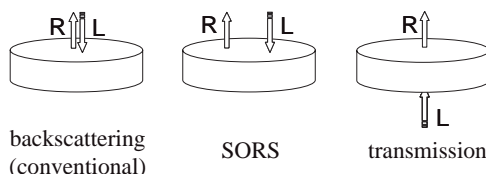
Figure 12.1 Basic types of Raman spectroscopy geometries with respect to the sample. Conventional backscattering Raman, SORS and Raman transmission geometries. R = Raman light; L = laser beam.

the accessible depths in living tissues are typically only several hundred micrometers, many of the tissue's components, such as bones and deep cancerous tissues, will be beyond the reach of this technique.

A substantial extension to the penetration depth of Raman spectroscopy was recently accomplished using the diffuse component of light, in analogy with NIR absorption tomography [3–5] or fluorescence spectroscopy [6–9], where corresponding concepts have been used previously. In this chapter we review recent developments in this area, and provide examples of several practical applications. Although these approaches are targeted primarily on the chemical characterization of subsurface domains within turbid media, they also hold considerable potential for extracting spatial information (in analogy with NIR tomography). This latter aspect, which is outlined in Section 12.4, is only now beginning to be explored.

12.2
Techniques for Deep, Noninvasive Raman Spectroscopy

Several deep, noninvasive approaches have been developed following earlier extensive investigations into the photon migration process [3, 10–12]. The methods can be divided into two basic classes, namely temporal and spatial.

12.2.1
Temporal Methods: Ultrafast Gating

The discrimination of layers within a stratified turbid sample can be accomplished with the temporal approach, using impulsive Raman excitation and fast temporal gating of the backscattered Raman signal using, for example, a 1 ps optical Kerr gate. This concept builds on the earlier studies of Wu *et al.* [10], who used a somewhat slower photon counting approach to accomplish this task. The role of the gate is to separate the earlier-arriving surface Raman photons from delayed Raman photons born at greater depths.

The recovery of the full Raman spectrum of a deeply buried layer in a turbid sample was accomplished using the Kerr gating approach by Matousek and coworkers [13], on a two-layer powder sample, building upon pioneering research

into Raman photon migration by Everall *et al.* [11, 12] and Morris *et al.* [14] and the preceding investigations on Raman Kerr gating fluorescence rejection [15–17]. A more extensive description of the concepts and underlying mechanisms is provided in a tutorial review [18].

The Kerr-gated Raman concept proved to be effective, although the complexity and high peak intensities involved in these experiments precluded its wider use. These limitations were lifted by the subsequent development of the spatial concepts for deep, noninvasive spectroscopy.

12.2.2
Spatial Methods: Spatially Offset Raman Spectroscopy (SORS)

The spatial Raman methods are related to widely used tomographic concepts such as NIR absorption [3] and subsurface fluorescence spectroscopy [6]. The basic concept, known as spatially offset Raman spectroscopy (SORS) [19], utilizes the differences in the spatial distribution of Raman photons emerging at the surface from different depths of the probed sample. In this approach, Raman spectra are collected from regions on the sample surface that are spatially offset by different amounts from the point of laser incidence (see Figures 12.1 and 12.2). These spectra contain varying relative Raman contributions from layers located at different depths within the sample. This difference is brought about by the wider lateral diffusion of photons emerging from greater depths [3, 11, 12].

The feasibility of the SORS concept as a tool for obtaining Raman signals from deeply buried layers in turbid media was first demonstrated in a collaborative investigation [19] (see Figure 12.3). The experiments were performed on a two-layer sample composed of a 1 mm-thick poly(methyl methacrylate) (PMMA) powder layer placed on top of a *trans*-stilbene powder layer using 514 nm as the probe wavelength. The results of these measurements are shown in Figure 12.4. The zero-offset spectrum represents a conventional Raman spectrum. By increasing the spatial offset, the surface layer signal (PMMA) diminishes much more quickly that that of the sublayer (*trans*-stilbene) such that, at a spatial offset of >2 mm, an order of magnitude improvement in the intensity ratio is achieved. The same report also detailed improvements in the relative ratio between the Raman signals of the two layers by a factor of 19 at a 3.5 mm spatial offset. Interestingly, the quality of the spectra obtained in these measurements was substantially higher
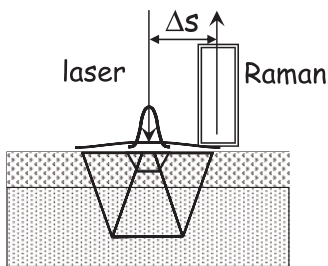
Figure 12.2 Principle of the spatial SORS concept for the discrimination of subsurface signals.
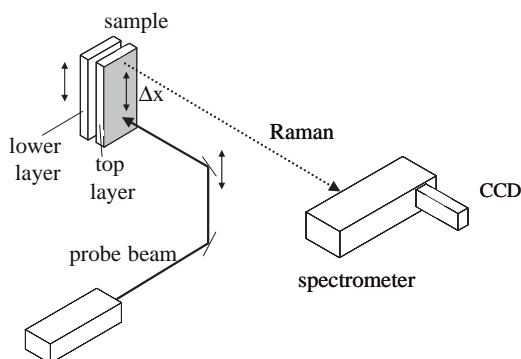
Figure 12.3 Schematic diagram of a basic SORS experimental set-up. Reprinted with permission from Ref. [19]; © 2005, The Society for Applied Spectroscopy.
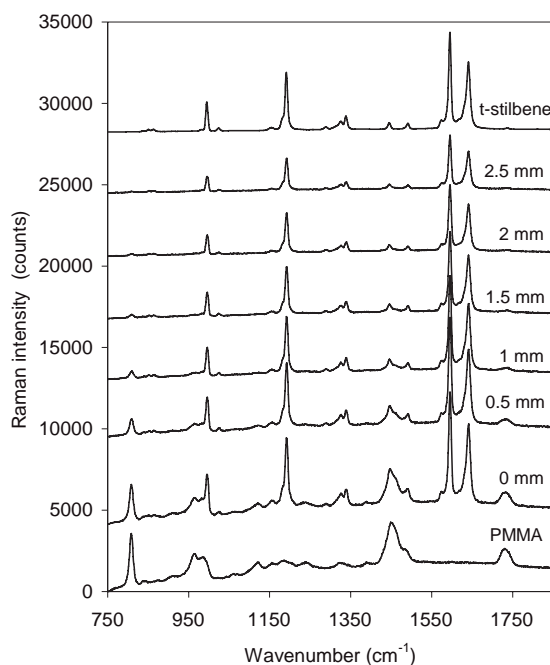
Figure 12.4 A set of SORS spectra collected from a two-layer system consisting of a 1 mm-thick layer of PMMA made from 20 µm-diameter spheres followed by a 2 mm-layer of *trans*-stilbene powder measured using 514 nm as the probe wavelength. The spectra are shown for different spatial offsets. The top and bottom spectra are those of the individual layers obtained in separate measurements. The spectra are offset for clarity. The acquisition time was 100 s for each spectrum, and the average laser power 12 mW. Reprinted with permission from Ref. [19]; © 2005, The Society for Applied Spectroscopy.

than was achieved using the more complex Kerr-gated system [13]. The improvement is ascribed to the higher intensity of the Raman signal detected, due to the fact that SORS integrates the Raman signal across the entire time domain, unlike with the temporal approach, where only a narrow temporal slice is obtained.

If a higher degree of separation of the subsurface signals from the surface contribution is required, then this can be accomplished, for a two-layer system, by a simple scaled subtraction of two spectra obtained at different spatial offsets to cancel the Raman contribution from the surface layer. For a stratified sample with more than two layers, a multivariate data analysis approach including factor analysis can be applied, using a more extensive data set. An example of such a procedure is band target entropy minimization (BTEM) [20–24]. A major advantage of these approaches is that a stratified system can be decomposed with no *a priori* knowledge of its composition.

The SORS concept can be combined, in a relatively straightforward manner, with a fiber optic collection scheme developed for conventional Raman spectroscopy earlier [25] to provide a substantial enhancement of the Raman collection efficiency. In this approach, fibers collecting the Raman signal from the sample arranged typically in a ring or disk pattern are reorganized on the spectrograph slit into a linear pattern to match the slit geometry. The use of this concept in SORS was discussed, from a theoretical standpoint, in studies by Matousek and colleagues [19, 26], and first experimentally demonstrated by Schulmerich *et al.* [27], who used a commercial fiber probe with the fibers arranged at the center of the probe with global illumination configuration [28]. The concept was employed subsequently by Matousek *et al.* [29], who utilized fibers distributed on annuli of different radii (see Figure 12.5), with each different radius being presented to a different horizontal section of a two-dimensional (2-D) CCD detector. Similar concepts were also used in fluorescence tomography [6–9].
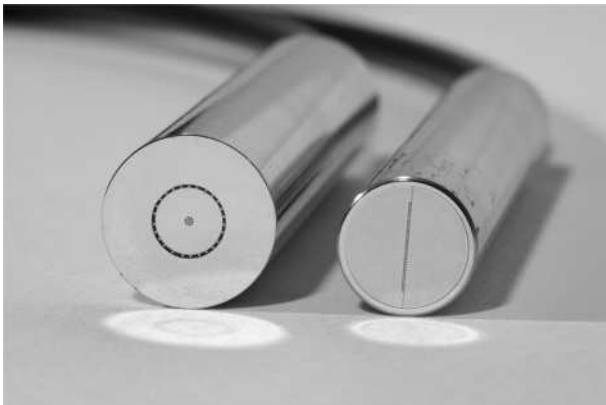
Figure 12.5 A photograph of the SORS ring fiber probe (left = input side, right = output side). Reprinted with permission from Ref. [29]; © 2006, The Society for Applied Spectroscopy.

The application of SORS in its basic form provides information on the chemical composition of individual layers, but no spatial information about their distribution within the sample. Additional studies performed by Schulmerich and coworkers [28] demonstrated how SORS could also be deployed as a tomographic tool.

Another SORS variant was described [30] for which the concept relies on the separation of signals in stratified media by defocusing a conventional Raman instrument. Although less effective than a fully optimized SORS method, the technique can be sufficiently effective with less-challenging samples, and may provide a convenient first stepping stone for those groups first encountering this area of research.

12.2.3
Inverse SORS

Further research in the area of SORS led to the development of a more effective SORS modality, termed inverse SORS. This improved concept removes some of the artifactual limitations inherent to the conventional SORS approach, and permits the use of higher laser powers through the provision of a wider illumination zone at the sample. This is beneficial in applications where maximum illumination intensity limits exist, such as when probing living tissue *in vivo* and in explosive powder environments.

The concept, which was proposed and demonstrated independently by Schulmerich and colleagues [31, 32] and Matousek [33], relies on the collection of Raman light through a group of fibers at the center of a probe, and the delivery of the laser beam through a ring-shaped area centered on the collection zone (see Figure 12.6). The ring radius defines the SORS spatial offset. In this concept, it is also beneficial that, in each read-out of the CCD detector, an arbitrary illumination ring radius can be set, thus enabling a better tailoring of the experimental conditions to the sample parameters than was possible with conventional SORS probes, where rings are built into the fiber probe. The laser beam ring profile can be generated using an axicon (conical lens), and the spatial offsets set either by adjusting the distance of the axicon from the sample [33] or by varying the magnification of a telescope inserted between the sample and the axicon [31, 32].
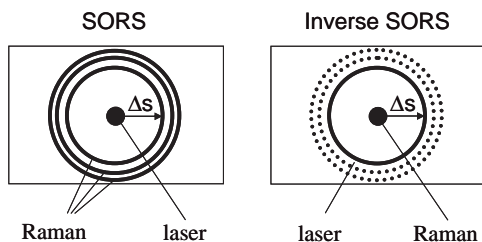
Figure 12.6 Schematic diagram of conventional SORS and inverse SORS concepts showing Raman collection and laser beam delivery geometries. Reprinted with permission from Ref. [33]; © 2006, The Society for Applied Spectroscopy.

12.2.4
Transmission Raman Spectroscopy

In some analytical applications the primary goal of the measurement can be the assessment of the overall bulk content of the probed sample, instead of the composition of individual layers. This is, for example, the case in the bulk analysis of pharmaceutical tablets, when the requirement is to establish the overall tablet content. Matousek *et al.* [34] recently showed that a transmission Raman geometry is particularly well suited for such an analysis (see Figure 12.1). Although this geometry was introduced during the 'early days' of Raman spectroscopy [35], it became largely forgotten and its benefits for the analysis of pharmaceutical products were unrecognized. In sharp contrast with the conventional backscattering Raman geometry, where the signal is biased towards surface layers of the probed sample, the transmission Raman mode exhibits gross insensitivity to the depth of a probed layer. This in turn eliminates the so-called 'subsampling' problem, when sample heterogeneity can limit the accuracy of the prediction of the overall sample content [36]. Previous attempts to minimize this effect have included the use of special devices to rotate the pharmaceutical tablets in front of a conventional backscattering Raman microscope.

This exceptionally useful feature of the transmission Raman mode was confirmed both experimentally and using Monte Carlo simulations [34]. The numerical results (see Figure 12.7) show that if a thin 'impurity' layer is relocated from the surface to a depth of 3 mm within a typical tablet medium, then its conventional backscattering Raman signal is diminished by four orders of magnitude,
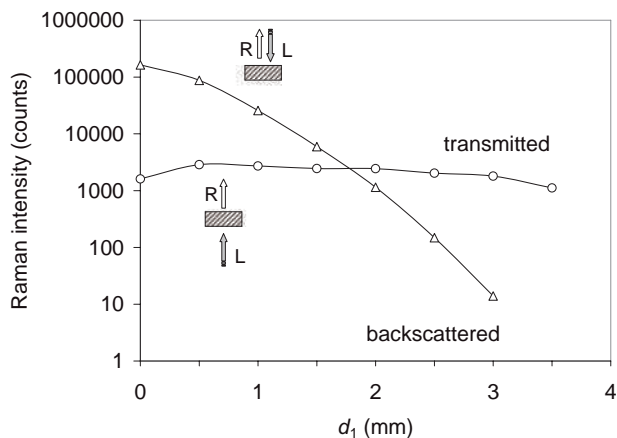
Figure 12.7 Plot of Raman intensities for the backscattering and transmission geometries versus depth (d_1) of the interlayer (impurity) within a pharmaceutical tablet-like medium. The dependencies are the results of Monte Carlo simulations. Reprinted with permission from Ref. [34]; © 2006, The Society for Applied Spectroscopy.

and typically is lost in the dominant signal coming from the surface layers. On the other hand, the transmission geometry yields a largely unperturbed signal, which shows that the transmission concept is much better suited to probing of the bulk content of turbid media. The results of these studies also showed that a good level of Raman signal can be obtained in the transmission geometry with pharmaceutical tablets [34].

In many pharmaceutical and biomedical applications, such as the noninvasive probing of colored capsules, coated tablets and subsurface tissue spectroscopy, it is also beneficial that the transmission Raman method very effectively diminishes the Raman and fluorescence signals originating from the surface layers of the probed sample compared to conventional backscattering Raman geometry [37].

12.2.5
Raman Signal Enhancement Using a Bandpass Filter

In situations where the laser light delivery point and Raman collection area are spatially separated – as for SORS, inverse SORS and transmission Raman spectroscopy – a simple method [38] can be used to substantially enhance the detected Raman signals. Such an enhancement is achieved by using a multilayer dielectric optical element, such as a bandpass filter, placed in the laser beam over the sample. This prevents the loss of laser photons, which re-emerge from the medium at the critical point where the laser beam enters the sample and in its vicinity, where major photon loss occurs. This leads to a substantial increase in the coupling of laser radiation into the sample. Consequently, an enhanced laser photon–medium interaction process is present, which boosts the overall Raman signal yield in the concerned geometries. In its basic form, the method requires that the coupling sample surface is flat.

The method utilizes the angular dependence of the dielectric filter on impacting photon direction, with its transmission spectral profile shifting to the blue, in line with the increase in the deviation of photons away from normal incidence. This feature enables the filter to serve as a unidirectional mirror, passing a semi-collimated laser beam through unhindered from one side while at the other side reflecting any photons emerging from the sample predominantly at random directions, back into the sample.

Figure 12.8 shows the results of a feasibility experiment carried out in transmission Raman geometry on a standard paracetamol (acetaminophen) tablet, with and without a bandpass filter. The bandpass filter was centered at 830 nm and its bandwidth was 3.2 nm. The Raman spectra are shown in a raw form, without any numerical preprocessing. A substantial enhancement (×6.5) was observed upon the insertion of the bandpass filter into the proximity of the tablet. Such a large enhancement could be very difficult, and in many cases impossible, to reproduce by other means. The use of a bandpass filter permits the collection of Raman spectra of higher quality, and consequently a more sensitive analysis of sample can be accomplished, or higher penetration depths attained. It is also worth noting

(a)

(b)
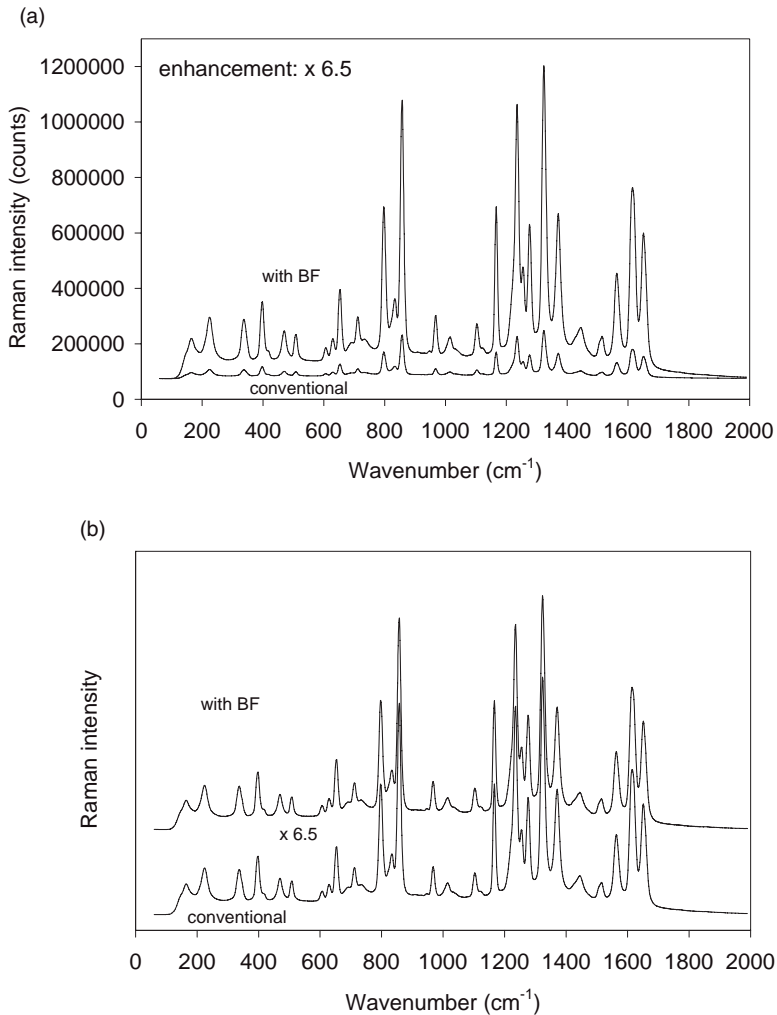
Figure 12.8 Experimental demonstration of the enhancement of the transmission Raman signal using a standard dielectric bandpass filter (BF) placed within the laser beam into the proximity of sample. (a) The Raman spectra are those of a standard paracetamol (acetaminophen) tablet measured with ('with BF') and without ('conventional') BF; (b) The same spectra scaled to the identical size to illustrate the uniformity of the enhancement across the entire spectral range. The preservation of the overall spectral pattern is important in many analytical applications involving complex analytes. The spectra are offset for clarity. The acquisition times were 10 s in both cases with a laser power of 50 mW (827 nm). Reprinted with permission from Ref. [38]; © 2007, The Society for Applied Spectroscopy.

here that the signal enhancement is uniform across the entire spectrum (see Figure 12.8b), and no spectral fluctuations were observed. Such a feature would be important in many analytical applications where the spectral pattern serves as a means of identifying the individual chemical components and determining the relative concentrations of subcomponents.

The simplicity and robustness of the method makes it well suited to a number of practical analytical applications, such as sensitive noninvasive *in vivo* disease diagnosis, security screening and the quality control of pharmaceutical tablets. The concept is also potentially applicable to fluorescence spectroscopy, NIR tomography of turbid media and other general applications, where the enhanced coupling of laser radiation into a turbid medium is beneficial; an example is the case of photodynamic therapy in cancer treatment of subsurface tissues.

12.3
Examples of Application Areas

12.3.1
Probing of Bones through Skin for Disease Diagnosis

As discussed in Chapter 4, there is considerable benefit to be obtained from applying Raman spectroscopy to the analysis of bone matrices. The ability to perform such interrogation noninvasively and safely through soft overlaying tissue reveals a host of potential applications, including the diagnosis of brittle bone disease and osteoporosis [14, 39, 40]. For example, at present dual-energy X-ray absorptiometry (DEXA), which represents the 'gold standard' screening for the diagnosis of osteoporosis, is only 60–70% accurate in the prediction of osteoporotic fracture. Such inaccuracy most likely stems from the inability of DEXA to probe the protein (mainly collagen) components within the bones that not only constitute about one-third of the bone matrix but also contribute significantly to bone strength. Recently, both the temporal and spatial Raman approaches have been applied successfully to this problem, building on the pioneering studies of Morris *et al.* [14, 41] in this area.

A collaborative team led by Draper [39] recently reported the successful, noninvasive, detection of osteogenesis imperfecta (brittle bone disease) in mouse limbs, through approximately 1 mm of overlaying soft tissue, using the temporal Kerr-gated Raman approach. The presence of the condition was apparent from a substantial relative intensity change between the collagen and mineral components in the spectra (see Figure 12.9). These studies represented a milestone in the noninvasive Raman spectroscopy of bone, showing for the first time the feasibility of such an approach. Unfortunately, however, major issues remain to be resolved with this technique. Apart from the high complexity and associated cost of the instrumentation, the experiments necessitate the use of laser intensities two to three orders of magnitude higher than those permissible for the safe illumination of human skin [29]. However, these hurdles were surmounted through the
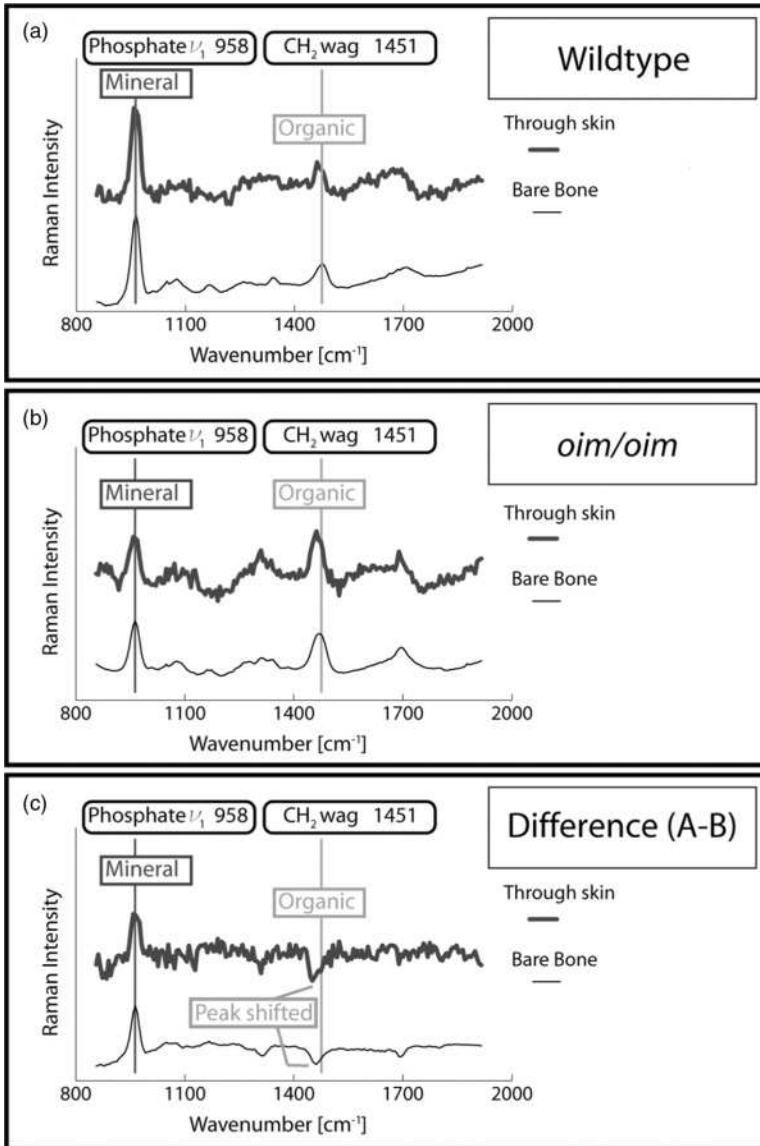
Figure 12.9 Raman spectra of bone measured from two genotypes; wild-type mice and osteogenesis imperfecta (*oim/oim*) mice. The spectra were recorded both through the overlying skin and directly on bare bone using the ultrafast Raman Kerr-gated method. (a) Raman spectra of wild-type mice; (b) Raman spectra of *oim/oim* mice; (c) Difference Raman spectra obtained by subtracting the spectra from the two genotypes. The acquisition times were 7–15 min for each spectrum and the laser pulse energy was 340 μJ (average power 340 mW, 1 kHz repetition rate). Reproduced with permission from Ref. [39]; © American Society for Bone and Mineral Research.

subsequent development of the SORS concept, which is compatible with much safer continuous-wave laser beams.

The first use of SORS in the area of noninvasive probing of bones was reported by Schulmerich *et al.* [27], who succeeded in recovering the Raman spectra of bones transcutaneously from depths of several millimeters in both animal and human cadavers. Subsequently, with an improved instrumentation based around a ring illumination geometry (equivalent to inverse SORS), Schulmerich *et al.* [31] reached another key milestone by demonstrating the feasibility of measuring Raman spectra noninvasively from a depth of 4 mm from chicken tibia, with a better than 8% accuracy in terms of the relative Raman band intensities between the phosphate (95 cm^{-1}) and carbonate (1070 cm^{-1}) bands. These successes opened the prospect for the potential detection of osteoporosis, which is likely to require the level of accuracy as indicated by McCreadie and coworkers on excised bones [40]. In these investigations (the results of which are shown in Figure 12.10), the measurements were performed using 785 nm as the probe wavelength.

Parallel research conducted by Matousek and coworkers [29] demonstrated the feasibility of recovering the Raman spectra of bones from humans *in vivo*. Although the obtained spectra were of limited quality, with some overlaying tissue signals still present, the study results showed that the key bone features could be measured transcutaneously *in vivo*, under totally safe illumination conditions. The measurements were performed with the laser power attenuated to a mere 2 mW – that is, well within the maximum permissible exposure limit and approximately equal to the power of a laser pointer. The spectra were collected using a ring fiber probe (see Figure 12.5) with zero and 3 mm spatial offsets, and then scaled-subtracted to remove the surface layer contributions. The measurements were performed on the thumb distal phalanx bone of volunteers through approximately 2 mm of overlaying soft tissue. The overall acquisition time was 200 s, and the probe wavelength 830 nm; three typical processed Raman spectra are shown in Figure 12.11. The accuracy achieved in these studies was limited by the signal-to-noise ratio (SNR) of the spectra obtained at the very low laser power, and did not reach the level required for the diagnosis of conditions such as osteoporosis [40]. However, further improvement of the *in vivo* Raman spectra might be feasible by using the inverse SORS approach [31–33], which permits substantially higher laser powers to be delivered safely into the tissues.

12.3.2
Chemical Identification of Calcifications in Breast Cancer Lesions

Another potential application area for these techniques is in the noninvasive detection of calcifications within breast tissue, as demonstrated by the groups of Baker [42], Stone [43] and Matousek [44], using the Raman Kerr-gated, SORS and transmission Raman methods, respectively, with chicken breast tissue phantoms. These groups achieved respective penetration depths of 0.9, 8.7 and 16 mm in these experiments. Given the potential for recognizing malignant and benign
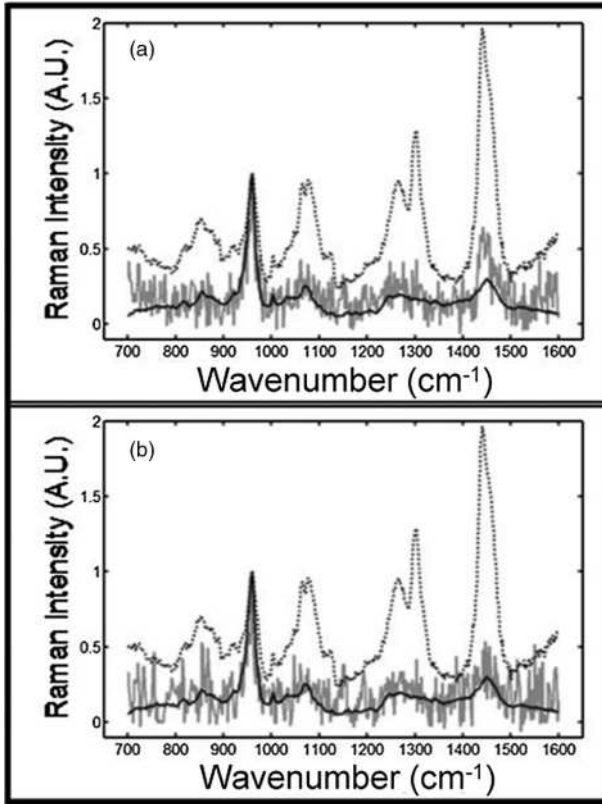
Figure 12.10 Measurements made through 4 mm of overlying tissue on a chicken tibia at the mid diaphysis using the SORS approach. Transcutaneous (dotted), recovered bone factor (gray), exposed bone (black). (a) Recovered bone factor using data from all 50 collection fibers; (b) Recovered bone factor using data from the 32 innermost collection fibers. The laser power was 110 mW and the acquisition time 120 s. Reprinted with permission from Ref. [31].; © 2006, The Society of Photo-Optical Instrumentation Engineers.

lesions from the chemical constituency of the calcifications, the techniques hold great promise for providing additional diagnostic power to conventional techniques such as X-ray mammography, which cannot identify the chemical make-up of the calcifications noninvasively, nor the type of lesion. At present, detection of the presence of suspected calcifications is usually followed by a needle biopsy which, in 70–90% of cases, uncovers only benign lesions.

The above investigations built upon the pioneering studies of Haka *et al.* [45], by showing that excised calcifications were identifiable by Raman spectroscopy and separable into groups: type I, containing calcium oxalate dihydrate (cod); and type II, containing calcium hydroxyapatite (hap). Calcium oxalate crystals are mainly found in benign ductal cysts, while calcium hydroxyapatite crystals
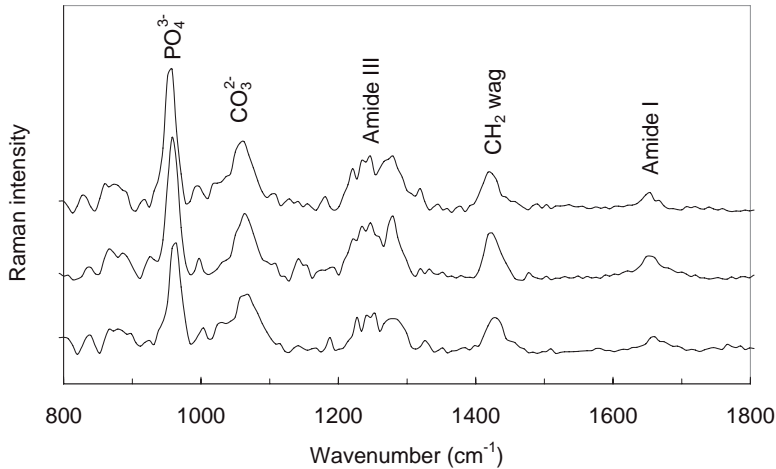
Figure 12.11 The estimates of pure Raman spectra of human bone *in vivo* measured transcutaneously at the distal phalanx of the thumb bones. Three different measurements are shown decomposed from the raw SORS spectra obtained at the zero and 3 mm spatial offsets. The spectra were obtained using a continuous-wave laser operating at 827 nm with skin-safe laser power (2 mW). The spectra are offset for clarity. The acquisition time was 200 s for each spectrum. Reprinted with permission from Ref. [29]; © 2006, The Society for Applied Spectroscopy.

are found both in carcinoma and in benign breast tissue. There is, however, a recognizable spectroscopic difference between calcium hydroxyapatite crystals originating from malignant and non-malignant sources.

In this application, the transmission Raman method has, to date, achieved the greatest penetration depth. This method yields a strong suppression of skin fluorescence originating at the NIR wavelengths, predominantly from melanin components, but is grossly insensitive to the depth of the probed calcifications [44]. The results of the reported feasibility study [44] are shown in Figure 12.12. These experiments were performed at 830 nm with a laser spot diameter of around 4 mm, and the Raman light was collected using a fiber bundle consisting of 33 individual optical fibers. The study was performed on a 'phantom' lesion made from a 16 mm slab of chicken tissue with a thin calcified material layer (100–300 μm) placed within its interior. While recognizable chemical signatures were obtained with both calcification types, further studies are clearly required as the amount of calcification used exceeded (by about two orders of magnitude) the clinically relevant level. Substantial improvements in the technique are, nonetheless, possible and these were also proposed in the study report [44]. While this application represents an ongoing challenge, if proved to be successful it could play a significant role in breast cancer diagnosis, as well as contributing to the diagnostic potential of existing techniques.
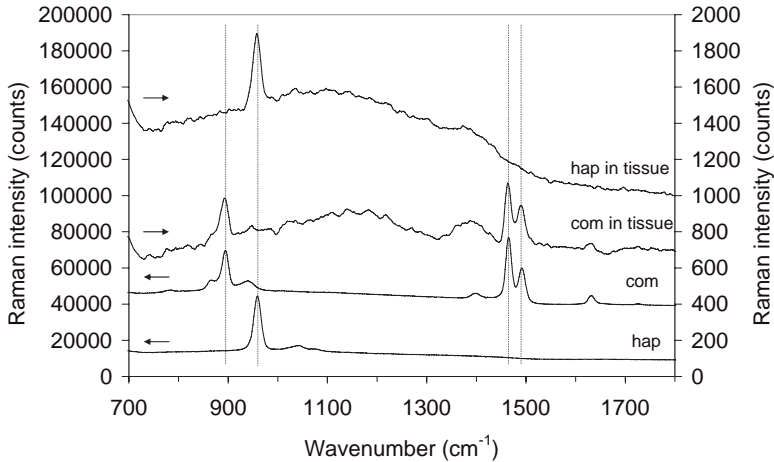
Figure 12.12 Raman spectra of two types of calcified materials (a 100–300 μm-thick layer) recovered from a 16 mm-thick slab of chicken tissue ('hap in tissue', 'com in tissue'; see text for details). The spectra were obtained by subtracting raw transmission Raman spectra of tissue only from those of tissue containing calcified material. The pure Raman spectra of individual calcified materials are also shown. The acquisition time was 100 s with a laser power of 60 mW. The spectra are offset for clarity. Reprinted with permission from Ref. [44]; © 2007, The Society of Photo-Optical Instrumentation Engineers.

12.3.3
Probing of Pharmaceutical Tablets in Quality Control

In many pharmaceutical process analytical technology (PAT) applications it is necessary to ascertain the overall bulk content of a tablet. Ideally, this should be accomplished both quickly and noninvasively, and with high chemical specificity. An investigation by Matousek *et al*. [34] outlined the potential of the transmission Raman approach [35] in this area, demonstrating its ability to provide bulk information on the probed object. Moreover, a substantial improvement of subsurface probing capability over the conventional backscattering Raman approach was demonstrated. The experiments were carried out on a standard 3.9 mm-thick paracetamol tablet with a simulated impurity layer (a 2 mm *trans*-stilbene powder layer) placed either at the front or back of the tablet. The measurements were performed using an 830 nm probe, with a laser beam diameter of 4 mm. The results (see Figure 12.13) demonstrated the known presence of a strong surface bias of the conventional backscattering Raman geometry (often referred to as a subsampling problem), yielding Raman signatures of solely the surface layers that were presented to the instrument. However, the transmission geometry provided mixed Raman signatures originating from both the tablet and the 'impurity', irrespective of whether the impurity was at the top or bottom of the tablet being examined.
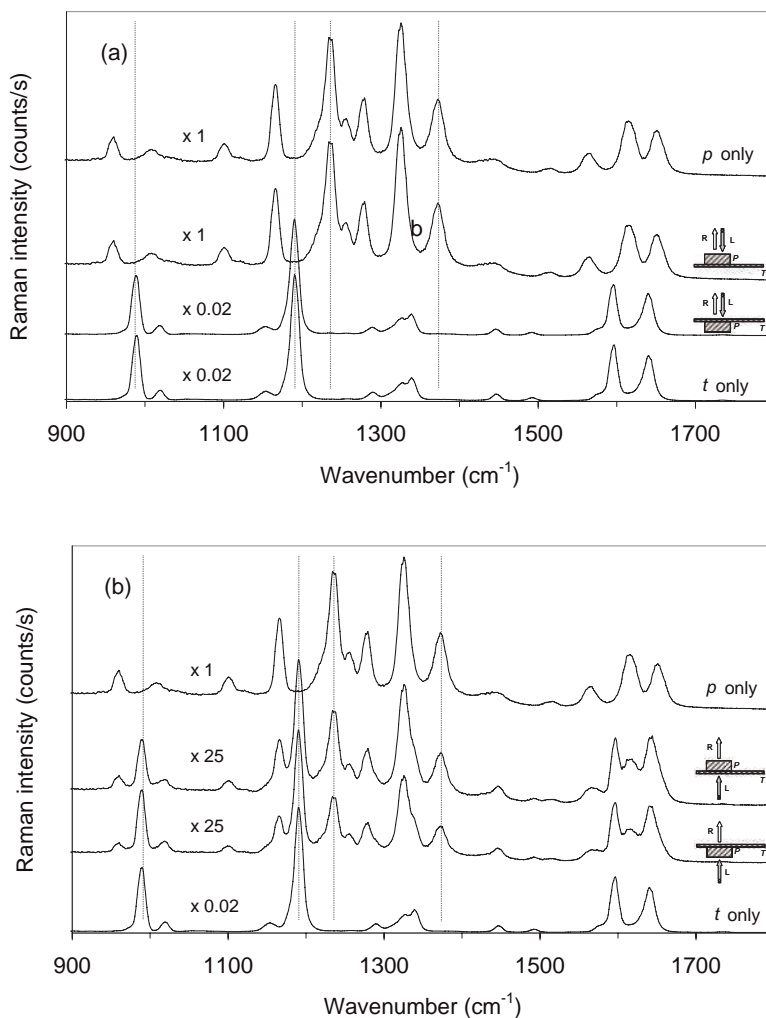
Figure 12.13 The Raman spectra obtained from a two-layer sample (3.9 mm-thick paracetamol tablet and 2 mm-thick *trans*-stilbene powder 'impurity' layer) using: (a) conventional backscattering geometry; and (b) transmission geometry. The measurements were performed at two sample orientations, with paracetamol at the top and bottom of the *trans*-stilbene cell, as indicated in the graphs. The top and bottom spectra are those of paracetamol and *trans*-stilbene, respectively, obtained in separate experiments. The acquisition times were between 0.2 and 10 s, with a laser power of 80 mW. The spectra are offset for clarity. Legend: *P* = paracetamol, *T* = *trans*-stilbene, *R* = Raman light, *L* = laser beam. Reprinted with permission from Ref. [34]; © 2006, The Society for Applied Spectroscopy.

The overall Raman signal intensity of the tablet alone in the transmission geometry was only 12-fold lower than that observed with the conventional backscattering approach. A further increase in the transmission signal and a reduction in acquisition time are possible, however, by increasing the laser power permitted by larger illumination areas available in the transmission geometry and/or by using an enhancing dielectric bandpasss filter [38]. These improvements have the potential to bring the acquisition times to well within a fraction of a second, as would be required for example in a PAT applications on a production line.

The properties of the transmission Raman geometry are well suited to the requirements of pharmaceutical production lines, thus underlining the potential of this method to displace existing NIR absorption spectroscopy in applications where a higher chemical specificity is required. However, further studies are required to establish the technique's sensitivity limits and to validate its potential. The results of some very recent investigations by Johansson *et al.* [46] and Eliasson *et al.* [47] showed that the quantification of active pharmaceutical ingredients in tablets and capsules is feasible by using the transmission approach, with a few percent relative accuracy.

12.3.4
Probing of Pharmaceutical Capsules in Quality Control

A similar need exists in the quality control of pharmaceutical capsules and coated tablets, where their bulk content may be required. Although in many applications conventional Raman spectroscopy has proven to be very effective, in some cases the Raman signal or interfering fluorescence emanating from the capsule shell or tablet coating can severely reduce the sensitivity of conventional Raman spectroscopy.

A recent study conducted by Matousek and coworkers [37] demonstrated that transmission Raman geometry could also dramatically reduce the fluorescence background originating from surface layers, thus permitting a more sensitive spectroscopic interrogation of the bulk capsule content. The results of comparative measurements using transmission and conventional Raman geometries on a variety of colored capsules are shown in Figure 12.14. Here, the spectra are displayed in their raw form as acquired. It is clear that with many colored capsules the surface fluorescence significantly deteriorates the overall Raman SNR, thus reducing the sensitivity of the conventional Raman approach [18]. The transmission Raman method does not suffer from this problem to the same extent, however, as it inherently suppresses the surface-born fluorescence and permits a much more sensitive measurement of the internal content.

12.3.5
Noninvasive Detection of Counterfeit Drugs

Another important analytical area includes the noninvasive detection of counterfeit drugs, through the plastic or glass bottles and blister packs in which they are
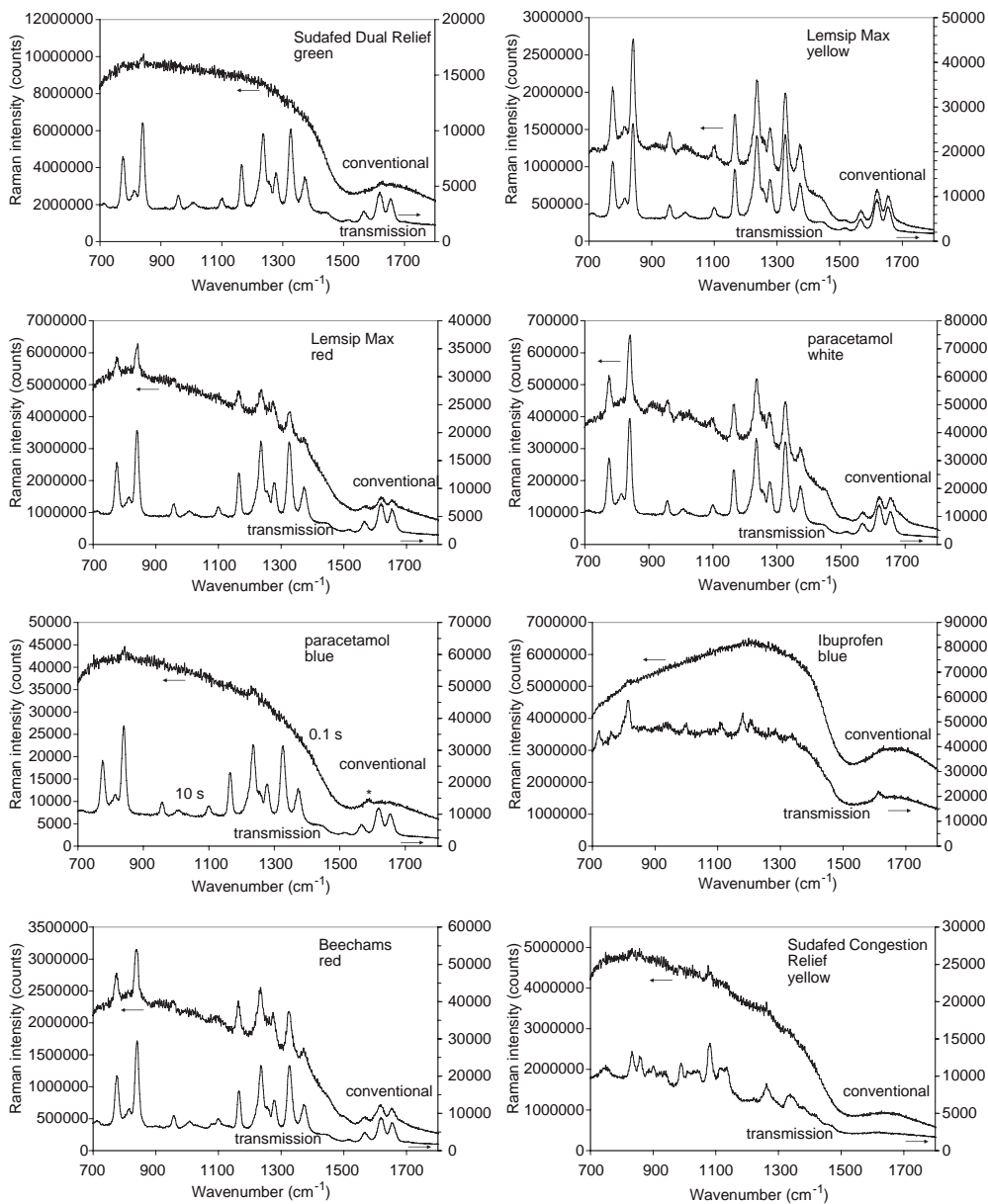
Figure 12.14 Comparison of performance of the conventional backscattering and transmission Raman geometries in probing various pharmaceutical capsules. The acquisition times were 10 s, unless indicated otherwise, with a laser power of 80 mW. * designates Raman band originating from capsule shell. Reprinted with permission from Ref. [37]; © 2007, John Wiley & Sons.

contained. Counterfeit drugs can present a serious health risk which, in extreme situations may even be life-threatening; an example is the counterfeiting of anti-malarial tablets in eastern Asia [48–50]. Although NIR absorption spectroscopy is used in this analytical area, its limited chemical specificity restricts its effectiveness. Likewise, while Raman spectroscopy has a high chemical specificity, its effectiveness will vary depending on the color and thickness of the packaging. Although the technique can be used to analyze, quite readily, any lightly colored capsules and tablets held in blister packs, any darkly colored capsules or thicker packaging (e.g., white plastic bottles) will generate excessive amounts of Raman and/or fluorescence emission, causing a substantial reduction in sensitivity.

Eliasson *et al.* [51] showed that SORS could very effectively suppress the surface Raman and fluorescence signals originating from the capsule, coating or packaging, and thus provide a substantially higher degree of chemical sensitivity than could conventional Raman spectroscopy. The use of SORS and conventional back-scattering Raman geometry in the noninvasive probing of white plastic pharmaceutical bottles containing paracetamol tablets is shown in Figure 12.15. The conventional Raman approach is ineffective in this case, yielding a massive Raman signal originating from the container wall. In contrast, the SORS approach, after the scaled subtraction of two SORS spectra obtained at spatial offsets of 0 and 3 mm, provided a clean Raman spectrum of the tablets held within the bottle. A practical use of this method was subsequently demonstrated by Ricci *et al.* on the detection of anti-malarial tablets [52].
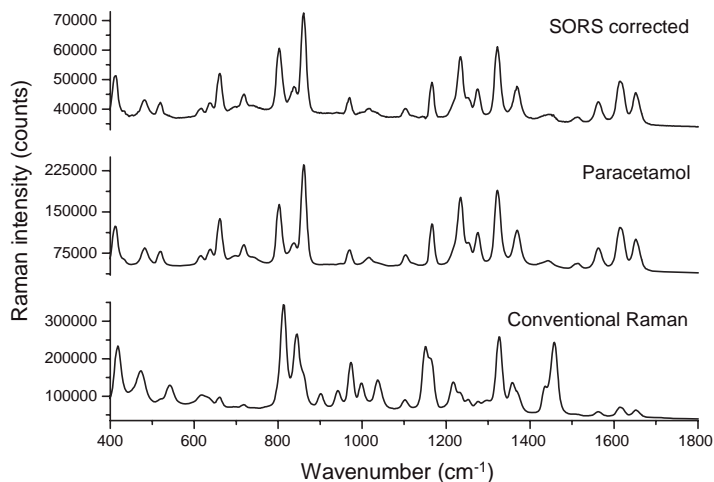
Figure 12.15 Noninvasive Raman spectra of paracetamol tablets measured through a white, diffusely scattering 1.7 mm-thick plastic container in drug authentication. Conventional Raman and SORS raw data are shown together with the tablets reference Raman spectrum. The acquisition time was 10 s and the laser beam power 50 mW. Reprinted in part with permission from Ref. [51]; © American Chemical Society.

As the SORS concept can be easily incorporated into existing commercial, hand-held Raman instruments, it holds great promise for the more accurate and sensitive identification of drugs in the entire supply chain. Yet, the applicability of this method stretches well beyond this area, and includes applications such the non-invasive detection of powder and liquid explosives and illicit drugs [33, 53].

12.4
Outlook on Raman Tomography

Today, a number of avenues exists for the further improvement of these techniques, beyond the optimization of the sensitivity through improved data collection methods and numerical data processing. The SORS approach has tremendous imaging potential, which only now is becoming apparent. Such potential was first recognized in the studies conducted by Schulmerich and colleagues [28, 54] where, in addition to chemical information on the sample composition, the ability to resolve spatial information was demonstrated. This development allows SORS to be used as a tomographic tool, in analogy with NIR absorption tomography, such that highly chemical-specific images of subsurface sample components in tissues and powdered samples can be formed. Moreover, these studies continue to make rapid progress, with Schulmerich *et al.* [55] recently demonstrating the feasibility of 3-D tomographic imaging through a canine hind limb section with thickness of up to 45 mm, using transmission Raman spectroscopy. Other alternatives include the combination of this method with other techniques, such as ultrasound and X-ray computed tomography, to provide an interesting modality whereby SORS would complement the greater spatial imaging capability of the established methods by providing detailed chemical information on the composition of subsurface structures.

12.5
Conclusions

The advent of new, noninvasive Raman spectroscopic techniques promises to have a significant impact on many biomedical, security and industrial analytical applications. Although many additional studies must be conducted, a host of new and exciting practical applications are already 'looming on the horizon'. Examples of these include the diagnosis of diseases such as osteoporosis, brittle bone and breast cancer, the quality control and authentication of pharmaceutical products, and also the detection of powder and liquid explosives through packaging.

References

1 Pelletier, M.J. (1999) *Analytical Applications of Raman Spectroscopy*, Blackwell Science, Oxford, UK.

2 Pivonka, D.E., Chalmers, J.M. and Griffiths, P.R. (2007) *Applications of Vibrational Spectroscopy in Pharmaceutical Research and Development*, John Wiley & Sons, Ltd, Chichester, UK.

3 Das, B.B., Liu, F. and Alfano, R.R. (1997) *Rep. Prog. Phys.*, **60**, 227–92.

4 Hebden, J.C., Gibson, A., Yusof, R., Everdell, N., Hillman, E.M.C., Delpy, D.T., Arridge, S.R., Austin, T., Meek, J.H. and Wyatt, J.S. (2002) *Phys. Med. Biol.*, **47**, 4155–66.

5 Koizumi, H., Yamashita, Y., Maki, A., Yamamoto, T., Ito, Y., Itagaki, H. and Kennan, R. (1999) *J. Biomed. Opt.*, **4**, 403–13.

6 Pfefer, T.J., Schomacker, K.T., Ediger, M.N. and Nishioka, N.S. (2002) *Appl. Opt.*, **41**, 4712–21.

7 Ghosh, N., Majumder, S.K., Patel, H.S. and Gupta, P.K. (2005) *Opt. Lett.*, **30**, 162–4.

8 Quan, L. and Ramanujam, N. (2002) *Opt. Lett.*, **27**, 104–6.

9 Gebhart, S.C., Majumder, S.K. and Mahadevan-Jansen, A. (2007) *Appl. Opt.*, **46**, 1343–60.

10 Wu, J., Wang, Y., Perelman, L., Itzkan, I., Dasari, R. and Feld, M.S. (1995) *Appl. Opt.*, **34**, 3425–30.

11 Everall, N., Hahn, T., Matousek, P., Parker, A.W. and Towrie, M. (2001) *Appl. Spectrosc.*, **55**, 1701–8.

12 Everall, N., Hahn, T., Matousek, P., Parker, A.W. and Towrie, M. (2004) *Appl. Spectrosc.*, **58**, 591–7.

13 Matousek, P., Everall, N., Towrie, M. and Parker, A.W. (2005) *Appl. Spectrosc.*, **59**, 200–5.

14 Morris, M.D., Matousek, P., Towrie, M., Parker, A.W., Goodship, A.E. and Draper, E.R.C. (2005) *J. Biomed. Opt.*, **10**, 014014.

15 Matousek, P., Towrie, M., Stanley, A. and Parker, A.W. (1999) *Appl. Spectrosc.*, **53**, 1485–9.

16 Matousek, P., Towrie, M., Ma, C., Kwok, W.M., Phillips, D., Toner, W.T. and Parker, A.W. (2001) *J. Raman Spectrosc.*, **32**, 983–8.

17 Matousek, P., Towrie, M. and Parker, A.W. (2002) *J. Raman Spectrosc.*, **33**, 238–42.

18 Matousek, P. (2007) *Chem. Soc. Rev.*, **36**, 1292–304.

19 Matousek, P., Clark, I.P., Draper, E.R.C., Morris, M.D., Goodship, A.E., Everall, N., Towrie, M., Finney, W.F. and Parker, A.W. (2005) *Appl. Spectrosc.*, **59**, 393–400.

20 Widjaja, E., Li, C.Z. and Garland, M. (2002) *Organometallics*, **21**, 1991–7.

21 Chew, W., Widjaja, E. and Garland, M. (2002) *Organometallics*, **21**, 1982–90.

22 Li, C.Z., Widjaja, E. and Garland, M. (2003) *J. Catal.*, **213**, 126–34.

23 Widjaja, E., Li, C.Z., Chew, W. and Garland, M. (2003) *Anal. Chem.*, **75**, 4499–507.

24 Widjaja, E., Crane, N.J., Chen, T.C., Morris, M.D., Ignelzi, M.A. and McCreadie, B.R. (2003) *Appl. Spectrosc.*, **57**, 1353–62.

25 Ma, J.Y. and Ben-Amotz, D. (1997) *Appl. Spectrosc.*, **51**, 1845–8.

26 Matousek, P., Morris, M.D., Everall, N., Clark, I.P., Towrie, M., Draper, E., Goodship, A. and Parker, A.W. (2005) *Appl. Spectrosc.*, **59**, 1485–92.

27 Schulmerich, M.V., Finney, W.F., Popescu, V., Morris, M.D., Vanasse, T.M. and Goldstein, S.A. (2006) Transcutaneous Raman spectroscopy of bone tissue using a non-confocal fiber optic array probe, in Proceedings of SPIE 6093, Biomedical Vibrational Spectroscopy III: Advances in Research and Industry (eds A. Mahadevan-

Jansen and W.H. Petrich), Paper 60930O.

28 Schulmerich, M.V., Finney, W.F., Fredricks, R.A. and Morris, M.D. (2006) *Appl. Spectrosc.*, **60**, 109–14.

29 Matousek, P., Draper, E.R.C., Goodship, A.E., Clark, I.P., Ronayne, K.L. and Parker, A.W. (2006) *Appl. Spectrosc.*, **60**, 758–63.

30 Eliasson, C., Claybourn, M. and Matousek, P. (2007) Deep subsurface Raman spectroscopy of turbid media by defocused collection system. *Appl. Spectrosc.*, **61**, 1123–7.

31 Schulmerich, M.V., Dooley, K.A., Morris, M.D., Vanasse, T.M. and Goldstein, S.A. (2006) *J. Biomed. Opt.*, **11**, 060502.

32 Schulmerich, M.V., Morris, M.D., Vanasse, T.M. and Goldstein, S.A. (2007) Transcutaneous Raman spectroscopy of bone global sampling and ring/disk fiber optic probes, in Proceedings of SPIE 6430, Advanced Biomedical and Clinical Diagnostic Systems, V (eds T. Vo-Dinh, W.S. Grundfest, D.A. Benaron, G.E. Cohn and R. Raghavachari), Paper 643009.

33 Matousek, P. (2006) *Appl. Spectrosc.*, **60**, 1341–7.

34 Matousek, P. and Parker, A.W. (2006) *Appl. Spectrosc.*, **60**, 1353–7.

35 Schrader, B. and Bergmann, G. (1967) *Z. Anal. Chem. Fres.*, **225**, 230–47.

36 Johansson, J., Pettersson, S. and Folestad, S. (2005) *J. Pharm. Biomed.*, **39**, 510–16.

37 Matousek, P. and Parker, A.W. (2007) *J. Raman Spectrosc.*, **38**, 563–7.

38 Matousek, P. (2007) *Appl. Spectrosc.*, **61**, 845–54.

39 Draper, E.R.C., Morris, M.D., Camacho, N.P., Matousek, P., Towrie, M., Parker, A.W. and Goodship, A.E. (2005) *J. Bone Miner. Res.*, **20**, 1968–72 and references therein.

40 McCreadie, B.R., Morris, M.D., Chen, T., Rao, D.S., Finney, W.F., Widjaja, E. and Goldstein, S.A. (2006) *Bone*, **39**, 1190–5.

41 Carden, A. and Morris, M.D. (2000) *J. Biomed. Opt.*, **5**, 259–68.

42 Baker, R., Matousek, P., Ronayne, K.L., Parker, A.W., Rogers, K. and Stone, N. (2007) *Analyst*, **132**, 48–53.

43 Stone, N., Baker, R., Rogers, K., Parker, A.W. and Matousek, P. (2007) *Analyst*, **132**, 899–905.

44 Matousek, P. and Stone, N. (2007) *J. Biomed. Opt.*, **12**, 024008.

45 Haka, A.S., Shafer-Peltier, K.E., Fitzmaurice, M., Crowe, J., Dasari, R.R. and Feld, M.S. (2002) *Cancer Res.*, **62**, 5375–80.

46 Johansson, J., Sparen, A., Svensson, O., Folestad, S. and Claybourn, M. (2007) *Appl. Spectrosc.*, **61**, 1211–18.

47 Eliasson, C., Macleod, N.A., Jayes, L., Clarke, F.C., Hammond, S., Smith, M.R. and Matousek, P. (2008) Non-invasive quantitative assessment of the content of pharmaceutical capsules using transmission Raman spectroscopy. *J. Pharm. Biomed. Anal.*, **47**, 221–9.

48 Newton, P.N., Green, M.D., Fernández, F.M., Day, N.P.J. and White, N.J. (2006) *Lancet Infect. Dis.*, **6**, 602–13.

49 Witkowski, M.R. (2005) *Am. Pharm. Rev.*, **8**, 56–60.

50 Mukhopadhyay, R. (2007) *Anal. Chem.*, **79**, 2622–7.

51 Eliasson, C. and Matousek, P. (2007) *Anal. Chem.*, **79**, 1696–701.

52 Ricci, C., Eliasson, C., Macleod, N.A., Newton, P., Matousek, P. and Kazarian, S.G. (2007) *Anal. Bioanal. Chem.*, **389**, 1525–32.

53 Eliasson, C., Macleod, N.A. and Matousek, P. (2007) Non-invasive detection of concealed liquid explosives using laser spectroscopy. *Anal. Chem.*, **79**, 8185–9.

54 Schulmerich, M.V., Dooley, K.A., Vanasse, T.M., Goldstein, S.A. and Morris, M.D. (2007) *Appl. Spectrosc.*, **61**, 671–8.

55 Schulmerich, M.V., Cole, J.H., Dooley, K.A., Morris, M.D., Kreider, J.M., Goldstein, S.A., Srinivasan, S. and Pogue, B.W. (2008) *J. Biomed. Opt.*, **13**, 020506.

13
Planar Array Infrared Spectroscopy and 1-D Imaging

Christian Pellerin

13.1
Introduction

In Chapter 1, details were provided of how focal plane array (FPA) detectors could be coupled to infrared (IR) spectrometers to enable the hyperspectral imaging of samples. When working in the mid-IR spectral range, these spectrometers are virtually always Fourier-transform IR (FT-IR) spectrometers. Indeed, their multiplex (Fellgett), throughput (Jacquinot) and frequency precision (Connes) advantages are well documented and, together, have caused the near-disappearance of dispersive mid-IR instruments from the laboratory [1]. In stark contrast, dispersive instruments have remained the standard instrumentation for spectroscopy in other spectral ranges, including that of Raman spectroscopy, in part because of the availability of large and sensitive detector arrays, most notably charge-coupled device (CCD) cameras. It is, then, no surprise that the recent availability of mid-IR FPAs has renewed interest in the use of dispersive mid-IR spectrometers in a spectrographic mode.

In this chapter, we present details of the coupling of mid-IR spectrographs with FPA detectors into so-called planar array IR (PA-IR) spectrographs. Such instruments allow the recording of broadband IR spectra in a few milliseconds, or less, with a good signal-to-noise ratio (SNR), and with an intrinsic one-dimensional (1-D) spatial resolution. The concept and basic instrumental aspects of this technology will first be presented. Details concerning the performances of PA-IR spectroscopy will then follow, including the technique's advantages and drawbacks as compared to FT-IR spectroscopy. Finally, application examples of this young and developing technique will be presented.

13.2
Concept and Instrumentation

The two main differences between a PA-IR spectrograph and a conventional mid-IR dispersive spectrometer are the use of a large planar array detector rather than

a single-element detector, and the absence of an exit slit on the monochromator. This has the obvious advantage of allowing the acquisition of a broad range of wavelengths in a single measurement, without any moving part. The acquisition time is thus dramatically reduced, typically to a few milliseconds or less, and is only limited by the frame rate of the FPA. In addition, removing the exit slit increases the throughput of the instrument.

The first known use of a dispersive IR spectrometer in a multidetector configuration dates from 1951, when Agnew *et al.* coupled a prism spectrograph with 10 detectors through light pipes, allowing as many resolution elements to be measured simultaneously [2]. It was only during the early 1990s that linear array detectors became available. Richardson *et al.* described a spectrometer that used a 32-element InSb linear array [3] which could be use to measure spectra in the 2400–2650 cm^{-1} region with a nominal resolution of 32 cm^{-1} and a time resolution of 4 μs. Subsequently, Hamm *et al.* built a spectrometer that used a monochromator to disperse the light from a broadband femtosecond IR pulse on a mercury cadmium telluride (MCT) 10-element array, yielding a 65 cm^{-1} bandwidth with 3–10 cm^{-1} resolution [4]. Heilweil *et al.* were the first to couple a large 256 × 256 InSb FPA with a dispersive system [5]. By using a difference-frequency mixing laser as a broadband source, they obtained spectra over a range of 400 cm^{-1} and with a resolution of 15 cm^{-1}.

The first PA-IR spectrograph was developed in 2002 by Rabolt *et al.* [6]. It also used a 256 × 256 InSb FPA and provided a 850 cm^{-1} bandwidth tunable between 3400 and 2000 cm^{-1} and with an average resolution of 8 cm^{-1}. In 2004, Pellerin *et al.* extended the technique to the full mid-IR range (from 4000 to 975 cm^{-1}) by using a 256 × 256 MCT FPA [7]. In 2007, Sommer *et al.* [8] went further back in the history of dispersive IR spectrometers by demonstrating the possibility of PA-IR spectroscopy using a prism-based spectrograph rather than a grating system.

Figure 13.1 shows the typical layout of a grating-based PA-IR spectrograph. In contrast with the set-up of Heilweil *et al.* [5], an inexpensive continuous-wave broadband IR source is used, thus decreasing the cost and complexity of the

S: Slit
G: Grating
L: Lens
FPA: Focal plane array

IRS: Infrared source
M: Concave mirrors
F: Long-pass filter
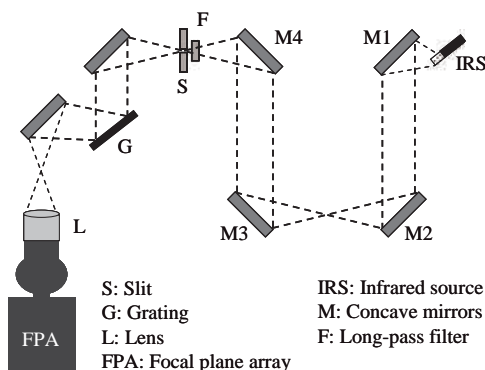
Figure 13.1 Schematic representation of the optical layout of a planar array infrared spectrograph.

instrument. Although such a source provides sufficient power (often 100 W), its height limits the focusing capability. The IR radiation is collected and collimated by a concave mirror (M1), typically a spherical or an off-axis parabolic mirror with a 5–8 cm diameter and a 15 cm focal length. A series of identical concave mirrors (M2–M4) first focus the beam onto the sample holder or accessory, and then onto an order-sorting long-pass filter (F) and the entrance slit (S) of the spectrograph. Any standard FT-IR accessories (specular reflection, ATR, etc.) can be used with a PA-IR spectrograph, as long as the focal length of both the M2 and M3 mirrors is similar to that of an FT-IR. The long-pass filter is used to reject the second or higher diffraction orders from the grating, and is thus critical for quantitative measurements. The slit width is often set at 200–300 μm as a compromise between spectral resolution (favored by narrow slits) and throughput (favored by large slits).

A Czerny–Turner spectrograph is used to disperse the different wavelengths and to focus the diffracted light on a focal plane for detection by the FPA. A short-focal length (10–15 cm) system and a planar ruled grating with a low groove density are normally used in order to provide an appropriate dispersion of the radiation. Diffraction gratings with 40 to 150 grooves mm^{-1} are typically used for measurements in the fingerprint region, whereas a grating with 300 grooves mm^{-1} is appropriate for measurements above 2000 cm^{-1}.

The FPA can be aligned directly at the focal plane of the spectrograph, as in most CCD-based systems; however, in most cases a compound lens is used (as in Figure 13.1) to reimage the focal plane on the FPA with a controlled demagnification. Indeed, the size of (affordable) FPAs is smaller than that of the focal plane of the spectrograph, and thus becomes a limiting factor for the spectral bandwidth. In contrast to standard 1-inch (2.5 cm) CCD cameras, a 256×256 mid-IR FPA covers only about 40% of the width of the focal plane of the spectrograph. Although the compound lens increases the cost of the system, it does allow the measurement of a larger spectral range; alternatively, it can be used to optimize the field of view along the spatial dimension of the spectral images (*vide infra*).

The sensitivity and noise level of a PA-IR spectrograph are affected by the source power and the overall throughput of the instrument (reflectivity of the surfaces, slit width, etc.). The dominant factor is, nevertheless, the performance of the FPA, the most expensive element of the spectrometer. Up to now, most results have been obtained using liquid nitrogen-cooled FPAs (MCT or InSb) with dimensions from 64×64 up to 256×320 pixels, sometimes originally intended for use with FT-IR imaging microscopes. Liquid nitrogen-cooled FPAs offer the best sensitivity and noise level, with noise equivalent power temperature (NEPT) of 15 mK. Thermoelectrically cooled microbolometer arrays can, nevertheless, constitute a cheap and convenient alternative. These allow measurements to be made at lower frequencies than MCT FPAs (700 versus 975 cm^{-1}), albeit at the expense of a greater noise level (NEPT of 80 mK), a decreased time resolution, and a high-wavenumber response limited to approximately 1400 cm^{-1}. The demand for IR cameras in civil applications is prompting the development of uncooled or thermoelectrically cooled IR FPAs with improved performance and lower cost.

The frame rate of the FPA directly determines the time resolution of a PA-IR spectrograph, while its size can limit the achievable bandwidth/resolution and the field of view. Maximum frame rates vary between 100 μs and 17 ms per spectrum, depending on FPA type and size. Such time resolutions are similar or significantly better than those possible with continuous-scanning FT-IR spectrometers. It should be pointed out that the limiting factor is often not the detection of the IR radiation, but rather the time necessary for the read-out and data transfer. Perfectly optimized electronics could eventually enable a ~70 μs time resolution.

13.3
PA-IR Spectroscopy

Figure 13.2a shows a spectral image recorded by a PA-IR spectrograph for a polystyrene (PS) sample. The spectrograph disperses the radiation along the horizontal axis (spectral dimension) so that a pixel row corresponds to a single beam spectrum of the sample. In this specific case, the image ranges from about 1850 to 1100 cm^{-1} from left to right. The bright color is due to high intensity in the single beam spectrum, while dark vertical stripes are due to absorption by PS or by water vapor.

It is clear in Figure 13.2a that a PA-IR spectral image is several pixels high and offers an intrinsic 1-D spatial resolution. Each row contains the spectral information originating from a specific height along the long direction of the entrance slit. This is illustrated in Figure 13.2b, in which only a narrow strip of PS was inserted in the middle of the beam. As a consequence, PS absorption bands are only observed in the middle of the image (as noted by an arrow), while the rest of the spectral image can be used as a single-beam background spectrum. The spatial resolution depends on the focal length of the mirrors and the compound lens, as
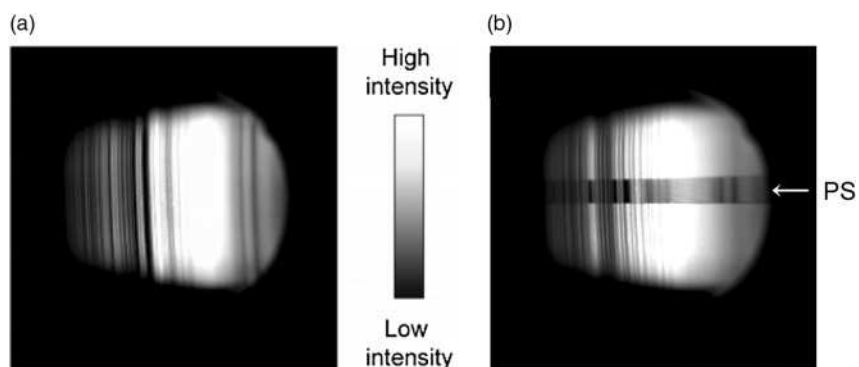
Figure 13.2 Spectral image recorded for a polystyrene (PS) thin film covering: (a) the full IR beam; and (b) only the middle section of the IR beam. Panel (a) reproduced with permission from Ref. [7].

well as on the pixel size. The resolution is about 150 μm per pixel for the set-up of Figure 13.1, when no particular magnification or demagnification is introduced. Different uses of the spatial dimension, such as multisample and multibeam experiments, will be described in the following sections. As Figure 13.2b suggests, this spatial dimension also allows the simultaneous recording of both sample and background spectra [9, 10].

A spectral image in absorbance units can be calculated pixel by pixel as:

$$A = -\log\left(\frac{I_{sample} - I_{dbk}}{I_{background} - I_{dbk}}\right)$$

where I_j is the intensity (counts) detected for the sample, background and dark background (dbk), respectively. The background is a standard open beam spectrum that can either be measured in a separate acquisition or on the same image as the sample, as in Figure 13.2b. The dark background is recorded with a shutter blocking the entrance slit of the spectrograph. Its purpose is to take into account stray light reaching the FPA. Such correction is necessary because the FPA works in DC mode and is sensitive to IR emission from the environment (including itself). As with any dispersive spectrometer, the spectral axis of a PA-IR spectrum must be converted to wavenumbers using a frequency calibration standard. A PS secondary standard card is often used for this purpose.

Figure 13.3 compares the PA-IR spectra of poly(ethylene naphthalate) (PEN) and PS recorded with InSb and MCT FPAs, respectively, with FT-IR spectra recorded at different resolutions [6, 7]. As expected, the PA-IR spectra are similar to their FT-IR counterparts. An InSb PA-IR spectrograph with a 300 grooves mm^{-1} grating (first-order diffraction) provides an approximately 850 cm^{-1} bandwidth that can be tuned in the 3400–2000 cm^{-1} range, with an average resolution of 8 cm^{-1} [6]. A system based on an MCT FPA can provide a bandwidth up to 750 cm^{-1} over the 3400–975 cm^{-1} range, with a resolution that varies between 7 and 14 cm^{-1} [7]. This resolution range is due to the fact that the spectral resolution of a dispersive instrument is constant in wavelength units, not wavenumbers. The spectral resolution for any given configuration is always better at low wavenumbers (long wavelengths). An uncooled microbolometer FPA can also be used to record spectra down to 700 cm^{-1}, below the cut-off of MCT detectors [8].

In contrast to FT-IR spectroscopy, it is not possible to dissociate bandwidth and resolution in a PA-IR experiment. Both are limited by the size of the FPA that dictates the number of resolution elements that can be recorded in a single acquisition. Up to now, bandwidth has usually been favored over resolution because moderate resolutions are often sufficient, especially for time-resolved studies. As a rough rule of thumb, doubling the groove density doubles the spectral resolution but halves the bandwidth (as long as the slit width and FPA pixel size do not become limiting factors). The ideal way of achieving both high spectral resolution and large bandwidth is to use larger arrays, as in Raman spectroscopy with 1024 pixel-wide CCD cameras. However, such mid-IR FPAs are currently prohibitively expensive.

(a)

(b)
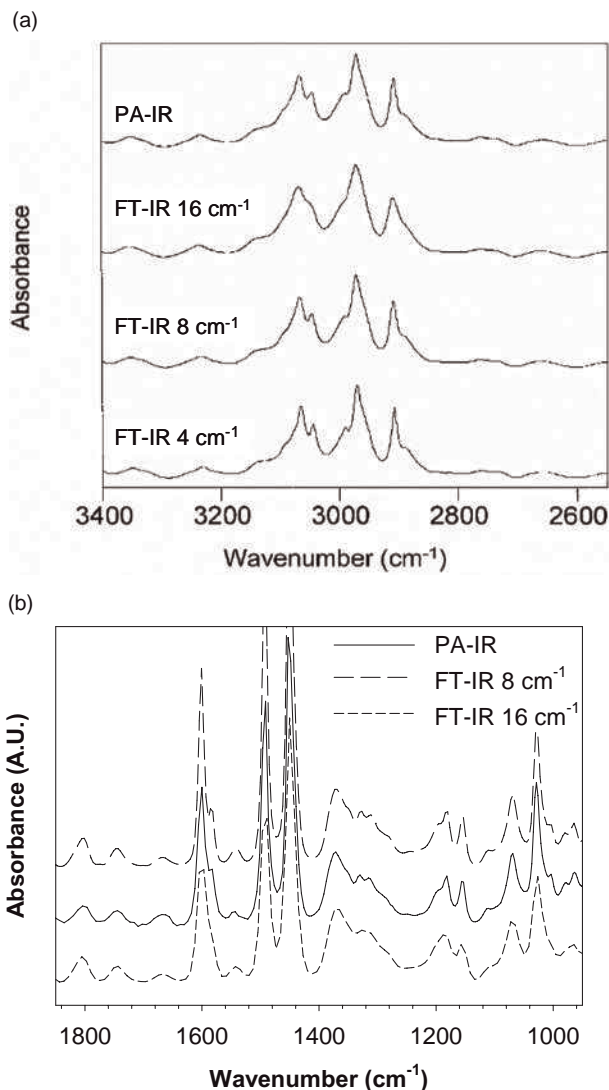
Figure 13.3 Comparison of the PA-IR and FT-IR spectra recorded for: (a) Poly(ethylene naphthalate) in the high-frequency range with an InSb FPA; (b) Polystyrene recorded in the fingerprint region with an MCT FPAs. Panels (a) and (b) adapted from Refs [6] and [7], respectively.

An alternative approach recently proposed by Sommer *et al.* is the use of a single or double-pass prism monochromator rather than a grating system [8]. This provided a large bandwidth, up to $3000 \, cm^{-1}$, at the expense of a reduced spectral resolution, especially in the C—H stretching region. Another recently described approach to extend the spectral coverage was to stack two gratings with a low and

high groove density, respectively, in order to simultaneously record two spectral ranges in the same image. Such mosaic grating architecture allowed the recording of spectra in the C—H stretching and fingerprint regions, simultaneously [9].

PA-IR spectroscopy allows very rapid measurements, with millisecond or submillisecond time resolution, with good to excellent SNRs. By measuring 100% lines spectra, Rabolt *et al.* reported that a peak-to-peak noise level of 2.7×10^{-3} absorbance units can be obtained in 17 ms using an InSb FPA system [6]. A similar value was obtained in 8.7 ms with an MCT FPA system [7]. As expected, longer acquisition times lead to increased SNRs. The data in Figure 13.4 show that peak-to-peak noise level in PA-IR spectra decreases with acquisition time, with a slope close to the expected square root improvement [1, 7]. Noise levels are similar to those obtained with an FT-IR spectrometer for the same measurement time. An important feature of PA-IR spectroscopy is that, when a sample is homogeneous, the spectra recorded from multiple rows can be averaged (pixel binned) to improve the SNR of the mean spectrum. Again, the data in Figure 13.4 show that, when averaging 100 rows, a peak-to-peak noise of 2.4×10^{-4} absorbance units can be obtained with an MCT PA-IR spectrograph in a single frame of 8.7 ms. A noise level in the low milliabsorbance range has also been reported for a prism-based PA-IR spectrograph for an acquisition time of 2 s [8].

It should be pointed out that, in good part because of the use of large off-axis mirrors, optical aberrations can lead to significant curvature of the images under certain instrumental configurations. This has a detrimental impact on spectral resolution when multiple rows are binned. Pelletier *et al.* have reported a data processing procedure to minimize this effect for situations where experimental limitations prevent improving the optical set-up [9]. In future commercial
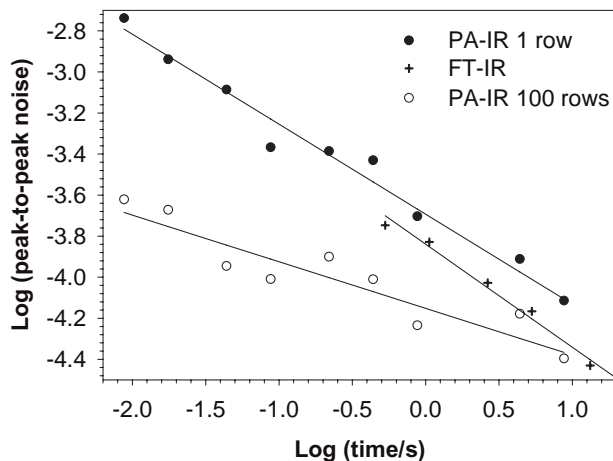
Figure 13.4 Evolution of the peak-to-peak noise level in 100% noise spectra as a function of acquisition time using an MCT PA-IR spectrograph (with an without pixel binning) and an FT-IR spectrometer. Reproduced with permission from Ref. [7].

implementations of PA-IR spectroscopy, proper optical design should minimize this effect, for instance by using of a curved slit or an aberration-correcting toroidal mirror.

13.4
Applications

13.4.1
Ultrathin Films

The first reported applications of PA-IR spectroscopy and imaging dealt with the characterization of ultrathin organic films deposited on solid substrates [11–13]. IR spectroscopy is a very useful tool for characterizing various aspects of such systems [14]. In particular the density or surface coverage of the ultrathin film can be determined from the absorbance of IR bands with known absorption index, while the position and width of some bands provide information about the conformation and structure of the molecules. For instance, the position of the methylene symmetric stretching band around $2850\,cm^{-1}$ is often used to evaluate if the alkyl chains are in all-*trans* conformation or contain gauche defects [15], while the splitting of the methylene bending band at 1463 and $1473\,cm^{-1}$ is indicative of a crystalline structure with an orthorhombic packing [16]. IR polarization measurements also allow the quantitative determination of the molecular orientation of the molecules [17].

Elmore *et al.* have used a PA-IR system equipped with a 320×256 InSb FPA to analyze a series of self-assembled monolayers (SAMs) of octadecyltrichlorosilane (OTS) on glass substrates [11]. The group studied the coverage and conformation of SAMs prepared using three different solvents: hexane, benzene and toluene, and showed that their PA-IR spectrograph was sufficiently sensitive to record the spectrum of a monolayer on glass in a tilted-transmission geometry. Spectral images covered the 3200–$2800\,cm^{-1}$ range with an average resolution of $6\,cm^{-1}$. The spectra were recorded in only 27 s, corresponding to approximately 256 FT-IR scans at the same resolution. Of course, FT-IR spectroscopy would provide a complete mid-IR spectrum, but this would not be a major advantage for glass substrates because of their limited transmission range.

The advantage of PA-IR spectroscopy for this study was the possibility of recording a series of 1-D, spatially resolved spectra [11]. Indeed, although the recorded spectral image was ~100 pixels high, the binning of only four pixel rows was found to be sufficient to yield a spectrum with good SNR. Each image was thus converted to 28 spectra spatially resolved along the height of the slit. Figure 13.5 shows the line spectra recorded for the SAMs prepared from solutions in the three solvents. It can be observed that the mean absorbance varies by up to a factor of four, depending on the solvent used for the deposition. Based on the known absorbance of the antisymmetric H—C—H stretching band ($2920\,cm^{-1}$) for a full monolayer of OTS, it was concluded that deposition from hexane produced almost complete
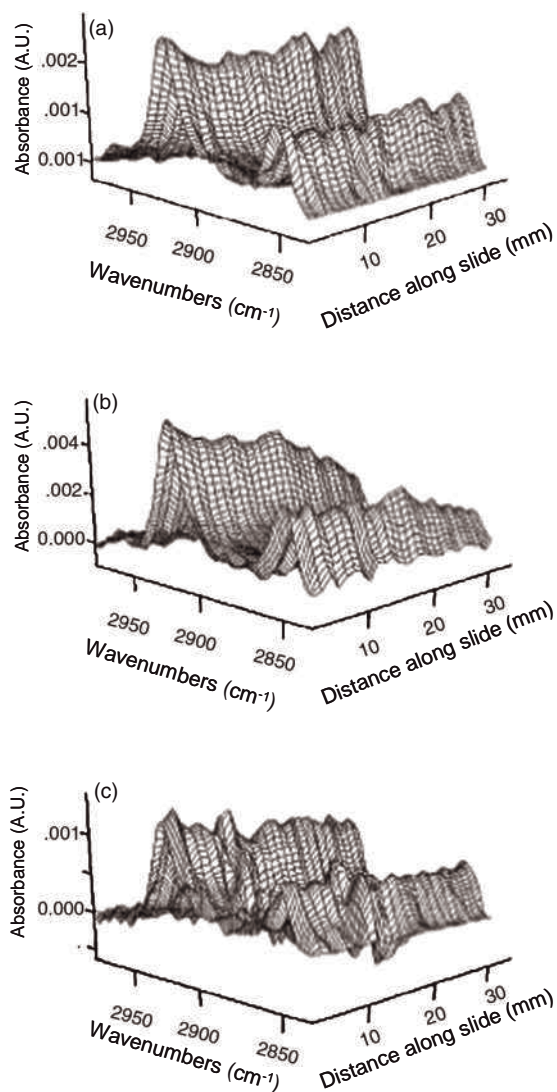
Figure 13.5 Line images of self-assembled OTS monolayers on a glass substrate produced using (a) benzene; (b) hexane; and (c) toluene. Adapted from Ref. [11].

monolayers. In contrast, benzene and toluene yielded partial monolayers composed of domains that covered ~50% and ~25% of the glass surface, respectively. In a different study, a similar trend was observed in SAMs of the short-chain *n*-propyltrichlorosilane prepared from the same solvents [12]. It can be observed in Figure 13.5 that the surface coverage is not uniform across a given sample. Statistical analysis indicated that the largest relative standard deviation in absorbance is observed for the SAMs prepared from hexane. Such variation in coverage would

obviously have been missed by recording a single averaged spectrum instead of a line image.

The position of the antisymmetric H—C—H stretching band also revealed significant variations of conformational order in the different samples and with position within a sample [11]. Not unexpectedly, SAMs prepared from hexane showed the lowest average band position at $2919\,\text{cm}^{-1}$, which is indicative of higher order, while the SAMs with lower surface coverage had frequencies as high as $2923\,\text{cm}^{-1}$, indicative of high *gauche* conformation content. In fact, Figure 13.6 shows that there is a relationship between band position and surface coverage. It was noted that, interestingly, the shape of this plot is similar to that of a Langmuir pressure–area isotherm. An apparent transition from a disordered to an ordered state is found between 18 and 40% coverage, followed by a plateau-like region, and a second transition at higher surface coverage. These results are in agreement with those obtained using sum-frequency generation spectroscopy and contact angle measurements [18].

Monolayers and ultrathin films are often prepared or deposited on metallic surfaces and studied using FT-IR reflection-absorption spectroscopy (FT-IRRAS) [14]. Rabolt *et al.* showed that such measurements are also possible using a PA-IR spectrograph [13] by studying the evolution of orientation and conformation in monolayers of octadecylthiol self-assembled on gold substrates as a function of dipping time. In contrast to the previous study [11], 1-D spectral imaging indicated the formation of rather uniform monolayers for all dipping times, even after only a few seconds. The conformational order of the SAMs, observed through the antisymmetric H—C—H stretching band position, nevertheless increased rapidly during the first 5 min of dipping, and then very slowly over a 40 h period. Finally, it was shown recently that PA-IR reflectance spectra can be recorded in a dual-beam fashion by covering only half of the metallic or dielectric substrate with the sample [10]. The second half of the beam can be used to record, simultaneously,
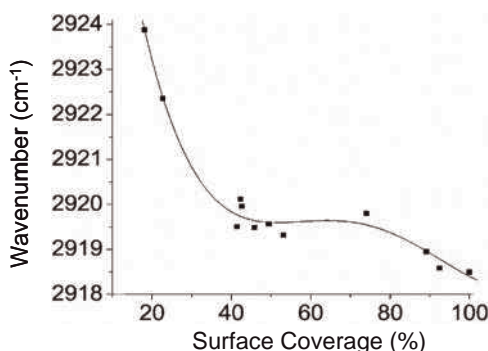
Figure 13.6 Evolution of the frequency of the H—C—H antisymmetric stretching band as a function of monolayer coverage for OTS SAM on glass substrates. Adapted from Ref. [11].

a background spectrum, which allows compensation to be made for fluctuations in the water vapor concentration and drifts of the instrument.

13.4.2
Time-Resolved Studies

Because of its intrinsic millisecond or submillisecond time resolution, a natural application of PA-IR spectroscopy is the dynamic characterization of complex chemical and physical systems. Continuous-scanning FT-IR spectroscopy is currently the tool of choice to probe phenomena with characteristic times on the order of hundreds of milliseconds or more, although its time resolution is limited by the need to accelerate and decelerate the moving mirror during each scan [19]. A prototype interferometer designed by Manning *et al.* circumvented this problem by using a rotating wedged mirror [20]. A time resolution of 10 ms has been demonstrated for the study of polymer deformation using this spectrometer [21]. In spite of this, the time resolution for continuous-scanning FT-IR imaging is limited to several seconds per image, because relatively slow scanning speeds must be used in order for the Fourier frequencies to be appropriately sampled by the FPA digitizing electronics [22].

Step-scan FT-IR spectroscopy is a technique that decouples the temporal response of the chemical system from the Fourier frequencies of the interferometer, thus enabling a time resolution in the nanosecond range for single-point studies [19]. When coupled with an FPA, a time resolution of 2.5 ms has been demonstrated by Bhargava and Levin for the electric field-induced Freedericksz transition of liquid crystals (LCs) [23]. However, a serious limitation of step-scan FT-IR, both for imaging and nonimaging studies, is that it is strictly limited to phenomena that can be perfectly repeated hundreds or even thousands of times without any evolution of the sample response. This, unfortunately, prevents its use for a large number of interesting systems [20].

In this context, PA-IR spectroscopy can overcome some of the limitations of FT-IR spectrometers by providing millisecond or submillisecond time resolution for the study of nonrepeatable events, while still providing a 1-D spatial resolution. If imaging is not needed, the spatial dimension of the FPA can still be used to increase the SNR of the spectrum by pixel binning, or to record information from two beams simultaneously. In a proof-of-principle study, Rabolt *et al.* demonstrated the possibility of millisecond time-resolved PA-IR spectroscopy by probing the electric field-induced reorientation of a LC, 4-*n*-pentyl-4′-cyanobiphenyl (5CB) [7]. The dynamics of 5CB and other low-molecular-weight LCs have been widely studied using step-scan FT-IR spectroscopy, in order to better understand the parameters affecting the performance of LC display devices; an example is the influence of the alignment layers on dynamic response [24]. It should be recognized that whilst this phenomenon is in fact highly repeatable, it was treated as nonrepeatable for demonstration purposes.

Figure 13.7a shows a spectral image of the 5CB sample inserted between two germanium plates covered by a rubbed poly(vinyl alcohol) (PVA) alignment layer.

(a)

p polarization

s polarization

(b)

(c)
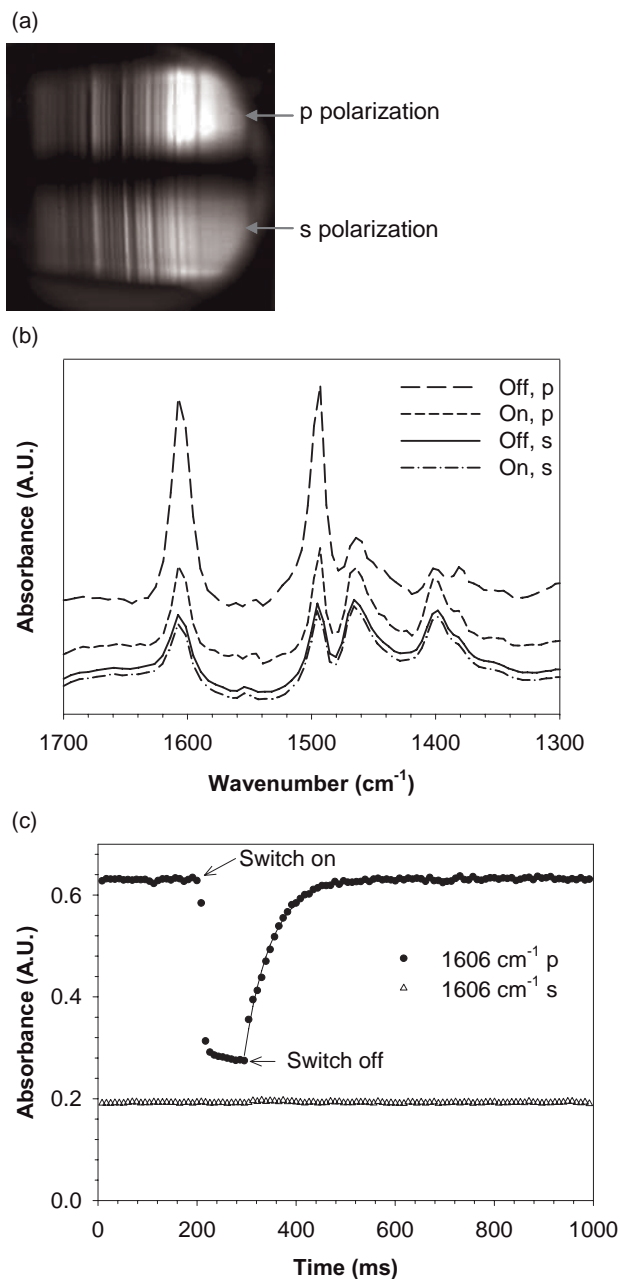
Figure 13.7 (a) Multiple beams PA-IR spectral image: the top and bottom images are p- and s- polarized, respectively, before application of the electric field; (b) p- and s- polarized spectra of 5CB recorded before (Off) and during (On) a 100 ms electric field pulse; (c) Dynamics of 5CB submitted to a single 100 ms electric field pulse. The continuous curve is a single exponential fit of the reorientation kinetics. Adapted from Ref. [7].

It is often interesting to record time-resolved IR spectra with the radiation polarized parallel (p) and perpendicular (s) to the rubbing direction, in order to extract molecular orientation information. This normally requires two independent experiments to be performed, ideally under rigorously identical conditions, to record two sets of time-resolved data. In these studies, the spatial dimension of the FPA and two stacked mutually perpendicular polarizers were used to detect simultaneously two polarized beams. The top and bottom portions of Figure 13.7a thus contain p- and s-polarized spectra, respectively. It should be noted that the pixel rows in each portion of the image still correspond to different positions along the height of the sample.

Figure 13.7b shows the average polarized spectra, and reveals that the PVA layers introduced a preferential in-plane orientation of the LC prior to application of the electric field (Off). For instance, the $1606\,cm^{-1}$ band, attributed to aromatic C=C stretching, is much more intense in the p-polarized spectrum. On the other hand, the $1398\,cm^{-1}$ band, due to C—H deformation of the tail aliphatic groups, preferentially absorbs s-polarized radiation. An orientation function [25] of 0.47 was determined for the LC using the $1606\,cm^{-1}$ band, while a perfect orientation would have yielded a maximum theoretical value of 1. When the electric field was applied (On), the parallel and perpendicular bands in the p-polarized spectrum decreased and increased, respectively. In contrast, no significant variation occurred in the s-polarized spectrum. This is the expected behavior for a nematic LC reorienting along the electric field direction when cylindrical symmetry is preserved [26].

Figure 13.7c shows the time-resolved absorbance changes for the $1606\,cm^{-1}$ band before, during and after the application of a 100 ms electric field pulse. An abrupt decrease in absorbance was observed in the first few milliseconds in the p-polarized curve when the field was switched on, followed by a slower process during the following ~80 ms. When the field was switched off, the LC molecules reoriented back to their initial state, parallel to the alignment layer. Curve fitting with a single exponential function yielded a relaxation time of 55 ms for the reorientation process. As expected from Figure 13.7b, no significant change can be observed in the s-polarized curve with the application of the electric field. This curve, nevertheless, shows the sensitivity of time-resolved PA-IR spectroscopy. A very low scatter in the data (<0.005 absorbance units) is observed around the mean value in spite of a short 8.7 ms acquisition time. It should be stressed that the results of Figure 13.7c were obtained by applying a single pulse, without any averaging other than pixel binning.

Snively *et al.* used a PA-IR spectrograph equipped with a 64×64 MCT rolling-mode FPA to push the time resolution of PA-IR spectroscopy to less than 100 μs per spectrum [27]. The small size and the acquisition mode of this FPA, both contributed to enable such time resolution. First, a smaller FPA allows faster frame rates than a larger one (3.2 ms per image in this specific case), at the expense of bandwidth and/or resolution. Second, the 100% duty cycle of a rolling-mode FPA was put to profit. In a snapshot-mode FPA, all pixels measure the signal intensity simultaneously for ~100 μs, but the electronic read-out time can be as

much as 100 times longer and effectively limits the time resolution of the instrument. The actual duty cycle depends on the FPA size and on the number of acquisition channels. In contrast, only two pixel rows integrate the signal at any given time in a rolling-mode FPA. The electronic read-out is then performed while the next rows probe the IR signal. A full spectral image is then, in fact, constituted of 32 'time slices' recorded at 99 μs intervals. By addressing each time slice (pair of rows) separately, the time resolution of the instrument effectively becomes sub-100 μs. A trade-off of such an experimental scheme is that it prevents use of the spatial dimension of the spectral images for other purposes, and implicitly assumes that the dynamic response is uniform across the height of the sample.

Snively *et al.* demonstrated this experimental approach using the same model system as above: the Freedericksz transition of 5CB [27]. Because of the restricted number of pixels on a 64×64 FPA, the spectral image was centered on the 1606 cm^{-1} phenyl C=C stretching band, and covered about 154 cm^{-1} with an 8 cm^{-1} resolution. While this bandwidth is narrow, it is sufficient to probe the dynamics of the LC reorientation. Figure 13.8 shows the response of the LC when the electric field is switched on; here, the orientation of the LC along the electric field occurs very rapidly with a characteristic time of approximately 1.5 ms. The dynamics of the phenomenon could easily be resolved based on the 99 μs time resolution of the instrument. The noise level was significantly larger than that in experiments conducted with the larger 256×256 FPA (Figure 13.7c) [7], this being due in good part to the fact that only two pixel rows were averaged as compared to 20 in the previous study.

Although the previous demonstrations were performed on a repeatable event, they illustrated the performance that could be expected for truly nonrepeatable events. It should be pointed out here that some IR FPA detectors can be triggered by an external signal with a jitter time of <100 ns, thus allowing precise synchro-
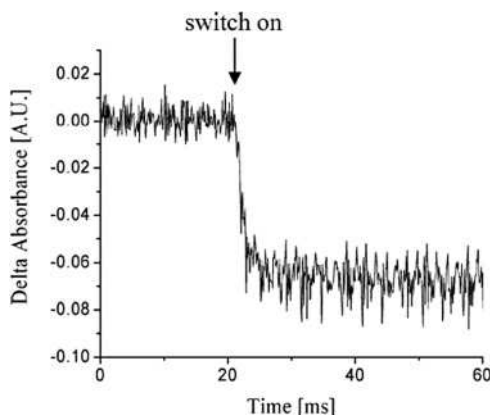
Figure 13.8 Sub-100 μs orientation dynamics of 5CB submitted to a single 100 ms electric field pulse. Reproduced with permission from Ref. [27].

nization of time-resolved experiments. One such example currently under study is the macroscopic deformation of polymers, for which the simultaneous measurement of p- and s-polarized spectra with a sub-millisecond time resolution should prove invaluable. Another potential application of time-resolved PA-IR imaging is the study of diffusion kinetics, such as the dissolution of polymers or pharmaceutical tablets. Although this phenomenon is currently investigated using FT-IR imaging (see Chapter 9), it would be naturally amenable to PA-IR 1-D imaging as spatial resolution is only necessary along the diffusion gradient. In fact, the hyperspectral FT-IR images are sometimes reduced to a single line (1-D imaging) to improve the SNR of the spectra.

As noted above, step-scan FT-IR can provide a better time resolution than PA-IR spectroscopy for time-resolved studies, as well as full spectra at the desired resolution. On the other hand, its major limitation is that the phenomenon under study must be perfectly repeatable – information which often is not available before an experiment is carried out. Another problematic aspect to consider is that sufficient relaxation time must be allocated for the sample to return to its initial state between consecutive perturbations. Unfortunately, this parameter is also often not known *a priori* before the experiment is performed, and may risk artifacts appearing in the data. In contrast, a single perturbation is required in a PA-IR experiment to record the time-resolved data, eliminating the requirements of repeatability and an *a priori* knowledge of the relaxation time. PA-IR spectroscopy was used to assess directly the repeatability of the orientation/reorientation cycles for 5CB [27]. Table 13.1 shows the switch-on and switch-off time constants determined individually for a series of 300 consecutive reorientation cycles. As expected for this well-studied LC, the time constants did not evolve systematically as a function of the number of cycles. In this case, however, the repeatability was demonstrated experimentally and not only assumed, as is often necessary in step-scan studies.

Table 13.1 Time constants obtained from the switch-on and switch-off portions of the response curves for 5CB as a function of the number of cycles.

Cycle #	Switch-on time constant (ms)	Error (±)	Switch-off time constant (ms)	Error (±)
1	1.40	0.10	19.5	1.5
2	1.53	0.14	17.6	1.5
3	1.49	0.11	18.8	1.5
4	1.55	0.11	14.6	1.6
5	1.72	0.13	19.4	1.6
6	1.76	0.12	13.3	1.4
7	1.45	0.11	20.5	1.8
8	1.47	0.11	17.2	1.7
9	2.03	0.11	15.0	1.3
10	1.35	0.10	16.8	1.8
100	1.49	0.09	13.9	0.9
300	1.33	0.11	20.3	1.5

Even when a phenomenon is proven to be perfectly repeatable, PA-IR spectroscopy can still constitute an attractive approach when its time resolution is sufficient. Potential advantages include 1-D spatial imaging, multiple beam capability, as well as a shorter experiment duration. In the previous example [7], a single 1 s experiment was necessary to record both p- and s-polarized orientation/reorientation curves of the 5CB liquid crystal. In contrast, a similar step-scan FT-IR study would have required the application at least 512 perturbation cycles for each polarization, leading to a measurement time more than two orders of magnitude longer. Such a significant reduction in measurement time would clearly be advantageous for high-throughput experiments.

13.4.3
Dynamic IR Linear Dichroism

Some processes possess dynamics that are too rapid to be studied with continuous-scanning FT-IR spectroscopy, and for which the requirement of perfect repeatability limits the applicability of step-scan FT-IR. A noteworthy illustration is dynamic IR linear dichroism (DIRLD), a technique developed by Noda, Marcott and Dowrey that couples dynamic mechanical analysis (DMA) with polarized IR spectroscopy [28, 29]. In DIRLD, the samples are subjected to cyclic deformations, during which their dynamic response is measured in-phase and 90° out-of-phase (quadrature) with respect to the applied strain. These two components are related to the elastic and viscous properties of the polymer, respectively. Detailed information regarding the viscoelastic properties of the material, such as its glass transition temperature (T_g), can obtained by studying its response as a function of temperature or deformation frequency. Indeed, in contrast to DMA, DIRLD provides molecular-level information – a feature which is especially useful for the study of complex systems such as blends, copolymers and semi-crystalline polymers [29, 30]. However, a significant trade-off is that, while DMA experiments are rapid and applicable to most polymer samples, DIRLD experiments require several minutes to reach an acceptable SNR. In addition, the process must be repeated at several temperatures, without any modification of the sample or fatigue, in order to yield meaningful data. As a consequence, DIRLD has found most of its success for elastomeric samples that could withstand cyclic deformation for a very long time without deterioration [30].

Pellerin *et al.* have evaluated the possibility of overcoming this important limitation of DIRLD by performing faster experiments using PA-IR spectroscopy [31]. They used a spectrograph equipped with a 256×256 MCT FPA, a 50 grooves mm^{-1} grating and a PM-100 polymer modulator (Manning Applied Technology, Troy, ID, USA). Figure 13.9 shows the static and DIRLD spectra obtained for isotactic polypropylene (iPP), a well-studied sample. The in-phase dynamic spectrum obtained using PA-IR spectroscopy was in good agreement with that obtained with an FT-IR spectrometer (spectrum inverted for clarity) and with previously published results [32]. As expected, the dynamic quadrature spectrum was much weaker than the in-phase spectrum because the experiments were performed well
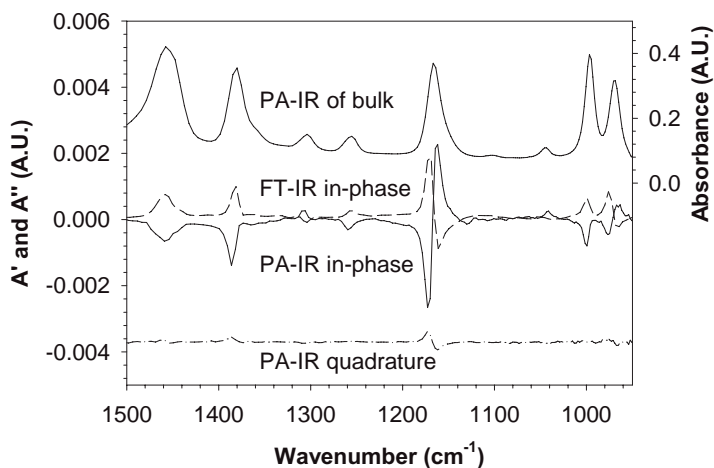
Figure 13.9 Comparison of the DIRLD in-phase spectra of isotactic polypropylene recorded in 20 s with a PA-IR spectrograph and in 34 min using a step-scan FT-IR spectrometer. The FT-IR spectrum has been inverted for clarity. The dynamic quadrature spectrum and the static PA-IR spectrum of the bulk sample are also shown. Reproduced with permission from Ref. [31].

above the T_g of iPP. PA-DIRLD experiments were performed with dynamic strains ranging from 0.021% to 0.14% [31]. A linear relationship between spectral intensity and strain confirmed the reproducibility and quantitative nature of the technique.

A key difference between the step-scan FT-IR and PA-IR approaches to DIRLD is the shortest achievable acquisition time. The PA-IR experiment only requires, in principle, a single deformation cycle. On the other hand, at least one deformation cycle must be applied for each of the 512 steps required to generate a typical step-scan FT-IR spectrum with a 2000 cm^{-1} bandwidth and an 8 cm^{-1} resolution. In practice, several cycles must normally be averaged to obtain an acceptable SNR because of the very weak DIRLD signal (see the y-axis scale of Figure 13.9).

Unpolarized in-phase iPP spectra were recorded with decreasing acquisition times in order to determine the minimum achievable measurement time for a PA-DIRLD experiment. Figure 13.10 shows that very good spectra could be obtained in 52, 8, and even 1 s. An excellent peak-to-peak noise level of $\sim 5 \times 10^{-5}$ A.U. was found for the 1 s spectrum, good enough to observe most spectral features. A further experiment attempted to record the dynamic spectra of iPP in 70 ms, corresponding to a single deformation cycle at a 14 Hz stretching frequency. Although the noise level observed in Figure 13.10 is quite large, it is still possible to quantify the most intense bisignate band at 1167 cm^{-1}. Performing such single-cycle DIRLD experiments is obviously not realistic for most systems; nevertheless, this demonstration opens the door to the characterization of a wide range of
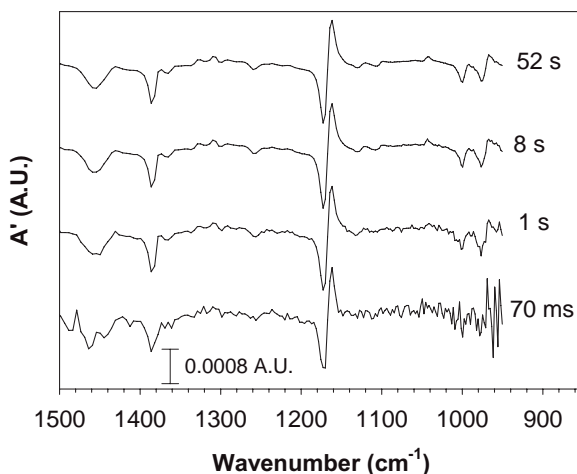
Figure 13.10 Unpolarized PA-DIRLD in-phase spectra of isotactic polypropylene deformed at 14.36 Hz and recorded in a total acquisition time of 52 s, 8 s, 1 s and 70 ms, respectively. Reproduced with permission from Ref. [31].

nonelastomeric samples that can be studied using conventional DMA but that were not amenable to DIRLD using current methods.

13.4.4
Emission PA-IR Imaging

The IR absorption and emission phenomena involve transitions between the same vibrational energy levels and thus, in principle, convey the same molecular information. In spite of this, the first phenomenon largely dominates its counterpart for most applications because of its sampling convenience, better SNR, etc. Emission IR spectroscopy (IRES) is nevertheless sometimes the best or even the only possible sampling approach, for instance in astronomy when there is no source for transmission measurements [33]. This technique is also used in the laboratory (for thermally, chemically or electronically excited species [34]), in field applications (for standoff detection of pollutants or potential threats [35]), and in industrial settings [36]. IRES is usually performed with an FT-IR spectrometer, but the astronomy community already uses large (up to 2048 × 2048) IR FPAs in a spectrographic mode in various telescopes. Considering the weakness of the emitted signal, these detectors are normally cryocooled using liquid helium (4 K) rather than liquid nitrogen (77 K), thereby reducing the thermal background signal that can plague the measurements.

Pellerin *et al.* assessed the feasibility of IRES measurements with a PA-IR spectrograph equipped with a liquid nitrogen-cooled MCT FPA [37]. They measured the spectrum of different polymer thin films heated to temperatures between 60 and 120 °C. Spectra with a good SNRs were obtained in the fingerprint region for

samples maintained at 80 °C or more, while spectra recorded at 60 °C showed a larger noise level but still allowed identification of the samples. The PA-IRES spectra were very similar to those obtained using absorption spectroscopy in the transmission mode, but quantitative differences were nevertheless observed because of the approximate nature of the blackbody source used as a reference.

FT-IR emission spectroscopy has been used to perform kinetic studies, for instance to probe the thermal degradation of polymers [34], although its time resolution is limited by the time required to obtain a sufficient SNR. As demonstrated above, an interest of PA-IR spectroscopy is that it provides good SNRs in short acquisition times. Figure 13.11 shows the PA-IR emission spectra of a thin polystyrene film recorded at 120 °C in 870, 87 and 17.4 ms. The quality of these spectra demonstrates that sub-20 ms time-resolved acquisition times are readily achievable in PA-IR emission spectroscopy. Such time resolution should prove beneficial for a technique referred to as transient infrared spectroscopy (TIRS) [36]. In this technique, a sample in motion is exposed to a hot air stream to create a thin surface layer which is warmer than the bulk of the sample. This allows the recording of emission IR spectra of thick samples that otherwise would be saturated. FT-TIRS is currently applied to the characterization of samples such as polymers, glasses and wood chips, but requires relatively long acquisition times [36]. The consequence is that each spectrum is an average over several samples or a long distance (for continuous processes). Pellerin *et al.* recently showed that PA-IR spectroscopy could be used to perform much faster TIRS measurements by recording PA-TIRS spectra of different packaging polymers with a time resolution below 100 ms [38].

In addition to high-speed measurements, PA-IR spectroscopy distinguishes itself from FT-IR by the possibility of performing 1-D imaging. Figure 13.12a
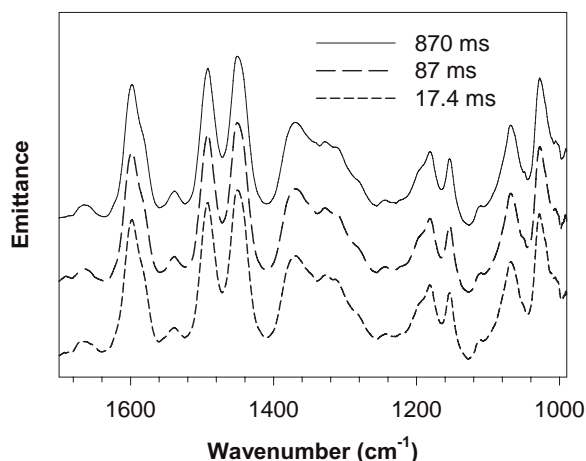
Figure 13.11 PA-IR emittance spectra of a polystyrene film recorded at 120 °C with acquisition times ranging from 870 to 17.4 ms. Reproduced with permission from Ref. [37].

(a)

(b)
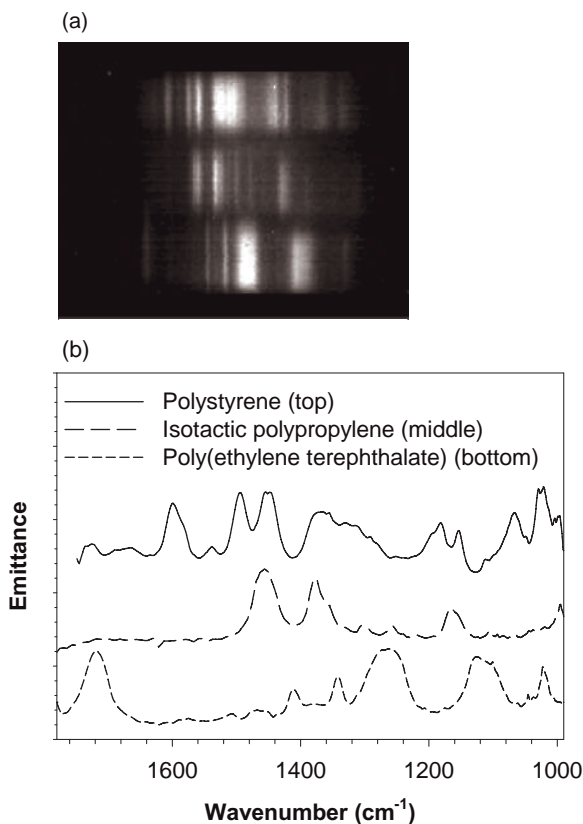
Figure 13.12 (a) Spatially resolved PA-IR emittance spectral image recorded for a stack of three polymer thin films heated to 120°C; (b) The corresponding emittance spectra. Reproduced with permission from Ref. [37].

shows a PA-IRES spectral image obtained for a stack of polymer samples [37]. As this image was recorded in emission mode, the sample-specific bands appeared as bright stripes on a dark background, in contrast to Figure 13.2 where the bands appeared as dark stripes on a bright envelope created by the IR source. The spectral image clearly showed three distinct sections along the vertical axis, with each containing features due to a different material. Figure 13.12b shows that the recorded emittance spectra allow the identification of PS, isotactic polypropylene and poly(ethylene terephthalate). The spatial resolution along the vertical axis of Figure 13.12a was ~150 μm per pixel, and the total vertical field of view 15 mm. The combination of millisecond IRES acquisition times with 1-D spatial resolution could allow, for example, the real-time imaging of warm moving targets such as extrudates, blown films or items on a conveyer belt.

13.4.5
PA-IR Microscopy

In Figures 13.2b and 13.12a, the spatial resolution along the height of the slit was shown to be on the order of 150 μm per pixel, using a typical PA-IR spectrograph. In principle, nothing prevents the field of view of the spectrometer from being expanded or reduced, by using appropriate optics. For example, demagnification would be useful for recording the 1-D-resolved spectra of large objects, while magnification would be of obvious interest for microscopic 1-D imaging with very rapid acquisition times.

In a recent study, Sommer *et al.* have combined a commercial IR microscope with a prism-based spectrograph into a micro-PA-IR system [8]. Out of necessity, the microscope was inserted prior to the spectrograph and its aperture played the dual role of area-defining element and entrance slit. Figure 13.13 shows a spectral image recorded for a cross-sectioned photographic film; this reveals a clear distinction between the poly(vinyl acetate) substrate (vertical pixels 122–160) and a ~10 μm-thick polyamide layer (pixels 110–122). The characteristic amide A, I and II bands of the polyamide layer can be observed at the horizontal pixels 5, 150 and 180, respectively, while the C=O and C—O—C bands of poly(vinyl acetate) are located at pixels 135 and 235, respectively. In this image, the polyamide layer spans across a height of 12 pixels, leading to an apparent spatial resolution on the order of 1 μm per pixel. The diffraction limit for far-field microscopy is on the order of the radiation's wavelength, 3–10 μm in the mid-IR, which means that Figure 13.13 is oversampled. Although the recorded spectra had a limited SNR, which is to be
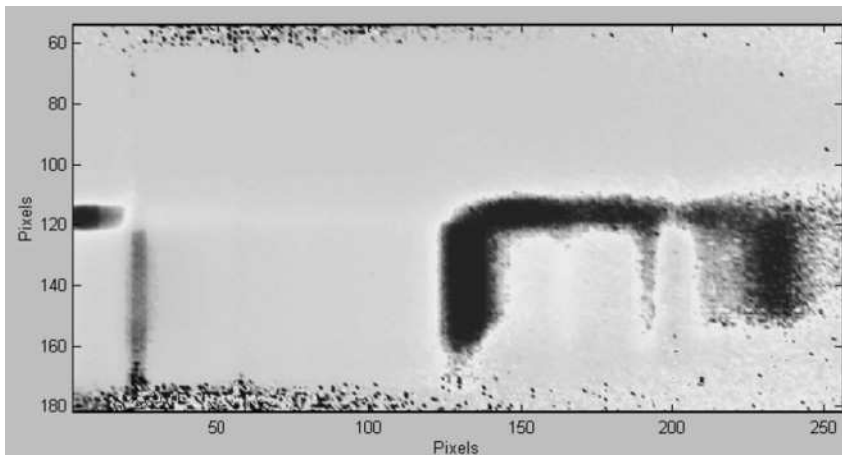
Figure 13.13 Spectral image of a cross-sectioned photographic film recorded using a prism-based PA-IR spectrograph coupled to an infrared microscope. Reproduced with permission from Ref. [8].

expected for prototype instruments, these results show much promise for future applications of micro-PA-IR spectroscopy.

13.5
Conclusions

Although still in its early stage of development, PA-IR spectroscopy represents a promising approach to mid-IR spectroscopy. The combination of focal plane array detectors with a spectrograph can:

Provide sufficient sensitivity for challenging experiments such as the study of ultrathin films and emission measurements.
Follow the dynamics of repeatable and nonrepeatable events with sub-millisecond time resolution.
Provide a 1-D spatial resolution that can be used for macro- or micro-imaging.
Be used for multisample or multibeam experiments.

The main drawbacks of the technique are a limited spectral bandwidth and/or spectral resolution, and the loss of frequency precision found in FT-IR spectrometers. For these reasons, it should not be considered as a replacement method but rather as being complementary to the ubiquitous FT-IR spectrometer. It is expected that technological developments and the increasing use of mid-IR array detectors in civil applications will lead to larger and cheaper (uncooled) FPAs with improved performance, thereby overcoming some of the current limitations of PA-IR spectroscopy.

References

1 Griffiths, P.R. and de Haseth, J.A. (2007) *Fourier Transform Infrared Spectrometry*, 2nd edn, John Wiley & Sons, Inc., Hoboken, NJ.

2 Agnew, J.T., Franklin, R.G. and Benn, R.E. (1951) *J. Opt. Soc. Am.*, **41**, 76.

3 Alawi, S.M., Krug, T. and Richardson, H.H. (1993) *Appl. Spectrosc.*, **47**, 1626.

4 Hamm, P., Wiemann, S., Zurek, M. and Zinth, W. (1994) *Opt. Lett.*, **19**, 1642.

5 Arrivo, S.M., Kleiman, V.D., Dougherty, T.P. and Heilweil, E.J. (1997) *Opt. Lett.*, **22**, 1488.

6 Elmore, D.L., Tsao, M.W., Frisk, S., Chase, D.B. and Rabolt, J.F. (2002) *Appl. Spectrosc.*, **56**, 145.

7 Pellerin, C., Snively, C.M., Chase, D.B. and Rabolt, J.F. (2004) *Appl. Spectrosc.*, **58**, 639.

8 Keltner, Z., Kayima, K., Lanzarotta, A., Lavalle, L., Canepa, M., Dowrey, A.E., Story, G.M., Marcott, C. and Sommer, A.J. (2007) *Appl. Spectrosc.*, **61**, 909.

9 Pelletier, I., Pellerin, C., Chase, D.B. and Rabolt, J.F. (2005) *Appl. Spectrosc.*, **59**, 156.

10 Kim, Y.S., Snively, C.M., Rabolt, J.F. and Chase, D.B. (2007) *Appl. Spectrosc.*, **61**, 916.

11 Elmore, D.L., Leverette, C.L., Chase, D.B., Kalambur, A.T., Liu, Y.J. and Rabolt, J.F. (2003) *Langmuir*, **19**, 3519.

12 Elmore, D.L., Chase, D.B., Liu, Y.J. and Rabolt, J.F. (2004) *Vib. Spectrosc.*, **34**, 37.

13 Liu, Y.J., Kalambur, A.T., Rabolt, J.F. and Chase, D.B. (2004) *Langmuir*, **20**, 816.

14 Gregoriou, V.G. and Rodman, S.E. (2001) Vibrational spectroscopy of thin organic films, in *Handbook of Vibrational Spectroscopy*, Vol. **4** (eds P.R. Griffiths and

J.M. Chalmers), John Wiley & Sons, Ltd, Chichester, p. 2670.

15 Mendelsohn, R., Davies, M.A., Brauner, J.W., Schuster, H.F. and Dluhy, R.A. (1989) *Biochemistry*, **28**, 8934.

16 Pelletier, I., Laurin, I., Buffeteau, T., Desbat, B. and Pézolet, M. (2003) *Langmuir*, **19**, 1189.

17 Pelletier, I., Laurin, I., Buffeteau, T. and Pézolet, M. (2004) *J. Phys. Chem. B*, **108**, 7162.

18 Liu, Y., Wolf, L.K. and Messmer, M.C. (2001) *Langmuir*, **17**, 4329.

19 Smith, G.D. and Palmer, R.A. (2001) Fast time-resolved mid-infrared spectroscopy using an interferometer, in *Handbook of Vibrational Spectroscopy*, Vol. **1** (eds P.R. Griffiths and J.M. Chalmers), John Wiley & Sons, Ltd, Chichester, p. 625.

20 Griffiths, P.R., Hirsche, B.L. and Manning, C.J. (1999) *Vib. Spectrosc.*, **19**, 165.

21 Pellerin, C., Pézolet, M. and Griffiths, P.R. (2006) *Macromolecules*, **39**, 6546.

22 Snively, C.M., Katzenberger, S., Oskarsdottir, G. and Lauterbach, J. (1999) *Opt. Lett.*, **24**, 1841.

23 Bhargava, R. and Levin, I.W. (2004) *J. Phys. Chem. A*, **108**, 3896.

24 Klimov, E., Fuelleborn, M. and Siesler, H.W. (2003) *Appl. Spectrosc.*, **57**, 499.

25 Buffeteau, T. and Pézolet, M. (2001) Linear dichroism in infrared spectroscopy, in *Handbook of Vibrational Spectroscopy*, Vol. **1** (eds P.R. Griffiths and J.M. Chalmers), John Wiley & Sons, Ltd, Chichester, p. 693.

26 Siesler, H.W., Zebger, I., Kulinna, C., Okretic, S., Shilov, S. and Hoffmann, U. (1999) Segmental mobility of liquid crystals and liquid-crystalline polymers under external fields: characterization by fourier-transform infrared polarization spectroscopy, in *Modern Polymer Spectroscopy* (ed. G. Zerbi), Wiley-VCH Verlag GmbH, Weinheim, p. 33.

27 Snively, C.M., Pellerin, C., Rabolt, J.F. and Chase, D.B. (2004) *Anal. Chem.*, **76**, 1811.

28 Noda, I., Dowrey, A.E. and Marcott, C. (1983) *J. Polym. Sci. Part C-Polym. Lett.*, **21**, 99.

29 Marcott, C. and Noda, I. (2001) Dynamic linear dichroism spectroscopy, in *Handbook of Vibrational Spectroscopy*, Vol. **4** (eds P.R. Griffiths and J.M. Chalmers), John Wiley & Sons, Ltd, Chichester, p. 2576.

30 (a) Steeman, P.A.M., Meier, R.J., Simon, A. and Gast, J. (1997) *Polymer*, **38**, 5455; (b) Wang, H.C., Graff, D.K., Schoonover, J.R. and Palmer, R.A. (1999) *Appl. Spectrosc.*, **53**, 687.

31 Pellerin, C., Frisk, S., Rabolt, J.F. and Chase, D.B. (2004) *Appl. Spectrosc.*, **58**, 799.

32 (a) Budevska, B.O., Manning, C.J., Griffiths, P.R. and Roginski, R.T. (1993) *Appl. Spectrosc.*, **47**, 1843; (b) Palmer, R.A., Manning, C.J., Chao, J.L., Noda, I., Dowery, A.E. and Marcott, C. (1991) *Appl. Spectrosc.*, **45**, 12.

33 Lisse, C.M., VanCleve, J., Adams, A.C., A'Hearn, M.F., Fernandez, Y.R., Farnham, T.L., Armus, L., Grillmair, C.J., Ingalls, J., Belton, M.J.S., Groussin, O., McFadden, L.A., Meech, K.J., Schultz, P.H., Clark, B.C., Feaga, L.M. and Sunshine, J.M. (2006) *Science*, **313**, 635.

34 George, G.A., Celina, M., Vassallo, A.M. and Coleclarke, P.A. (1995) *Polym. Deg. Stab.*, **48**, 199.

35 Bacsik, Z., Mink, J. and Keresztury, G. (2005) *Appl. Spectrosc. Rev.*, **40**, 327.

36 (a) Jones, R.W. and McClelland, J.F. (1989) *Anal. Chem.*, **61**, 650. (b) Jones, R.W., McClelland, J.F. and Bajic, S.J. (2001) Transient Infrared Spectroscopy, in *Handbook of Vibrational Spectroscopy*, Vol. 2 (eds P.R. Griffiths and J.M. Chalmers), John Wiley & Sons, Ltd, Chichester, p. 1215. (c) Jones, R.W., Meglen, R.R., Hames, B.R. and McClelland, J.F. (2002) *Anal. Chem.*, **74**, 453.

37 Pellerin, C., Pelletier, I., Rabolt, J.F. and Chase, D.B. (2007) *Anal. Chem.*, **79**, 2037.

38 Pellerin, C. (2008) *Macromol. Symp.*, **265**, 21.

14
Biomedical Applications of Infrared Microspectroscopy Using Synchrotron Radiation

Lisa M. Miller

14.1
Introduction

Infrared (IR) microscopes equipped with conventional IR sources have been used to examine biological samples for almost 20 years, having been used to examine numerous plant and animal tissues [1]. For complex samples such as human tissues, an IR spectrum can provide a direct indication of sample biochemistry. For example, Figure 14.1 illustrates the IR spectra of a common phospholipid, dimyristoylphosphatidycholine (DMPC), protein (myoglobin), nucleic acid (poly-A) and carbohydrate (sucrose). The dominant absorption features in the lipid spectrum are found in the region 2800–3000 cm^{-1}, and are assigned to antisymmetric and symmetric C—H stretching vibrations of CH_3 (2956 and 2874 cm^{-1}) and antisymmetric and symmetric C—H stretching vibrations of CH_2 (2922 and 2852 cm^{-1}). In addition, the strong band at 1736 cm^{-1} arises from ester C=O groups in the lipid. The protein spectrum has two primary features, the Amide I (1600–1700 cm^{-1}) and Amide II (1500–1560 cm^{-1}) bands, which arise primarily from the C=O and C—N stretching vibrations of the peptide backbone, respectively. The frequency of the Amide I band is particularly sensitive to protein secondary structure [2, 3]. The nucleic acid spectrum also displays C=O stretching vibrations from the purine (1717 cm^{-1}) and pyrimidine (1666 cm^{-1}) bases. In addition, the region between 1000–1500 cm^{-1} contains contributions from antisymmetric (1224 cm^{-1}) and symmetric (1087 cm^{-1}) PO_2^- stretching vibrations.

When examining the chemical make-up of biological cells and tissues, it is important to achieve subcellular spatial resolution. Although conventional IR microspectroscopy has proven extremely valuable for resolving the chemical components in biological samples, the long wavelengths of IR light limit the spatial resolution that can be achieved, and the high brightness of a synchrotron source has recently opened the door to improving the spatial resolution of the technique.
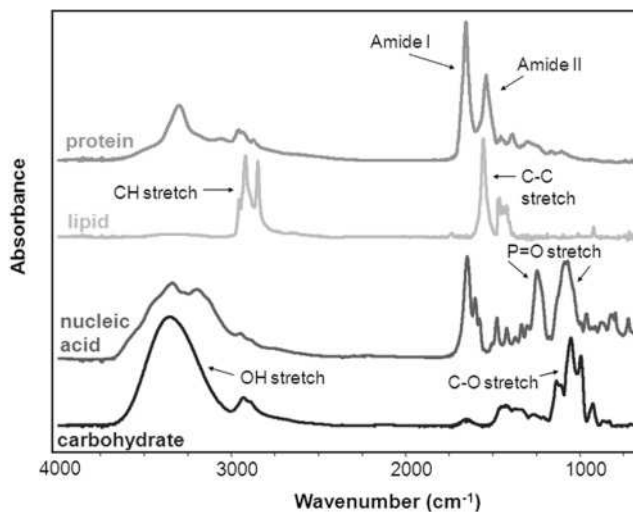
Figure 14.1 Infrared spectra of biological components highlighting the most prominent absorption features. Spectra for a protein (myoglobin), lipid (dimyristoylphosphatidylcholine, DMPC), nucleic acid (poly-A) and carbohydrate (sucrose) are shown.

14.2
Spatial Resolution Considerations

Typically, IR microscopes are configured in one of two ways – for FT-IR microspectroscopy (FT-IRM) or FT-IR imaging (FT-IRI) (Figure 14.2). In a few cases, single IR microscopes can operate in both configurations. For an FT-IRM instrument, a small area (a 'point') is spectroscopically sampled by the instrument, and an image built up by raster-scanning the specimen through the focused beam. Since only a single point is sampled at a time, these instruments use a single-element detector. The microscope uses reflecting Schwarzschild-type objectives to avoid absorption and chromatic aberrations over the large mid-IR spectral range (cf. Chapter 1). One objective serves to focus the light onto the specimen, while the other collects the light and relays it on to the detector. An aperture is used to constrain the illuminated or detected area on the specimen.

In an FT-IRI microscope, Schwarzschild objectives are also used, but the system is apertureless – that is, it does not provide any spatial discrimination. Instead, the first objective illuminates a rather large area, and this illuminated region is then imaged onto a focal plane array (FPA) detector by the second Schwarzschild objective [5, 6]. Spatial discrimination is provided by the individual pixels of the detector, each one serving as its own 'aperture'. Because there is no matching aperture for the illumination objective, this system does not operate in a confocal arrangement. However, being a FPA system, the speed at which large IR images can be collected is dramatically improved.
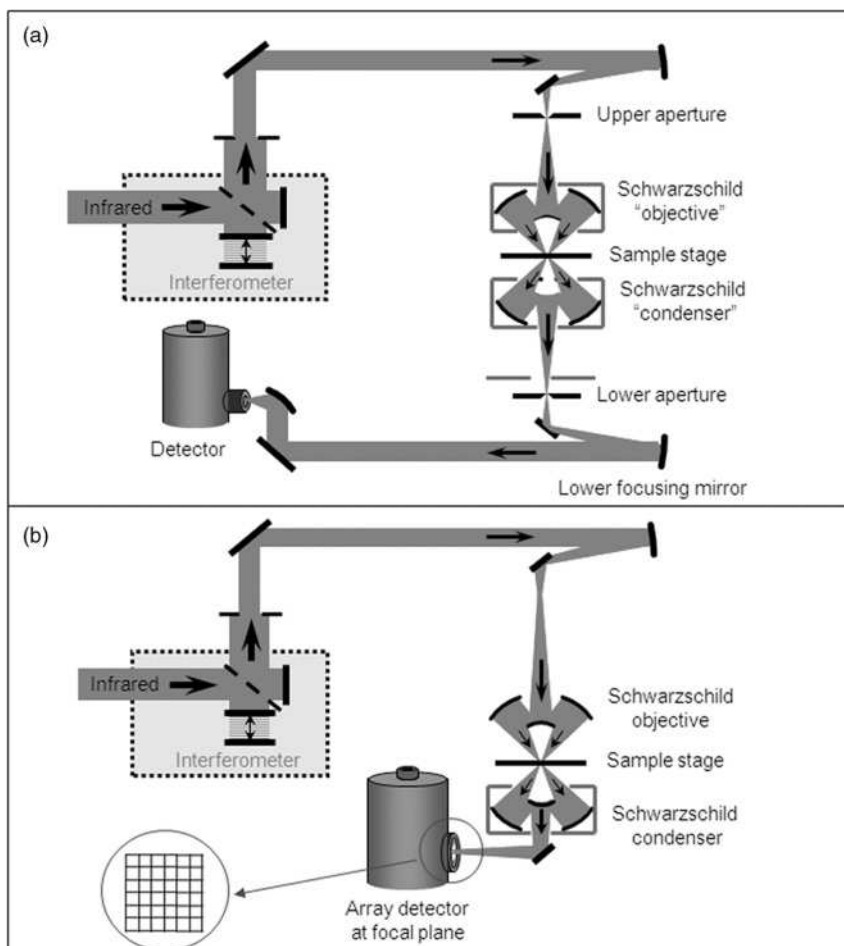
Figure 14.2 (a) Schematic for a scanning (FT-IRM) microspectrometer system using a single-element detector and the possibility for confocal operation where aperturing is used both before and after the sample; (b) Schematic for an imaging (FT-IRI) microspectrometer system using an FPA detection system. Reproduced with permission from Ref. [4].

When examining the chemical make-up of biological cells and tissues with an IR microscope, it is important to achieve subcellular spatial resolution. For both FT-IRM and FT-IRI, the spatial resolution is limited by the wavelengths of IR light, which are longer than visible light wavelengths used for conventional optical microscopy. The diffraction-limited spatial resolution is dependent upon the wavelength of light and the numerical aperture (NA) of the focusing optic (Chapter 1 and [7]). Typical IR microscopes utilize Schwarzschild objectives with NA-values of ~0.6. In an FT-IRM experiment, the apertures confine the beam to the sample's

area of interest, with some microscopes utilizing a single aperture before the sample, thus controlling the region that is illuminated. With a single aperture, the diffraction-limited spatial resolution is approximately $2\lambda/3$ [8]. Thus, for the mid-IR range, the diffraction-limited spatial resolution is approximately 1.7 μm (at 4000 cm^{-1}) –13 μm (at 500 cm^{-1}). Other microscopes operate in a confocal arrangement, where a second aperture is used after the sample to define the region being sensed by the IR detector. For such a confocal microscope, where objectives and apertures are placed both before and after the sample, the spatial resolution is improved to $\sim\lambda/2$ [8]. In addition, the confocal arrangement also reduces the Schwarzschild's first- and higher-order diffraction rings, dramatically improving image contrast [8].

In an FT-IRI experiment, no physical apertures are used to limit the illumination area of the IR beam. Instead, an array of IR detector elements is used to collect the projected image of the unmasked IR beam on the sample. While FPA systems dramatically improve the rate at which IR images can be collected, the spatial resolution is poorer than that of a confocal FT-IRM microscope because an FT-IRI instrument cannot operate in a confocal arrangement.

14.3
Advantages of a Synchrotron IR Source

In an FT-IRM experiment, as the aperture size is decreased, so does the IR flux that reaches the detector, and hence the signal-to-noise ratio (SNR) decreases. A conventional globar source illuminates light into a ~100 μm area; consequently the typical aperture settings are 20 to 100 μm.

A synchrotron IR source is 100 to 1000-fold brighter than a conventional thermal (e.g., globar) source [9]. This brightness advantage is not because the synchrotron produces more power, but rather because the effective source size is small and the light is emitted into a narrow range of angles. The high brightness (i.e., flux density) of the synchrotron source allows smaller regions to be probed with acceptable SNR [10, 11]. As a synchrotron IR source typically fills a 10–20 μm area, a synchrotron source provides no advantage over the thermal source for larger aperture settings (~20 μm or greater). Figure 14.3a demonstrates the difference in brightness between a synchrotron and globar source by comparing the throughput as a function of aperture size [12]. As can be seen, the globar source transmits very little light through a 10 μm aperture, whereas >80% of the synchrotron IR light passes through the same size aperture. However, with a 70 μm aperture, the synchrotron source provides no advantage. Figure 14.3b shows the IR spectra of a single red blood cell collected with a $5 \times 5 \, \mu m^2$ aperture, illustrating how the brightness advantage of the synchrotron leads to a dramatically improved SNR.

In addition to its high brightness, synchrotron IR light has other advantages of over the conventional thermal source: it has a pulsed time structure and a high degree of polarization (when a bending magnet is used for producing the IR
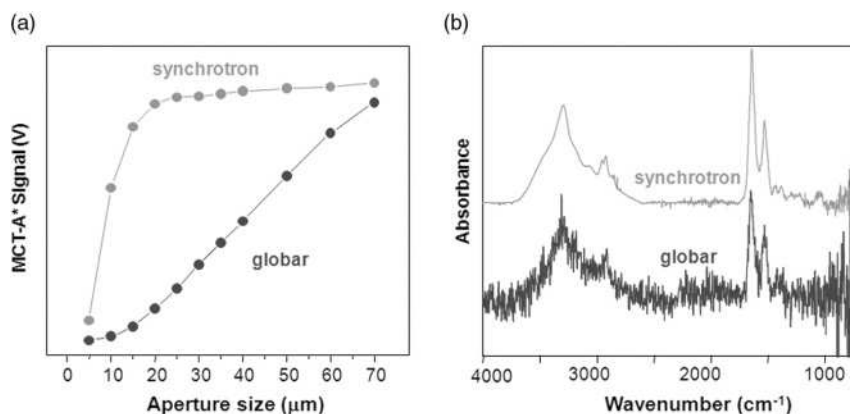
Figure 14.3 (a) Infrared signal through various aperture sizes using a synchrotron versus globar source. A confocal IR microscope was used with a single-point detector; (b) Infrared spectra of a single red blood cell collected with a synchrotron versus globar source. A square aperture of $5 \times 5 \mu m^2$ was used.

photons). The pulsed nature of the light derives from the intrinsic characteristics of synchrotron radiation, where the specific pulse structure (10 s to 100 s of pico-second-long pulses) is determined by the electron bunch structure in the storage ring [13]. The polarization of the synchrotron IR beam depends on both the geometrical and optical characteristics of the beamline [4, 14, 15].

The first demonstration of FT-IRM with a synchrotron IR source was made during the early 1990s, when a custom-built IR microscope was installed at the National Synchrotron Light Source (Upton, NY, USA) [16, 17], while similar efforts were underway at UVSOR in Japan at the same time [18]. The first commercial IR microscope was installed at the NSLS a few years later [10, 19]. Since then, IR microscopes have been installed on over 15 beamlines at synchrotrons worldwide, and an equal number are currently in the planning or construction stages.

14.4
Instrumentation

14.4.1
Infrared Beamlines

A synchrotron is an electron storage ring that produces intense broadband light from X-rays through microwaves. Synchrotron light is emitted as relativistic electrons are accelerated along a circular trajectory [20]. Infrared beamlines worldwide collect synchrotron light from bending magnets in the electron storage ring. For bending magnet radiation, the 'natural opening angle' (the total angle required to

transmit 90% of the emitted light) is given by a simple formula: $\theta_v \cong 1.6 \, (\rho v)^{-1/3}$, where ρ is the electron bend radius (in cm) and v is the frequency of light (in cm^{-1}). As an example, the VUV-IR ring at the NSLS (Brookhaven National Laboratory) has a bending magnet radius of 1.91 m, giving a natural opening angle of 28 mrad at 10 μm, and ~62 mrad at 100 μm. The IR microscope beamlines at the NSLS are designed around an extraction system that collects ~40 mrad, the storage ring – an opening angle that collects essentially all of the IR light down to 250 cm^{-1} (λ = 40 μm), and the collection efficiency decreases slowly with frequencies below this value. As a general rule, the light collected from a bending magnet is linearly polarized in the plane of the electron beam orbit, while the off-axis radiation is elliptically polarized [15]. Engineering constraints on newer, third-generation synchrotrons prohibit the large vertical opening angles required to extract long-wavelength IR photons [15]. In this case, the smaller opening angle of radiation produced at the entrance or exit edge of a bending magnet provides an advantage [21]. Today, several synchrotron IR beamlines utilize radiation from the edge of the dipole magnet, which is emitted along the straight section axis in a hollow cone [22–24]. While the emission pattern and properties of edge-radiation differ from ordinary synchrotron light (e.g., edge radiation beamlines produce radially polarized light [14, 25]), these beamlines provide comparable flux and brightness [4, 14, 21, 25].

Extraction of the synchrotron light from the storage ring is generally accomplished with a combination of gold- or aluminum-coated plane and toroid/ellipsoid or spherical mirrors (Figure 14.4). The first extraction mirror must handle the heat load of higher-energy photons (i.e., X-rays), so water-cooling, water-cooled masks and/or slotted mirrors are often employed. The IR radiation is focused through an IR-transparent window (usually diamond, but in a few cases IR transparent
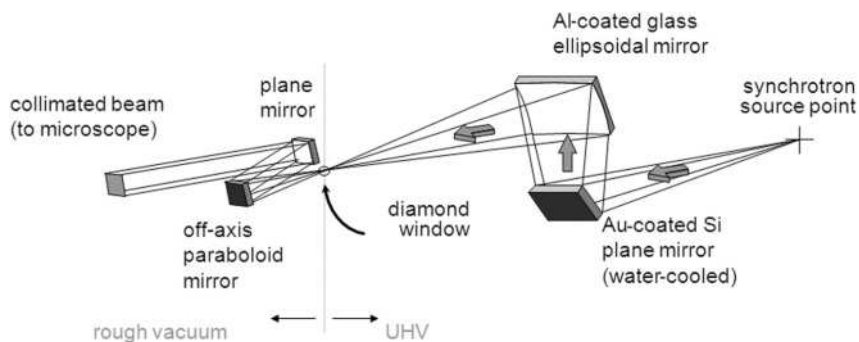
Figure 14.4 Schematic of synchrotron IR beamline extraction optics at the NSLS. All components before the diamond window are at ultra-high vacuum. The beamline operates at rough vacuum and the IR microscope is purged with dry N_2. Reproduced with permission from Ref. [20].

windows such as KBr, ZnSe and KRS5 have been used), which separates the ultrahigh vacuum (UHV) conditions of the storage ring (10^{-9}–10^{-10} Torr) and the rough vacuum of the IR beamline (10^{-3}–10^{-4} Torr). The beam is then recollimated and directed into the IR microscope. IR beamlines are generally terminated with an IR-transparent window (KBr, CsI, polyethylene) to isolate the beamline vacuum from the ambient pressure of the microscope. Although IR light passes easily through air, any water vapor and carbon dioxide (CO_2) in the air are highly absorbing; consequently, IR microscopes are typically purged with dry nitrogen or dry air.

14.4.2
Synchrotron Infrared Microscopes

Infrared microscopes are commercially available from a number of companies worldwide, and operate much like conventional visible light microscopes. The IR radiation follows the same path as the sample illumination light, so that IR microspectroscopy can be performed on the sample at the center of the viewing field. Because of their design, they are also equipped with a number of convenient methods for enhanced sample visualization. These include polarized light (visible and IR), fluorescence illumination and differential interference contrast (DIC), all of which are well known and frequently used to identify biological sample histology.

Very little modification is needed to adapt a commercial FT-IR microscope for a synchrotron IR source, where a single synchrotron point source is used to illuminate a single IR detector element. The collimated beam of synchrotron IR radiation follows the same beam path as the conventional thermal IR source. Thus, in general, a simple flat mirror is used to easily switch between the thermal and synchrotron sources. From the end of the beamline, the collimated beam of synchrotron IR light first enters the FT-IR spectrometer and is then directed towards the IR microscope. For FT-IRI microscopes, coupling the synchrotron light to the size and arrangement of the individual detector elements is more difficult. To date, FT-IRI microscopes have not been optimized for a synchrotron-powered IR microscope, although a number of efforts are currently under way (see Section 14.4.3).

Both, FT-IRM and FT-IRI instruments are designed with two paths from the sample to the detector, namely transmission and reflection:

- In transmission mode, the IR radiation passes through the sample and is collected by a second IR objective that recollimates the beam and sends it to the IR detector.

- In reflection mode, the IR radiation reflects off of the sample and passes back through the illuminating objective. In this configuration, approximately 40–50% of the incident IR radiation is blocked by a mirror that collects the reflected light. This fraction can be reduced significantly with a synchrotron IR source,

providing a large throughput advantage over the conventional thermal source in reflection mode.

14.4.3
Infrared Detectors

Infrared microscopes are generally equipped with detectors of high responsivity, generally liquid nitrogen-cooled, broadband or narrow-band mercury cadmium telluride (MCT). The long wavelength cut-off for this tunable alloy system is usually set to 650 cm^{-1}, which provides a good compromise between the spectral range and the SNR. Longer-wavelength MCT detectors (e.g., down to 450 cm^{-1}) are also available, the intrinsic detectivity of which is lower, and this reduced the achieved SNR by a factor of 2 to 5 compared to the 650 cm^{-1} cut-off MCT detectors. One drawback of the MCT detector is its nonlinear response, where the high brightness of the synchrotron source leads to a highly localized intensity on the detector. A better linearity in detector response is achieved with extrinsic germanium photoconductor detectors [20]. As a synchrotron IR source produces light well into the far-IR region, IR microscopes are also equipped with low-frequency detectors (e.g., Cu-doped Ge, B-doped Si, bolometer). These detectors are generally large in size because they are cooled with liquid helium, and mounted externally to the IR microscope [26]. However, new developments in micro-bolometric detectors have been recently reported [27].

The most recent development in IR detectors involves the coupling of an IR FPA detector to an interferometer [5, 6]. To date, the size and arrangement of the individual detector elements have not been optimized for a synchrotron-powered IR microscope, primarily because of their optical design and light coupling. Specifically, the FPA collects the projected image of the IR beam onto the sample, which is quite large due to the large source size of the conventional globar (a few mm^2). Each FPA detector element records the spectrum of the corresponding projected pixel size onto the sample. With the small inherent source size of the synchrotron beam, the brightness advantage would be lost if the beam were expanded to accommodate the same projected size. However, early attempts using an FPA with 64×64 elements have already shown the great advantage of using the synchrotron source [28].

14.5
Biological Sample Preparation and Modes of Data Collection

Sample preparation is perhaps the most critical part of a successful IR microspectroscopy experiment. In the same way that the IR microscope can be used in a number of ways to collect spectra, so too can sample preparation can approached in a variety of ways. As biological materials are most frequently probed in either transmission mode or reflection mode, these methods will be described here. Other methods are also available, however, such as grazing incidence and attenuated total reflection (ATR) [1].

14.5.1
Transmission Mode

For transmission mode, which is perhaps the preferred means of collecting IR microspectra, it is essential to have thin samples. Although being very sample-dependent, the typical thickness for transmission measurements ranges from 5 to 30 μm. Polymers, unmineralized biological tissues and other organic materials are generally prepared with thicknesses of 10–15 μm. Minerals (both biological and geological) are much more variable, depending on the specific material; for example, a fully mineralized bone is typically sectioned at 3–5 μm.

The method of choice for preparing thin sections of biological tissue is cryogenic sectioning, using a microtome, as this best preserves the original state of the tissue and does not involve embedding materials. However, cryosectioning is often not possible, and in these cases the thin samples are often prepared by embedding the sample in a matrix and then cutting with a microtome. The embedding compounds are generally chosen to match the hardness of the sample. For mineralized tissues and other hard materials, a variety of polymers are available [29], while for soft tissues paraffin is often used. Most importantly, great care must be taken to choose an embedding process that does not affect the chemistry of the sample. Also, as these compounds usually penetrate throughout the sample, a material should be chosen that does not have IR absorption features which overlap those of the sample. For example, paraffin is often used to embed unmineralized biological tissues because its most intense absorbance features are limited to the C—H stretch region (2800–3000 cm^{-1}). However, weaker C—C stretching modes fall near 1465 cm^{-1}, which can also interfere with the sample spectrum. Moreover, the process of paraffin-embedding requires sample dehydration and fixation, which can alter the chemistry of the sample to be probed. Consequently, the sample component(s) of interest must be robust enough to handle this process.

When a thin section has been cut it is placed on an IR-transparent material with thickness ranging from nanometers to millimeters. For biological materials, transparent, water-insoluble substrates such as CaF_2 and BaF_2 are most common. When using IR-transparent substrates and working with the small spot sizes of a synchrotron IR source, the effect of dispersion must also be considered during data collection [8]. Specifically, most of the IR-transparent materials have some degree of dispersion in the visible, IR (or both) regions. For typical thicknesses of these materials (1–2 mm), this dispersion leads to focusing errors of 20 μm or more, and a severe loss of signal or spatial resolution may occur over part, or all, of the spectral range of interest. In order to compensate for substrate dispersion, defocusing of the collection optics (i.e., condenser) is critical (Figure 14.5).

14.5.2
Reflection Mode

Another method of collecting IR microspectra is that of reflection mode. Samples probed in reflection mode are most often: (i) highly reflective or polished samples
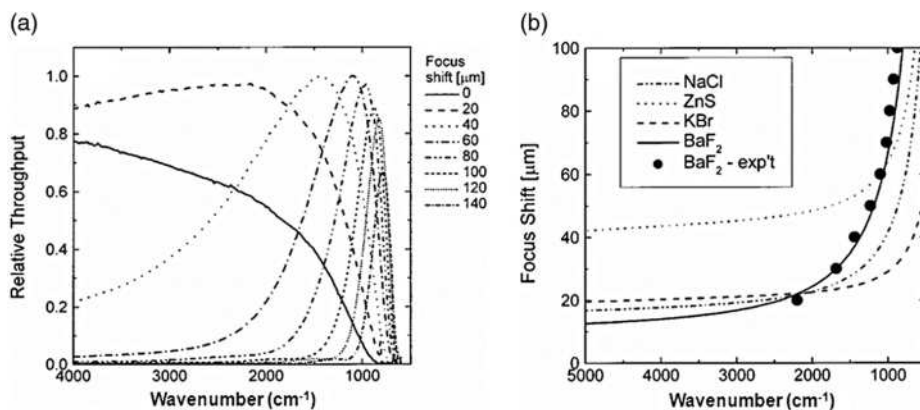
Figure 14.5 (a) Relative transmission through a 2 mm-thick BaF$_2$ substrate at various focus settings; (b) Lines: Calculated focus shift for several common IR materials (all 2 mm thick) including BaF$_2$. The solid circles indicate the measured focus shift for BaF$_2$. Reproduced with permission from Ref. [8].

that cannot be cut to thin sections; or (ii) microtomed thin sections that are placed on an IR-reflective substrate instead of an IR-transparent substrate. Recently, reflection mode has become more popular for probing microtomed thin sections that have been placed on IR-reflective substrates. For these experiments, the IR beam penetrates through the sample, reflects off the substrate, and then passes back through the sample again. As the beam passes through the sample twice, the result is a 'double-absorption' spectrum. For this reason, the thin sections should be cut to approximately half of the thickness used for a transmission mode measurement.

Semi-reflective and polished samples are also probed in reflection mode. As the SNR of the spectra relies heavily on collection of the reflected light back into the IR objective, it is important that these samples have a smooth, flat surface and are correctly oriented. Samples with smooth surfaces that are not flat can be mounted into a micro-goiniometer, so as to adjust the tilt of the sample with respect to the incoming beam. Even simpler, samples can also be pressed into a small sphere of putty so that the sample surface is parallel to the microscope stage.

While thin sections are often easier to prepare on IR-reflective substrates, the use of IR-reflective substrates does come at a cost to the IR data collection process, and even spectral quality. As noted above, the incident flux in reflection mode is reduced by almost 50% compared to transmission mode, as only half of the focusing objective is used to direct the beam onto the sample, while the second half is used for collecting the reflected beam. In addition, any inhomogeneities in the thin section can cause interference effects (e.g., oscillations) in the background of the IR spectra. These artifacts can alter peak shapes, intensities and frequencies. Thus, care must be taken with sample preparation, and only certain (generally homogeneous) samples can be investigated well in this mode.

14.6
Biological and Medical Applications of Synchrotron IR Microspectroscopy

Infrared microspectroscopy was used to examine numerous plant and animal tissues long before the union of the IR microscope and the synchrotron source [30]. For complex samples such as human tissues, an IR spectrum can provide a direct indication of sample biochemistry.

With the high spatial resolution of the synchrotron, individual cells within a tissue can be probed with subcellular resolution. For example, the structures of misfolded protein aggregates in neurological protein folding diseases have been identified in the brain tissue of Alzheimer's disease patients [31–33], while infectious prion proteins have been characterized in scrapie [34–37]. Additional biochemical changes have also been observed in the fingerprint regions of Alzheimer's [38], Parkinson's [39] and scrapie-infected tissues [40].

Bone composition, such as mineralization, carbonate accumulation, crystallinity and collagen crosslinking, has been shown to change with age [41], and is correlated with the bone's mechanical properties [42, 43]. In microdamaged bone, the collagen crosslinking is altered but the mineralization and crystallinity are unaffected [44] (Figure 14.6). Alterations in bone composition have been observed in diseases such as osteoporosis [45], osteopetrosis [46] and osteoarthritis [47]. The treatment of osteoporosis with nandrolone decanoate, an anabolic steroid, was shown to alter the cortical bone composition [48], whereas treatment with bisphosphonates had little effect [49].

Synchrotron-based FT-IRM has been used to observe a decreased lipid and an increased collagen content in the myocardium in heart disease [50], and which can be partially normalized by treatment with losartan [51]. Biochemical changes caused during peridural scarring have also been observed with FT-IRM, and their reversal by the use of anti-inflammatory agents is currently being assessed [52]. Changes in collagen content have also been observed in liver fibrosis, making FT-IRM a possible diagnostic tool for the early stages of the disease [53].

The high spatial resolution of a synchrotron IR source has permitted the subcellular chemical mapping of single living cells for the first time (Figure 14.7). In this technique, sample heating has been shown to be negligible, which means that single cells can be analyzed over long time scales, of hours to days [55, 56]. Individual mouse hybridoma B cells have been examined during necrosis, at the end phases of mitosis [57], and also during the process of apoptosis [58]. Metal–cyanobacteria sorption reactions have also been characterized in detail [59]. In addition, spectral differences have been noted between normal and cancerous oral epithelial cells [54, 60–62], between healthy and nutrient-repleted *Micrasterias hardyi* algal cells [63], and in HepG2 cells exposed to low doses of 2,3,7,8-tetrachlorodibenzo-*p*-dioxin [64]. Variations in DNA/RNA content and packing have also been demonstrated during the cell cycle of human lung epithelial cells [65], and correlated with the degree of differentiation and proliferative capacity of stem cell populations in the human corneal epithelium [66, 67].
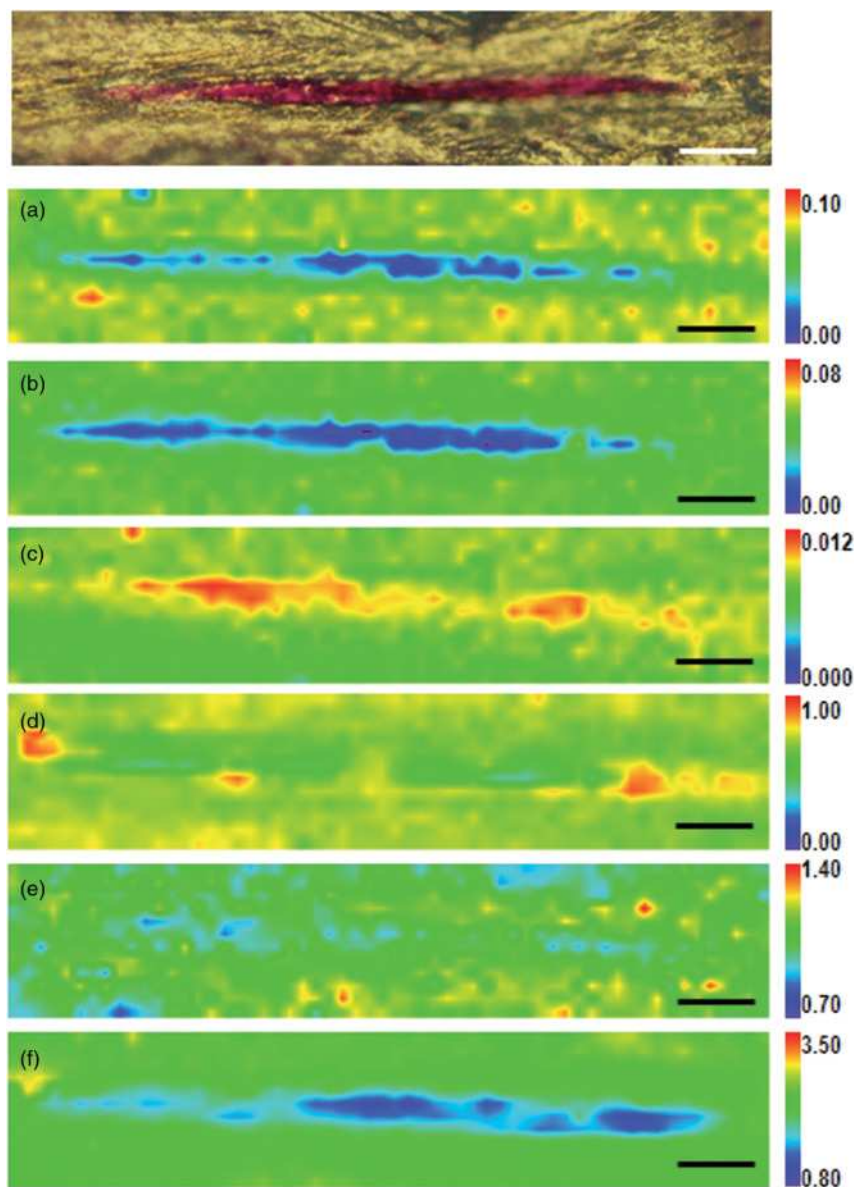
Figure 14.6 Top panel: Visible image of a microcrack indicating the area imaged with the IR microscope. The fuchsin stain (magenta) highlights the microcrack. Data were collected within the crack and from the surrounding area. (a–f) Corresponding IR images of the same area. The individual images illustrate the: (a) carbonate/phosphate ratio; (b) carbonate/protein ratio; (c) acid phosphate/total phosphate ratio; (d) phosphate/protein ratio; (e) crystallinity; and (f) collagen crosslinking. Scale bar = 25 μm. Adapted from Ref. [44].
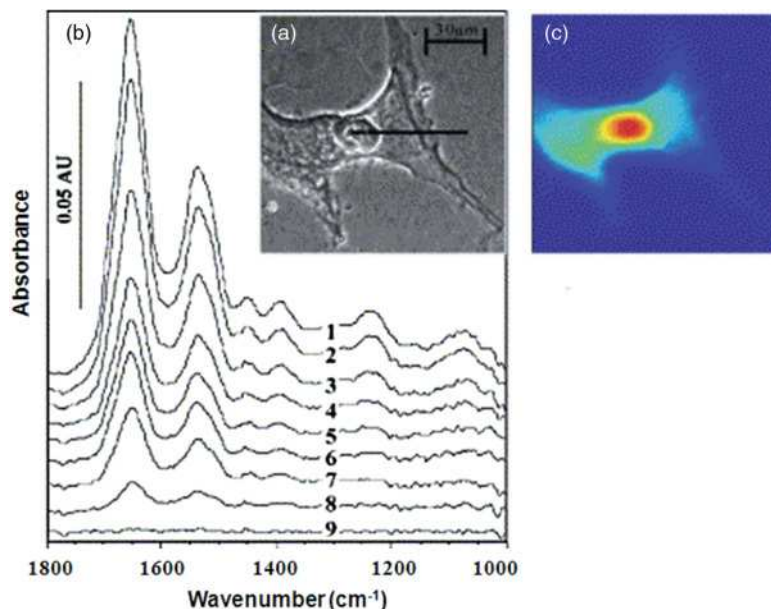
Figure 14.7 Synchrotron IR imaging of a benign human skin fibroblast showing: (a) the visual image; (b) representative IR spectra acquired along the black line in (a); and (c) protein IR image. Cells were grown onto a CaF$_2$ slide, and treated with ethanol and RNAse to remove phospholipids and RNA, respectively. Thus, the nucleic acid vibrations observed at ca. 1080 and 1235 cm^{-1} are due to DNA. The spectra were collected with a square aperture of 8×8 µm, in transmission mode. Reproduced with permission from Ref. [54].

Recently, FT-IRM has been combined simultaneously with epifluorescence microscopy [68, 69] to probe 5 µm-wide layers of newly deposited bone [42, 45, 48, 49], plaques in Alzheimer's disease [32], and the different stages of apoptosis [58]. The means by which epifluorescence microscopy was used to visualize the various stages of apoptosis, and synchrotron FT-IRM used simultaneously to assess changes in protein and nucleic acid composition, are illustrated in Figure 14.8. Other visualization techniques include the use of polarized light and DIC. At the cellular and subcellular level, these techniques can be used to visualize fluorescent tags bound to particular cellular components, and even antibodies to individual proteins and, once identified, the IR microscope can be used to analyze the chemical environment in and around that region of interest. It should be noted that, as fluorescent labels are generally present in extremely low (i.e., nanomolar) concentrations, they do not interfere with the IR technique; rather, they are used exclusively for visualizing a region of interest.

A considerable analytical effort has been expended recently on the chemical composition of human hair, for which the synchrotron IR source can provide the ability to probe, separately, the cuticle (~5 µm width), cortex (~40–80 µm width) and medulla (~10 µm width) substructures (Figure 14.9) [70, 71]. The results of
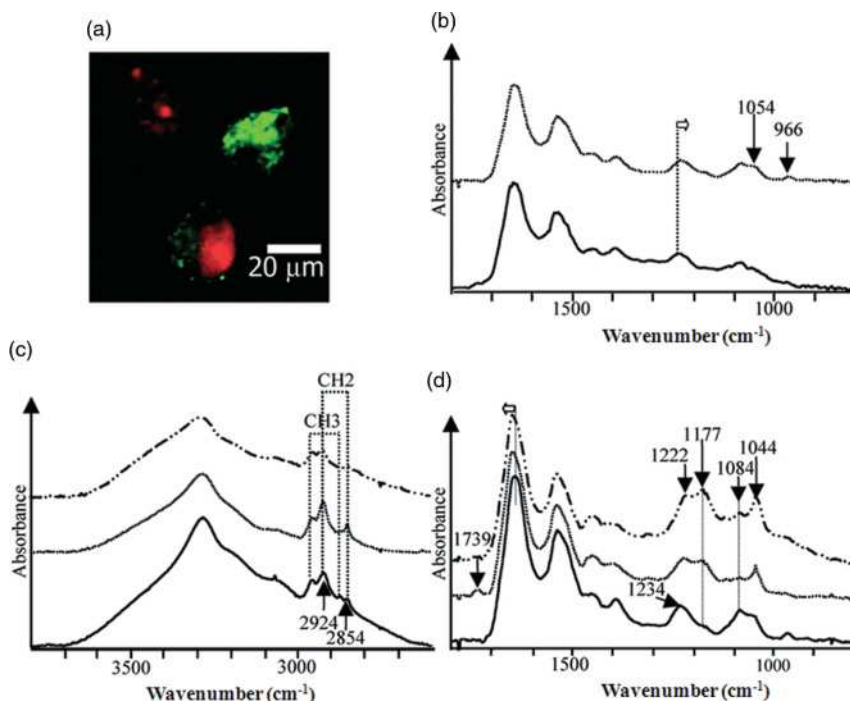
Figure 14.8 (a) Visual image of Jurkat cells treated with the anti-Fas DX2 monoclonal antibody (mAb) under fluorescence illumination with the IR microscope. The green and red fluorescence signify early and late apoptosis, respectively; (b) A comparison of the fingerprint region of untreated cells (AV⁻/PI⁻) (—) with those treated with the anti-Fas DX2 mAb (----); (c, d) A comparison of the IR spectra of (—) AV⁻/PI⁻, (----) AV⁺/PI⁻ and (– ·· –) AV⁺/PI⁺ cells. The (c) 3800–2600 cm⁻¹ and (d) fingerprint regions are shown. The spectra were collected with an aperture of $11 \times 11 \,\mu m^2$ centered on the nucleus. Scale bar = 20 μm. Adapted from Ref. [58].

these investigations have shown lipid concentrations to be elevated in the medulla, whereas variations in protein structure exist among the different regions [70, 72]. The bleaching of hair affects the hydration level of the cuticle, and also causes the formation of sulfonate (S=O) groups in the cortex [73]. Keratin disorganization has been observed in the hair of ancient Egyptian mummies, most likely due to peptide bond breakage [74], while narcotics have also been identified in human hair [75].

As IR spectroscopy probes the vibrational frequency of a bond, elemental isotopes can be used as targets to study biochemical processes. For example, when the transport of D_2O from the gut to the brain was studied in adult rats [76], the CD:CH and ND,OD:NH,OH ratios were shown to be highest in the molecular layer of the brain, and lowest in the white matter. The findings in the molecular layer were consistent with the active synthesis and recycling at synapses, which are abundant structures in this layer, while the low levels in white matter
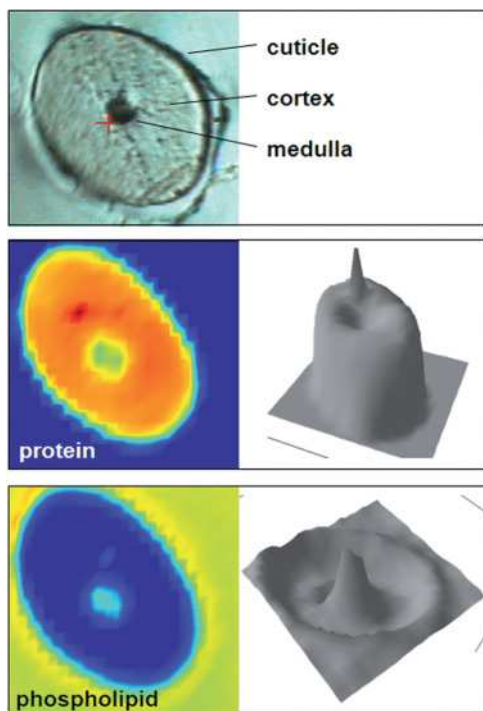
Figure 14.9 Synchrotron IR images of the cross-section of a human hair. Hair contains three substructures that can only be resolved with the high spatial resolution of a synchrotron IR source. From the center outward, these substructures and their thicknesses are: medulla (10–20 μm), cortex (30–100 μm) and cuticle (2–5 μm). IR imaging of these regions shows that the protein concentration (1700–1600 cm^{-1}) is highest in the cortex, while phospholipid (1750–1700 cm^{-1}) concentrations are highest in the medulla and cuticle. Scale bar = 25 μm.

(confirmed using radiolabels) highlighted a slow turnover of proteins and lipids in myelin, the main constituent of that region.

Synchrotron FT-IRM has also been used in less-traditional ways to study biological systems. For example, a synchrotron IR microscope has been coupled to a rapid-mix flow cell in order to study protein folding [77, 78] and the binding of an antibiotic to a tripeptide [79], on a time scale as short as microseconds. The small spot size of the synchrotron beam permitted a faster time resolution of the technique and the use of smaller volumes of sample.

Another recent, 'nontraditional' investigation involved the use a of pump-probe technique to study the laser-ablation of tooth enamel [80] and the influence of an optically thick water layer applied onto the tooth surface [81]. Laser ablation was performed in the presence and absence of water, and synchrotron FT-IRM used to probe the chemical composition of the enamel in the thus-formed crater. FT-IRM revealed the formation of new mineral phases deposited along the crater walls after repetitive laser pulses, while the nonapatitic phases reduced the efficiency of

the ablation. The application of a water layer led to the removal of any loosely adherent phases, thus maintaining efficient ablation during multiple-pulse irradiation.

14.7
Future Directions for Synchrotron IR Microspectroscopy

To date, the vast majority of synchrotron FT-IRM experiments have been performed on static systems, at ambient pressure and temperature, and in the mid-IR region (some of the few exceptions have been described above).

Future FT-IRM experiments promise to include time-resolved measurements, ranging from long time scales (minutes to hours) to time scales that take advantage of the pulsed structure of the synchrotron beam (10 s to 100 s of picoseconds). Although the pulse duration is significantly longer than what can be achieved with ultra-fast lasers (10 s to 100 s of femtosecond pulses), the synchrotron is a 'white' source that allows complete spectral information to be acquired. This provides a unique opportunity to study dynamics associated with chemical bonds. It is possible that future generations of synchrotron light sources will produce pulses with durations of ~100 fs or less.

Other areas of growth include applications to systems studied over wide temperature and pressure ranges, and spectra recorded over a much broader spectral range, including far-IR or terahertz (THz or T-Ray) FT-IRM. Many IR studies have shown that protein and lipid membrane structures are sensitive to temperature and pressure, yet none has involved spatially resolved IR imaging [82–85]. The throughput limits of cryogenic and/or high-pressure microspectroscopy and the brightness limits of X-ray/far-IR microspectroscopy represent a particular challenge that only a synchrotron source can fulfill. Both, proteins and nucleic acids have also been studied in the far-IR regime [86, 87] and, while some have utilized the high brightness of free electron laser sources [88–90], none has yet taken advantage of the high spatial resolution of a synchrotron IR microscope.

At the other end of the spectrum, combined X-ray (fluorescence, absorption and diffraction) and IR microscopic analyses on the same sample represent an activity of growing interest among the biomedical community. For example, protein misfolding has been correlated with trace metal uptake in Alzheimer's disease [32], Parkinson's disease [91], scrapie [36] and amyotrophic lateral sclerosis [91]. Likewise, in human hair the protein and lipid composition of the cuticle, cortex and medulla have been correlated with trace metal content associated with mummification techniques [74], and with environmental metal exposure [92].

Finally, while current synchrotron FT-IRM measurements provide the highest possible spatial resolution, they are time-consuming because they utilize a confocal arrangement with a single-element IR detector. Raster-scanned images of a single biological cell can take more than an hour to collect, while the subcellular imaging of significant regions of tissue can take several days. To date, a comprehensive FT-IRI study with a FPA detector has not been performed on with a

synchrotron source, although the rapid speed at which FPA detectors collect data make them an appealing alternative for some chemical imaging measurements.

When imaging biological systems at the diffraction limit, a confocal optical arrangement can improve the spatial resolution and image contrast. However, this optical configuration is inherently incompatible with FPA detection systems having contiguous pixels. Nonetheless, having an accurate knowledge of the diffraction pattern implies that a mathematical correction for diffraction is possible by deconvolution methods. Unfortunately, for acceptable results, deconvolution requires both high spatial oversampling and an excellent SNR, and it seems unlikely that these requirements can be achieved using a conventional thermal source. Although high-resolution sampling can be accomplished using an FPA and a high-magnification objective, the flux incident on each pixel may be more than 100-fold smaller, such that the SNR is insufficient for a successful deconvolution [4]. The synchrotron source has the potential to correct for diffraction effects and to improve the spatial resolution of FT-IRI over regions of modest size (Figure 14.10). Thus, it is expected that the synchrotron and thermal sources will most likely play complementary roles, with the thermal source being capable of illuminating large regions and well suited to surveying large areas. In contrast, synchrotron has its intensity concentrated into a small area, and is typically used for microsampling (i.e., collecting spectra from small objects with minimal contamination from neighboring regions) or for producing high spatial resolution images of small areas (typically <100 μm on a side). A similar role is anticipated for the
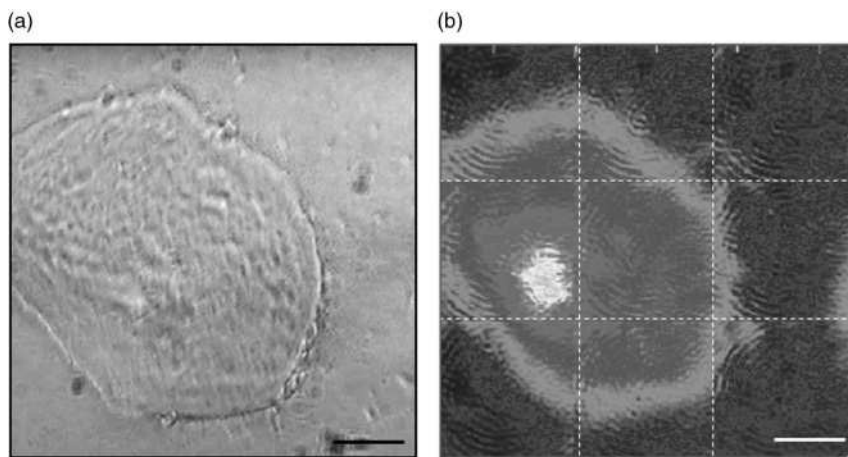
Figure 14.10 (a) Bright-field visible image of a human oral mucosal cell; (b) Synchrotron FPA image of the protein (Amide I) absorbance in the oral mucosal cell. The sample was illuminated with a low-magnification objective (36×, 0.6 NA) for long working distance and collected with a high-magnification (74×, 0.6 NA) objective. A 64 × 64 pixel MCT FPA detector was used to image the cell, where the resulting field of view on the FPA was 35 × 35 μm^2 with 0.54 μm per pixel. The IR image (192 × 192 pixels) was generated in 72 min with a 64 × 64 pixel FPA detector (200 scans, 6 cm^{-1} resolution). Scale bar = 20 μm.

FPA detector, with the thermal source surveying areas many millimeters on a side and offering excellent performance down to approximately 10 μm spatial resolution. With the synchrotron, the resolution limit may be extended down to around 1 μm, but over a much more limited area.

Acknowledgments

Abbreviations

IR   Infrared
FT-IRM   Fourier transform infrared microspectroscopy
FT-IRI   Fourier transform infrared imaging
FPA   Focal plane array
MCT   Mercury cadmium telluride
SNR   Signal-to-noise ratio

References

1 Humecki, H. (ed.) (1995) *Practical Guide to Infrared Microspectroscopy*, Marcel Dekker, Inc., New York.

2 Goormaghtigh, E., Ruysschaert, J.M. and Raussens, V. (2006) *Biophys. J.*, **90**, 2946–57.

3 Byler, D.M. and Susi, H. (1986) *Biopolymers*, **25**, 469–87.

4 Carr, G.L., Chubar, O. and Dumas, P. (2006) *Spectrochemical Analysis Using Infrared Detectors* (eds R. Bhargava and I.W. Levin), Blackwell Publishing, pp. 56–84.

5 Lewis, E.N., Treado, P.J., Reeder, R.C., Story, G.M., Dowrey, A.E., Marcott, C. and Levin, I.W. (1995) *Anal. Chem.*, **67**, 3377–81.

6 Huffman, S.W., Bhargava, R. and Levin, I.W. (2002) *Appl. Spectrosc.*, **56**, 965–9.

7 Messerschmidt, R.G. (1995) *Practical Guide to Infrared Microspectroscopy* (ed. H. Humecki), Marcel Dekker, Inc., New York, pp. 3–40.

8 Carr, G.L. (2001) *Rev. Sci. Instrum.*, **72**, 1613–19.

9 Duncan, W. and Williams, G.P. (1983) *Appl. Opt.*, **22**, 2914.

10 Carr, G.L., Reffner, J.A. and Williams, G.P. (1995) *Rev. Sci. Instrum.*, **66**, 1490–2.

11 Reffner, J.A., Martoglio, P.A. and Williams, G.P. (1995) *Rev. Sci. Instrum.*, **66**, 1298.

12 Miller, L.M. and Smith, R.J. (2005) *Vib. Spectrosc.*, **38**, 237–40.

13 Carr, G.L. (1999) *Vib. Spectrosc.*, **19**, 53–60.

14 Bosch, R.A. (2002) *Nucl. Instrum. Methods Phys. Res. A*, **492**, 284–98.

15 Nucara, A., Lupi, S. and Calvani, P. (2003) *Rev. Sci. Instrum.*, **74**, 3934–42.

16 Williams, G.P. (1992) *Rev. Sci. Instrum.*, **63**, 1535.

17 Hanfland, M., Hemley, R.J., Mao, H.K. and Williams, G.P. (1992) *Phys. Rev. Lett.*, **69**, 1129–32.

18 Ugawa, A., Ishii, H., Yakushi, K., Okamoto, H., Mitani, T., Watanabe, M., Sakai, K., Suzui, K. and Kato, S. (1992) *Rev. Sci. Instrum.*, **63**, 1551–4.

19 Carr, G.L., Hanfland, M. and Williams, G.P. (1995) *Rev. Sci. Instrum.*, **66**, 1643–5.

20 Carr, G.L. and Williams, G.P. (1997) *SPIE Conf. Proc.*, **3153**, 51–9.

21 Bosch, R.A. (2000) *Nucl. Instrum. Methods Phys. Res. A*, **454**, 497–505.

22 Schade, U., Roseler, A., Korte, E.H., Scheer, M. and Peatman, W.B. (2000) *Nucl. Instrum. Methods Phys. Res. A*, **455**, 476–86.

23 Bosch, R.A. (2002) *Rev. Sci. Instrum.*, **73**, 1423–6.

24 Mathis, Y.L., Gasharova, B. and Moss, D. (2003) *J. Biol. Phys.*, **29**, 313–18.

25 Bosch, R.A. (1999) *Nucl. Instrum. Methods Phys. Res. A*, **431**, 320–33.

26 Miller, L.M., Smith, G.D. and Carr, G.L. (2003) *J. Biol. Phys.*, **29**, 219–30.

27 Kreisler, A.J. and Gaugue, A. (2000) *Supercond. Sci. Technol.*, **13**, 1235–45.

28 Moss, D., Gasharova, B. and Mathis, Y.L. (2006) *Infrared Phys. Technol.*, **49**, 53–6.

29 Aparicio, S., Doty, S.B., Camacho, N.P., Paschalis, E.P., Spevak, L., Mendelsohn, R. and Boskey, A.L. (2002) *Calcif. Tissue Int.*, **70**, 422–9.

30 Wetzel, D.L. and LeVine, S.M. (1999) *Science*, **285**, 1224–5.

31 Choo, L.P., Wetzel, D.L., Halliday, W.C., Jackson, M., LeVine, S.M. and Mantsch, H.H. (1996) *Biophys. J.*, **71**, 1672–9.

32 Miller, L.M., Wang, Q., Telivala, T.P., Smith, R.J., Lanzirotti, A. and Miklossy, J. (2005) *J. Struct. Biol.*, **155**, 30–7.

33 Rak, M., Del Bigio, M.R., Mai, S., Westaway, D. and Gough, K. (2007) *Biopolymers*, **87**, 207–17.

34 Kneipp, J., Miller, L.M., Joncic, M., Kittel, M., Lasch, P., Beekes, M. and Naumann, D. (2003) *Biochim. Biophys. Acta*, **1639**, 152–8.

35 Kneipp, J., Miller, L.M., Spassov, S., Sokolowski, F., Lasch, P., Beekes, M. and Naumann, D. (2004) *Biopolymers*, **74**, 163–7.

36 Wang, Q., Kretlow, A., Beekes, M., Naumann, D. and Miller, L. (2005) *Vib. Spectrosc.*, **38**, 61–9.

37 Kretlow, A., Wang, Q., Kneipp, J., Lasch, P., Beekes, M., Miller, L. and Naumann, D. (2006) *Biochim. Biophys. Acta*, **1758**, 948–59.

38 Gallant, M., Rak, M., Szeghalmi, A., Bigio, M.R. Del, Westaway, D., Yang, J., Julian, R. and Gough, K.M. (2006) *J. Biol. Chem.*, **281**, 5–8.

39 Szczerbowska-Boruchowska, M., Dumas, P., Kastyak, M.Z., Chwiej, J., Lankosz, M., Adamek, D. and Krygowska-Wajs, A. (2007) *Arch. Biochem. Biophys.*, **459**, 241–8.

40 Kneipp, J., Lasch, P., Baldauf, E., Beekes, M. and Naumann, D. (2000) *Biochim. Biophys. Acta*, **1501**, 189–99.

41 Fuchs, R.K., Allen, M.R., Ruppel, M.E., Diab, T., Phipps, R.J., Miller, L.M. and Burr, D.B. (2008) *Matrix Biol.*, **27**, 34–41.

42 Busa, B., Miller, L.M., Rubin, C.T., Qin, Y.X. and Judex, S. (2005) *Calcif. Tissue Int.*, **77**, 386–94.

43 Miller, L.M., Little, W., Schirmer, A., Sheik, F., Busa, B. and Judex, S. (2007) *J. Bone Miner. Res.*, **22**, 1037–45.

44 Ruppel, M.E., Burr, D.B. and Miller, L.M. (2006) *Bone*, **39**, 318–24.

45 Huang, R.Y., Miller, L.M., Carlson, C.S. and Chance, M.R. (2002) *Bone*, **30**, 492–7.

46 Miller, L.M., Vairavamurthy, V., Chance, M.R., Mendelsohn, R., Paschalis, E.P., Betts, F. and Boskey, A.L. (2001) *Biochim. Biophys. Acta*, **1527**, 11–19.

47 Miller, L.M., Novatt, J.T., Hamerman, D. and Carlson, C.S. (2004) *Bone*, **35**, 498–506.

48 Huang, R.Y., Miller, L.M., Carlson, C.S. and Chance, M.R. (2003) *Bone*, **33**, 514–21.

49 Burr, D.B., Miller, L., Grynpas, M., Boyde, J.L.i, A., Mashiba, T., Hirano, T. and Johnston, C.C. (2003) *Bone*, **33**, 960–9.

50 Wang, Q., Sanad, W., Voigt, A., Klingel, K., Kandolf, R., Stangl, K., Baumann, G. and Miller, L.M. (2005) *Vib. Spectrosc.*, **38**, 61–9.

51 Gough, K.M., Zelinski, D., Wiens, R., Rak, M. and Dixon, I.M.C. (2003) *Anal. Biochem.*, **316**, 232–42.

52 Wiens, R., Rak, M., Cox, N., Abraham, S., Juurlink, B.H., Kulyk, W.M. and Gough,

K.M. (2007) *Anal. Bioanal. Chem.*, **387**, 1679–89.

53 Liu, K.Z., Man, A., Shaw, R.A., Liang, B., Xu, Z., and Gong, Y. (2006) *Biochim. Biophys. Acta*, **1758**, 960–7.

54 Diem, M., Romeo, M., Matthaus, C., Miljkovic, M., Miller, L. and Lasch, P. (2004) *Infrared Phys. Technol.*, **45**, 331–8.

55 Holman, H.Y.N., Martin, M.C. and McKinney, W.R. (2003) *J. Biol. Phys.*, **29**, 275–86.

56 Martin, M.C., Tsvetkova, N.M., Crowe, J.H. and McKinney, W.R. (2001) *Appl. Spectrosc.*, **55**, 111–13.

57 Jamin, N., Dumas, P., Moncuit, J., Fridman, W.H., Teillaud, J.L., Carr, G.L. and Williams, G.P. (1998) *Proc. Natl Acad. Sci. USA*, **95**, 4837–40.

58 Jamin, N., Miller, L., Moncuit, J., Fridman, W.H., Dumas, P. and Teillaud, J.L. (2003) *Biopolymers*, **72**, 366–73.

59 Yee, N., Benning, L.G., Phoenix, V.R. and Ferris, F.G. (2004) *Environ. Sci. Technol.*, **38**, 775–82.

60 Tobin, M.J., Chesters, M.A., Chalmers, J.M., Rutten, F.J.M., Fisher, S.E., Symonds, I.M., Hitchcock, A., Allibone, R. and Dias-Gunasekara, S. (2004) *Faraday Discuss.*, **126**, 27–39.

61 Lasch, P., Boese, M., Pacifico, A. and Diem, M. (2002) *Vib. Spectrosc.*, **28**, 147–57.

62 Diem, M., Chiriboga, L., Lasch, P. and Pacifico, A. (2002) *Biopolymers*, **67** (4-5), 349–53.

63 Heraud, P., Wood, B.R., Tobin, M.J., Beardall, J. and McNaughton, D. (2005) *FEMS Microbiol. Lett.*, **249**, 219–25.

64 Holman, H.Y.N., Goth-Goldstein, R., Martin, M.C., Russell, M.L. and McKinney, W.R. (2000) *Environ. Sci. Technol.*, **34**, 2513–17.

65 Holman, H.N., Martin, M.C., Blakely, E.A., Bjornstad, K. and McKinney, W.R. (2000) *Biopolymers*, **57**, 329–35.

66 German, M.J., Pollock, H.M., Zhao, B., Tobin, M.J., Hammiche, A., Bentley, A., Cooper, L.J., Martin, F.L. and Fullwood, N.J. (2006) *Invest. Ophthalmol. Vis. Sci.*, **47**, 2417–21.

67 Bentley, A.J., Nakamura, T., Hammiche, A., Pollock, H.M., Martin, F.L., Kinoshita, S. and Fullwood, N.J. (2007) *Mol. Vis.*, **13**, 237–42.

68 Tague, T. and Miller, L.M. (2000) *Microsc. Today*, **2**, 26–32.

69 Miller, L.M., Dumas, P., Jamin, N., Teillaud, J.L., Miklossy, J. and Forro, L. (2002) *Rev. Sci. Instrum.*, **73**, 1357–60.

70 Dumas, P. and Miller, L. (2003) *Vib. Spectrosc.*, **32**, 3–21.

71 Chan, K.L., Kazarian, S.G., Mavraki, A. and Williams, D.R. (2005) *Appl. Spectrosc.*, **59**, 149–55.

72 Briki, F., Busson, B., Kreplak, L., Dumas, P. and Doucet, J. (2000) *Cell. Mol. Biol. (Noisy-le-grand)*, **46**, 1005–16.

73 Bantignies, J.L., Carr, G.L., Lutz, D., Marull, S., Williams, G.P. and Fuchs, G. (2000) *J. Cosmet. Sci.*, **51**, 73–90.

74 Bertrand, L., Doucet, J., Dumas, P., Simionovici, A., Tsoucaris, G. and Walter, P. (2003) *J. Synchrotron. Radiat.*, **10**, 387–92.

75 Kalasinsky, K.S. (1998) *Cell. Mol. Biol. (Noisy-le-grand)*, **44**, 81–7.

76 Wetzel, D.L., Slatkin, D.N. and Levine, S.M. (1998) *Cell. Mol. Biol. (Noisy-le-grand)*, **44**, 15–27.

77 Marinkovic, N.S., Adzic, A.R., Sullivan, M., Kovacs, K., Miller, L.M., Rousseau, D.L., Yeh, S.R. and Chance, M.R. (2000) *Rev. Sci. Instrum.*, **71**, 4057–60.

78 Marinkovic, N.S., Huang, R., Bromberg, P., Sullivan, M., Toomey, J., Miller, L.M., Sperber, E., Moshe, S., Jones, K.W., Chouparova, E., Lappi, S., Franzen, S. and Chance, M.R. (2002) *J. Synchrotron Radiat.*, **9**, 189–97.

79 Kaun, N., Kulka, S., Frank, J., Schade, U., Vellekoop, M.J., Harasek, M. and Lendl, B. (2006) *Analyst*, **131**, 489–94.

80 Fan, K., Bell, P. and Fried, D. (2006) *J. Biomed. Opt.*, **11**, 064008.

81 Fried, D., Ashouri, N., Breunig, T. and Shori, R. (2002) *Lasers Surg. Med.*, **31**, 186–93.

82 Beney, L., Mille, Y. and Gervais, P. (2004) *Appl. Microbiol. Biotechnol.*, **65**, 457–64.

83 Carrier, D. and Wong, P.T.T. (1997) *Eur. J. Solid State Inorg. Chem.*, **34**, 733–44.

84 Holtje, M., Forster, T., Brandt, B., Engels, T., von Rybinski, W. and Holtje, H.D. (2001) *Biochim. Biophys. Acta - Biomembr.*, **1511**, 156–67.

85 Park, S.Y., Hannemann, R.E. and Franses, E.I. (1999) *Colloids Surf. B - Biointerfaces*, **15**, 325–38.

86 Xie, A., He, Q., Miller, L.M., Sclavi, B. and Chance, M.R. (1999) *Biopolymers*, **49**, 591–603.

87 Globus, T.R., Woolard, D.L., Samuels, A.C., Gelmont, B.L., Hesler, J., Crowe, T.W. and Bykhovskaia, M. (2002) *J. Appl. Phys.*, **91**, 6105–13.

88 Williams, G.P. (2006) *Rep. Prog. Phys.*, **69**, 301–26.

89 Edwards, G.S., Allen, S.J., Haglund, R.F., Nemanich, R.J., Redlich, B., Simon, J.D. and Yang, W.C. (2005) *Photochem. Photobiol.*, **81**, 711–35.

90 Neil, G.R., Carr, G.L., Gubeli, J.F., Jordan, K., Martin, M.C., McKinney, W.R., Shinn, M., Tani, M., Williams, G.P. and Zhang, X.C. (2003) *Nucl. Instrum. Methods Phys. Res. A*, **507**, 537–40.

91 Szczerbowska-Boruchowska, M., Chwiej, J., Lankosz, M., Adamek, D., Wojcik, S., Krygowska-Wajs, A., Tomik, B., Bohic, S., Susini, J., Simionovici, A., Dumas, P. and Kastyak, M. (2005) *X-Ray Spectrom.*, **34**, 514–20.

92 Miller, L.M., Wang, Q., Smith, R.J., Zhong, H., Elliott, D. and Warren, J. (2007) *Anal. Bioanal. Chem.*, **387**, 1705–15.

15

Spectroscopic Imaging with Nanometer Resolution Using Near-Field Methods

Boon-Siang Yeo[*], *Thomas Schmid*[*], *Weihua Zhang, and Renato Zenobi*

15.1
Introduction

Methods for performing *in situ* and nondestructive chemical analysis with nanometer spatial resolution are in great demand due to rapid developments in nanoscience and nanotechnology. These techniques are required to answer outstanding questions in surface chemistry (e.g., where are the 'hot sites' on a catalyst surface?); in biology (e.g., where are membrane proteins located in the lipid bilayer of a cell?); and in materials science (e.g., what is the nanoscale architecture of the tires of a Formula 1 racing car that hardly skids during a rainy race day?). It can be observed that these problems demand answers that give more than just a number, spectrum or a topographic image of the analyte. Rather, they require full spectroscopic information for every pixel of the sample; that is, chemical imaging is needed.

The requirements for methods that provide such information are clearly stringent, necessitating simultaneously excellent spatial resolution, chemical identification without the use of labels and good sensitivity, often with *in situ* probing of the sample (to prevent degradation). These effectively rule out the established workhorses of modern chemical analysis such as nuclear magnetic resonance, infrared (IR) spectroscopy and electron microscopy.

In this chapter, we will review near-field optical methods and their applications to problems in biology and materials science. Near-field techniques provide nanometer spatial resolution by overcoming the Abbe diffraction limit, and can be used to investigate many types of sample *in situ*. Here, emphasis is placed on near-field methods that provide vibrational information (i.e., 'molecular fingerprints') of the analytes. Finally, the current challenges faced by these methods and their potential in nanoscale chemical analysis in the near future are discussed.

---

[*] These authors contributed equally to this work.

15.2
Methods

15.2.1
Scanning Near-Field Optical Microscopy with Aperture Probes

In order to break the optical diffraction limit, the most straightforward idea is to create a point light source which can then be scanned over the sample surface in close proximity (in the optical near-field) to perform optical mapping. The spatial resolution is in this case not restricted by the diffraction limit (cf. Chapter 1), but is determined by the size of the light source. Although this idea was first proposed in 1928 by Synge [1], due to the difficulties in the fabrication, as well as the precise positioning and scanning with such a light source, the real techniques of scanning near-field optical microscopy (SNOM) was only realized during the 1980s, following the invention of scanning tunneling microscopy (STM) [2, 3]. Early on, a metal-coated fiber tip was used to create a nanoscale optical aperture, as shown in Figure 15.1a. The size of the aperture – and hence the light source – may be down to 50 nm, several times smaller than the diffraction limit using visible light. This type of SNOM is referred to as aperture-SNOM (a-SNOM). Following its invention, a-SNOM achieved huge success during the 1990s, for example, by imaging the fluorescence of single molecules at room temperature [4], and the mapping of luminescence from a quantum well with unprecedented spatial resolution [5].

However, a-SNOM faces two fundamental difficulties: (i) the power emitted from the aperture is usually on the order of nanoWatts, and too weak for collecting a spectrum with a short acquisition time; (ii) its spatial resolution is limited to 50 nm in practice, and is insufficient for true nanoscale analysis [6]. In order to overcome these problems, alternatives have been developed during the past 10 years, namely, tip-enhanced Raman spectroscopy (TERS) [7, 8] (Figure 15.1b) and scattering SNOM (s-SNOM), which is mainly used in the IR spectral range (Figure 15.1c) [9]. In this chapter, we focus primarily on these two methods.
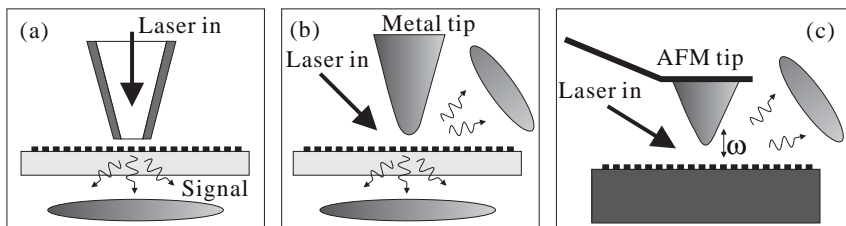
Figure 15.1 Schematic drawings of different SNOM methods.
(a) Aperture SNOM (a-SNOM); (b) Tip-enhanced Raman
spectroscopy; (c) Scattering SNOM (s-SNOM).

15.2.2
Tip-Enhanced Raman Spectroscopy

Raman scattering is known to be an extremely weak process. Its scattering cross-section is approximately 10^{-29} cm^2, some 14 orders of magnitude smaller than the absorption cross-section of fluorescence. In order to collect a spectrum with a reasonable signal-to-noise ratio (SNR) and speed, signal enhancement techniques are required, and this is made possible by using TERS.

The origin of TERS arose from studies of localized surface plasmons, which suggested that an electric field could be greatly enhanced and confined by certain metal nanostructures [10–12]. Following reports of single-molecule surface-enhanced Raman spectroscopy (SERS) of Rhodamine 6G and crystal violet dye molecules made in 1997 [13, 14], the feasibility of creating a localized light source at the apex of a sharp metal tip was further investigated. Simulations and subsequent experimental results demonstrated that the electric field could be laterally confined into a small area with a diameter less than 30 nm, while the light intensity could be enhanced tens of times (see Figure 15.2) [15]. In 2000, the use of TERS was reported by Stöckle *et al.* [8], and almost simultaneously by Anderson and Kawata *et al.* [7, 16]. A new era of near-field spectroscopy had begun!

The heart of the TERS technique is a 'hot' tip, which can highly confine and enhance the electric field at the tip apex. A brief introduction of the origins of the field enhancement is now given here. There are two main types of field enhancement: (i) that powered by localized plasmon resonance which is highly frequency-dependent; and (ii) shape-induced enhancement which does not depend on the frequency. To yield a good enhancement, one can either tune the excitation wavelength to coincide with the resonant frequency (or *vice versa*), or use a structure which can provide enhancement over a wide spectral range.

The first approach was recently successfully demonstrated by our group [17, 18]. It was found that the resonance frequency of Ag-coated AFM tips could be tuned
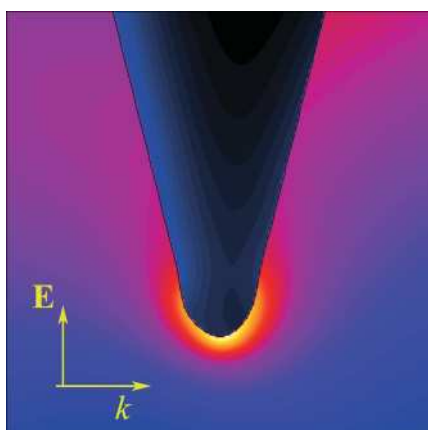
Figure 15.2 The lightning rod effect. When the polarization of the incident radiation is parallel to the tip axis, the electric field will be highly enhanced at the tip apex.

by modifying the optical constants of the dielectric tips. In these studies, Ag was coated on AFM tips made from, or precoated with, different materials such as Si_3N_4, SiO_2 and AlF_3 (Figure 15.3). An AFM tip made of a low-refractive index material gave the best enhancement with 488 nm illumination. Further theoretical studies have verified that the resonance frequency will indeed red-shift when the refractive index of the AFM tip increases [19]. This provides a methodology to fabricate 'hot' tips with a high yield.

In addition to the possibility of tuning the resonance of the tip by choice of the underlying material, two types of structure supporting a strong field enhancement over a broad spectral range have been identified. The first of these structures uses sharp metal tips (Figure 15.4) that benefit from the 'lightning rod' effect [10, 12]; this means that the electromagnetic field is always highly enhanced at sharp protrusions [12, 20]. A simple example is provided by a cigar-shaped ellipsoid. Besides the plasmon resonance-induced enhancement, another type of resonance exists
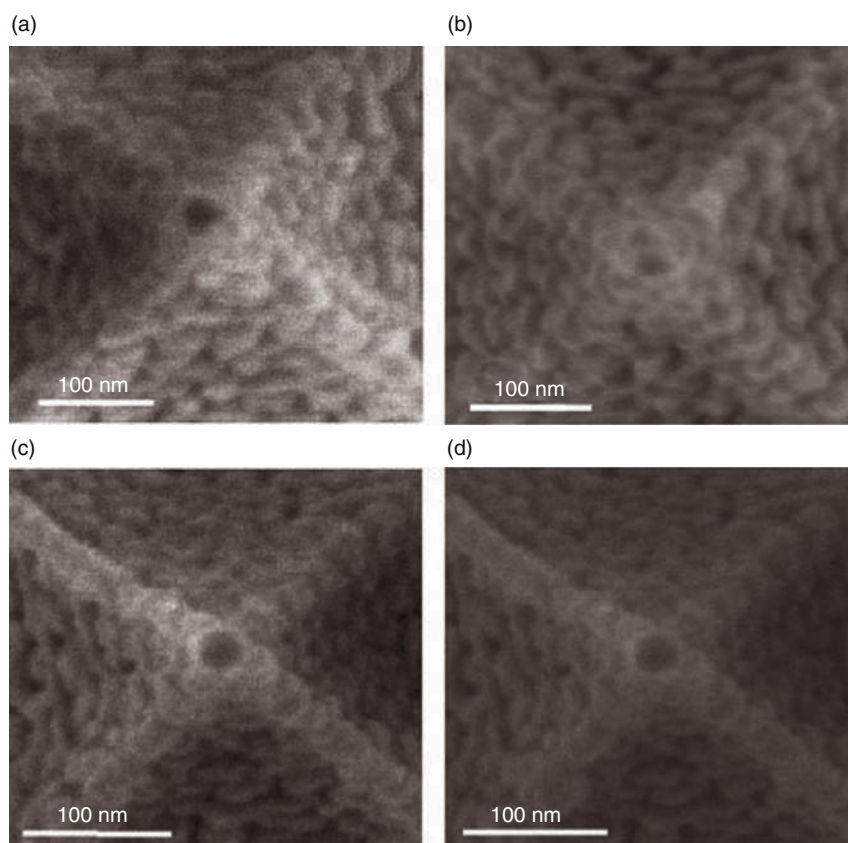
Figure 15.3 Scanning electron microscopy images of Ag-coated AFM tips. (a, b) Tips precoated with SiO_x; (c, d) Tips precoated with AlF_3. Adapted from Ref. [17].
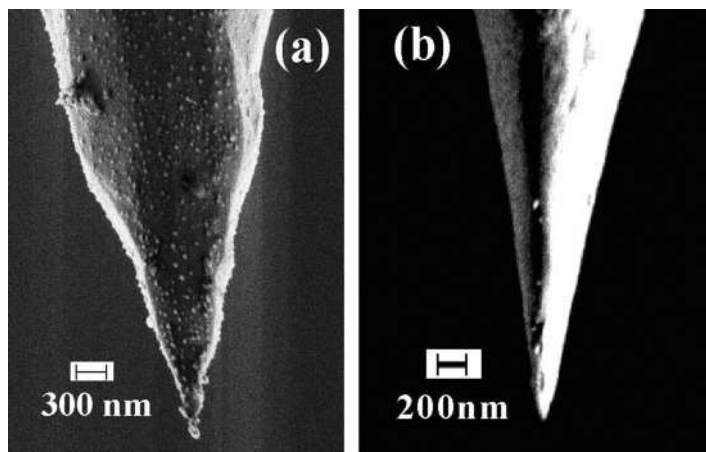
Figure 15.4 Scanning electron microscopy images of electrochemically etched (a) Au and (b) Ag tips.

which is only determined by the sharpness of the end of the ellipsoid – the sharper the nanostructure, the higher the field enhancement. This conclusion was supported by numerical simulations on tapered metal tips [10, 11]. To date, many TERS measurements have been reported using sharp Au or Ag tips, based on the lightning rod effect; an example is a series of investigations on carbon nanotubes (CNTs) conducted by Novotny and coworkers [21–25]. Unfortunately, the enhancement afforded by this type of tip is rather low, and this prevents its application to samples consisting of weak Raman scatterers. However, it was recently predicted that a field enhancement 100-fold better than the present result is possible if the radius of curvature of the tip apex were to be reduced to 1 nm [26]. Such a finding highlights the untapped potential of this approach.

The second approach is gap-mode TERS, which is essentially a broadband antenna [27]. Compared to the production of ultrasharp tips, the creation of a nanometer gap between a metal tip and a metal substrate is much easier. In the case of an electrochemically etched Au tip with a radius of curvature less than 25 nm, a Raman enhancement better than 10^6 can be achieved, with a good reproducibility [27, 28].

The most significant achievement of gap-mode TERS is its demonstration of single-molecule Raman spectroscopy [29, 30], the first attempt at which was reported by Neacsu *et al.* [31]. Here, the sample was an Au substrate covered by a monolayer of malachite green, a dye molecule which shows a strong resonance Raman effect. Significant spectral fluctuations were observed, and the intensity histogram showed a Poisson distribution-like pattern, which was taken as evidence for single molecule detection. However, the spectra presented were not consistent with the fingerprint vibrational modes of the analyte used. Stronger evidence of single-molecule TERS was independently reported by Domke *et al.*, and shortly afterwards by our group [29, 30]. In these investigations, TER spectra identical to

the normal Raman spectra of the analyte were observed. Several lines of evidence, such as intensity which was dependent on sample coverage as well as discrete signal losses, prove unambiguously that the sensitivity of TERS can reach the single-molecule level. Two interesting observations were made from these studies. First, the signal enhancement was only ~10^7, and several orders of magnitude lower than expected. Second, no significant mode shifts or new modes were observed, indicating that the surface selection rules for Raman scattering remained valid under such high field intensity. This also implied that existing Raman spectrum databases could be employed for interpretation of the TERS data.

15.2.3
Scattering SNOM

The TERS strategy is not suitable for IR absorption spectroscopy (IRAS). This is because a broadband light source is used in IRAS and it is difficult to create a constant enhancement over the entire spectral range. Another problem stems from the much longer wavelength of IR compared to visible light. In other words, the far-field excitation area will be much larger than in the case of TERS, and the SNR will deteriorate. In order to overcome these problems, s-SNOM is commonly used for near-field IRAS [32].

Figure 15.1c shows the basic set-up of a s-SNOM. The tip–sample system is illuminated from the side, the near-field signal (i.e., the interaction between the tip and sample) is modulated by the oscillation of the tip, and harmonic signal components in the scattered light that correspond to the near-field information are recorded to form an optical image. In a simplified model, the tip can be treated as a spherical particle, the polarizability of which is $\alpha = 4\pi r^3(\varepsilon_p - \varepsilon_m)/(\varepsilon_p + 2\varepsilon_m)$, where r is the radius of the sphere, and ε_p and ε_m are the permittivities of the tip and the surrounding medium, respectively. The image dipole of the tip in the sample is $\alpha\beta$, where $\beta = (\varepsilon_s - 1)/(\varepsilon_s + 1)$ and ε_s denotes the permittivity of the sample. The tip–sample coupling can be described as a dipole–dipole coupling, and the effective polarizability of the scattering of this system will be [33]:

$$\alpha_{eff} = \frac{\alpha(1+\beta)}{1 - \dfrac{\alpha\beta}{16\pi(r+z)^3}} \tag{15.1}$$

where z is the tip–sample distance. Using this equation, the optical constants of the sample can be deduced. In other words, the IR absorption spectrum is recorded by this s-SNOM. To date, the best s-SNOM results were collected by Hillenbrand *et al.* [33–36], who achieved spatial resolutions of 10 nm or even lower. Unfortunately, s-SNOM suffers from several problems. First, it only functions at a single wavelength at a time, and consequently it is impossible to obtain a full near-field IR absorption spectrum. The second problem is the complexity of the tip–sample coupling. Equation 15.1 assumes that the sample surface is perfectly flat, which is at best an approximation. Therefore, there is still room for improvement in the development of s-SNOM.

15.2.4
Comparison of the Near-Field Spectroscopic Methods

Table 15.1 shows a comparison of all near-field spectroscopic methods. It is clear that a-SNOM is not suitable for vibrational spectroscopic imaging because of its poor sensitivity. While s-SNOM provides a good spatial resolution and sensitivity, it suffers from two problems: (i) the difficulties in image interpretation; and (ii) it does not provide a full spectrum. TERS is more promising, although the fabrication of 'hot' tips can be tricky. As discussed above, much progress has been made with TERS during the past few years, and it is predicted that TERS will grow into a reliable nanoscale analytical method in the near future, when the tip fabrication methods have been optimized.

15.2.5
Imaging

Spectroscopic imaging with nanometer spatial resolution is a very attractive proposition. Having full spectroscopic information available at every pixel is also crucial for obtaining simultaneous chemical information for unknown, heterogeneous samples, or when following transient events. Detailed information from small frequency shifts (not available from fixed-frequency imaging) can also be obtained. Fast spectroscopic imaging will further facilitate the high-throughput investigation

Table 15.1 Comparison of different near-field spectroscopic methods.

	Aperture SNOM	TERS	Scattering SNOM
Spatial resolution	50 nm	10 nm	10 nm
Sensitivity	Poor	Single molecule level(gap-mode TERS)	~100 molecules (estimated from its spatial resolution)
Sample topography	No requirement	No requirement (Flat sample is required for gap-mode TERS)	Flat sample surface
Tip preparation	Difficult	Difficult	Easy
Instrumentation	Complex	Complex	Complex
Spectral range	Full spectrum (for Raman)	Full spectrum	Single wavelength
Collection time of one full spectrum	10 min	1 s	–

of complex samples, reduce drift and sample damage, and will also allow dynamic processes to be followed. Unfortunately, almost all of the published research has presented either fixed-frequency intensity maps or show topographic scans with spectroscopic data taken at a very small number of points, which is most likely due to the lack of sensitivity and inadequate recording speed of existing instruments. Further technical improvements will enable this analytical method to provide more complete solutions to the difficult problems in the nanosciences.

15.3
Applications

In this section, various applications of near-field vibrational spectroscopies in materials and biological sciences are presented.

15.3.1
Carbon Nanotubes

The imaging of single-walled carbon nanotubes (SWNTs) has become the most frequent application of TERS [23–25]. SWNTs have generated intense interest due to their potential applications in nanotechnology. Four types of Raman mode are usually observed in the TER spectra of SWNT: the radial breathing modes (RBM), two graphitic bands (G, G'), and the disordered (D) band. The positions of these bands are vibrational signatures of the state of the SWNT, for example, its defect density, chirality, and so on.

Defect-density imaging has been demonstrated for an isolated SWNT produced by the arc discharge method [22]. Bumps of 5 nm in height have been observed on top of the SWNT in the topography image, and these have been assigned to Ni/Y catalyst particles. When TERS measurements were performed on locations of the SWNT close to or on the Ni/Y catalyst, the frequencies and intensities of the D and G bands changed. Differences in the local tube structure, which may be due to defects, junctions or interactions with the glass substrate, may also be revealed from the TERS variation of the RBM frequency (diameter sensitive) and intensity.

The simultaneous near-field photoluminescence and Raman imaging of isolated SWNTs with a spatial resolution better than 15 nm has also been reported [21]. Highly localized and intense photoluminescence was observed from certain sections (20–30 nm) of an arc-discharge-produced SWNT, and has been assigned to the presence of localized excited states. These states may originate from localized chirality variations occurring from defects or from local environmental perturbations. However, for micelle-encapsulated SWNTs, the photoluminescence emission extends along the tube length (several hundreds of nanometers). By simultaneously acquiring near-field Raman and photoluminescence images, it is desired that a correlation between structural defects and the photoluminescence properties of individual SWNTs is obtained.
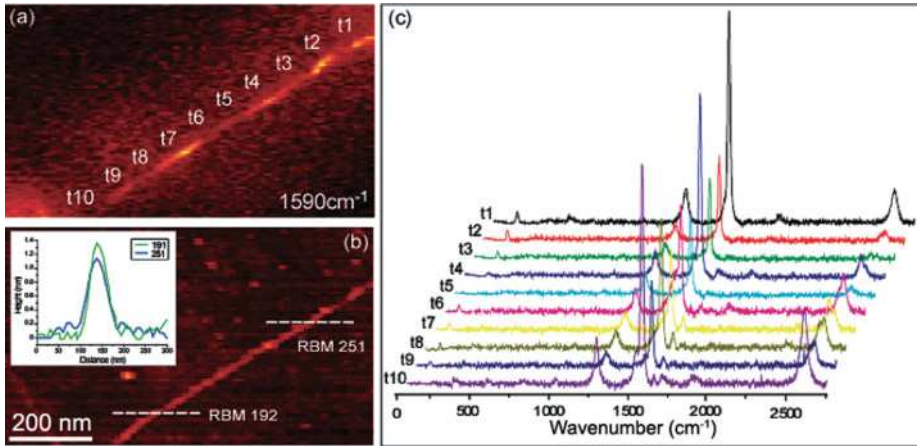
Figure 15.5 (a) TERS image and (b) corresponding topography image of an isolated single-walled nanotube (SWNT), where the optical resolution was determined to be 40 nm; (c) A series of TER spectra acquired along the length of the SWNT. Two resonant RBM phonons are detected. One RBM phonon frequency is detected at 251 cm^{-1}, assigned to semiconducting chirality; the second RBM phonon frequency recorded from the lower section of the SWNT is centered at 192 cm^{-1}, and is assigned to metallic chirality. The inset in panel (b) displays two cross-sectional profiles acquired from both the upper and lower sections, respectively, revealing that the expected diameter change occurs as the SWNT undergoes transition from a semiconducting to metallic chirality. Scale bar = 200 nm (panels a and b). Adapted from Ref. [23].

The feasibility of CNTs as components in molecular electronics (e.g., intramolecular junctions) is intimately related to their conducting or semiconducting properties. Here, these properties along a nanotube have been measured by the near-field recording of the resonant phonon frequencies along spatially isolated SWNTs (Figure 15.5). The determination of changes in chirality is based on shifts in the RBM mode, and supported by changes in the D band. Chirality transitions from semiconducting to metal and metal to metal at the single nanotube level have been mapped. A spatial extension of the transition region of 40–100 nm has been found [23].

The near-field imaging of SWNTs covered with an overlayer of SiO$_x$ has also been performed [24], the results having implications for biological processes and in semiconductor technology because the functional units found in cells and silicon chips are located in the subsurface.

15.3.2
Semiconductors

Stress, strain and impurities in Si samples can be detected based on frequency, intensity, shape and width changes of the Si phonon band. Due to the ongoing miniaturization of semiconductor structures, there is a need for imaging of these features with nanometer-scale resolution.

The TERS mapping of a Si device consisting of 380 nm-wide SiO$_2$ lines separated by 300 nm has been demonstrated by Sun and Shen [37–40]. Poborchii *et al.* used a depolarization configuration for TERS in order to suppress the far-field signal and to improve the intensity contrast of the Si phonon band at 520 cm^{-1} from 0.5× to 2× [41]. This group analyzed 100 nm pitches in Si that had been oxidized by thermal annealing using an Ag-coated quartz AFM tip. The phonon frequency has been found to increase at the proximity of the pitch, which demonstrates that compression at the Si/SiO$_2$ boundary between the pitch and the remainder of the substrate has occurred during the thermal oxidation process. Further improvements of this depolarization approach, as assessed by the group of Sokolov, yielded contrasts of up to 12, which was partially attributed to reflection of the incident light by the metal-coated tip and thus to a higher irradiance at the sample [42, 43]. Without this contribution, the contrast was still on a high level of ≥3.4 and allowed a mapping using the intensity of the Si phonon band with a lateral resolution of ~20 nm and an acquisition time of 2 s per pixel (Figure 15.6) [42].

Recently, the research laboratories of the microchip producer AMD began to use TERS for characterizing patterned silicon surfaces. Metallized AFM tips that have been prepared by sputter deposition of thin Ag films onto quartz tips and sharpened by focused ion beam (FIB) milling were used. With a top-illumination set-up, line profiles of patterned samples were recorded and the influence of laser deflection at the tip and laser heating on silicon stress measurements were studied [44–46].

Subsurface structures in silicon were also studied using apertureless s-SNOM in the IR range. Lahrech *et al.* have shown successfully that implanted boron lines in silicon can be detected with a lateral resolution of ~400 nm, even in the absence of any topographical contrast [47]. Knoll and Keilmann have performed near-field
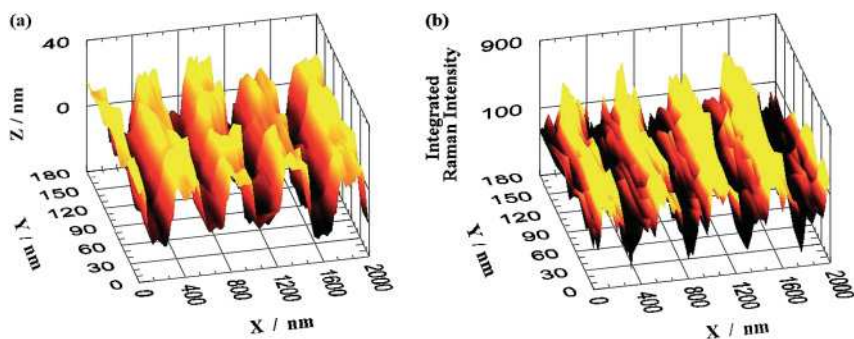
Figure 15.6 Three-dimensional scanning images (10 × 100 pixels, 180 × 2000 nm^2) of (a) topography and (b) integrated Si phonon signal (TERS, 2 s acquisition time per pixel) for a silicon sample coated with 30 nm-thick and 250 nm-wide stripes of SiO$_x$ with a distance of 250 nm between the structures. Reprinted with permission from Ref. [42].

IR measurements on doped Si and shown that the subsurface mobile carriers can be probed by their response to an IR near-field with a spatial resolution of 30 nm [48]. The group of Havenith presented a scanning near-field infrared microscopy (SNIM) system; this is an IR s-SNOM set-up based on a continuous-wave optical parametric oscillator (OPO) as an excitation source with a much wider tunability compared to the usually applied CO_2 lasers [49]. With this set-up, a subsurface pattern of implanted gallium ions in a topographically flat silicon wafer was imaged with a lateral resolution of ≤30 nm.

In the context of semiconductor samples, the pattern characterization of deep-UV photoresists by a-SNOM IR imaging should be mentioned. The set-up used by Dragnea *et al.* is based on an illumination-mode SNOM with a color center laser as a tunable IR source and collection of the light transmitted through the sample by an IR objective [50]. Samples were prepared by mask-assisted deep-UV patterning of poly(*tert*-butylmethacrylate) thin films, leading to poly(methacrylic acid) and poly(*tert*-butylmethacrylate) in the exposed and unexposed regions, respectively. Imaging was performed at 2.80 μm and 2.94 μm, and resulted in a chemical contrast due to O–H stretching vibrations at 2.94 μm only present in the exposed regions (Figure 15.7). The lateral resolution was ~290 nm, which is clearly below the diffraction limit. These studies were extended to measurements of water vapor uptake by photolithographic polymers [51]. Consequently, the entire SNOM set-up, excluding the laser source, was built inside a bell-jar chamber in order to generate a controlled environment around the sample.

All studies mentioned in this section have been single-wavelength/single-frequency maps, and thus restricted to the imaging of changes in band intensities, such as the Si phonon band of strained silicon. Important information that can
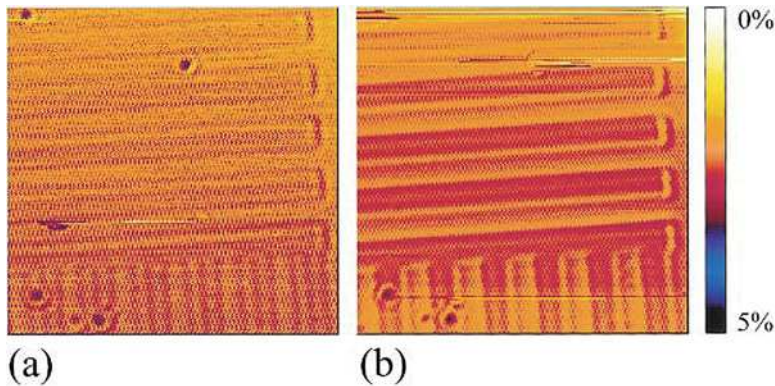
Figure 15.7 Aperture SNOM IR images of a 8 μm/8 μm line/space pattern obtained by mask-assisted deep-UV exposure of a 1 μm-thick photoresist layer. The images were collected at 2.80 μm (a) and 2.94 μm (b). IR absorption at the OH stretching vibration frequency at 2.94 μm leads to the dark contrast of the exposed regions in (b). Reprinted with permission from Ref. [50].

be derived from changes in band frequencies and shapes is yet to be reported in near-field imaging experiments. In IR approaches, this is due to the need to tune the laser in order to obtain spectrally resolved information. Scanning the same part of a sample sequentially many times, while tuning the wavelength over the range of interest, is not feasible in practice, due to the long measurement time and long-term drifts of the set-up. A complete spectrum can, alternatively, be obtained in one attempt by using near-field Raman spectroscopy with detector arrays (e.g., CCDs). With the improvements of TERS with regards to the optical contrast mentioned above, and more efficient collection optics/detectors, full spectroscopic imaging of semiconductor samples with nanometer-scale resolution is expected in the near future.

15.3.3
Polymers and Other Materials

Imaging with material-specific spectral contrast using excitation at a fixed IR wavelength in an apertureless s-SNOM configuration can be achieved with excellent spatial resolution and relatively rapidly, as no spectral scanning or dispersion in a spectrometer is needed. This has been demonstrated for the recognition of components in polymer blends, as well as in metal–dielectric composites, and on silicon surfaces. Polymer blends are a very interesting and promising area of application for near-field spectroscopic imaging. Such blends often show segregation of the polymer phases, forming domains with sizes in the 100 nm range and below. Fillers such as small silica or graphite particles and other additives add to the complexity of such samples, especially in materials of industrial relevance. State-of-the-art Raman microspectrometry has a spatial resolution on the order of 1 µm, and is thus not capable of resolving nanosize polymer phase domains or filler particles [52].

The group of Keilmann has applied IR s-SNOM at fixed wavelengths to image polymer mixtures, polymer films and polymer beads, with excellent spatial resolution [53–55]. A high contrast can be achieved between metals and high-refractive index dielectric compounds [9], and a spatial resolution of <10 nm has been reported [36] even at IR wavelengths of $\lambda \approx 10$ µm, corresponding to a resolution of $\lambda/1000$. While the contrast is material-dependent, the spatial resolution is not, and is determined solely by the properties of the tip. Figure 15.8 shows the imaging of a poly(methylmethacrylate)/polystyrene (PMMA/PS) polymer blend with a resolution of <70 nm carried out at different IR wavelengths in the 5.5–6 µm range [56]. This example demonstrates very nicely how spectroscopic contrast is achieved at an appropriate (fixed) wavelength, and how the contrast is completely reversed at another wavelength.

Akhremitchev *et al.* presented a set-up based on the same principle, namely IR s-SNOM with a side-illuminated AFM tip, and employed it to characterize nanostructured polymer blends that were used as minimally adhesive surface coatings to prevent biofouling [57, 58]. Raschke *et al.* used sharp Au-coated, forward-pointing ('nose-type') AFM probes with a radius of 10–15 nm, and obtained fixed-

(a)

(b)
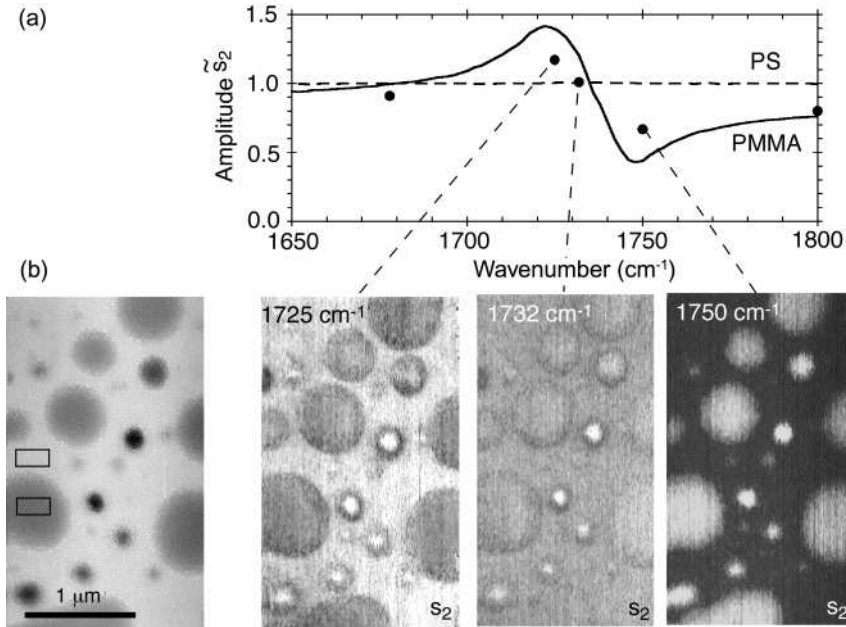
Figure 15.8 s-SNOM analysis of polystyrene (PS) in a PMMA matrix. (a) Calculated s-SNOM amplitude spectra of PMMA (solid line) and of PS (dashed line); (b) Topography (left) and IR amplitude (right) s-SNOM images of a 70 nm-thick polymer blend film on Si at three different wavenumbers, as indicated in (a). The extracted IR contrast of PMMA relative to PS obtained by averaging in the regions indicated in the topography is shown as experimental data points in (a). Adapted from Ref. [56].

frequency s-SNOM images with a lateral resolution of ≤10 nm [59] in block copolymer blend samples of poly(styrene-*b*-2-vinylpyridene) and poly(styrene-*b*-ethyleneoxide).When probed at 3.39 μm (2950 cm⁻¹), individual domains of the two polymers could be distinguished, based on the degree of resonance of their C—H stretching vibration with the excitation wavelength. Images with a size of $300 \times 300 \, nm^2$ were collected within 1–2 h, and spatial resolutions down to 8 nm were found.

The IR s-SNOM approach can also be applied to other materials. For example, Keilmann and coworkers have shown examples ranging from SiC partially covered with Au [33] to metal/Si/polymer three-component samples [60] and even subsurface imaging in such three-component systems [61].

An approach to full spectroscopic near-field imaging in the IR range was presented by Michaels *et al.* [62], whose illumination-mode a-SNOM set-up was based on a Ti:sapphire-pumped optical parametric amplifier (OPA) coupled into a tapered fluoride glass optical fiber. The OPA system provides tunable broadband IR radiation with output powers in the milli Watt range. After passing the thin film sample, the transmitted light is collected by a CaF₂ lens and coupled into a monochromator with a detector array. Broadband illumination with a bandwidth

of 200 cm^{-1} (e.g., 2800–3000 cm^{-1}) in combination with the array detector allows the collection of the IR transmission spectrum of the sample over 200 cm^{-1} within 2 s. For a 2 μm thickness of PS, a good agreement was found between its near-field and the FT-IR reference spectra. The transmission SNOM measurements with subdiffraction resolution is limited to sample thicknesses well below the excitation wavelength. This is because, as the sample thickness increases beyond the near-field regime, the lateral resolution becomes increasingly dominated by diffraction rather than by the dimensions of the aperture. Therefore, for spatially resolved measurements with this set-up, a 300 nm-thick layer of poly(ethyl acrylate) (PEA) with embedded PS domains was used as a sample [63]. The chemical nature of the domains was determined by AFM reference measurements after a hydrolytic etching treatment that is selective for PEA. The spectroscopic imaging of an area of 8 × 8 μm^2 with 50 × 50 pixels and a collection time of 2 s per pixel, was performed within ~1.5 h. From the spectra, images at three characteristic frequencies, where the far-field spectra of the two components show significant differences, were constructed. No clear differences between the images were observed, which indicates that IR absorption is not the major source of contrast in samples with a thickness within the near-field regime, but rather scattering/near-field coupling effects play a significant role. From some pixels with high signal intensity, absorption spectra with a reasonable agreement with the reference spectrum of PS could be derived. This transmission mode a-SNOM approach with broadband excitation represents an interesting step towards real spectroscopic near-field imaging in the IR range, but is currently limited to thin film samples with subwavelength thickness. Moreover, the contrast mechanisms are not fully understood.

15.3.4
Biological Applications – I: IR a-SNOM of Fibroblasts

In IR a-SNOM experiments of biological samples, free-electron lasers (FELs) have often been employed due to their wide tunability and high output power in the IR range. Due to the need for an electron accelerator with an appropriate shielding, as well as the size and costs of such systems, FELs are available only at very few research centers, usually associated with particle accelerators. Hong *et al.* presented an interesting approach to near-field IR imaging in liquids [64], where FEL radiation was coupled into the chalcogenide fiber of an illumination-mode SNOM, while the tapered end of the fiber was placed in the near-field of a sample coated onto a CaF$_2$ window, which was scanned using piezoelectric transducers. The transmitted signal was detected using optics below the CaF$_2$ window. Several advantages become apparent when both the sample and tip are in water. First, because of the small distance between fiber tip and sample, the IR spectral range is accessible; this would otherwise be obscured by strong water absorption in conventional far-field IR microscopy. Second, metal coating of the tip to prevent the leaking of IR radiation was not necessary, due to the strong IR absorption by the surrounding water. Third, high laser powers can be coupled into the fiber probe because of the dramatically increased damage threshold due to water cooling

of the tip. With this set-up, living fibroblast cells were imaged in water at several characteristic IR wavelengths, such as 6.06 μm (Amide I), 6.45 μm (Amide II) and 5.76 μm (C=O stretching band characteristic for lipids), and significant chemical contrast was demonstrated (Figure 15.9).

As the size of the aperture is defined by the IR absorption of water, the lateral resolution clearly depends on the wavelength, with the best results obtained in regions of the spectrum where water absorbs strongly. The authors reported that, with such an approach, a resolution in the range of 10 nm or λ/600 is within reach. On the other hand, images taken at different wavelengths cannot be directly compared due to the wavelength-dependent lateral resolution. In addition, aperture transmission-mode arrangements are limited to sample thicknesses below the excitation wavelength, because the high-resolution information from the aperture

(a)

(b)
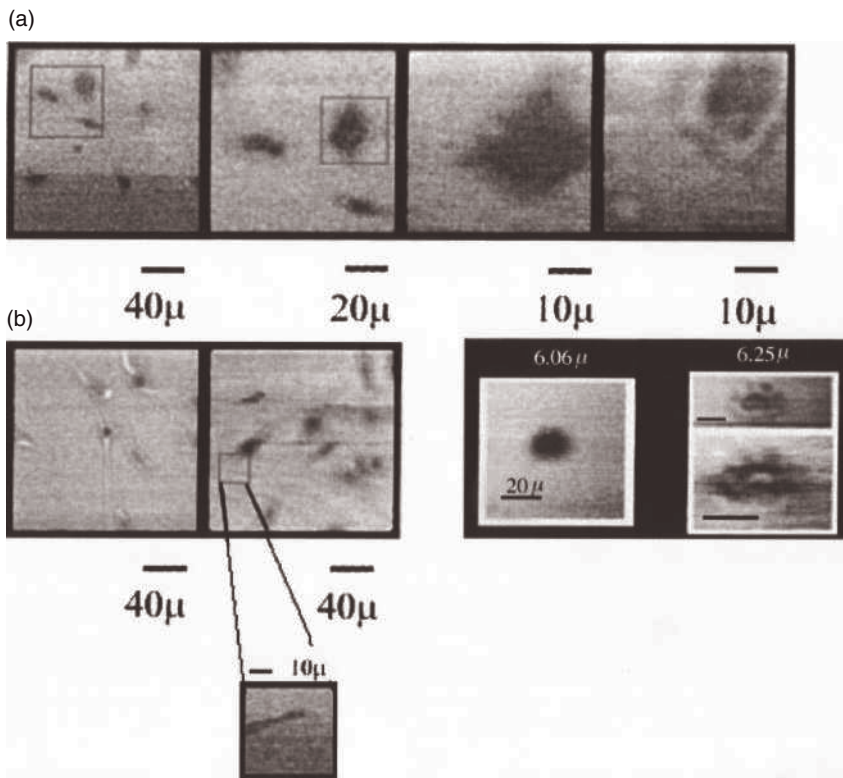
Figure 15.9 IR a-SNOM of fibroblasts. (a) Fibroblast cells imaged in water by IR a-SNOM at different wavelengths and different magnifications. The first three images were obtained at 6.06 μm (amide I), whereas the image at the right shows the different chemical contrast that was obtained at 6.25 μm; (b) Left: Fibroblast cells imaged at 6.06 μm and 6.45 μm (Amide II). The high-resolution scan at the bottom shows a surprisingly high chemical contrast of a lamellopodium imaged at 5.76 μm (C=O band assigned to lipids). Right: Images of single human hybridoma cells obtained at 6.06 μm (Amide I) and 6.25 μm, respectively. Reprinted with permission from Ref. [64].

point source vanishes with increasing sample thickness, due to diffraction. Cricenti *et al.* presented near-field IR images of partially dried cell samples that were collected in reflection by a collection-mode SNOM set-up in air using unfocused FEL radiation for excitation [65]. The group obtained images with a lateral resolution of 0.1 μm or λ/70, and a chemical contrast that could be explained by absorption bands of the cell material and components of the buffer/nutrient solution.

15.3.5
Biological Applications – II: DNA

The apertureless s-SNOM IR imaging of biopolymer samples was demonstrated by Akhremichev *et al.* [66], who prepared 5 μm-wide monolayer stripes of 24 base pairs-long DNA and hexadecanethiol on Au-coated glass surfaces and performed s-SNOM measurements. With this approach, IR images with a lateral resolution of ~200 nm were obtained that showed a clear chemical contrast based on the phosphate absorption band of DNA at 980 cm^{-1}. The stripe pattern revealed by IR contrast was not observable in the topography images.

Tip-enhanced coherent anti-Stokes Raman scattering (TE-CARS) for near-field Raman imaging of DNA samples has been performed [67]. CARS is based on a nonlinear effect, whereby two laser pulses with a constant pump frequency ω_1 and a tunable Stokes frequency ω_2 (with $\omega_1 > \omega_2$) are synchronized at the sample and generate an anti-Stokes field at $\omega_{as} = 2\omega_1 - \omega_2$; this corresponds to the Raman signal at $\omega_R = \omega_1 - \omega_2$. The advantages of CARS are the enhancement of anti-Stokes signals, the confinement of the volume probed to the center of the laser focus due to the nonlinear effect, and the absence of any fluorescence background, which is often present in biological samples. Figure 15.10 shows TE-CARS images of a dried DNA network; this system was prepared by spin-coating a solution of an alternating copolymer of 2′-deoxyribosyladenine and 2′-deoxyribosylthymine (poly(dA-dT)) onto a glass slide and drying at room temperature.

The AFM topography image revealed a network consisting of single DNA strands as well as bundles of up to 10 DNA molecules (Figure 15.10a). TE-CARS measurements were performed with an Ag-coated tip in contact with the sample, irradiated using an inverted microscope set-up by means of a high-NA objective. Images collected at the resonant frequency $\omega_R = 1337$ cm^{-1} corresponding to the ring breathing mode of the purine ring of adenine and at an off-resonant frequency 1278 cm^{-1}, are shown in Figures 15.10b and c, respectively. The on-resonant image differs clearly from the corresponding off-resonant image, which can also be seen in the line profiles in Figure 15.10d. Thus, the on-resonant image is based on a spectroscopic contrast, which allows the imaging of adenine-containing parts of the DNA sample. The active volume in these TE-CARS experiments was estimated to have a diameter of 20 nm and a height of 2.5 nm, which corresponds to ~1 zl. Determination of the SNR led to a smallest detectable DNA volume of ~0.25 zl. Thus, TE-CARS is a powerful tool for spectroscopically resolved imaging of biopolymer networks in their native state at the nanometer scale, and provides vibrational spectral information from a subzeptoliter volume.
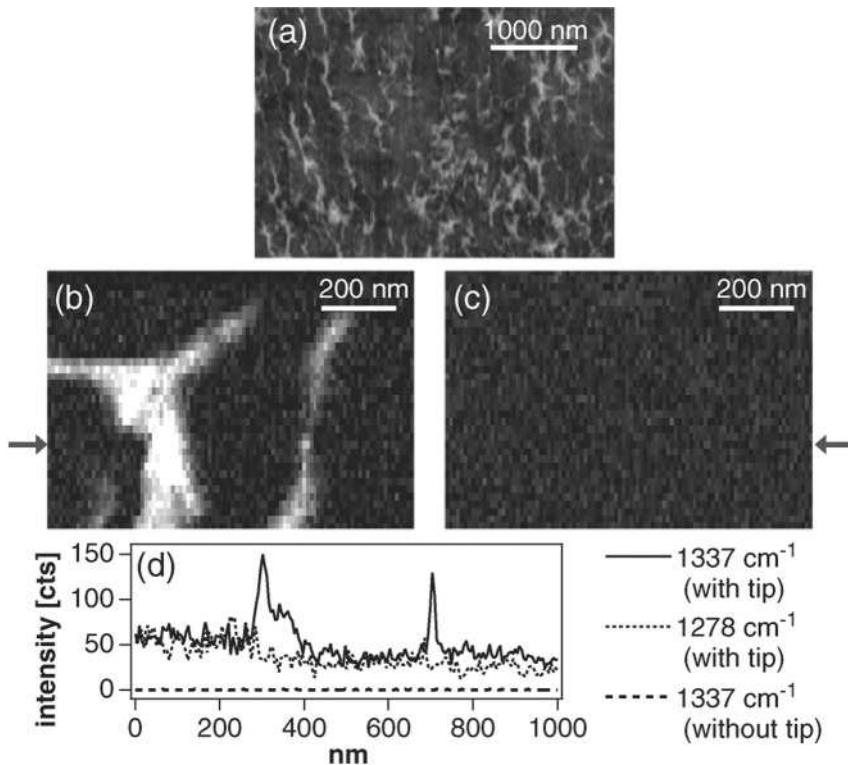
Figure 15.10 TE-CARS imaging of the DNA network. (a) Topographic AFM image; (b) TE-CARS image at on-resonant frequency of adenine (1337 cm^{-1}); (c) TE-CARS image at off-resonant frequency (1278 cm^{-1}); (d) Cross-sections along the line indicated by the arrows. Reprinted with permission from Ref. [67].

15.3.6
Biological Applications – III: AFMIR of Escherichia coli

Dazzi *et al.* have presented a new approach to apertureless s-SNOM in the IR range, which is based on photoacoustic spectroscopy [68]. In their set-up, the sample is coated onto a ZnSe prism and irradiated through the prism by IR pulses from a FEL or CO$_2$ laser. If the IR wavelength matches an absorption band of the sample, the absorbed energy leads to local heating and thermal expansion of the sample. The pressure waves generated by this effect are detected by an AFM tip/cantilever that is in contact with the opposite side of the sample. The signals are detected in the form of oscillations of the feedback signal, which decay within hundreds of microseconds and the amplitudes of which depend on the IR absorption of the sample at the excitation wavelength. This technique (termed AFMIR)

was applied to the imaging of *Escherichia coli* cells [69]. First, spectra at single spots on one cell were collected and compared to the FT-IR reference spectra of bulk samples. The two types of spectra showed good resemblance and were dominated by bands assignable to proteins (amide I, amide II and amide III) and DNA, which is a proof for the spectroscopic information obtainable with AFMIR. In a further step, imaging was performed at two on-resonant frequencies $1650\,cm^{-1}$ (amide I) and $1550\,cm^{-1}$ (amide II), as well as at an off-resonant frequency ($1800\,cm^{-1}$). The data from resonant signals showed good resemblance with the corresponding topography measurements, whereas at the off-resonance frequency, no contrast was obtained, indicating a clear chemical contrast in AFMIR imaging (Figure 15.11). Inhomogeneities inside the image of the bacterium were mainly attributed to the inhomogeneous illumination of the sample. The smallest details in the AFMIR images had a size of ~100 nm, corresponding to a lateral resolution of ~λ/60.

This combination of near-field imaging with the photoacoustic effect is very promising: if the time delay between the laser pulse and signal detection is
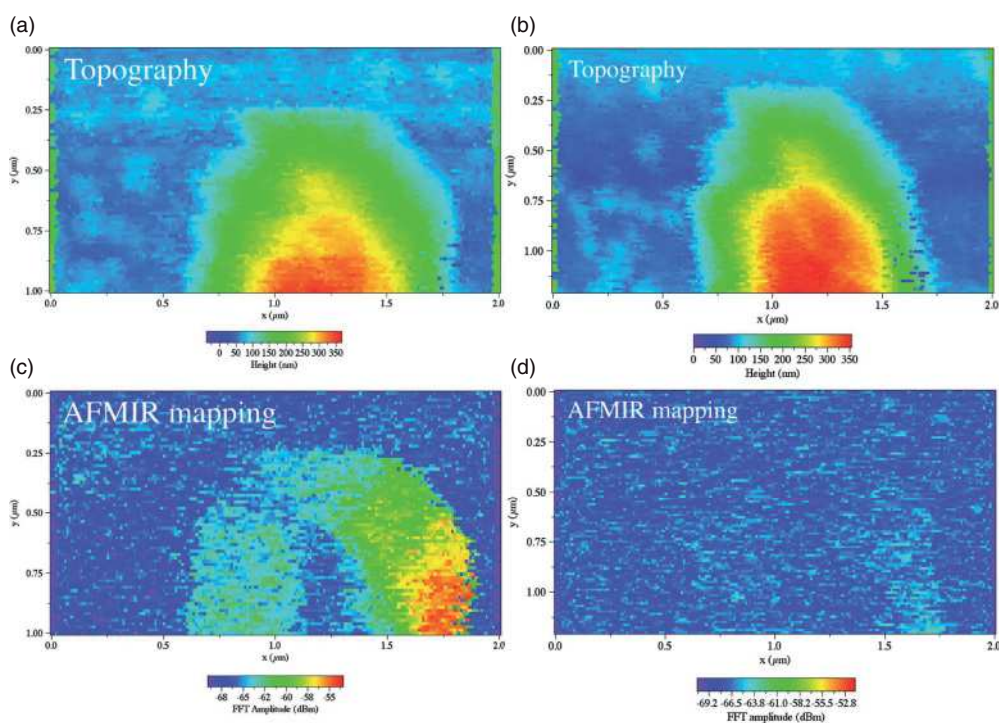
Figure 15.11 (a, b) AFM topography and (c, d) corresponding AFMIR images of an *E. coli* cell. The AFMIR images were collected at the Amide I band ($1650\,cm^{-1}$, left) and at an off-resonant frequency ($1800\,cm^{-1}$, right). Reprinted with permission from Ref. [69].

additionally analyzed, then depth-resolved investigations could be performed. On the other hand, AFMIR is far from being a tool for the imaging of nanometer-sized objects. As mentioned above, inhomogeneities found inside the micrometer-sized bacterium were attributed to the uneven distribution of the IR radiation, and were not due to real subcellular structures. The good agreement between AFMIR spectra and FT-IR bulk measurements is also an argument against the possibility of detecting nanoinhomogeneities by AFMIR. It is not clear which volume fraction of the sample is represented by the AFMIR spectra; this is mainly due to acoustic effects, which complicate the data interpretation. The laterally resolved information is only preserved if plane acoustic waves are generated inside the sample and detected by the AFM tip. If other acoustic waveforms are generated – for example, in small absorbing objects that are point sources of spherical acoustic waves – then the acoustic energy will propagate both perpendicularly to the substrate and in lateral directions, which blurs the lateral resolution. In other words, AFMIR is complicated by the fact that the tip has to be within both, the optical and the acoustic near-field of the sample. These issues must be solved before AFMIR can be used as a tool for nanometer-scale IR imaging.

15.3.7
Biological Applications – IV: Towards Full Spectroscopic Imaging

The techniques discussed in Sections 15.3.4–15.3.6 (including TE-CARS) were used to image samples at single wavelengths/frequencies. Such techniques can only be applied to biopolymer samples with known composition and known marker bands in the spectrum, or for the intensity mapping of well-known bands representing the most important chemical fractions in biological systems, such as proteins and lipids. A more detailed understanding of highly inhomogeneous biological systems consisting of a variety of chemical compounds is only possible on the basis of full spectra collection at every pixel. The most promising techniques for spectroscopic imaging of biological samples are near-field Raman spectroscopies, because they provide the whole spectrum at every pixel without the need of tuning the laser. Among these techniques, Raman a-SNOM is disadvantaged by its low sensitivity, which is insufficient to detect biomolecules with low Raman cross-sections. TERS provides enhanced spectra from a well-defined volume of the sample, which is the near-field under the tip, typically a few tens of nanometers, both laterally and in depth.

To date, the only a-SNOM Raman imaging experiments with biological material were conducted on dye-labeled samples, because of the low Raman scattering cross-section of the biomolecules alone [70]. 18-mer oligonucleotides were labeled with brilliant cresyl blue dye (BCB) and coated onto a SERS substrate consisting of Ag-coated Teflon nanospheres on a glass substrate. With an illumination-mode SNOM set-up, near-field Raman spectra were collected on 20×20 points over an area of $2 \times 2 \, \mu m^2$. The 488 nm excitation led to a partial resonance enhancement, because this wavelength is close to the rising edge of the BCB absorption band. With a collection time of 1 min per pixel, the experiment took ~6 h to complete.

From the data obtained, images representing BCB band intensities (at $1524\,cm^{-1}$ and $1655\,cm^{-1}$), as well as the intensity of the glass band at $800\,cm^{-1}$, were derived which showed a high similarity between the two BCB images, and significant differences between BCB and glass images; this was proof of the chemical nature of the contrast obtained. These study results demonstrated the potential of real spectroscopic imaging. A high-BCB signal at one pixel can originate from two causes that cannot be distinguished in single-frequency experiments: a high concentration of BCB-labeled DNA or a high reflectivity/surface enhancement at this spot. In these studies, the glass band intensity was used as a measure for the latter, and the BCB spectra were normalized using this band. Images representing the BCB-DNA distribution on the sample, with a lateral resolution of ~100 nm, were then constructed as shown in Figure 15.12.
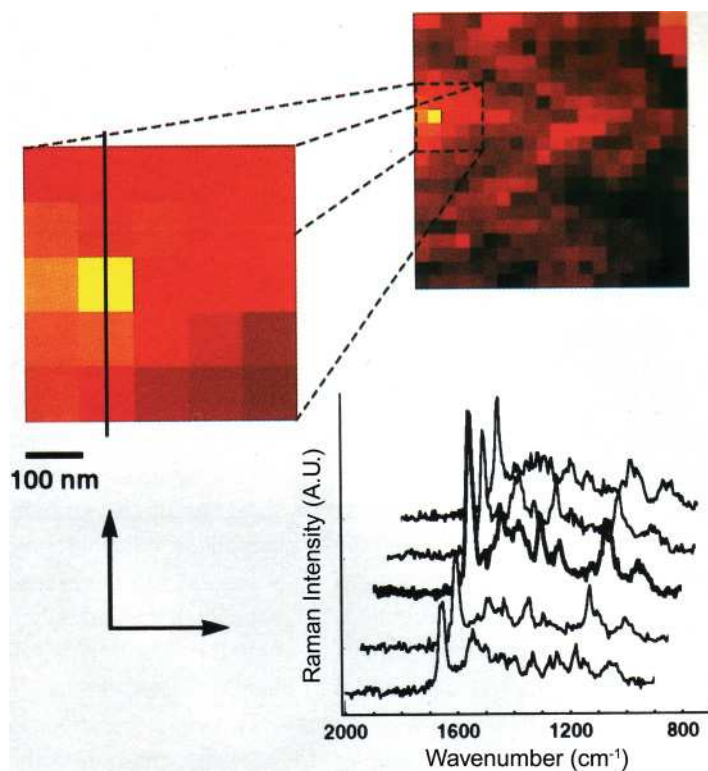
Figure 15.12 Higher-magnification of a corrected (see text) a-SNOM Raman image of BCB-labeled DNA based on the BCB band intensity at $1655\,cm^{-1}$ and full spectra collected along the line profile indicated in the magnified image. Whereas, the intensity of the glass band at ~$1100\,cm^{-1}$ remains constant, the BCB band intensities (e.g., at $1655\,cm^{-1}$) change, depending on the position. Adapted from Ref. [70].

A number of TER point spectroscopy experiments have been conducted to probe the contents of the cell wall of Staphylococcus epidermidis [71, 72]. The far-field spectra of the intact cell contain mainly proteins signals, while the TERS showed bands that were assigned to N-acetylglucosamine (NAG), a constituent of the biopolymer cell surface. Probing the cell at different times also reveals spectral fluctuations; this observation has been attributed to the detection of dynamic processes occurring at the cell surface. When TERS was also performed on pure NAG, some of the observed vibrational bands resembled those detected on the cell surface. However, the bands (from TERS of NAG) appeared very different from the Raman spectrum of the pure compound as reported in the literature, and no justifications were given [73]. Chemical enhancement/tip pressure/selection rules might cause band shifting, but such effects are not easily derived from the data. Further investigations are required to verify the identity of the bands.

In contrast to dye molecules or CNTs, biomolecules are often weak Raman scatterers, and consequently background fluorescence, as well as Raman signals of amorphous carbon and other contaminants present in the sample or on the tip surface, can significantly affect the TER spectra (see Section 15.4.3). In the interpretation of TER spectra, these artifacts can be ruled out by demonstrating a resemblance between TERS data and reference spectra of the bulk material, or by numerical simulations. Highly reproducible, sharp Raman bands are evidence against carbon contamination signals, because the latter will fluctuate randomly in intensity and frequency, and usually average out to two broad bands centered at ~1360 cm^{-1} and 1590 cm^{-1} when spectra with long acquisition times (>10 s) are collected [74]. In order to interpret the TER spectra, reference materials for bulk measurements must be selected very carefully. The group of Kawata has shown that, in some cases, direct chemical interactions between the binding sites of a molecule (e.g., lone-pairs of nitrogen atoms or certain functional groups) and the metal surface of the tip can cause band shifts of a few tens of wavenumbers, and can even lead to the appearance of new bands that are not visible in the bulk spectrum of the pure analyte molecule [75, 76]. For example, adenine can interact with the Ag surface of a TERS tip via each of its four nitrogen atoms. Numerical simulations of the four corresponding isomers of the adenine–Ag complex resulted in spectra with good resemblance to the TERS data. The interpretation of TER spectra of biopolymers is additionally complicated by inhomogeneities in chain length, molecular mass and sequence, as well as by the high number of functional groups and other potential binding sites for the metal surface of the tip. These are currently open questions that will have to be addressed by the investigation of pure biopolymer compounds and comparison of their TER spectra with normal Raman, SER and Ag or Au colloid-enhanced Raman spectra. TERS is only useful as a nanoscale chemical analytical technique for biological structures if differences between the TER and bulk spectra can be satisfactorily explained by chemical interactions with the metal surface or tip pressure effects, and if other influences such as carbon contaminations can be ruled out.

15.4
Current Challenges

Although a number of difficulties still hamper the development of TERS, overcoming these will surely lead to TERS maturing into a technology for robust nanochemical analysis. Some of these challenges are outlined in the following sections.

15.4.1
Performance of the Tips

A major limitation of any TERS tip is its durability. Besides strongly enhancing the Raman signals of the analytes, an ideal tip should also be mechanically robust so that, even in the event of a tip-to-sample contact, the apex is not destroyed (this is especially important for mineralogy studies). Furthermore, the tip should be chemically inert so that an analysis can be performed over a long period of time. At present, Ag-coated or etched tips become TERS-inactive within one to two days of fabrication and are discarded. Metallic alloys rather than pure Ag or Au (the two metals generally used for TERS tips, as both are relatively soft) should be considered as alternative materials for TERS tips. Theoretical studies on such materials could guide the search for higher-quality 'hot' tips.

15.4.2
TERS Signal Modulation by Surface Roughness

Artifacts in gap-mode TERS imaging have been found to occur due to local roughness of the metal substrate [77]. By scanning an etched Ag tip across a benzenethiol monolayer adsorbed onto a rough Au surface, and recording both the topology of the substrate and the TERS signals, it has been found that small local morphological features of 2 nm can modulate the signal intensity by more than 10-fold (Figure 15.13).

The roughness can also induce an offset between the TERS map and the corresponding topography image. This occurs when the enhanced field is asymmetrically distributed with respect to the tip axis instead of being directly below it. The offset may be tens of nanometers, and larger than the resolution of the gap-mode experiment. Hence, in order to obtain reliable data a planar substrate without steep edges – that is, a corrugation <1 nm – is necessary. This is a true 'catch 22' situation, since it is known from surface science studies that catalytic activity on surfaces usually occurs at steps, edges, and so on. However, if nanoscale corrugations of the surface can induce an offset, then reliable information on the true nature of these sites would be elusive. On the other hand, research studies have shown that sharp edges on a metal surface could be exploited as near-ideal sites to form nano gaps for very high field enhancement and single-molecule detection [77].
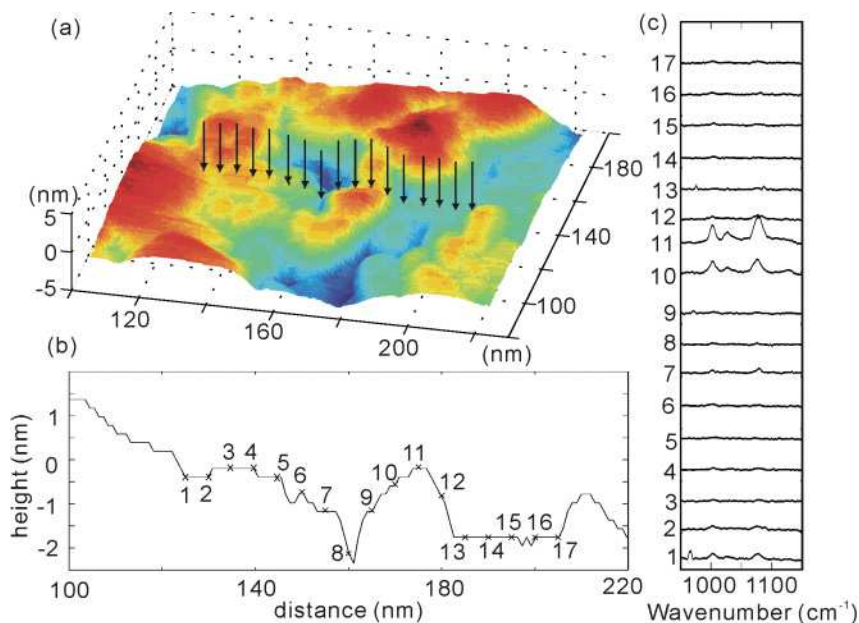
Figure 15.13 TERS mapping on a rough Au surface, demonstrating changes in spectra intensity as a function of surface morphology. An STM image of the sample is shown in (a); TERS data were collected at the positions indicated by the arrows. The cross-section of the topography image is shown in (b), where the TERS collection sites are labeled with crosses; (c) The corresponding TERS sequence. The numbers denote the sites where the spectra were collected. Adapted from Ref. [77].

15.4.3
Tip Contamination, Analyte Dissociation and 'Blinking'

One unsolved problem in TERS is that of carbon contamination signals arising from the dissociation of analyte molecules and/or from pre-adsorbed contamination on the tip [78]. These signals often fluctuate, and could even be mistaken as signatures of single molecules, in analogy to single-molecule fluorescence spectroscopy [79, 80]. However, the bands in blinking spectra are often at completely different Raman frequencies compared to bands of the bulk molecules. Verification of the identity of these TERS bands may be made by comparing them with the far-field bulk spectra. Assuming that adsorption onto the metal surface does not significantly perturb the chemical bonds of the analyte, these TER spectra should show a resemblance to the far-field Raman data. This has been demonstrated by two independent single-molecule studies on malachite green and BCB adsorbed, respectively, onto smooth Au surfaces [29, 30].

The dissociation of an analyte may also be induced by the high local electromagnetic field intensity, and presumably also from the associated temperature rise

[78]. In experiments, a compromise between a high intensity of the incident laser power and a short data collection time must be found. Robust analytes are able to tolerate greater heating, while fragile molecules (e.g., dyes with high absorption cross-sections) will be more prone to thermal or field-induced dissociation. Finally, the high temperatures created in nano gaps may also lead to thermal annealing and morphology changes of the Ag surface and the tip, along with dissociation of the analyte. All of these phenomena may lead to an irreversible signal loss during the analysis.

15.5
Summary and Outlook

In this chapter, we have reviewed the current state of the art in near-field optical technologies for spectroscopic imaging, and applications to CNTs, semiconductors, polymer-based nanomaterials and biological samples. A general observation is that full spectroscopic imaging has only been realized in a handful of studies, with most publications focusing on point spectroscopy or single-frequency imaging. Consequently, a very large potential for development in this area still exists.

Far-field Raman imaging using confocal microscopy is gradually becoming a standard technique, with several instruments now available commercially that possess true spectroscopic imaging capabilities. The spatial resolution is of course diffraction-limited, and the collection time can be somewhat long, because the incident laser power must be limited in order to avoid photodecomposition of the sample. But, compared to Raman – and especially to IR imaging – TERS has a significantly better spatial resolution; the spectral acquisition times are also shorter due to enhancement from the tip. With the first commercial TERS instruments becoming available only six to seven years after the method was developed, currently important technical areas include the long-term stability and low drift of the scanning unit, the efficient collection of the Raman scattered light, and the integration of the controls for the SPM and optical systems into a single unit. Sensitive CCD cameras are now also available that allow shorter spectral acquisition times to be realized.

In the past, TERS has not often achieved high sensitivity in terms of detection, and its application to many 'real-world' samples is still far from routine. However, the technique has shown vast improvements over the past few years as a result of better tips, and single-molecule sensibility has been achieved. This detection capability surpasses the sensitivity of most other analytical methods, including IR spectroscopy. Clearly, with a better theoretical understanding of the various field-enhancement mechanisms exhibited by TERS, routine procedures with 'very hot' tips can be expected in the near future.

Today, both TERS and TERS imaging are utilized and being developed by many groups, ranging from basic studies such as adsorption onto single crystal metal surfaces, to materials science and biological applications, such as the stretching

of DNA or polypeptide chains on very flat substrates for 'sequencing'. Most encouragingly, the most recent studies have incorporated new-generation TERS optical set-ups with parabolic mirrors that focus into an ultra-high vacuum chamber, thus providing access to nanoscale investigations of catalytic processes under highly controlled conditions [81]. It is predicted that chemical and biological applications, in particular, will stimulate the development of near-field spectroscopic imaging even further. Perhaps most importantly, because TERS is not affected adversely by the presence of water in a sample, it may become applicable to a host of *in situ* applications where IR imaging would be impossible.

Acknowledgments

References

1 Synge, E. (1928) *Philos. Mag.*, **6**, 356–62.

2 Pohl, D.W., Denk, W. and Lanz, M. (1984) *Appl. Phys. Lett.*, **44**, 651.

3 Lewis, A., Isaacson, M., Harootunian, A. and Muray, A. (1984) *Ultramicroscopy*, **13**, 227–31.

4 Betzig, E. and Trautman, J.K. (1992) *Science*, **257**, 189–95.

5 Hess, H.F., Betzig, E., Harris, T.D., Pfeiffer, L.N. and West, K.W. (1994) *Science*, **264**, 1740–5.

6 DeAro, J.A., Weston, K.D. and Buratto, S.K. (1999) *Phase Transitions*, **68**, 27–57.

7 Anderson, M.S. (2000) *Appl. Phys. Lett.*, **76**, 3130–2.

8 Stöckle, R.M., Suh, Y.D., Deckert, V. and Zenobi, R. (2000) *Chem. Phys. Lett.*, **318**, 131–6.

9 Knoll, B. and Keilmann, F. (1999) *Nature*, **399**, 134–7.

10 Novotny, L., Bian, R.X. and Xie, X.S. (1997) *Phys. Rev. Lett.*, **79**, 645–8.

11 Novotny, L., Sanchez, E.J. and Xie, X.S. (1998) *Ultramicroscopy*, **71**, 21–9.

12 Zayats, A.V. (1999) *Opt. Commun.*, **161**, 156–62.

13 Nie, S.M. and Emory, R. (1997) *Science*, **275**, 1102–6.

14 Kneipp, K., Wang, Y., Kneipp, H., Perelman, L.T., Itzkan, I., Dasari, R. and Feld, M.S. (1997) *Phys. Rev. Lett.*, **78**, 1667–70.

15 Sanchez, E.J., Novotny, L. and Xie, X.S. (1999) *Phys. Rev. Lett.*, **82**, 4014–17.

16 Hayazawa, N., Inouye, Y., Sekkat, Z. and Kawata, S. (2000) *Opt. Commun.*, **183**, 333–6.

17 Yeo, B.S., Schmid, T., Zhang, W.H. and Zenobi, R. (2007) *Anal. Bioanal. Chem.*, **387**, 2655–62.

18 Yeo, B.S., Zhang, W., Vannier, C. and Zenobi, R. (2006) *Appl. Spectrosc.*, **60**, 1142–7.

19 Cui, X., Zhang, W., Yeo, B.S., Zenobi, R., Hafner, C. and Erni, D. (2007) *Opt. Express*, **15**, 8309–16.

20 Xu, H.X., Aizpurua, J., Kall, M. and Apell, P. (2000) *Phys. Rev. E*, **62**, 4318–24.

21 Hartschuh, A., Qian, H., Meixner, A.J., Anderson, N. and Novotny, L. (2005) *Nano Lett.*, **5**, 2310–13.

22 Anderson, N., Hartschuh, A., Cronin, S. and Novotny, L. (2005) *J. Am. Chem. Soc.*, **127**, 2533–7.

23 Anderson, N., Hartschuh, A. and Novotny, L. (2007) *Nano Lett.*, **7**, 577–82.

24 Anderson, N., Anger, P., Hartschuh, A. and Novotny, L. (2006) *Nano Lett.*, **6**, 744–9.

25 Hartschuh, A., Sanchez, E.J., Xie, X.S. and Novotny, L. (2003) *Phys. Rev. Lett.*, **90**, 095503.

26 Downes, A., Salter, D. and Elfick, A. (2006) *Opt. Express*, **14**, 11324–9.

27 Pettinger, B., Ren, B., Picardi, G., Schuster, R. and Ertl, G. (2004) *Phys. Rev. Lett*, **92**, 096101.

28 Ren, B., Picardi, G. and Pettinger, B. (2004) *Rev. Sci. Instrum.*, **75**, 837–41.

29 Zhang, W.H., Yeo, B.S., Schmid, T. and Zenobi, R. (2007) *J. Phys. Chem. C*, **111**, 1733–8.

30 Domke, K.F., Zhang, D. and Pettinger, B. (2006) *J. Am. Chem. Soc.*, **128**, 14721–7.

31 Neacsu, C.C., Dreyer, J., Behr, N. and Raschke, M.B. (2006) *Phys. Rev. B.*, **73**, 193406.

32 Novotny, L. and Stranick, S.J. (2006) *Annu. Rev. Phys. Chem.*, **57**, 303–31.

33 Hillenbrand, R., Taubner, T. and Keilmann, F. (2002) *Nature*, **418**, 159–62.

34 Hillenbrand, R. and Keilmann, F. (2000) *Phys. Rev. Lett.*, **85**, 3029–32.

35 Hillenbrand, R., Keilmann, F., Hanarp, P., Sutherland, D.S. and Aizpurua, J. (2003) *Appl. Phys. Lett.*, **83**, 368–70.

36 Hillenbrand, R. and Keilmann, F. (2002) *Appl. Phys. Lett.*, **80**, 25–7.

37 Sun, W.X. and Shen, Z.X. (2001) *Mater. Phys. Mech.*, **4**, 17–21.

38 Sun, W.X. and Shen, Z.X. (2003) *J. Raman Spectrosc.*, **34**, 668–76.

39 Sun, W.X. and Shen, Z.X. (2003) *Ultramicroscopy*, **94**, 237–44.

40 Sun, W.X., Shen, Z.X., Cheong, F.C., Yu, G.Y., Lim, K.Y. and Lin, J.Y. (2002) *Rev. Sci. Instrum.*, **73**, 2942–7.

41 Poborchii, V., Tada, T. and Kanayama, T. (2005) *Jpn. J. Appl. Phys.*, **44**, L202–4.

42 Lee, N., Hartschuh, R.D., Mehtani, D., Kisliuk, A., Maguire, J.F., Green, M., Foster, M.D. and Sokolov, A.P. (2007) *J. Raman Spectrosc.*, **38**, 789–96.

43 Mehtani, D., Lee, N., Hartschuh, R.D., Kisliuk, A., Foster, M.D., Sokolov, A.P. and Maguire, J.F. (2005) *J. Raman Spectrosc.*, **36**, 1068–75.

44 Georgi, C., Hecker, M. and Zschech, E. (2007) *Appl. Phys. Lett.*, **90**, 171102.

45 Georgi, C., Hecker, M. and Zschech, E. (2007) *J. Appl. Phys.*, **101**, 123104.

46 Zhu, L., Georgi, C., Hecker, M., Rinderknecht, J., Mai, A., Ritz, Y. and Zschech, E. (2007) *J. Appl. Phys.*, **101**, 104305.

47 Lahrech, A., Bachelot, R., Gleyzes, P. and Boccara, A.C. (1997) *Appl. Phys. Lett.*, **71**, 575–7.

48 Knoll, B. and Keilmann, F. (2000) *Appl. Phys. Lett.*, **77**, 3980–2.

49 Samson, J.S., Wollny, G., Brundermann, E., Bergner, A., Hecker, A., Schwaab, G., Wieck, A.D. and Havenith, M. (2006) *Phys. Chem. Chem. Phys.*, **8**, 753–8.

50 Dragnea, B., Preusser, J., Szarko, J.M., Leone, S.R. and Hinsberg, W.D. (2001) *J. Vac. Sci. Technol. B*, **19**, 142–52.

51 McDonough, L.A., Dragnea, B., Preusser, J., Leone, S.R. and Hinsberg, W.D. (2003) *J. Phys. Chem. B*, **107**, 4951–4.

52 Zerda, T.W., Song, G., and Waddell, W.H. (2003) Proceedings Spring ACS Rubber Division Meeting, 76, pp. 769–78.

53 Keilmann, F. (2002) *Vib. Spectrosc.*, **29**, 109–14.

54 Keilmann, F. (2004) *J. Electron. Microsc.*, **53**, 187–92.

55 Keilmann, F. and Hillenbrand, R. (2004) *Philos. Trans. R. Soc. A*, **362**, 787–805.

56 Taubner, T., Hillenbrand, R. and Keilmann, F. (2004) *Appl. Phys. Lett.*, **85**, 5064–6.

57 Akhremitchev, B.B., Pollack, S. and Walker, G.C. (2001) *Langmuir*, **17**, 2774–81.

58 Akhremitchev, B.B., Bemis, J.E., Al-Maawali, S., Sun, Y.J., Stebounova, L. and Walker, G.C. (2003) *Biofouling*, **19**, 99–104.

59 Raschke, M.B., Molina, L., Elsaesser, T., Kim, D.H., Knoll, W. and Hinrichs, K. (2005) *Chem. Phys. Chem.*, **6**, 2197–203.

60 Taubner, T., Hillenbrand, R. and Keilmann, F. (2003) *J. Microsc.*, **210**, 311–14.

61 Taubner, T., Keilmann, F. and Hillenbrand, R. (2005) *Opt. Express*, **13**, 8893–9.

62 Michaels, C.A., Stranick, S.J., Richter, L.J. and Cavanagh, R.R. (2000) *J. Appl. Phys.*, **88**, 4832–9.

63 Michaels, C.A., Gu, X.H., Chase, D.B. and Stranick, S.J. (2004) *Appl. Spectrosc.*, **58**, 257–63.

64 Hong, M.K., Jeung, A.G., Dokholyan, N.V., Smith, T.I., Schwettman, H.A., Huie, P. and Erramilli, S. (1998) *Nucl. Instrum. Methods Phys. Res. B*, **144**, 246–55.

65 Cricenti, A., Generosi, R., Luce, M., Perfetti, P., Margaritondo, G., Talley, D., Sanghera, J.S., Aggarwal, I.D., Tolk, N.H., Congiu-Castellano, A., Rizzo, M.A. and Piston, D.W. (2003) *Biophys. J.*, **85**, 2705–10.

66 Akhremitchev, B.B., Sun, Y.J., Stebounova, L. and Walker, G.C. (2002) *Langmuir*, **18**, 5325–8.

67 Ichimura, T., Hayazawa, N., Hashimoto, M., Inouye, Y. and Kawata, S. (2004) *Phys. Rev. Lett.*, **92**, 220801.

68 Dazzi, A., Prazeres, R., Glotin, E. and Ortega, J.M. (2005) *Opt. Lett.*, **30**, 2388–90.

69 Dazzi, A., Prazeres, R., Glotin, F. and Ortega, J.M. (2006) *Infrared Phys. Technol.*, **49**, 113–21.

70 Deckert, V., Zeisel, D., Zenobi, R. and Vo-Dinh, T. (1998) *Anal. Chem.*, **70**, 2646–50.

71 Neugebauer, U., Rosch, P., Schmitt, M., Popp, J., Julien, C., Rasmussen, A., Budich, C. and Deckert, V. (2006) *Chem. Phys. Chem.*, **7**, 1428–30.

72 Neugebauer, U., Schmid, U., Baumann, K., Ziebuhr, W., Kozitskaya, S., Deckert, V., Schmitt, M. and Popp, J. (2007) *Chem. Phys. Chem.*, **8**, 124–37.

73 She, C.Y. and Tu, A.T. (1974) *Biochim. Biophys. Acta*, **372**, 345–57.

74 Kudelski, A. and Pettinger, B. (2000) *Chem. Phys. Lett.*, **321**, 356–62.

75 Watanabe, H., Ishida, Y., Hayazawa, N., Inouye, Y. and Kawata, S. (2004) *Phys. Rev. B.*, **69**, 155418.

76 Hayazawa, N., Watanabe, H., Saito, Y. and Kawata, S. (2006) *J. Chem. Phys.*, **125**, 244706.

77 Zhang, W.H., Cui, X.D., Yeo, B.S., Schmid, T., Hafner, C. and Zenobi, R. (2007) *Nano Lett.*, **7**, 1401–5.

78 Domke, K.F., Zhang, D. and Pettinger, B. (2007) *J. Phys. Chem. C*, **111**, 8611–16.

79 Domke, K.F. and Pettinger, B. (2007) *Phy. Rev. B.*, **75**, 236401.

80 Neacsu, C.C., Dreyer, J., Behr, N. and Raschke, M.B. (2007) *Phys. Rev. B.*, **75**, 236402.

81 Steidtner, J. and Pettinger, B. (2007) *Rev. Sci. Instrum.*, **78**, 103104.

Index